VERÖFFENTLICHUNGEN

des Grundbauinstitutes
der Technischen Universität Berlin

Herausgegeben von S.A. Savidis

HEFT 62

An Arbitrary Lagrangian-Eulerian Method for Penetration into Sand at Finite Deformation

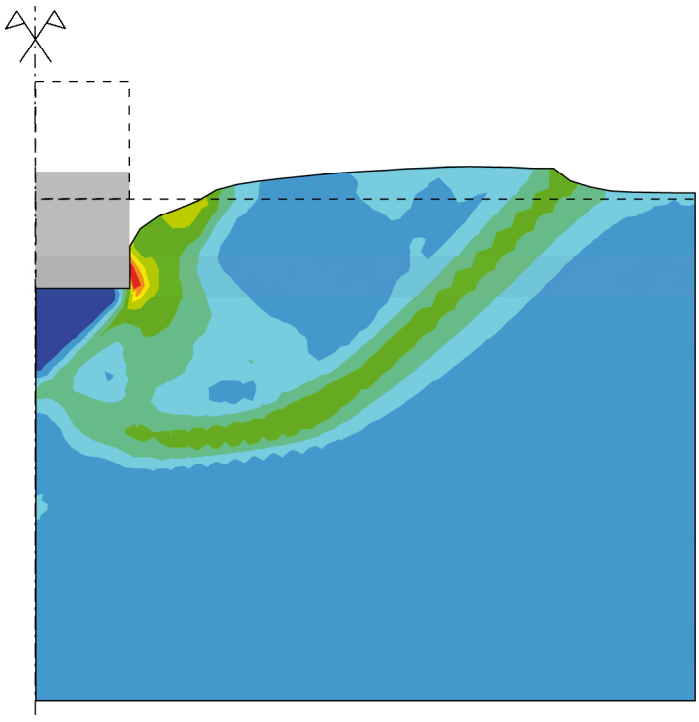

Daniel Aubram

Berlin 2013

Bibliographic information published by the Deutsche Nationalbibliothek
The Deutsche Nationalbibliothek lists this publication in the Deutsche Nationalbibliografie; detailed bibliographic data are available in the internet at http://dnb.d-nb.de.

Zugl.: Berlin, Techn. Univ., Diss., 2013

Adresse des Instituts:

Fachgebiet Grundbau und Bodenmechanik - Degebo
Technische Universität Berlin
Sekr. TIB1-B7
Gustav-Meyer-Allee 25
13355 Berlin

Telefon: (030) 314-72341
Telefax: (030) 314-72343
E-Mail: info@grundbau.tu-berlin.de
Internet: http://www.grundbau.tu-berlin.de

Das Titelbild ist eine Stilisierung der Abbildung auf S. 226.

Printed in Germany.

ISBN 978-3-8440-2507-1
ISSN 0342-3905

Shaker Verlag GmbH • P.O. BOX 101818 • D-52018 Aachen
Phone: 0049/2407/9596-0 • Telefax: 0049/2407/9596-9
Internet: www.shaker.de • e-mail: info@shaker.de

An Arbitrary Lagrangian-Eulerian Method for Penetration into Sand at Finite Deformation

vorgelegt von
Dipl.-Ing. Daniel Aubram
aus Berlin

Von der Fakultät VI – Planen Bauen Umwelt
Technische Universität Berlin
zur Erlangung des akademischen Grades

Doktor der Ingenieurwissenschaften
– Dr.-Ing. –

genehmigte Dissertation

Gutachter:	Univ.-Prof. Dr.-Ing. habil. Stavros A. Savidis
	Univ.-Prof. Dr.-Ing. habil. Dr. h.c. mult. Peter Wriggers
	Prof. Dr.-Ing. Frank Rackwitz
Vorsitzender:	Univ.-Prof. Dr.-Ing. habil. Yuri Petryna

Tag der wissenschaftlichen Aussprache: 12. Dezember 2013

Berlin 2013
D 83

(This page intentionally left blank)

Preface by the Editor

The design of foundations and geotechnical structures and the prediction of their deformation and mechanical response based on numerical simulations require detailed knowledge of the local state of the soil as well as sufficiently realistic models for the nonlinear soil behavior. This is particularly true for sand whose behavior depends among others on the stress state, density state, and loading history. The local state is a result of loading history, hence the construction processes of structural elements must generally be taken into account. Common numerical models in geotechnical engineering, however, consider the construction process as a simplified staged construction by assuming an initial state of the soil and taking the structural elements as wished-in-place. The research work reported here is a step towards more realistic modeling.

The present work submitted by Daniel Aubram is concerned with the penetration into sand as a typical geotechnical process and its numerical simulation by using the finite element method (FEM). Apart from the highly nonlinear mechanical behavior of sand and the presence of non-stationary material interfaces this challenging problem is characterized by large local material deformations for which the classical Lagrangian and Eulerian approaches are inapplicable. In this work a new arbitrary Lagrangian-Eulerian (ALE) method is developed and implemented in which the material and mesh deformations are uncoupled. Its unique features are an advanced hypoplastic rate constitutive equation for sand and an efficient and robust optimization-based algorithm to ensure a quality FE mesh during the entire calculation. The method is validated by results from the literature and specifically conducted experimental model tests.

This thesis addresses a wide range of topics of continuum mechanics, soil mechanics, and computational mechanics. Daniel Aubram has acquired advanced knowledge of all these fields during his comprehensive research work. Finally, he achieved both unusual depth and coherence of his thesis by means of a modern mathematical language and consistent notation. Most of the background needed is in the main text or can be found in the noteworthy appendix. Beyond that, Daniel Aubram has set up the necessary computer code and supervised the experimental program.

Parts of this research work have been carried out under the financial support from the German Research Foundation (DFG) through grants SA 310/21-1 and SA 310/21-2 which is gratefully acknowledged.

Stavros A. Savidis
Berlin, December 2013

Preface by the Author

The work presented in this thesis was carried out between 2006 and 2011 when I was a research associate at the Chair of Soil Mechanics and Geotechnical Engineering at the Technische Universität Berlin.

I would like to express my deepest gratitude to my advisor and principal reviewer Prof. Dr.-Ing. Stavros A. Savidis for giving me the opportunity to work on this interesting topic and for the freedom to develop and implement my own ideas while continuously guiding and supporting me during all stages of my research work. Moreover, I thank Prof. Savidis for his encouragement and support in presenting the results of my research work on several national and international conferences. I am also indebted to Prof. Dr.-Ing. Peter Wriggers from Leibniz Universität Hannover for his interest in my work and preparing the second review of my thesis. Being a well-known expert in the field of computational mechanics he enriched the area of research addressed by this work and its interdisciplinary aspects. I am grateful to my former colleague at TU Berlin and third reviewer Prof. Dr.-Ing. Frank Rackwitz from Ostbayerische Technische Hochschule Regensburg for several fruitful discussions and helpful suggestions. In addition, I wish to acknowledge Prof. Dr.-Ing. Yuri Petryna for his feedback and taking the chair of the doctoral committee.

I would like to thank my former and present colleagues at the Chair of Soil Mechanics and Geotechnical Engineering at TU Berlin for the very pleasant working atmosphere. Many of them were always willing to discuss ideas and to answer questions, first of all Dipl.-Ing. Winfried Schepers, Dr.-Ing. H. Ercan Taşan, Dipl.-Ing. Ralf Glasenapp, and Dipl.-Ing. Marcel Ney. Moreover, I thank the technical staff of our geotechnical laboratory, especially Mr. Rüdiger von König and Mr. Harald Lorenz, for helping to realize the experimental model tests. Preliminary work for the experimental part of this thesis was carried out at the institute by several undergraduate students within the scope of their final theses, which is also gratefully acknowledged.

Finally, I am deeply grateful to my family for unconditionally supporting me during my whole life, especially my parents Bärbel and Stefan Aubram. Above all, I thank my wife Janine for her constant patience and support in successfully finishing this thesis and for being a loving mother to our son Konstantin.

Daniel Aubram
Berlin, December 2013

Abstract

The penetration into sand is one of the most challenging problems in soil mechanics and its numerical simulation, particularly by the widely-used finite element method (FEM), still poses a great challenge. In order to overcome the problems associated with the classical Lagrangian and Eulerian formulations of FEM, an arbitrary Lagrangian-Eulerian (ALE) method particularly suitable for plane and axisymmetric penetration into sand is developed in this thesis based upon the theoretical foundations.

The developed ALE method applies an operator-split which breaks up solution of the governing equations over a time step into a Lagrangian step, a mesh regularization step, and a transport step. The operator-split makes implementation into existing Lagrangian FE codes possible, which is shown using the example of ANSYS. A unique feature of the ALE method is its combination with an advanced hypoplastic rate constitutive equation for sand which enables realistic prediction of stress and density changes within the soil even at large deformations. In addition, an optimization-based algorithm for mesh regularization is developed in order to smooth out the non-convexly distorted mesh regions that occur below a penetrator. The ALE method is verified and validated by benchmarks, basic initial boundary value problems, and by specifically conducted penetration tests in chambers filled with sand.

Keywords: arbitrary Lagrangian-Eulerian; large deformations; finite element method; penetration; pile; sand; soil mechanics; continuum mechanics; computational mechanics; geotechnical engineering

Zusammenfassung

Die Penetration in Sand zählt zu den kompliziertesten Problemstellungen in der Bodenmechanik, und ihre numerische Simulation insbesondere mit der weit verbreiteten Finite Elemente Methode (FEM) stellt bis heute eine große Herausforderung dar. Um die Probleme im Zusammenhang mit den klassischen Lagrange und Euler Formulierungen der FEM zu überwinden, wird in der vorliegenden Arbeit eine allgemeine Lagrange-Euler (engl.: arbitrary Lagrangian-Eulerian, kurz: ALE) Methode aus den theoretischen Grundlagen heraus speziell für die ebene und axialsymmetrische Penetration in Sand entwickelt.

Die entwickelte ALE Methode basiert auf einer Operator-Spaltung, welche die Lösung der maßgeblichen Gleichungen über ein Zeitinkrement aufteilt in einen Lagrange Schritt, einen Schritt der Netzregularisierung und einen Transportschritt. Die Operator-Spaltung gestattet die Implementierung in bestehende Lagrange FE Programmsysteme, was am Beispiel von ANSYS erläutert wird. Ein Alleinstellungsmerkmal der ALE Methode ist ihre Kombination mit einem hochentwickelten hypoplastischen Materialmodell für Sand, das wirklichkeitsnahe Prognosen der Spannungs- und Dichteänderungen im Boden auch bei großen Verformungen ermöglicht. Ein optimierungsbasierter Algorithmus zur Netzregularisierung wird darüber hinaus entwickelt, um die unterhalb eines Eindringkörpers auftretenden nicht-konvex verzerrten Netzregionen zu glätten. Die ALE Methode wird anhand von Benchmarks, grundlegenden Anfangsrandwertproblemen und eigens durchgeführten Eindringversuchen in sandbefüllten Versuchskammern verifiziert und validiert.

Schlagworte: Arbitrary Lagrangian-Eulerian; große Verformungen; Finite Elemente Methode; Penetration; Pfahl; Sand; Bodenmechanik; Kontinuumsmechanik; Numerische Mechanik; Geotechnik

To my family

(This page intentionally left blank)

Contents

List of Figures

List of Tables

List of Algorithms

Notation

General Conventions

Calligraphic ($\mathcal{M}, \mathcal{N}, \ldots$)	sets, vector spaces, and manifolds
Italic lightface ($a, b, A, B, \ldots$)	points, scalars, scalar-valued functions, vector- and tensor components, coordinates, coordinate indices, labels, and general functions
Greek lightface ($\alpha, \beta, \Phi, \Psi \ldots$)	point mappings, coordinates, and coordinate indices
Boldface ($\boldsymbol{v}, \boldsymbol{\alpha}, \boldsymbol{A}, \boldsymbol{\mathfrak{T}}, \boldsymbol{c}, \ldots$)	linear maps, vectors, tensors, linear forms, differential forms, and tensor-valued functions
Sans serif (usermat, ...)	program subroutine names

Vector and tensor components with respect to some coordinate system use the same kernel symbol in lightface. Italics is also used for theorems, propositions, and terminology just defined. The Halmos symbol ■ indicates the end of a proof, ♢ indicates the end of a definition, and △ indicates the end of a remark. Equations, definitions, theorems, and propositions are consecutively numbered by using the same counter for all these environments.

Index of Symbols

Latin Letters

a	edge length
a	hypoplastic response function
$\bar{\boldsymbol{a}}$	static acceleration field
$\boldsymbol{a}$	fourth-order material tangent tensor
A	area measure
A_j	area measure of $\mathcal{A}_j$
A	generic material state variable (material description)
$\boldsymbol{A}$	material acceleration
$\mathcal{A}_j$	cross-sectional area of control volume

$\mathfrak{A}(\mathcal{M})$	atlas of a manifold $\mathcal{M}$
$\boldsymbol{\mathfrak{A}}$	set of corotated material state variables
b	edge length
b	generic source per unit spatial volume
$\boldsymbol{b}$	left Cauchy-Green tensor field
B	breadth of a foundation
$B(\mathcal{V},\mathcal{W})$	set of all bounded linear operators of $\mathcal{V}$ to $\mathcal{W}$
$\boldsymbol{B}^I_{\mathrm{s}}$	matrix of symmetrized derivatives of interpolation function N^I
$\mathcal{B}$	reference configuration of a material body in the ambient space
$\tilde{\mathcal{B}}$	spatial approximation to the reference configuration of a body
$\mathcal{B}_0$	ball (cluster) of elements associated with node P_0
$\mathfrak{B}$	body manifold
c	edge length
c_{u}	undrained shear strength
$\boldsymbol{c}$	convective velocity field
$\boldsymbol{c}_{j,k}$	averaged convective velocity field on $\Gamma_{j,k}$
C_{c}	contact contributions
C_{c}	curvature of grain size distribution curve
C_{u}	coefficient of non-uniformity
$\boldsymbol{C}$	right Cauchy-Green tensor
$\boldsymbol{C}$	global damping matrix
$\mathcal{C}$	configuration space
$\mathcal{C}$	space of admissible configurations
$\mathcal{C}$	set of all control volumes in a tessellation
$\mathcal{C}'$	set of control volumes in a tessellation affected by mesh motion
Co	Courant number; CFL number
d_{10}, d_{30}, d_{60}	characteristic grain size
d_{50}	mean grain size (characteristic grain size)
d_{im}	image distance; focal length
d_{iso}	equivalent shear strain rate
d_{ob}	object distance
d_{vol}	volumetric strain rate
$\boldsymbol{d}$	descent direction
$\boldsymbol{d}$	spatial (or Eulerian) rate of deformation tensor
$\vec{\boldsymbol{d}}$	direction of spatial rate of deformation
D	diameter of a pile
D_{r}	relative density

$\boldsymbol{D}$	material (or Lagrangian) rate of deformation tensor
$\mathbf{d}\square$	Riemannian volume form on the parent element
$\mathbf{d}(\partial\square)$	Riemannian area form on the parent element
$\mathbf{d}\boldsymbol{a}$	Riemannian area form on the ambient space
$\mathbf{d}\hat{\boldsymbol{a}}$	Riemannian area form on the reference domain
$\mathbf{d}\boldsymbol{A}$	Riemannian area form on the material body
$\mathbf{d}\boldsymbol{v}$	Riemannian volume form on the ambient space
$\mathbf{d}\hat{\boldsymbol{v}}$	Riemannian volume form on the reference domain
$\mathbf{d}\boldsymbol{V}$	Riemannian volume form on the material body
$\partial_{\mathrm{c}}\mathcal{B}$	boundary of the material body with contact constraints
$\partial_{\mathrm{c}}(\varphi_t(\mathcal{B}))$	boundary of the current config. of the body with contact constraints
$\partial_{\mathrm{d}}\mathcal{B}$	boundary of the material body with prescribed displacement
$\partial_{\mathrm{v}}(\varphi_t(\mathcal{B}))$	boundary of the current config. of the body with prescribed velocities
$\partial_{\tau}\mathcal{B}$	boundary of the material body with prescribed traction
$\partial_{\tau}(\varphi_t(\mathcal{B}))$	boundary of the current config. of the body with prescribed traction
e	spatial void ratio
e_{c}	characteristic void ratio (hypoplasticity)
e_{c0}	crit. void ratio at zero pressure (hypoplastic material constant)
e_{d}	characteristic void ratio (hypoplasticity)
e_{d0}	min. void ratio at zero pressure (hypoplastic material constant)
e_{i}	characteristic void ratio (hypoplasticity)
e_{i0}	max. void ratio at zero pressure (hypoplastic material constant)
e_{int}	spatial specific internal energy
$\hat{e}_{\mathrm{int}}$	referential specific internal energy
$\boldsymbol{e}$	spatial logarithmic strain tensor; Hencky strain
$\boldsymbol{e}$	conceptual spatial finite strain tensor
$\boldsymbol{e}_a$	vectors of the spatial canonical basis
E	Young's modulus (material constant)
E_{int}	material specific internal energy
E^{t}	tangent modulus
E^{p}	plastic modulus (material constant)
$\boldsymbol{E}$	Green-Lagrange strain tensor field
$\boldsymbol{E}_A$	vectors of the material canonical basis
f_{b}	hypoplastic barotropy function
f_{d}	hypoplastic pycnotropy function
f_{e}	hypoplastic pycnotropy function
$\boldsymbol{f}$	relative incremental deformation gradient

$\boldsymbol{f}(q)$	flux density of q governed by the spatial velocity
$\boldsymbol{f}^{\text{ext}}, \boldsymbol{f}_g^{\text{ext}}$	global applied external nodal force vector
$\boldsymbol{f}^{\text{int}}, \boldsymbol{f}_g^{\text{int}}$	global internal nodal force vector
$\hat{\boldsymbol{f}}^{\text{ext}}$	effective load vector
$\mathfrak{f}$	response function for corotated Cauchy stress increment
F	penetration force
F	hypoplastic response function
$F^q_{j,k}$	numerical averaged convective flux density of q (1d: $F^q_{j\pm1/2}$, $F^q_{j,j\pm1}$)
$F^V_{j,k}$	averaged convective volume flux density (1d: $F^V_{j\pm1/2}$, $F^V_{j,j\pm1}$)
$\boldsymbol{F}$	deformation gradient
$\boldsymbol{F}_\theta$	tangent of parent element map
$\boldsymbol{F}_\Phi$	relative deformation gradient
$\boldsymbol{F}_\Psi$	referential deformation gradient
$\mathcal{F}(\mathcal{V}_j)$	set of facets of control volume $\mathcal{V}_j$
$\mathfrak{F}$	response function for $F^q_{j,k}$
g	Earth's standard acceleration due to gravity
g_{ij}	coefficients of the spatial metric
g^{ij}	coefficients of the inverse spatial metric
g_{N}	gap function
$\hat{g}_{\alpha\beta}$	coefficients of the referential metric
$\boldsymbol{g}$	metric tensor on the ambient space (spatial metric)
$\boldsymbol{g}_i$	basis vectors
$\boldsymbol{g}^i$	vectors of the dual basis
$\boldsymbol{g}_{\text{T}}$	tangential relative displacement function
G	shear modulus
G_{IJ}	coefficients of the material metric
G^{IJ}	coefficients of the inverse material metric
$\boldsymbol{G}$	metric tensor on the material body (material metric)
$\mathfrak{G}$	grid manifold
$\boldsymbol{\mathfrak{G}}$	corotated spatial metric
h_{s}	granulate hardness (hypoplastic material constant)
$\boldsymbol{h}$	response function for Cauchy stress rate
$\boldsymbol{h}_\alpha$	basis vectors
H	past material history element
$\boldsymbol{H}_w$	Hessian of element objective function w
$\boldsymbol{H}_W$	Hessian of local objective function W
$\mathcal{H}$	set of past material histories

$\mathfrak{H}$	corotated intergranular strain
$\boldsymbol{i}$	second-order identity tensor on the ambient space
$\boldsymbol{i}_\nu$	basis vectors of the image plane
I	local node number
I	image intensity; luminance
I_1, I_2, I_3	principal invariants
I_{search}	image intensity field associated with search patch
I_{test}	image intensity field associated with test patch
$\boldsymbol{I}$	second-order identity tensor on the material body
$\boldsymbol{I}$	identity matrix; identity map
$\boldsymbol{I}^\varphi$	second-order identity two-point tensor over a map φ
$\mathcal{I}$	image
$\mathbf{1}$	fourth-order symmetric identity tensor; symmetrizer
id	identity map
$\boldsymbol{j}$	response function for intergranular strain rate (hypoplasticity)
$\boldsymbol{j}_\alpha$	basis vectors of the camera space
$\boldsymbol{j}_3$	optical axis
J	Jacobian of the motion φ_t
J_2	negative second principal invariant of the Cauchy stress deviator
J_θ	Jacobian of the parent element map θ_t
J_Φ	Jacobian of the relative motion Φ_t
J_Ψ	Jacobian of the referential motion Ψ_t
$\hat{J}$	referential picture of Jacobian J
K	bulk modulus; modulus of compression
K_0	coefficient of earth-pressure at-rest
$\boldsymbol{K}$	global stiffness matrix
$\boldsymbol{K}_e^{\text{geo}}$	geometric element stiffness matrix
$\boldsymbol{K}_e^{\text{mat}}$	material element stiffness matrix
$\hat{\boldsymbol{K}}$	effective stiffness matrix
$\boldsymbol{l}$	spatial velocity gradient
$\bar{\boldsymbol{l}}$	hypoelastic response function
$L_{j,k}$	length measure of $\mathcal{L}_{j,k}$
$\boldsymbol{L}$	hypoelastic material tangent tensor
$\mathcal{L}_{j,k}$	control volume facet in the pseudo-Cartesian plane
m_{R}	stiffness factor (hypoplastic material constant)
m_{T}	stiffness factor (hypoplastic material constant)
$\boldsymbol{m}$	fourth-order material tangent tensor

M	magnification
$\boldsymbol{M}, \boldsymbol{M}_g$	(consistent) global mass matrix
$\mathcal{M}$	model for the material body
$\mathcal{M}$	mesh
$\mathfrak{M}$	material manifold
n	spatial porosity
n	hypoplastic material constant
n_{bnd}	number of sub-boundaries
n_{cv}	number of control volumes
n_{dim}	number of dimensions
n_{nd}	number of nodes of an element
n_{Q}	number of element quadrature points (Gauss points)
$\boldsymbol{n}_{j,k}$	averaged outward normal field on $\Gamma_{j,k}$
$\boldsymbol{n}^*$	outward normals related to the ambient space
$\bar{\boldsymbol{n}}$	nonlinear hypoplastic response function
$\hat{\boldsymbol{n}}^*$	outward normals related to the reference domain
$\boldsymbol{n}^*$	outward normals on the parent element boundary
N	material specific entropy per unit mass
N	function for cross correlation normalization (PIV)
N_{c}	cone factor
N^I	interpolation function (shape function, ansatz function) for node I
$\boldsymbol{N}$	nonlinear hypoplastic response function
$\boldsymbol{N}$	matrix of interpolation functions
$\boldsymbol{N}^*$	outward normals related to the material body
$\mathcal{N}$	set of all nodes in a mesh
$\mathcal{N}(\mathcal{V}_j)$	set of neighbors of control volume $\mathcal{V}_j$
$\mathcal{N}'$	set of flagged nodes intended for relocation
$\mathcal{N}_\partial$	set of boundary nodes
$\mathcal{N}_{\partial\partial}$	set of corner nodes
$\mathcal{N}_{\mathrm{edg}}$	set of edge nodes
$\mathcal{N}_{\mathrm{int}}$	set of nodes included in the interior of the mesh
$\mathbb{N}$	set of natural numbers
o, O	origin
p	negative mean Cauchy stress
p	projective center of camera aperture (pinhole)
p'	negative mean effective stress
p_{a}	atmospheric pressure at sea level

p_{N}	contact pressure
p_{w}	pore water pressure
P	functional of virtual power
$\boldsymbol{P}$	first Piola-Kirchhoff stress
Pe	Péclet number
q	generic physical field (spatial description)
q	von Mises stress; equivalent shear stress; deviator stress
q	principal point on the image plane $\mathcal{Y}$
$q^{\blacksquare}$	piecewise constant field associated with a storage point
q_{c}	static cone resistance
q_j	discrete average of the field q in a control volume $\mathcal{V}_j$
$q^{\star}_{j,k}$	approximation to the field q at $\Gamma_{j,k}$ (1d: $q^{\star}_{j\pm1/2}$, $q^{\star}_{j,j\pm1}$)
$\dot{q}$	material time derivative of the spatial field q
$\hat{q}$	generic physical field (referential description)
$\hat{q}'$	total time derivative of the referential field $\hat{q}$
$\bar{q}_j$	average of the field q in a control volume $\mathcal{V}_j$
$\boldsymbol{q}$	stress-like internal plastic variables
$\boldsymbol{q}$	spatial heat flux density
Q	generic physical field (material description)
Q	quality measure
$\boldsymbol{Q}$	material heat flux density
r	spatial heat supply per unit mass
r	incircle radius of a simplex
$\boldsymbol{r}$	vector of residuals
R	circumcircle radius of a simplex
R	max. intergranular strain (hypoplastic material constant)
R	cross correlation of I_{test} and I_{search}
R	pseudo-radius
R_j	averaged pseudo-radius associated with $\mathcal{A}_j$
$R_{j,k}$	averaged pseudo-radius associated with $\mathcal{L}_{j,k}$
R_{ref}	reference radius for a simplex
$\bar{R}$	normalized cross correlation of I_{test} and I_{search}
$\boldsymbol{R}$	material rotation tensor field
$\mathcal{R}$	reference domain for the material body
$\tilde{\mathcal{R}}$	spatial approximation to the reference domain for the material body
$\mathfrak{R}$	reference grid for the material body
$\mathfrak{R}$	rotation related to a corotational rate

$\mathbb{R}$	set of real numbers
$\mathbb{R}^m$	m-dimensional real coordinate space; m-dimensional Euclidian space
$\mathbb{R}^m$	set of real $(m \times 1)$- or $(1 \times m)$-matrices; set of rows; set of columns
$\mathbb{R}^{m \times n}$	set of real $(m \times n)$-matrices
s	time; curve parameter
s	semiperimeter of a triangle
$s_{\max}$	PIV search range
$s^1_{\text{peak}}, s^2_{\text{peak}}$	components of the image vector $\boldsymbol{s}$ at the correlation peak
$\boldsymbol{s}$	image vector
S	combined generic source per unit spatial volume
S	minimal boundary distance
$S_{j,k}$	area measure of $\Gamma_{j,k}$
$\hat{S}$	referential picture of combined generic source S
$\boldsymbol{S}$	second Piola-Kirchhoff stress
$\mathfrak{S}$	corotated Cauchy stress
$\mathrm{SE}(\mathcal{M})$	special or proper Euclidian group of a point space $\mathcal{M}$
$\mathrm{SO}(\mathcal{V})$	special or proper orthogonal group of a vector space $\mathcal{V}$
sub	constant for subincrementation
t	time; curve parameter
$\boldsymbol{t}$	Cauchy traction vector field
$T^p_q(\mathcal{M})$	$\binom{p}{q}$-tensor bundle of $\mathcal{M}$
$T_X\mathcal{M}$	tangent space at $X \in \mathcal{M}$
$T^*_X\mathcal{M}$	cotangent space at $X \in \mathcal{M}$; dual space
$T\mathcal{M}$	tangent bundle of a manifold $\mathcal{M}$
$T^*\mathcal{M}$	cotangent bundle of $\mathcal{M}$
$T\mathbb{R}^m$	trivial tangent bundle of $\mathbb{R}^m$
$T\varphi$	tangent of a map φ
$\mathcal{T}$	control volume tessellation
$\mathfrak{T}^p_q(\mathcal{M})$	set of all $\binom{p}{q}$-tensor fields on $\mathcal{M}$
$\mathscr{T}$	topology
$\boldsymbol{u}$	generic source per unit spatial area
$\boldsymbol{u}$	(incremental) spatial displacement
$\boldsymbol{u}_{\text{im}}$	image of (incremental) spatial displacement
$\boldsymbol{U}$	(incremental) material displacement
$\boldsymbol{U}$	right stretch tensor
$\boldsymbol{v}$	spatial velocity field of the material; spatial velocity of φ_t
$\boldsymbol{v}_e$	element nodal velocity vector

$\hat{\boldsymbol{v}}$	referential picture of spatial velocity field $\boldsymbol{v}$
$\dot{\boldsymbol{v}}$	spatial acceleration field
$\dot{\boldsymbol{v}}, \dot{\boldsymbol{v}}_g$	global nodal acceleration vector
V	volume measure
V_j	volume measure of $\mathcal{V}_j$
$\boldsymbol{V}$	material velocity field
$\boldsymbol{V}$	left stretch tensor
$\mathcal{V}'$	representative volume element
$\mathcal{V}_j$	control volume
$\mathcal{V}_t$	space of admissible spatial variations
w	element objective function for mesh smoothing
w_q	weight associated with the q-th quadrature point
$\boldsymbol{w}$	relative velocity field; mesh velocity; spatial velocity of Φ_t
W	local objective function for mesh smoothing
$\mathcal{W}$	space of admissible velocities
x	point in the ambient space; object point
x^i	general coordinates of the ambient space
$\boldsymbol{x}$	position vector of a spatial point
$\boldsymbol{x}_0$	position vector of the vertex of a ball of elements
X	place of a material particle in the reference configuration
X^I	general coordinates of the body in the reference configuration
$\boldsymbol{X}$	position vector of a particle in the reference configuration
y	image point
y_c	centroid of interrogation window (test patch, search patch)
$\mathcal{Y}$	image plane
z	penetration depth; vertical coordinate of the pile tip
z^a	Cartesian coordinates of the ambient space
Z^A	Cartesian coordinates of the body in the reference configuration

Greek Letters

α	generic material state variable (spatial description)
α	hypoplastic material constant
α	donor-cell weighting factor
$\alpha_1, \alpha_2, \alpha_3$	internal angles of a triangle

$\boldsymbol{\alpha}$	set of generic material state variables (spatial description)
β	material chart map
β	problem type specifier (plane: $\beta = 0$, axisymmetric: $\beta = 1$)
β_{r}	hypoplastic material constant
$\gamma_i{}^j{}_k$	coefficients of the connection on the ambient space
$\bar{\boldsymbol{\gamma}}^1_\alpha$	vectors of the covariant basis on a contact surface
$\mathit{\Gamma}(T\mathcal{M})$	set of all vector fields (bundle sections) on $\mathcal{M}$
$\mathit{\Gamma}_{\mathrm{c}}$	(actual) contact surface
$\mathit{\Gamma}_{j,k}$	control volume facet
δ_{ij}	Kronecker delta ($\delta_{ij} = \delta^{ij} = \delta^i{}_j = \delta_i{}^j$)
$\boldsymbol{\delta}$	intergranular strain (hypoplasticity)
$\vec{\boldsymbol{\delta}}$	direction of intergranular strain (hypoplasticity)
Δt	time increment
$\Delta\tilde{\boldsymbol{e}}$	algorithmic finite strain increment; incremental finite strain tensor
$\Delta\mathfrak{E}$	corotated algorithmic finite strain increment
$\Delta\tilde{\boldsymbol{r}}$	algorithmic finite rotation increment
$\Delta\mathfrak{R}$	relative rotation of configurations; incremental rotation
$\Delta\mathfrak{S}$	corotated Cauchy stress increment
ϵ_{N}	penalty parameter associated with the normal direction
ϵ_{T}	penalty parameter associated with the tangential direction
ε	tolerance
ε^{p}	equivalent plastic strain
$\boldsymbol{\varepsilon}$	material logarithmic strain tensor
ζ^ν	image plane coordinates
η	spatial specific entropy per unit mass
$\hat{\eta}$	referential specific entropy per unit mass
$\boldsymbol{\eta}_t$	admissible spatial variation; virtual velocity
θ	spatial absolute temperature
θ_t	parent element map
$\mathit{\Theta}$	material absolute temperature
$\boldsymbol{\vartheta}$	referential velocity field
κ	placement of the material body in space
λ	Lamé constant
λ	step size for line search
λ_{N}	Lagrange multiplier associated with the normal direction
$\boldsymbol{\lambda}_{\mathrm{T}}$	Lagrange multiplier associated with the tangential direction
$\boldsymbol{\mathit{\Lambda}}$	spin tensor

μ	Lamé constant
μ	sliding friction coefficient
μ_t	grid motion
ν	Poisson's ratio (material constant)
ξ_q	natural coordinate associated with the q-th quadrature point
ξ^α	element coordinates; natural coordinates of the parent element
ξ^α	camera space coordinates
π	phase function
π	projection
π	permutation
$\mathit{\Pi}_k$	set of all permutations on a set with k elements
ϱ	referential chart map
ρ	spatial mass density
ρ	normalized magnitude of intergranular strain (hypoplasticity)
ρ'	spatial effective mass density
ρ_d	spatial bulk density
ρ_s	spatial grain mass density
ρ_w	spatial water mass density
ρ_ref	spatial mass density in the reference configuration
$\hat{\rho}$	referential picture of spatial mass density ρ
σ	spatial chart map
σ_0	total overburden stress
σ^y	yield stress in uniaxial tension
$\sigma^{\mathrm{y}0}$	initial yield stress (material constant)
$\boldsymbol{\sigma}$	Cauchy stress
$\boldsymbol{\sigma}'$	effective Cauchy stress
$\tilde{\boldsymbol{\sigma}}$	dimensionless effective stress ratio (hypoplasticity)
$\hat{\boldsymbol{\sigma}}$	referential picture of Cauchy stress $\boldsymbol{\sigma}$
$\mathring{\boldsymbol{\sigma}}$	corotational rate of Cauchy stress
$\mathring{\boldsymbol{\sigma}}^\mathrm{ZJ}$	Zaremba-Jaumann rate of Cauchy stress
$\mathring{\boldsymbol{\sigma}}^\mathrm{GN}$	Green-Naghdi rate of Cauchy stress
ϕ'	angle of internal friction
ϕ_c	friction angle at critical state (hypoplastic material constant)
φ_t	motion of a material body in space
$\mathit{\Phi}_t$	relative motion
χ	reference point
χ	hypoplastic material constant

χ^α	general coordinates of the reference domain
ψ	spatial free energy
$\boldsymbol{\psi}(q)$	convective flux density of q governed by the convective velocity
Ψ	material free energy
Ψ_t	referential motion
$\boldsymbol{\omega}$	spatial vorticity tensor
Ω	finite element; reference configuration of the parent element
$\Omega_\square$	parent element domain
$\Omega^k(\mathcal{M})$	set of all fields of differential k-forms on a manifold $\mathcal{M}$
$\hat{\Omega}$	reference configuration of the parent element (ALE formulation)
$\boldsymbol{\Omega}$	spatial rate of rotation

Subscripts

0	initial value
bnd	boundary
c	centroid
c	critical state
cv	control volume
∂	boundary
$\partial\partial$	corner
dev	deviator of a second-order tensor
dim	dimension
edg	edge
el	element
im	image
int	internal
iso	isochoric
max	maximum
min	minimum
n	associated with time t_n
$n+1$	associated with time t_{n+1}
$n+\theta$	associated with time $t_{n+\theta}$, with $\theta \in [0,1]$
N	normal part with respect to a surface
peak	peak value

sub	subincrementation
T	tangential part with respect to a surface
vol	volumetric
$a, b, \ldots$	spatial coordinate indices
$A, B, \ldots$	material coordinate indices
$\alpha, \beta, \ldots$	referential coordinate indices, and other

Superscripts

$-$	associated with time t_{n+1}^{-} (end of Lagrangian step)
$+$	associated with time t_{n+1}^{+} (end of mesh motion and transport steps)
e	elastic
ep	elasto-plastic
i	associated with iteration step i
$i+1$	associated with iteration step $i+1$
p	plastic
y	yielding
$a, b, \ldots$	spatial coordinate indices
$A, B, \ldots$	material coordinate indices
$\alpha, \beta, \ldots$	referential coordinate indices, and other

Operators and Special Symbols

$\cdot$	contraction of tensors
:	double contraction of tensors
$\pm$	either $+$ or $-$
$\times$	cartesian product; direct product of sets; cross product
$\circ$	composition of maps
$\otimes$	tensor product
$*$	convolution
$\star$	cross-correlation
$\wedge$	exterior product; wedge product

$\bigwedge^k$	k-th exterior power of a tensor bundle
$\subset$	(proper) subset
$\supset$	(proper) superset
$\in$	set membership ("is an element of")
$\cup$, $\bigcup$	union of sets
$\cap$, $\bigcap$	intersection of sets
$\setminus$	set complement; set-theoretic difference
$=$	equality in terms of identity
$\stackrel{\text{def}}{=}$	equality by definition
$\equiv$	equality for all elements in the domain of definition
$(\cdot)_\star$	pushforward by $(\cdot)$
$(\cdot)^\star$	pullback by $(\cdot)$
$(\cdot)^\flat$	index lowering; associate of a tensor $(\cdot)$ with all indices lowered
$(\cdot)^\sharp$	index raising; associate of a tensor $(\cdot)$ with all indices raised
$(\cdot)^{-1}$	inverse of $(\cdot)$
$(\cdot)^{\mathrm{T}}$	transpose of $(\cdot)$
$\dot{(\cdot)}$	material time derivative of $(\cdot)$
$\mathring{(\cdot)}$	corotational rate
$\mathring{(\cdot)}^\star$	generic spatially objective rate
$\mathring{(\cdot)}^{\mathrm{ZJ}}$	Zaremba-Jaumann rate
$\mathring{(\cdot)}^{\mathrm{GN}}$	Green-Naghdi rate
$\langle\cdot\rangle$	spatial average
$\langle\cdot,\cdot\rangle$	inner product
$\lvert\cdot\rvert$	absolute value
$\lVert\cdot\rVert$	norm
$\overrightarrow{PQ}$	vector pointing from P to Q
$\boldsymbol{\nabla}$	connection
$\boldsymbol{\nabla}(\cdot)$	covariant derivative of $(\cdot)$; gradient of $(\cdot)$
$\boldsymbol{\nabla}^{\mathrm{s}}(\cdot)$	symmetrized covariant derivative of $(\cdot)$; symmetrized gradient of $(\cdot)$
$\boldsymbol{\nabla}_{\boldsymbol{v}}(\cdot)$	covariant derivative of $(\cdot)$ along a vector field $\boldsymbol{v}$
$\boldsymbol{\nabla}^\star$	induced connection
$\hat{\boldsymbol{\nabla}}$	connection on the reference domain
$\widetilde{\boldsymbol{\nabla}}$	material gradient operator
$\sqrt{\langle\cdot,\cdot\rangle}$	Euclidian norm
$\triangle$	simplex; triangle element
$\emptyset$	empty set
∞	infinity

$\forall$	universal quantification (“for all”)
alt	alternation mapping
$\arg\max$	argument of the maximum
$\arg\min$	argument of the minimum
cl	closure of a set
cof	cofactor of a regular tensor
d	(total) differential
$\mathbf{d}$	differential; exterior derivative
d	subincrement
d	metric
$d(P,Q)$	distance of the points P, Q
D	Fréchet derivative
det	determinant
dim	dimension
div	divergence; divergence related to the ambient space
Div	divergence related to the reference domain
DIV	divergence related to the material body
$\frac{\mathrm{d}}{\mathrm{d}(\cdot)}$	total derivative with respect to $(\cdot)$
∂	boundary of a set
∂	partial derivative
$\frac{\boldsymbol{\partial}}{\boldsymbol{\partial}(\cdot)}$	vector of a holonomic basis associated with $(\cdot)$
$\exists$	existential quantifier (“there exists”)
$\boldsymbol{H}_f$	Hessian matrix of a real function f
$\boldsymbol{i}_{\boldsymbol{u}}$	interior product in terms of a vector field $\boldsymbol{u}$
int	interior of a set
J_φ	Jacobian of a map φ with respect to certain volume forms
$\mathrm{L}_{\boldsymbol{v}}$	Lie derivative along a vector field $\boldsymbol{v}$
$\pounds_{\boldsymbol{v}}$	autonomous Lie derivative along a vector field $\boldsymbol{v}$
lim	limes
$\mathrm{LIN}_{\boldsymbol{u}}$	linearization about a vector $\boldsymbol{u}$
max	maximum
min	minimum
sgn	sign
tr	trace of a second-order tensor
$\boldsymbol{\Delta}$	increment

Acronyms

ALE	Arbitrary Lagrangian-Eulerian
CEL	Coupled Eulerian-Lagrangian
DOF	Degrees Of Freedom
FDM	Finite Difference Method
FEM	Finite Element Method
FVM	Finite Volume Method
IBVP	Initial Boundary Value Problem
IVP	Initial Value Problem
MMALE	Multi-Material Arbitrary Lagrangian-Eulerian
OSMOT	Optimization-based SMOothing of Triangle meshes
PDE	Partial Differential Equation
PIV	Particle Image Velocimetry
PP	Pile Penetration
RITSS	Remeshing and Interpolation Technique with Small Strain
SALE	Simplified Arbitrary Lagrangian-Eulerian
SP	Shallow Penetration
SOM	Swept Out of Memory

Chapter 1

Introduction

1.1 Motivation and Objectives

The last decades witnessed an increasing interest in the application of computational scientific methods for engineering problems by both academic institutions and industry. The reason is that numerical simulation, now established as a "third pillar" beside theory and experiment, can considerably improve the understanding of the natural processes that take place and may assist in the interpretation of measured data. By numerical simulation using appropriate models, one is able to predict the response of structures and workpieces, and may even replace testings of physical prototypes. The main purpose of this endeavor is to ensure quality products at least costs and resources.

Although the user can choose between various methods for numerical simulation, the *finite element method (FEM)* [e.g. Zienkiewicz and Taylor, 2000a,b,c; Belytschko et al., 2000; Bathe, 1996; Wriggers, 2008] has become the dominating tool in computational mechanics because of its broad applicability and technological sophistication. Surprisingly, soil mechanics and geotechnical engineering were among the first areas of application of the FEM [Zienkiewicz and Cheung, 1964, 1965]. In geotechnical engineering, it is primarily employed to predict soil deformations under earth- and water pressures and the applied loads. These deformations need to be known beforehand since they may have an impact on the serviceability and stability of buildings and infrastructure and may also put a risk on the geotechnical project itself.

Unfortunately, FE models in practice often underestimate deformations. During the realization of large geotechnical projects in urban area, for example the Potsdamer Platz and the Berlin Central Station (Fig. 1.1), it was found that the final deformations of the walls of several deep excavation pits were generally larger than those predicted by the FE simulations. Investigations highlighted that the construction processes, particularly the installation of anchoring piles for the base slab, played an important role [Triantafyllidis, 1998; Savidis and Mittag, 1999]. In these specific cases, however, the FE models used for the numerical simulations did not include the pile installation process. The construction process was modeled as a simplified *staged construction* by

Figure 1.1: View of the construction site of Berlin Central Station on September 1, 1997. Deep excavation pit dewatered after underwater concreting revealing the pile heads of the base slab (center), Lehrter Stadtbahnhof (above), diverted River Spree (middle) – (Photo: Copyright © 2001 Oltmann Reuter, Luftbild Berlin; from [Reuter, 2001, p. 61], picture L 181 recorded on September 1, 1997).

assuming an initial state of the soil and with the readily-installed piles *wished-in-place*. This is a common approach in geotechnical engineering.

The present work is concerned with the numerical simulation of penetration into sand. Penetration, e.g. of piles, is the archetype of geotechnical installation processes —the first types of piles can be dated back to the late Neolithic Age [Kérisel, 1985; Ulitskii, 1995]. Being one of the oldest problems in soil mechanics, it turned out to be also one of the most challenging. Rigorous modeling of penetration problems is very difficult because of the large local deformations in the vicinity of the penetrator, the evolution of material interfaces and free surfaces, the changing contact conditions, the large stiffness variations, the interaction between the grain skeleton and pore fluids, and the complex nonlinear mechanical behavior of the soil material. The co-occurrence of these phenomena makes the classical Lagrangian and Eulerian descriptions of motion in continuum mechanics and their FEM implementation inappropriate (Fig. 1.2).

The Lagrangian form of the governing equation, which is standard in solid mechanics, is in many respects the most attractive formulation for problems where path-dependent material response and evolving interfaces are present. By using the Lagrangian description the finite element mesh follows the material as it deforms, thus providing a natural form of an adaptive solution. However, if material deformations are large then severe element distortion may occur as illustrated in Fig. 1.2. Distorted finite elements are problematic because they may slow down or even terminate the calculation. The generation of a new mesh and the projection of the variables onto the new mesh at some stage in the Lagrangian calculation (so-called *rezoning*) require user intervention, are computationally expensive, and usually introduce excessive numerical diffusion.

In the Eulerian description, which is common in fluid dynamics, the discretized computational domain is fixed in space (Fig. 1.2 below). Since no element distortion occurs the Eulerian methods impose no restrictions on the magnitude of material deformations. Many problems that cannot be addressed by Lagrangian methods will compute with little user intervention when using Eulerian methods. The weakness of a fixed computational mesh, however, is found in following moving interfaces as well as in the proper treatment of complex path-dependent materials. Additional sophisticated techniques for material tracking are required in these cases.

In order to overcome the difficulties arising from the classical approaches, the research objective of the present work is the development and application of an *arbitrary Lagrangian-Eulerian (ALE)* method particularly suitable for the penetration into sand at finite deformation. ALE methods have been originally developed in the 1960-70's at US laboratories [Frank and Lazarus, 1964; Trulio, 1966; Hirt et al., 1974]. Since that time ALE methods have been developed to be a powerful analysis tool for free surface flows, fluid-structure interaction, and large deformation problems in solid mechanics [e.g. Belytschko and Kennedy, 1978; Donea et al., 1981, 1982; Hughes et al., 1981; Huétink, 1982; Liu et al., 1986, 1988; Ramaswamy and Kawahara, 1987; Benson, 1989; Rodríguez-Ferran et al., 1998, 2002]. Applications of ALE to soil mechanical and geotechnical problems are still rare and mostly incorporate simple constitutive equations to model the nonlinear soil behavior [e.g. Susila and Hryciw, 2003; Nazem et al., 2006, 2008; Di et al., 2007; Liyanapathirana, 2009; Sheng et al., 2009].

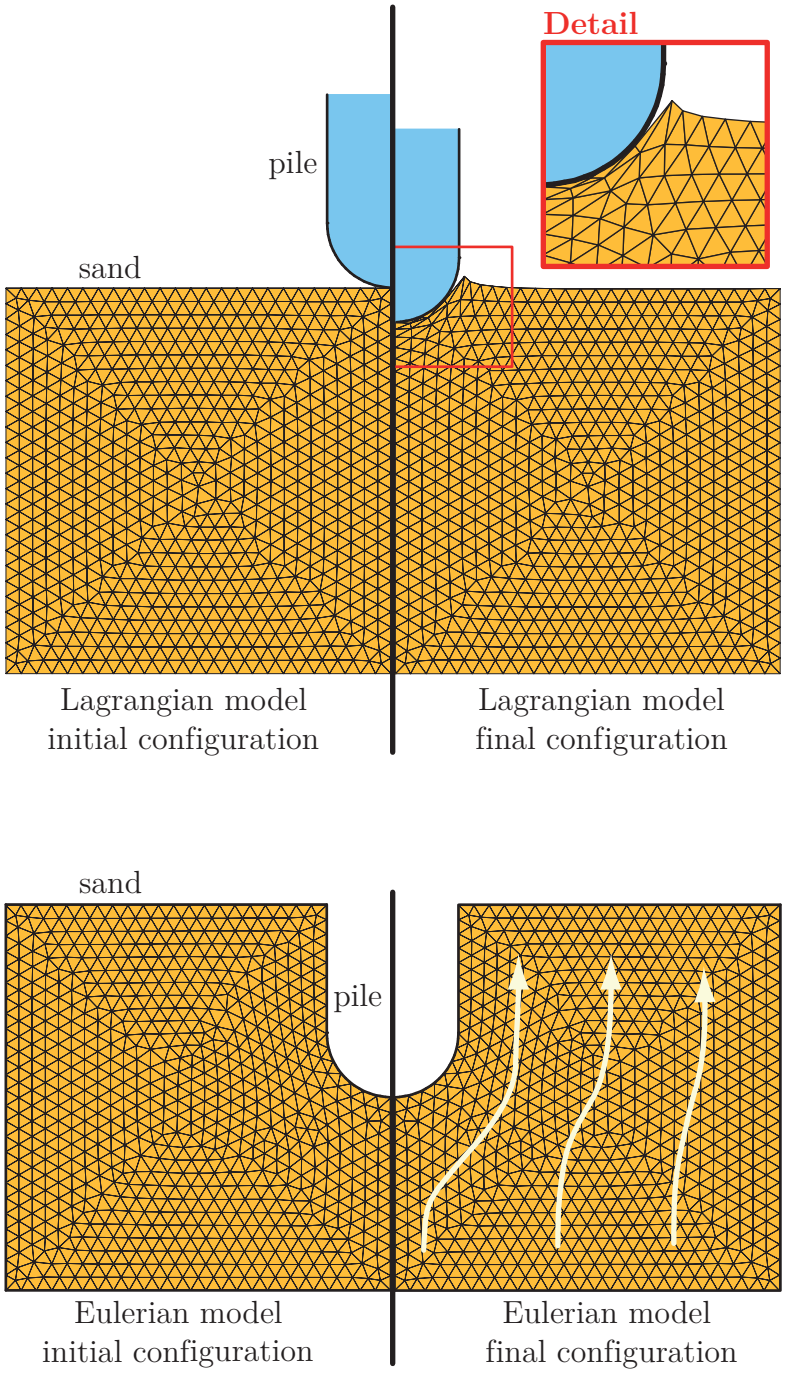

Figure 1.2: Schematic diagram highlighting the differences and drawbacks of the classical Lagrangian (above) and Eulerian (below) methods when applied to the problem of pile penetration into sand.

In ALE methods, the computational mesh is regarded as a reference domain which is not fixed but can move independent of the material at an arbitrary velocity. The ALE description of motion generalizes the purely Lagrangian and purely Eulerian formulations and includes them as special cases. Instead of applying remeshing or mesh refinement algorithms, the ALE mesh is continuously *smoothed* at fixed connectivity such that element distortion is reduced. Since mesh topology is kept unchanged, all elements have the same neighbors during the whole calculation. This permits the application of *advection algorithms* borrowed from the field of computational fluid dynamics (CFD) in order to remap the solution variables onto the improved mesh in a conservative manner.

Most of the references about ALE published are technical papers including engineering applications that prefer spaces as simple as possible. This is because the arbitrary Lagrangian-Eulerian approach has been recognized as a purely numerical tool for a long time. First attempts to a comprehensive treatment of continuum mechanics on arbitrarily moving domains with both linear and nonlinear background spaces have been made recently [Scovazzi and Hughes, 2007; Aubram, 2009]. The present work is intended to continue this activity.

With the objective to provide a sufficiently general and unified presentation of the fundamentals of continuum mechanics in the Lagrangian, Eulerian, and ALE descriptions, a *modern differential geometrical approach* like in [Marsden and Hughes, 1994; Romano and Baretta, 2009; Aubram, 2009] has been found to be compelling. This goes along with the notion of *manifolds* and the relinquishment of the common Euclidian space. Differential geometry [Abraham et al., 1983; Bishop and Goldberg, 1968; Spivak, 1999; Synge and Schild, 1978] is unquestionably the appropriate setting for continuum mechanics and tensor analysis. The mathematical rigor required for this endeavor will also be pursued in other parts of the present work.

Besides the mathematical description and the solution techniques appropriate to handle the geometrical nonlinear nature of the problem, a realistic numerical simulation of penetration into sand also requires the nonlinear soil response to be taken into account. The mechanical behavior of sand, or cohesionless granular material in general, is very complex and has many influencing factors. Dilatancy and the dependency on the mean effective stress are two important characteristics that distinguish sand as a granular solid from other materials. The latter results in a strength tending to zero near the unloaded ground surface, a fact which causes problems in finite element analysis. Sand response does also depend on material history, the degree of saturation, and on drainage conditions. A saturated sand under cyclic loading and undrained conditions may completely loose shear resistance, which is referred to as *liquefaction*, or may show *cyclic mobility* with limited shear deformation. This behavior generally depends on the confining pressure, the loading amplitude, and the initial density.

Just a few constitutive equations for soils need only a single set of material constants and then are able to simulate the mechanical behavior of sand at finite deformation and under complex loading paths over a wide range of densities and stress states. Precisely these conditions, however, are present during penetration processes. The ALE method developed in the present work is combined with an advanced *hypoplastic*

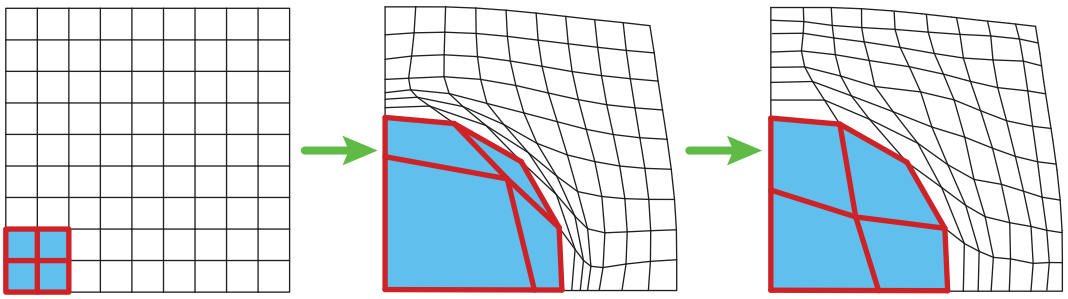

Figure 1.3: Schematic diagram of the operator-split ALE method. The blue area indicates a material zone which is assigned to an element patch highlighted in red.

rate constitutive equation for sand [Gudehus, 1996; von Wolffersdorff, 1996; Niemunis and Herle, 1997] which incorporates the stress state, the void ratio, and a measure for material history as internal state variables. Hypoplasticity has been proven to be a powerful constitutive theory to model soil behavior and has since become widely-used, especially in Germany.

The ALE formulation of governing equations introduces convective terms. This is similar to the Eulerian formulation used in fluid dynamics and entails that material is allowed to flow through the computational mesh. Since material motions are not tracked the incorporation of path-dependent materials, especially those complex materials one has to deal with in soil mechanics, is complicated. Similar problems are encountered for contact conditions. The numerical treatment of the convective terms has a significant influence on the accuracy, stability, and robustness of the ALE method. Instead of solving the monolithic problem including both the sources and the convective terms, an *operator-split* technique [Benson, 1992] is applied in the present work which allows simpler and more robust algorithms. Another advantage grows from the facility to upgrade existing Lagrangian finite element codes; the general purpose commercial code ANSYS® is employed here. Operator-splitting is the proven technology for solid mechanical ALE methods. It divides the solution to the initial boundary value problem into a Lagrangian step and a Eulerian or remap step (Fig. 1.3).

In the Lagrangian step, convective terms are not present because the mesh follows the material motion. The spatially discretized system of governing equations can thus be advanced in time by almost standard *updated Lagrangian (UL)* finite element procedures for solid mechanical problems. The Lagrangian step contains the sources and constitutive equations, and the evolution equations are integrated over the time step by ensuring *incremental objectivity* [Hughes and Winget, 1980; Hughes, 1984; Simo and Hughes, 1998] at large deformation. Density changes must explicitly be accounted for in order to conserve mass with respect to a moving mesh. This means that in contrast to purely Lagrangian FE methods that implicitly conserve mass, ALE methods must update the mass density if the material is compressible or dilatant, like sand.

Physical time elapses only during the Lagrangian step but will be “frozen” in the subsequent remap step. In other words, the remap step constitutes an instantaneous

projection of the variables from the old mesh onto a smoother mesh. The remap step accounts for the convective terms arising from the relative motion between the body and the ALE reference domain, by leaving the material state unchanged. However, the latter is hard to achieve from a numerical viewpoint. Remapping in the operator-split ALE method is further subdivided into a mesh motion step and a transport step.

Mesh motion is defined by nodes relocation that smoothes out the element distortion occurring during the Lagrangian step. The mesh connectivity is retained such that each node in the mesh is shared by the same ball of elements throughout the entire calculation. Since ALE methods frequently relocate the mesh nodes, efficient and stable algorithms for automatic mesh smoothing are preferable. The strategy of material boundary (or interface) consideration in the computational domain imposes further restrictions on the mesh motion scheme and distinguishes two different ALE approaches [cf. Benson, 1992; Mair, 1999; Freßmann and Wriggers, 2007].

Virtually all arbitrary Lagrangian-Eulerian codes for solid mechanical problems and also the one developed in this work is based on the *simplified ALE (SALE)* approach. In SALE methods, the material interfaces are aligned with element edges, thus remain Lagrangian in normal direction (Fig. 1.3). This makes the design of a stable mesh motion scheme a difficult task particularly for the non-convex regions that necessarily occur along with penetration problems. In the *multi-material ALE (MMALE)* approach on the other hand, material interfaces may move through the mesh so that elements may contain two or more materials. Therefore, multi-material elements generally require a discrete material interface model. MMALE methods are far more complex than SALE methods and are beyond the scope of the present work.

The transport step, which is the last step in a calculational cycle of the operator-split ALE method, has more in common with computational fluid dynamics than with solid mechanics. In contrast to many other methods which employ non-conservative interpolative remaps based on the element shape functions the ALE method developed here will be equipped with an *conservative advection scheme* for variable transfer between the Lagrangian and the smoothed mesh. Advection schemes numerically solve hyperbolic conservation laws and often use a *finite volume* discretization. They require calculation of the material flux across element boundaries caused by the mesh motion.

By using the developed ALE method, computational models for penetration into sand can be designed and these models should be validated by experimental tests. However, reports of experimental tests in the literature can rarely be used for this purpose because they generally do not provide a sufficiently detailed description of the properties of the test sand. Therefore, *experimental model tests* are carried out within the scope of this research work in addition to the theoretical and numerical work. Besides the intended validation of the ALE models, these *qualitative* tests should provide more insight into the phenomenology of penetration into sand. The tests are conducted in chambers with observing window and they involve the quasi-static penetration of different model piles and foundations into dry sand at different initial densities. The processes are digitally photographed through the window which enables the application of an image correlation method to analyze the soil motion without on-sample instrumentation. The present work employs a special method based on *particle im-*

age velocimetry (PIV) [Adrian, 1984, 1991, 2005; Pickering and Halliwell, 1984; White, 2002; White et al., 2003; Nübel and Weitbrecht, 2002; Hauser and Walz, 2004].

In this thesis different attempts are made to set up fundamental concepts for the "general case" without any unnecessary assumption or restriction. On the other hand, issues concerning the actual numerical implementation are tried to be kept as simple as possible in order to reach the objectives with reasonable effort. The basic assumption is that of a *continuum representation* for the soil assembly of distinct particles in order to benefit from the highly developed mathematics and concepts of continuum mechanics. A drastic but reasonable simplification then arises from the consideration of sand as a *single-phase medium*, that is to say, the mathematically modeled and numerically treated sand is either dry or fully saturated with water, in which case it is also locally drained. Moreover, only *plane strain* and *axisymmetric* problems are considered in the numerical treatment. The ALE method is designed for *quasi-static* and not for fully transient penetration. The penetrator is assumed to be either *smooth* (zero friction) or *perfectly rough* (no sliding). *3-node triangles with 1-point integration* (constant strain triangles) are used for the spatial discretization.

In summary, the objectives of the present work are:

1. Mathematical formulation and continuum mechanical modeling of the initial boundary value problem of penetration into sand at finite deformation by using the ALE description. Only those problems are considered in which the sand is either dry or fully saturated with water and locally drained.

2. Development and implementation of algorithms for the Lagrangian step, the mesh motion step, and the transport step in the context of an operator-split ALE method for plane strain and axisymmetric quasi-static penetration into sand.

3. Carrying out experimental tests in chambers with observing window concerning the penetration of model piles and foundations into dry sand at different initial densities. The soil velocity and strain fields are indirectly measured using the PIV method.

4. Application of the developed ALE method, verification of the algorithms, and validation of the ALE method by using results of the experimental model tests.

In consideration of the preceding assumptions and restrictions, the method will permit the realistic prediction of the stress and density changes during penetration into sand and other granular material.

1.2 Structure of the Work

Literature related to soil penetration is reviewed in Chapter 2. Both cohesive and cohesionless soils are considered, but the main focus is on penetration into sand. The review is divided into three parts. In the first part, the experimental investigations undertaken to analyze the mechanical soil behavior are examined. Experimental analysis is mostly concerned with soil deformations, stress and density distributions, as well

as with the evolution of the base resistance and shaft friction at the penetrator. The second part of the review is devoted to the semi-empirical and analytical methods that have been developed to deduce soil properties from a penetrating sounding tool or to predict the ultimate bearing capacity of a pile. Most of these methods involve drastic simplification in the mechanical soil behavior, contact or boundary conditions. Numerical models which are reviewed in the last part of Chapter 2 generally do not have these limitations and can handle large deformations, complex material behavior, and changing contact conditions. The present models, however, can only address certain aspects of soil penetration, which is highlighted in the review.

The introduction of the continuum mechanical basis related to the ALE method starts in Chapter 3 with the fundamental equations of kinematics and balance principles. Depending on the choice of the reference domain used for the derivation these can be equivalently set up in either a Lagrangian, a Eulerian or an arbitrary Lagrangian-Eulerian form. Chapter 3 pays attention to all three formulations in order to highlight their differences and interrelations. Concerning the ALE formulation, it has been tried to consolidate fundamental concepts and results which are scattered among the literature on the subject. Differential geometry on manifolds provides the requisite tools for a sufficiently general formulation of the continuum mechanical basis. Because this subject does not belong to the standard repertoire of civil and mechanical engineers, it is briefly introduced in Appendix A. This supplemented material also contains important topics in classical linear geometry.

Chapter 4 deals with the constitutive theory and completes the continuum mechanical part of this work. After providing the fundamentals and general principles those classes of rate constitutive equations are introduced which respect finite deformation theory and dominate in arbitrary Lagrangian-Eulerian computational methods. Another important topic the chapter deals with is the mechanical response of sand under monotonic and cyclic loading and how to mathematically model this. The hypoplastic rate constitutive equation applied in the present work is formulated subsequently. This model —insiders just call it *hypoplasticity with intergranular strain*— has become widely used by the soil mechanics and geotechnical engineering community because it comprehensively describes the behavior of sand and other granular materials. Besides the mathematical formulation of hypoplasticity with intergranular strain and its ALE description in Chapter 4, the determination of material constants is commented and the constants of different granular materials are listed.

The mechanical initial boundary value problem associated with penetration into sand as well as general finite element discretization and solution methods are described in Chapter 5. Ambient space is assumed to be linear from this point on but the geometric point of view is kept up throughout the work as it delivers valuable insight. The focus of the chapter is on the updated Lagrangian (UL) finite element technique commonly applied to solid mechanical large deformation problems. This is due to the fact that the operator-split ALE solution approach adopted in the present work defines a Lagrangian step where the UL finite element technique plays a central role. Chapter 5, moreover, introduces integration algorithms for rate constitutive equations

respecting the constitutive axiom of material frame indifference (or objectivity) at large material deformation on a discrete level.

Chapter 6 is central to the present thesis. It is concerned with the numerical procedures related to the proposed arbitrary Lagrangian-Eulerian method and their numerical implementation. The chapter is divided into six parts. In the first part, the origins of ALE methods are reviewed and the basic monolithic and operator-split ALE approaches are discussed. Part two of the chapter describes the incremental operator-split ALE finite element solution procedure for quasi-static problems which is applied in the present work. The procedure consists of a Lagrangian step, a mesh motion step, and a transport step, each of which is studied in the subsequent third, fourth, and fifth part of Chapter 6, respectively. It is pointed out here that a new optimization-based mesh smoothing algorithm is proposed in part four, which requires computation of the gradient and Hessian matrix of an objective function. This is based on the exact formulas included in Appendix C. Finally, the sixth part of Chapter 6 is devoted to the aspects of numerical implementation and how the coded ALE capabilities have been added to the proprietary ANSYS® simulation software used for the studies.

The experimental model tests conducted during this research are reported in Chapter 7. As introduced previously, these tests were primarily intended to deliver qualitative information about the phenomenology of penetration into sand which is accessible for back-calculation. After some general remarks concerning the conceptual design, the chapter describes the design and construction of the test equipment and the employed instrumentation, and then the experimental program is outlined. The part that follows provides a brief introduction of particle image velocimetry (PIV) and the particular method that has been applied for the indirect measurement of the incremental soil displacement resp. of the soil velocity field. This PIV method has also been used to deduce the volumetric strain rate and the maximum shear strain rate from the velocity field. The test results are discussed in the final part of the chapter.

Chapter 8 presents example applications of the developed ALE method. Two groups of example problems are considered. The first group includes test cases for particular algorithms of the method. Running these test cases enables determination whether the particular algorithm or federation of algorithms is working under specific conditions correctly or not. The second group of numerical examples in Chapter 8 consists of large deformation solid mechanical and soil mechanical problems for which analytical, numerical, or experimental results are available that can be back-calculated. Among these are some of the penetration tests carried out in Chapter 7 as well as example problems from literature. Within the scope of validation of the developed ALE method, then, the available results are compared with respective results obtained through back-calculation by using ALE computational models.

The present work closes with concluding remarks and outlook in Chapter 9.

Chapter 2

Previous Research on Soil Penetration

This chapter reviews the literature related to research on soil penetration, in which the penetrator can be represented by a pile, a sounding tool, or a shallow foundation. The analysis of soil penetration embodies an important topic of research. Nevertheless, early research of soil penetration was content with the development of design methods for already installed piles. A prediction model that yields detailed information about the change in state during penetration particularly of granular soils is yet missing. Because the penetration process is one of the main influencing factors of the axial load capacity of driven and pressed-in (resp. jacked) piles as well as of in-situ cone penetration test data, there is an extensive amount of literature in this field available. This review concentrates on soil mechanical studies, although penetration also plays an important role in other scientific disciplines. Even in respect thereof, the review cannot be exhaustive as it expresses the author's view on the subject. For further studies the interested reader is referred to the bibliographies in the references cited.

The research on soil penetration consists of experimental analysis, semi-empirical and analytical methods, and numerical models. Each of these approaches can provide information only of particular phenomena and not of the entire process. For example, the pile penetration forces in granular materials can be measured with high accuracy in experimental tests but the density distribution in the vicinity of the pile can hardly be determined without disturbance. On the other hand, the use of sophisticated constitutive equations for sand enable high resolution of stress and density fields in a finite element model, but the resulting pile penetration force is strongly influenced by mesh quality and element technology. A realistic and accurate numerical model can thus be obtained only through validation based on experimental tests.

The following sections are self-explanatory. The only background knowledge needed is that a representative volume element filled with soil, called the *soil element*, consists of a partial solid volume and a partial pore volume. The ratio of the partial pore and partial solid volumes is called the *void ratio*. For sand resp. cohesionless granular

soil a *relative density* can be defined which allows to specify whether a soil element is relatively *loose* or *dense*. The formal definitions are given in Section 4.2.1.

2.1 Experimental Analysis

2.1.1 Soil Deformations and Relative Density Distribution

In an early paper, Pogany [1953] reports on experimental small-scale model tests in which model piles were pressed into wet sand-cement mixtures with pigmented sand layers. By cutting open the cured mixture in the final stage of penetration, Pogany could visualize the magnitudes of total deformation. However, neither the deformation process (flow field) nor changes in relative density could be extracted. Moreover, the soil response during the penetration process remained hidden.

Kérisel [1961, 1964] conducted large-scale model tests with local density measurement. In a large testing container filled with sandy soil, piles with a diameter up to 320 mm were pressed into the soil about 7 m starting at the ground surface. Ground heaving was observed along with penetration which gradually decreased at continued penetration. Sensors indicated the development of a zone of densified soil below the conical pile tip. This zone loosened after the pile tip had passed, indicating that it was subjected to a cyclic loading path. After digging out the pile it was found that the pile tip was surrounded by a zone of densified soil, which was again surrounded by a loosened zone. Tensile cracks appeared next to the lower part of the pile shaft.

Berezantsev et al. [1961] carried out tests with a model pile in layered sand. The observed deformation pattern during quasi-static penetration revealed a series of distinct slip surfaces beside the pile. From this, Berezantsev et al. deduce a limit equilibrium solution for pile base capacity depending on the internal angle of friction of the sand.

Based on the tests documented by Berezantsev et al. [1961], Robinsky and Morrison [1964] installed model piles of about 30 mm diameter in dry medium dense to loose quartz sand with interspersed layers of lead shots. Installation was done by jacking and an X-ray method was applied to track the lead shot motion along with penetration. Robinsky and Morrison [1964] use the resulting displacement vectors in order to deduce contours of volumetric strain. They conclude that a conical zone would be formed below the pile tip in which the sand would be compressed and displaced in primarily vertical direction. Loosening and vertical motion dominate outside the compression zone. The results, however, are questionable because horizontal deformations could not properly measured.

An X-ray method was also used by Heinz [1970] at the chair of Soil Mechanics and Geotechnical Engineering, Technische Universität Berlin (TU Berlin), to deduce relative density changes. In contrast to [Robinsky and Morrison, 1964], the thesis of Heinz is concerned with density changes in granular soil below small-scale shallow foundation models. The width of the foundation model is 40 mm. Heinz reports four experimental tests that cover the range of initially loose to initially dense sand. The isopycnic

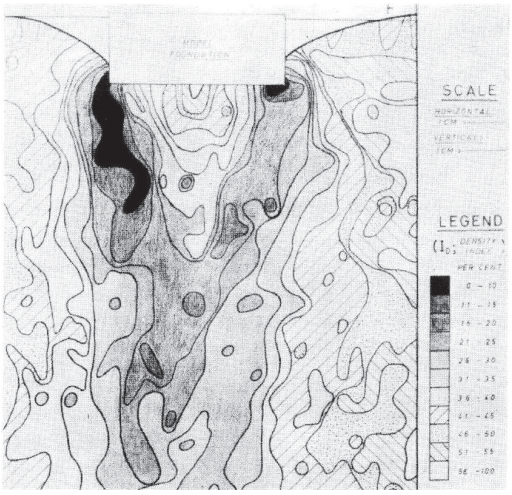

Figure 2.1: Distribution of the relative density (isopycnic lines) under a model foundation on initially medium dense sand ($D_{r0} = 0.56$); reprint from Heinz [1970, p. 51].

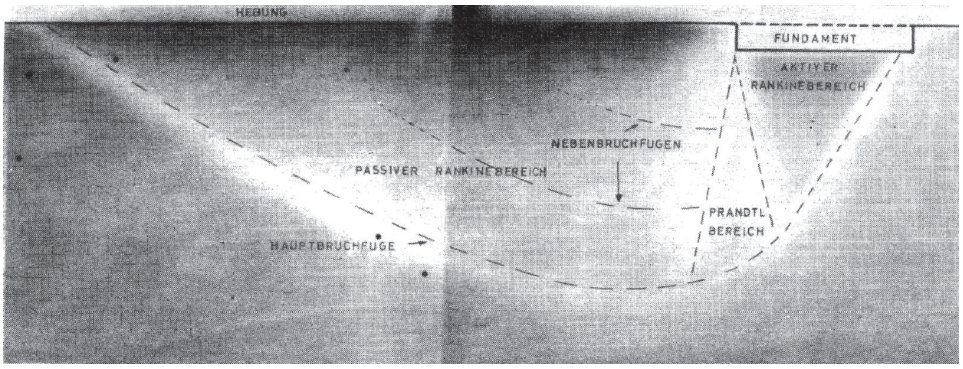

Figure 2.2: X-ray photograph of initially medium dense sand below a penetrated model foundation. State of base failure. Light zones indicate loosening resp. plastic yielding; reprint from Heinz [1970, p. 72].

lines, that is, the distribution of the relative density on initially medium dense sand ($D_{r0} = 0.56$) close to the collapse load is shown in Fig. 2.1. The grey shadings indicate reduction in relative density; the black color is for a relative density $0 \leq D_{r0} \leq 0.1$. It can be seen from the figure that a wedge is formed under the foundation which is surrounded by zones of severe loosening. Heinz [1970, sec. 8.2] points out that these zones can be identified with zones of plastic yielding. No significant density changes were measured within the wedge, thus Heinz [1970, p. 68] calls this the *elastic core* ("elastischer Kern").

Fig. 2.2 reprinted from [Heinz, 1970] shows an X-ray photograph of initially medium dense sand below a penetrated foundation model at the state of base failure. Light zones indicate reduction in relative density. These zones are adjacent to the distinct primary and secondary slip surfaces (dashed lines) that occur. The wedge directly under the foundation behaves monolithically without plastification. Heinz [1970, sec. 8.3] notes that the apex angle of the wedge increases along with increasing initial relative density.

The small-scale pile penetration experiments conducted by Mikasa and Takada [1973] are geometrically similar to those of Berezantsev et al. [1961]. However, all the experiments of Berezantsev et al. were carried out without surcharging the soil ($1g$ tests), whereas Mikasa and Takada use a centrifuge to obtain more realistic initial stress states. Displacement or veloctiy pattern of the soil were not quantitatively but only qualitatively measured by stereoscopic photography. Mikasa and Takada show that a compressive zone around the pile tip is governed by the surcharge pressure. They concluded that this behavior is due to stress-dependent dilatancy.

At TU Berlin, Linder [1977] conducted an extensive test program to study the penetration- and load-bearing behavior of small-scale model piles in dry and initially dense quartz sand. For this purpose a cylindrical soil container with pneumatic pressure pad equipment had been constructed to allow surcharging of the ground surface resp. to realize larger initial embedding depths of the model piles. Moreover, the soil container was instrumented with a large number of vertically and radially aligned extensometers for displacement measurements in a close-mesh grid. The distortion of these grid cells enabled quantification of local volume resp. density changes. The instrumented flat-ended model piles with diameters of 60 mm, 80 mm, and 100 mm featured measurement of base resistance and local shaft friction. The piles were pressed into the ground not by starting from the ground surface but from different embedding depths with and without surcharge pressure.

To check the measured deformation data and to deduce soil deformations at larger penetration depths, Linder [1977] conducted additional experiments with frost bodies. For this purpose the soil container had been flooded and the soil had been frozen at the end of pile penetration tests into sand with layers of markers. The final deformation state could then be visualized by cutting open a frost body.

Linder [1977] describes three phases during quasi-static pile penetration into dense dry sand. The soil would collapse due to a *general shear failure* ("allgemeiner Scherbruch") in phase 1, forming blocks of failure and sliding surfaces reaching up to the ground level (Fig. 2.3). This mechanism is similar to base failure under shallow foundations. Zones of severe loosening surround the shear localization zones (sliding surfaces). Moreover, a hemispherical *dead zone* or *core* arises which is similar to the one reported by Heinz [1970] and which is shielded by a soil arch. The volume of the ground heaving is larger than this of the penetrated pile.

In phase 2, zones of shearing and loosening would enclose a compression cone which is formed under the pile [see also Robinsky and Morrison, 1964]. This is depicted in Fig. 2.4. Within the compression cone the soil would densify and grain crushing occurs, whereupon the general shear failure passes into a *local shear failure* ("lokaler Scherbruch" [Linder, 1977]) and finally into a *punching shear failure* ("Verdichtungs- und Verdrängungsbruch" [Linder, 1977]) —the modes of general shear failure, local shear failure, and punching shear failure are described in [Terzaghi, 1943; Vesic, 1963, 1973; Craig, 2007]. The shear zone would transform the vertical motion of the soil particles into a radial motion. From a global viewpoint phase 2 approximately describes an isochoric motion, meaning that the volume of the ground heaving equals the volume of the penetrated pile.

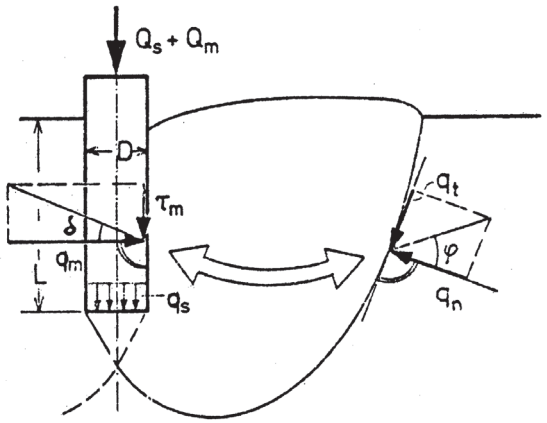

Figure 2.3: Failure mechanism at small penetration depths in phase 1; reprint from Linder [1977, p. 105].

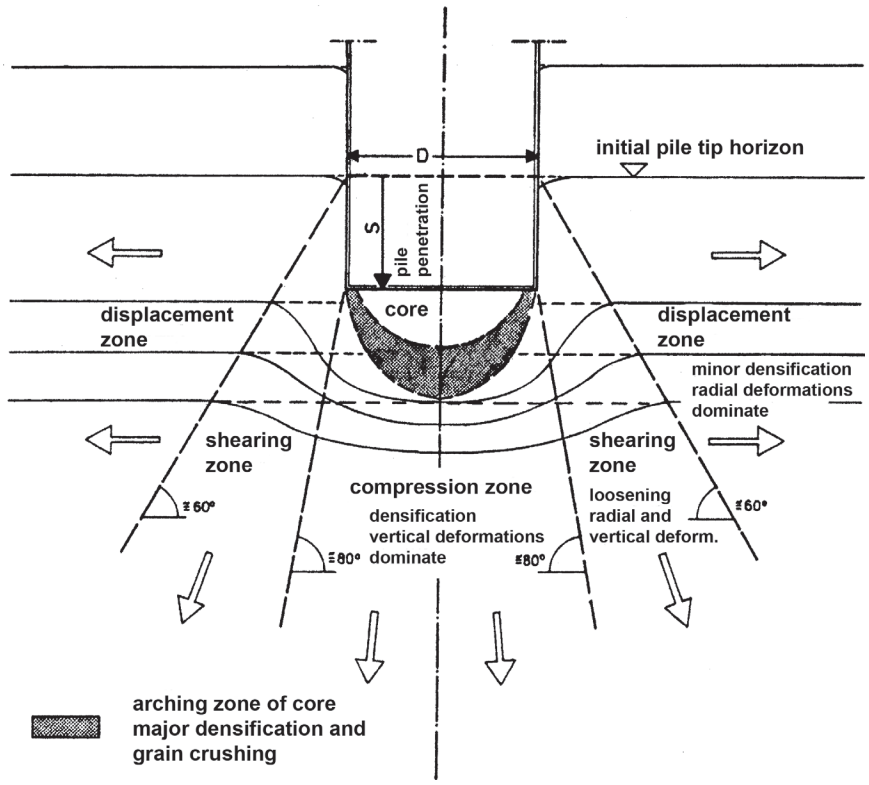

Figure 2.4: Deformations and relative density changes in dense sand at medium penetration depths in phase 2; schematic diagram according to Linder [1977, p. 174].

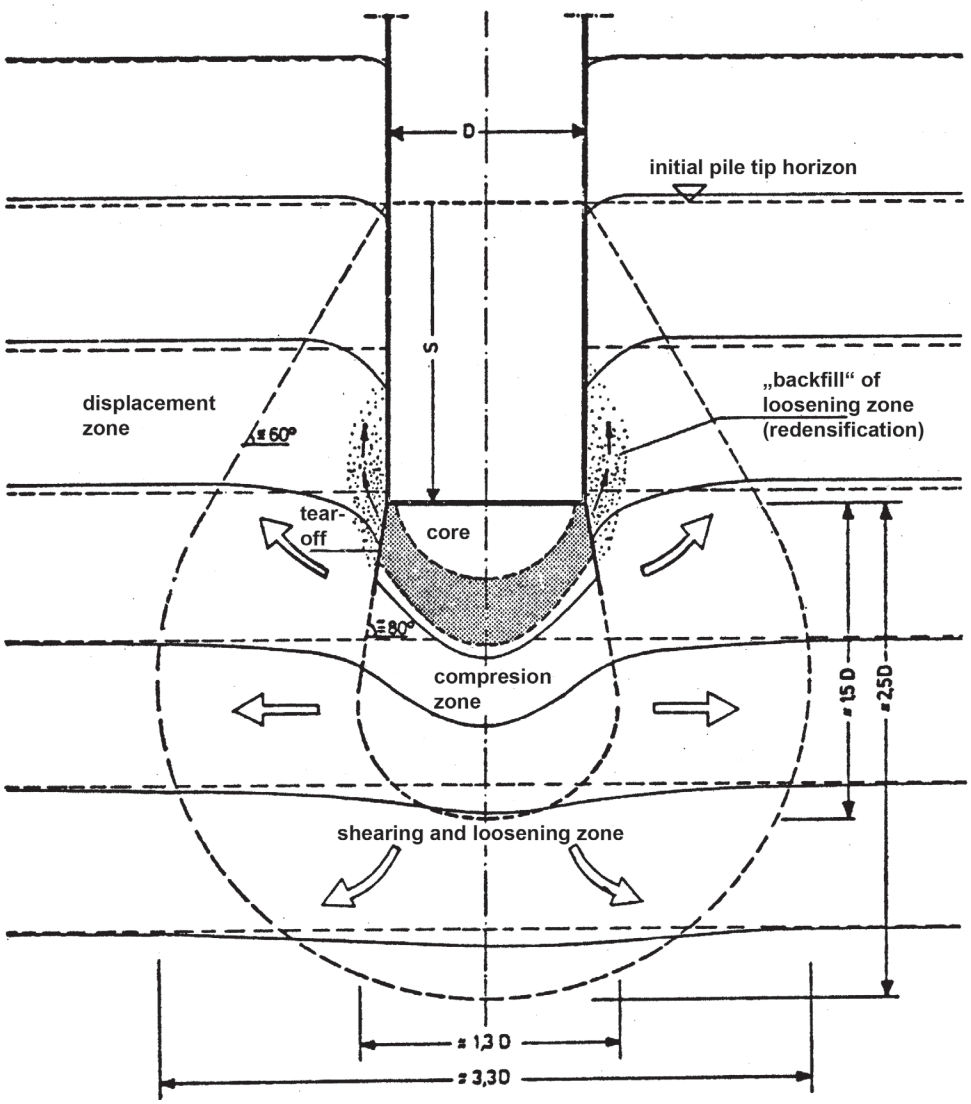

Figure 2.5: Deformations and relative density changes in dense sand at large penetration depths in phase 3; schematic diagram according to Linder [1977, p. 182].

In phase 3 the soil under the pile base would be compressed normal to the core boundary. Then, the shearing zone running ahead of the compression zone would displace the soil in radial and upward direction (Fig. 2.5). Sand would loosen moderately within this shearing zone [see also Kérisel, 1961, 1964] and would experience redensification along with displacement. The shearing and loosening zone in phase 3 has a diameter of about $3.5D$ and reaches into a depth up to $2.5D$ under the pile base, where D is the diameter of the pile. The shearing zone is enclosed by a compression resp. displacement zone like the lower part of the pile shaft. An important phenomenon in phase 3 is that initially dense soil elements are subjected to significant structural changes governed by grain crushing once they are grabbed by the compression zone right below the pile tip.

The results of the tests reported by Linder [1977] were influenced by the initial embedding depth of the model piles. At the same amount of penetration the behavior in

phases 1 and 2 would differ for small and large embedding depths. In phase 3 the soil response behavior would be almost independent of the initial embedding depth.

At the University of Cambridge, White [2002] conducted pile penetration tests in a chamber at plane strain conditions. A small-scale model pile (in fact, a wall segment) was pressed along an observing window into different types of sand with different initial densities. White developed a system for deformation measurement that combines techniques of *particle image velocimetry (PIV)* and close range photogrammetry. A vertical stress boundary condition to the soil mass could be applied by a pair of rubber surcharge bags in order to achieve higher and more realistic stress levels.

White [2002] identifies three zones of soil motion during a penetration increment. A core zone would be formed right below the flat pile base similar to the core noticed by Heinz [1970] and Linder [1977], and in which the soil would be compressed. The second, cone-shaped zone would be located ahead of the core and would expand downwards with an inclination angle of about 55° relative to the horizontal. Within this second zone the soil would be compressed in vertical direction. A third zone would be observed above and lateral to the cone in which the soil would be compressed in horizontal direction but is allowed to expand in vertical direction.

By using the PIV method, which is a special kind of particle imaging technique (see Chapter 7), White [2002] was able to measure soil velocity and to deduce soil strains with high resolution and accuracy. Motion tracking was implemented by integrating the velocity field in time. Hauser and Walz [2004] and other research groups approve the applicability of the PIV method to experimental soil mechanics. It is also applied in the present work.

2.1.2 Soil Stress, Base Resistance, and Shaft Friction

A large number of experimental penetration tests is reported in which the penetrator and/or the soil was instrumented. Most of the laboratory and on-site pile penetration experiments focus on the pile shaft friction, because the base resistance does not significantly change at large penetration depths; see [Linder, 1977] and below.

De Nicola [1996] and Bruno [1999] conducted tests in a centrifuge at the University of Western Australia in order to examine the distribution of the shaft friction. A miniature pile driving actuator had been constructed to install instrumented open-ended model piles in-flight by hammering. The scale of the model required satisfaction of laws of similitude for dynamic installation. This was achieved by either particle size reduction or by using a pore fluid with higher viscosity than water.

In their theses, de Nicola [1996] and Bruno [1999] report not only a drop of shaft friction at increasing distance from the pile base but also a gradually loss of friction along the pile shaft as driving proceeds. The latter phenomenon is referred to as *friction fatigue* [Heerema, 1980]. Randolph et al. [1994] attribute the loss of shaft friction to a decreasing earth-pressure coefficient owing to dynamic shear deformation. The rate of fatigue is governed by the compressibility of the soil and its sensitivity to grain

crushing, as well as by the pile roughness, the energy impact due to driving, and the local soil motion next to the pile base [Randolph et al., 1994]. Soil compressibility is related to the plastic volume change of a soil element.

Chow [1997] reports on an extensive program of large-scale on-site tests. He used a 7 m long instrumented pile that allows for measurement of both friction and radial stress at three locations along the shaft. The pile was driven by hammering. Friction fatigue was quantified in addition to a significant increase in radial effective stress at a given pile shaft level during installation. Chow attributes this increase to dilation at the pile-soil interface, that is, to the increasing volume due to shear loading.

To examine the soil stress around the pile in the course of pile penetration, Leung et al. [1996, 2001] performed experiments in a centrifuge. The soil was instrumented by an array of buried vertical and horizontal total stress transducers, and pile models were driven into the soil by pressing. The measured horizontal stress remained nearly constant as the pile tip passed. In larger depths the vertical stress behaved similar. However, near to the ground surface the vertical stress would drop below the geostatic level. As the pile reached a desired penetration depth, Leung et al. [1996] applied a constant load for a specific period of time to investigate time-dependent behavior. It turned out that the base resistance gradually decreased whereas shaft friction increased. Such time-dependent phenomena are also reported by Chow [1997] and Chow et al. [1997], among many others. These, however, are not considered in the present work.

The evolution of the pile base resistance at initiating penetration, on the other hand, is an important issue. Linder [1977] gives a detailed report of the base resistance during the three phases of pile penetration described above. He deduced a schematic enveloping load-displacement curve from his test results in which he identified phase transitions with points of inflection (Fig. 2.6). In a relative penetration resp. embedding depth of $L/D \geq 1.0$ to 2.0, where L is the penetration depth and D is the pile diameter, the general shear failure of phase 1 would pass into a local shear failure which initiates phase 2 and the first inflection point on the load-displacement curve. Accordingly, the stress at the flat pile base highly increases along with penetration. Compared to phase 1 the base resistance in phase 2 would be predominantly governed by the compressibility of the soil, whereas its shear resistance would become less important.

Phase 3 would be marked by the second inflection point on the load-displacement curve in relative penetration depths of $L/D \geq 8.0$ to 12.0. The enveloping load-displacement curve depicted in Fig. 2.6 approaches a straight line of quasi-constant base resistance. This quasi-constancy is also reported by Kérisel [1964]. Practically, the base resistance in phase 3 would be governed only by the compressibility and displacement ability of the soil, and by the response of the powdered material running ahead of the core zone.

2.1.3 Influencing Factors

Many experimental laboratory and on-site tests have been conducted in the past in order to investigate the influence of the relative density of sand on shaft resistance and base resistance of piles and sounding tools. As one would expect, there is a trend of

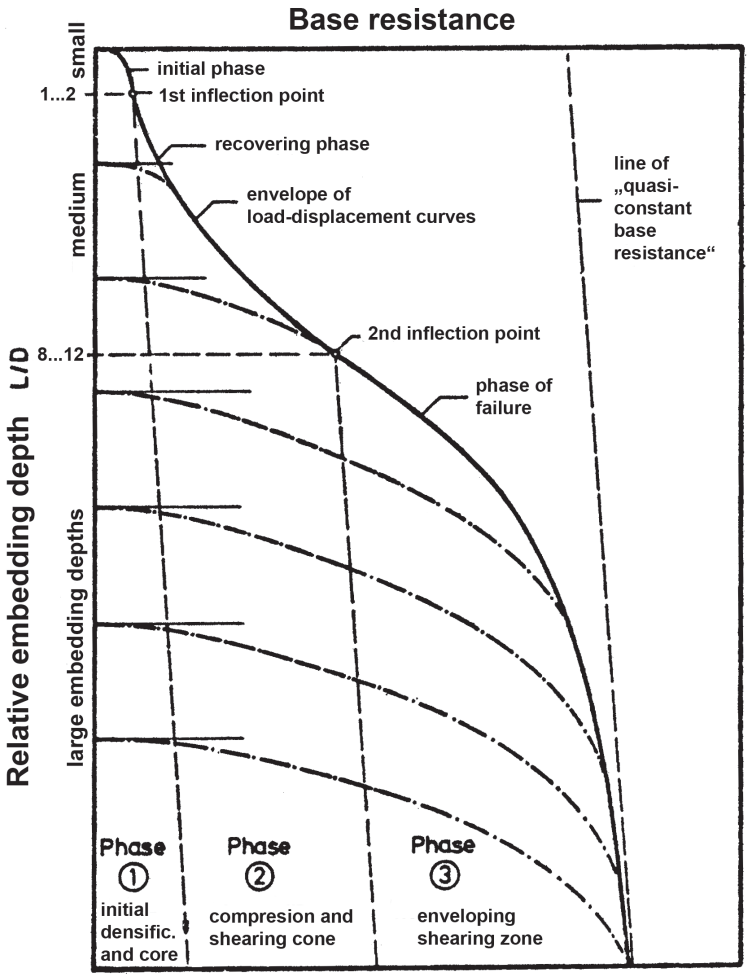

Figure 2.6: Phases during pile penetration in dense sand. Progress of base resistance; schematic diagram according to Linder [1977, p. 171].

base resistance increasing with relative density. However, a mechanically well-founded direct correlation has not been found yet. According to Klotz and Coop [2001], the relative density would not be not sufficient to deduce the base resistance from. Based on conducted small-scale pile penetration tests in a centrifuge, Klotz and Coop instead suggest to use a so-called *state parameter* as the basic variable, which is a scalar-valued quantity comprising both the stress and density state of sand. The state parameter was introduced by Been and Jefferies [1985]; see also Section 4.2.

In early design methods to determine the bearing capacity of displacement piles, the angle of internal friction is the only soil parameter. Vesic [1963] concluded that this would be indeed a reasonable assumption for cohesionless soil provided that the angle of internal friction would be considered as a function of the relative density. He reports on a series of conducted large-scale shallow penetration and pile penetration on-site tests to investigate the bearing capacity of deep foundations in sand. The tests reveal that all three modes of shear failure (i.e. global shear failure, local shear failure, and punching shear failure) may occur within cohesionless soil under a shallow foundation

dependent on the initial relative density. At greater depths only punching shear failure would take place irrespective of the relative density. Moreover, Vesic [1963] concluded that shaft resistance and base resistance would reach constant values at relative depths of $L/D > 15$ which are independent of the overburden pressure and appear to be a function of the relative density of sand only. The bearing capacity would generally increase with increasing relative density.

Yasufuku et al. [2001] carried out experiments with pile models in calcareous sands and quartz sands, and recorded a considerable influence of soil compressibility. They improve the *cavity expansion method* of Vesic [1972], see below, for back-calculation of their experimental results. From these back-calculations, Yasufuku et al. [2001] deduce a relationship between soil compressibility and base resistance at different overburden stress. However, details about the dimensions of the plastic zones due to soil compressibility are not given.

The penetration phenomenology, load-bearing behavior, and particularly the shaft friction and base resistance of displacement piles is affected by the installation method. For example, Chow [1997], de Nicola and Randolph [1997], and White et al. [2000] report that the friction fatigue phenomenon would be more significant in case of vibrodriving than if the pile would be driven by pressing or hammering. However, as the current research is concerned only with quasi-static penetration of piles, any influence of the pile installation method is left unconsidered.

2.2 Semi-Empirical and Analytical Methods

Several attempts have been made to predict the ultimate bearing capacity of driven and pressed-in piles and to deduce soil properties from penetrating sounding tools on a *semi-empirical* basis. The in-situ static cone penetration test is a widely used procedure to give rough estimates of engineering soil properties. By now semi-empirical relations have been deduced between the measured static cone resistance and the internal friction angle, the relative density, the undrained shear strength, and the stiffness of the soil near the cone. For example, the static cone resistance q_c can be related to the undrained shear strength c_u according to the well-known formula [van den Berg and Vermeer, 1988; DIN 4094-1]

$$q_c \stackrel{\text{def}}{=} N_c \, c_u + \sigma_0 \,, \tag{2.2.1}$$

where σ_0 is the total overburden stress and N_c is the so-called cone factor. Cone resistance has also been related to the limiting values of base resistance and shaft friction of driven and pressed-in piles in both cohesive and granular soils [Meyerhof, 1951, 1956; DIN 1054].

The semi-empirical method of Meyerhof [1976] combines bearing capacity theory with experimental test data. The proposed bearing capacity factor and earth pressure coefficient incorporate the influence of the pile installation method on base resistance and shaft friction, respectively. However, due to its simplifying assumptions the method of Meyerhof does not feature the prediction of soil property changes during installation

or the computation of stress and density distributions. This is because semi-empirical approaches in general are intended for engineering practice, having reduced complexity compared to analytical or numerical methods.

Analytical approaches to soil penetration include [cf. Susila and Hryciw, 2003; van den Berg, 1994]: *bearing capacity theories* by limit plasticity [Meyerhof, 1951, 1956] that originate from the work of Prandtl [1920], *cavity expansion theories* [Hill, 1998; Vesic, 1972; Randolph and Wroth, 1979], and the *strain path method* [Baligh, 1985; Teh and Houlsby, 1991]. However, none of these methods is able to realistically predict density changes along with penetration.

Methods that are based on bearing capacity theories, like the one proposed by Meyerhof [1951], are among the earliest approaches to soil penetration and pile resistance. These methods are restricted to ideal (or rigid) plastic constitutive behavior of the soil without any plastic volume changes, i.e. they ignore the influence of soil compressibility. Therefore, ultimate bearing capacity of cohesive soils can generally be estimated from bearing capacity theory and the shear strength of undisturbed samples. For cohesionless soils, however, this approach would not be practical [cf. Meyerhof, 1956, 1976]. Moreover, the penetration process changes the initial properties of the soil near the pile or sounding tool governing the bearing capacity, thus results are not reliable.

Cavity expansion theories are reasonably applicable to cohesive soils. The method of Hill [1998, sec. XI.4] is valid only for ideal plastic soil with zero internal friction, which is approximately the case for fully saturated undrained clay. Vesic [1972] extends ideal plastic cavity expansion theory by soil compressibility. The main assumption is that the plastic zone is governed by the Mohr-Coulomb limit condition. This in turn means that plastic volumetric strain can only result from shear failure, which contradicts the real behavior of sand (see Section 4.2). Irreversible volume changes in sand may also be due to isotropic loading.

The cavity expansion theories of Randolph and Wroth [1979], Randolph et al. [1979] and Carter et al. [1979] allow for the simplified analysis of the effects of pile penetration with subsequent consolidation in saturated clays. This is achieved through the implementation of more advanced elasto-plastic constitutive equations for the soil. Moreover, Yu and Houlsby [1996] extends the range of applicability of cavity expansion theories to finite deformations, and Maisch [2000] combines cavity expansion with hypoplasticity. Hypoplasticity is a constitutive framework different to elasto-plasticity that is also applied in this research work; see Sections 4.1.3 and 4.3.

The advantage of the strain path method of Baligh [1985] is that geometry and kinematics of penetration deep below ground surface can be accurately reproduced. In order to determine the stress and pore pressure fields within the soil, initial values have to be assumed and a constant penetration velocity has to be prescribed. Thereafter, a flow resp. strain rate field around the rigid penetrator must be estimated, and then the deformation and strain paths are deduced from the flow field by integration. Once the strain history is known, the stress and pore pressure can be obtained from a constitutive equation. The strain path method has been successfully applied to the penetration of piles with different pile tip geometries [Baligh, 1985], and to analyze the cone pen-

etration in-situ test [Teh and Houlsby, 1991]. However, the method is restricted to undrained cohesive soils because of the basic hypothesis that soil deformations and strains are independent of the shearing resistance of the soil [Baligh, 1985].

2.3 Numerical Models

As outlined in the introductory chapter and highlighted in the preceding sections, the problem of soil penetration is highly nonlinear due to large soil deformations, complex material behavior, and changing contact conditions. In the current age of personal computers with multi-core processors and sophisticated application software the solution of such a problem by numerical methods is advocated. There are two main groups of methods to build a numerical model for soil penetration. The first group regards both the soil and the penetrator formed by assemblies of distinct (or discrete) contacting particles, whereas the methods of the second group are based upon the continuum assumption. Combinations of both approaches are at an early stage [e.g. Avci and Wriggers, 2012].

2.3.1 Discrete Element Models and Meshless Models

The *discrete element method (DEM)* developed by Cundall and Strack [1979] is based on discrete mechanics. The basic ingredients of this method are the particle assembly and a constitutive law for interparticle contact. The microscopic response can provide response of the particle assembly under loading on the macro level. Therefore, the macroscopic behavior is strongly affected by the particle shape, particle size and its distribution, as well as by the contact model. Research on DEM in soil mechanics and geotechnical engineering is at an early stage. The current limitations of the DEM include its inability to solve true-to-scale problems with millions of particles. Simulation of consolidation and fluid flow in the interspace requires coupling with continuum-based methods. Nevertheless, promising works on soil penetration do exist [e.g. Jiang et al., 2006; Heesen, 2010].

The majority of numerical models and solution techniques in soil mechanics are based on the assumption of a soil continuum. Soil penetration is then understood as an initial boundary value problem that can be solved by either *mesh-based methods* or *meshless methods*.

Meshless methods, which are also called *point-based methods*, were developed with the objective to eliminate the problems associated with mesh-based methods at extremely large material deformation or propagating discontinuities; the reader is referred to the review articles of Belytschko et al. [1996] and Monaghan [1985] for detailed information. Meshless methods for solid mechanical problems originated from the particle-based methods for hydrodynamics, including the *particle-in-cell (PIC) method* [Harlow, 1957] and *smoothed particle hydrodynamics (SPH)* [Gingold and Monaghan, 1977; Lucy, 1977]. Sulsky and Schreyer [1996] extend the PIC method for the appli-

cation to dynamic solid mechanical problems, referred to as the *material point method (MPM)*. An alternative approach is the *element-free Galerkin (EFG) method* developed by Belytschko et al. [1994], which is based on a *moving least squares* [Lancaster and Salkauskas, 1981] approximation. However, many of the meshless methods resort to a background mesh at least in parts of the method, and there are only a few applications in soil mechanics and geotechnical engineering [e.g. Więckowski et al., 1999; Vermeer et al., 2008; Bui et al., 2008, 2011; Beuth, 2012].

2.3.2 Lagrangian Finite Element Models

The most widely-used mesh-based numerical tool in nonlinear solid mechanics is the *finite element method (FEM)* [e.g. Wriggers, 2008; Belytschko et al., 2000; Zienkiewicz and Taylor, 2000a,b; Bathe, 1996; Oden, 1972]. FEM calculations can be carried out on both structured as well as unstructured meshes. The finite difference method, which requires a logically regular mesh, is mostly applied to fluid dynamical and impact problems [Benson, 1992]. A challenge that is to be met for FE modeling of general penetration processes is constituted by the large local deformations in the vicinity of the penetrator. Moreover, numerical models for penetration of soils, in particular granular soils, require advanced constitutive equations to ensure that the stress and density fields and soil deformations are feasible and realistic.

Typical finite element models in solid mechanics are based on a *Lagrangian description*, in which a configuration of the material is chosen as the reference domain for the solution of the considered initial boundary value problem (cf. Chapter 5). In this case the motion of the element mesh is an approximation to the material deformation. If material deformations are large, excessive element distortions and mesh tangling may occur that slow down convergence of solution or even terminate the calculation. One of the earliest Lagrangian FE models for soil penetration was set up by Griffiths [1982]. Based on infinitesimal deformation theory and by using a simple elasto-plastic material model with Tresca's yield condition, he investigated load-bearing capacity of deep foundations resp. smooth piles placed in a "pre-bored hole" in cohesive soil. This basic idea of a soil penetration starting in pre-bored holes is also called the *wished-in-place* approach. It is adopted by many researchers, e.g. by de Borst and Vermeer [1984]; Teh and Houlsby [1991], and Kiousis et al. [1988], in order to prevent severe element distortion and to bypass numerical problems related to small shear strength at the unloaded ground surface.

The penetration model of de Borst and Vermeer [1984] is based on the assumption of infinitesimal deformations. Teh and Houlsby [1991] combine the strain path method with small-strain finite element analysis to study the cone penetration test in clay. Kiousis et al. [1988] extended a large deformation FE framework proposed previously [Kiousis et al., 1986], but the smooth penetrometer with conical tip also starts at a certain depth to keep soil deformations moderate. The constitutive equations for the soil employed in these early models are rather simple and do not include state variables in addition to stress, like the void ratio. For example, de Borst and Vermeer [1984]

apply the Mohr-Coulomb elasto-plastic model to their analysis, and Kiousis et al. [1988] use the model of DiMaggio and Sandler [1971] for granular materials.

It should be obvious that the calculated load-bearing capacity of wished-in-place numerical pile models generally differs from that of pile models where the installation process has been simulated. This is because the stress and material state of the soil changes during penetration. An alternative approach which also limits mesh deformations along with penetration in a Lagrangian FE model is to use a special modeling technique for the penetrating object, which is referred to as the *pilot-hole* or *zipper-type* technique. When using such an approach the pile is regarded as a rigid slideline or rail in two dimensions and as a rigid tube in three dimensions (Fig. 2.7). The rail resp. tube supports the modeled soil continuum in normal direction. Alternatively, the pile with conical tip can be modeled by solid elements. In any of these cases the "centerline" of the soil domain has to be given a hypothetical small thickness. By the pile moving downward the vertical axis of penetration, the soil is displaced and contact between pile and soil can be established. The contact constraints, which may include separation, adhesion, or sliding friction, are treated in the common way.

One of the earliest finite element models for penetration using the zipper-type technique is reported by Cividini and Gioda [1988]. In their two-dimensional model shown in Fig. 2.7 above, the rail representing the pile consists of a series of straight segments to which the soil is constrained by rollers. The rollers do not support tensile forces in normal direction. In tangential direction, the interaction between pile and soil includes frictional response together with adhesion.

Mabsout and Tassoulas [1994] incorporate a more advanced constitutive equation for undrained cohesive soil based on the bounding surface plasticity framework in their numerical model. The pile is installed dynamically by hammering. Transmitting boundaries of the viscous type have been used to prevent wave reflection at the boundaries of the finitely extended mesh for the soil mass. Lateral and overburden soil pressure on the radial and upper horizontal boundary, respectively, is applied using special pressure elements. The method for contact constraint treatment permits large relative slip between pile and soil, and allows separation along the interface. Sliding friction is modeled using the Coulomb law.

In a series of research projects carried out at the Technical Universities of Karlsruhe and Hamburg-Harburg, Germany, the zipper-type modeling technique in combination with highly-developed hypoplastic rate constitutive equations for the soil (see Chapter 4) was applied to analyze static, quasi-static cyclic, and dynamic penetration of sand and its influence on adjacent structures [Cudmani, 2001; Mahutka and Grabe, 2005; Grabe and König, 2006; Mahutka, 2007; König, 2008; Henke, 2008, 2010; Grabe et al., 2009; Mahutka and Henke, 2009]. The axisymmetric finite element models used in these works are similar to the one reported by Mabsout and Tassoulas [1994], including discretizations of the pile with both a smooth and a non-smooth surface.

Henke [2010] refines the zipper-type technique to model not only piles with full circular cross section but also pipe piles and fully three-dimensional steel piles with different cross sections (Fig. 2.7 below). In the latter case, both the model generation and finite

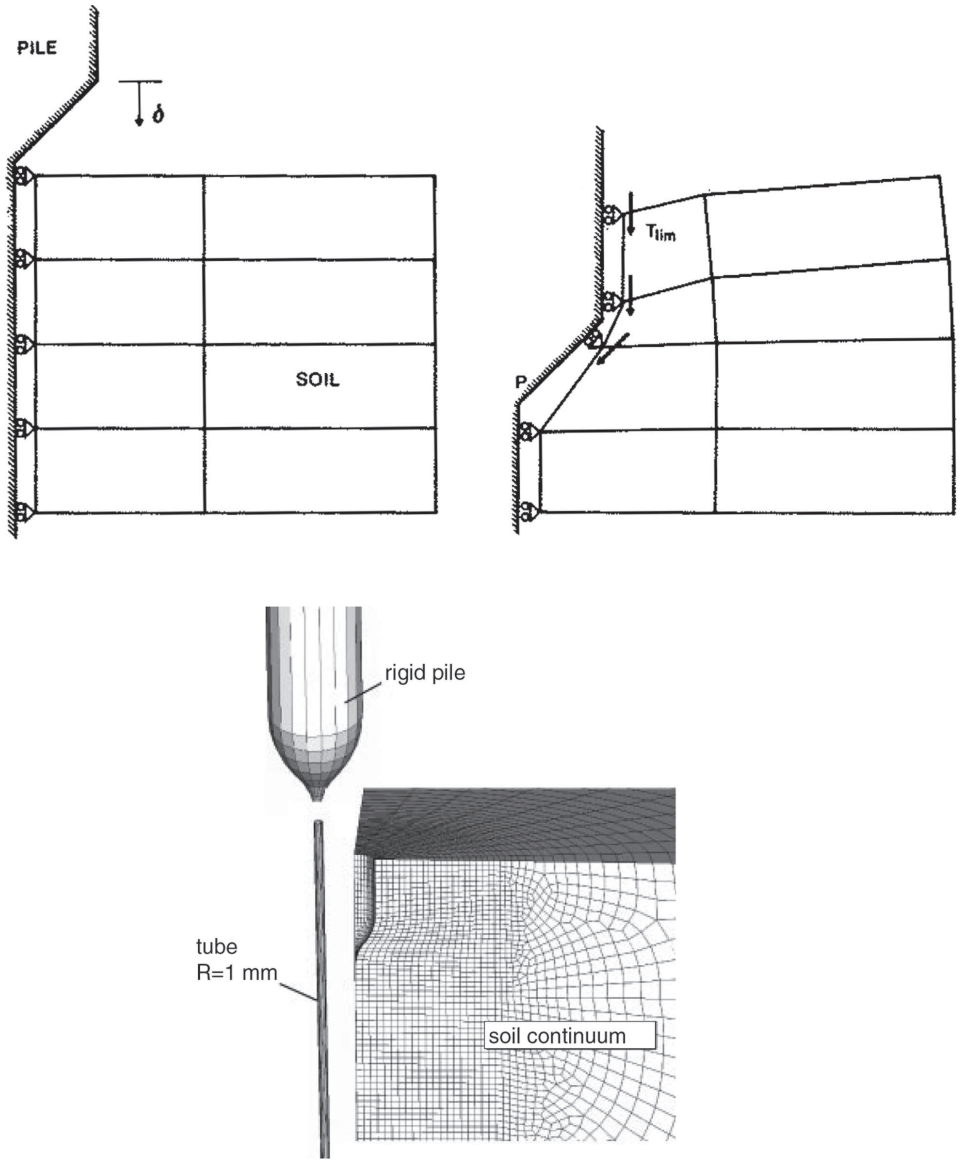

Figure 2.7: Special modeling techniques for soil penetration in Lagrangian FEM. *Above:* two-dimensional model with rigid rail; reprint from Cividini and Gioda [1988, p. 1046]. *Below:* three-dimensional model with rigid tube; reprint from Henke [2010, p. 1192] – (Copyright © 2009 John Wiley & Sons, Ltd.).

element solution process could be quite time-consuming. The results of numerical analysis show that the influence of pile installation on stress and density distribution in sand and on adjacent structures depends on the initial density, the installation method, the pile geometry, and the roughness of the pile shaft. The additional loading on adjacent structures due to pile penetration generally increases with increasing initial density of the soil. Earth-pressure built-up adjacent to pressed-in piles is larger than for piles which are vibro-driven.

Sheng et al. [2005] simulate the installation of pressed-in axisymmetric piles in cohesive soil in a Lagranigan finite element model by placing emphasis on the modeling of the contact zone between pile and soil. The *modified Cam-Clay* constitutive equation

[Roscoe and Burland, 1968] is used to model the mechanical behavior of the soil. The pile with conical tip is meshed by solid elements of finite stiffness to allow for stress evaluation within the pile. The FE model and contact methods applied in [Sheng et al., 2005] is improved by Sheng et al. [2006]. They show that the load-displacement curve related to the pile penetration process is strongly influenced by the discretization of the pile-soil contact interface. If the solid mesh is coarse and the interface is discretized by straight segments, then the load-displacement curve has a *zig-zag* form which is a manifestation of spurious oscillation. This phenomenon has already been reported by Simo and Meschke [1993] and is caused by the periodical release of the finite element nodal forces whenever a node loses contact with the pile cone. Oscillation can be reduced by smoothing the contact interface segments [Sheng et al., 2006].

The zipper-type approach, albeit widely-used, has some undesirable limitations. Since the direction of penetration is predefined, drifting and/or twisting of the modeled penetrator are precluded. Moreover, the penetrator is required to be sufficiently smooth and to have a beneficial geometry to limit material deformations resp. deformations of the Lagrangian mesh along with penetration. Conical or "dagger-like" pile tips that cut open the soil, i.e. which predominantly displace the soil horizontally instead of compressing it in vertical direction, are highly recommended.

2.3.3 Rezoned and Non-Lagrangian Finite Element Models

If element distortions in Lagrangian FE models for penetration processes become unacceptably large, then a new FE model has to be generated and the solution variables have to be remapped onto the new mesh. This complex process is generally called *rezoning* or *adaptive remeshing*. Rezoning can be applied to any of the FE models mentioned but is difficult to implement for large strain finite element formulations. By contrast, the *remeshing and interpolation technique with small strain (RITSS)* proposed by Hu and Randolph [1998] is much simpler because it is based on the assumption of infinitesimal deformations. RITSS basically is a rezoning method for small-strain Lagrangian finite element technology to simulate large deformation problems. However, results are questionable since large deformation effects e.g. due to finite material rotations are neglected. Nevertheless, RITSS has been applied to several problems, including installation of spudcan foundations [Hu and Randolph, 1998] and penetration tests [Lu et al., 2004; Zhou and Randolph, 2007].

Element distortion will not occur in the *Eulerian* finite element or finite difference models in which the mesh is kept spatially fixed during the entire calculation. The material flows through the fixed mesh, hence tracking of free surfaces and material motion thus becomes non-trivial. However, if the stationary process of deep penetration into homogeneous soil is intended to be simulated by neglecting the ground surface, the penetrator can be regarded as spatially fixed so that Eulerian FE model generation and solution is considerably simplified. This latter approach was investigated to simulate cone penetration in both homogeneous [van den Berg and Vermeer, 1988] and layered [van den Berg, 1994; van den Berg et al., 1996] cohesive soil. Liyanapathirana et al. [2000] uses a Eulerian model to simulate driving of a pipe pile by hammering. Effort

has been made to include free surfaces and material interface evolution in the so-called *multi-material Eulerian* codes [e.g. McGlaun et al., 1990; Benson, 1995, 1997, 2000], but these are much more complex and have not been applied yet to quasi-static soil penetration involving complex constitutive response.

The *coupled Eulerian-Lagrangian (CEL) method* proposed by Noh [1964] in the context of finite difference methods couples overlapping but distinct Eulerian and Lagrangian meshes. In CEL methods, a Lagrangian mesh is generally used to discretize the penetrator whereas an Eulerian mesh is used for the target, representing the soil in the present case. The boundary of the Lagrangian mesh represents the actual interface between the penetrator and the target, and interface models need to be employed to couple the responses of the Lagrangian and Eulerian meshes. Typical interface models use the velocity of the Lagrangian boundary as a kinematic constraint to the Eulerian mesh, and the stress within the Eulerian elements is applied as a traction boundary condition to the Lagrangian mesh [see Benson, 1992; Brown et al., 2002]. Usually the deviatoric stress contribution generating interface friction is ignored, because most of the CEL codes are intended to solve highly dynamic, pressure-dominated problems.

Noh [1964] applies his method to fluid-structure interaction problems, and Brown et al. [2002] discusses CEL in the context of hypervelocity earth penetrating weapon applications. The commercial finite element code ABAQUS® provides a CEL feature that incorporates a model to handle interface friction. Henke et al. [2010] combined this feature with an advanced hypoplastic constitutive equation for the target material to simulate pile penetration into sand.

As outlined in the introductory Chapter 1, the *arbitrary Lagrangian-Eulerian (ALE) description* of finite element models, taken as the basis for the present work, was developed to overcome the difficulties encountered in the purely Lagrangian and Eulerian descriptions, and to combine their advantages. The origins and state of the art of ALE procedures and their detailed examination will be presented in Chapter 6 and not at this point here. Implementation of ALE methods is complex, and the need for elaborated constitutive equations to realistically model the mechanical behavior of soils further increases complexity. Therefore, there are currently only few ALE finite element models for soil penetration reported in the literature. Moreover, in these models the constitutive equations employed (Mohr-Coulomb, Drucker-Prager, modified Cam-Clay, etc.) are not applicable to reproduce the stress- and density-dependent response of sand and granular materials under monotonic and cyclic loading. This is because relative density and material history do not constitute internal state variables to the governing equations (sand behavior is investigated in Section 4.2).

Susila and Hryciw [2003] and Liyanapathirana [2009] employ the automatic adaptive remeshing (rezoning) technique implemented in ABAQUS® to simulate the cone penetration test in normally consolidated sand and soft clay, respectively. The adaptive remeshing technique can be regarded as an *operator-split ALE method* because after a purely *Lagrangian solution step* a new mesh is generated from the old mesh by node relocation (r-adaption). *Node relocation* resp. *mesh smoothing* improves the quality of the mesh without changing mesh topology. Therefore, mechanically consistent *advection algorithms* borrowed from computational fluid dynamics can be used to *remap*

the solution variables onto the new mesh. An operator-split ALE method will be also developed in the present work; see Chapter 6.

The algorithm for node relocation in ABAQUS® used in the finite element models of Susila and Hryciw [2003] and Liyanapathirana [2009] is an averaging procedure that moves the vertex node shared by a group of elements to the centroid of this group. It is a simple algorithm that is not qualified to handle non-convex mesh patches and to account for mesh grading. The advection algorithm is based on the work of van Leer [1977] which has a maximum accuracy of second order. The cone-soil interface accounts for shaft friction by using the Coulomb law. Susila and Hryciw [2003] and Liyanapathirana [2009] investigate cone tip resistance and stress distribution within the soil. The simple Drucker-Prager constitutive equation has been chosen by Susila and Hryciw [2003] to model the mechanical behavior of sandy soil. Therefore, the FE model cannot capture relative density development and response due to cyclic loading.

Nazem et al. [2006, 2008] develop an operator-split ALE method to solve large deformation geomechanical initial boundary value problems under different drainage conditions. This ALE method is applied to shallow foundations on fully drained and fully undrained soil [Nazem et al., 2006] as well as to consolidation problems [Nazem et al., 2008]. The latter requires a two-equation model for the soil together that accounts for solid-fluid coupling. The constitutive equations used for the soil include those of Mohr-Coulomb and Tresca, as well as the modified Cam-Clay model. A new algorithm has been developed and implemented in order to smooth the finite element mesh based on physical considerations.

The ALE method employed by Di et al. [2007] allows for a wide range of geomechanical applications. It is also based on the operator-split solution procedure. The soil is modeled as a saturated porous medium with solid-fluid coupling, and the mechanical behavior of the solid phase is described by a hypoelasto-plastic rate constitutive equation using non-linear kinematic hardening and non-associated flow rules. Strain and pore water pressure accumulations during cyclic loading are taken into account in addition to static consolidation effects. By these features, Di et al. [2007] can analyze large deformation response of an embankment made up of saturated soil mass and subjected to vertical and horizontal earthquake excitation. The finite element model was laterally bounded by infinite elements to avoid wave reflection. Di et al. point out that computational stability would be lost and the running of the program would be stopped when using a purely Lagrangian mesh. In contrast, the ALE finite element mesh would remain smooth so that the computation can be continued.

Sheng et al. [2009] combine the zipper-type FE model for quasi-static pile penetration set up by Sheng et al. [2006], see above, with the ALE method of Nazem et al. [2006], but included some improvements to the node relocation scheme. They conclude that the ALE method together with contact interface smoothing would be able to considerably advance the simulation of soil penetration problems involving friction and would not cause much increase in computing time compared to a purely Lagrangian simulation. This comparison, nota bene, can be done only at penetration stages at which the Lagrangian simulation has not yet been terminated due to severe element distortion.

Chapter 3

Kinematics and Balance Principles

Roughly speaking, continuum mechanics consists of kinematics, balance principles, and constitutive theory. The following chapter is concerned with the former two fields, whereas constitutive theory with applications to sand response is investigated in the next chapter. Kinematics is the description of material bodies and their motion in the ambient space without considering the causes of motion. The balance principles are the laws of dynamics that govern the motion of bodies including mechanical as well as thermal effects. Depending on the choice of reference points and volume elements, kinematics and the balance principles can be set up in Lagrangian (or material), Eulerian (or spatial), and arbitrary Lagrangian-Eulerian (ALE or referential) form.

The classical Lagrangian and Eulerian formulations are usually applied to continuum mechanics, and a large body of literature is available that treats classical continuum mechanics in Euclidian linear spaces [e.g. Truesdell and Toupin, 1960; Malvern, 1969; Gurtin, 1981; Truesdell and Noll, 2004; Ciarlet, 1988; Holzapfel, 2000]. Continuum mechanics on manifolds has been developed with increasing speed during the last few decades [Carter and Quintana, 1972; Wang and Truesdell, 1973; Marsden and Hughes, 1994; Ebin and Marsden, 1970; Simo and Marsden, 1984; Simo et al., 1988; Epstein and Segev, 1980; Segev, 1986, 2000, 2013; Stumpf and Hoppe, 1997; Romano and Baretta, 2009; Aubram, 2009]. In the majority of cases, it is more practical to apply the Lagrangian description to general solid mechanical problems because these are characterized by complex nonlinear inelastic materials with strength. The Eulerian description is commonly used for pressure-dominated fluid dynamical problems that involve very large deformation of materials without memory. The Lagrangian approach has to satisfy less complex governing equations than the Eulerian approach, because convective terms are absent. However, this advantage is gained through material tracking that requires knowledge of an initial (or reference) configuration of the body, which is not necessary in non-Lagrangian descriptions.

Along with the advent of computational mechanics and the demand for advanced and interdisciplinary finite element applications, the classical Lagrangian and Eulerian formulations have revealed some inevitable disadvantages (see Chapters 1 and 2). An almost arbitrary reference domain uncoupled from the material body and its spatial configurations is introduced in the ALE formulation in order to unify both classical con-

cepts, and to overcome their shortcomings. The earliest references concerned with the arbitrary resp. mixed Lagrangian-Eulerian treatment of continuum mechanical equations include [Trulio and Trigger, 1961; Guo, 1963; Frank and Lazarus, 1964].

The following chapter derives the basic equations of kinematics and balance principles in the Lagrangian, Eulerian, and ALE descriptions. These descriptions will be given proper definitions, which are missing in the available literature. The treatises of Marsden and Hughes [1994], Scovazzi and Hughes [2007], and Aubram [2009] serve as an orientation, and the geometric concepts summarized in Appendix A are adopted consistently in order to obtain an ALE setting of continuum mechanics on manifolds. Notwithstanding this aspect of generality, the present outline takes space and time as different concepts, like in non-relativistic classical mechanics.

As a general convention, upper case Latin is used for coordinates, vectors, and tensors of the reference configuration, and objects related to the Lagrangian formulation. Lower case Latin relates to the current configuration, the ambient space, or to the Eulerian formulation.

3.1 Kinematics

3.1.1 Motion of a Body in Space

The basic mathematical object in the proper formulation of continuum mechanics is that of a differentiable manifold. In this spirit, let $\mathfrak{M}$ be a sufficiently smooth *material manifold*, and let its *particles* or *material points* carry the properties of the material under consideration. A subset $\mathfrak{B} \subset \mathfrak{M}$ is referred to as a *material body* resp. a *body manifold* [Lodge, 1951; Noll, 1967, 1972; Krawietz, 1986]. $\mathfrak{B}$ is usually noticed in a Riemannian ambient space $\mathcal{S}$, which is a differentiable manifold with metric $\boldsymbol{g}$, symmetric connection $\boldsymbol{\nabla}$, and volume form $\mathbf{d}\boldsymbol{v}$. Let the *placement* $\kappa : \mathfrak{B} \to \mathcal{S}$ be an embedding such that $\mathfrak{B} \to \kappa(\mathfrak{B})$ is a diffeomorphism, and call $\mathcal{B} \stackrel{\text{def}}{=} \kappa(\mathfrak{B}) \subset \mathcal{S}$ the *reference configuration of the body in* $\mathcal{S}$, or simply the *body*. The points $X \in \mathcal{B}$ are the *places of the particles of the body in the reference configuration*, but they are just called the *particles* for brevity. The situation is illustrated in Fig. 3.1.

Let $[0, T] \subset \mathbb{R}$ be a time interval. An embedding

$$\begin{aligned} \varphi_t : \quad & \mathcal{B} \to \mathcal{S} \\ & X \mapsto x = \varphi_t(X) \end{aligned} \tag{3.1.1}$$

is called a *configuration* of $\mathcal{B}$ in $\mathcal{S}$ at time $t \in [0, T]$, and the set $\mathcal{C} \stackrel{\text{def}}{=} \{\varphi_t \,|\, \varphi_t : \mathcal{B} \to \mathcal{S}\}$ is called the *configuration space*. The *deformation* of the body then is the diffeomorphism $\mathcal{B} \to \varphi_t(\mathcal{B})$. A *motion* of $\mathcal{B}$ in $\mathcal{S}$ is a family of configurations dependent on time $t \in [0, T]$, i.e. a curve $c : [0, T] \to \mathcal{C}$, $t \mapsto c(t) = \varphi_t$, and with $\varphi_t(\cdot) \stackrel{\text{def}}{=} \varphi(\cdot, t)$ at fixed t. $\varphi_t(\mathcal{B})$ is referred to as the *current configuration* of the body at time t, so $x = \varphi_t(X)$ is the *current location* of the particle X.

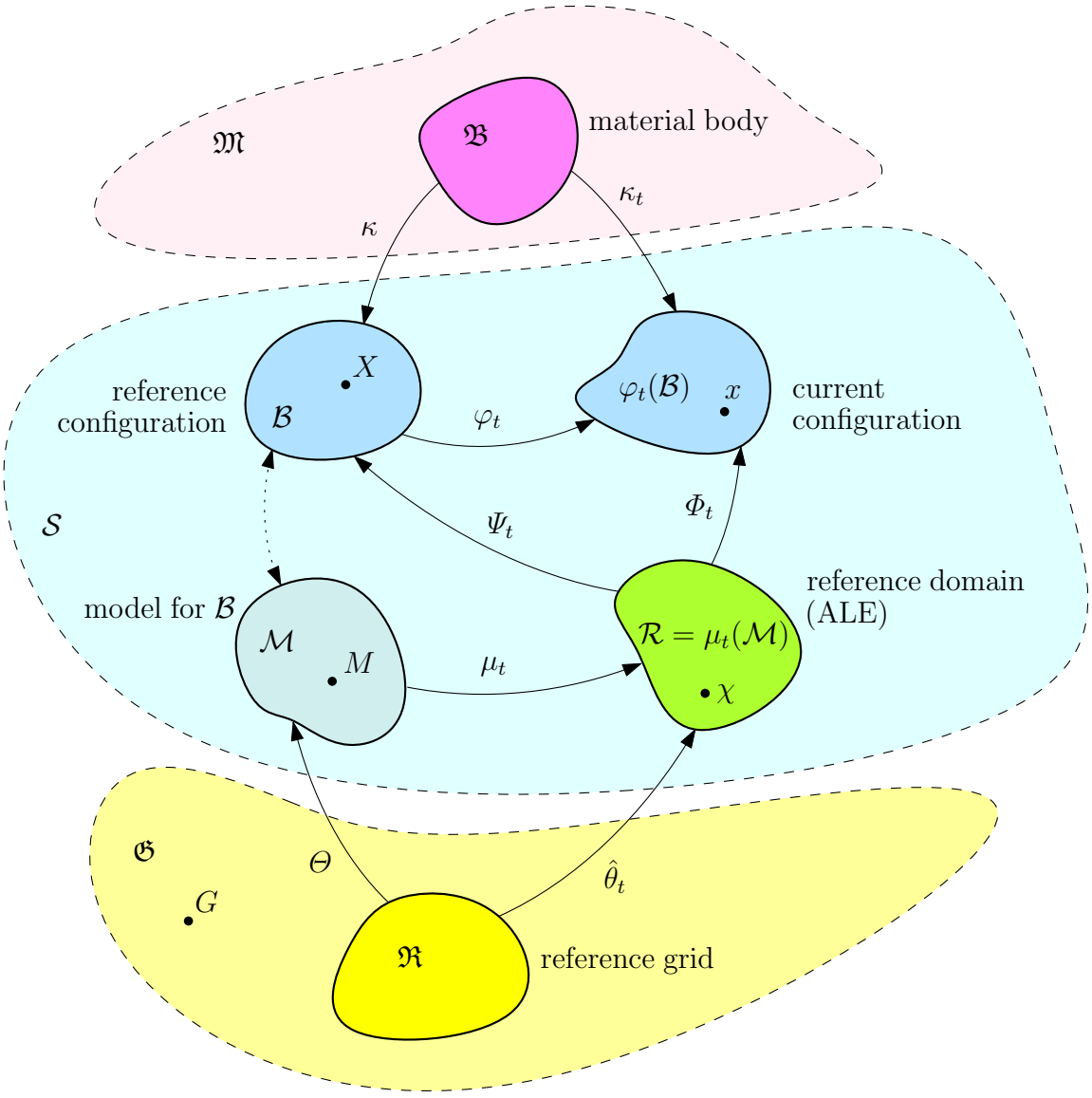

Figure 3.1: Manifolds and mappings related to the Lagrangian, Eulerian, and arbitrary Lagrangian-Eulerian descriptions; according to Aubram [2009, fig. 4.4].

Remark 3.1.2. If $\varphi_0 = \mathrm{id}_{\mathcal{B}}$ is the identity map on $\mathcal{B}$, then $\mathcal{B} = \varphi_0(\mathcal{B})$, i.e. the body is in its reference configuration at $t = 0$. $\mathcal{B}$ is then called the *initial configuration* of the body. However, the choice of a initial configuration is not necessary to describe the motion of the body, but it has historical significance in continuum mechanics. $\triangle$

For simplicity, it is throughout assumed that the dimensions of the body and the ambient space are the same, i.e. $\dim(\mathcal{B}) = \dim(\mathcal{S}) \stackrel{\text{def}}{=} m$. Both $\mathcal{B}$ and $\mathcal{S}$ have differentiable atlases by Definition A.4.4. The charts of the open neighborhoods $\mathcal{U}(X) \subset \mathcal{B}$ will be denoted by $(\mathcal{U}, \beta)$, where $\beta : \mathcal{U} \to \mathcal{Y} \subset \mathbb{R}^m$ is a homeomorphism and $\{X^1, \dots, X^m\}_X \stackrel{\text{def}}{=} \{X^I\}_X = \beta(X) \in \mathbb{R}^m$ are local coordinate functions. Consequently, $\left\{\frac{\partial}{\partial X^1}, \dots, \frac{\partial}{\partial X^m}\right\}_X \stackrel{\text{def}}{=} \left\{\frac{\partial}{\partial X^I}\right\}_X \in T_X\mathcal{B}$ establishes a holonomic basis of the tangent space at X, and the coordinate differentials form its dual $\{\mathbf{d}X^I\}_X \in T_X^*\mathcal{B}$ in the cotangent space. Regularity of the local coordinate systems is demanded everywhere and at all times, hence fracture and interpenetration are precluded. It was assumed above that the ambient space $\mathcal{S}$ has a metric, so $\mathcal{B}$ also has. The metric coefficients at every $X \in \mathcal{U}$ with respect to the $\{X^I\}_X$ are $G_{IJ}(X) \stackrel{\text{def}}{=} \left\langle \frac{\partial}{\partial X^I}, \frac{\partial}{\partial X^J} \right\rangle_X$.

The differentiable atlas of the ambient space $\mathcal{S}$ consists of charts $(\mathcal{V}, \sigma)$, where $\mathcal{V}(x) \subset \mathcal{S}$ is an open neighborhood of the spatial point $x \in \mathcal{S}$, $\sigma : \mathcal{U} \to \mathcal{X} \subset \mathbb{R}^m$ is a homeomorphism, and $\{x^1, \dots, x^m\}_x \stackrel{\text{def}}{=} \{x^i\}_x = \sigma(x) \in \mathbb{R}^m$. As before, the local vector basis at x is $\left\{\frac{\partial}{\partial x^i}\right\}_x \in T_x\mathcal{S}$, and $\{\mathbf{d}x^i\}_x \in T_x^*\mathcal{S}$ is its dual. The metric coefficients at every $x \in \mathcal{V}$ are be denoted by $g_{ij}(x) \stackrel{\text{def}}{=} \left\langle \frac{\partial}{\partial x^i}, \frac{\partial}{\partial x^j} \right\rangle_x$ at every $x \in \mathcal{V}$. The ambient space should have a symmetric connection denoted by $\boldsymbol{\nabla}$, with coefficients $\gamma_i{}^j{}_k$. It is assumed that $\mathcal{B}$ and $\mathcal{S}$ are orientable, with Riemannian volume forms denoted by $\mathbf{d}\boldsymbol{V}$ and $\mathbf{d}\boldsymbol{v}$, respectively. Finally, let $\boldsymbol{I}$ and $\boldsymbol{i}$, with components $\delta^I{}_J$ and $\delta^i{}_j$, be the identity tensors on $\mathcal{B}$ and $\mathcal{S}$, respectively.

Definition 3.1.3. Let $\varphi_t : \mathcal{B} \to \mathcal{S}$ be the motion of a material body, and $(\mathcal{U}, \beta)$, $(\mathcal{V}, \sigma)$ be coordinate charts as defined previously. Let $\varphi_t^{-1}(\mathcal{V}) \cap \mathcal{U} \neq \emptyset$, then by (A.4.5), the *localization of the motion* is the map

$$\sigma \circ \varphi_t \circ \beta^{-1}\Big|_{\beta\left(\varphi_t^{-1}(\mathcal{V}) \cap \mathcal{U}\right)} ,$$

and

$$\varphi_t^i(X^I) \stackrel{\text{def}}{=} (x^i \circ \varphi_t \circ \beta^{-1})(X^I) \qquad \text{resp.} \qquad \varphi_t^i \stackrel{\text{def}}{=} x^i \circ \varphi_t \circ \beta^{-1}$$

are the spatial coordinates associated with $\varphi_t(\mathcal{B})$ at time t. The so-called *convected coordinates* on $\varphi_t(\mathcal{B})$ are given by the inverses of φ_t^i, i.e. $X^I \circ \varphi_t^{-1} \circ \sigma^{-1}$. These are lines scribed on $\mathcal{B}$ following its motion in $\mathcal{S}$. $\diamondsuit$

Remark 3.1.4. The previous definitions include the standard Euclidian point space and motions therein as a special case. Assume that $\mathcal{S} = \mathbb{R}^m$ is an m-dimensional Euclidian point space, and that $\mathcal{B} \subset \mathbb{R}^m$ is the reference configuration of the body having the same dimensions. $\mathbb{R}^m$ is affine, thus has the global chart $(\mathbb{R}^m, \mathrm{id})$. To make a difference, write $(\mathbb{R}^m, Z = \mathrm{id})$ for the global chart on $\mathcal{B}$, and $(\mathbb{R}^m, z = \mathrm{id})$

for the global chart on $\mathcal{S}$. The tangent bundle of $\mathbb{R}^m$ is just $T\mathbb{R}^m = \mathbb{R}^m \times \mathbb{R}^m$ (see Remark A.4.11).

Now, let $O, o \in \mathcal{S}$ be arbitrary points. In $\mathbb{R}^m$, a material particle $X \in \mathcal{B}$ in the reference configuration can be identified with the position vector

$$\boldsymbol{X}_O = (O, \boldsymbol{X}) \qquad \in T_O\mathbb{R}^m = \{O\} \times \mathbb{R}^m \,,$$

with $\boldsymbol{X} \stackrel{\text{def}}{=} \overrightarrow{OX}$, and spatial points $x \in \mathcal{S}$ can be identified with $\boldsymbol{x}_o = (o, \boldsymbol{x}) \in T_o\mathbb{R}^m$, where $\boldsymbol{x} \stackrel{\text{def}}{=} \overrightarrow{ox}$. Let the chart $(\mathbb{R}^m, Z = \mathrm{id})$ be centered at $O \in \mathbb{R}^m$, so that $(O, \boldsymbol{E}_A)$ is a frame and the basis $\{\boldsymbol{E}_1, \ldots, \boldsymbol{E}_m\} \stackrel{\text{def}}{=} \{\boldsymbol{E}_A\} \in \mathbb{R}^m$ is ortho-normalized. Then, material Cartesian coordinates Z^A can be determined from $\overrightarrow{OX} = Z^A(X)\,\boldsymbol{E}_A \in \mathbb{R}^m$, or, equivalently, $\overrightarrow{Ox} = Z^A(x)\,\boldsymbol{E}_A \in \mathbb{R}^m$, since $(\mathbb{R}^m, \mathrm{id})$ is a global chart. Similarly, spatial Cartesian coordinates z^a can be determined from $\overrightarrow{ox} = z^a(x)\,\boldsymbol{e}_a \in \mathbb{R}^m$, where $(o, \boldsymbol{e}_a)$, and $\{\boldsymbol{e}_1, \ldots, \boldsymbol{e}_m\} \stackrel{\text{def}}{=} \{\boldsymbol{e}_a\} \in \mathbb{R}^m$ is likewise ortho-normalized. Note that such ortho-normalized bases are always available in $\mathbb{R}^m$ (see Section A.1).

Let $x \in \mathcal{S}$ be any point, then $\overrightarrow{Ox} = \overrightarrow{Oo} + \overrightarrow{ox}$. The Cartesian, that is, affine coordinates of x in the two frames $(O, \boldsymbol{E}_A)$ and $(o, \boldsymbol{e}_a)$ transform according to the well-known rules

$$Z^A(x) = B^A{}_a z^a(x) + c^A \quad \text{and} \quad z^a(x) = B^a{}_A Z^A(x) + b^a \,, \qquad \text{with} \quad b^a = -c^A B^a{}_A \,.$$

Here $B^A{}_a = (B^a{}_A)^{-1}$ are the components of the inverse matrix of the change of basis $\boldsymbol{E}_A = B^a{}_A \boldsymbol{e}_a$, $\boldsymbol{I}(\overrightarrow{ox}) = z^a(x) B^A{}_a \boldsymbol{E}_A$ and $\overrightarrow{Oo} \stackrel{\text{def}}{=} c^A \boldsymbol{E}_A = -b^a \boldsymbol{e}_a \stackrel{\text{def}}{=} -\overrightarrow{oO}$ [cf. Aubram, 2009, sec. 2.2].

If $\varphi : \mathcal{B} \times [0, T] \to \mathcal{S}$, $(X, t) \mapsto x = \varphi(X, t)$ is a motion of the material body, then its vector-valued counterpart is defined through

$$\begin{aligned} \boldsymbol{\varphi} : \ & \mathbb{R}^m \times [0, T] \to \mathbb{R}^m \\ & (\boldsymbol{X}, t) \mapsto \overrightarrow{O\varphi(X, t)} \stackrel{\text{def}}{=} \boldsymbol{\varphi}(\boldsymbol{X}, t) \,. \end{aligned}$$

If $\mathcal{B}$ is in its reference configuration at $t = 0$, one has $\boldsymbol{X} = \boldsymbol{\varphi}(\boldsymbol{X}, 0)$. A local representative is $\boldsymbol{\varphi} = Z^A(\varphi(X, t))\,\boldsymbol{E}_A \stackrel{\text{def}}{=} \varphi^A_Z(X, t)\,\boldsymbol{E}_A$, as well as

$$\boldsymbol{\varphi} = (B^A{}_b z^b(\varphi(X, t)) + c^A)\,\boldsymbol{E}_A = (B^a{}_A B^A{}_b z^b(\varphi(X, t)) - b^a)\,\boldsymbol{e}_a = (\varphi^a_z(X, t) - b^a)\,\boldsymbol{e}_a$$

by applying the transformation rules, and $\varphi^a_z(X, t) \stackrel{\text{def}}{=} z^a(\varphi(X, t))$. The vector field $\boldsymbol{U}_t : \mathcal{B} \to T\mathcal{B}$ defined through

$$\boldsymbol{U}(X, t) \stackrel{\text{def}}{=} (X, \boldsymbol{\varphi}(\boldsymbol{X}, t) - \boldsymbol{X}) = \left(X, \overrightarrow{X\varphi(X, t)}\right)$$

is called the *material displacement*. This is only defined in $\mathbb{R}^m$. Using the previous results, the displacements components with respect to $(O, \boldsymbol{E}_A)$ are

$$U^A(X, t) = \varphi^A_Z(X, t) - Z^A(X) = B^A{}_a \varphi^a_z(X, t) - Z^A(X) + c^A \,.$$

Let $(\mathcal{U},\beta)$ and $(\mathcal{V},\sigma)$ be general charts on $\mathcal{B}\subset\mathbb{R}^m$ and $\mathcal{S}=\mathbb{R}^m$, respectively, where $\mathcal{U}(X)\subset\mathcal{B}$, $\mathcal{V}(x)\subset\mathcal{S}$ are open neighborhoods. If X^I and x^i are general curvilinear coordinates related to these charts, then their local basis vectors are given by the transformation rules

$$\frac{\boldsymbol{\partial}}{\boldsymbol{\partial} X^J}=\frac{\partial Z^A(X)}{\partial X^J}\,\boldsymbol{E}_A\qquad\text{and}\qquad\frac{\boldsymbol{\partial}}{\boldsymbol{\partial} x^i}=\frac{\partial z^a(x)}{\partial x^i}\,\boldsymbol{e}_a\,,$$

respectively (evaluated at the appropriate points). Therefore, $\boldsymbol{E}_A=\frac{\boldsymbol{\partial}}{\boldsymbol{\partial} Z^A}$ and $\boldsymbol{e}_a=\frac{\boldsymbol{\partial}}{\boldsymbol{\partial} z^a}$ are the holonomic basis vectors associated with the Cartesian coordinates. △

Definition 3.1.5. Let φ_t be at least 1-fold continuous differentiable, i.e. a C^1-motion of $\mathcal{B}$ in $\mathcal{S}$, then

$$\boldsymbol{V}_t(X)\overset{\text{def}}{=}\frac{\partial\varphi_t}{\partial t}(X)\overset{\text{def}}{=}\left.\frac{\partial\varphi_t^i}{\partial t}\right|_{\beta(X)}\frac{\boldsymbol{\partial}}{\boldsymbol{\partial} x^i}\overset{\text{def}}{=}V_t^i(X)\frac{\boldsymbol{\partial}}{\boldsymbol{\partial} x^i}(x)$$

is called the *Lagrangian* or *material velocity field over* φ_t *at* X, where $x=\varphi_t(X)$ and $\boldsymbol{V}_t(X)\overset{\text{def}}{=}\boldsymbol{V}(X,t)$ if t is regarded fixed. In fact, $\boldsymbol{V}_t:\mathcal{B}\to T\mathcal{S}$ is an honest vector field neither on $\mathcal{B}$, nor on $\mathcal{S}$: it is a section of $T\mathcal{S}$ *induced* by the map φ_t; see Section A.6 for a general definition of induced sections. Provided that φ_t is regular, one can make $\boldsymbol{V}_t$ a vector field on $\varphi_t(\mathcal{B})\subset\mathcal{S}$ by switching the point arguments,

$$\boldsymbol{v}_t\overset{\text{def}}{=}\boldsymbol{V}_t\circ\varphi_t^{-1}:\quad\varphi_t(\mathcal{B})\to T\mathcal{S}\,,$$

which is then called the *spatial* or *Eulerian velocity field of* φ_t. The spatial velocity is the "instantaneous" velocity at $x\in\varphi_t(\mathcal{B})\subset\mathcal{S}$, and $\boldsymbol{V}(X,t)=\boldsymbol{v}(\varphi(X,t),t)$. By abuse of language, both $\boldsymbol{V}$ and $\boldsymbol{v}$ are occasionally called the *material velocity* in order to distinguish it from other, non-material velocity fields. ♢

Proposition 3.1.6. *For a regular C^1-motion, the Lie derivative of an arbitrary, possibly time-dependent, spatial tensor field $\boldsymbol{t}_t\in\mathfrak{T}^p_q(\mathcal{S})$ along the spatial velocity $\boldsymbol{v}$ is*

$$\mathrm{L}_{\boldsymbol{v}}\boldsymbol{t}_t=\varphi_{t\star}\frac{\mathrm{d}}{\mathrm{d}t}(\varphi_t^\star\,\boldsymbol{t}_t)\,.$$

Proof. From the definition of the Lie derivative, $\mathrm{L}_{\boldsymbol{v}}(\boldsymbol{t}_t)=\psi_{\star t,s}\frac{\mathrm{d}}{\mathrm{d}t}(\psi_{t,s}^\star\boldsymbol{t}_t)$, where $\psi_{t,s}$, with $s,t\in[t_0,T]\subset\mathbb{R}$, is the time-dependent flow generated by the spatial velocity on $\mathcal{S}$; cf. (A.7.7). By Definition 3.1.5, the latter is obtained from

$$\psi_{t,s}=\varphi_t\circ\varphi_s^{-1}:\ \mathcal{S}\supset\varphi_s(\mathcal{B})\to\varphi_t(\mathcal{B})\subset\mathcal{S}\,.$$

The assertion follows by applying the chain rule for pushforwards and pullbacks, and noting that $(\varphi_s^\star)^{-1}=(\varphi_s^{-1})^\star=\varphi_{s\star}$ [see also Marsden and Hughes, 1994, sec. 1.6]. ∎

Time-dependency is dropped for the moment, so $\varphi:\mathcal{B}\to\mathcal{S}$ is just a configuration, not a motion. The tangent of φ at $X\in\mathcal{B}$, $\boldsymbol{F}(X)\overset{\text{def}}{=}T\varphi(X):T_X\mathcal{B}\to T_{\varphi(X)}\mathcal{S}$, is a two-point tensor called the *deformation gradient*. $\boldsymbol{F}$ has the local representative

$$\boldsymbol{F}(X)=F^i_I(X)\frac{\boldsymbol{\partial}}{\boldsymbol{\partial} x^i}\otimes\mathbf{d}X^I\,,\tag{3.1.7}$$

in which $F^i_{\ I} = \frac{\partial \varphi^i}{\partial X^I}$. Note that globally, $\boldsymbol{F} : \mathcal{B} \to \varphi^\star T\mathcal{S} \otimes T^*\mathcal{B}$ is a two-point tensor field, where $\varphi^\star T\mathcal{S}$ denotes the induced bundle of $T\mathcal{S}$ over φ; so $\frac{\partial}{\partial x^i}$ attached to $\varphi(X)$ is being understood. From (A.5.16) and (A.5.17), the transposed deformation gradient is

$$\boldsymbol{F}^{\mathrm{T}}(x) = g_{ij} \left(F^i_{\ I} \circ \varphi^{-1}\right) \left(G^{IJ} \circ \varphi^{-1}\right) \frac{\boldsymbol{\partial}}{\boldsymbol{\partial} X^J} \otimes \mathbf{d}x^j \,, \tag{3.1.8}$$

which is simply $\boldsymbol{F}^{\mathrm{T}} = F^i_{\ I}\, \mathbf{d}X^I \otimes \frac{\boldsymbol{\partial}}{\partial x^i}$ by index raising and index lowering, and by dropping the compositions with the point map.

Definition A.6.8 can be applied to obtain the pushforward and pullback of arbitrary tensor fields on $\mathcal{B}$ and $\mathcal{S}$, respectively. In particular, the following calculation formulas can be obtained.

Proposition 3.1.9. *For $\boldsymbol{t} \in \mathfrak{T}^0_2(\mathcal{S})$, $\boldsymbol{s} \in \mathfrak{T}^2_0(\mathcal{S})$, $\boldsymbol{T} \in \mathfrak{T}^0_2(\mathcal{B})$, and $\boldsymbol{S} \in \mathfrak{T}^2_0(\mathcal{B})$, one has*

$$\begin{aligned}
\varphi^\star \boldsymbol{t} &= \boldsymbol{F}^{\mathrm{T}} \cdot \boldsymbol{t} \cdot \boldsymbol{F} && \in \mathfrak{T}^0_2(\mathcal{B})\,, \\
\varphi^\star \boldsymbol{s} &= \boldsymbol{F}^{-1} \cdot \boldsymbol{s} \cdot \boldsymbol{F}^{-\mathrm{T}} && \in \mathfrak{T}^2_0(\mathcal{B})\,, \\
\varphi_\star \boldsymbol{T} &= \boldsymbol{F}^{-\mathrm{T}} \cdot \boldsymbol{T} \cdot \boldsymbol{F}^{-1} && \in \mathfrak{T}^0_2(\mathcal{S})\,, \quad \textit{and} \\
\varphi_\star \boldsymbol{S} &= \boldsymbol{F} \cdot \boldsymbol{S} \cdot \boldsymbol{F}^{\mathrm{T}} && \in \mathfrak{T}^2_0(\mathcal{S})\,,
\end{aligned}$$

respectively. Compositions with point mappings have been suppressed.

Remark 3.1.10. The pullback and pushforward operators involve the tangent map $T\varphi = \boldsymbol{F}$, and not φ itself. This circumstance would justify the replacement of $\varphi^\star$ by the symbol $\boldsymbol{F}^\star$, referred to as the $\boldsymbol{F}$*-pullback*, and $\varphi_\star$ by $\boldsymbol{F}_\star$, called the $\boldsymbol{F}$*-pushforward*. △

The deformation gradient includes all deformations, that is, stretches as well as rotations, thus it is not a suitable strain measure. Instead, the *right Cauchy-Green tensor* or *deformation tensor (field)*

$$\boldsymbol{C} \stackrel{\text{def}}{=} (\boldsymbol{F}^{\mathrm{T}} \circ \varphi) \cdot \boldsymbol{F} \quad \in \mathfrak{T}^1_1(\mathcal{B}) \tag{3.1.11}$$

is a proper strain measure on $\mathcal{B}$, and the *Green-Lagrange strain* or *material strain* $\boldsymbol{E} \stackrel{\text{def}}{=} \frac{1}{2}(\boldsymbol{C} - \boldsymbol{I})$ also is. $\boldsymbol{E}^\flat = \frac{1}{2}(\boldsymbol{C}^\flat - \boldsymbol{G})$ denotes the associated tensor of $\boldsymbol{E}$ with all indices lowered, where $\boldsymbol{G} \stackrel{\text{def}}{=} G_{IJ}\, \mathbf{d}X^I \otimes \mathbf{d}X^J$ is the metric on $\mathcal{B}$. Spatial or Eulerian strain measures can be defined as symmetric mappings $T\mathcal{S} \to T\mathcal{S}$ for every $x \in \varphi(\mathcal{B})$. For example, the *left Cauchy-Green tensor* is defined through $\boldsymbol{b} \stackrel{\text{def}}{=} (\boldsymbol{F} \circ \varphi^{-1}) \cdot \boldsymbol{F}^{\mathrm{T}} \in \mathfrak{T}^1_1(\mathcal{S})$.

Proposition 3.1.12. *Let $\boldsymbol{g} \in \mathfrak{T}^0_2(\mathcal{S})$ be the spatial metric tensor field, and φ a regular configuration, then $\boldsymbol{C}^\flat = \varphi^\star \boldsymbol{g}$.*

Proof. A proof of can be done in local coordinates by using the formulas presented in this section [see also Aubram, 2009]. ∎

If $\varphi : \mathcal{B} \to \mathcal{S}$ is a regular configuration, then the deformation gradient has a unique *right polar decomposition* $\boldsymbol{F} = \boldsymbol{R} \cdot \boldsymbol{U}$, and a unique *left polar decomposition* $\boldsymbol{F} = \boldsymbol{V} \cdot \boldsymbol{R}$. The two-point tensor $\boldsymbol{R}(X) : T_X\mathcal{B} \to T_x\mathcal{S}$, where $x = \varphi(X)$, includes the rotatory part

of the deformation and is proper orthogonal, that is, $\boldsymbol{R}^{-1} = \boldsymbol{R}^{\mathrm{T}}$ and $\det \boldsymbol{R} = +1$. The *right stretch tensor* $\boldsymbol{U}(X) : T_X\mathcal{B} \to T_X\mathcal{B}$ and the *left stretch tensor* $\boldsymbol{V}(x) : T_x\mathcal{S} \to T_x\mathcal{S}$ are symmetric and positive definite for every $X \in \mathcal{B}$ and $x \in \mathcal{S}$, respectively —it will be clear from the context whether $\boldsymbol{V}$ denotes the left stretch tensor or the material velocity.

The *Lagrangian* or *material logarithmic strain* is defined through the spectral decomposition

$$\boldsymbol{\varepsilon} \stackrel{\text{def}}{=} \ln \boldsymbol{U} = \sum_{\alpha=1}^{3} (\ln \lambda_\alpha)\, \boldsymbol{\Psi}_{(\alpha)} \otimes \boldsymbol{\Psi}_{(\alpha)} \quad \in \mathfrak{T}^1_1(\mathcal{B})\,, \tag{3.1.13}$$

where λ_α and $\boldsymbol{\Psi}_\alpha$, with $\alpha \in \{1,2,3\}$, are the eigenvalues and eigenvectors of $\boldsymbol{U}$, respectively. The eigenvalues play the role of *principal stretches*. From this, the *Eulerian* or *spatial logarithmic strain* is given by $\boldsymbol{e} \stackrel{\text{def}}{=} \ln \boldsymbol{V} = \boldsymbol{R} \cdot \boldsymbol{\varepsilon} \cdot \boldsymbol{R}^{\mathrm{T}} = \boldsymbol{R}_\star \boldsymbol{\varepsilon}$. It is often referred to as the *Hencky strain* in the literature.

Let $\varphi : \mathcal{B} \times [0,T] \to \mathcal{S}$ be a motion being continuously differentiable with respect to time. The *Lagrangian* or *material rate of deformation tensor* is then defined by

$$2\boldsymbol{D}(X,t) \stackrel{\text{def}}{=} \frac{\partial}{\partial t}\boldsymbol{C}(X,t) = 2\frac{\partial}{\partial t}\boldsymbol{E}(X,t)\,. \tag{3.1.14}$$

Definition 3.1.15. Let $\varphi_t : \mathcal{B} \to \mathcal{S}$ be a regular C^1-motion and $\boldsymbol{D}$ the material rate of deformation on $\mathcal{B}$, then the *Eulerian* or *spatial rate of deformation tensor field* $\boldsymbol{d}$ (also called the *stretching*) is defined by $\boldsymbol{d}_t^\flat \stackrel{\text{def}}{=} \varphi_{t\star}(\boldsymbol{D}_t^\flat)$, where $\boldsymbol{d}_t : \varphi_t(\mathcal{B}) \to T\mathcal{S} \otimes T^*\mathcal{S}$.$_\diamondsuit$

Proposition 3.1.16. *Let $\boldsymbol{v}$ be the spatial velocity and $\boldsymbol{g}$ the spatial metric, then*

$$\boldsymbol{d}^\flat = \tfrac{1}{2}\, \mathrm{L}_{\boldsymbol{v}} \boldsymbol{g}\,.$$

Proof. The assertion follows from (3.1.14) and the previous Definition, together with Propositions 3.1.12 and 3.1.6. An alternative proof can be found in [Marsden and Hughes, 1994, p. 98]. ∎

Using the definition of the spatial rate of deformation tensor and noting that $\nabla_i g_{jk} = 0$, i.e. $\boldsymbol{\nabla}(\boldsymbol{u}^\flat) = (\boldsymbol{\nabla}\boldsymbol{u})^\flat$ for any spatial vector field $\boldsymbol{u} \in \Gamma(T\mathcal{S})$, it can be shown that $d_{ij} = \frac{1}{2}(\nabla_i v_j + \nabla_j v_i)$. Accordingly, the *spatial velocity gradient*,

$$\boldsymbol{l} \stackrel{\text{def}}{=} \boldsymbol{\nabla}\boldsymbol{v} = \boldsymbol{d} + \boldsymbol{\omega} \qquad \stackrel{\text{def}}{=} \left(\frac{\partial \boldsymbol{F}}{\partial t} \cdot \boldsymbol{F}^{-1}\right) \circ \varphi^{-1}\,, \tag{3.1.17}$$

can be decomposed into the symmetric part $\boldsymbol{d}$ and the skew-symmetric part $\boldsymbol{\omega} \stackrel{\text{def}}{=} \frac{1}{2}(\boldsymbol{\nabla}\boldsymbol{v} - (\boldsymbol{\nabla}\boldsymbol{v})^{\mathrm{T}})$, called the *spin* or *vorticity tensor*.

The *material Riemannian volume form* $\mathbf{d}\boldsymbol{V} \in \Omega^m(\mathcal{B})$ on orientable $\mathcal{B}$ is related to the *spatial Riemannian volume form* $\mathbf{d}\boldsymbol{v} \in \Omega^m(\mathcal{S})$ by

$$\varphi_t^\star \mathbf{d}\boldsymbol{v} = \mathbf{d}\boldsymbol{v} \circ \varphi_t = J\, \mathbf{d}\boldsymbol{V}\,, \tag{3.1.18}$$

in accordance with (A.8.20). $J(X,t)$ is the *Jacobian of the motion* φ_t, associated with material particle X and time t.

Proposition 3.1.19.

$$\frac{\partial J}{\partial t} = J(\operatorname{tr} \boldsymbol{d}) \circ \varphi_t \,.$$

PROOF. $(\varphi^\star \mathbf{d}\boldsymbol{v})(X,t) = J(X,t)\,\mathbf{d}\boldsymbol{V}(X)$ by (A.8.20), so $J\,\mathbf{d}\boldsymbol{V}$ is a time-dependent volume form on $\mathcal{B}$. Hence, from Propositions A.8.22 and 3.1.6,

$$\frac{\partial}{\partial t}(J\,\mathbf{d}\boldsymbol{V}) = \varphi_t^\star \pounds_{\boldsymbol{v}} \mathbf{d}\boldsymbol{v} = \varphi_t^\star((\operatorname{div}\boldsymbol{v})\,\mathbf{d}\boldsymbol{v}) = ((\operatorname{div}\boldsymbol{v}) \circ \varphi_t)\, J\,\mathbf{d}\boldsymbol{V}\,,$$

that is, $\frac{\partial}{\partial t} J = J(\operatorname{div}\boldsymbol{v}) \circ \varphi_t$. Since skew-symmetric tensors have zero trace, $\operatorname{div}\boldsymbol{v} = \operatorname{tr}\boldsymbol{l} = \operatorname{tr}\boldsymbol{d}$. ∎

3.1.2 Arbitrarily Moving Reference Domains

The choice of a reference configuration is arbitrary [Noll, 1967, 1972; Truesdell and Noll, 2004; Krawietz, 1986]. Therefore, one may describe the geometry and kinematics of a material body independent of its initial configuration and current configuration, that is, with respect to an arbitrarily moving domain which has some one-to-one correspondence to these configurations of the body. This concept is rather general and had been employed before arbitrary Lagrangian-Eulerian computational methods were developed [e.g. Guo, 1963].

Let $\mathfrak{G}$ be a manifold, which shall be called the *grid manifold* based upon its significance in computational mechanics, and the elements $G \in \mathfrak{G}$ are called the *grid nodes*. Descriptively, the grid manifold is a continuum that has no further properties apart from its topology. However, the topology of $\mathfrak{G}$ should be restricted by the topology of $\mathfrak{B}$ in the following way:

Definition 3.1.20. A subset $\mathfrak{R} \subset \mathfrak{G}$ is referred to as the *reference grid for the material body* provided that the map $\mathfrak{R} \to \mathfrak{B}$ is a homeomorphism (Fig. 3.1). ◊

By definition, the reference grid $\mathfrak{R}$ inherits the topology of the body. The homeomorphism ensures the one-to-one correspondence of grid nodes and particles of the body. In general, the reference grid is neither a differentiable manifold, nor has an inner product or affine connection, hence $\mathfrak{R}$ is embedded topologically into the ambient space by the map $\Theta : \mathfrak{R} \to \mathcal{M} \subset \mathcal{S}$. The differentiable manifold $\mathcal{M} = \Theta(\mathfrak{R})$, which shall be called the *model for* $\mathcal{B}$, is the reference configuration of $\mathfrak{R}$ in $\mathcal{S}$.

Definition 3.1.21. A *grid motion* in the ambient space is an embedding

$$\begin{aligned} \mu_t : \;& \mathcal{M} \to \mathcal{S} \\ & M \mapsto \mu_t(M) \stackrel{\text{def}}{=} \chi\,, \end{aligned}$$

where $\mu_t(M) = \mu(M,t)$ and $t \in [0,T] \subset \mathbb{R}$. The current configuration of $\mathcal{M}$ at time t, $\mathcal{R} \stackrel{\text{def}}{=} \mu_t(\mathcal{M}) \subset \mathcal{S}$, is a submanifold of $\mathcal{S}$ called the *reference domain of the body* ($\neq$ reference configuration), and $\chi \in \mathcal{R}$ denotes the *reference points* (Fig. 3.1). To rule out relativistic effects, it is assumed that the parameter "time" is universal, i.e. all processes on $\mathcal{R}$, $\mathcal{B}$ and $\mathcal{S}$ are synchronous, thus involve the same t. ◊

The arbitrarily moving reference domain $\mathcal{R}$ is differentiable through its embedding in $\mathcal{S}$, and $\dim(\mathcal{R}) = \dim(\mathcal{B}) = \dim(\mathcal{S}) = m$ by definition. Let $\mathcal{W}(\chi) \subset \mathcal{R}$ be an open neighborhood and $(\mathcal{W}, \varrho)$ a chart with local coordinates $\{\chi^1, \dots, \chi^m\}_\chi \stackrel{\text{def}}{=} \{\chi^\alpha\}_\chi = \varrho(\chi) \in \mathbb{R}^n$, then $\{\frac{\boldsymbol{\partial}}{\boldsymbol{\partial}\chi^\alpha}\} \in T_\chi\mathcal{R}$ is a basis of the tangent space at $\chi \in \mathcal{R}$, and $\{\mathbf{d}\chi^\alpha\} \in T^*_\chi\mathcal{R}$ is its dual. The metric coefficients on $\mathcal{W}$ are denoted by $\hat{g}_{\alpha\beta}(\chi) \stackrel{\text{def}}{=} \langle \frac{\boldsymbol{\partial}}{\boldsymbol{\partial}\chi^\alpha}, \frac{\boldsymbol{\partial}}{\boldsymbol{\partial}\chi^\beta} \rangle_\chi$. The symmetric connection associated with the metric coefficients is denoted by $\hat{\boldsymbol{\nabla}}$. Coordinate indices related to the reference domain will usually be denoted by lower case Greek, and vectors, tensors etc. will be marked with a caret if necessary.

Definition 3.1.22. Let

$$\begin{aligned} \Phi_t : \ \mathcal{R} &\to \mathcal{S} \\ \chi &\mapsto x = \Phi_t(\chi) \end{aligned}$$

be a time-dependent embedding of $\mathcal{R}$ in $\mathcal{S}$, and

$$\begin{aligned} \Psi_t : \ \mathcal{R} &\to \mathcal{B} \\ \chi &\mapsto X = \Psi_t(\chi) \end{aligned}$$

a time-dependent diffeomorphism, in which $\Phi_t(\cdot) = \Phi(\cdot, t)$ and $\Psi_t(\cdot) = \Psi(\cdot, t)$ at fixed t. The embedding Φ_t is chosen such that $\Phi_t(\mathcal{R}) = \varphi_t(\mathcal{B})$ at instant t. Clearly, the physical motion $\varphi_t : \mathcal{B} \to \mathcal{S}$ of the body is defined through

$$\varphi_t \stackrel{\text{def}}{=} \Phi_t \circ \Psi_t^{-1} \,,$$

so that $x = \varphi(X, t) = \Phi(\Psi^{-1}(X, t), t) \in \mathcal{S}$ holding t fixed. The maps Φ_t and Ψ_t so defined are then called the *relative map* (or *relative motion*) and the *referential map* (or *referential motion*) of $\mathcal{R}$, respectively. ♢

Recall that the chart of an open neighborhood $\mathcal{U}(X) \subset \mathcal{B}$ is denoted by $(\mathcal{U}, \beta)$, with local coordinate functions $\{X^I\}_X = \beta(X) \in \mathbb{R}^n$. A spatial chart is the pair $(\mathcal{V}, \sigma)$, where $\mathcal{V}(x) \subset \mathcal{S}$ is open, and $\{x^i\}_x = \sigma(x) \in \mathbb{R}^n$. In accordance with Definition 3.1.3, the localizations of the relative map $\Phi_t : \mathcal{R} \to \mathcal{S}$ and the inverse referential map $\Psi_t^{-1} : \mathcal{B} \to \mathcal{R}$ are $\Phi_t^i \stackrel{\text{def}}{=} x^i \circ \Phi_t \circ \varrho^{-1}$ for $\chi \in \mathcal{W} \subset \mathcal{R}$, and $(\Psi_t^{-1})^\alpha \stackrel{\text{def}}{=} \chi^\alpha \circ \Psi_t^{-1} \circ \beta^{-1}$ for $X \in \mathcal{U} \subset \mathcal{B}$, respectively. Therefore, one has

$$\varphi_t^i = x^i \circ \Phi_t \circ \Psi_t^{-1} \circ \beta^{-1} \qquad \text{resp.} \qquad \varphi^i(X^I, t) = \Phi^i(\Psi^{-1}(X^I, t), t) \tag{3.1.23}$$

by Definition 3.1.22 and holding t fixed.

Definition 3.1.24. Let Ψ_t^{-1} and Φ_t defined through 3.1.22 be at least C^1-continuous, then the *referential velocity field on* $\mathcal{R}$ and the *relative velocity field on* $\mathcal{S}$ are defined by their local representatives

$$\begin{aligned} \left(\frac{\partial (\Psi_t^{-1})^\alpha}{\partial t} \circ \Psi_t \right) \frac{\boldsymbol{\partial}}{\boldsymbol{\partial}\chi^\alpha} &\stackrel{\text{def}}{=} \vartheta_t^\alpha(\chi) \frac{\boldsymbol{\partial}}{\boldsymbol{\partial}\chi^\alpha} = \boldsymbol{\vartheta}_t(\chi) \quad \in T_\chi\mathcal{R} \qquad \text{and} \\ \left(\frac{\partial \Phi_t^i}{\partial t} \circ \Phi_t^{-1} \right) \frac{\boldsymbol{\partial}}{\boldsymbol{\partial} x^i} &\stackrel{\text{def}}{=} w_t^i(x) \frac{\boldsymbol{\partial}}{\boldsymbol{\partial} x^i} = \boldsymbol{w}_t(x) \quad \in T_x\mathcal{S} \,, \end{aligned}$$

respectively, so that $\boldsymbol{\vartheta}_t \in \Gamma(T\mathcal{R})$ and $\boldsymbol{w}_t \in \Gamma(T\mathcal{S})$. As usual, $\boldsymbol{\vartheta}_t \overset{\text{def}}{=} \boldsymbol{\vartheta}(\cdot, t)$ and $\boldsymbol{w}_t \overset{\text{def}}{=} \boldsymbol{w}(\cdot, t)$ at fixed t. The referential velocity is the apparent particle velocity on the moving reference domain. $\boldsymbol{w}_t$, which also called the *mesh velocity* in numerical approaches, is the spatial velocity of Φ_t resp. of the reference points χ, generating the generally time-dependent flow $\Phi_t \circ \Phi_s^{-1}$, for $t, s \in \mathcal{I} \subset \mathbb{R}$. ♢

Definition 3.1.25. The tangent maps $T\Psi_t : T\mathcal{R} \to T\mathcal{B}$ and $T\Phi_t : T\mathcal{R} \to T\mathcal{S}$ can be identified with the two-point tensor fields $\boldsymbol{F}_{\Psi t}$ and $\boldsymbol{F}_{\Phi t}$ on $\mathcal{R}$, respectively. Locally, one has

$$\boldsymbol{F}_\Psi(\chi, t) \overset{\text{def}}{=} T_\chi \Psi = \frac{\partial \Psi^I}{\partial \chi^\alpha} \frac{\boldsymbol{\partial}}{\boldsymbol{\partial} X^I} \otimes \mathbf{d}\chi^\alpha \,, \qquad \text{and}$$
$$\boldsymbol{F}_\Phi(\chi, t) \overset{\text{def}}{=} T_\chi \Phi = \frac{\partial \Phi^i}{\partial \chi^\alpha} \frac{\boldsymbol{\partial}}{\boldsymbol{\partial} x^i} \otimes \mathbf{d}\chi^\alpha \,,$$

with $\Psi^I \overset{\text{def}}{=} X^I \circ \Psi \circ \varrho^{-1}$. $\boldsymbol{F}_\Psi$ is called the *referential deformation gradient*, and $\boldsymbol{F}_\Phi$ is called the *relative deformation gradient*. ♢

From the chain rule and Definition 3.1.22, $T\varphi_t = T(\Phi_t \circ \Psi_t^{-1}) = T\Phi_t \circ T(\Psi_t^{-1})$, hence the total deformation gradient is given by the composition

$$\boldsymbol{F}_t = \left(\boldsymbol{F}_{\Phi t} \cdot \boldsymbol{F}_{\Psi t}^{-1}\right) \circ \Psi_t^{-1} \,, \tag{3.1.26}$$

where $\boldsymbol{F}_{\Psi t}^{-1} = T(\Psi_t^{-1}) \circ \Psi_t$.

Theorem 3.1.27 (Convective Velocity). *Let $\boldsymbol{v}$, $\boldsymbol{w}$, and $\boldsymbol{\vartheta}$ be the spatial, relative, and referential velocity fields, respectively. Define the* convective velocity field *on $\mathcal{S}$ through $\boldsymbol{c}_t \overset{\text{def}}{=} \boldsymbol{v}_t - \boldsymbol{w}_t \in \Gamma(T\mathcal{S})$, then*

$$\boldsymbol{c}_t = \Phi_{t\star} \boldsymbol{\vartheta}_t \,.$$

Proof. For vector fields $\boldsymbol{\xi}$ on $\mathcal{R}$, (A.6.5) gives

$$\Phi_{t\star}\boldsymbol{\xi} = T\Phi_t \circ \boldsymbol{\xi} \circ \Phi_t^{-1} = (\boldsymbol{F}_{\Phi t} \cdot \boldsymbol{\xi}) \circ \Phi_t^{-1} \qquad \in \Gamma(T\mathcal{S}) \,,$$

in components $(\frac{\partial \Phi_t^i}{\partial \chi^\alpha} \xi^\alpha) \circ \Phi_t^{-1}$. Now substituting (3.1.23) for the components of the spatial velocity, and keeping track of the point arguments involved yields

$$\begin{aligned} v_t^i &= \frac{\partial \varphi_t^i}{\partial t} \circ \varphi_t^{-1} = \frac{\partial (x^i \circ \Phi_t \circ (\chi^{-1} \circ \chi) \circ \Psi_t^{-1})}{\partial t} \circ \varphi_t^{-1} \\ &= \frac{\partial \Phi_t^i}{\partial t} \circ \Phi_t^{-1} + \frac{\partial \Phi_t^i}{\partial \chi^\alpha} \left(\frac{\partial (\Psi_t^{-1})^\alpha}{\partial t} \circ \Psi_t \right) \circ \Phi_t^{-1} \\ &= w_t^i + \left(\frac{\partial \Phi_t^i}{\partial \chi^\alpha} \vartheta_t^\alpha \right) \circ \Phi_t^{-1} \end{aligned}$$

at $x \in \mathcal{S}$, hence $\boldsymbol{v}_t = \boldsymbol{w}_t + \Phi_{t\star}\boldsymbol{\vartheta}_t$, as desired. ∎

The convective velocity is a proper vector field on $\mathcal{S}$, and forms a fundamental link between the body, its configurations and the reference domain. It denotes the relative

velocity between the particles $X = \varphi_t^{-1}(x)$ and the reference points $\chi = \Phi_t^{-1}(x)$ as measured from the places x.

Let $\mathcal{R} = \Psi_t^{-1}(\mathcal{B})$ be oriented and $\Phi_t : \mathcal{R} \to \mathcal{S}$ orientation preserving, and let $\mathbf{d}\hat{\boldsymbol{v}}$ be the Riemannian volume form on $\mathcal{R}$. According to (A.8.20), $\mathbf{d}\hat{\boldsymbol{v}}$ is related to the Riemannian volume forms $\mathbf{d}\boldsymbol{v}$ on $\varphi_t(\mathcal{B}) = \Phi_t(\mathcal{R}) \subset \mathcal{S}$ and $\mathbf{d}\boldsymbol{V}$ on $\mathcal{B}$ through

$$\Phi_t^\star \mathbf{d}\boldsymbol{v} = J_\Phi \, \mathbf{d}\hat{\boldsymbol{v}} \,, \qquad (\Psi_t^{-1})^\star \mathbf{d}\hat{\boldsymbol{v}} = J_{\Psi^{-1}} \mathbf{d}\boldsymbol{V} \,, \qquad \text{with} \quad J = (J_\Phi \circ \Psi_t^{-1}) \, J_{\Psi^{-1}} \,. \tag{3.1.28}$$

$J_\Phi(\chi, t) \stackrel{\text{def}}{=} \det\left(\frac{\partial \Phi^i}{\partial \chi^\alpha}\right) \frac{\left(\sqrt{\det g_{ij}}\right) \circ \Phi_t}{\sqrt{\det \hat{g}_{\alpha\beta}}}$, by (A.8.21), is the Jacobian of Φ_t and defined as a function of the reference points χ and time t. On the other hand, $J_{\Psi^{-1}}(X, t) = J_\Psi^{-1}(X, t)$ is the Jacobian of Ψ_t^{-1} and taken with respect to a material particle X and time t. The last identity in (3.1.28) is by the chain rule and Definition 3.1.22. As the metric on $\mathcal{R}$ is not explicitly time-dependent, $\mathbf{d}\hat{\boldsymbol{v}}(\chi)$ is also not.

Similar to Proposition 3.1.19, the relations in (3.1.28) yield

$$\frac{\partial J_\Phi}{\partial t} = J_\Phi (\operatorname{div} \boldsymbol{w}) \circ \Phi_t \qquad \text{and} \qquad \frac{\partial J_{\Psi^{-1}}}{\partial t} = J_{\Psi^{-1}} (\operatorname{Div} \boldsymbol{\vartheta}) \circ \Psi_t^{-1} \,, \tag{3.1.29}$$

because the relative velocity $\boldsymbol{w}$ generates the flow $\Phi_t \circ \Phi_s^{-1} : \Phi_s(\mathcal{R}) \to \Phi_t(\mathcal{R})$, and the referential velocity $\boldsymbol{\vartheta}_t$ generates the flow $\Psi_t^{-1} \circ \Psi_s : \Psi_s^{-1}(\mathcal{B}) \to \Psi_t^{-1}(\mathcal{B})$, for all $t, s \in \mathcal{I} \subset \mathbb{R}$. Recall that $\boldsymbol{\vartheta}_t \in \Gamma(T\mathcal{R})$ is a vector field on the reference domain, calling for a proper divergence operator Div on $\mathcal{R}$.

Finally, let $\mathbf{d}\hat{\boldsymbol{a}}$ be the area form on $\partial\mathcal{R}$, then from Nanson's formula A.8.25, the outward normals on $\mathbf{d}\boldsymbol{a}$ and $\mathbf{d}\hat{\boldsymbol{a}}$ are related by

$$\boldsymbol{n}^* = \Phi_{t\star}(J_\Phi \hat{\boldsymbol{n}}^*) = (J_\Phi \circ \Phi_t^{-1}) \boldsymbol{F}_{\Phi t}^{-\mathrm{T}} \cdot \hat{\boldsymbol{n}}^* \,. \tag{3.1.30}$$

and $x \stackrel{\text{def}}{=} \varphi(X, t) \in \mathcal{S}$ for every $X \in \mathcal{B}$ and $t \in \mathcal{I} \subset \mathbb{R}$

3.1.3 Total Derivatives and the ALE Operator

In Section 3.1.1 a distinction has been drawn between the material and the spatial fields, but a proper definition of that terminology is still pending.

Definition 3.1.31. Let $\varphi : \mathcal{B} \times \mathcal{I} \to \mathcal{S}$ be the motion of a material body and define $\mathcal{D} \stackrel{\text{def}}{=} \varphi(\mathcal{B}, t) \subset \mathcal{S}$. Then, depending on whether $x \stackrel{\text{def}}{=} \varphi(X, t) \in \mathcal{S}$ or $X \in \mathcal{B}$ serve as the independent point variables describing a physical field, one refers to $q_t : \mathcal{D} \to T_s^r(\mathcal{S})$ as the *Eulerian* or *spatial representation* and to $Q_t \stackrel{\text{def}}{=} (q_t \circ \varphi_t) : \mathcal{B} \to T_s^r(\mathcal{S})$ as the *Lagrangian* or *material representation* of the field at time t, respectively. The *convected representation* of the field is defined by pulling back the spatial field to the reference configuration, leading to $\varphi_t^\star q_t : \mathcal{B} \to T_s^r(\mathcal{B})$ [cf. Simo et al., 1988]. ♢

The definition generalizes the notion of the Lagrangian and Eulerian velocity fields related by $\boldsymbol{V}_t \stackrel{\text{def}}{=} \boldsymbol{v}_t \circ \varphi_t$. Note that the Eulerian field at fixed t, $q_t(x) \stackrel{\text{def}}{=} q(x, t) = q(\varphi(X, t), t)$, is an honest spatial tensor field, and Q_t is a tensor field over φ_t.

Definition 3.1.32. The *material time derivative* of a field $q(x,t)$ on $\mathcal{S}$ is defined through

$$\dot{q} \stackrel{\text{def}}{=} \frac{\partial q}{\partial t} + \boldsymbol{\nabla}_{\boldsymbol{v}} q \qquad \text{resp.} \qquad \dot{q}(x,t) \stackrel{\text{def}}{=} \left.\frac{\partial q}{\partial t}\right|_x (x,t) + \left(\boldsymbol{\nabla}_{\boldsymbol{v}} q\right)(x,t)\,,$$

where $x = \varphi(X,t)$. The term $\frac{\partial}{\partial t} q$ resp. $\left.\frac{\partial}{\partial t}\right|_x q(x,t)$ is called the *local* or *spatial time derivative* of $q(x,t)$. $\boldsymbol{\nabla}$ denotes the connection on $\mathcal{S}$, and the convective term $\boldsymbol{\nabla}_{\boldsymbol{v}} q$ is the covariant derivative of q along the spatial velocity $\boldsymbol{v}$. ◇

It should be clear that $\boldsymbol{\nabla}_{\boldsymbol{v}} q$ is due to $x = \varphi(X,t)$, thus legitimating the term *material*. By the chain rule, $\dot{q}(\varphi(X,t),t) = \frac{\partial Q}{\partial t}$ resp. $\dot{q}_t = \left(\frac{\partial}{\partial t}\left(q_t \circ \varphi_t\right)\right) \circ \varphi_t^{-1}$. Hence, *total* or *substantial derivatives* of $Q(X,t)$ and $q(x,t)$, with $x = \varphi(X,t)$, can be defined through

$$\frac{\partial Q}{\partial t}(X,t) \qquad \text{and} \qquad \dot{q}(x,t)\,, \tag{3.1.33}$$

respectively.

Definition 3.1.34. Let $\varphi_t = \Phi_t \circ \Psi_t^{-1} : \mathcal{B} \to \mathcal{S}$ be the motion of a material body, $q_t : \varphi_t(\mathcal{B}) \to T^r_s(\mathcal{S})$ the spatial formulation of a field, and $\mathcal{R} = \Psi_t^{-1}(\mathcal{B})$ the arbitrarily moving reference domain, then $\hat{q}_t \stackrel{\text{def}}{=} (q_t \circ \Phi_t) : \mathcal{R} \to T^r_s(\mathcal{S})$ is called the *arbitrary Lagrangian-Eulerian (ALE)* or *referential representation* of the field at fixed t. ◇

Definitions (3.1.31) and the latter yield

$$q_t = \hat{q}_t \circ \Phi_t^{-1} \qquad \text{and} \qquad Q_t = \hat{q}_t \circ \Psi_t^{-1}\,. \tag{3.1.35}$$

The general ALE operator stated next relates the Lagrangian, Eulerian, and ALE time derivatives on manifolds. Its derivation makes use of a preliminary result that accounts for the total time derivative on the reference domain.

Proposition 3.1.36. *Let the mappings Φ_t and Ψ_t^{-1} be at least C^1, and let $\mathcal{R} \stackrel{\text{def}}{=} \Psi_t^{-1}(\mathcal{B})$ be a reference domain of the body. Let $\hat{q}_t = (q_t \circ \Phi_t) : \mathcal{R} \to T^r_s(\mathcal{S})$ be the ALE formulation of a field $q_t(x) = q(x,t)$, $\boldsymbol{\vartheta}$ the referential velocity of Definition 3.1.24, and let $\boldsymbol{\nabla}^\star$ be the Φ_t-induced connection on $\mathcal{R}$ of the spatial connection $\boldsymbol{\nabla}$ according to Theorem A.7.2. Then, the total time derivative of $\hat{q}$, denoted as $\hat{q}'$, is given by*

$$\hat{q}'(\chi,t) = \left.\frac{\partial \hat{q}}{\partial t}\right|_\chi (\chi,t) + \boldsymbol{\nabla}^\star_{\boldsymbol{\vartheta}} \hat{q}(\chi,t)\,,$$

where $\chi = \Psi_t^{-1}(X) \in \mathcal{R}$.

Proof. Recall that the Eulerian field $q_t \in \mathfrak{T}^r_s(\mathcal{S})$ is an honest tensor field on $\mathcal{S}$, and the ALE field $\hat{q}_t = q_t \circ \Phi_t$ is a tensor field over Φ_t, that is, a Φ_t-induced section of the tensor bundle $T^r_s(\mathcal{S})$; see Section A.6. Therefore, $\hat{q}'$ and the terms on the right hand side also are. Now assume without loss of generality that $q_t \in \Gamma(T\mathcal{S})$ is a vector field having the local representative $q_t(x) = q_t^i(x)\frac{\partial}{\partial x^i}$ in a chart $(\mathcal{V},\sigma)$ on $\mathcal{S}$, so that

$\hat{q}_t(\chi) = (q_t^i \circ \Phi_t)(\chi) \frac{\partial}{\partial x^i}$. The components $(q_t^i \circ \Phi_t)$ functionally depend on the coordinates $\{\chi^\alpha\}$ of a subset $\mathcal{W} \subset \mathcal{R}$.

The covariant derivative of vector-valued $\hat{q}$, $\boldsymbol{\nabla}^\star \hat{q}_t \in \Gamma(T^*\mathcal{R} \otimes \Phi_t^\star T\mathcal{S})$, is a two-point tensor field for fixed t, calling for the Φ_t-induced connection $\boldsymbol{\nabla}^\star$ on $\mathcal{R}$ (see Theorem A.7.2). Thus, for the proposed time derivative to make sense, $\boldsymbol{\nabla}^\star \hat{q}_t$ must be contracted by an honest vector field on $\mathcal{R}$, say $\boldsymbol{\vartheta} = \vartheta^\alpha \frac{\partial}{\partial \chi^\alpha} \in \Gamma(T\mathcal{R})$. In local coordinates, and by keeping track of the point arguments,

$$\boldsymbol{\nabla}^\star_{\boldsymbol{\vartheta}} \hat{q}\,(\chi, t) = \left(\frac{\partial (q^i \circ \Phi)}{\partial \chi^\alpha} \vartheta^\alpha + \vartheta^\alpha (q^j \circ \Phi) \left(\gamma_j{}^i{}_k \circ \Phi \right) (\boldsymbol{F}_\Phi)^k{}_\alpha \right) \frac{\boldsymbol{\partial}}{\boldsymbol{\partial} x^i}\,,$$

where $\gamma_j{}^i{}_k(x)$ are the coefficients of $\boldsymbol{\nabla}$ on $\mathcal{S}$, and $(\gamma_j{}^i{}_k (\boldsymbol{F}_\Phi)^k{}_\alpha)(\chi, t)$ are the coefficients of $\boldsymbol{\nabla}^\star$.

To show that $\boldsymbol{\vartheta}$ in the convective term $\boldsymbol{\nabla}^\star_{\boldsymbol{\vartheta}} \hat{q}$ must be the referential velocity, and to proof the assertion, use the condition that for $\Phi_t = \mathrm{id}_\mathcal{S}$, the proposed material time derivative for $\hat{q}$ must reduce to the material time derivative of q defined by 3.1.32. Indeed, in this case $\boldsymbol{\nabla}^\star = \boldsymbol{\nabla}$, $\Psi_t^{-1} = \varphi_t$, and $(\mathrm{id}_\mathcal{S})_\star \boldsymbol{\vartheta} = \boldsymbol{v}$ by 3.1.27. ∎

Theorem 3.1.37 (General ALE Operator). *Let Q, q and $\hat{q}$, respectively, be the Lagrangian, Eulerian and ALE formulation of the same time-dependent tensor-valued physical field, then*

$$\frac{\partial Q}{\partial t} \circ \Psi = \frac{\partial \hat{q}}{\partial t} + \boldsymbol{\nabla}_{(\boldsymbol{c} \circ \Phi)} q\,,$$

where $\boldsymbol{c}$ is the convective velocity of Theorem 3.1.27.

Proof. From Theorem 3.1.27, $\boldsymbol{c}_t \circ \Phi_t = T\Phi_t(\boldsymbol{\vartheta}_t)$, hence

$$(\boldsymbol{\nabla}^\star_{\boldsymbol{\vartheta}} \hat{q})(\chi, t) = (\boldsymbol{\nabla}_{(\boldsymbol{c} \circ \Phi)} q)(\chi, t)$$

by Theorem A.7.2. As $Q_t = \hat{q}_t \circ \Psi_t^{-1}$ is the corresponding Lagrangian field, $\frac{\partial Q}{\partial t} = \hat{q}'(\Psi^{-1}(X, t), t)$ resp. $\hat{q}'_t = (\frac{\partial}{\partial t}(\hat{q}_t \circ \Psi_t^{-1})) \circ \Psi_t$ again by the chain rule. Replacing the respective terms in Proposition 3.1.36 then finally gives the desired result. ∎

Remark 3.1.38. The Lagrangian and Eulerian formulations are special cases of the ALE formulation. If $\Psi_t = \mathrm{id}_\mathcal{R}$, then $\boldsymbol{w} = \boldsymbol{v}$ and $\boldsymbol{c} = \boldsymbol{0}$, and the Lagrangian formulation is obtained: the observer moves with the particles. If $\Phi_t = \mathrm{id}_\mathcal{R}$ on the other hand, then $\boldsymbol{w} = \boldsymbol{0}$ and $\boldsymbol{c} = \boldsymbol{v}$, which is the basic principle of the Eulerian formulation: the observer permanently takes up the same spatial points. △

Remark 3.1.39. In the literature, the point-dependency of the ALE operator is often ignored in order to simplify notation. Without indicating the points, and by suppressing the arguments, Theorem 3.1.37 reads

$$\dot{q} = \frac{\partial \hat{q}}{\partial t} + \boldsymbol{\nabla}_{\boldsymbol{c}} q\,.$$

It is crucial to keep in mind that the local time derivative $\frac{\partial}{\partial t} \hat{q}$ is an abbreviation for $\frac{\partial (q \circ \Phi)}{\partial t} \circ \Phi^{-1}$. △

3.2 Balance Principles

The balance principles presented in this section include the basic dynamical equations of continuum mechanics and inequalities from thermodynamics: conservation of mass, balance of linear and angular momentum, balance of energy (first law of thermodynamics), and the entropy production inequality (second law of thermodynamics). The principles will largely be set up in both integral and local forms for all Lagrangian (material), Eulerian (spatial), and ALE (referential) formulations. Both the convective and conservative forms of local balance principles will be presented.

The notations and definitions of Section 3.1 are used throughout. The body $\mathcal{B}$, the space $\mathcal{S}$, and the reference domain $\mathcal{R}$ are same dimensional Riemannian manifolds, that is, differentiable, metrizable, and with symmetric connections. Charts include the coordinate functions X^I, x^i, and χ^α, respectively, and chart transitions are assumed to be regular. The physical motion $\varphi_t \overset{\text{def}}{=} (\Phi_t \circ \Psi_t^{-1}) : \mathcal{B} \to \mathcal{S}$ is at least C^1, and $\boldsymbol{V}(X,t)$ is the material velocity, $\boldsymbol{v}(x,t)$ is the spatial velocity of φ, and $\boldsymbol{c}(x,t)$ is the convective velocity. $\mathcal{B}$, $\mathcal{S}$, and $\mathcal{R}$ are orientable, with Riemannian volume forms denoted by $\mathbf{d}\boldsymbol{V}$, $\mathbf{d}\boldsymbol{v}$, and $\mathbf{d}\hat{\boldsymbol{v}}$, respectively. $J(X,t)$ is the Jacobian of φ_t, $J_\Phi(\chi,t)$ is the Jacobian of Φ_t, and $J_{\Psi^{-1}}(X,t)$ is the Jacobian of Ψ_t^{-1}. As $\mathcal{B}$, $\mathcal{S}$, and $\mathcal{R}$ are postulated to have their own metrics and connections, they also provide divergence operators distinguished by DIV, div, and Div, respectively.

Subsets $\mathcal{U} \subset \mathcal{B}$, $\varphi_t(\mathcal{U}) \subset \varphi_t(\mathcal{B})$, and $\mathcal{W} \subset \mathcal{R}$ are called *nice* if they have at least piecewise C^1-continuous boundaries $\partial\mathcal{U}$, $\partial(\varphi_t(\mathcal{U})) = \varphi_t(\partial\mathcal{U})$, and $\partial\mathcal{W}$, respectively. Note that at each of these boundaries the Riemannian volume form can be represented by the exterior product of the outward normals and area form of the boundary. That is, $\mathbf{d}\boldsymbol{V} \overset{\text{def}}{=} \boldsymbol{N}^* \wedge \mathbf{d}\boldsymbol{A}$, $\mathbf{d}\boldsymbol{v} \overset{\text{def}}{=} \boldsymbol{n}^* \wedge \mathbf{d}\boldsymbol{a}$, and $\mathbf{d}\hat{\boldsymbol{v}} \overset{\text{def}}{=} \hat{\boldsymbol{n}}^* \wedge \mathbf{d}\hat{\boldsymbol{a}}$, respectively. Additional assumptions and restrictions will be specified as needed.

3.2.1 Transport Theorems and Master Balance Principles

Before deriving relations for the rate of change of integral quantities (extensive quantities), those conditions are formalized under which the Lagrangian, Eulerian, and ALE integral quantities are equivalent.

Proposition 3.2.1. *In addition to the above assumptions, let φ_t, Φ_t, and Ψ_t, with $\varphi_t = \Phi_t \circ \Psi_t^{-1}$, be orientation preserving, and let $\mathcal{U}$ and $\mathcal{W}$ instantaneously occupy the same region of space at time t, i.e. $\varphi_t(\mathcal{U}) = \Phi_t(\mathcal{W}) \subset \mathcal{S}$.*

(i) Let $q : \varphi_t(\mathcal{U}) \to \mathbb{R}$ be a $\mathbf{d}\boldsymbol{v}$-integrable spatial scalar field, then

$$\int_{\varphi_t(\mathcal{U})} q\, \mathbf{d}\boldsymbol{v} = \int_{\mathcal{U}} QJ\, \mathbf{d}\boldsymbol{V} = \int_{\mathcal{W}} \hat{q} J_\Phi\, \mathbf{d}\hat{\boldsymbol{v}} = \int_{\Phi_t(\mathcal{W})} q\, \mathbf{d}\boldsymbol{v}\ .$$

(ii) Let $h : \varphi_t(\mathcal{U}) \to \mathbb{R}$ be a $\mathbf{d}\boldsymbol{a}$-integrable spatial scalar field, then

$$\int_{\partial\varphi_t(\mathcal{U})} h\, \mathbf{d}\boldsymbol{a} = \int_{\partial\mathcal{U}} HJ \sqrt{\boldsymbol{N}^* \cdot (\boldsymbol{C}^{-1})^\sharp \cdot \boldsymbol{N}^*}\, \mathbf{d}\boldsymbol{A} = \int_{\partial\mathcal{W}} \hat{h} J_\Phi \sqrt{\hat{\boldsymbol{n}}^* \cdot \Phi_t^\star(\boldsymbol{g}^\sharp) \cdot \hat{\boldsymbol{n}}^*}\, \mathbf{d}\hat{\boldsymbol{a}}$$

provided that $\boldsymbol{N}^*$, $\boldsymbol{n}^*$, *and* $\hat{\boldsymbol{n}}^*$ *have unit length.*

PROOF. According to 3.1.31 and 3.1.34, the Lagrangian and ALE descriptions of any scalar-valued spatial function f are defined through $F \overset{\text{def}}{=} f \circ \varphi$ and $\hat{f} \overset{\text{def}}{=} f \circ \Phi$, respectively.

(i) From (A.8.20) and (3.1.28), $\varphi^\star \mathbf{d}\boldsymbol{v} = J\,\mathbf{d}\boldsymbol{V}$ and $\Phi^\star \mathbf{d}\boldsymbol{v} = J_\Phi\,\mathbf{d}\hat{\boldsymbol{v}}$. Then apply the change of variables formula A.8.15, and the chain rule for pullbacks $(\text{A.6.6})_1$.

(ii) The image $H = h \circ \varphi$ of h is well-defined on $\partial\mathcal{U}$, and $\hat{h} = h \circ \Phi$ is defined on $\partial\mathcal{W}$, because both φ_t and Φ_t are assumed diffeomorphisms [Abraham et al., 1983, lemma 7.2.4]. Note $\varphi_t(\partial\mathcal{B}) = \partial\varphi_t(\mathcal{B})$, then Theorem A.8.26 proofs the assertion. ∎

Theorem 3.2.2 (Transport Theorem). *Let* $\varphi_t : \mathcal{B} \to \mathcal{S}$ *be the motion of a material body,* $\mathcal{U} \subset \mathcal{B}$ *a nice* n*-dimensional subset, and* $\boldsymbol{\mu}_t \in \Omega^n(\mathcal{S})$ *a time-dependent* n*-form (resp. volume form) on* $\mathcal{S}$*, then*

$$\frac{\mathrm{d}}{\mathrm{d}t}\int_{\varphi_t(\mathcal{U})} \boldsymbol{\mu} = \int_{\varphi_t(\mathcal{U})} \mathrm{L}_{\boldsymbol{v}}\boldsymbol{\mu}\,.$$

PROOF. This should be proven for the well-known case $\boldsymbol{\mu}(x,t) \overset{\text{def}}{=} q(x,t)\,\mathbf{d}\boldsymbol{v}(x)$, where $q : \mathcal{S}\times\mathbb{R} \to \mathbb{R}$ is a time-dependent spatial scalar field. As $\mathrm{L}_{\boldsymbol{v}}$ is a derivation, $\mathrm{L}_{\boldsymbol{v}}(q\,\mathbf{d}\boldsymbol{v}) = (\mathrm{L}_{\boldsymbol{v}}q)\,\mathbf{d}\boldsymbol{v} + q\,\mathrm{L}_{\boldsymbol{v}}(\mathbf{d}\boldsymbol{v})$ by Leibniz' rule. Then for the first term,

$$\mathrm{L}_{\boldsymbol{v}}q = \frac{\partial q}{\partial t} + \boldsymbol{i}_{\boldsymbol{v}}\mathbf{d}q = \frac{\partial q}{\partial t} + \mathbf{d}q \cdot \boldsymbol{v} = \dot{q}$$

by Cartan's formula (A.8.9) together with (A.4.12), and

$$\mathrm{L}_{\boldsymbol{v}}(\mathbf{d}\boldsymbol{v}) = \frac{\partial(\mathbf{d}\boldsymbol{v})}{\partial t} + \boldsymbol{i}_{\boldsymbol{v}}\mathbf{d}(\mathbf{d}\boldsymbol{v}) + \mathbf{d}\boldsymbol{i}_{\boldsymbol{v}}(\mathbf{d}\boldsymbol{v}) = \mathbf{d}\boldsymbol{i}_{\boldsymbol{v}}(\mathbf{d}\boldsymbol{v}) = (\operatorname{div}\boldsymbol{v})\,\mathbf{d}\boldsymbol{v}\,,$$

in which the condition $\mathbf{d}\mathbf{d}\boldsymbol{v} = \mathbf{0}$ and Proposition A.8.22 have been used. Then proving the preliminary result

$$\frac{\mathrm{d}}{\mathrm{d}t}\int_{\varphi_t(\mathcal{U})} q\,\mathbf{d}\boldsymbol{v} = \int_{\varphi_t(\mathcal{U})} (\dot{q} + q\operatorname{div}\boldsymbol{v})\,\mathbf{d}\boldsymbol{v}$$

is a standard exercise that can be found in the textbooks on continuum mechanics [e.g. Gurtin, 1981; Marsden and Hughes, 1994]. ∎

The result 3.2.2 is sometimes called the generalized transport theorem, because it has been set up for general n-forms and not only for scalar fields. However, note there is an even more generalized version on arbitrarily moving reference domains:

Theorem 3.2.3 (Generalized Transport Theorem). *Let* $\varphi_t = \Phi_t \circ \Psi_t^{-1}$ *be the motion of a material body, and* $\mathcal{R} = \Psi_t^{-1}(\mathcal{B})$ *an arbitrarily moving reference domain. Let* $\mathcal{U} \subset \mathcal{B}$ *and* $\mathcal{W} \subset \mathcal{R}$ *be nice* n*-dimensional subsets, and* $\boldsymbol{\mu}_t \in \Omega^n(\mathcal{S})$ *a time-dependent* n*-form on* $\mathcal{S}$*, then*

$$\frac{\mathrm{d}}{\mathrm{d}t}\int_{\varphi_t(\mathcal{U})} \boldsymbol{\mu} = \frac{\mathrm{d}}{\mathrm{d}t}\int_{\Phi_t(\mathcal{W})} \boldsymbol{\mu} + \int_{\varphi_t(\mathcal{U})} \pounds_{\boldsymbol{c}}\boldsymbol{\mu}\,.$$

PROOF. From the property $\mathrm{L}_{\boldsymbol{v}} = \mathrm{L}_{\boldsymbol{w}+\boldsymbol{c}} = \pounds_{\boldsymbol{w}} + \mathrm{L}_{\boldsymbol{c}} = \mathrm{L}_{\boldsymbol{w}} + \pounds_{\boldsymbol{c}}$ of the Lie derivative, Theorem 3.2.2 becomes $\frac{\mathrm{d}}{\mathrm{d}t}\int_{\varphi_t(\mathcal{U})} \boldsymbol{\mu} = \int_{\varphi_t(\mathcal{U})} \mathrm{L}_{\boldsymbol{w}}\boldsymbol{\mu} + \int_{\varphi_t(\mathcal{U})} \pounds_{\boldsymbol{c}}\boldsymbol{\mu}$. For the first term on the right hand side, note that

$$\int_{\varphi_t(\mathcal{U})} \mathrm{L}_{\boldsymbol{w}}\boldsymbol{\mu} = \int_{\mathcal{U}=\Psi_t(\mathcal{W})} \varphi_t^\star(\mathrm{L}_{\boldsymbol{w}}\boldsymbol{\mu}) = \int_{\mathcal{W}} (\Psi_t^\star \circ \varphi_t^\star)(\mathrm{L}_{\boldsymbol{w}}\boldsymbol{\mu}) = \int_{\mathcal{W}} \Phi_t^\star(\mathrm{L}_{\boldsymbol{w}}\boldsymbol{\mu}) = \int_{\Phi_t(\mathcal{W})} \mathrm{L}_{\boldsymbol{w}}\boldsymbol{\mu}$$

by the change of variables formula A.8.15 and the chain rule for pullbacks. Since the domain $\mathcal{W}$ over which should be integrated is kept fixed with respect to Φ_t, and $\boldsymbol{w}$ is the spatial velocity of Φ_t,

$$\int_{\mathcal{W}} \Phi_t^\star(\mathrm{L}_{\boldsymbol{w}}\boldsymbol{\mu}) = \int_{\mathcal{W}} \frac{\partial}{\partial t}(\Phi_t^\star\boldsymbol{\mu}) = \frac{\mathrm{d}}{\mathrm{d}t}\int_{\mathcal{W}} \Phi_t^\star\boldsymbol{\mu} = \frac{\mathrm{d}}{\mathrm{d}t}\int_{\Phi_t(\mathcal{W})} \boldsymbol{\mu}$$

by Proposition 3.1.6 and changing the variables again. Substitution into the transport theorem 3.2.2 finally proofs the assertion. ∎

To the best knowledge of the author, 3.2.3 is the first statement of a generalized transport theorem for arbitrarily moving manifolds. The version 3.2.2 is recovered by choosing $\Phi_t = \mathrm{id}_{\mathcal{R}}$, for which $\boldsymbol{w} = \boldsymbol{0}$, $\frac{\mathrm{d}}{\mathrm{d}t}\int_{\mathcal{W}=\varphi_t(\mathcal{U})} \boldsymbol{\mu} = \int_{\varphi_t(\mathcal{U})} \frac{\partial}{\partial t}\boldsymbol{\mu}$, and $\boldsymbol{c} = \boldsymbol{v}$. On the other hand, setting $\Psi_t = \mathrm{id}_{\mathcal{R}}$ yields $\boldsymbol{w} = \boldsymbol{v}$, $\boldsymbol{c} = \boldsymbol{0}$, and the identity $\frac{\mathrm{d}}{\mathrm{d}t}\int_{\varphi_t(\mathcal{U})} \boldsymbol{\mu} = \int_{\mathcal{U}} \frac{\partial}{\partial t}(\varphi_t^\star\boldsymbol{\mu})$ by changing variables.

With the transport theorems at hand one can pass over to balance principles. Most of the basic dynamical equations or inequalities of continuum mechanics can be cast in an abstract master balance principle as follows.

Definition 3.2.4. Let $q(x,t)$, $b(x,t)$, and $u(x,t,\boldsymbol{n}^*(x))$ be spatial scalar fields defined for every $x \in \varphi_t(\mathcal{B})$, $t \in \mathcal{I} \subset \mathbb{R}$, and let $\boldsymbol{n}^* \in \Gamma(T^*(\varphi_t(\mathcal{U})))$ be the unit outward normals on $\partial(\varphi_t(\mathcal{U}))$. Let $\mathcal{U} \subset \mathcal{B}$ be nice, then q, b, and u satisfy the *Eulerian* or *spatial master balance principle* provided that

$$\frac{\mathrm{d}}{\mathrm{d}t}\int_{\varphi_t(\mathcal{U})} q(x,t)\,\mathbf{d}\boldsymbol{v} = \int_{\varphi_t(\mathcal{U})} b(x,t)\,\mathbf{d}\boldsymbol{v} + \int_{\partial\varphi_t(\mathcal{U})} u(x,t,\boldsymbol{n}^*(x))\,\mathbf{d}\boldsymbol{a}\,,$$

and the time derivation of $\int_{\varphi_t(\mathcal{U})} q\,\mathbf{d}\boldsymbol{v}$ together with the integrals do exist. The functions b and u can be regarded given *sources* per unit volume and unit area, respectively. ♢

Definition 3.2.5. The quantities q, b, and u defined before are said to satisfy the *Eulerian* or *spatial master inequality principle* if

$$\frac{\mathrm{d}}{\mathrm{d}t}\int_{\varphi_t(\mathcal{U})} q(x,t)\,\mathbf{d}\boldsymbol{v} \geq \int_{\varphi_t(\mathcal{U})} b(x,t)\,\mathbf{d}\boldsymbol{v} + \int_{\partial\varphi_t(\mathcal{U})} u(x,t,\boldsymbol{n}^*(x))\,\mathbf{d}\boldsymbol{a}\,.$$

The quantity q is called *balanced* if "=", and *produced* if ">". ♢

Definition 3.2.6. In the two definitions above, the quantity q is said to be *conserved* with respect to the moving domain $\varphi_t(\mathcal{U})$ if it is balanced and the sources b and u are both zero. ♢

The form of the integrand $u(x,t,\boldsymbol{n}^*(x))$ in the spatial master balance principle is related to a cornerstone of continuum mechanics; for a proof, see [Marsden and Hughes, 1994, ch. 2]:

Theorem 3.2.7 (Cauchy's Theorem). *Let $q(x,t)$, $b(x,t)$, and $u(x,t,\boldsymbol{n}^*(x))$ be C^0-continuous time-dependent spatial scalar fields that satisfy the spatial master balance principle 3.2.4 on $\mathcal{V} = \varphi_t(\mathcal{U}) \subset \mathcal{S}$, then there exists a unique time-dependent spatial vector field $\boldsymbol{u}_t \in \Gamma(T\mathcal{V})$ such that*

$$u(x,t,\boldsymbol{n}^*(x)) = \boldsymbol{u}(x,t) \cdot \boldsymbol{n}^*(x)\,,$$

that is, u depends linearly on the surface normal $\boldsymbol{n}^*$.

Definition 3.2.8. Let $\varphi_t = (\Phi_t \circ \Psi_t^{-1}) : \mathcal{B} \to \mathcal{S}$ be the motion of a material body, $\mathcal{U} \subset \mathcal{B}$, $\mathcal{W} \subset \mathcal{R}$, and $\varphi_t(\mathcal{U}) = \Phi_t(\mathcal{W}) \subset \mathcal{S}$. Let $q : \varphi_t(\mathcal{U}) \to T^r_s(\mathcal{S})$ be a spatial $\binom{r}{s}$-tensor field.

(i) The *flux density of the field q governed by the material velocity field* $\boldsymbol{v} = (\frac{\partial}{\partial t}\varphi_t) \circ \varphi_t^{-1}$ is a generally nonlinear function $\boldsymbol{f}(q) \stackrel{\text{def}}{=} \boldsymbol{h}(q,\boldsymbol{v})$ having values in the tensor space $T^{r+1}_s(\mathcal{S}) = T^r_s(\mathcal{S}) \otimes T\mathcal{S}$. The flux density is called *linear* if $\boldsymbol{f}(q) = q \otimes \boldsymbol{v}$, respectively $\boldsymbol{f}(q) = q\boldsymbol{v}$ for $q_t : \varphi_t(\mathcal{U}) \to \mathbb{R}$ being scalar-valued.

(ii) The *convective flux density of the field q governed by the convective velocity field* $\boldsymbol{c} = \boldsymbol{v} - \boldsymbol{w}$ is the function defined through [cf. Lesoinne and Farhat, 1996]

$$\boldsymbol{\psi}(q) \stackrel{\text{def}}{=} \boldsymbol{f}(q) - q \otimes \boldsymbol{w}\,,$$

where $\boldsymbol{w} = (\frac{\partial}{\partial t}\Phi_t) \circ \Phi_t^{-1}$ is the spatial velocity of the map Φ_t, and $\boldsymbol{f}(q)$ is the flux density of (i). In the simplest linear case one has $\boldsymbol{\psi}(q) = q \otimes \boldsymbol{c}$, respectively $\boldsymbol{\psi}(q) = q\boldsymbol{c}$ if $q_t : \varphi_t(\mathcal{U}) \to \mathbb{R}$ is scalar-valued. ♢

Proposition 3.2.9. *Let the quantities $q(x,t)$, $b(x,t)$, and $u(x,t,\boldsymbol{n}^*(x))$ satisfy the spatial master balance principle 3.2.4, and let the source per unit area moreover satisfy Cauchy's theorem 3.2.7. Then,*

$$\frac{\partial q}{\partial t} + \operatorname{div} \boldsymbol{f}(q) = b + \operatorname{div} \boldsymbol{u}\,,$$

where $\boldsymbol{f}(q) = q\boldsymbol{v}$.

Proof. By the transport theorem 3.2.2 and the divergence theorem A.8.24 together with the requirement that the resulting equation holds for any nice subset $\varphi_t(\mathcal{U})$. ∎

A special case of this form is obtained when the sources b and $\boldsymbol{u}$ vanish. Taking the integral over a spatially fixed control volume $\mathcal{V}$ and applying the applying the divergence theorem results in the generic *integral conservation law*

$$\int_{\mathcal{V}} \frac{\partial q}{\partial t}\, \mathbf{d}\boldsymbol{v} + \int_{\partial\mathcal{V}} \boldsymbol{f}(q) \cdot \boldsymbol{n}^*\, \mathbf{d}\boldsymbol{a} = 0\,. \tag{3.2.10}$$

The integral conservation law is a basic element in computational fluid dynamics.

Definition 3.2.11. Proposition 3.2.9 provides the so-called *conservation form* of the *localized spatial master balance principle*. The equivalent *convective form* of the localized spatial master balance principle reads

$$\frac{\partial q}{\partial t} + \mathbf{d}q \cdot \boldsymbol{v} = b + \operatorname{div} \boldsymbol{u} - q \operatorname{div} \boldsymbol{v} \,.$$

The *Lagrangian* or *material form* of the spatial balance principle employs the material time derivative 3.1.32 to get

$$\dot{q} = b + \operatorname{div} \boldsymbol{u} - q \operatorname{div} \boldsymbol{v} \,. \qquad \diamondsuit$$

Another material version of the master balance principle can be obtained from the spatial version, 3.2.4, by changing the domain of the integral to $\mathcal{U}$, applying the change of variables theorem A.8.15, and stipulating

$$\begin{aligned} Q(X,t) &\stackrel{\text{def}}{=} q(\varphi(X,t),t)\,, \\ B(X,t) &\stackrel{\text{def}}{=} b(\varphi(X,t),t)\,, \text{ and} \\ \boldsymbol{U}(X,t) &\stackrel{\text{def}}{=} J(X,t)(\boldsymbol{F}^{-1})(X,t) \cdot (\boldsymbol{u}(\varphi(X,t),t))\,, \end{aligned} \tag{3.2.12}$$

so that $\boldsymbol{U}$ is the Piola transform of $\boldsymbol{u}$, and $x = \varphi(X,t)$. Then Q, B, and $\boldsymbol{U}$ are said to satisfy the *Lagrangian* or *material master balance principle* provided that

$$\frac{\mathrm{d}}{\mathrm{d}t} \int_{\mathcal{U}} Q(X,t) J(X,t) \, \mathbf{d}\boldsymbol{V} = \int_{\mathcal{U}} B(X,t) J(X,t) \, \mathbf{d}\boldsymbol{V} + \int_{\partial \mathcal{U}} \boldsymbol{U}(X,t) \cdot \boldsymbol{N}^*(X) \, \mathbf{d}\boldsymbol{A}\,, \tag{3.2.13}$$

where $\boldsymbol{N}^* \in \Gamma(T^*\mathcal{U})$ are the unit outward normals on $\partial\mathcal{U}$. The *Lagrangian* or *material master inequality principle* is obtained by replacing "=" with "≥".

Definition 3.2.14. The *convective form of the localized ALE master balance principle*,

$$\frac{\partial \hat{q}}{\partial t} \circ \Phi_t^{-1} + \boldsymbol{\nabla}_{\boldsymbol{c}} q = b + \operatorname{div} \boldsymbol{u} - q \operatorname{div} \boldsymbol{v}\,,$$

is obtained by substituting the ALE operator 3.1.37 for the material time derivative of the field $q(x,t)$ in the localized spatial master balance principle 3.2.9 resp. its material form. $\diamondsuit$

The previous definition provides one means of an ALE master balance principle. From a computational point of view, however, the integral form of the modified spatial master balance principle stated next is more common [cf. Zhang et al., 1993; Scovazzi, 2007; Scovazzi and Hughes, 2007].

Theorem 3.2.15 (Quasi-Spatial Master Balance Principle). *Let $\hat{q}_t = q_t \circ \Phi_t : \mathcal{R} \to \mathbb{R}$ be the referential field corresponding to $q(x,t)$, and $\Phi_t(\mathcal{W}) = \varphi_t(\mathcal{U}) \subset \mathcal{S}$, then the spatial master balance principle can be written*

$$\int_{\Phi_t(\mathcal{W})} \Phi_{t\star} \left(J_\Phi^{-1} \frac{\partial \hat{q} J_\Phi}{\partial t} \right) \mathbf{d}\boldsymbol{v} = \int_{\varphi_t(\mathcal{U})} b \, \mathbf{d}\boldsymbol{v} + \int_{\partial \varphi_t(\mathcal{U})} (\boldsymbol{u} - \boldsymbol{\psi}(q)) \cdot \boldsymbol{n}^* \, \mathbf{d}\boldsymbol{a}\,,$$

where $\boldsymbol{\psi}(q) = q\boldsymbol{c}$ is the flux density of q governed by the convective velocity.

PROOF. The generalized transport theorem provides $\frac{\mathrm{d}}{\mathrm{d}t}\int_{\varphi_t(\mathcal{U})} q\,\mathbf{d}\boldsymbol{v} = \frac{\mathrm{d}}{\mathrm{d}t}\int_{\Phi_t(\mathcal{W})} q\,\mathbf{d}\boldsymbol{v} + \int_{\varphi_t(\mathcal{U})} \pounds_{\boldsymbol{c}}(q\,\mathbf{d}\boldsymbol{v})$, in which the first term on the right hand side can be written as

$$\begin{aligned}\frac{\mathrm{d}}{\mathrm{d}t}\int_{\Phi_t(\mathcal{W})} q\,\mathbf{d}\boldsymbol{v} &= \frac{\mathrm{d}}{\mathrm{d}t}\int_{\mathcal{W}} \Phi_t^\star(q\,\mathbf{d}\boldsymbol{v}) = \int_{\mathcal{W}} \frac{\partial \hat{q} J_\Phi}{\partial t}\,\mathbf{d}\hat{\boldsymbol{v}} \\ &= \int_{\mathcal{W}} J_\Phi^{-1}\frac{\partial \hat{q}\, J_\Phi}{\partial t}\,\Phi_t^\star \mathbf{d}\boldsymbol{v} = \int_{\Phi_t(\mathcal{W})} \Phi_{t\star}\left(J_\Phi^{-1}\frac{\partial \hat{q} J_\Phi}{\partial t}\right)\mathbf{d}\boldsymbol{v}\end{aligned}$$

by the change of variables theorem. For the second term on the right hand side,

$$\begin{aligned}\int_{\varphi_t(\mathcal{U})} \pounds_{\boldsymbol{c}}(q\,\mathbf{d}\boldsymbol{v}) &= \int_{\varphi_t(\mathcal{U})} (\pounds_{\boldsymbol{c}} q)\,\mathbf{d}\boldsymbol{v} + \int_{\varphi_t(\mathcal{U})} (q \operatorname{div}\boldsymbol{c})\,\mathbf{d}\boldsymbol{v} \\ &= \int_{\varphi_t(\mathcal{U})} (\mathbf{d}q\cdot\boldsymbol{c} + q\operatorname{div}\boldsymbol{c})\,\mathbf{d}\boldsymbol{v} = \int_{\varphi_t(\mathcal{U})} \operatorname{div}(q\boldsymbol{c})\,\mathbf{d}\boldsymbol{v} \\ &= \int_{\partial\varphi_t(\mathcal{U})} q\boldsymbol{c}\cdot\boldsymbol{n}^*\,\mathbf{d}\boldsymbol{a}\end{aligned}$$

by the chain rule and the divergence theorem A.8.24. Substitution into the master balance principle 3.2.4 and rearranging yields the desired result. ∎

The next important result follows immediately.

Proposition 3.2.16. *Suppose that the motion of a material body is the composition $\varphi_t = \Phi_t \circ \Psi_t^{-1}$, and that Q, B, $\boldsymbol{U}$, and q, b, $\boldsymbol{u}$ are related by (3.2.12), and $\hat{q} = q \circ \Phi$. Then Q, B, $\boldsymbol{U}$ satisfy the material master balance principle if and only if q, b, $\boldsymbol{u}$ satisfy the spatial master balance principle, and if and only if $\hat{q}$, b, $\boldsymbol{u}$ satisfy the quasi-spatial master balance principle.*

3.2.2 Balance Principles in the Spatial and Material Settings

Suitable substitutions for the quantities and sources in the master balance principle (resp. master inequality principle) will lead to the particular balance principles typically employed in continuum mechanics. This section provides the classical spatial (Eulerian) and material (Lagrangian) settings of these principles. Full proofs are omitted as they are almost straightforward when using the general relations derived in the previous section. Moreover, derivations of the spatial and material formulations of the balance principles are presented in most textbooks on continuum mechanics; see reference lists at the beginning of this chapter. The reader is particularly referred to Marsden and Hughes [1994], whose notation is close to the present one.

Conservation of Mass

Definition 3.2.17. Let the motion $\varphi_t : \mathcal{B} \to \mathcal{S}$ be a one-parameter group of orientation-preserving C^1-diffeomorphisms for each time $t \in [0, T]$ such that $\varphi_0(\mathcal{B}) = \mathcal{B}$ is the initial configuration, $J(X, 0) = 1$, and $J(X, t) > 0$ for every $X \in \mathcal{B}$ and time t. Let

$\mathcal{U} \subset \mathcal{B}$ be a nice subset, then the *spatial mass density* $\rho(x,t) \geq 0$ obeys *conservation of mass* if

$$\frac{\mathrm{d}}{\mathrm{d}t} \int_{\varphi_t(\mathcal{U})} \rho \, \mathbf{d}\boldsymbol{v} = 0 \,,$$

so that the mass of $\mathcal{U}$ is constant in every configuration $\varphi_t(\mathcal{U})$. ♢

Proposition 3.2.18. *Conservation of mass is equivalent to*

(i) the Lagrangian form

$$\rho(\varphi(X,t),t)\, J(X,t) = \rho_{\mathrm{ref}}(X) \,,$$

where $\rho_{\mathrm{ref}}(X) \stackrel{\mathrm{def}}{=} \rho(\varphi(X,0),0)$ *is the mass density at time* $t = 0$*,*

(ii) the Eulerian conservation form

$$\frac{\partial}{\partial t}\rho(x,t) + \mathrm{div}(\rho\, \boldsymbol{v})(x,t) = 0 \,,$$

which is referred to as the continuity equation.

Balance of Momentum

The concept of stress distinguishes continuum mechanics from particle mechanics. The existence of a *Cauchy traction vector field* $\boldsymbol{t}(x,t,\boldsymbol{n}^*(x))$ is presumed, which represents the force per unit area acting on an oriented surface element with unit outward normal $\boldsymbol{n}^*$, and evaluated at time t and a point $x \in \partial(\varphi_t(\mathcal{B}))$ on the boundary of the body.

Definition 3.2.19. Let $\rho(x,t)$ be the spatial mass density, $\boldsymbol{b}_t : \mathcal{S} \to T\mathcal{S}$, with $\boldsymbol{b}_t(x) = \boldsymbol{b}(x,t)$, the *external force per unit mass* vector field, and let $\mathcal{U} \subset \mathcal{B}$ be nice, then *spatial balance of linear momentum* is satisfied if

$$\frac{\mathrm{d}}{\mathrm{d}t} \int_{\varphi_t(\mathcal{U})} \rho\boldsymbol{v} \, \mathbf{d}\boldsymbol{v} = \int_{\varphi_t(\mathcal{U})} \rho\boldsymbol{b} \, \mathbf{d}\boldsymbol{v} + \int_{\partial\varphi_t(\mathcal{U})} \boldsymbol{t} \, \mathbf{d}\boldsymbol{a} \,. \qquad ♢$$

It is important to realize that the equation has to be evaluated componentwise in Cartesian coordinates because vector fields cannot be integrated. Therefore, it is not a tensorial equation [see also Marsden and Hughes, 1994, p. 134].

Provided that the traction vector field $\boldsymbol{t}$ is a continuous function of its arguments, there exists a unique time-dependent spatial $\binom{2}{0}$-tensor field $\boldsymbol{\sigma}_t \in \mathfrak{T}^2_0(\mathcal{S})$ such that

$$\boldsymbol{t}(x,t,\boldsymbol{n}^*(x)) = \boldsymbol{\sigma}(x,t) \cdot \boldsymbol{n}^*(x) \,, \qquad \text{in spatial coordinates } x^i, \quad t^i = \sigma^{ij} n_j \,. \tag{3.2.20}$$

This follows from Cauchy's theorem 3.2.7. The tensor $\boldsymbol{\sigma}(x,t) = \sigma^{ij}(x,t)\, \frac{\boldsymbol{\partial}}{\boldsymbol{\partial} x^i} \otimes \frac{\boldsymbol{\partial}}{\boldsymbol{\partial} x^j}$, as well as its associates with components $\sigma^i{}_j$, $\sigma_i{}^j$ and σ_{ij}, respectively, are referred to as the *Cauchy stress tensor field*, or just as the *Cauchy stress*.

Proposition 3.2.21. *Let balance of linear momentum and conservation of mass be satisfied, then the proper tensorial equation*

$$\rho\dot{\boldsymbol{v}} = \rho\boldsymbol{b} + \operatorname{div}\boldsymbol{\sigma}\,,$$

manifests a localized spatial balance of linear momentum.

Let $\varphi_0(\mathcal{B}) = \mathcal{B}$ be the configuration of the body at $t = 0$, $\boldsymbol{B}(X,t) \overset{\text{def}}{=} \boldsymbol{b}(\varphi(X,t),t)$, and $\boldsymbol{V}(X,t)$ be the material velocity, then balance of linear momentum has the *Lagrangian* resp. *material form*

$$\rho_{\text{ref}}\boldsymbol{A} = \rho_{\text{ref}}\boldsymbol{B} + \operatorname{DIV}\boldsymbol{P}\,, \tag{3.2.22}$$

where $\boldsymbol{A}(X,t) \overset{\text{def}}{=} \frac{\partial}{\partial t}\boldsymbol{V}(X,t)$ is the material acceleration.

Applying the Piola transformation, defined by A.8.27, to the second leg of the Cauchy stress tensor gives the *first Piola-Kirchhoff stress tensor field* $\boldsymbol{P}_t : \mathcal{B} \to T\mathcal{S} \otimes T^*\mathcal{B}$, that is,

$$\boldsymbol{P}_t(X) \overset{\text{def}}{=} J_t(X)\left((\boldsymbol{\sigma}_t \cdot \boldsymbol{F}_t^{-\mathrm{T}}) \circ \varphi_t\right)(X) \tag{3.2.23}$$

for every $X \in \mathcal{B}$, and $\boldsymbol{\sigma} = \boldsymbol{\sigma}^\sharp$ being understood. The placement of parentheses and the composition with the point map are important: as $\boldsymbol{\sigma}(x,t) \cdot \boldsymbol{F}^{-\mathrm{T}}(x,t)$ has its values at (x,t), one has to switch the point arguments. In material coordinates $\{X^I\}$, spatial coordinates $\{x^i\}$, and by omitting the point maps and arguments, the component equation of the previous reads $P^{iI} = J\sigma^{ij}(\boldsymbol{F}^{-1})_j{}^I$. Similar to the deformation gradient, $\boldsymbol{P}(X)$ is a two-point tensor at every $X \in \mathcal{B}$. While $\boldsymbol{\sigma} \cdot \boldsymbol{n}^* = \boldsymbol{t}$ is the force per unit of deformed area in the current configuration of the body, $\boldsymbol{P} \cdot \boldsymbol{N}^* = \boldsymbol{T}$, resp. $N^I P^{iI} = T^i$, is the same force per unit of undeformed area. That is to say, the traction vectors $\boldsymbol{t}(x,t,\boldsymbol{n}^*(x))$ and $\boldsymbol{T}(X,t,\boldsymbol{N}^*(X))$ are parallel throughout the motion φ, and $(\boldsymbol{t}\,\mathrm{d}\boldsymbol{a}) \circ \varphi = \boldsymbol{T}\,\mathrm{d}\boldsymbol{A}$ by Proposition A.8.29.

Two additional stress measures should be defined. The *second Piola-Kirchhoff stress tensor* $\boldsymbol{S}_t \in \mathfrak{T}^2_0(\mathcal{B})$ plays a fundamental role in constitutive theory. It is obtained by pulling the first leg of $\boldsymbol{P}$ back to $\mathcal{B}$:

$$\boldsymbol{S}_t \overset{\text{def}}{=} \boldsymbol{F}_t^{-1} \cdot \boldsymbol{P}_t = J_t\boldsymbol{F}_t^{-1} \cdot \left((\boldsymbol{\sigma}_t \cdot \boldsymbol{F}_t^{-\mathrm{T}}) \circ \varphi_t\right)\,. \tag{3.2.24}$$

In components, $S^{IJ} = J(\boldsymbol{F}^{-1})^I{}_i(\boldsymbol{F}^{-1})_j{}^J\sigma^{ij}$, and $\boldsymbol{S}_t(X) = \boldsymbol{S}(X,t)$. The *corotated Cauchy stress* is a stress measure which is convenient for the development of objective stress update algorithms in finite strain computational mechanics (see Section 5.5). It is defined through the $\boldsymbol{R}$-pullback of the Cauchy stress, clearly,

$$\mathfrak{S}_t^\sharp \overset{\text{def}}{=} \boldsymbol{R}_t^\star\boldsymbol{\sigma}_t^\sharp = \boldsymbol{R}_t^{-1} \cdot \left((\boldsymbol{\sigma}_t^\sharp \cdot \boldsymbol{R}_t^{-\mathrm{T}}) \circ \varphi_t\right) = \left((\boldsymbol{R}_t^{\mathrm{T}} \cdot \boldsymbol{\sigma}_t^\sharp) \circ \varphi_t\right) \cdot \boldsymbol{R}_t \tag{3.2.25}$$

by using Proposition 3.1.9, in which $\boldsymbol{R}$ denotes the rotation two-point tensor obtained from the polar decomposition of the deformation gradient.

Definition 3.2.26. Let ρ, $\boldsymbol{b}$, etc., be as before. Let the ambient space be $\mathcal{S} = \mathbb{R}^n$, and $\boldsymbol{x}$ the position vector pointing from the origin to x, then *spatial balance of angular momentum* is satisfied for every nice $\mathcal{U} \subset \mathcal{B}$ provided that

$$\frac{\mathrm{d}}{\mathrm{d}t}\int_{\varphi_t(\mathcal{U})} \rho(\boldsymbol{x} \times \boldsymbol{v})\,\mathrm{d}\boldsymbol{v} = \int_{\varphi_t(\mathcal{U})} \rho(\boldsymbol{x} \times \boldsymbol{b})\,\mathrm{d}\boldsymbol{v} + \int_{\partial\varphi_t(\mathcal{U})} \boldsymbol{x} \times (\boldsymbol{\sigma} \cdot \boldsymbol{n}^*)\,\mathrm{d}\boldsymbol{a}\,,$$

where $\times$ denotes the usual cross product. $\diamondsuit$

If balance of linear momentum and conservation of mass hold, the previous postulate yields the symmetry of the Cauchy stress, that is,

$$\boldsymbol{\sigma} = \boldsymbol{\sigma}^{\mathrm{T}} \qquad \text{resp.} \qquad \sigma^{ij} = \sigma^{ji}\,, \tag{3.2.27}$$

and $\boldsymbol{S} = \boldsymbol{S}^{\mathrm{T}}$.

Balance of Energy

Definition 3.2.28. Let $\varphi_t : \mathcal{B} \to \mathcal{S}$ be a C^1-motion with spatial velocity $\boldsymbol{v}(x,t)$, and $\mathcal{U} \subset \mathcal{B}$ a nice subset, mapped onto $\varphi_t(\mathcal{U}) \subset \mathcal{S}$ with boundary $\partial(\varphi_t(\mathcal{U}))$. Let $\rho(x,t)$ be the spatial mass density, $\boldsymbol{b}(x,t)$ the external force per unit mass, and $\boldsymbol{t}(x,t,\boldsymbol{n}^*)$ the Cauchy traction vector field. The motion φ_t satisfies *balance of energy* if

$$\frac{\mathrm{d}}{\mathrm{d}t}\int_{\varphi_t(\mathcal{U})} \rho\left(e_{\mathrm{int}} + \tfrac{1}{2}\left\langle \boldsymbol{v},\boldsymbol{v}\right\rangle\right)\mathbf{d}\boldsymbol{v} = \int_{\varphi_t(\mathcal{U})} \rho\left(\left\langle \boldsymbol{b},\boldsymbol{v}\right\rangle + r\right)\mathbf{d}\boldsymbol{v} + \int_{\partial\varphi_t(\mathcal{U})}\left(\left\langle \boldsymbol{t},\boldsymbol{v}\right\rangle + h\right)\mathbf{d}\boldsymbol{a}\,,$$

where $e_{\mathrm{int}}(x,t)$ is the *internal energy* per unit mass (*specific internal energy*), $r(x,t)$ is the *heat supply* per unit mass, and $h(x,t,\boldsymbol{n}^*(x))$ is the *heat flux* across the area with outward normals $\boldsymbol{n}^*$. The *total energy* per unit mass is defined through $e_{\mathrm{tot}} \stackrel{\mathrm{def}}{=} e_{\mathrm{int}} + \frac{1}{2}\left\langle \boldsymbol{v},\boldsymbol{v}\right\rangle$ $\diamondsuit$

Proposition 3.2.29. *Let φ_t be regular and C^1-continuous, and let both the traction $\boldsymbol{t}$ and the heat flux h satisfy Cauchy's theorem 3.2.7. Moreover, assume that conservation of mass, balance of linear and angular momentum, and balance of energy hold. Then, for every $x \in \varphi_t(\mathcal{B})$, and $t \in \mathcal{I} \subset \mathbb{R}$, the localized balance of energy reads*

$$\rho\dot{e}_{\mathrm{int}} = \boldsymbol{\sigma} : \boldsymbol{d} + \rho r - \operatorname{div}\boldsymbol{q}\,,$$

where the field $\boldsymbol{q}_t : \varphi_t(\mathcal{U}) \to T\mathcal{S}$ defined through $h(x,t,\boldsymbol{n}^*(x)) = -\boldsymbol{n}^*(x)\cdot\boldsymbol{q}(x,t)$ is called the heat flux vector field *or* heat flux density*.*

To obtain a material version of localized balance of energy 3.2.29, let the configuration at time $t = 0$ be the initial configuration of the body, i.e. $\varphi_0(\mathcal{B}) \stackrel{\mathrm{def}}{=} \mathcal{B}$, and let $E_{\mathrm{int}}(X,t) \stackrel{\mathrm{def}}{=} e_{\mathrm{int}}(\varphi(X,t),t)$, $R(X,t) \stackrel{\mathrm{def}}{=} r(\varphi(X,t),t)$, and $\boldsymbol{Q}(X,t) \stackrel{\mathrm{def}}{=} J(X,t)(\boldsymbol{F}^{-1})(X,t)\cdot(\boldsymbol{q}(\varphi(X,t),t))$. Then from $\rho(\varphi(X,t),t)\,J(X,t) = \rho_{\mathrm{ref}}(X)$ by Proposition 3.2.18(i), one has

$$\rho_{\mathrm{ref}}\frac{\partial E_{\mathrm{int}}}{\partial t} = \boldsymbol{S} : \boldsymbol{D} + \rho_{\mathrm{ref}}R - \operatorname{DIV}\boldsymbol{Q}\,. \tag{3.2.30}$$

Entropy Production Inequality

Definition 3.2.31. Let $\varphi_t : \mathcal{B} \to \mathcal{S}$ be a C^1-motion, and $\mathcal{U} \subset \mathcal{B}$ a nice subset. In addition to $\rho(x,t)$, $r(x,t)$, and $h(x,t,\boldsymbol{n}^*)$ introduced in the previous sections, let

$\eta(x,t)$ and $\theta(x,t) > 0$ be functions called the *specific entropy* per unit mass and the *absolute temperature*, respectively. These functions are said to satisfy the *spatial entropy production inequality* (also called the *Clausius-Duhem inequality*, or the *second law of thermodynamics*) if

$$\frac{\mathrm{d}}{\mathrm{d}t}\int_{\varphi_t(\mathcal{U})}\rho\eta\,\mathbf{d}\boldsymbol{v} \geq \int_{\varphi_t(\mathcal{U})}\frac{\rho r}{\theta}\,\mathbf{d}\boldsymbol{v} + \int_{\partial\varphi_t(\mathcal{U})}\frac{h}{\theta}\,\mathbf{d}\boldsymbol{a}\,, \qquad \diamond$$

Proposition 3.2.32. *Assume $h(x,t,\boldsymbol{n}^*) = -\boldsymbol{q}(x,t)\cdot\boldsymbol{n}^*$, and that conservation of mass holds, then the localized form of the spatial entropy production inequality is*

$$\rho\dot{\eta}(x,t) - \frac{\rho r}{\theta}(x,t) + \frac{1}{\theta}\operatorname{div}\boldsymbol{q}\,(x,t) - \frac{1}{\theta^2}\langle\boldsymbol{q},\boldsymbol{\nabla}\theta\rangle(x,t) \geq 0\,,$$

for r being C^0-, and $\boldsymbol{q}$ and θ being C^1-continuous.

Let $\psi(x,t)$ be a function, called the *free energy*, which is related to the internal energy $e_{\mathrm{int}}(x,t)$ through

$$\psi(x,t) = e_{\mathrm{int}}(x,t) - \theta(x,t)\,\eta(x,t) \tag{3.2.33}$$

It can be shown [see Marsden and Hughes, 1994, pp. 197–198], that (3.2.33) is a *Legendre transformation* of e to ψ, and that entropy and temperature are conjugate variables. Assuming Proposition 3.2.32 and balance of energy 3.2.29 to hold, then, by noting that $\theta\dot{\eta} = \dot{e}_{\mathrm{int}} - \eta\dot{\theta} - \dot{\psi}$,

$$\rho\left(\eta\dot{\theta} + \dot{\psi}\right) - \boldsymbol{\sigma} : \boldsymbol{d} + \frac{1}{\theta}\left\langle\boldsymbol{q},\boldsymbol{\nabla}\theta\right\rangle \leq 0\,, \tag{3.2.34}$$

which is referred to as the *spatial reduced dissipation inequality*.

Let $\varphi_0(\mathcal{B}) \overset{\mathrm{def}}{=} \mathcal{B}$ be the initial configuration of the body at time $t = 0$. Additional to $\boldsymbol{S}$, $\boldsymbol{D}$, and $\boldsymbol{Q}$ already defined, let $N(X,t) \overset{\mathrm{def}}{=} \eta(\varphi(X,t),t)$, $\Theta(X,t) \overset{\mathrm{def}}{=} \theta(\varphi(X,t),t)$, and $\Psi(X,t) \overset{\mathrm{def}}{=} \psi(\varphi(X,t),t)$. By conservation of mass holds, then, the *Lagrangian* resp. *material reduced dissipation inequality* reads

$$\rho_{\mathrm{ref}}\left(N\frac{\partial\Theta}{\partial t} + \frac{\partial\Psi}{\partial t}\right) - \boldsymbol{P} : \frac{\partial\boldsymbol{F}}{\partial t} + \frac{1}{\Theta}\left\langle\boldsymbol{Q},\widetilde{\boldsymbol{\nabla}}\Theta\right\rangle \leq 0 \tag{3.2.35}$$

at every $X \in \mathcal{B}$ and time t. Here $\widetilde{\boldsymbol{\nabla}}$ should denote the gradient operator for material scalar-valued functions of X, i.e. $\widetilde{\boldsymbol{\nabla}}\Theta = G^{IJ}\frac{\partial\Theta}{\partial X^J}\frac{\boldsymbol{\partial}}{\boldsymbol{\partial} X^I}$ in local coordinates. Note that for the second term, $\boldsymbol{P} : \frac{\partial\boldsymbol{F}}{\partial t} = \boldsymbol{S} : \boldsymbol{D}$.

3.2.3 Convective and Conservation Forms in ALE Setting

The convective and conservation forms of the balance principles is of fundamental importance in the development of ALE methods. The following section provides some more details frequently used in this context.

In accordance with Definition 3.2.14, the convective form of the continuity equation, balance of linear momentum, and balance of energy read

$$\begin{aligned} \frac{\partial\hat{\rho}}{\partial t}\circ\Phi_t^{-1} + \mathbf{d}\rho\cdot\boldsymbol{c} + \rho\,\mathrm{div}\,\boldsymbol{v} &= 0\,, \\ \rho\,\frac{\partial\hat{\boldsymbol{v}}}{\partial t}\circ\Phi_t^{-1} + \rho\,\boldsymbol{\nabla}_{\boldsymbol{c}}\boldsymbol{v} &= \rho\boldsymbol{b} + \mathrm{div}\,\boldsymbol{\sigma}\,, \\ \rho\,\frac{\partial\hat{e}_{\mathrm{int}}}{\partial t}\circ\Phi_t^{-1} + \rho\,\mathbf{d}e_{\mathrm{int}}\cdot\boldsymbol{c} &= \boldsymbol{\sigma}:\boldsymbol{d} + \rho r - \mathrm{div}\,\boldsymbol{q} \end{aligned} \tag{3.2.36}$$

on $\Phi(\mathcal{R},t)\subset\mathcal{S}$, where $\hat{\rho}\overset{\mathrm{def}}{=}\rho\circ\Phi$, $\hat{\boldsymbol{v}}\overset{\mathrm{def}}{=}\boldsymbol{v}\circ\Phi$, etc. Note that for scalar fields like the mass density, $\boldsymbol{\nabla}_{(\boldsymbol{c}\circ\Phi)}\rho = (\mathbf{d}\rho\cdot\boldsymbol{c})\circ\Phi$, evaluated at $\chi\in\mathcal{R}$ and time t.

Recall from Theorem 3.2.15 that the *quasi-spatial master balance principle* takes the form

$$\frac{\mathrm{d}}{\mathrm{d}t}\int_{\Phi(\mathcal{W},t)} q\,\mathbf{d}\boldsymbol{v} = \int_{\varphi(\mathcal{U},t)} b\,\mathbf{d}\boldsymbol{v} + \int_{\partial\varphi(\mathcal{U},t)} (\boldsymbol{u}-q\boldsymbol{c})\cdot\boldsymbol{n}^*\,\mathbf{d}\boldsymbol{a}\,, \tag{3.2.37}$$

where $\Phi(\mathcal{W},t) = \Phi_t(\mathcal{W}) = \varphi_t(\mathcal{U})$, $\partial\Phi_t(\mathcal{W}) = \partial\varphi_t(\mathcal{U})$, $\hat{q}_t = q_t\circ\Phi_t : \mathcal{R}\to\mathbb{R}$ is the referential description of a sufficiently smooth time-dependent spatial scalar field $q(x,t)$, and $b(x,t)$ and $\boldsymbol{u}(x,t)$ are external sources. If $q(x,t)$ is tensor-valued, then the integral form makes sense only if the ambient space is $\mathcal{S} = \mathbb{R}^{m_{\mathrm{dim}}}$ and if the integrals are evaluated with respect to Cartesian coordinates. Note that the spatial master balance principle, defined through 3.2.4, is included in the above equation as the particular case where $\Phi_t = \mathrm{id}_{\mathcal{R}}$, so that $J_\Phi = 1$ and $\boldsymbol{c} = \boldsymbol{v}$.

The *generic ALE integral conservation law* for the quantity q can be derived from (3.2.37) by setting the sources to zero:

$$\frac{\mathrm{d}}{\mathrm{d}t}\int_{\Phi_t(\mathcal{W})} q\,\mathbf{d}\boldsymbol{v} + \int_{\partial\Phi_t(\mathcal{W})} q\boldsymbol{c}\cdot\boldsymbol{n}^*\,\mathbf{d}\boldsymbol{a} = 0\,. \tag{3.2.38}$$

Proposition 3.2.39 (Geometric Conservation Laws). *Let the quantity q satisfy the conservation law (3.2.38) on a domain $\mathcal{D}\subset\mathcal{S}$, and let the material flow be steady and uniform, and oriented in the arbitrary direction $\boldsymbol{y}:\mathcal{D}\to T\mathcal{S}$. Then,*

(i)

$$\frac{\mathrm{d}}{\mathrm{d}t}\int_{\mathcal{V}}\mathbf{d}\boldsymbol{v} = \int_{\partial\mathcal{V}}\boldsymbol{w}\cdot\boldsymbol{n}^*\,\mathbf{d}\boldsymbol{a}\,, \qquad \textit{where } \mathcal{V} = \Phi_t(\mathcal{W})\subset\mathcal{D} \textit{ and } \boldsymbol{w}_t = \tfrac{\partial\Phi_t}{\partial t}\circ\Phi_t^{-1}\,.$$

(ii)

$$\int_{\partial\mathcal{V}}\boldsymbol{y}\cdot\boldsymbol{n}^*\,\mathbf{d}\boldsymbol{a} = 0\,, \qquad \textit{with } \mathcal{V}\subset\mathcal{D} \textit{ fixed.}$$

The *geometric conservation laws (GCL)* are purely geometric identities which must hold independently of any material or physical situation. They establish two additional balance principles whose discrete counterparts play an important role in Eulerian and arbitrary Lagrangian-Eulerian numerical methods, respectively [Trulio and Trigger, 1961; Thomas and Lombard, 1979; Demirdžić and Perić, 1988, 1990; Vinokur, 1989;

Zhang et al., 1993; Lesoinne and Farhat, 1996; Farhat et al., 2001; Donea et al., 2004]. The GCL 3.2.39(i) is also called the *volume conservation law*, *space conservation law* or *conservation of space*. The GCL 3.2.39(ii), referred to as the *surface conservation law*, is usually ignored, or assumed to be automatically satisfied. This is why the geometric conservation law is frequently identified with volume conservation alone.

Definition 3.2.40. By suitable substitutions for q, b, and $\operatorname{div} \boldsymbol{u}$ in the quasi-spatial master balance principle (3.2.37), it can be easily shown that the balance principles for space, mass, momentum, and energy, respectively, can be recast in the form [cf. Bird, 1957; Bird et al., 1960; Trulio and Trigger, 1961; Frank and Lazarus, 1964; Slattery, 1972; Thompson, 1972; Hirt et al., 1974; Addessio et al., 1990; Demirdžić and Perić, 1990; Donea and Huerta, 2003; Donea et al., 2004]

$$\begin{aligned}
\frac{\mathrm{d}}{\mathrm{d}t}\int_{\Phi_t(\mathcal{W})} \mathbf{d}\boldsymbol{v} - \int_{\partial\Phi_t(\mathcal{W})} \boldsymbol{w}\cdot\boldsymbol{n}^*\,\mathbf{d}\boldsymbol{a} &= 0\,,\\
\frac{\mathrm{d}}{\mathrm{d}t}\int_{\Phi_t(\mathcal{W})} \rho\,\mathbf{d}\boldsymbol{v} + \int_{\partial\Phi_t(\mathcal{W})} \rho\boldsymbol{c}\cdot\boldsymbol{n}^*\,\mathbf{d}\boldsymbol{a} &= 0\,,\\
\frac{\mathrm{d}}{\mathrm{d}t}\int_{\Phi_t(\mathcal{W})} \rho\boldsymbol{v}\,\mathbf{d}\boldsymbol{v} + \int_{\partial\Phi_t(\mathcal{W})} (\rho\boldsymbol{v}\otimes\boldsymbol{c}-\boldsymbol{\sigma})\cdot\boldsymbol{n}^*\,\mathbf{d}\boldsymbol{a} &= \int_{\Phi_t(\mathcal{W})} \rho\boldsymbol{b}\,\mathbf{d}\boldsymbol{v}\,,\\
\frac{\mathrm{d}}{\mathrm{d}t}\int_{\Phi_t(\mathcal{W})} \rho e_{\mathrm{int}}\,\mathbf{d}\boldsymbol{v} + \int_{\partial\Phi_t(\mathcal{W})} (\boldsymbol{q}+\rho e_{\mathrm{int}}\boldsymbol{c})\cdot\boldsymbol{n}^*\,\mathbf{d}\boldsymbol{a} &= \int_{\Phi_t(\mathcal{W})} (\boldsymbol{\sigma}:\boldsymbol{d}+\rho r)\,\mathbf{d}\boldsymbol{v}\,.
\end{aligned}$$

This is called the *integral conservation form of ALE balance principles*. The third equation should again be interpreted componentwise in Cartesian coordinates. ♢

Proposition 3.2.41. *Let the function q be continuously differentiable on a nice subset $\Phi_t(\mathcal{W}) \subset \mathcal{S}$ occupied by the body at time t, and let $\hat{S} \stackrel{\text{def}}{=} (b + \operatorname{div}\boldsymbol{u}) \circ \Phi$ be the combined source for each t. Then q satisfies the quasi-spatial master balance principle 3.2.15 resp. (3.2.37) if and only if it satisfies the localized quasi-spatial master balance principle*

$$\frac{\partial \hat{q} J_\Phi}{\partial t} + J_\Phi\,(\operatorname{div}\boldsymbol{\psi}(q)) \circ \Phi = \hat{S} J_\Phi\,,$$

where $\boldsymbol{\psi}(q)$ is the convective flux density of q.

Proof. Assume that q is scalar-valued, and recall that

$$\frac{\mathrm{d}}{\mathrm{d}t}\int_{\Phi_t(\mathcal{W})} q\,\mathbf{d}\boldsymbol{v} = \int_{\Phi_t(\mathcal{W})} \Phi_{t\star}\left(J_\Phi^{-1}\frac{\partial \hat{q} J_\Phi}{\partial t}\right)\mathbf{d}\boldsymbol{v}\,.$$

Rewriting the quasi-spatial master balance principle by the divergence theorem results in

$$\int_{\Phi_t(\mathcal{W})} \Phi_{t\star}\left(J_\Phi^{-1}\frac{\partial \hat{q} J_\Phi}{\partial t}\right)\mathbf{d}\boldsymbol{v} = \int_{\varphi_t(\mathcal{U})} (b + \operatorname{div}(\boldsymbol{u} - q\boldsymbol{c}))\,\mathbf{d}\boldsymbol{v}\,.$$

Define $\Omega \stackrel{\text{def}}{=} \hat{\Omega} \circ \Phi^{-1} = b + \operatorname{div} \boldsymbol{u}$, then the change of variables formula and the pullback rule for scalars yield

$$\begin{aligned} 0 &= \int_{\Phi_t(\mathcal{W})} \Phi_{t\star}\left(J_\Phi^{-1} \frac{\partial \hat{q} J_\Phi}{\partial t} \right) \mathbf{d}\boldsymbol{v} + \int_{\varphi_t(\mathcal{U})} (\operatorname{div}(q\boldsymbol{c}) - \Omega)\, \mathbf{d}\boldsymbol{v} \\ &= \int_{\mathcal{W}} \left(J_\Phi^{-1} \frac{\partial \hat{q} J_\Phi}{\partial t} + \Phi_t^\star(\operatorname{div}(q\boldsymbol{c})) - \Phi_t^\star \Omega \right) \Phi_t^\star \mathbf{d}\boldsymbol{v} \\ &= \int_{\mathcal{W}} \left(J_\Phi^{-1} \frac{\partial \hat{q} J_\Phi}{\partial t} + \operatorname{div}(q\boldsymbol{c}) \circ \Phi_t - \Omega \circ \Phi_t \right) J_\Phi \, \mathbf{d}\hat{\boldsymbol{v}} \,. \end{aligned}$$

This holds for arbitrary $\mathcal{W}$, hence

$$\frac{\partial \hat{q} J_\Phi}{\partial t} + (\operatorname{div}(q\boldsymbol{c}) \circ \Phi_t)\, J_\Phi - \hat{\Omega} J_\Phi = 0 \,.$$

The generalization applying to tensor-valued q is in accordance with the product rule for divergence, (A.7.5). The assertion then follows if the flux density is defined by $\boldsymbol{\psi}(q) \stackrel{\text{def}}{=} q\boldsymbol{c}$ for $q_t : \Phi_t(\mathcal{W}) \to \mathbb{R}$ being scalar-valued, and by $\boldsymbol{\psi}(q) \stackrel{\text{def}}{=} q \otimes \boldsymbol{c}$ for $q_t : \Phi_t(\mathcal{W}) \to T^r_s(\mathcal{S})$ being $\binom{r}{s}$-tensor-valued. ∎

The next fundamental result is readily obtained [see also Lesoinne and Farhat, 1996].

Proposition 3.2.42. *A continuously differentiable field q which is conserved with respect to $\varphi_t(\mathcal{U}) = \Phi_t(\mathcal{W})$ satisfies (3.2.38) if and only if it satisfies the generic ALE conservation law*

$$\frac{\partial \hat{q} J_\Phi}{\partial t} + J_\Phi \,(\operatorname{div} \boldsymbol{\psi}(q)) \circ \Phi = 0 \,.$$

Using Proposition 3.2.41, the ALE description of balance principles can be easily recast in conservation form by appropriate substitutions for the quantity $\hat{q}$ and the source $\hat{\Omega}$ [cf. Donea et al., 1981, 1982; Benson, 1989, 1992; Scovazzi and Hughes, 2007]. Accordingly, the conservation of mass, momentum, energy, and the conservation form of localized entropy production inequality read

$$\begin{aligned} \frac{\partial \hat{\rho} J_\Phi}{\partial t} + J_\Phi \operatorname{div}(\rho \boldsymbol{c}) \circ \Phi &= 0 \,, \\ \frac{\partial \hat{\rho} \hat{\boldsymbol{v}} J_\Phi}{\partial t} + J_\Phi \operatorname{div}(\rho \boldsymbol{v} \otimes \boldsymbol{c}) \circ \Phi &= J_\Phi \,(\rho \boldsymbol{b} + \operatorname{div} \boldsymbol{\sigma}) \circ \Phi \,, \\ \frac{\partial \hat{\rho} \hat{e}_{\text{int}} J_\Phi}{\partial t} + J_\Phi \operatorname{div}(\rho e_{\text{int}}\, \boldsymbol{c}) \circ \Phi &= J_\Phi \,(\boldsymbol{\sigma} : \boldsymbol{d} + \rho r - \operatorname{div} \boldsymbol{q}) \circ \Phi \,, \qquad \text{and} \\ \frac{\partial \hat{\rho} \hat{\eta} J_\Phi}{\partial t} + J_\Phi \operatorname{div}(\rho \eta\, \boldsymbol{c}) \circ \Phi &\geq J_\Phi \left(\frac{\rho r}{\theta} - \frac{1}{\theta} \operatorname{div} \boldsymbol{q} + \frac{1}{\theta^2} \langle \boldsymbol{q}, \boldsymbol{\nabla} \theta \rangle \right) \circ \Phi \,, \end{aligned} \tag{3.2.43}$$

respectively.

Some solution variables of continuum mechanical problems, like the stress and the material state variables, may have evolution equations but do not obey a conservation law or balance principle (see Chapter 4). For numerical solution using ALE methods,

it is highly desirable to have some conservation form of these evolution equations available. The ALE conservation form of spatial rate equations can be obtained as follows.

Proposition 3.2.44. *Let $\dot{q} \stackrel{\text{def}}{=} f(\ldots)$ be an evolution equation for the time-dependent spatial tensor field $q_t : \mathcal{V} \to T^r_s(\mathcal{S})$ resp. $q_t \in \mathfrak{T}^r_s(\mathcal{S})$, with $\mathcal{V} = \Phi_t(\mathcal{W}) \subset \mathcal{S}$, $q_t(x) = q(x,t)$, and $x \in \mathcal{V}$. Provided that the convective velocity $\boldsymbol{c}$ is continuously differentiable in space, this spatial rate equation is equivalent to*

$$\frac{\partial \hat{q} J_\Phi}{\partial t} + J_\Phi \operatorname{div}(q \otimes \boldsymbol{c}) \circ \Phi = J_\Phi \left(f(\ldots) + q \operatorname{div} \boldsymbol{v}\right) \circ \Phi \,,$$

where $\hat{q} = q \circ \Phi$.

Proof. Applying the ALE operator 3.1.37 yields

$$\frac{\partial \hat{q}}{\partial t} \circ \Phi_t^{-1} + \boldsymbol{\nabla}_{\boldsymbol{c}} q = f(\ldots) \,.$$

By the product rule for divergence, (A.7.5), one has

$$\frac{\partial \hat{q}}{\partial t} + \operatorname{div}(q \otimes \boldsymbol{c}) \circ \Phi_t = \left(f(\ldots) + q \operatorname{div} \boldsymbol{c}\right) \circ \Phi \,.$$

After multiplication with J_Φ and expanding the left hand side with $\hat{q} \cdot 0 = \hat{q}(\frac{\partial}{\partial t} J_\Phi - J_\Phi \left(\operatorname{div} \boldsymbol{w}\right) \circ \Phi)$ using (3.1.29), it follows that

$$\frac{\partial \hat{q}}{\partial t} J_\Phi + \hat{q} \left(\frac{\partial J_\Phi}{\partial t} - J_\Phi \left(\operatorname{div} \boldsymbol{w}\right) \circ \Phi \right) + J_\Phi \operatorname{div}(q \otimes \boldsymbol{c}) \circ \Phi = J_\Phi \left(f(\ldots) + q \operatorname{div} \boldsymbol{c}\right) \circ \Phi \,.$$

The assertion follows by slight rearrangement and noting that $\operatorname{div} \boldsymbol{v} = \operatorname{div}(\boldsymbol{w} + \boldsymbol{c})$. ∎

Chapter 4

Constitutive Theory and Behavior of Sand

The basic equations and balance principles derived in the previous chapter are not enough to solve mechanical problems. Constitutive theory provides a functional form to the unknown variables to make the set of equations formally well-posed. The following chapter gives a rough introduction of the fundamentals of constitutive theory, and then the mechanical behavior of sand will be investigated. The chapter closes with a description of the hypoplastic model for sand which has been implemented into the proposed ALE method. Deeper knowledge of constitutive theory can be gained from the continuum mechanical textbooks listed in the previous chapter, particularly [Marsden and Hughes, 1994, ch. 3]. The author also refers to [Eringen, 1980; Krawietz, 1986; Ogden, 1997; Simo and Hughes, 1998; Chen and Han, 1988], and to the classical papers and lecture notes [Noll, 1958, 1967, 1972, 1973; Coleman and Noll, 1963; Coleman and Mizel, 1964; Coleman and Gurtin, 1967; Green and Naghdi, 1965]. Additional citations are in the text.

4.1 Fundamentals and Constitutive Equations

The basic equations derived in the previous chapter, and set up in the material description, are as follows:

$$\begin{aligned}
&\text{(i) conservation of mass:} && \rho_{\mathrm{ref}} = \rho\, J \\
&\text{(ii) balance of linear momentum:} && \rho_{\mathrm{ref}} \boldsymbol{A} = \rho_{\mathrm{ref}} \boldsymbol{B} + \mathrm{DIV}\, \boldsymbol{P} \\
&\text{(iii) balance of angular momentum:} && \boldsymbol{S} = \boldsymbol{S}^{\mathrm{T}} \\
&\text{(iv) balance of energy:} && \rho_{\mathrm{ref}} \frac{\partial E_{\mathrm{int}}}{\partial t} = \boldsymbol{S} : \boldsymbol{D} + \rho_{\mathrm{ref}} R - \mathrm{DIV}\, \boldsymbol{Q} \\
&\text{(v) reduced dissipation inequality:} && \rho_{\mathrm{ref}} \left(N \frac{\partial \Theta}{\partial t} + \frac{\partial \Psi}{\partial t} \right) - \boldsymbol{P} : \frac{\partial \boldsymbol{F}}{\partial t} + \frac{1}{\Theta} \langle \boldsymbol{Q}, \widetilde{\boldsymbol{\nabla}} \Theta \rangle \leq 0 \\
&\text{(vi) Legendre transformation:} && \Psi = E_{\mathrm{int}} - \Theta\, N
\end{aligned}$$

Generally the motion $\varphi : \mathcal{B} \times \mathcal{I} \to \mathcal{S}$, the temperature field $\Theta : \mathcal{B} \times \mathcal{I} \to \mathbb{R}$, and the temperature gradient $\widetilde{\boldsymbol{\nabla}}\Theta : \mathcal{B} \times \mathcal{I} \to T\mathcal{B}$, where $\mathcal{I} \subset \mathbb{R}$ is a time interval, are treated as the primary variables. The fields ρ_{ref}, $\boldsymbol{B}$, and R are usually given. If φ is a regular C^k motion, $k > 0$, then $\boldsymbol{F} = T\varphi$ does exist, and the second Piola-Kirchhoff stress $\boldsymbol{S}$ can be determined from $\boldsymbol{P}$ by (3.2.24), and vice versa. The material acceleration $\boldsymbol{A}$ is known by the knowledge of φ. The Jacobian J is a function of X and t through φ, and the current density ρ can thus be determined from (i). The internal energy E_{int} is related to the free energy Ψ and the specific entropy N by (vi), so one has not enough equations left to solve for $\boldsymbol{P}$, $\boldsymbol{Q}$, Ψ, and N. In mathematical language, the set of equations (i.e. the model) is said *not closed*. Closure of the model can be achieved by determining $\boldsymbol{P}$, $\boldsymbol{Q}$, Ψ, and N from suitable response functions resp. constitutive equations. Only *rate-independent* material will be considered in what follows.

4.1.1 Axioms of Constitutive Theory

Based on rational thermomechanical principles, a set of axioms can be postulated to constrain and simplify the constitutive equations. Some of the classical axioms are addressed in the following section, by referring to [Eringen, 1980; Truesdell and Noll, 2004; Marsden and Hughes, 1994].

Axiom 4.1.1 (Determinism). *The fields $\boldsymbol{P}$, $\boldsymbol{Q}$, Ψ, and N on a material body are determined by the past history of φ, Θ, and $\widetilde{\boldsymbol{\nabla}}\Theta$ of that body only.*

To formalize the axiom, let the set of all *past motions* up to time T be defined through [Marsden and Hughes, 1994, p. 181]

$$\mathcal{M}_T \overset{\text{def}}{=} \{\varphi : \mathcal{B} \times]-\infty, T] \to \mathcal{S} \,\big|\, \varphi \text{ is } C^k \text{ and regular for all } -\infty < t \leq T\}\,. \tag{4.1.2}$$

One can similarly define the set of all *past temperature fields* $\mathcal{T}_T$, and *past temperature gradient fields* $\mathcal{G}_T$ up to time T such that the set of *past histories* phrased in axiom 4.1.1 can be written

$$\mathcal{H} \overset{\text{def}}{=} \bigcup_{T \in \mathbb{R}} (\mathcal{M}_T \times \mathcal{T}_T \times \mathcal{G}_T \times \mathcal{B} \times \{T\})\,. \tag{4.1.3}$$

Definition 4.1.4. The *general constitutive equation for the first Piola-Kirchhoff stress field* $\boldsymbol{P}$ is a mapping

$$\bar{\boldsymbol{P}} : \mathcal{H} \to \mathfrak{T}_2^{\varphi}(\mathcal{B}, \mathcal{S})\,,$$

where $\mathfrak{T}_2^{\varphi}(\mathcal{B}, \mathcal{S}) \overset{\text{def}}{=} \Gamma(\varphi^{\star} T\mathcal{S} \otimes T^*\mathcal{B})$ denotes the set of all sections of the second-order two-point tensor bundle $\varphi^{\star} T\mathcal{S} \otimes T^*\mathcal{B} = \bigcup_{X \in \mathcal{B}} T_{\varphi(X)}\mathcal{S} \otimes T^*_X\mathcal{B}$ over φ. Let $H \overset{\text{def}}{=} (\varphi_{[t]}, \Theta_{[t]}, \widetilde{\boldsymbol{\nabla}}\Theta_{[t]}, X, t) \in \mathcal{H}$ be a past history element, in which $\varphi_{[t]}$, for example, means φ restricted to $]-\infty, t]$. Then, a particular first Piola-Kirchhoff stress $\boldsymbol{P}$ associated with $\bar{\boldsymbol{P}}$ and H is defined through

$$\boldsymbol{P}(X,t) \overset{\text{def}}{=} \bar{\boldsymbol{P}}(H) \overset{\text{def}}{=} \bar{\boldsymbol{P}}^t_{\tau=-\infty}(\varphi(Y,\tau), \Theta(Y,\tau), \widetilde{\boldsymbol{\nabla}}\Theta(Y,\tau), X, t)\,,$$

where $Y \in \mathcal{B}$ denotes any particle. $\diamond$

Generally the functional $\bar{\boldsymbol{P}}$ explicitly depends on the choice of the particle X and time t. If it is independent of both X and t, then the material body is called *homogenous* and *non-aging* with respect to $\bar{\boldsymbol{P}}$, respectively [Gummert, 1999]. In this case one is allowed to write $\boldsymbol{P}(X,t) = \bar{\boldsymbol{P}}^{t}_{\tau=-\infty}(\varphi, \Theta, \widetilde{\boldsymbol{\nabla}}\Theta)(X,t)$, where $\varphi = \varphi(Y,\tau)$, $\Theta = \Theta(Y,\tau)$ etc., trying to say that the functional is just to be evaluated at the particle X and time t.

Axiom 4.1.5 (Equipresence). *A quantity present as an independent variable in one constitutive equation should be so present in all, unless its presence contradicts some general law of physics.*

Axiom 4.1.6 (Locality). *Let $\mathcal{U}(X) \subset \mathcal{B}$ be an open neighborhood of X, then for any two past history elements $H_1, H_2 \in \mathcal{H}$ that coincide on $\mathcal{U}$ for all $\tau \leq t$, it is assumed that*

$$\bar{\boldsymbol{P}}(H_1) = \bar{\boldsymbol{P}}(H_2)$$

on $\mathcal{U}$. The same applies to the constitutive equations $\bar{\boldsymbol{Q}}$, $\bar{\Psi}$, and $\bar{N}$.

A set of possibly tensor-valued *internal state variables* or *history variables* $A_i(X,t) \stackrel{\text{def}}{=} \{A_1(X,t), \ldots, A_m(X,t)\}$ is postulated in order to deal with material history and to include dissipative effects in addition to heat conduction. The internal state variables are treated as additional unknowns which exclusively carry the information of the material history [Coleman and Gurtin, 1967].

As a consequence of the axiom of equipresence and Definition 4.1.4, the general constitutive equations for $\boldsymbol{P}$, $\boldsymbol{Q}$, Ψ, N, and the rate of change of the internal state variables $\frac{\partial}{\partial t}A_i$ must have identical lists of arguments. If, moreover, the axiom of locality holds, then it can be shown that the constitutive functionals depend only on X and t, and the point values at (X,t) of the deformation gradient $\boldsymbol{F}$, temperature Θ, temperature gradient $\widetilde{\boldsymbol{\nabla}}\Theta$, and the internal state variables A_i [Noll, 1958; Truesdell and Noll, 2004; Marsden and Hughes, 1994]. In what follows, let C_i denote an evolution equation for the history variable A_i, that is, a rate constitutive equation.

Axiom 4.1.7 (Entropy Production). *For any φ_t, Θ_t, $\widetilde{\boldsymbol{\nabla}}\Theta_t$, and A_{it}, the constitutive equations $\bar{\boldsymbol{P}}$, $\bar{\boldsymbol{Q}}$, $\bar{\Psi}$, $\bar{N}$, and C_i are assumed to satisfy the entropy production inequality resp. the reduced dissipation inequality*

$$\rho_{\text{ref}}\left(N\frac{\partial\Theta}{\partial t} + \frac{\partial\Psi}{\partial t}\right) - \boldsymbol{P} : \frac{\partial \boldsymbol{F}}{\partial t} + \frac{1}{\Theta}\langle \boldsymbol{Q}, \widetilde{\boldsymbol{\nabla}}\Theta\rangle \leq 0$$

for all particles $X \in \mathcal{B}$ and at each time t.

The following fundamental theorem formalizes the consequences of the axioms discussed and drastically simplifies the general constitutive equations. The theorem comprehends results that have originally been proposed by Coleman and Noll [1963]; Coleman and Mizel [1964]; Coleman and Gurtin [1967]. For thermoelastic materials without any internal state variables, rate and memory effects, a proof can be also found in [Marsden and Hughes, 1994, pp. 190–192].

Theorem 4.1.8. *Let the constitutive equations for $\boldsymbol{P}$, $\boldsymbol{Q}$, Ψ, N, and $\frac{\partial A_i}{\partial t}$ satisfy the axioms of determinism, equipresence, locality, and entropy production, and let the material be non-aging. Then the following assertions hold:*

(i) The functionals $\bar{\boldsymbol{P}}$, $\bar{\Psi}$, and $\bar{N}$ are independent of the temperature gradient $\widetilde{\boldsymbol{\nabla}}\Theta$.

(ii) $\bar{N} = -\partial\bar{\Psi}/\partial\Theta$.

(iii) $\bar{\boldsymbol{P}} = \rho_{\mathrm{ref}}\, \boldsymbol{g}^{\sharp}\, \partial\bar{\Psi}/\partial\boldsymbol{F}$.

(iv) $\bar{\boldsymbol{Q}}$, $\bar{\Psi}$, and C_i obey the dissipation inequality $(\partial\bar{\Psi}/\partial A_i)\cdot C_i + \langle\bar{\boldsymbol{Q}}, \widetilde{\boldsymbol{\nabla}}\Theta\rangle \leq 0$.

For the rest of this thesis, thermal effects are ignored, that is, the dependency on Θ and $\widetilde{\boldsymbol{\nabla}}\Theta$ will be dropped. By setting $\widetilde{\boldsymbol{\nabla}}\Theta \equiv \boldsymbol{0}$ one can also omit the heat flux $\boldsymbol{Q}$. With the assumptions and results of Theorem 4.1.8, the constitutive equations for $\boldsymbol{P}$, Ψ, and $\frac{\partial}{\partial t}A_i$ then reduce to

$$\begin{aligned} \boldsymbol{P}(X,t) &= \rho_{\mathrm{ref}}(X)\, \boldsymbol{g}^{\sharp}(\varphi_t(X))\, \frac{\partial\bar{\Psi}}{\partial\boldsymbol{F}}\left(\boldsymbol{F}_t(X), A_{it}(X), X\right), \\ \Psi(X,t) &= \bar{\Psi}(\boldsymbol{F}_t(X), A_{it}(X), X), \\ \frac{\partial A_i}{\partial t}(X,t) &= C_i(\boldsymbol{F}_t(X), A_{it}(X), X), \quad \text{with } \frac{\partial\bar{\Psi}}{\partial A_i}\cdot C_i \leq 0. \end{aligned} \tag{4.1.9}$$

The present section closes with some key facts about the constitutive axiom of material frame indifference. For more details, the reader is referred to [Aubram, 2009] and to the monographs cited at the beginning of this chapter. The axiom was introduced by Noll [1958] with the intention to further reduce the general form of the constitutive equations. It is based on the fundamental concept of *objectivity* phrased in Definition A.6.9: let $\theta : \mathcal{S} \to \mathcal{S}$ be a spatial diffeomorphism, then a tensor $\boldsymbol{s}$ is called objective if $\boldsymbol{s}' = \theta_{\star}\boldsymbol{s}$, that is, if it transforms in the usual way. In classical treatises, however, θ represents a superposed rigid body motion, which is characterized by a proper orthogonal tangent map $T_x\theta : T_x\mathcal{S} \to T_{x'}\mathcal{S}$ for all $x \in \mathcal{S}$, with $x' = \theta(x)$. Superposed rigid body motions are spatial isometries leaving the spatial metric $\boldsymbol{g}$ unchanged.

Consider a *path-independent* or *elastic* material whose constitutive behavior remains unaffected by material history. By (4.1.9) and assuming material homogeneity, then, the general constitutive equation for the first Piola-Kirchhoff stress takes the form $\boldsymbol{P}(X,t) = \bar{\boldsymbol{P}}(\boldsymbol{F})(X,t)$; see also Definition 4.1.4.

Axiom 4.1.10 (Material Frame Indifference). *Let the constitutive functional $\bar{\boldsymbol{P}}$ representing elastic material satisfy the axioms of determinism, equipresence, and locality, and let the material be path-independent, homogenous and non-aging, so that $\boldsymbol{P} = \bar{\boldsymbol{P}}(\boldsymbol{F})$. Then, $\bar{\boldsymbol{P}}$ is functionally invariant under a superposed rigid body motion $\theta : \mathcal{S} \to \mathcal{S}$, that is,*

$$\boldsymbol{P}' = \bar{\boldsymbol{P}}(\boldsymbol{F}'),$$

where $\boldsymbol{F}'(X) : T_X\mathcal{B} \to T_{x'}\mathcal{S}$, $x' = \theta(x) = \theta(\varphi(X)) \in \mathcal{S}$, and $\boldsymbol{F}' = \theta_{\star}\boldsymbol{F}$ and $\boldsymbol{P}' = \theta_{\star}\boldsymbol{P}$ are the objective transformations of $\boldsymbol{F}$ and $\boldsymbol{P}$, respectively.

If the constitutive functional of Axiom 4.1.10 satisfies material frame indifference, then it depends only on the right Cauchy-Green tensor $\boldsymbol{C} = (\boldsymbol{F}^{\mathrm{T}} \circ \varphi) \cdot \boldsymbol{F}$, that is, $\boldsymbol{P} = \tilde{\boldsymbol{P}}(\boldsymbol{C})$. To obtain the corresponding constitutive equations for the second Piola-Kirchhoff stress $\boldsymbol{S}$ and the Cauchy stress $\boldsymbol{\sigma}$ from $\boldsymbol{P} = \tilde{\boldsymbol{P}}(\boldsymbol{C})$, one has to apply the transformation rule (3.2.24), yielding $\boldsymbol{S} = \bar{\boldsymbol{S}}(\boldsymbol{C}) = (\boldsymbol{F}^{-1} \cdot \tilde{\boldsymbol{P}})(\boldsymbol{C})$ and $\boldsymbol{\sigma} = \bar{\boldsymbol{\sigma}}(\boldsymbol{C}) = (J^{-1}\tilde{\boldsymbol{P}} \cdot \boldsymbol{F}^{-1})(\boldsymbol{C})$, respectively. Since the right Cauchy-Green tensor is a function of $\boldsymbol{F}(X)$ and the spatial metric $\boldsymbol{g}(x)$ through $\boldsymbol{C} = \varphi^{\star}\boldsymbol{g}$, one may set $\tilde{\boldsymbol{\sigma}}(\boldsymbol{F}, \boldsymbol{g}) \stackrel{\text{def}}{=} \bar{\boldsymbol{\sigma}}(\boldsymbol{C}(\boldsymbol{F}, \boldsymbol{g}))$.

4.1.2 Objective and Corotational Rates

The index "t" indicating time-dependency of the involved mappings will be dropped for notational brevity, and dependency on a point mapping will be usually clear from the context.

Material frame indifference 4.1.10 includes the postulate that the tensor fields related to a constitutive functional transform objectively under some spatial maps. There are two levels of objectivity on general differentiable manifolds that should be distinguished [Marsden and Hughes, 1994, p. 102].

Definition 4.1.11. A tensor field $\boldsymbol{s}$ on the ambient space $\mathcal{S}$ which transforms objectively with $\boldsymbol{s}' = \theta_{\star}\boldsymbol{s}$ under superposed rigid motions $\theta \colon \mathcal{S} \to \mathcal{S}$ is just called *objective*. If $\boldsymbol{s}$ transforms objectively under arbitrary spatial diffeomorphisms θ, then it is called *spatially covariant*. ♢

Spatial covariance is a stronger (or more general) version of objectivity: every spatially covariant tensor is objective under isometries, but the converse is false. Note that the claim for spatial covariance is automatically satisfied by honest tensor fields $\boldsymbol{T} \in \mathfrak{T}^p_q(\mathcal{B})$ on the material body. Spatial and two-point tensor fields, on the other hand, might be objective or even spatially covariant, but their material time derivative (Definition 3.1.32) is generally not. This is particularly true for the Cauchy stress $\boldsymbol{\sigma}(x, t)$ [Truesdell and Noll, 2004].

The preceding observation plays an important role in constitutive theory, and a large amount of literature to recent days is concerned with the discussion and/or development of objective rates. In fact, any possible objective rate of spatial second-order tensors is a particular manifestation of the spatial Lie derivative [Marsden and Hughes, 1994; Simo and Marsden, 1984; Simo and Hughes, 1998]. The Lie derivative introduced in Section A.7 is a geometric object that has an important property: if a tensor is spatially covariant, then its Lie Derivative also is. In this context, see [Marsden and Hughes, 1994, pp. 101–102] and [Aubram, 2009, prop. 4.6.18].

Objective and even spatially covariant stress rates do not commute with index raising and index lowering if the respective rates of the metric tensor do not vanish. Consequently, the stress invariants which are formed by the metric tensor would not be stationary at zero stress rate. This fact, however, conflicts with Prager's requirement [Prager, 1961; Naghdi and Wainwright, 1961; Guo, 1963] and constitutes a drawback

in plasticity theory [Xiao et al., 2000; Bruhns et al., 2004]. The so-called *corotational rates* circumvent this drawback.

Definition 4.1.12. Let $\boldsymbol{s}$ be a time-differentiable second-order objective tensor field on the ambient space, and let $\boldsymbol{\Lambda} = -\boldsymbol{\Lambda}^{\mathrm{T}}$ be a spin tensor, then

$$\mathring{\boldsymbol{s}} \stackrel{\text{def}}{=} \dot{\boldsymbol{s}} - \boldsymbol{\Lambda} \cdot \boldsymbol{s} + \boldsymbol{s} \cdot \boldsymbol{\Lambda}$$

is called the *corotational rate* of $\boldsymbol{s}$ defined by the spin $\boldsymbol{\Lambda}$. This definition is the same for all associated tensors $\boldsymbol{s} \in \mathfrak{T}^1_1(\mathcal{S})$, $\boldsymbol{s}^\sharp \in \mathfrak{T}^2_0(\mathcal{S})$, and $\boldsymbol{s}^\flat \in \mathfrak{T}^0_2(\mathcal{S})$ irrespective of index placement because all corotational rates commute with index raising and index lowering. ♢

Let $\boldsymbol{\Lambda}(x,t) = -\boldsymbol{\Lambda}^{\mathrm{T}}(x,t)$ be a given spin tensor for all $x \in \varphi(\mathcal{B},t)$ and $t \in [0,T]$, with $\varphi(\mathcal{B},0) = \mathcal{B}$. Consider the following evolution equation

$$\frac{\partial \boldsymbol{\mathfrak{R}}}{\partial t} = (\boldsymbol{\Lambda} \circ \varphi) \cdot \boldsymbol{\mathfrak{R}}\,, \qquad \text{with} \qquad \boldsymbol{\mathfrak{R}}|_{t=0} = \boldsymbol{I}\,, \tag{4.1.13}$$

where $\boldsymbol{\mathfrak{R}}(X,t) : T_X\mathcal{B} \to T_{\varphi(X,t)}\mathcal{S}$ is a proper orthogonal two-point tensor for fixed $X \in \mathcal{B}$ and each $t \in [0,T]$, such that $\boldsymbol{\mathfrak{R}}^{\mathrm{T}} \cdot \boldsymbol{\mathfrak{R}} = \boldsymbol{I}_{\mathcal{B}}$, $\boldsymbol{\mathfrak{R}} \cdot \boldsymbol{\mathfrak{R}}^{\mathrm{T}} = \boldsymbol{I}_{\mathcal{S}}$, and $\det \boldsymbol{\mathfrak{R}} = +1$. Solutions to the problem (4.1.13) generate a *one-parameter group of rotations* to which $\boldsymbol{\mathfrak{R}}$ belongs, thus $\boldsymbol{\Lambda}$ is called the *generator* of that group [Hughes, 1984; Simo and Hughes, 1998].

From this, the term "corotational" can be justified as follows. In a rotating Euclidian frame with spin $\boldsymbol{\Lambda} = \dot{\boldsymbol{\mathfrak{R}}} \cdot \boldsymbol{\mathfrak{R}}^{\mathrm{T}}$ the tensor $\boldsymbol{s}$ is given by $\boldsymbol{\mathfrak{S}} = \boldsymbol{\mathfrak{R}}^\star \boldsymbol{s} = \boldsymbol{\mathfrak{R}}^{\mathrm{T}} \cdot \boldsymbol{s} \cdot \boldsymbol{\mathfrak{R}}$. Then, the corotational rate $\mathring{\boldsymbol{s}}$ represents the rate of change of $\boldsymbol{\mathfrak{S}}$ observed in the *fixed frame* where $\boldsymbol{s}$ is measured. Clearly,

$$\mathring{\boldsymbol{s}} = \boldsymbol{\mathfrak{R}} \cdot \dot{\boldsymbol{\mathfrak{S}}} \cdot \boldsymbol{\mathfrak{R}}^{\mathrm{T}}\,. \tag{4.1.14}$$

There are infinitely many objective rates and corotational rates. Not every corotational rate is objective, and vice versa. Whether or not a corotational rate is objective depends on its defining spin tensor. For example, the corotational *Zaremba-Jaumann rate of Cauchy stress* $\boldsymbol{\sigma}$ [Zaremba, 1903; Jaumann, 1911] is obtained by setting $\boldsymbol{\Lambda} = \boldsymbol{\omega}$, where $\boldsymbol{\omega} = \frac{1}{2}(\boldsymbol{l} - \boldsymbol{l}^{\mathrm{T}}) \in \mathfrak{T}^1_1(\mathcal{S})$ is the vorticity tensor according to (3.1.17):

$$\mathring{\boldsymbol{\sigma}}^{\mathrm{ZJ}} \stackrel{\text{def}}{=} \dot{\boldsymbol{\sigma}} - \boldsymbol{\omega} \cdot \boldsymbol{\sigma} + \boldsymbol{\sigma} \cdot \boldsymbol{\omega}\,. \tag{4.1.15}$$

Another corotational rate arises from the right polar decomposition $\boldsymbol{F} = \boldsymbol{R} \cdot \boldsymbol{U}$ of the deformation gradient. Similar to the velocity gradient given by the relation $\frac{\partial}{\partial t}\boldsymbol{F} = (\boldsymbol{l} \circ \varphi) \cdot \boldsymbol{F}$, the *spatial rate of rotation* $\boldsymbol{\Omega}$ is defined through

$$\frac{\partial \boldsymbol{R}}{\partial t} \stackrel{\text{def}}{=} (\boldsymbol{\Omega} \circ \varphi) \cdot \boldsymbol{R}\,. \tag{4.1.16}$$

$\boldsymbol{\Omega} \in \mathfrak{T}^1_1(\mathcal{S})$ is a kind of angular velocity field describing the rate of rotation of the material, whereas $\boldsymbol{\omega}$ describes the rate of rotation of the principal axes of the rate of

deformation tensor $\boldsymbol{d} = \boldsymbol{l} - \boldsymbol{\omega}$ [Dienes, 1979]. Choosing the spin $\boldsymbol{\Lambda} = \boldsymbol{\Omega}$ then defines the corotational *Green-Naghdi stress rate* [Green and Naghdi, 1965],

$$\mathring{\boldsymbol{\sigma}}^{\mathrm{GN}} \stackrel{\mathrm{def}}{=} \dot{\boldsymbol{\sigma}} - \boldsymbol{\Omega} \cdot \boldsymbol{\sigma} + \boldsymbol{\sigma} \cdot \boldsymbol{\Omega} \,. \tag{4.1.17}$$

Remark 4.1.18. Time differentiation of $\boldsymbol{F} = \boldsymbol{R} \cdot \boldsymbol{U}$ yields a relation between vorticity $\boldsymbol{\omega} = \frac{1}{2}(\boldsymbol{l} - \boldsymbol{l}^{\mathrm{T}})$ associated with the Zaremba-Jaumann rate and spatial rate of rotation $\boldsymbol{\Omega} = \dot{\boldsymbol{R}} \cdot \boldsymbol{R}^{\mathrm{T}}$ associated with the Green-Naghdi rate:

$$\boldsymbol{\omega} = \boldsymbol{\Omega} + \tfrac{1}{2}\boldsymbol{R} \cdot (\dot{\boldsymbol{U}} \cdot \boldsymbol{U}^{-1} - \boldsymbol{U}^{-1} \cdot \dot{\boldsymbol{U}}) \cdot \boldsymbol{R}^{\mathrm{T}} \,.$$

In contrast to $\boldsymbol{\Omega}$, the vorticity tensor $\boldsymbol{\omega}$ also contains terms due to stretching. Therefore, the Green-Naghdi rate (4.1.17) is identical to the material time derivative of the Cauchy stress in the absence of rigid body rotation, while the Zaremba-Jaumann rate (4.1.15) is generally not. The Green-Naghdi rate requires knowledge of total material deformation through $\boldsymbol{R} = T\varphi \cdot \boldsymbol{U}^{-1}$, while the Zaremba-Jaumann rate, by virtue of vorticity, is derivable from the instantaneous motion at current time. This makes the Zaremba-Jaumann rate more attractive to problems where a past material motion is unavailable (see Chapter 6). By using the equation above, it can be shown that $\boldsymbol{\omega} = \boldsymbol{\Omega}$ resp. $\mathring{\boldsymbol{\sigma}}^{\mathrm{ZJ}} = \mathring{\boldsymbol{\sigma}}^{\mathrm{GN}}$ if and only if the motion of the material body is a rigid rotation, a pure stretch, or if the current configuration has been chosen as the reference configuration such that $\boldsymbol{F} = \boldsymbol{R} = \boldsymbol{I}^{\varphi}$, $\boldsymbol{U} = \boldsymbol{I}$, and $\dot{\boldsymbol{F}} = \dot{\boldsymbol{R}} + \boldsymbol{I}^{\varphi} \cdot \dot{\boldsymbol{U}}$; see also [Truesdell and Noll, 2004, pp. 54–55] and [Dienes, 1979, 1986; Cheng and Tsui, 1992]. △

It can be summarized that the Zaremba-Jaumann rate and the Green-Naghdi rate are corotational, objective, and satisfy Prager's requirement, but they are not spatially covariant. The Oldroyd rate and the Truesdell rate meet the much stronger condition of spatial covariance, but they include stretching parts, thus are not corotational, and they do not commute with index raising and lowering applied to their argument.

4.1.3 Spatial Rate Constitutive Equations

There are basically two main groups of rate-independent constitutive equations (or material models) that are used in computational solid mechanical applications at large deformation. The elements of the first group are typically based on thermodynamical principles postulated at the outset, and they are commonly addressed with the prefix "hyper": *hyperelasticity* , *hyperelasto-plasticity*, and *hyperplasticity*. The constitutive equations belonging to the second group usually ignore balance of energy and the axiom of entropy production 4.1.7. Many of them are are based on an *ad hoc* extension of existing small-strain constitutive equations to the finite deformation range. Elements of the second group are called *Eulerian* or *spatial rate constitutive equations* and are commonly addressed with the prefix "hypo": *hypoelasticity*, *hypoelasto-plasticity*, and *hypoplasticity*.

The following section is concerned with the second group because spatial rate constitutive equations have also been implemented into the ALE method developed during

this research. It has been pointed out by several researchers on the subject [e.g. Simo and Pister, 1984; Simo and Hughes, 1998] that, in spite of their shortcomings, these material models remain widely used in computational mechanics. This is because the same integration algorithms can be employed at both infinitesimal and finite deformations; cf. Section 5.5. Most of the commercial finite element codes, including ANSYS®, LS-DYNA®, and ABAQUS®, apply rate constitutive equations for problems involving small or large inelastic deformations. In what follows, only rate constitutive equations accounting for finite deformation are addressed. Readers who are not familiar with elasticity and classical elasto-plasticity at small strains should consult introductory texts on plasticity theory [e.g. Chen and Han, 1988; Simo and Hughes, 1998].

It is assumed that the constitutive functionals satisfy the axioms of determinism, locality, and material frame indifference, and the underlying materials are assumed homogeneous and non-aging. Without indicating it further, stress measures are taken with all indices raised, and strain measures with all indices lowered, e.g. $\boldsymbol{\sigma} \overset{\text{def}}{=} \boldsymbol{\sigma}^\sharp$ and $\boldsymbol{d} \overset{\text{def}}{=} \boldsymbol{d}^\flat$. This is consistent with the majority of bibliography on that topic.

Definition 4.1.19. In constitutive theory it proves convenient to define the following measures of stress and rate of deformation.

(i) The *negative mean Cauchy stress* and the *Cauchy stress deviator*

$$p \overset{\text{def}}{=} -\tfrac{1}{3}\operatorname{tr}\boldsymbol{\sigma} \qquad \text{and} \qquad \boldsymbol{\sigma}_{\text{dev}} \overset{\text{def}}{=} \boldsymbol{\sigma} + p\,\boldsymbol{g}^\sharp\,,$$

respectively.

(ii) The *von Mises stress* or *equivalent shear stress*

$$q \overset{\text{def}}{=} \sqrt{3J_2} = \sqrt{\tfrac{3}{2}}\,\|\boldsymbol{\sigma}_{\text{dev}}\|\,,$$

in which

$$J_2 \overset{\text{def}}{=} \tfrac{1}{2}\operatorname{tr}(\boldsymbol{\sigma}^2_{\text{dev}}) = \tfrac{1}{3}\left(I_1(\boldsymbol{\sigma})\right)^2 - I_2(\boldsymbol{\sigma}) \qquad \geq 0$$

is the negative second principal invariant of the Cauchy stress deviator according to the general formulas (A.5.20), and $I_1(\boldsymbol{\sigma})$, $I_2(\boldsymbol{\sigma})$ are the first and second the principal invariants of the Cauchy stress, respectively.

(iii) The *equivalent shear strain rate* and the *volumetric strain rate*

$$d_{\text{iso}} \overset{\text{def}}{=} \sqrt{\frac{2}{3}\operatorname{tr}(\boldsymbol{d}^2_{\text{dev}})} \qquad \text{and} \qquad d_{\text{vol}} \overset{\text{def}}{=} \operatorname{tr}\boldsymbol{d} = d^k{}_k\,,$$

respectively, with $\boldsymbol{d}_{\text{dev}} \overset{\text{def}}{=} \boldsymbol{d} - \tfrac{1}{3}(\operatorname{tr}\boldsymbol{d})\boldsymbol{g}$. ♢

Hypoelasticity

According to Section 4.1, the general constitutive equation of homogenous isotropic elasticity in the material and spatial settings read

$$\boldsymbol{S} = \bar{\boldsymbol{S}}(\boldsymbol{C}, \boldsymbol{G}) \qquad \text{and} \qquad \boldsymbol{\sigma} = \bar{\boldsymbol{\sigma}}(\boldsymbol{F}, \boldsymbol{g})\,, \tag{4.1.20}$$

respectively. However, there is only a limited number of materials, e.g. rubber, whose stress state can be derived as a whole, either from a finite strain measure (say $\boldsymbol{C}$), or a free energy function. This observation led to the development of *hypoelastic* rate constitutive equations [Truesdell, 1955b,a; Truesdell and Noll, 2004]. The general hypoelastic rate constitutive equation can be written in the form

$$\mathring{\boldsymbol{\sigma}}^{\star} \stackrel{\text{def}}{=} \boldsymbol{h}(\boldsymbol{\sigma}, \boldsymbol{g}, \boldsymbol{d}) = \boldsymbol{a}(\boldsymbol{\sigma}, \boldsymbol{g}) : \boldsymbol{d} \qquad \text{(linearity in } \boldsymbol{d}) \,, \tag{4.1.21}$$

where $\mathring{\boldsymbol{\sigma}}^{\star}$ can be any spatially objective rate of the Cauchy stress, $\boldsymbol{a}(\boldsymbol{\sigma}, \boldsymbol{g})$ is a spatial fourth-order tensor-valued function, and the spatial metric $\boldsymbol{g}$ is necessary to form invariants of the stress tensor, if desired. If only rate-independent response should be modeled by (4.1.21), then $\boldsymbol{h}$ must be *positively homogeneous of first degree* in $\boldsymbol{d}$, i.e. $\boldsymbol{h}(\boldsymbol{\sigma}, \boldsymbol{g}, a\boldsymbol{d}) = a\boldsymbol{h}(\boldsymbol{\sigma}, \boldsymbol{g}, \boldsymbol{d})$ for all $a > 0$. Moreover, due to material frame-indifference 4.1.10, the response function $\boldsymbol{h}$ for the stress rate must be isotropic in $\boldsymbol{\sigma}$, $\boldsymbol{g}$, and $\boldsymbol{d}$. Hence $\boldsymbol{a}$ is likewise isotropic.

A material is said to be *hypoelastic of grade* n, if $\boldsymbol{a}(\boldsymbol{\sigma}, \boldsymbol{g})$ is a polynomial of degree n in the components of $\boldsymbol{\sigma}$ [Truesdell, 1955b; Truesdell and Noll, 2004]. For $n = 0$, representing *hypoelasticity of grade zero*, the tensor $\boldsymbol{a}(\boldsymbol{g})$ is independent of $\boldsymbol{\sigma}$. The simplest *ad hoc* choice compatible with this idea is the constant isotropic elasticity tensor

$$a^{ijkl} = K\, g^{ij} g^{kl} + 2G(g^{ik} g^{jl} + g^{il} g^{jk} - \tfrac{1}{3}\, g^{ij} g^{kl}) \,. \tag{4.1.22}$$

Here g^{ij} are the components of the inverse metric, $K = \lambda + \frac{2}{3}\mu$ is the *bulk modulus* or *modulus of compression*, $G = \mu$ is the *shear modulus*, and λ, μ are the *Lamé constants*. Since the deviator of a symmetric $\binom{0}{2}$-tensor $\boldsymbol{t} \stackrel{\text{def}}{=} \boldsymbol{t}^{\sharp}$ is defined through $\boldsymbol{t}_{\text{dev}} \stackrel{\text{def}}{=} \boldsymbol{t} - \frac{1}{3}(\operatorname{tr} \boldsymbol{t})\boldsymbol{g}^{\sharp}$, the considered grade-zero hypoelastic rate constitutive equation takes the form

$$\mathring{\boldsymbol{\sigma}}^{\text{ZJ}} \stackrel{\text{def}}{=} K(\operatorname{tr} \boldsymbol{d})\, \boldsymbol{g}^{\sharp} + 2G\, \boldsymbol{d}^{\sharp}_{\text{dev}} \qquad \text{resp.} \qquad (\mathring{\boldsymbol{\sigma}}^{\text{ZJ}})^{ij} \stackrel{\text{def}}{=} K d^{k}{}_{k}\, g^{ij} + 2G\, d^{ij}_{\text{dev}} \,, \tag{4.1.23}$$

by choosing $\mathring{\boldsymbol{\sigma}}^{\star}$ to be the Zaremba-Jaumann stress rate (4.1.15). Note that deviators are traceless, and that the deviator of rate of deformation reflects purely isochoric deformations.

Remark 4.1.24. Within the hypoelasticity framework the stress is not necessarily path-independent such that hypoelastic constitutive equations generally produce non-zero dissipation in a closed cycle. Additional conditions must be satisfied so that the model represents a properly elastic or hyperelastic material [Simo and Pister, 1984; Simo and Hughes, 1998]. △

Hypoelasto-Plasticity

In classical plasticity theory, plastic flow is understood as an irreversible process characterized in terms of the past material history. Let the past material history up to current time $t \in \mathbb{R}$, in accordance with the fundamentals of Section 4.1, be defined as

$$]-\infty, t] \ni \tau \mapsto \{\boldsymbol{\sigma}(x, \tau), \boldsymbol{q}(x, \tau)\} \,. \tag{4.1.25}$$

$\boldsymbol{q}(x,\tau) \stackrel{\text{def}}{=} \{q_1(x,\tau),\dots,q_m(x,\tau)\}$ is a set of (possibly tensor-valued) internal state variables, often referred to as the *hardening parameters* or *plastic variables*. Here $\boldsymbol{q}$ are understood as stress-like variables, like the yield stress, which are conjugate to a set $\boldsymbol{\alpha} \stackrel{\text{def}}{=} \{\alpha_1,\dots,\alpha_m\}$ of strain-like internal variables.

Definition 4.1.26. Let $\mathfrak{T}^2_{\text{sym}}$ be the set of symmetric $\binom{2}{0}$-tensor fields, and let the stress-like internal plastic variables $\boldsymbol{q} \stackrel{\text{def}}{=} \{q_1,\dots,q_m\}$ belong to the set identified through $\mathcal{H} \stackrel{\text{def}}{=} \{\boldsymbol{q} \,|\, \boldsymbol{q} \in \mathcal{H}\}$. A *state* of an elasto-plastic material is the pair $(\boldsymbol{\sigma},\boldsymbol{q}) \in \mathfrak{T}^2_{\text{sym}} \times \mathcal{H}$. The ad hoc extension of classical small-strain elasto-plasticity to the finite deformation range then consists of the following elements [cf. Simo and Hughes, 1998]:

(i) *Additive decomposition.* The spatial rate of deformation tensor is additively decomposed into elastic and plastic parts:

$$\boldsymbol{d} \stackrel{\text{def}}{=} \boldsymbol{d}^{\text{e}} + \boldsymbol{d}^{\text{p}}\,, \qquad \text{in components,} \qquad d_{ij} \stackrel{\text{def}}{=} d^{\text{e}}_{ij} + d^{\text{p}}_{ij}\,.$$

(ii) *Stress response.* A hypoelastic rate constitutive equation of the form

$$\mathring{\boldsymbol{\sigma}}^{\star} = \boldsymbol{a}(\boldsymbol{\sigma},\boldsymbol{g}) : (\boldsymbol{d} - \boldsymbol{d}^{\text{p}})$$

characterizes the *"elastic" response*, where $\mathring{\boldsymbol{\sigma}}^{\star}$ represents any objective stress rate.

(iii) *Elastic domain* and *yield condition.* A differentiable function $f : \mathfrak{T}^2_{\text{sym}} \times \mathfrak{T}^2_{\text{sym}} \times \mathcal{H} \to \mathbb{R}$ is called the *yield condition*, and

$$\mathcal{A}_{\boldsymbol{\sigma}} \stackrel{\text{def}}{=} \{(\boldsymbol{\sigma},\boldsymbol{q}) \in \mathfrak{T}^2_{\text{sym}} \times \mathcal{H} \,|\, f(\boldsymbol{\sigma},\boldsymbol{g},\boldsymbol{q}) \le 0\}$$

is the set of *admissible states* in stress space; the explicit dependency on the metric $\boldsymbol{g}$ is necessary in order to define invariants of $\boldsymbol{\sigma}$ and $\boldsymbol{q}$. An admissible state $(\boldsymbol{\sigma},\boldsymbol{q}) \in \mathcal{A}_{\boldsymbol{\sigma}}$ satisfying $f(\boldsymbol{\sigma},\boldsymbol{g},\boldsymbol{q}) < 0$ is said to belong to the *elastic domain* or to be an *elastic state*, and for $f(\boldsymbol{\sigma},\boldsymbol{g},\boldsymbol{q}) = 0$ the state is an *elasto-plastic state* lying on the *yield surface*. States with $f > 0$ are not admissible.

(iv) *Flow rule* and *hardening law.* The evolution equations for $\boldsymbol{d}^{\text{p}}$ and $\boldsymbol{q}$ are called the *flow rule* and *hardening law*, respectively:

$$\boldsymbol{d}^{\text{p}} \stackrel{\text{def}}{=} \lambda\, \boldsymbol{m}(\boldsymbol{\sigma},\boldsymbol{g},\boldsymbol{q}) \qquad \text{and} \qquad \mathring{\boldsymbol{q}}^{\star} \stackrel{\text{def}}{=} -\lambda\, \boldsymbol{h}(\boldsymbol{\sigma},\boldsymbol{g},\boldsymbol{q})\,.$$

Here $\boldsymbol{m}$ and $\boldsymbol{h}$ are prescribed functions, and $\lambda \ge 0$ is called the *consistency parameter* or *plastic multiplier*. The flow rule is called *associated* if $\boldsymbol{m} = D_{\boldsymbol{\sigma}} f$, and *non-associated* if $\boldsymbol{m}$ is obtained from a *plastic potential* $g \neq f$ as $\boldsymbol{m} = D_{\boldsymbol{\sigma}} g$. Within the *isotropic* hardening laws $\boldsymbol{q}$ usually represents the current radius of the yield surface, whereas $\boldsymbol{q}$ represents the center of the yield surface (*back stress*) in *kinematic* hardening laws.

(v) *Loading/unloading* and *consistency conditions.* It is assumed that $\lambda \ge 0$ satisfies the *loading/unloading conditions*

$$\lambda \ge 0\,, \qquad f(\boldsymbol{\sigma},\boldsymbol{g},\boldsymbol{q}) \le 0\,, \qquad \text{and} \qquad \lambda\, f(\boldsymbol{\sigma},\boldsymbol{g},\boldsymbol{q}) = 0\,,$$

as well as the *consistency condition*

$$\lambda\, \dot{f}(\boldsymbol{\sigma}, \boldsymbol{g}, \boldsymbol{q}) = 0\,. \qquad \diamondsuit$$

As an example, consider a well-known hypoelasto-plastic rate constitutive equation which is commonly referred to as *J_2-plasticity with isotropic hardening* or *von Mises plasticity* in computational solid mechanics [e.g. Nagtegaal and Veldpaus, 1984; Hughes, 1984; Simo and Hughes, 1998]. This model is applicable to metals and other materials because it includes the *von Mises yield condition*

$$f(\boldsymbol{\sigma}, \boldsymbol{g}, \sigma^{\mathrm{y}}) \stackrel{\mathrm{def}}{=} q(\boldsymbol{\sigma}, \boldsymbol{g}) - \sigma^{\mathrm{y}}\,, \tag{4.1.27}$$

where q is the von Mises stress (Definition 4.1.19), and σ^{y} is the current yield stress given by the linear relation

$$\sigma^{\mathrm{y}}(\varepsilon^{\mathrm{p}}) \stackrel{\mathrm{def}}{=} \sigma^{\mathrm{y}0} + E^{\mathrm{p}}\, \varepsilon^{\mathrm{p}}\,. \tag{4.1.28}$$

The *initial yield stress* $\sigma^{\mathrm{y}0}$ and the *plastic modulus* E^{p} are material constants in addition to the elastic constants E and ν (or K and G), and the *equivalent plastic strain* ε^{p} is understood as a function of the *plastic rate of deformation tensor* $\boldsymbol{d}^{\mathrm{p}}$.

Including (4.1.28) produces bilinear elasto-plastic response with isotropic hardening mechanism. Bilinear in this context means that a one-dimensional bar in simple tension behaves elastic with Young's modulus E until reaching the initial yield stress. Then plastic flow occurs, the material hardens by satisfying (4.1.28), and the *elasto-plastic tangent modulus* is given by the constant

$$E^{\mathrm{t}} \stackrel{\mathrm{def}}{=} \frac{E\, E^{\mathrm{p}}}{E + E^{\mathrm{p}}}\,. \tag{4.1.29}$$

Now, let the hypoelastic response be characterized by

$$\mathring{\boldsymbol{\sigma}}^{\mathrm{ZJ}} = \boldsymbol{a}(\boldsymbol{g}) : (\boldsymbol{d} - \boldsymbol{d}^{\mathrm{p}})\,, \tag{4.1.30}$$

where $\boldsymbol{a}(\boldsymbol{g})$ is the constant isotropic elasticity tensor given by (4.1.22). Plastic flow is assumed to be associated, that is,

$$\boldsymbol{d}^{\mathrm{p}} \stackrel{\mathrm{def}}{=} \boldsymbol{d}^{\mathrm{p}}_{\mathrm{dev}} \stackrel{\mathrm{def}}{=} \lambda\, \frac{\partial f}{\partial \boldsymbol{\sigma}} = \lambda\, \frac{3}{2q}\, \boldsymbol{\sigma}^{\flat}_{\mathrm{dev}} = \lambda \sqrt{\frac{3}{2}}\, \boldsymbol{n}^{\flat}\,, \tag{4.1.31}$$

where $\boldsymbol{n} \stackrel{\mathrm{def}}{=} \boldsymbol{\sigma}_{\mathrm{dev}}/\|\boldsymbol{\sigma}_{\mathrm{dev}}\|$, with $\operatorname{tr} \boldsymbol{n} = 0$. Therefore, plastic straining is purely deviatoric, and the *hardening law*, representing the evolution of the radius of the von Mises yield surface, is given by

$$\dot{\sigma}^{\mathrm{y}} = E^{\mathrm{p}}\, \dot{\varepsilon}^{\mathrm{p}} = E^{\mathrm{p}} \sqrt{\frac{2}{3} \operatorname{tr}((\boldsymbol{d}^{\mathrm{p}})^2)} = \lambda\, E^{\mathrm{p}} \qquad \text{resp.} \qquad \dot{\varepsilon}^{\mathrm{p}} = \lambda\,. \tag{4.1.32}$$

After substitution into the consistency condition during plastic loading, the plastic multiplier is obtained as

$$\lambda = \frac{2G}{3G + E^{\mathrm{p}}} \sqrt{\frac{3}{2}}\, \boldsymbol{n} : \boldsymbol{d}_{\mathrm{dev}}\,, \tag{4.1.33}$$

which completes the model. Some algebraic manipulation finally results in the hypo-elasto-plastic spatial rate constitutive equation

$$\mathring{\boldsymbol{\sigma}}^{\mathrm{ZJ}} = \boldsymbol{a}^{\mathrm{ep}}(\boldsymbol{\sigma}, \boldsymbol{g}, \varepsilon^{\mathrm{p}}) : \boldsymbol{d} \,, \tag{4.1.34}$$

in which the *elasto-plastic material tangent tensor* is given by

$$\boldsymbol{a}^{\mathrm{ep}}(\boldsymbol{\sigma}, \boldsymbol{g}, \varepsilon^{\mathrm{p}}) \stackrel{\mathrm{def}}{=} \boldsymbol{a}(\boldsymbol{g}) - \frac{6G^2}{3G + E^{\mathrm{p}}}\, \boldsymbol{n} \otimes \boldsymbol{n} \tag{4.1.35}$$

at plastic loading, and by $\boldsymbol{a}^{\mathrm{ep}}(\boldsymbol{\sigma}, \boldsymbol{g}, \varepsilon^{\mathrm{p}}) = \boldsymbol{a}(\boldsymbol{g})$ at elastic loading and unloading, and neutral loading, respectively. The distinction of these types of loading is done with the aid of (4.1.27) in conjunction with (4.1.28), that is, the dependency of the function $\boldsymbol{a}^{\mathrm{ep}}$ on ε^{p} is implicit.

Hypoplasticity

The notion of *hypoplasticity*, which is entirely different from that of hypoelasto-plasticity, has been introduced by Kolymbas [1991a], but the ideas behind are much older. The earliest hypoplastic constitutive equations have been developed to model the behavior of soils [Kolymbas, 1978; Gudehus and Kolymbas, 1979; Kolymbas, 1988]. Hypoplasticity can be understood as a generalization of hypoelasticity, and the general hypoplastic rate constitutive equation for isotropic materials takes the form

$$\mathring{\boldsymbol{\sigma}}^{\star} \stackrel{\mathrm{def}}{=} \boldsymbol{h}(\boldsymbol{\sigma}, \boldsymbol{g}, \boldsymbol{\alpha}, \boldsymbol{d}) \,, \tag{4.1.36}$$

where $\mathring{\boldsymbol{\sigma}}^{\star}$ represents any objective stress rate, and $\boldsymbol{\alpha}(x,t) \stackrel{\mathrm{def}}{=} \{\alpha_1(x,t), \ldots, \alpha_m(x,t)\}$ is a set of (possibly tensor-valued) internal state variables. In contrast to hypoelasticity, the hypoplastic response function $\boldsymbol{h}$ is generally *nonlinear* in $\boldsymbol{d}$ in order to describe dissipative behavior. Hypoplastic constitutive modeling basically means to fit the almost arbitrary tensor-valued response function $\boldsymbol{h}$ to experimental data.

Consider the simple case where $\mathring{\boldsymbol{\sigma}}^{\star} \stackrel{\mathrm{def}}{=} \boldsymbol{h}(\boldsymbol{\sigma}, \boldsymbol{g}, \boldsymbol{d})$. If rate-independent material should be described, then $\boldsymbol{h}$ is required to be positively homogeneous of first degree in $\boldsymbol{d}$, so that for every $a > 0$, $\boldsymbol{h}(\boldsymbol{\sigma}, \boldsymbol{g}, a\boldsymbol{d}) = a\boldsymbol{h}(\boldsymbol{\sigma}, \boldsymbol{g}, \boldsymbol{d})$. In this case, however,

$$\boldsymbol{h}(\boldsymbol{\sigma}, \boldsymbol{g}, \boldsymbol{d}) = \frac{\partial \boldsymbol{h}(\boldsymbol{\sigma}, \boldsymbol{g}, \boldsymbol{d})}{\partial \boldsymbol{d}} : \boldsymbol{d} = \boldsymbol{m}(\boldsymbol{\sigma}, \boldsymbol{g}, \boldsymbol{d}) : \boldsymbol{d} \tag{4.1.37}$$

by *Euler's theorem on homogeneous functions*, where $\boldsymbol{m}$ is a spatial fourth-order-tensor-valued function that does explicitly depend on $\boldsymbol{d}$. The values of $\boldsymbol{m}$ are referred to as *material tangent tensors*, as for other classes of rate constitutive equations.

A detailed description of the hypoplastic constitutive equation for sand that has been implemented into the developed ALE method is provided in Section 4.3.

Figure 4.1: Optical microscope photograph of dry silica sand (here: Berlin sand); courtesy of Dr.-Ing. U. Schran [see also Schran, 2003].

4.2 Modeling the Behavior of Sand

The following section introduces the basic mechanical characteristics of sand under monotonic and cyclic loading. Readers who are not familiar with basic topics of theoretical and experimental soil mechanics should consult one of the standard textbooks [e.g. Terzaghi, 1943; Wood, 1990; Craig, 2007; Bardet, 1997; Das, 2008]. Advanced papers on the cyclic behavior of soils can be found in [Pande and Zienkiewicz, 1982; Triantafyllidis, 2004]. In order to properly model the behavior of fully and partially saturated soil, it should be dealt with as a porous medium or immiscible mixture [e.g. Lewis and Schrefler, 1998; de Boer, 2000; Dormieux et al., 2006; Pinder and Gray, 2008]. Additional literature will be cited in the text.

4.2.1 Assumptions, Terminology, and Basic Relations

Soil generally is a mixture consisting of a solid phase and one or more fluid phases (e.g. water, air and water, water and oil). The solid phase is built up of contacting soil grains forming a soil skeleton, and the fluid phases fill the pores (voids) in between. Sand resp. cohesionless granular material is characterized by contact forces acting between the grains which are dominated by the mean stress and friction, whereas surface forces due to cohesion are neglected.

Fig. 4.1 indicates that sand is a heterogeneous material at the microscale of grain size, so that the actual physical fields are microscopically distributed over the constituents. The balance principles derived in Chapter 3 can be assumed to apply in the interior of each constituent on the microscale, whereas jump conditions express the balances at

the interfaces. In order to distinguish between the solid phase and all other phases in a specimen of sand on the microscopic scale, a *phase function* is defined through [Drew, 1983]

$$\pi(x,t) \stackrel{\text{def}}{=} \begin{cases} 1 & \text{if } x \text{ is in the void or fluid region at time } t \\ 0 & \text{else.} \end{cases} \tag{4.2.1}$$

The matter of concern in most practical engineering problems is the somehow averaged field and not its actual microscopic distribution. When employing *spatial averaging*, an averaging volume or *representative volume element (RVE)*, $\mathcal{V}' \subset \mathcal{S}$, has to be specified [Drew, 1983; Lewis and Schrefler, 1998; Pinder and Gray, 2008]. The RVE must contain a sufficient number of microscopic heterogeneities and fluctuations to be statistically representative. On the other hand, it must not be too large in order to retain macroscopic variations of the problem under consideration.

Definition 4.2.2. Let $\mathcal{V} \subset \varphi_t(\mathcal{B})$ be a fixed spatial domain occupied by the body at time $t \in [0,T]$, and let $V' \stackrel{\text{def}}{=} \int_{\mathcal{V}'} \mathbf{d}\boldsymbol{v}$ be the spatial volume measure of the representative volume element $\mathcal{V}'$. Then, the *volume average* of a microscopic scalar field $q : \mathcal{V} \times [0,T] \to \mathbb{R}$ over the RVE is defined pointwise through

$$\langle q \rangle(x,t) \stackrel{\text{def}}{=} \frac{1}{|V'|} \int_{\mathcal{V}'} q(x+\boldsymbol{\xi},t)\, \mathbf{d}\boldsymbol{v}\,,$$

with $\boldsymbol{\xi} = x' - x$, $x \in \mathcal{V}$, $x' \in \mathcal{V}'$, and $\lim_{V' \to 0} \langle q \rangle(x,t) = q(x,t)$. ◇

Spatial averaging enables a proper definition of basic soil mechanical quantities and notions.

Definition 4.2.3. Assume that all voids in the sand specimen under consideration are interconnected, then

(i) the spatial *porosity* $n_t : \varphi_t(\mathcal{B}) \to \mathbb{R}$ of the material body is defined as the volume average of the phase function, that is,

$$n(x,t) \stackrel{\text{def}}{=} \langle \pi \rangle(x,t)\,,$$

where $x = \varphi_t(X)$ and $n(x,t) = n_t(x)$.

(ii) The spatial *void ratio* $e(x,t)$, with $e_t : \varphi_t(\mathcal{B}) \to \mathbb{R}$ by holding t fixed, is the ratio of the partial volume of interconnected voids and the partial solid volume in the RVE. It is related to the porosity by $e = n/(1-n)$, so $n = e/(1+e)$. ◇

This thesis is concerned with quasi-static analysis of sand under isothermal conditions, so that effects due to inertia and temperature can be ignored. It is assumed throughout that the sand under consideration is either dry or fully saturated with water, so that the RVE consists of a solid phase and a single fluid phase. Surface effects like capillarity, cemented bridges, etc. are absent, and rate effects are negligible. The sand grains and the water are assumed to be incompressible, and the sand grains are permanent,

i.e. they are non-abrasive and cannot crush. Moreover, the bulk modulus and density of air are negligibly small compared to the bulk modulus and density, respectively, of the soil skeleton. If a sand specimen is fully saturated with water, then it is postulated to be also fully drained in the vicinity of every material particle. This means that the solid and fluid phases are uncoupled, and that consolidation effects will not occur. The impact of pore water on the grain skeleton is only due to buoyant forces occurring under static acceleration fields (i.e. gravitation). Due to all these assumptions, sand can be modeled as a one-phase porous material.

The macroscopic or averaged spatial mass densities of the dry sand and of the fully saturated sand can be written as

$$\rho_{\mathrm{d}}(x,t) \stackrel{\mathrm{def}}{=} (1-n(x,t))\,\rho_{\mathrm{s}}(x) \qquad \text{and} \qquad \rho_{\mathrm{r}}(x,t) \stackrel{\mathrm{def}}{=} \rho_{\mathrm{d}}(x,t) + n(x,t)\,\rho_{\mathrm{w}}(x)\,, \quad (4.2.4)$$

respectively. ρ_{d} is also called the *bulk mass density*, ρ_{s} denotes the *grain mass density*, that is, the density of the solid material, and ρ_{w} is the *water mass density*. Since both the sand grains and the pore water were assumed to be incompressible, ρ_{s} and ρ_{w} do not depend on time. Moreover, for the purpose of this work it is sufficient to use spatially constant values $\rho_{\mathrm{s}} = 2.65\,\mathrm{g\,cm^{-3}}$ for quartz resp. silica sand [see Herle and Gudehus, 1999; Rackwitz, 2003], and $\rho_{\mathrm{w}} = 1.0\,\mathrm{g\,cm^{-3}}$. The *effective mass density* of the sand is then defined through

$$\rho'(x,t) \stackrel{\mathrm{def}}{=} \rho_{\mathrm{r}}(x,t) - \rho_{\mathrm{w}} = (1-n(x,t))(\rho_{\mathrm{s}} - \rho_{\mathrm{w}})\,, \quad (4.2.5)$$

which leads to the fundamental *principle of effective stresses* for fully saturated soils [Terzaghi, 1943, art. 6]:

$$\boldsymbol{\sigma}'(x,t) \stackrel{\mathrm{def}}{=} \boldsymbol{\sigma}(x,t) + p_{\mathrm{w}}(x,t)\,\boldsymbol{g}^{\sharp}(x)\,. \quad (4.2.6)$$

Here $\boldsymbol{\sigma}$ is the *total stress* which represents the common measurable macroscopic stress, p_{w} is the *pore water pressure*, and $\boldsymbol{\sigma}'$ is the *effective stress* acting as a macroscopic variable within the soil skeleton. In soil mechanics, constitutive equations are usually postulated for $\boldsymbol{\sigma}'$. If no water is present, then $\boldsymbol{\sigma}' = \boldsymbol{\sigma}$.

Remark 4.2.7. A general convention in soil mechanics takes compression positive, so that (4.2.6) would read $\boldsymbol{\sigma}' = \boldsymbol{\sigma} - p_{\mathrm{w}}\,\boldsymbol{g}^{\sharp}$ at compression. This thesis, however, is also to be seen in the context of general mechanics. The common sign convention is applied throughout, that is, compressive stress is taken with negative sign. Regardless of these convention, pressure has positive sign whenever stress is compressive, otherwise it has negative sign. △

Proposition 4.2.8. *Let the motion $\varphi_t : \mathcal{B} \to \mathcal{S}$ be a one-parameter group of C^1-diffeomorphisms such that $\varphi_0(\mathcal{B}) = \mathcal{B}$ is the initial configuration of a sand specimen, and assume that conservation of mass holds. Then, incompressibility of the grains implies that the evolution of spatial void ratio is given by*

$$\dot{e}(x,t) = (1+e(x,t))\,\mathrm{tr}\,\boldsymbol{d}(x,t)\,.$$

PROOF. From conservation of mass 3.2.18(i), and $(4.2.4)_1$ it follows that for incompressible grains

$$(1 - n(\varphi(X,t),t))\, J(X,t) = 1 - n_0(X)$$

holds, in which $J(X,t)$ is the Jacobian of the motion φ, and $n_0(X) = n(\varphi(X,0),0)$ is the *initial porosity*. Since the void ratio is related to the porosity through $e = n/(1-n)$, the equation above is equivalent to $e = (1+e_0)J-1$. Taking the material time derivative on both sides and applying Proposition 3.1.19 then proves the assertion. ∎

The current void ratio e of a specimen of sand is bounded between a minimum value $e_{\min}$ and a maximum value $e_{\max}$. In general these are not material constants but depend on the confining pressure.

Definition 4.2.9. The *relative density* defined through

$$D_{\mathrm{r}} \overset{\mathrm{def}}{=} \frac{e_{\max} - e}{e_{\max} - e_{\min}}$$

allows to specify whether a specimen is relatively *loose* or *dense*:

	D_{r}	≤ 0.15	very loose
$0.15 <$	D_{r}	≤ 0.35	loose
$0.35 <$	D_{r}	≤ 0.65	medium dense
$0.65 <$	D_{r}	≤ 0.85	dense
$0.85 <$	D_{r}		very dense .

D_{r} is identical to I_{D} used in the German literature. ♢

An important characteristic that distinguishes sand response from that of other solids is the tendency of granular material to expand or contract in bulk volume due to shear loading, which is referred to as *dilatancy* [Reynolds, 1885]; to ease formulation, the term dilatancy is adopted here for both, positive (contractive) and negative (dilative) volume changes. Li et al. [1999] and Li and Dafalias [2000] show that dilatancy of sand is a function of both the stress state and the density state. These dependencies are also referred to as the *barotropy* and the *pycnotropy* of sand, respectively [Kolymbas, 1991a].

It should be mentioned that the finite deformation theory of soil mechanics is still little developed, although deformations often exceed infinitesimal values, e.g. during pile penetration, slope failure, or in triaxial and oedometric experimental laboratory tests. This is because until recent dates the basic tools of geotechnical engineering have been small-strain elasticity and limit design [cf. Kiousis et al., 1986]. Another reason is that the mathematical formulation of soil behavior results in rather complex relations compared to constitutive equations for metals or fluids, and finite deformation theory would further increase complexity. Therefore, the following two sections describe the behavior of sand under the assumption of small strains.

4.2.2 Monotonic Loading

Sand exposes several characteristics when subjected to different loading, boundary, and drainage conditions. Monotonic loading can be viewed as a limit of cyclic loading, and several experimental laboratory testing devices are available in order to investigate the associated mechanical behavior of sand. The triaxial device allows the application of shear deformation without rotating the principal stress axes. In an axisymmetric triaxial setting loading can be applied in axial (index "1") and radial (index "3") direction. Under these conditions and by recalling Definition 4.1.19, the negative mean effective stress resp. the effective pressure becomes $p' = -\frac{1}{3}(\sigma'_1 + 2\sigma'_3)$, and the von Mises stress boils down to $q' = q = |\sigma_1 - \sigma_3|$. In soil mechanics, however, the von Mises is usually replaced with the *deviator stress* $q \overset{\text{def}}{=} \sigma_1 - \sigma_3$. Moreover, the triaxial versions of volumetric strain rate and equivalent shear strain rate are $\dot{\varepsilon}_{\text{vol}} = \dot{\varepsilon}_1 + 2\dot{\varepsilon}_3$ and $\dot{\varepsilon}_{\text{iso}} = \frac{2}{3}(\dot{\varepsilon}_1 - \dot{\varepsilon}_3)$, respectively, where $\boldsymbol{\varepsilon} = \frac{1}{2}(\boldsymbol{\nabla u} + (\boldsymbol{\nabla u})^{\text{T}})$ is the infinitesimal strain tensor and $\boldsymbol{u} : \mathcal{B} \to T\mathcal{S}$ is the infinitesimal deformation imposed on the reference configuration $\mathcal{B}$. Under triaxial conditions the axial component $\dot{\varepsilon}_1$ is a measure of shear strain rate [see also Wood, 1990, sec. 1.4].

The dilative behavior of Toyoura sand under triaxial compression ($-\sigma_1 > -\sigma_3$) with different initial densities under the same initial stress state ($p_0 = 1000\,\text{kPa}$ and $q_0 = 0\,\text{kPa}$) is shown in Fig. 4.2; note that all the plotted curves presented in this section are results of numerical simulations. A specimen of sand with a sufficient low initial density ($D_{\text{r0}} = 0.15$) contracts monotonically and leads to a monotonically increasing shear strength (Fig. 4.2b). If the initial density is sufficient high, say medium dense ($D_{\text{r0}} = 0.64$), then sand shows little contraction at small shear strains. Under continued shear loading, the deviatoric stress increases until reaching a peak value, and the sand dilates until a residual strength is reached. Obviously, medium dense and dense sands pass a reversal point which marks the *phase transformation state* [Ishihara et al., 1975; Verdugo and Ishihara, 1996; Li and Dafalias, 2000], at which the density remains constant (Fig. 4.2a).

Analogous results to that of Fig. 4.2 can be obtained by a variation of the confining pressure instead of the initial density, indicating that both barotropy and pycnotropy of sand have an intrinsic relation. This is depicted in Fig. 4.3. The dilative responses of a medium dense sand under high confining pressures and a loose sand under intermediate confining pressures are comparable. One can also locate a peak value of deviator stress in the ε_1-q-plane for a sufficient dense sand or a sufficient low confining pressure, respectively. Irrespective of the initial conditions, sand exhibits an isochoric response at constant p' and q if shearing exceeds a certain value (Fig. 4.2), which is referred to as the *critical state* [Roscoe et al., 1958; Roscoe and Schofield, 1963]. The set of all critical states forms a curve in the ε_1-p'-q-plane [Wood, 1990], which means that the state of sand under monotonic loading is governed by both the stress state and the density state.

Li and Wang [1998] show that the amount of void ratios at critical state can be fitted to a straight line $e_{\text{c}} = e_\Gamma - \lambda_{\text{c}}(p'/p_{\text{a}})^\xi$ in the e-$(p'/p_{\text{a}})^\xi$-plane, where e_Γ, λ_{c}, and ξ are material constants, and the atmospheric pressure at sea level $p_{\text{a}} = 101\,\text{kPa}$ is included

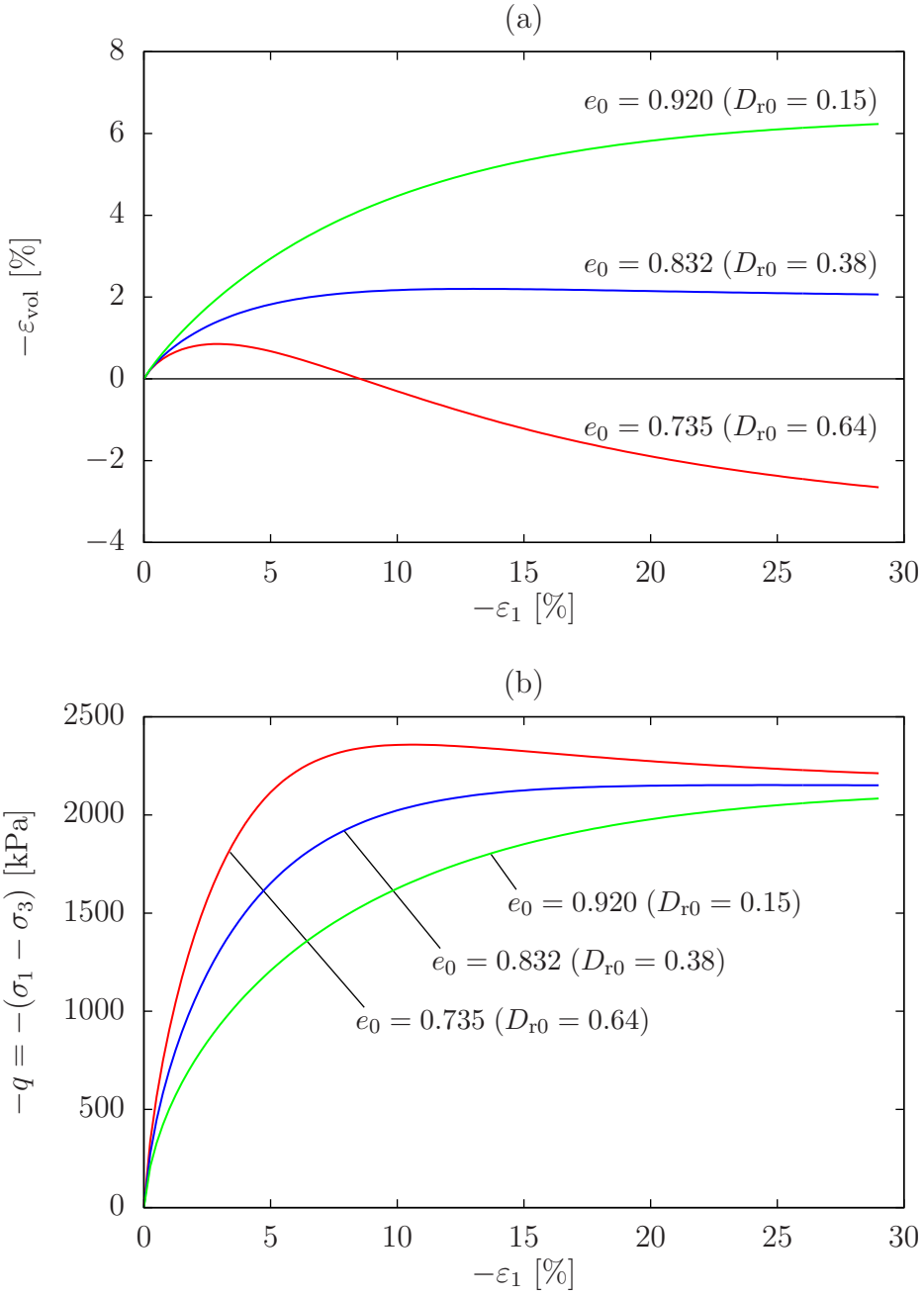

Figure 4.2: Simulated dilative behavior of sand under drained triaxial compression: dependency on the density state (pycnotropy). Toyoura sand, $p_0 = 1000\,\mathrm{kPa}$.

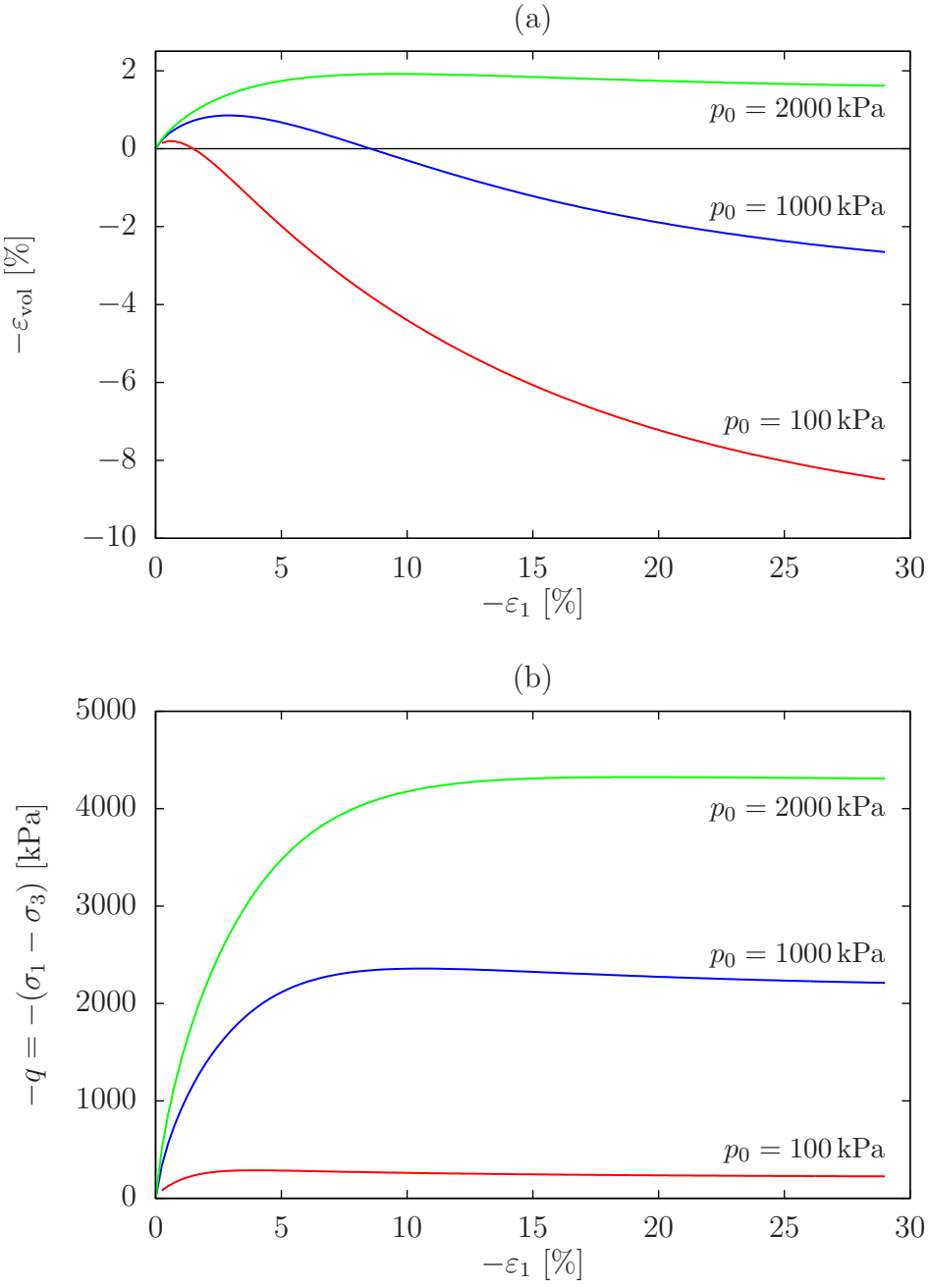

Figure 4.3: Simulated dilative behavior of sand under drained triaxial compression: dependency on the stress state (barotropy). Toyoura sand, $e_0 = 0.735$ ($D_{\mathrm{r0}} = 0.64$).

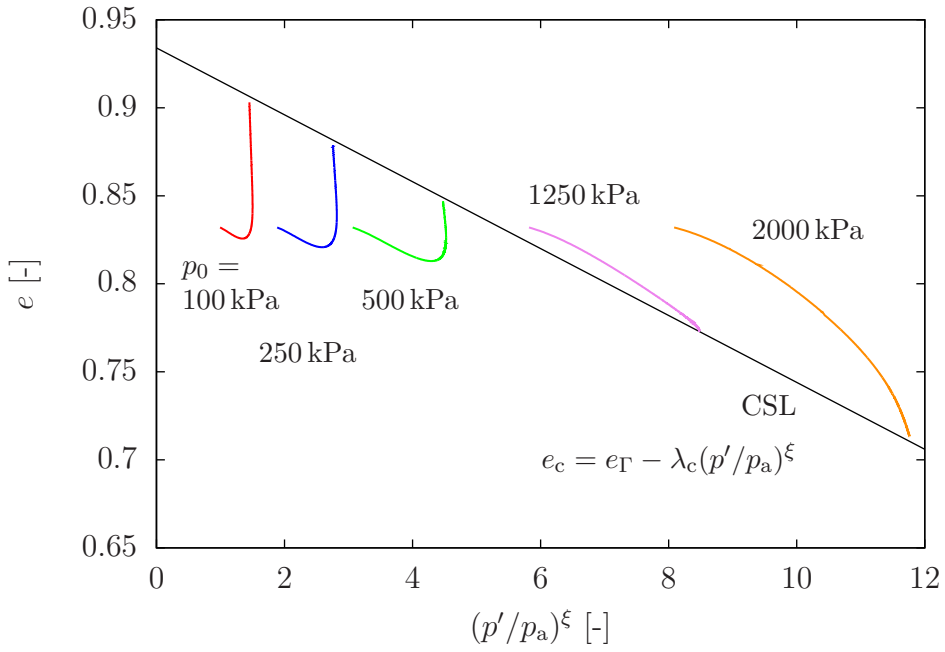

Figure 4.4: Simulated critical state line (CSL) in the e-$(p'/p_a)^\xi$-plane obtained for Toyoura sand, $e_0 = 0.832$ ($D_{r0} = 0.38$). The void ratios at critical state can be fitted to a straight line $e_c \stackrel{\text{def}}{=} e_\Gamma - \lambda_c(p'/p_a)^\xi$, with material constants $e_\Gamma = 0.934$, $\lambda_c = 0.019$, and $\xi = 0.7$ for Toyoura sand [Li and Dafalias, 2000].

for normalization. This critical state line (CSL) is plotted in Fig. 4.4 for Toyoura sand in triaxial compression at $e_0 = 0.832$ ($D_{r0} = 0.38$) and different confining pressures p_0. Now let a *state parameter* [Been and Jefferies, 1985] be defined through $\psi = e - e_c$. Then at the beginning of loading, the specimens with $p_0 = 100\,\text{kPa}$, $250\,\text{kPa}$, and $500\,\text{kPa}$ are said to be in a relatively dense state ($\psi < 0$) and behave dilative, whereas the specimens with $p_0 = 1250\,\text{kPa}$ and $2000\,\text{kPa}$ are in a relatively loose state ($\psi > 0$) and behave contractive [Li and Dafalias, 2000].

The dilative behavior of sand can also be observed under undrained conditions where $\dot{\varepsilon}_{vol} = 0$. Fig. 4.5 shows the results of undrained triaxial compression tests with Toyoura sand at the same confining pressure, but with three different densities. If a shear loading increment from a particular stress ratio $-q/p'$ is applied, the loose sand contracts and the dense sand dilates, resulting in a reduction or production of effective mean normal stress, respectively. These facts contradicts the stress-dilatancy approach introduced by Rowe [1962], in which the dilatancy is uniquely related to the stress ratio. Rowe's relation is based on the assumption that the rate of internal work done is a minimum, and thus density effects are eliminated [Li and Dafalias, 2000].

The drainage conditions have a dramatic impact on the shear strength of sand, even under monotonic loading. The results of comparative calculations are shown in Fig. 4.6. In each Fig. 4.6a and 4.6b, two specimen of sand under the same initial stress and density states are considered, but with one subjected to drained and the other to subjected undrained triaxial compression. If the initial density is sufficiently high

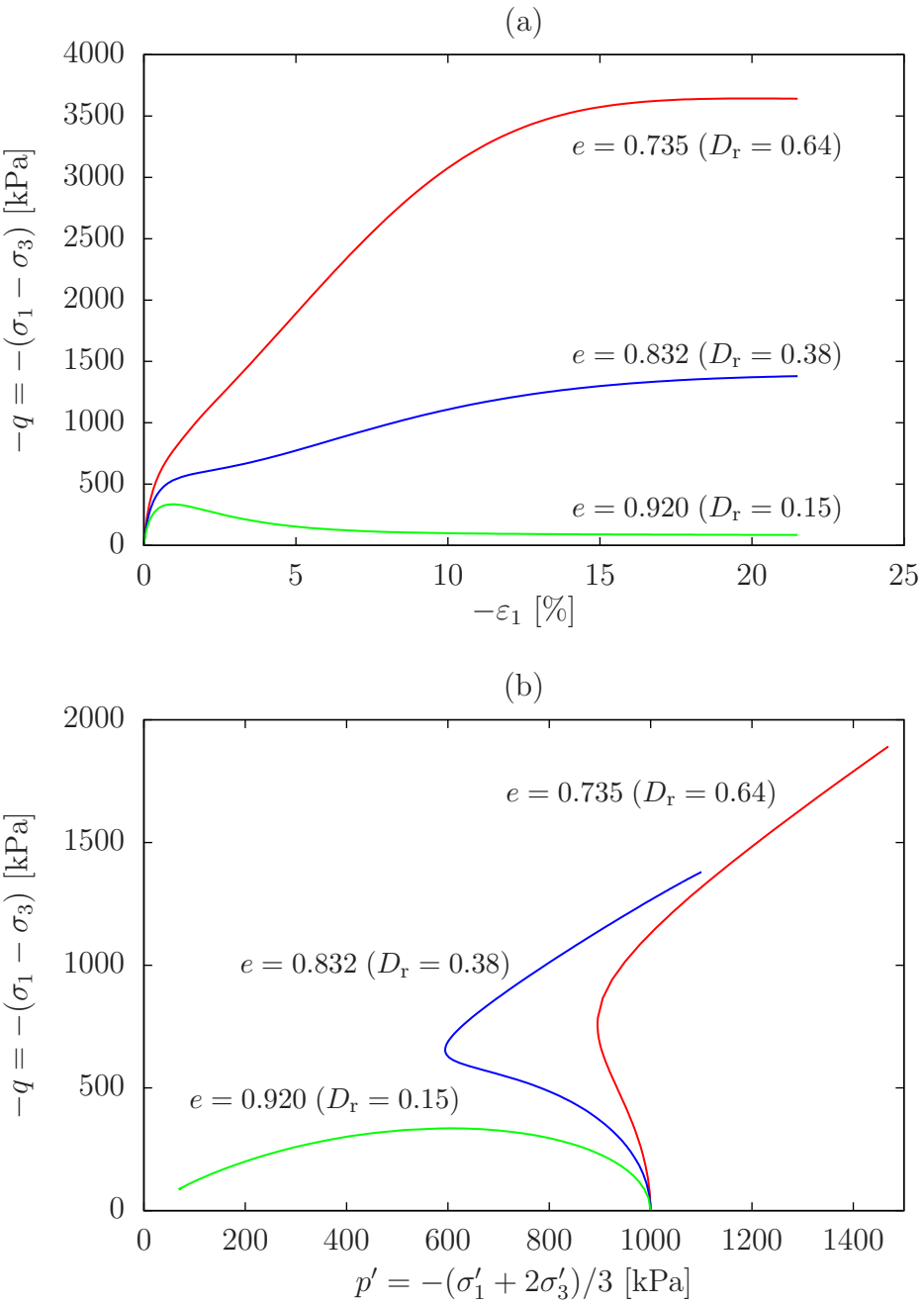

Figure 4.5: Simulated pycnotropy of sand under undrained triaxial compression. Toyoura sand, $p_0 = 1000\,\mathrm{kPa}$.

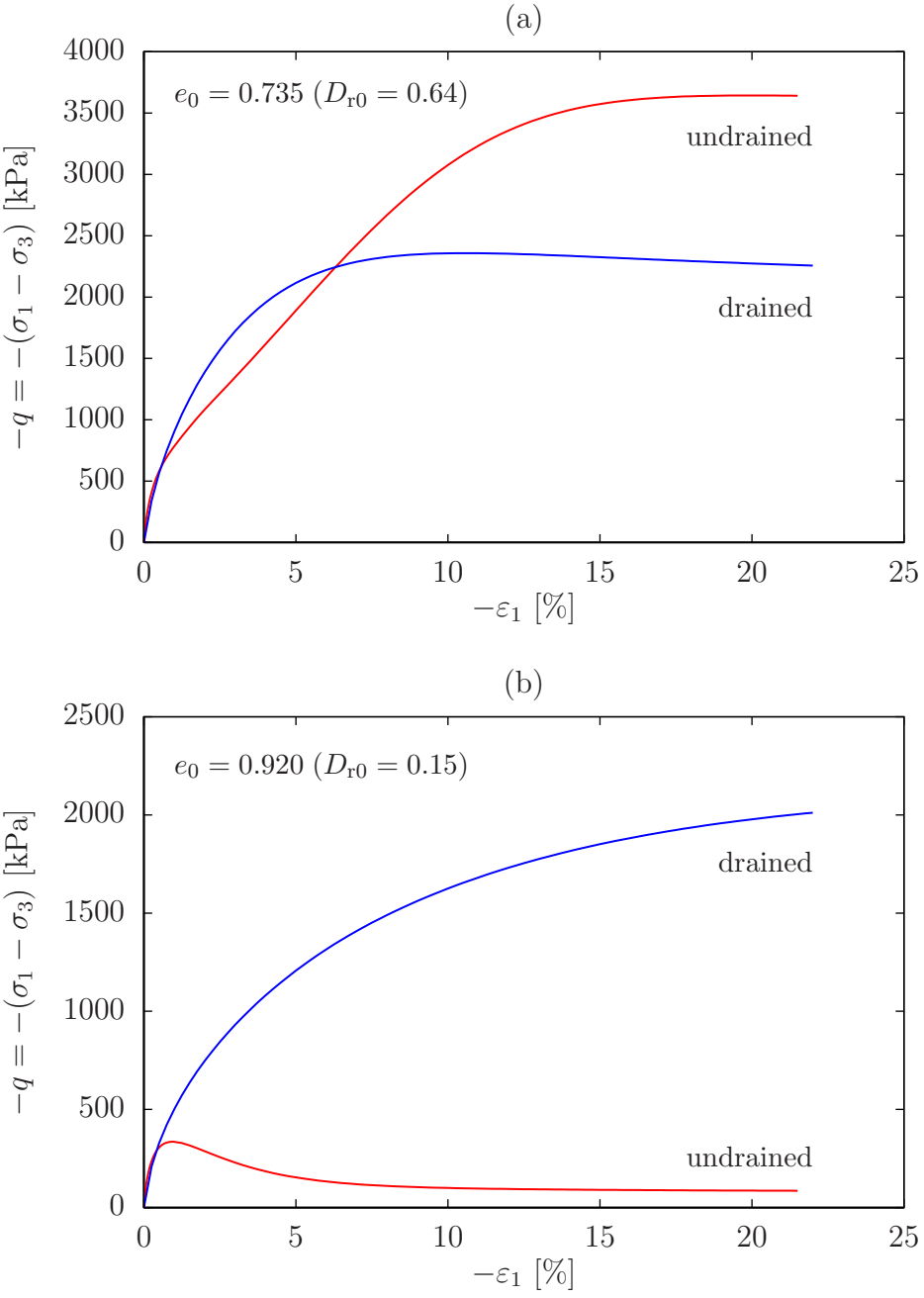

Figure 4.6: Simulated behavior of sand under drained and undrained conditions at different initial densities. Toyoura sand, $p_0 = 1000\,\mathrm{kPa}$.

(Fig. 4.6a) undrained sand hardens monotonically, resulting in a residual shear strength higher than under drained conditions. By contrast, the rearrangement of grains due to dilatancy leads to a build-up of excess pore water pressure under undrained conditions if the initial density is sufficient low (Fig. 4.6b). This goes along with a loss of grain contacts and a reduction of the mean effective stress, so that the shear strength drops down to a very small value. In the limit, *static liquefaction* will occur.

In standard axisymmetric triaxial compression and extension tests the loading is always *proportional*, meaning that $\dot{\boldsymbol{\sigma}} = a\,\boldsymbol{\sigma}$, with $a > 0$. However, in many practical applications loading is generally non-proportional, e.g. during wave loading acting on seabeds, and multidirectional earthquakes at ground level [Li, 2006]. Non-proportional loading paths in experimental laboratory testing of sand can be realized in the bi-directional simple shear device [Ishihara and Yamazaki, 1980], in the torsional shear device [Ishihara and Towhata, 1983; Towhata and Ishihara, 1985; Yoshimine et al., 1998], and in the true triaxial device [Hambly, 1969; Goldscheider, 1975; Yamada and Ishihara, 1979, 1981, 1983]. All these results point out that the incorporation of a non-proportional loading mechanism plays a crucial in realistic constitutive modeling of sand.

Goldscheider [1975], Ishihara and Yamazaki [1980], and Yamada and Ishihara [1981, 1983], among others, show that under non-proportional loading the generation of plastic deformations is also affected by the shape of the loading path in the stress-deviator-plane. This dependency on the direction of the stress rate renders the stress-strain relations incrementally nonlinear or hypoplastic [Dafalias, 1986; Wang et al., 1990; Li and Dafalias, 2004; Li, 2006]. Moreover, Vaid and Thomas [1995] carried out tests showing that the shear strength of an undrained sand at the same density is different in triaxial compression and triaxial extension, thus depends on the direction of the principle stress axes. This fabric or inherent anisotropy of sand deposits, under either proportional or non-proportional loading, has also been observed by other experimental researchers [e.g. Yamada and Ishihara, 1979, 1981, 1983; Ishihara and Towhata, 1983; Towhata and Ishihara, 1985; Yoshimine et al., 1998].

4.2.3 Cyclic Loading

A loading function is called *cyclic* if it includes at least two reversals in loading direction. For example, during pile penetration the soil is subjected to cyclic loading because it will be compressed, sheared, and then released if the pile tip passes (see Chapter 2). The mechanical behavior of sand is different under monotonic and cyclic loading, i.e. it depends on material history or how the current stress and density states have been reached. Therefore, the stress and density are not enough to describe the state of sand, and so additional state variables are needed.

As already pointed out in the previous section, the drainage conditions severely influence the strength of sand dependent on its relative density, and this would be crucial under cyclic loading. Undrained sand under monotonic loading is usually not encountered *in situ*, but can only be realized in the laboratory. However, under cyclic loading the loading direction changes faster than the sand consolidates due to the new loading

Figure 4.7: Effects of soil liquefaction: Loss of support of buildings during the 1964 Niigata, Japan earthquake. Photograph taken from `http://en.wikipedia.org/wiki/Soil_liquefaction`

conditions. This results in a gradual increase of the excess pore water pressure governed by the relative density, the confining pressure, the loading amplitude and frequency. Loose sand may be subjected to a complete loss of shear resistance and large deviatoric strains, which is also referred to as *liquefaction* (Fig. 4.7). Because it is often a major cause of damage during earthquakes, the experimental research on soil liquefaction has grown up since the 1960's [Seed and Lee, 1966; Peacock and Seed, 1968; Seed and Peacock, 1971; Seed, 1979; Finn et al., 1970, 1971; Castro, 1975; Ishihara et al., 1975; Ishihara and Yamazaki, 1980; Ishihara and Towhata, 1983; Savidis and Schuppe, 1982; Martin et al., 1975; Towhata and Ishihara, 1985; Vaid and Thomas, 1995]. In contrast to that, a sufficient dense sand regains its shear stiffness after a couple of loading cycles and shows *cyclic mobility* by limiting shear deformation [Castro, 1975].

Figs. 4.8 and 4.9 show the results of undrained cyclic triaxial tests with Toyoura sand under a confining pressure of $p_0 = 300\,\mathrm{kPa}$ (isotropic consolidation). The cyclic stress ratio was chosen to $q_{\max}/p_0 = 0.2$. Due to excess pore water pressure build-up the mean effective stress p' decreases cycle by cycle for both a loose and a medium dense specimen. However, in case of the loose specimen ($D_\mathrm{r} = 0.15$, Figs. 4.8a and 4.9a) the stress path already reaches a kind of failure surface indicated by the straight lines after a few cycles, and then moves slowly along the surface until reaching the final state. This behavior corresponds to the path in the γ-q-plane shown in Fig. 4.9a, where $\gamma = \varepsilon_1 - \varepsilon_3$ is the shear strain. As long as the stress path stays inside the failure surface, the shear deformation is relatively small or, conversely, the soil stiffness is relatively large. If the stress path approaches a failure state on the surface, then the shear stiffness drops quickly, leading to very large shear deformation.

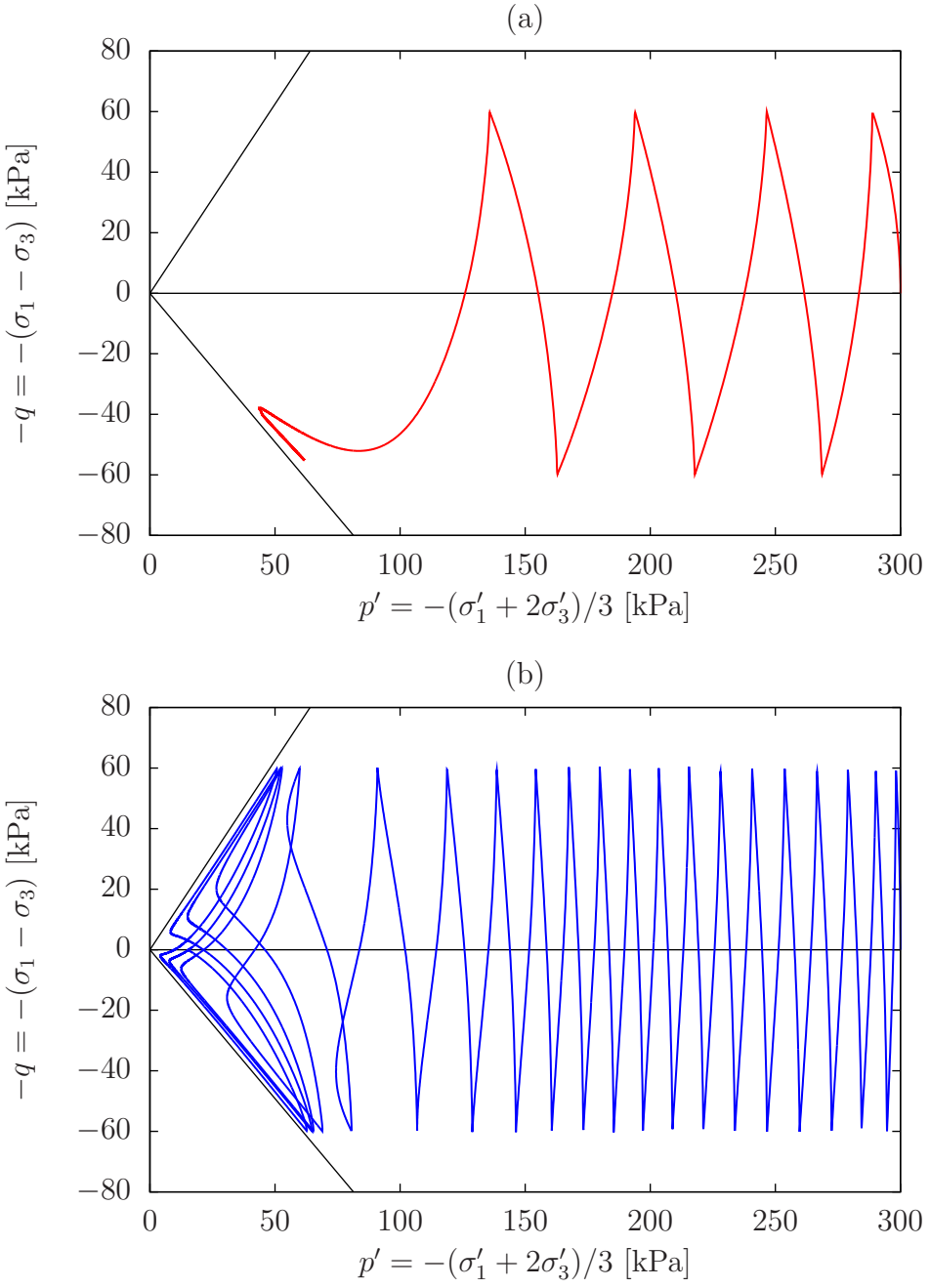

Figure 4.8: Simulated pycnotropy of Toyoura sand under undrained cyclic triaxial loading. Stress path at (a) $e = 0.920$ ($D_\mathrm{r} = 0.15$), (b) $e = 0.735$ ($D_\mathrm{r} = 0.64$).

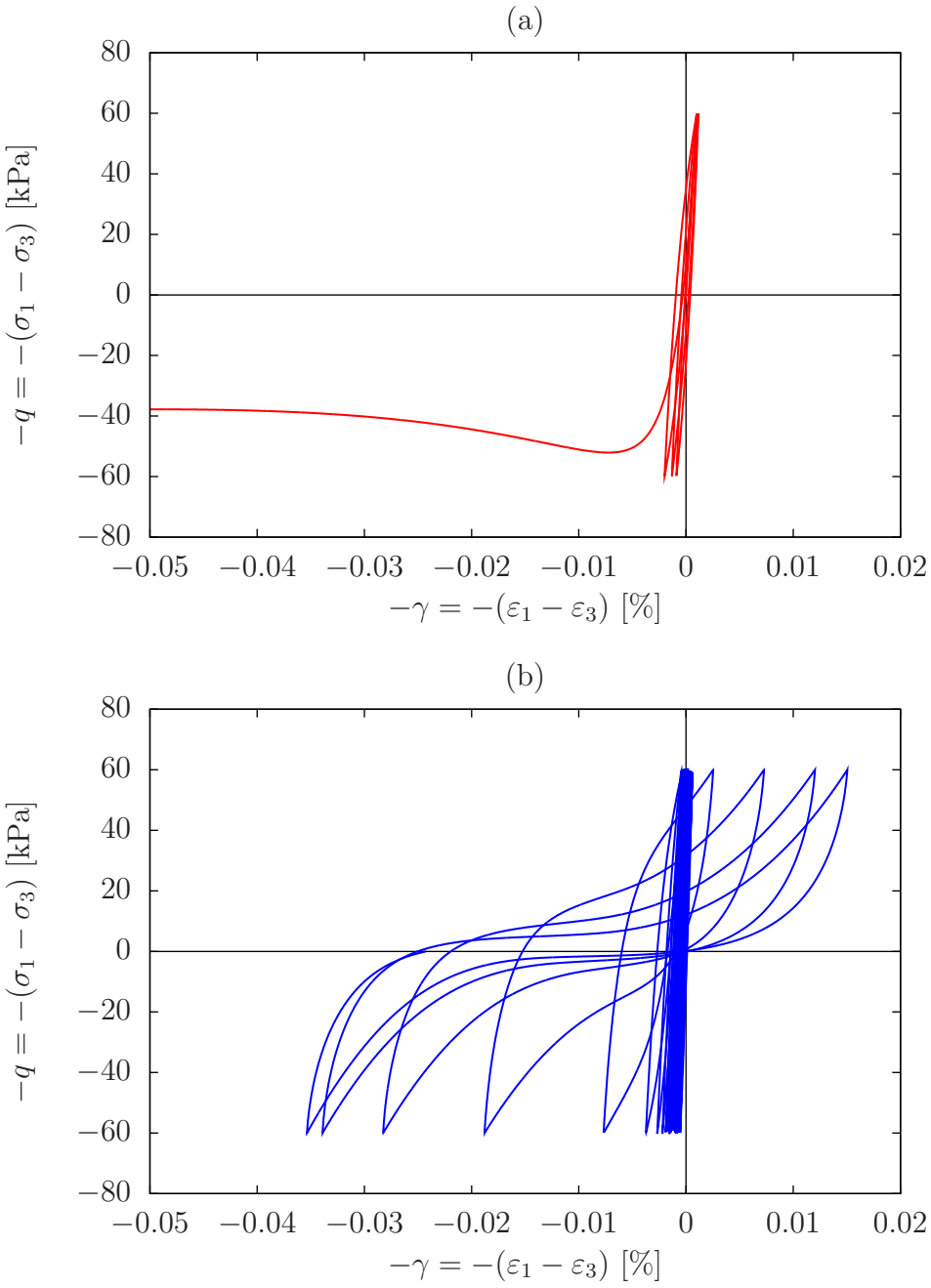

Figure 4.9: Simulated pycnotropy of Toyoura sand under undrained cyclic triaxial loading. Stress-strain response at (a) $e = 0.920$ ($D_\mathrm{r} = 0.15$), (b) $e = 0.735$ ($D_\mathrm{r} = 0.64$).

The medium dense specimen ($D_r = 0.64$, Figs. 4.8b and 4.9b) also tends to contract during the cyclic loading process under undrained conditions. Compared to the loose specimen, however, the rate of mean effective stress reduction is smaller, so that the medium dense specimen bears several more loading cycles before reaching the failure surface. The different mechanical behavior becomes apparent at this point. Although the value of p' is considerably smaller than the minimum value for the loose specimen, the shear deformation is limited because the response switches from contractive to dilative in each cycle. This mobilizes the well-known "banana shapes" in the γ-q-plane (Fig. 4.9b). Beyond phase transformation, which appears as an inflection point in stress path, the sand regains it shear stiffness and shows cyclic mobility.

In the above examples, the number of loading cycles is relatively small ($N_{cycl} < 10^2$) and the shear strain amplitudes are large ($\gamma_{amp} > 10^{-3}$). This is typical for sand deposits subjected to earthquake loading or pile penetration. In geotechnical engineering, however, the consideration of long-term and high-cyclic behavior with $N_{cycl} \gg 10^2$ and small strain amplitudes ($\gamma_{amp} < 10^{-3}$) becomes more and more important, e.g. in the serviceability analysis of foundations for offshore wind turbines. Research activity on this field has been accelerated in recent years but is left unconsidered in the present work.

4.3 Hypoplastic Model for Isotropic Sand

From the discussion of sand behavior in the previous sections it can be concluded that an appropriate constitutive equation must include the void ratio as a state variable, a cyclic loading mechanism, and a kind of non-proportional loading mechanism preventing coaxiality of principal axes of plastic strain rate and stress. A constitutive equation for sand should also reflect incremental nonlinearity and dependency of the inelastic strain rate direction on the stress rate direction.

The constitutive equation for sand applied in this work is based on hypoplasticity (Section 4.1.3). Early attempts to hypoplastic constitutive modeling of soils were already made in the late 1970's [Kolymbas, 1978; Gudehus and Kolymbas, 1979], and research on this went on up to recent dates [Niemunis, 2003]. Hypoplasticity is an established and well-known constitutive framework in the German and international soil mechanics and geotechnical engineering community. Hypoplastic models have been successfully applied to several problems, including pile penetration processes [e.g. Cudmani, 2001; Grabe et al., 2009; Henke, 2010; Herle and Mayer, 1999; Mahutka and Grabe, 2005; Mahutka and Henke, 2009; Rackwitz, 2003; von Wolffersdorff and Schwab, 2009].

The particular hypoplastic model for sand used here has been proposed by Gudehus [1996] and Bauer [1996], and includes the limit state description of von Wolffersdorff [1996], and the intergranular strain extension of Niemunis and Herle [1997] to account for the mechanical behavior under cyclic loading. The model is *comprehensive* insofar as it is applicable to any granular material, not only sand [Gudehus, 1996]. The following section derives the basic formulas without making to much comments on the

long process that released these formulas; this can be found elsewhere [e.g. Kolymbas, 1978, 1988, 1991b; Wu and Bauer, 1994; Gudehus, 1996; Bauer, 1996; Niemunis, 2003].

Only effective stress $\boldsymbol{\sigma}'$ in terms of (4.2.6) is considered in what follows, but the superscribed dash is omitted for brevity. As within previous sections, the stress tensor has all indices raised, while the rate of deformation has all indices lowered, that is, $\boldsymbol{\sigma} \stackrel{\text{def}}{=} \boldsymbol{\sigma}^\sharp$ and $\boldsymbol{d} \stackrel{\text{def}}{=} \boldsymbol{d}^\flat$. The considered hypoplastic rate constitutive equation for sand then takes the form

$$\mathring{\boldsymbol{\sigma}}^{\text{ZJ}} \stackrel{\text{def}}{=} \boldsymbol{h}(\boldsymbol{\sigma}, \boldsymbol{g}, e, \boldsymbol{\delta}, \boldsymbol{d}) = \boldsymbol{m}(\boldsymbol{\sigma}, \boldsymbol{g}, e, \boldsymbol{\delta}, \boldsymbol{d}) : \boldsymbol{d} \,, \tag{4.3.1}$$

in which, as usual, the dependency on a set of material constants has been suppressed, and the material tangent tensor $\boldsymbol{m}$ is generally nonlinear in $\boldsymbol{d}$; see also (4.1.37). $\mathring{\boldsymbol{\sigma}}^{\text{ZJ}}(x,t)$ is the Zaremba-Jaumann rate of the effective Cauchy stress according to (4.1.15), $e(x,t)$ is the void ratio, and the spatial metric $\boldsymbol{g}(x)$ is included to form invariants of the tensorial arguments. The *intergranular strain* $\boldsymbol{\delta}(x,t)$ is an additional internal state variable whose rate is postulated to have a functional dependency on the spatial rate of deformation $\boldsymbol{d}(x,t)$ and some material constants. Therefore, the set of internal state variables extra to the stress is $\boldsymbol{\alpha}(x,t) = \{e(x,t), \boldsymbol{\delta}(x,t)\}$. By the assumptions of Section 4.2.1, Proposition 4.2.8 can be applied to obtain an evolution equation for the void ratio:

$$\dot{e} = (1+e)\,\operatorname{tr}\boldsymbol{d} \,. \tag{4.3.2}$$

From Section 4.1.3, the properties of $\boldsymbol{h}$ are isotropy and positively homogeneity of first degree in $\boldsymbol{d}$. In addition, the results of triaxial tests performed by Goldscheider and Gudehus [1973], Goldscheider [1976], and others suggest that under sufficiently long proportional deformation paths the stress response becomes also proportional (i.e. $\dot{\boldsymbol{\sigma}} = a\,\boldsymbol{\sigma}$, with $a > 0$), and vice versa. An asymptotical state where both stress and deformation are proportional is called a *swept out of memory (SOM) state* [von Wolffersdorff, 1996; Niemunis, 2003]. As a consequence, the response function must be positively homogeneous of degree $n > 0$ in $\boldsymbol{\sigma}$ [Kolymbas, 1988], that is,

$$\boldsymbol{h}(a\boldsymbol{\sigma}, \boldsymbol{g}, e, \boldsymbol{\delta}, \boldsymbol{d}) = a^n \boldsymbol{h}(\boldsymbol{\sigma}, \boldsymbol{g}, e, \boldsymbol{\delta}, \boldsymbol{d}) \,, \quad \forall\, a > 0 \,. \tag{4.3.3}$$

This, however, implies that tangent stiffness $\partial\boldsymbol{h}/\partial\boldsymbol{d}$ vanishes at $\boldsymbol{\sigma} = \boldsymbol{0}$, which is reasonable for sand, but imposes a major difficulty on the numerical simulation of pile penetration starting at the soil surface.

4.3.1 Reference Model for Monotonic Loading

For the case of monotonic loading with sufficiently large deformation, Gudehus [1996] and Bauer [1996] arrive at the following subclass of hypoplastic constitutive equations (4.3.1):

$$\mathring{\boldsymbol{\sigma}}^{\text{ZJ}} \stackrel{\text{def}}{=} f_{\text{b}}\, f_{\text{e}}\, \bar{\boldsymbol{l}}(\tilde{\boldsymbol{\sigma}}, \boldsymbol{g}, \boldsymbol{d}) + f_{\text{b}}\, f_{\text{e}}\, f_{\text{d}}\, \bar{\boldsymbol{n}}(\tilde{\boldsymbol{\sigma}}, \boldsymbol{g}) \|\boldsymbol{d}\| \,, \tag{4.3.4}$$

where $\bar{\boldsymbol{l}}(\tilde{\boldsymbol{\sigma}}, \boldsymbol{g}, \boldsymbol{d})$ is presumed linear in $\boldsymbol{d}$ (i.e. hypoelastic) as well as positive definite with respect to $\boldsymbol{d}$. Moreover, $\tilde{\boldsymbol{\sigma}} \stackrel{\text{def}}{=} \boldsymbol{\sigma}/\operatorname{tr}\boldsymbol{\sigma}$ is the *dimensionless effective stress ratio*, the factor $f_{\text{b}}(\boldsymbol{\sigma}, \boldsymbol{g})$ accounts for barotropy, and $f_{\text{e}}(\boldsymbol{\sigma}, \boldsymbol{g}, e)$ and $f_{\text{d}}(\boldsymbol{\sigma}, \boldsymbol{g}, e)$ are pycnotropy

factors. Pycnotropy and barotropy will be described by f_b, f_e, and f_d only. All three factors are scalar functions that will be specified in what follows. Since $\bar{\boldsymbol{l}}(\tilde{\boldsymbol{\sigma}}, \boldsymbol{g}, \boldsymbol{d})$ is linear in $\boldsymbol{d}$, (4.3.4) in a more compact form reads

$$\mathring{\boldsymbol{\sigma}}^{\mathrm{ZJ}} = \boldsymbol{L} : \boldsymbol{d} + \boldsymbol{N}\|\boldsymbol{d}\| \,, \tag{4.3.5}$$

where $\boldsymbol{N} \stackrel{\mathrm{def}}{=} f_\mathrm{b}\, f_\mathrm{e}\, f_\mathrm{d}\, \bar{\boldsymbol{n}}$ has been set. It can be seen that stress response becomes hypoelastic for $f_\mathrm{d} = 0$.

At SOM states, proportional stress states have been reached under proportional deformation (compression) paths, and vice versa. Clearly, such states are defined by

$$\boldsymbol{\sigma} = \boldsymbol{\sigma}_\mathrm{p} \,,\; e = e_\mathrm{p} \,,\; \boldsymbol{d} = \boldsymbol{d}_\mathrm{p} \,, \quad \mathring{\tilde{\boldsymbol{\sigma}}}_\mathrm{p}^{\mathrm{ZJ}} = \tilde{\boldsymbol{\sigma}}_\mathrm{p} \,, \quad \mathrm{tr}\, \boldsymbol{d}_\mathrm{p} < 0 \,, \quad \text{and} \quad f_\mathrm{d} = f_\mathrm{e} = \text{const.} \tag{4.3.6}$$

Critical states due to shear deformation paths (see Section 4.2.2) are defined through

$$\boldsymbol{\sigma} = \boldsymbol{\sigma}_\mathrm{c} \,,\; e = e_\mathrm{c} \,,\; \boldsymbol{d} = \boldsymbol{d}_\mathrm{c} \,, \quad \mathring{\boldsymbol{\sigma}}^{\mathrm{ZJ}} = \boldsymbol{0} \,, \quad \dot{e} = 0 \,, \quad \text{and} \quad f_\mathrm{d} = f_\mathrm{e} = 1 \,. \tag{4.3.7}$$

At critical states, (4.3.5) and $\vec{\boldsymbol{d}} \stackrel{\mathrm{def}}{=} \boldsymbol{d}/\|\boldsymbol{d}\|$ yield the *hypoplastic flow rule*

$$\vec{\boldsymbol{d}}_\mathrm{c} = -\boldsymbol{L}^{-1} : \boldsymbol{N} \,. \tag{4.3.8}$$

Flow becomes purely isochoric at critical states, i.e. $\mathrm{tr}\, \vec{\boldsymbol{d}}_\mathrm{c} = \mathrm{tr}(\boldsymbol{L}^{-1} : \boldsymbol{N}) = 0$, because $\dot{e} = 0$ is equivalent to $\mathrm{tr}\, \boldsymbol{d}_\mathrm{c} = 0$ through (4.3.2). Moreover, the property $\|\vec{\boldsymbol{d}}_\mathrm{c}\| = 1$ offers a kind of *hypoplastic yield condition* of the form [von Wolffersdorff, 1996; Niemunis, 2003]

$$y(\boldsymbol{\sigma}_\mathrm{c}, \boldsymbol{g}, e_\mathrm{c}) \stackrel{\mathrm{def}}{=} \|\boldsymbol{L}^{-1} : \boldsymbol{N}\| - 1 \,. \tag{4.3.9}$$

The condition (4.3.3) implies that $y(\boldsymbol{\sigma}_\mathrm{c}, \boldsymbol{g}, e_\mathrm{c}) = 0$ must represent a conical surface in principal stress space with vertex at the origin [von Wolffersdorff, 1996].

Now by choosing suitable forms of the $\binom{2}{0}$-tensor valued functions $\bar{\boldsymbol{l}}(\tilde{\boldsymbol{\sigma}}, \boldsymbol{g}, \boldsymbol{d})$ and $\bar{\boldsymbol{n}}(\tilde{\boldsymbol{\sigma}}, \boldsymbol{g})$ in (4.3.4), several yield conditions of classical elasto-plasticity can be incorporated into the hypoplastic yield condition (4.3.9). For example, von Wolffersdorff [1996] proposes the representations

$$\begin{aligned} \bar{\boldsymbol{l}}(\tilde{\boldsymbol{\sigma}}, \boldsymbol{g}, \boldsymbol{d}) &\stackrel{\mathrm{def}}{=} \frac{1}{\mathrm{tr}(\tilde{\boldsymbol{\sigma}}^2)} \Big(F^2\, \boldsymbol{d}^\sharp + a^2\, \tilde{\boldsymbol{\sigma}}\, \mathrm{tr}(\tilde{\boldsymbol{\sigma}} \cdot \boldsymbol{d}) \Big) \qquad \text{and} \\ \bar{\boldsymbol{n}}(\tilde{\boldsymbol{\sigma}}, \boldsymbol{g}) &\stackrel{\mathrm{def}}{=} \frac{aF}{\mathrm{tr}(\tilde{\boldsymbol{\sigma}}^2)} \left(\tilde{\boldsymbol{\sigma}} + \tilde{\boldsymbol{\sigma}}_\mathrm{dev} \right) \,, \end{aligned} \tag{4.3.10}$$

respectively, and then uses the yield condition for soils of Matsuoka and Nakai [1977]. By this and other assumptions not listed here, the scalar functions a and F in (4.3.10) result in

$$\begin{aligned} a &= \frac{\sqrt{3}(3 - \sin\phi_\mathrm{c})}{2\sqrt{2}\sin\phi_\mathrm{c}} \qquad \text{and} \\ F &= \sqrt{\frac{1}{8}\tan^2\psi + \frac{2 - \tan^2\psi}{2 + \sqrt{2}\tan\psi\, \cos 3\theta}} - \frac{1}{2\sqrt{2}}\tan\psi \,, \end{aligned} \tag{4.3.11}$$

respectively, in which

$$\tan\psi \stackrel{\text{def}}{=} \sqrt{3}\,\|\tilde{\boldsymbol{\sigma}}_{\text{dev}}\| \qquad \text{and} \qquad \cos 3\theta \stackrel{\text{def}}{=} -\sqrt{6}\frac{\text{tr}(\tilde{\boldsymbol{\sigma}}^3_{\text{dev}})}{\Big(\text{tr}(\tilde{\boldsymbol{\sigma}}^2_{\text{dev}})\Big)^{\frac{3}{2}}}\,. \tag{4.3.12}$$

θ is the so-called *Lode angle* located in the hyperplane spanned by the principal axes of $\tilde{\boldsymbol{\sigma}}_{\text{dev}} = \tilde{\boldsymbol{\sigma}} - (1/3)\,\boldsymbol{g}^\sharp$ (also called the π-plane).

The particular functions for the factors f_{b}, f_{e}, and f_{d} in (4.3.4) are carried over from [Gudehus, 1996] and [Bauer, 1996]. Gudehus [1996] introduces the characteristic void ratios $e_{\text{i}}(p)$, $e_{\text{c}}(p)$, and $e_{\text{d}}(p)$ as functions of the effective pressure p, with $e_{\text{i}} \geq e_{\text{c}} \geq e_{\text{d}}$. $e_{\text{i}}(p)$ represents the possible minimum density state under isotropic compression at a given pressure. $e_{\text{c}}(p)$ is the void ratio at critical state discussed in Section 4.2.2, and $e_{\text{d}}(p)$ represents the maximum density state which is usually reached after cyclic shearing. According to Gudehus [1996] and Bauer [1996] the characteristic void ratios are related through

$$\frac{e_{\text{i}}}{e_{\text{i0}}} \stackrel{\text{def}}{=} \frac{e_{\text{c}}}{e_{\text{c0}}} \stackrel{\text{def}}{=} \frac{e_{\text{d}}}{e_{\text{d0}}} \stackrel{\text{def}}{=} \exp\left(-\left(\frac{3p}{h_{\text{s}}}\right)^n\right)\,, \tag{4.3.13}$$

where n, h_{s}, e_{i0}, e_{c0}, and e_{d0}, with $e_{\text{i0}} \geq e_{\text{c0}} \geq e_{\text{d0}}$, are material constants. The so-called *granulate hardness* or *solid phase hardness* h_{s} is a reference pressure that renders the hypoplastic constitutive equation dimensionful. The exponential function in (4.3.13) causes the characteristic void ratio, say e_{i}, to have the limits $\lim_{p\to 0} e_{\text{i}} = e_{\text{i0}}$ and $\lim_{p\to\infty} e_{\text{i}} = 0$.

The pycnotropy functions are then prescribed by

$$f_{\text{e}}(\boldsymbol{\sigma}, \boldsymbol{g}, e) \stackrel{\text{def}}{=} \left(\frac{e_{\text{c}}}{e}\right)^{\beta} \tag{4.3.14}$$

and

$$f_{\text{d}}(\boldsymbol{\sigma}, \boldsymbol{g}, e) \stackrel{\text{def}}{=} \left(\frac{e - e_{\text{d}}}{e_{\text{c}} - e_{\text{d}}}\right)^{\alpha}\,, \tag{4.3.15}$$

and the barotropy function is

$$f_{\text{b}}(\boldsymbol{\sigma}, \boldsymbol{g}) \stackrel{\text{def}}{=} \frac{h_{\text{s}}}{n}\left(\frac{1+e_{\text{i}}}{e_{\text{i}}}\right)\left(\frac{e_{\text{i0}}}{e_{\text{c0}}}\right)^{\beta}\left(\frac{3p}{h_{\text{s}}}\right)^{1-n}\left(3 + a^2 - \sqrt{3}a\left(\frac{e_{\text{i0}} - e_{\text{d0}}}{e_{\text{c0}} - e_{\text{d0}}}\right)^{\alpha}\right)^{-1}\,, \tag{4.3.16}$$

with e_{i}, e_{c}, and e_{d} being obtained by applying (4.3.13), and α and β are additional material constants. Detailed theoretical justification of the functions is presented in [Gudehus, 1996; Bauer, 1996]. It can be summarized, however, that the pycnotropy function f_{e} relates the current void ratio to the void ratio at critical state. If the sand under consideration densifies, then f_{e} increases and the stiffness $\partial\boldsymbol{h}/\partial\boldsymbol{d}$ therefore also does. With the pycnotropy function f_{d} a critical state mechanism is included. The condition $e = e_{\text{c}}$ at critical state results in $f_{\text{d}} = 1$, and the stress response (4.3.5) becomes hypoelastic for $f_{\text{d}} = 0$ at $e = e_{\text{d}}$ (maximum density). Dilatancy and the increase of the peak friction angle ϕ_{p} with density for $e_{\text{c}} \geq e \geq e_{\text{d}}$ is accounted by $f_{\text{d}} < 1$. Finally, the barotropy function f_{b} ensures consistency of the hypoplastic model with the compression law (4.3.13).

4.3.2 Intergranular Strain Extension

Niemunis and Herle [1997] introduce the intergranular strain concept to improve the small strain response under changes of loading direction of the reference hypoplastic constitutive equation. In a strain range not exceeding the magnitude of $\sim 10^{-5}$ sand behavior is elastic with relatively high stiffness dependent on the stress and density states. Under the assumptions of Niemunis and Herle [1997], straining of a sand continuum results from rearrangement of the grain skeleton plus deformation of a intergranular interface layer, called *intergranular strain*.

Intergranular strain is assumed a time-dependent spatial $\binom{0}{2}$-tensor field $\boldsymbol{\delta}(x,t)$, with $\boldsymbol{\delta}_t : \mathcal{S} \to T^*\mathcal{S} \otimes T^*\mathcal{S}$ for fixed t. It is regarded as a macroscopic measure of microdeformations of the interface zone belonging to the solid phase of sand grains. The intergranular strain can grow up to a maximum value of $R \stackrel{\text{def}}{=} \max \|\boldsymbol{\delta}\|$, which is a material constant. In a simple one-dimensional model the interface layer remains deformed but the grains begin to slide if deformation is larger than R. At this stage the hypoplastic constitutive equation with intergranular strain extension is required to reduce to the reference model described in the previous section.

For the general three-dimensional case define the directions of $\boldsymbol{\delta} \neq \mathbf{0}$ and $\boldsymbol{d} \neq \mathbf{0}$ through $\vec{\boldsymbol{\delta}} \stackrel{\text{def}}{=} \boldsymbol{\delta}/\|\boldsymbol{\delta}\|$ and $\vec{\boldsymbol{d}} \stackrel{\text{def}}{=} \boldsymbol{d}/\|\boldsymbol{d}\|$, respectively, and set $\vec{\boldsymbol{\delta}} = \mathbf{0}$ for $\boldsymbol{\delta} = \mathbf{0}$, and $\vec{\boldsymbol{d}} = \mathbf{0}$ for $\boldsymbol{d} = \mathbf{0}$. The *normalized magnitude* ρ of $\boldsymbol{\delta}$ is defined through

$$\rho \stackrel{\text{def}}{=} \frac{\|\boldsymbol{\delta}\|}{R}\,, \qquad \text{with } \; 0 \le \rho \le 1\,. \tag{4.3.17}$$

Niemunis and Herle [1997] then propose the following discontinuous rate constitutive equation for intergranular strain:

$$\mathring{\boldsymbol{\delta}}^{\mathrm{ZJ}} \stackrel{\text{def}}{=} \boldsymbol{j}(\boldsymbol{\delta},\boldsymbol{g},\boldsymbol{d}) \stackrel{\text{def}}{=} \begin{cases} \boldsymbol{d} - \rho^{\beta_\mathrm{r}}\, \vec{\boldsymbol{\delta}} \otimes \vec{\boldsymbol{\delta}}^\sharp : \boldsymbol{d} & \text{for } \vec{\boldsymbol{\delta}}^\sharp : \boldsymbol{d} > 0\,, \\ \boldsymbol{d} & \text{for } \vec{\boldsymbol{\delta}}^\sharp : \boldsymbol{d} \le 0\,. \end{cases} \tag{4.3.18}$$

The exponent β_r is an additional material constant. As the rate of intergranular strain is likewise strain-like, it is also presumed to have both indices lowered, so that $\mathring{\boldsymbol{\delta}}^{\mathrm{ZJ}}_t, \boldsymbol{\delta}_t, \boldsymbol{d}_t \in \mathfrak{T}^0_2(\mathcal{S})$ at fixed t. The function $\boldsymbol{j}(\boldsymbol{\delta},\boldsymbol{g},\boldsymbol{d})$ acts between the bounds $\rho = 0$ and $\rho = 1$. Apart from its linearity in $\boldsymbol{d}$, the function has the following properties.

Firstly, $\max \|\mathring{\boldsymbol{\delta}}^{\mathrm{ZJ}}\| = \|\boldsymbol{d}\|$, meaning that intergranular strain is not evolving faster than $\boldsymbol{d}$ does. For $\rho = 0$ there is always $\mathring{\boldsymbol{\delta}}^{\mathrm{ZJ}} = \boldsymbol{d}$ independent of the current direction of $\boldsymbol{d}$. If deformation proceeds monotonically with $\boldsymbol{d} = \text{const.}$ starting from $\boldsymbol{\delta} = \mathbf{0}$, then $\dot\rho > 0$ and the directions of $\boldsymbol{\delta}$ and $\boldsymbol{d}$ coincide. For any $\boldsymbol{\delta}$ and $\boldsymbol{d}$ with $\vec{\boldsymbol{\delta}}^\sharp : \boldsymbol{d} > 0$ the function (4.3.18) describes a rotation of $\boldsymbol{\delta}$ towards $\boldsymbol{d}$, and the rate of intergranular strain becomes zero for $\vec{\boldsymbol{\delta}} = \vec{\boldsymbol{d}}$ at $\rho = 1$. Therefore, $\lim_{t\to\infty}\rho = 1$ and $\lim_{t\to\infty}\boldsymbol{\delta} = \frac{R}{\|d\|}\boldsymbol{d} = R\,\vec{\boldsymbol{d}}$. Beyond $\rho = 1$, sudden changes in loading direction which keep $\vec{\boldsymbol{\delta}}^\sharp : \boldsymbol{d} > 0$ do not change ρ, i.e. $\dot\rho = 0$, and the evolution of intergranular strain is $\mathring{\boldsymbol{\delta}}^{\mathrm{ZJ}} = \boldsymbol{d} - \vec{\boldsymbol{\delta}} \otimes \vec{\boldsymbol{\delta}}^\sharp : \boldsymbol{d}$. However, if for $0 \le \rho \le 1$ the loading direction changes suddenly such that $\vec{\boldsymbol{\delta}}^\sharp : \boldsymbol{d} \le 0$, which represents a loading reversal resp. unloading, then $\dot\rho < 0$ and $\boldsymbol{\delta}$ rotates faster towards

the new $\boldsymbol{d}$ than for $\vec{\boldsymbol{\delta}}^{\sharp} : \boldsymbol{d} > 0$ because now $\mathring{\boldsymbol{\delta}}^{\mathrm{ZJ}} = \boldsymbol{d}$. Intergranular strain is reduced until $\vec{\boldsymbol{\delta}}^{\sharp} : \boldsymbol{d} > 0$ again, but the state where $\rho = 0$ can only be reached if $\vec{\boldsymbol{d}}_{\mathrm{unload}} = -\vec{\boldsymbol{\delta}}$.

The general hypoplastic rate constitutive equation for the Cauchy stress $\boldsymbol{\sigma}(x,t)$ including the intergranular strain concept is provided by (4.3.1). At maximum intergranular strain with $\rho = 1$ and monotonic deformation paths with $\boldsymbol{d} = \vec{\boldsymbol{\delta}}\,\|\boldsymbol{d}\|$ the extended hypoplastic model is required to reduce to the reference model (4.3.5). This can be achieved by choosing

$$\boldsymbol{m} \stackrel{\mathrm{def}}{=} \boldsymbol{L} + \boldsymbol{N} \otimes \vec{\boldsymbol{\delta}}^{\sharp} \,. \tag{4.3.19}$$

A hypoelastic micro-rebound of the form

$$\boldsymbol{m} \stackrel{\mathrm{def}}{=} m_{\mathrm{R}}\, \boldsymbol{L} \tag{4.3.20}$$

is postulated for reversed loading with $\vec{\boldsymbol{d}} \approx -\vec{\boldsymbol{\delta}}$ at $\rho = 1$, where $m_{\mathrm{R}} > 1$ is another material constant. At neutral loading defined by $\vec{\boldsymbol{\delta}}^{\sharp} : \boldsymbol{d} = 0$ hypoelastic micro-rebound should take place with smaller stiffness, that is,

$$\boldsymbol{m} \stackrel{\mathrm{def}}{=} m_{\mathrm{T}}\, \boldsymbol{L} \,, \tag{4.3.21}$$

where $m_{\mathrm{R}} > m_{\mathrm{T}} > 1$. Finally, in the case where $\rho = 0$, e.g. during virgin loading, the stiffness is simply prescribed as $\boldsymbol{m} = m_{\mathrm{R}}\, \boldsymbol{L}$ independently of the loading direction $\boldsymbol{d}$. From these conditions together with (4.3.18), Niemunis and Herle [1997] propose the following interpolation for general $0 \le \rho \le 1$ and $\boldsymbol{d}$:

$$\boldsymbol{m} \stackrel{\mathrm{def}}{=} (\rho^{\chi} m_{\mathrm{T}} + (1-\rho^{\chi}) m_{\mathrm{R}}) \boldsymbol{L} + \begin{cases} \rho^{\chi}(1-m_{\mathrm{T}}) \boldsymbol{L} : \vec{\boldsymbol{\delta}} \otimes \vec{\boldsymbol{\delta}}^{\sharp} + \rho^{\chi} \boldsymbol{N} \otimes \vec{\boldsymbol{\delta}}^{\sharp} & \text{for } \vec{\boldsymbol{\delta}}^{\sharp} : \boldsymbol{d} > 0 \\ \rho^{\chi}(m_{\mathrm{R}} - m_{\mathrm{T}}) \boldsymbol{L} : \vec{\boldsymbol{\delta}} \otimes \vec{\boldsymbol{\delta}}^{\sharp} & \text{for } \vec{\boldsymbol{\delta}}^{\sharp} : \boldsymbol{d} \le 0 \,, \end{cases} \tag{4.3.22}$$

where χ is a material constant, and

$$\begin{aligned} \boldsymbol{L}(\tilde{\boldsymbol{\sigma}}, \boldsymbol{g}) &\stackrel{\mathrm{def}}{=} \frac{f_{\mathrm{b}}\, f_{\mathrm{e}}}{\mathrm{tr}(\tilde{\boldsymbol{\sigma}}^2)} \left(F^2\, \mathbf{1}^{\sharp} + a^2\, \tilde{\boldsymbol{\sigma}} \otimes \tilde{\boldsymbol{\sigma}} \right) \,, \\ \boldsymbol{N}(\tilde{\boldsymbol{\sigma}}, \boldsymbol{g}) &\stackrel{\mathrm{def}}{=} f_{\mathrm{b}}\, f_{\mathrm{e}}\, f_{\mathrm{d}} \frac{aF}{\mathrm{tr}(\tilde{\boldsymbol{\sigma}}^2)} \left(\tilde{\boldsymbol{\sigma}} + \tilde{\boldsymbol{\sigma}}_{\mathrm{dev}} \right) \end{aligned} \tag{4.3.23}$$

in accordance with the previous section. $\mathbf{1}^{\sharp}$ is the fourth-order symmetric identity tensor of (A.5.11) with all indices raised.

4.3.3 Determination of Material Constants

The comprehensive hypoplastic rate constitutive equation given by (4.3.1) together with (4.3.22), (4.3.18) and (4.3.2) contains the set $\{\phi_{\mathrm{c}}, h_{\mathrm{s}}, n, e_{\mathrm{i0}}, e_{\mathrm{c0}}, e_{\mathrm{d0}}, \alpha, \beta, R, m_{\mathrm{R}}, m_{\mathrm{T}}, \beta_{\mathrm{r}}, \chi\}$ of 13 material constants, in which the first 8 are related to the reference model and the last 5 are due to the intergranular strain extension. The determination of these material constants from experimental laboratory test is roughly described in the articles cited. More detailed information can be found in [Herle, 1997; Herle and Gudehus, 1999; Rackwitz, 2003]. Tab. 4.1 lists the description of the constants and

Table 4.1: Description and determination of hypoplastic material constants.

Constant	Unit	Description	Laboratory test
ϕ_c	°	friction angle at critical state	angle of repose
h_s	MPa	granulate hardness; ref. pressure	oedometer at e_{max}, or [1]
n	–	exponent; eq. (4.3.13)	oedometer at e_{max}, or [1]
e_{d0}	–	min. void ratio at zero pressure	cyclic shearing; $e_{d0} \approx e_{min}$
e_{c0}	–	crit. void ratio at zero pressure	pouring; $e_{c0} \approx e_{max}$
e_{i0}	–	max. void ratio at zero pressure	$1.15\, e_{c0}$ to $1.2\, e_{c0}$
α	–	exponent; eq. (4.3.15)	triaxial compression at e_{min}
β	–	exponent; eq. (4.3.14)	oedometer at e_{max} and e_{min}
R	–	max. intergranular strain	dynamic; strain reversal
m_R	–	stiffness factor; 180° reversal	dynamic; strain reversal
m_T	–	stiffness factor; 90° reversal	dynamic; strain reversal
β_r	–	exponent; eq. (4.3.18)	dynamic; strain reversal
χ	–	exponent; eq. (4.3.22)	dynamic; strain reversal

[1]=[Rackwitz, 2003]

the associated laboratory tests for their determination. Sets of the material constants associated with different granular materials are listed in Tab. 4.2.

The granulate hardness h_s and the exponent n are related to the compression curve (4.3.13). Their determination from oedometer tests with initially very loose specimens, as suggested by Herle [1997] and Herle and Gudehus [1999], is difficult because of their interrelation. However, approximation formulas are proposed in these references. It is important to notice that the hypoplastic model is valid only if the mean effective stress lies in the range of $20\,\text{kPa} < p' < 2\,\text{MPa}$, and for $n = 0.30$ the valid range of granulate hardness h_s is about [Herle, 1997; Herle and Gudehus, 1999]

$$10^{-5}\,(10^{-6}) \quad < \quad \frac{p'}{h_s} \quad < \quad 10^{-3}\,(10^{-2})\,. \tag{4.3.24}$$

The values in parentheses were suggested earlier by Gudehus [1996]. Conversely, one may argue that for a low mean effective stress, say $0\,\text{kPa} < p' < 20\,\text{kPa}$, as this is the case near unloaded ground surface, the granulate hardness constant must be restricted to $0\,\text{MPa} < h_s < 2000\,\text{MPa}$. So if (4.3.24) holds, then h_s must reflect the mean effective stress range. Certain values obtained at high pressures should be reduced for low pressure applications. In Tab. 4.2 the estimates of h_s for near-zero pressures are set in parentheses.

Chapter 7 describes experimental model tests with sand that have been performed in order to validate the ALE method incorporating the hypoplastic constitutive equation (4.3.1). The quartz sand used for the tests is described in Section 7.3. For realistic back-analysis of the model tests by applying the ALE framework, a complete set of hypoplastic material constant for that sand had to be determined, and these are listed in Tab. 4.2. The values of some constants were borrowed from those already determined for Berlin sand M [Rackwitz, 2003] and Hochstetten sand [Niemunis and Herle, 1997].

Table 4.2: Hypoplastic constants of some granular materials.

Material	ϕ_c [°]	h_s [MPa]	n [−]	e_{d0} [−]	e_{c0} [−]	e_{i0} [−]	α [−]	β [−]	R [−]	m_R [−]	m_T [−]	β_r [−]	χ [−]	Reference[a]
Berlin sand M	31.5	10000 (10)[b]	0.35	0.40	0.59	0.71	0.13	1.0	- 0.0001[c]	- 5.0[c]	- 2.0[c]	- 0.5[c]	- 6.0[c]	[1] this work
Berlin sand A	32.0	3730	0.20	0.46	0.75	0.90	0.14	1.0	-	-	-	-	-	[2]
	32.0	3730	0.20	0.46	0.75	0.90	0.14	1.0	0.0001[c]	5.0[c]	2.0[c]	0.4	6.0[c]	[3]
Berlin sand B	31.0	6650	0.26	0.48	0.81	0.97	0.12	1.0	-	-	-	-	-	[2]
	31.0	6650	0.26	0.48	0.81	0.97	0.12	1.0	0.0001[c]	5.0[c]	2.0[c]	0.4	6.0[c]	[3]
Berlin sand C	32.0	10700	0.24	0.53	0.84	1.00	0.12	2.2	-	-	-	-	-	[2]
	32.0	10700	0.24	0.53	0.84	1.00	0.12	1.0	0.0001[c]	5.0[c]	2.0[c]	0.4	6.0[c]	[3]
Hochstetten sand	33.0	1000	0.25	0.55	0.95	1.05	0.25	1.5	-	-	-	-	-	[4]
	33.0	1000	0.25	0.55	0.95	1.05	0.25	1.0	0.0001	5.0	2.0	0.5	6.0	[5]
	33.0	1500	0.28	0.55	0.95	1.05	0.25	1.0	-	-	-	-	-	[6]
Karlsruhe sand	30.0	5800	0.28	0.53	0.84	1.00	0.13	1.05	-	-	-	-	-	[7]
	30.0	5800	0.28	0.53	0.84	1.00	0.13	1.0	-	-	-	-	-	[6]
	32.0	5800	0.28	0.53	0.84	1.00	0.11	1.0	0.0001	5.0	2.0	0.1	2.0	[8]
Toyoura sand	30.0	2600	0.27	0.61	0.98	1.10	0.18	1.0	-	-	-	-	-	[7]
	30.0	2600	0.27	0.61	0.98	1.10	0.18	1.1	-	-	-	-	-	[6]
	32.0	120	0.69	0.61	0.98	1.13	0.12	1.0	-	-	-	-	-	[8]
Model test sand	31.5[d]	76500 (76.5)[b]	0.29	0.48	0.78	0.90	0.13[d]	1.0[d]	0.0001[c]	5.0[c]	2.0[c]	0.5[c]	6.0[c]	this work
Hochstetten gravel	36.0	32000	0.18	0.26	0.45	0.50	0.10	1.8	-	-	-	-	-	[7]
Polymer granulate[e]	32.0	110	0.33	0.53	0.73	0.80	0.08	1.0	-	-	-	-	-	[7]
Dried spring wheat	39.0	20	0.37	0.57	0.84	0.95	0.02	1.0	-	-	-	-	-	[7]

[a] [1]=[Rackwitz, 2003]; [2]=[Herle and Mayer, 1999]; [3]=[Mayer, 2000]; [4]=[von Wolffersdorff, 1996]; [5]=[Niemunis and Herle, 1997]; [6]=[Herle and Gudehus, 1999]; [7]=[Herle, 1997]; [8]=[Cudmani, 2001]

[b] estimated for pressures $0\,\text{kPa} < p < 20\,\text{kPa}$

[c] estimated, according to [Niemunis and Herle, 1997]

[d] estimated, according to [Rackwitz, 2003]

[e] elliptic cylinders with $h = 4\,\text{mm}$, $d_1 = 3\,\text{mm}$, and $d_2 = 4.5\,\text{mm}$

Chapter 5

Lagrangian Finite Element Methods

The main objective of the present work is the development of a finite element method (FEM) for the numerical simulation of penetration into sand. As introduced in Chapter 1, this initial boundary value problem is highly nonlinear. The following chapter addresses to the basic approaches and equations of the Lagrangian FEM to which the arbitrary Lagrangian-Eulerian capabilities will be added subsequently. After a definition of the mechanical initial boundary value problem, its variational or weak form will be derived and spatially discretized by finite elements. Temporal discretization and numerical solution of the resulting system of equations will be described, by placing emphasis on solution advancing implicitly in time (implicit FEM). Integration of the constitutive equations at large deformations will be outlined at the end of the chapter. Notation is kept consistent with previous chapters as far as algorithmic treatment permits.

Since the pioneering paper of Turner et al. [1956], the FEM has grown up to a powerful numerical tool that allows for a broad range of applications. Its versatility has made FEM a standard solution method, particularly in computational solid mechanics. Therefore, a large number of technical papers and monographs has been published. Some recommended textbooks dealing with nonlinear finite element analysis are those of Wriggers [2008]; Belytschko et al. [2000]; Zienkiewicz and Taylor [2000a,b]; Bathe [1996]; Oden [1972], and Simo and Hughes [1998]. Additional literature devoted to selected topics will be cited in the text.

5.1 Initial Boundary Value Problem

The finite element method is based on a weak resp. variational formulation of initial boundary value problems (IBVP). Stated loosely, an IBVP is a set of governing equations together with a set of certain initial conditions and boundary conditions that describe the problem (or process) under consideration. In the general case the solution must be established for every time station in a time interval. Due to the equivalence proposed in 3.2.16, there is generally no difference whether the solution process is carried out in the spatial (Eulerian), material (Lagrangian), or ALE descriptions.

Current finite element approaches for solid mechanical problems employ either the *total Lagrangian (TL)* description or the *updated Lagrangian (UL)* description. The TL finite element formulation uses the initial configuration of the body as the reference configuration, whereas the UL finite element formulation uses the current configuration of the body as the reference configuration. Note that in both approaches the material particles are the independent variables, that is, the finite element mesh is attached to the material. The following chapter is devoted to the updated Lagrangian description, which has been originally proposed by Yaghmai [1969] and Bathe et al. [1975].

As in previous chapters, the motion of a material body $\mathcal{B}$ in the ambient space $\mathcal{S}$ is the map $\varphi : \mathcal{B} \times [0,T] \to \mathcal{S}$, $(X,t) \mapsto x = \varphi(X,t)$, with $\varphi_t(X) \stackrel{\text{def}}{=} \varphi(X,t)$ by freezing t. The boundary $\partial\mathcal{B}$ of the body consists of parts $\partial_{\text{d}}\mathcal{B}$ with prescribed displacement, $\partial_{\tau}\mathcal{B}$ with prescribed traction, and $\partial_{\text{c}}\mathcal{B}$ with contact constraints, with $\partial_{\text{d}}\mathcal{B} \cap \partial_{\tau}\mathcal{B} \cap \partial_{\text{c}}\mathcal{B} \stackrel{\text{def}}{=} \emptyset$ and $\text{cl}(\partial_{\text{d}}\mathcal{B} \cup \partial_{\tau}\mathcal{B} \cup \partial_{\text{c}}\mathcal{B}) \stackrel{\text{def}}{=} \text{cl}(\partial\mathcal{B})$. The boundary $\varphi_t(\partial\mathcal{B}) = \partial(\varphi_t(\mathcal{B})) \stackrel{\text{def}}{=} \partial\varphi_t(\mathcal{B})$, with unit outward normals $\boldsymbol{n}^*$, is treated similarly. In the UL formulation of IBVP the current configuration of the body at time $s \in [0,T]$ serves as the reference configuration, i.e. $\varphi_s(\mathcal{B}) \stackrel{\text{def}}{=} \mathcal{B}$ at $t = s$, and any previous configuration is generally not available as a whole. The particles of the body in the reference configuration, $X \in \mathcal{B}$, are identified with their current locations at time $t = s$. Since $\varphi_s = \text{id}_{\mathcal{B}}$ is the identity map on $\mathcal{B}$, the material and spatial descriptions of balance of momentum coincide at $t = s$.

Balance of momentum in the UL formulation uses spatial variables and derivatives with respect to the spatial points $x = \varphi(X,t) \in \mathcal{S}$ resp. spatial coordinates $x^i = \varphi^i(X^I,t)$. However, for $t > s$ the solution is carried out in a Lagrangian fashion, meaning that all variables are taken with respect to the particles of the body in the reference configuration, $X \in \mathcal{B}$, which coincide with the locations of the particles at time $t = s$. Clearly, the velocity, the spatial mass density, the Cauchy stress, and the body force are given as functions of X and t, that is, $\boldsymbol{v}(\varphi(X,t),t)$, $\rho(\varphi(X,t),t)$, $\boldsymbol{\sigma}(\varphi(X,t),t)$, and $\bar{\boldsymbol{b}}(\varphi(X,t),t)$, respectively. Conservation of mass can thus be solved in algebraic form, and no solution of a separate differential equation is needed.

Definition 5.1.1. An *IBVP for mechanics in the updated Lagrangian description* is the problem of finding the spatial velocity $\boldsymbol{v}$, the spatial mass density ρ, the Cauchy stress $\boldsymbol{\sigma}$, and the internal material state on $\varphi_t(\mathcal{B})$ for every $t \in [0,T]$ provided that for a reference mass density $\rho_{\text{ref}}(X) = \rho(\varphi(X,0),0)\, J(X,0)$, with $J(X,0) = 1$, and a body force $\bar{\boldsymbol{b}}(\varphi(X,t),t)$ given,

(i) conservation of mass $\dot{\rho} = -\rho \operatorname{div} \boldsymbol{v}$,

(ii) balance of linear momentum $\rho\dot{\boldsymbol{v}} = \rho\bar{\boldsymbol{b}} + \operatorname{div}\boldsymbol{\sigma}$, and

(iii) balance of angular momentum $\boldsymbol{\sigma} = \boldsymbol{\sigma}^{\text{T}}$ hold,

(iv) the stress $\boldsymbol{\sigma}$ is obtained through integration of a spatial rate constitutive equation $\mathring{\boldsymbol{\sigma}}^{\star} = \boldsymbol{h}(\boldsymbol{\sigma}, \boldsymbol{d}, \ldots)$, and the evolution equations for the internal state variables are also known functions,

(v) for the boundary $\partial\varphi_t(\mathcal{B})$ of the body in its current configuration with unit outward normals $\boldsymbol{n}^*$ there are prescribed

(a) $\boldsymbol{v} = \bar{\boldsymbol{v}}$ on $\partial_{\mathrm{v}}(\varphi_t(\mathcal{B}))$ (*velocity boundary conditions*),
(b) $\boldsymbol{\sigma} \cdot \boldsymbol{n}^* = \bar{\boldsymbol{t}}$ on $\partial_{\tau}(\varphi_t(\mathcal{B}))$ (*traction boundary conditions*),
(c) contact constraints on $\partial_{\mathrm{c}}(\varphi_t(\mathcal{B}))$ (*contact boundary conditions*), and

(vi) $\boldsymbol{v}$, $\boldsymbol{\sigma}$, and the internal state variables are given at $t = 0$ (*initial conditions*). ♢

5.2 Weak Form of the IBVP

5.2.1 Principle of Virtual Power without Contact

The weak form of the IBVP for mechanics consists of the *principle of virtual work* resp. the *principle of virtual power*. In deriving the principle of virtual power in the updated Lagrangian formulation, some additional terminology is needed.

Definition 5.2.1. [See also Simo and Hughes, 1998; Marsden and Hughes, 1994] Let

$$\mathcal{C} \stackrel{\text{def}}{=} \{\varphi_t : \mathcal{B} \to \mathcal{S} \,|\, t \in [0,T] \text{ and } \varphi_t = \bar{\varphi}_t \text{ on } \partial_{\mathrm{d}}\mathcal{B} \text{ and } J_{\varphi_t} > 0\}$$

be the *space of admissible configurations*, where $\partial_{\mathrm{d}}\mathcal{B}$ is the part of the boundary of the body with prescribed displacements. The tangent space to $\mathcal{C}$ is given by $T_{\varphi_t}\mathcal{C} \stackrel{\text{def}}{=} \{\boldsymbol{V}_t : \mathcal{B} \to T\mathcal{S} \,|\, \tau_{\mathcal{S}} \circ \boldsymbol{V}_t = \varphi_t\}$, where $\tau_{\mathcal{S}} : T\mathcal{S} \to \mathcal{S}$ is a tangent bundle projection, and $\boldsymbol{V}_t$ is the material velocity. For specific $\varphi_t \in \mathcal{C}$, a vector field $\boldsymbol{\eta}_0 : \mathcal{B} \to T\mathcal{S}$ over φ_t is an element of $T_{\varphi_t}\mathcal{C}$. Let $\boldsymbol{\eta}_0 = \boldsymbol{0}$ on $\partial_{\mathrm{d}}\mathcal{B}$, then $\boldsymbol{\eta}_0 \in T_{\varphi_t}\mathcal{C}$ is called a *admissible material variation of* φ_t or a *material virtual displacement*.

In an updated Lagrangian formulation the space of admissible configurations is replaced with the *space of admissible velocities* on $\varphi_t(\mathcal{B})$,

$$\mathcal{W} \stackrel{\text{def}}{=} \{\boldsymbol{v}_t : \varphi_t(\mathcal{B}) \to T\mathcal{S} \,|\, \boldsymbol{v}_t = \bar{\boldsymbol{v}}_t \text{ on } \partial_{\mathrm{v}}\varphi_t(\mathcal{B})\}\,,$$

where $\partial_{\mathrm{v}}\varphi_t(\mathcal{B})$ is the part of the boundary of the current configuration with prescribed velocities. Defining the *admissible spatial variation* of φ_t through $\boldsymbol{\eta}_t \stackrel{\text{def}}{=} \boldsymbol{\eta}_0 \circ \varphi_t^{-1}$, then

$$\mathcal{V}_t \stackrel{\text{def}}{=} \{\boldsymbol{\eta}_t : \varphi_t(\mathcal{B}) \to T\mathcal{S} \,|\, \boldsymbol{\eta}_t = \boldsymbol{0} \text{ on } \partial_{\mathrm{v}}\varphi_t(\mathcal{B})\}$$

is called the *space of admissible spatial variations*. Note that $\boldsymbol{\eta}_t \in \mathcal{V}_t$ is often understood as a *virtual velocity*. It is emphasized that $\boldsymbol{\eta}_t$ is time-independent and a non-vanishing vector field only at the points $x \in \mathrm{cl}(\varphi_t(\mathcal{B}))\backslash\partial_{\mathrm{v}}\varphi_t(\mathcal{B})$ at fixed time t. In other words, the index in $\boldsymbol{\eta}_t$ serves as a label and not as a parameter. ♢

Assume that the strong form of balance of linear momentum 3.2.21, $\rho\dot{\boldsymbol{v}} - \operatorname{div}\boldsymbol{\sigma} - \rho\boldsymbol{b} = 0$, is satisfied at every $x \in \varphi_t(\mathcal{B})$ and $t \in [0,T]$. Then one may contract each term with a variation $\boldsymbol{\eta}_t \in \mathcal{V}_t$ and integrate over $\varphi_t(\mathcal{B})$:

$$\int_{\varphi_t(\mathcal{B})} \left(\rho\dot{\boldsymbol{v}} \cdot \boldsymbol{\eta}_t - (\operatorname{div}\boldsymbol{\sigma}) \cdot \boldsymbol{\eta}_t - \rho\bar{\boldsymbol{b}} \cdot \boldsymbol{\eta}_t\right) \mathbf{d}\boldsymbol{v} = 0\,. \tag{5.2.2}$$

Let $\boldsymbol{\eta}_t$ be likewise continuously differentiable, and assume that balance of angular momentum $\boldsymbol{\sigma} = \boldsymbol{\sigma}^{\mathrm{T}}$ holds, then by the product rule the second term becomes

$$(\operatorname{div}\boldsymbol{\sigma}) \cdot \boldsymbol{\eta}_t = \operatorname{div}(\boldsymbol{\sigma} \cdot \boldsymbol{\eta}_t) - \boldsymbol{\sigma} : \boldsymbol{\nabla}^{\mathrm{s}}\boldsymbol{\eta}_t \,, \tag{5.2.3}$$

where $\boldsymbol{\nabla}^{\mathrm{s}}\boldsymbol{\eta}_t \overset{\text{def}}{=} \frac{1}{2}\left(\boldsymbol{\nabla}\boldsymbol{\eta}_t + (\boldsymbol{\nabla}\boldsymbol{\eta}_t)^{\mathrm{T}}\right)$ is the symmetric part of $\boldsymbol{\nabla}\boldsymbol{\eta}_t$, thus $\boldsymbol{\nabla}^{\mathrm{s}}\boldsymbol{\eta}_t$ plays the role of a *virtual rate of deformation tensor*. Substitution into (5.2.2) and application of the divergence theorem A.8.24 then gives

$$\int_{\varphi_t(\mathcal{B})} \rho(\dot{\boldsymbol{v}} - \bar{\boldsymbol{b}}) \cdot \boldsymbol{\eta}_t \,\mathrm{d}\boldsymbol{v} + \int_{\varphi_t(\mathcal{B})} \boldsymbol{\sigma} : \boldsymbol{\nabla}^{\mathrm{s}}\boldsymbol{\eta}_t \,\mathrm{d}\boldsymbol{v} - \int_{\partial\varphi_t(\mathcal{B})} \boldsymbol{n}^* \cdot \boldsymbol{\sigma} \cdot \boldsymbol{\eta}_t \,\mathrm{d}\boldsymbol{a} = 0 \tag{5.2.4}$$

after some rearrangement. Note that $\boldsymbol{\eta}_t$ vanishes on $\partial_{\mathrm{v}}\varphi_t(\mathcal{B}) = \partial\varphi_t(\mathcal{B}) \cap \partial_{\tau}\varphi_t(\mathcal{B})$ by definition (contact constraints are left unconsidered here), and $\boldsymbol{\eta}_t$ is arbitrary on $\partial_{\tau}\varphi_t(\mathcal{B})$ where $\boldsymbol{\sigma} \cdot \boldsymbol{n}^* = \bar{\boldsymbol{t}}$ is prescribed. Therefore, the *weak form of balance of momentum* resp. the *principle of virtual power* can be stated as the functional

$$\begin{aligned} P(\boldsymbol{v}_t, \boldsymbol{\sigma}_t, \boldsymbol{\alpha}_t, \rho_t; \boldsymbol{\eta}_t) \overset{\text{def}}{=} & \int_{\varphi_t(\mathcal{B})} \rho(\dot{\boldsymbol{v}} - \bar{\boldsymbol{b}}) \cdot \boldsymbol{\eta}_t \,\mathrm{d}\boldsymbol{v} + \int_{\varphi_t(\mathcal{B})} \boldsymbol{\sigma} : \boldsymbol{\nabla}^{\mathrm{s}}\boldsymbol{\eta}_t \,\mathrm{d}\boldsymbol{v} \\ & - \int_{\partial_{\tau}\varphi_t(\mathcal{B})} \bar{\boldsymbol{t}} \cdot \boldsymbol{\eta}_t \,\mathrm{d}\boldsymbol{a} \\ & = 0 \,, \end{aligned} \tag{5.2.5}$$

in which $\boldsymbol{\alpha}_t(x) \overset{\text{def}}{=} \boldsymbol{\alpha}(x,t) \overset{\text{def}}{=} \{\alpha_1(x,t), \ldots, \alpha_k(x,t)\}$ denotes a set of (possibly tensor-valued) internal material state variables, with $x = \varphi(X,t)$. The material body $\mathcal{B}$ is said to be in a *state of equilibrium* at time $t \in [0,T]$ provided that (5.2.5) holds.

Definition 5.2.6. [Marsden and Hughes, 1994; Simo and Hughes, 1998] The *variational* or *weak form of the IBVP in UL description 5.1.1* without contact constraints is the problem of finding the velocity field $\boldsymbol{v}$, the stress field $\boldsymbol{\sigma}$, the mass density field ρ, and the internal state variables $\boldsymbol{\alpha}$ such that conservation of mass holds, and

$$P(\boldsymbol{v}_t, \boldsymbol{\sigma}_t, \boldsymbol{\alpha}_t, \rho_t; \boldsymbol{\eta}_t) = 0 \,, \quad \text{for all } \boldsymbol{\eta}_t \in \mathcal{V}_t \,,$$

subject to prescribed boundary and initial conditions. $P(\boldsymbol{v}_t, \boldsymbol{\sigma}_t, \boldsymbol{\alpha}_t, \rho_t; \boldsymbol{\eta}_t)$ is defined through (5.2.5). ♢

Remark 5.2.7. In the above equations, the index raising and index lowering operations, which make the equations well-posed, are hidden. It is understood that the involved quantities are compatible with respect to tensor contraction, that is, the spatial metric $\boldsymbol{g}$ is included in the weak balance of momentum to perform index raising and lowering. △

5.2.2 Treatment of Contact Contraints

In Section 5.1 the general initial boundary value problem (IBVP) for pure mechanics in the updated Lagrangian description has been defined. The general IBVP includes the

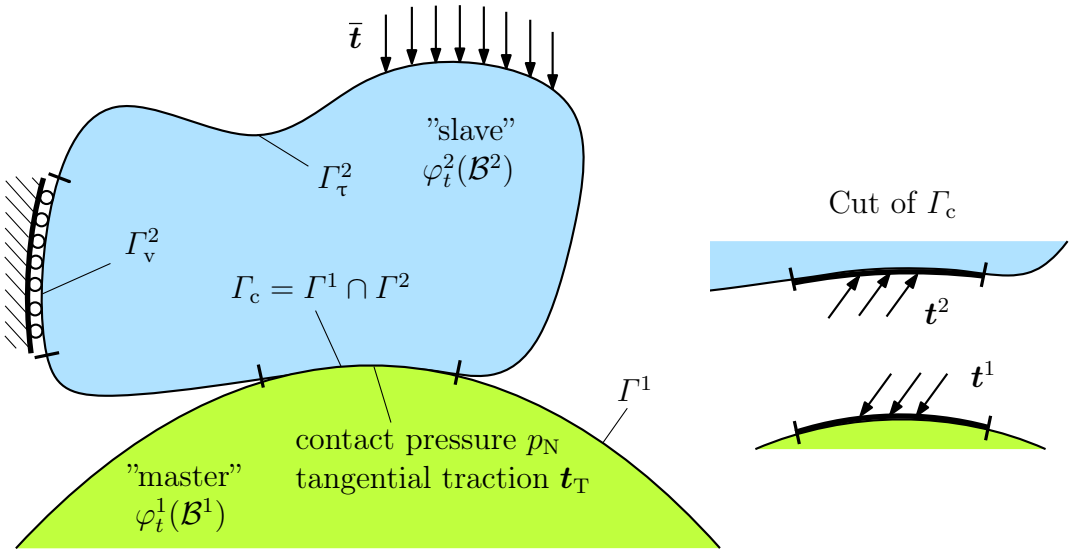

Figure 5.1: Contact of two material bodies.

constraints due to contact of two or more interacting material bodies, which have been left unconsidered in the previous section. Contact aspects of impenetrable bodies are normal contact with or without adhesion, tangential contact (*frictional contact*) with stick and/or slip, and deformation of the contact interface. The size and orientation of the contact zone is a function of time. The objective of the following section is to briefly introduce the governing equations to solve the contact problem on Lagrangian meshes. Comprehensive treatises are, for example, those of Kikuchi and Oden [1988], Wriggers [2006], and Belytschko et al. [2000, ch. 10].

General Definitions

Consider $N_{\text{bodies}} = 2$ material bodies $\mathcal{B}^1, \mathcal{B}^2$, and their motions $\varphi^J : \mathcal{B}^J \times [0,T] \to \mathcal{S}$, with $J \in \{1,2\}$, in the m-dimensional ambient space $\mathcal{S}$. Recall that the parts of the boundary $\partial\mathcal{B}^J$ with prescribed displacement, $\partial_v\mathcal{B}^J$, with prescribed traction, $\partial_\tau\mathcal{B}^J$, and with contact constraints, $\partial_c\mathcal{B}^J$, are regarded open sets, with $\partial_v\mathcal{B} \cap \partial_\tau\mathcal{B} \cap \partial_c\mathcal{B} = \emptyset$ and $\text{cl}(\partial_v\mathcal{B} \cup \partial_\tau\mathcal{B} \cup \partial_c\mathcal{B}) = \text{cl}(\partial\mathcal{B})$. On the current configuration, the partial boundary with prescribed contact constraints is denoted by

$$\Gamma_c^J \overset{\text{def}}{=} \partial_c\varphi_t^J(\mathcal{B}^J) = \varphi_t^J(\partial_c\mathcal{B}^J)\,. \tag{5.2.8}$$

Definition 5.2.9. Let two bodies $\mathcal{B}^1, \mathcal{B}^2$ be in contact at time $t \in [0,T]$, so $N_{\text{bodies}} = 2$, then the pair (Γ_c^1, Γ_c^2) is called the *contact surface pair*. Γ_c^1 and Γ_c^2 are not necessarily of equal size, and generally only a portion of these surfaces, $\Gamma_c \overset{\text{def}}{=} \Gamma^1 \cap \Gamma^2$, is the *actual contact surface* (Fig. 5.1). For convenience, one refers to Γ_c^1 as the *master* or *target surface*, and to Γ_c^2 as the *slave* or *contactor surface*. In a numerical treatment the actual contact surface Γ_c always refers to the master surface. ◇

Definition 5.2.10. The description of the contact surfaces and local contact kinematics includes the definition of a *gap* or *penetration function* g_N and a *tangential relative*

displacement function $\boldsymbol{g}_{\mathrm{T}}$. From this, the conditions of *impenetrability*, *slip*, and *stick* can be formalized as

$$g_{\mathrm{N}} \geq 0\,, \qquad \mathrm{L}_{\boldsymbol{v}}\boldsymbol{g}_{\mathrm{T}} \neq \boldsymbol{0}\,, \qquad \text{and} \qquad \boldsymbol{g}_{\mathrm{T}} = \mathrm{L}_{\boldsymbol{v}}\boldsymbol{g}_{\mathrm{T}} = \boldsymbol{0}\,,$$

respectively. $\mathrm{L}_{\boldsymbol{v}}$ denotes the Lie derivative along the spatial velocity $\boldsymbol{v}$. ◇

Weak IBVP and Finite Element Treatment

The weak form of the mechanical initial boundary value problem for a single body without contact constraints is given by Definition 5.2.6. The weak IBVP for two contacting bodies is defined in what follows.

Let $\boldsymbol{t}^1$ and $\boldsymbol{t}^2$ be the *spatial contact traction vector fields* acting on the contacting portions of Γ_{c}^1 and Γ_{c}^2, respectively. By definition, $\boldsymbol{t}^1$ and $\boldsymbol{t}^2$ vanish on non-contacting portions of Γ_{c}^1 and Γ_{c}^2, respectively, and $\boldsymbol{t}^1 = -\boldsymbol{t}^2$ through balance of momentum (Fig. 5.1). The contact traction vector field $\boldsymbol{t}^1 \in \Gamma(T\mathcal{S})$ is additively decomposed into normal and tangential parts to $\Gamma_{\mathrm{c}} \subset \Gamma_{\mathrm{c}}^1$, leading to

$$\boldsymbol{t}^1 \overset{\text{def}}{=} \boldsymbol{t}_{\mathrm{N}}^1 + \boldsymbol{t}_{\mathrm{T}}^1 = p_{\mathrm{N}}\,\bar{\boldsymbol{n}}^1 + (\boldsymbol{t}_{\mathrm{T}}^1)^{\alpha}\,\bar{\boldsymbol{\gamma}}_{\alpha}^1\,, \tag{5.2.11}$$

in which $\alpha \in \{1,2\}$, $p_{\mathrm{N}}(\bar{\xi}^{\alpha}) \overset{\text{def}}{=} p_{\mathrm{N}}^1(\bar{\xi}^{\alpha}) = p_{\mathrm{N}}^2(\bar{\xi}^{\alpha})$ is the contact pressure, $\xi^{\alpha} = \bar{\xi}^{\alpha}(t)$ are the (time-dependent) coordinates on Γ_{c} at minimal distance of the bodies, $\{\bar{\boldsymbol{\gamma}}_{\alpha}^1\} = \{\bar{\boldsymbol{\gamma}}_1^1, \bar{\boldsymbol{\gamma}}_2^1\}$ is the associated covariant vector basis, $\boldsymbol{t}_{\mathrm{T}}^1(\bar{\xi}^{\alpha}) = -\boldsymbol{t}_{\mathrm{T}}^2(\bar{\xi}^{\alpha})$, and $\bar{\boldsymbol{n}}^1 \overset{\text{def}}{=} \bar{\boldsymbol{\gamma}}_1^1 \times \bar{\boldsymbol{\gamma}}_2^1 / \|\bar{\boldsymbol{\gamma}}_1^1 \times \bar{\boldsymbol{\gamma}}_2^1\|$ is the field of unit outward normals.

The contact conditions on Γ_{c} can now be stated as follows. One always has $p_{\mathrm{N}} \leq 0$ provided that adhesive stresses are excluded. In case of contact one has the conditions $g_{\mathrm{N}} = 0$ and $p_{\mathrm{N}} < 0$. If there is a gap between the two bodies, then the conditions $g_{\mathrm{N}} > 0$ and $p_{\mathrm{N}} = 0$ hold. These conditions can be combined to the so-called Karush-Kuhn-Tucker conditions for contact.

Definition 5.2.12. The *weak form of the IBVP 5.1.1 with contact constraints* is the problem of finding the velocity field $\boldsymbol{v}$, the stress field $\boldsymbol{\sigma}$, the mass density field ρ, and the internal state variables $\boldsymbol{\alpha}$ for both bodies $\mathcal{B}^J$, with $J \in \{1,2\}$, such that conservation of mass holds, and

$$\sum_{J=1}^{2} P(\boldsymbol{v}_t^J, \boldsymbol{\sigma}_t^J, \boldsymbol{\alpha}_t^J, \rho_t^J; \boldsymbol{\eta}_t^J) + \int_{\Gamma_{\mathrm{c}}^1} \boldsymbol{t}^1 \cdot (\boldsymbol{\eta}_t^1 - \boldsymbol{\eta}_t^2)\,\mathbf{d}\boldsymbol{a} = 0\,, \quad \text{for all } \boldsymbol{\eta}_t^J \in \mathcal{V}_t^J\,,$$

subject to prescribed boundary and initial conditions, and subject to the *Karush-Kuhn-Tucker conditions* for frictionless contact without adhesion,

$$g_{\mathrm{N}} \geq 0\,, \qquad p_{\mathrm{N}} \leq 0\,, \quad \text{and} \quad g_{\mathrm{N}}\,p_{\mathrm{N}} = 0 \qquad \text{on } \Gamma_{\mathrm{c}}\,.$$ ◇

In the definition, $P(\boldsymbol{v}_t^J, \boldsymbol{\sigma}_t^J, \boldsymbol{\alpha}_t^J, \rho_t^J; \boldsymbol{\eta}_t^J)$ is the weak balance of momentum (5.2.5) with respect to the current configuration $\varphi_t^J(\mathcal{B}^J)$ of the body $\mathcal{B}^J$ without contact constraints,

and $\mathcal{V}_t^J$ is the space of admissible spatial variations (i.e. virtual velocities) taken with respect to the configuration $\varphi_t^J(\mathcal{B}^J)$.

If a *low contact precision* is sufficient, then the tangential contact traction $\boldsymbol{t}_{\mathrm{T}}^1$ is specified by a constitutive equation, called the *frictional law*, whereas the normal contact is treated as a unilateral geometrical constraint problem [Wriggers, 2006, ch. 5]. This is the common approach in most distributed finite element codes. The occurrence of stick or slip in the contact interface depends on its frictional response. The most commonly used constitutive equation to describe the frictional response is the *Coulomb law*,

$$\boldsymbol{t}_{\mathrm{T}}^1 \stackrel{\mathrm{def}}{=} -\mu|p_{\mathrm{N}}|\frac{\mathrm{L}_{\boldsymbol{v}}\boldsymbol{g}_{\mathrm{T}}}{\|\mathrm{L}_{\boldsymbol{v}}\boldsymbol{g}_{\mathrm{T}}\|} \qquad \text{if} \quad \|\boldsymbol{t}_{\mathrm{T}}^1\| > \mu|p_{\mathrm{N}}| \quad \text{(slip condition)}\,, \tag{5.2.13}$$

where μ is called the *sliding friction coefficient*. μ generally is a function of $\mathrm{L}_{\boldsymbol{v}}\boldsymbol{g}_{\mathrm{T}}$, p_{N}, surface roughness, temperature, and other variables, but it is constant in the classical Coulomb law.

Assume that the contact interface is known through a partial solution to the weak IBVP 5.2.12, and that contact is active at Γ_{c}. In this case weak balance of momentum with contact constraints can be written as

$$\sum_{J=1}^{2} P(\boldsymbol{v}_t^J, \boldsymbol{\sigma}_t^J, \boldsymbol{\alpha}_t^J, \rho_t^J; \boldsymbol{\eta}_t^J) + C_{\mathrm{c}} = 0\,, \quad \text{for all } \boldsymbol{\eta}_t^J \in \mathcal{V}_t^J\,, \tag{5.2.14}$$

where C_{c} shall denote the *contact contributions*. The specific form of C_{c} depends on the *contact algorithm* resp. *contact method* used. In many practical cases, contact methods that add constraints to the weak balance of momentum are favored over a direct application of constitutive equations. The most widely used methods are the *Lagrange multiplier method*, the *penalty method*, the *augmented Lagrangian method*, and the method of *direct constraint elimination*.

The *Lagrange multiplier (LM) method* introduces Lagrange multipliers λ_{N} and $\boldsymbol{\lambda}_{\mathrm{T}}$ together with their variations $\delta\lambda_{\mathrm{N}}$ and $\delta\boldsymbol{\lambda}_{\mathrm{T}}$ associated with the normal and tangential direction, respectively, which gives

$$C_{\mathrm{c}}^{\mathrm{LM}} \stackrel{\mathrm{def}}{=} \begin{cases} \int_{\Gamma_{\mathrm{c}}} (\lambda_{\mathrm{N}}\,\delta g_{\mathrm{N}} + \boldsymbol{\lambda}_{\mathrm{T}} \cdot \delta\boldsymbol{g}_{\mathrm{T}} + \delta\lambda_{\mathrm{N}}\, g_{\mathrm{N}} + \delta\boldsymbol{\lambda}_{\mathrm{T}} \cdot \boldsymbol{g}_{\mathrm{T}})\,\mathrm{d}\boldsymbol{a}, & \text{if stick,} \\ \int_{\Gamma_{\mathrm{c}}} (\lambda_{\mathrm{N}}\,\delta g_{\mathrm{N}} + \boldsymbol{t}_{\mathrm{T}}^1 \cdot \delta\boldsymbol{g}_{\mathrm{T}} + \delta\lambda_{\mathrm{N}}\, g_{\mathrm{N}})\,\mathrm{d}\boldsymbol{a}, & \text{if slip.} \end{cases} \tag{5.2.15}$$

If slip occurs, the integral $\int_{\Gamma_{\mathrm{c}}} \delta\boldsymbol{\lambda}_{\mathrm{T}} \cdot \boldsymbol{g}_{\mathrm{T}}\,\mathrm{d}\boldsymbol{a}$ is eliminated, and the tangential traction $\boldsymbol{t}_{\mathrm{T}}^1$ is to be determined from the constitutive equation for frictional slip, e.g. from the Coulomb law (5.2.13). The Lagrange multiplier method enforces zero penetration when contact is closed and zero slip when sticking contact occurs. Contact traction is added to the model, which introduces additional degrees of freedom. Therefore, the Lagrange multiplier method often increases the computational cost compared to other methods.

The *penalty method (PM)* introduces penalty parameters $\epsilon_{\mathrm{N}} > 0$ and $\epsilon_{\mathrm{T}} > 0$, which play the role of a normal and tangential "contact stiffness", respectively, in order to establish a relationship between the two contact surfaces. The contact contributions C_{c} in (5.2.14) then become

$$C_{\mathrm{c}}^{\mathrm{PM}} \stackrel{\mathrm{def}}{=} \begin{cases} \int_{\Gamma_{\mathrm{c}}} (\epsilon_{\mathrm{N}}\, g_{\mathrm{N}}\, \delta g_{\mathrm{N}} + \epsilon_{\mathrm{T}}\, \boldsymbol{g}_{\mathrm{T}} \cdot \delta\boldsymbol{g}_{\mathrm{T}})\,\mathrm{d}\boldsymbol{a}, & \text{if stick,} \\ \int_{\Gamma_{\mathrm{c}}} (\epsilon_{\mathrm{N}}\, g_{\mathrm{N}}\, \delta g_{\mathrm{N}} + \boldsymbol{t}_{\mathrm{T}}^1 \cdot \delta\boldsymbol{g}_{\mathrm{T}})\,\mathrm{d}\boldsymbol{a}, & \text{if slip,} \end{cases} \tag{5.2.16}$$

where $\boldsymbol{t}_{\mathrm{T}}^{1}$ is again to be determined from the constitutive equation for frictional slip. Penetration and tangential relative displacement (in case of stick) are generally non-zero if the penalty parameters take finite values.

The discretization and solution of the weak IBVP including contact constraints (Definition 5.2.12) is closely connected to the contact method and has grown a science of its own. The reader is referred to [Wriggers, 2006] for details.

5.3 Spatial Discretization

5.3.1 General Remarks

When employing the finite element method, the weak form of the governing equations of an initial boundary value problem is approximated by *discretizing* the computational domain by a set of finite elements. This procedure, which is outlined in the following section, results in a *semi-discrete weak form of the IBVP* derived subsequently.

Definition 5.3.1. Within the Lagrangian finite element methods the reference configuration of the material body $\mathcal{B}$ in the ambient space $\mathcal{S}$ is approximated by the disjoint (i.e. non-overlapping) union

$$\mathcal{B} \approx \tilde{\mathcal{B}} \stackrel{\text{def}}{=} \bigcup_{e=1}^{n_{\text{el}}} \Omega^e \qquad \subset \mathcal{S}$$

of n_{el} *finite elements* $\Omega^e \subset \mathcal{S}$. The superscribed e is dropped if a generic element Ω is considered. Each element is bounded by nodes (vertices), edges, and faces (only in 3d) defining a so-called *convex polytope*, which is a polygon in two dimensions or a polyhedron in three dimensions. The operator $\bigcup$ should be understood as an *assembly* which assigns a certain topology to $\tilde{\mathcal{B}}$. The boundary $\partial\mathcal{B}$ of the material body is approximated by

$$\partial\mathcal{B} \approx \partial\tilde{\mathcal{B}} \stackrel{\text{def}}{=} \bigcup_{e=1}^{b_{\text{el}}} \bar{\partial}\Omega^e \subset \bigcup_{e=1}^{b_{\text{el}}} \partial\Omega^e \,,$$

where b_{el} is the number of elements that have a part $\bar{\partial}\Omega^e \subset \partial\Omega^e$ of their boundary (i.e. one or more nodes, edges or faces) "aligned" to the boundary of $\mathcal{B}$.

Finite element methods usually consider motions $\varphi_t : \mathcal{B} \to \mathcal{S}$ of a material body $\mathcal{B} \subset \mathbb{R}^m$ in the standard m-dimensional Euclidian point space $\mathcal{S} = \mathbb{R}^m$; see also Remark 3.1.4 and Section A.1. The current configuration $\varphi_t(\mathcal{B}) \subset \mathcal{S}$ of the material body is approximated by the disjoint union $\varphi_t(\mathcal{B}) \approx \varphi_t(\tilde{\mathcal{B}}) \stackrel{\text{def}}{=} \bigcup_{e=1}^{n_{\text{el}}} \varphi_t(\Omega^e)$, and $\partial\varphi_t(\mathcal{B}) \approx \partial\varphi_t(\tilde{\mathcal{B}}) \stackrel{\text{def}}{=} \bigcup_{e=1}^{b_{\text{el}}} \bar{\partial}\varphi_t(\Omega^e)$ is the approximation of its boundary, with $\bar{\partial}\varphi_t(\Omega^e) \subset \partial\varphi_t(\Omega^e) = \varphi_t(\partial\Omega^e)$. ◇

Parent Element and Transformation Rules

Let the current configuration $\varphi_t(\Omega)$ of the generic finite element be a certain configuration of a parent element $\Omega_\square \subset \mathbb{R}^m$. This is formalized as an orientation-preserving C^1-embedding

$$\theta_t : \Omega_\square \to \mathcal{S} \tag{5.3.2}$$

which satisfies $\theta_t(\Omega_\square) = \varphi_t(\Omega) \subset \mathcal{S}$ for every $t \in [0,T]$ (Fig. 5.2). The property of this *parent element map* guarantees that $\Omega_\square$ and $\varphi_t(\Omega)$ possess the same differential topology, e.g. a mapped quadrilateral element remains a quadrilateral, probably with curved edges. As usual, $\theta_t(\cdot) \stackrel{\text{def}}{=} \theta(\cdot,t)$ is being understood.

Associated with the parent element domain $\Omega_\square$ there is a coordinate chart $(\Omega_\square, \omega)$ such that $\omega(\xi) = \{\xi^1,\dots,\xi^m\}_\xi \stackrel{\text{def}}{=} \{\xi^\alpha\}_\xi \in \mathbb{R}^m$, $\exists\omega^{-1}$, for a point $\xi \in \Omega_\square$. The ξ^α, $\alpha \in \{1,\dots,m\}$, are called *element coordinates* or *natural coordinates*. A local holonomic basis $\{\frac{\boldsymbol{\partial}}{\boldsymbol{\partial}\xi^\alpha}\}_\xi$ is associated with the element coordinates at $\xi \in \Omega_\square$, and $\{\mathbf{d}\xi^\alpha\}_\xi$ is the dual basis. Let $\mathcal{V} \stackrel{\text{def}}{=} \theta(\Omega_\square, t) \subset \mathcal{S} = \mathbb{R}^m$, and $(\mathcal{V},\sigma)$ a local chart of the ambient space. By applying the geometric language of Appendix A, the localization of the map θ is given by $\sigma\circ\theta\circ\omega^{-1}$, so that

$$\theta^i_t(\xi^\alpha) \stackrel{\text{def}}{=} (x^i \circ \theta_t \circ \omega^{-1})(\xi^\alpha) \tag{5.3.3}$$

defines generally curvilinear coordinates on $\mathcal{V} = \theta_t(\Omega_\square)$, with $\theta^i_t(\xi^\alpha) = \theta^i(\xi^\alpha,t)$. The global Cartesian coordinates z^b of the ambient space can likewise be expressed as functions of the element coordinates, viz. $\theta^b_z \stackrel{\text{def}}{=} z^b\circ\theta\circ\omega^{-1}$ on $\theta_t(\Omega_\square)$. The corresponding convected coordinates on $\theta_t(\Omega_\square)$ are defined through $(\theta_t^{-1})^\alpha(x^i) \stackrel{\text{def}}{=} (\xi^\alpha \circ \theta_t^{-1} \circ \sigma^{-1})(x^i)$ and $(\theta_t^{-1})^\alpha_z(z^b) \stackrel{\text{def}}{=} (\xi^\alpha \circ \theta_t^{-1} \circ z^{-1})(z^b)$.

The tangent of the map $\theta_t : \Omega_\square \to \mathcal{S}$, denoted by $T\theta_t \stackrel{\text{def}}{=} \boldsymbol{F}_{\theta t}$, is a two-point tensor field over θ_t, with $\boldsymbol{F}_{\theta t}(\xi) : T_\xi\Omega_\square \to T_{\theta_t(\xi)}\mathcal{S}$ evaluated at $\xi \in \Omega_\square$. Local representatives of $\boldsymbol{F}_{\theta t}(\cdot) \stackrel{\text{def}}{=} \boldsymbol{F}_\theta(\cdot,t)$ are

$$\boldsymbol{F}_\theta(\xi,t) = \frac{\partial\theta^i}{\partial\xi^\alpha}\,\frac{\boldsymbol{\partial}}{\boldsymbol{\partial}x^i} \otimes \mathbf{d}\xi^\alpha = \frac{\partial\theta^i}{\partial\xi^\alpha}\frac{\partial z^b}{\partial x^i}\,\boldsymbol{e}_b \otimes \mathbf{d}\xi^\alpha = \frac{\partial\theta^b_z}{\partial\xi^\alpha}\,\boldsymbol{e}_b \otimes \mathbf{d}\xi^\alpha\,, \tag{5.3.4}$$

where the relation $\frac{\boldsymbol{\partial}}{\boldsymbol{\partial}x^i} = \frac{\partial z^a(x)}{\partial x^i}\,\boldsymbol{e}_a$ has been used. $\{\boldsymbol{e}_1,\dots,\boldsymbol{e}_m\} \stackrel{\text{def}}{=} \{\boldsymbol{e}_a\} \in \mathbb{R}^m$ is the canonical basis of $\mathcal{S} = \mathbb{R}^m$.

The parent element $\Omega_\square$ is orientable with piecewise continuous orientable boundary $\partial\Omega_\square$ such that Riemannian volume and area forms, denoted by $\mathbf{d}\square$ and $\mathbf{d}(\partial\square)$, respectively, do exist. According to (A.8.20), $\mathbf{d}\square$ and the spatial Riemannian volume form $\mathbf{d}\boldsymbol{v}$ are related by

$$\theta^\star\mathbf{d}\boldsymbol{v} = J_\theta\,\mathbf{d}\square\,, \tag{5.3.5}$$

where $J_\theta > 0$ is the Jacobian of the orientation-preserving map θ.

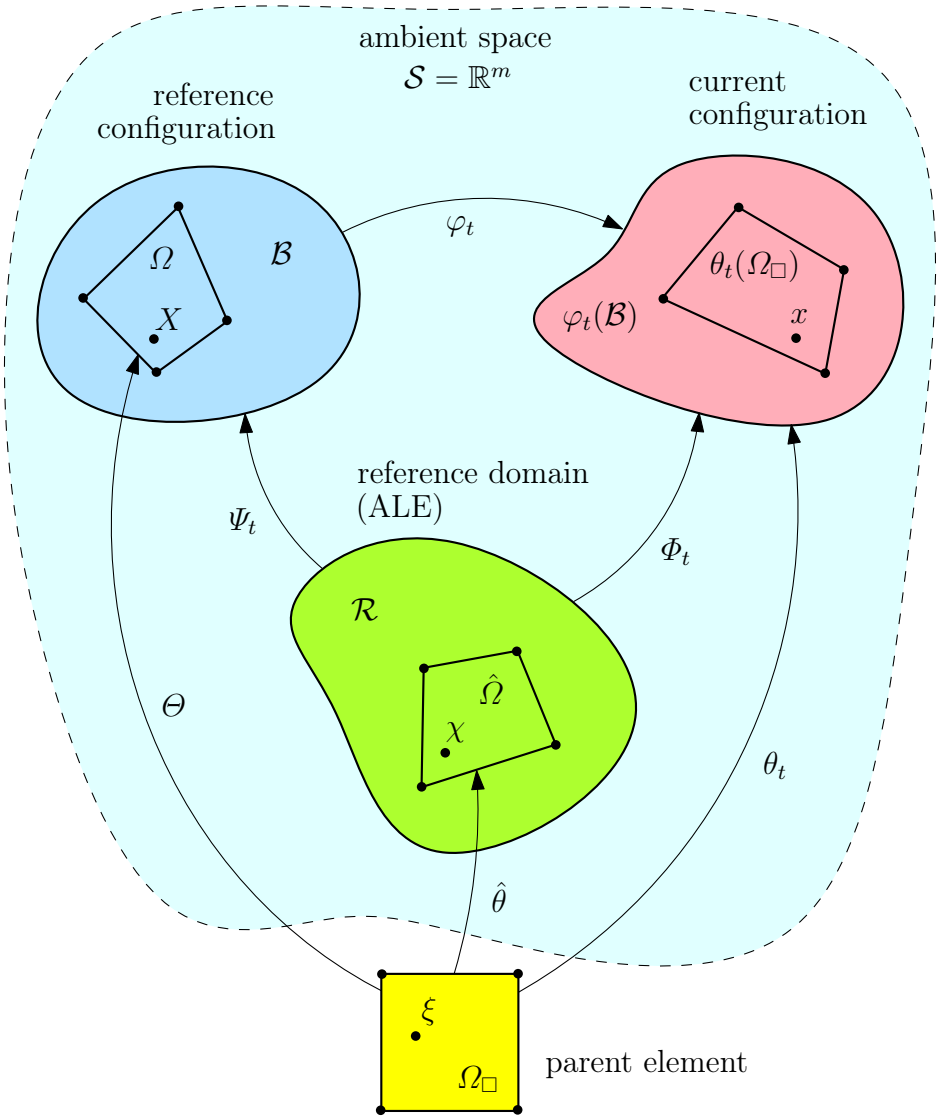

Figure 5.2: Parent element $\Omega_\square$ and configurations Ω, $\theta_t(\Omega_\square) = \varphi_t(\Omega)$, and $\hat{\Omega}$ associated with the reference and current configurations of the material body $\mathcal{B}$, and with the reference domain $\mathcal{R}$, respectively.

Furthermore, let $\boldsymbol{n}^*$ be the unit outward normals on piecewise smooth $\partial\varphi_t(\Omega)$ such that $\mathbf{d}\boldsymbol{v} = \boldsymbol{n}^* \wedge \mathbf{d}\boldsymbol{a}$. Let, on the other hand, $\boldsymbol{n}^*$ be the outward normals on $\partial\Omega_\square$ given by the relation $\mathbf{d}\square \overset{\text{def}}{=} \boldsymbol{n}^* \wedge \mathbf{d}(\partial\square)$. Then,

$$\theta^\star \mathbf{d}\boldsymbol{a} = \mathbf{d}\boldsymbol{a} \circ \theta = \|J_\theta \boldsymbol{F}_\theta^{-\mathrm{T}} \cdot \boldsymbol{n}^*\| \, \mathbf{d}(\partial\square) = J_\theta \sqrt{\boldsymbol{n}^* \cdot \theta^\star(\boldsymbol{g}^\sharp) \cdot \boldsymbol{n}^*} \, \mathbf{d}(\partial\square) \tag{5.3.6}$$

and $\boldsymbol{n}^* = (J_\theta \boldsymbol{F}_\theta^{-\mathrm{T}} \cdot \boldsymbol{n}^*)/\|J_\theta \boldsymbol{F}_\theta^{-\mathrm{T}} \cdot \boldsymbol{n}^*\|$ by Theorem A.8.26.

The specific form of the map (5.3.2) depends on the particular element in an assembly of finite elements. Concerning the e-th element Ω^e in the assembly, with $e \in \{1, \ldots, n_{\mathrm{el}}\}$, the map θ_t takes the form θ_t^e, and the Jacobian of θ_t^e is denoted by J_θ^e. On a finite element assembly the integrals of functions over the approximated spatial computational domain can then be transformed as follows.

Proposition 5.3.7. *Let f be a spatial real function defined on $\varphi_t(\mathcal{B})$, J_θ^e be the Jacobian of $\theta^e : \Omega_\square \times [0,T] \to \mathcal{S}$, $\theta_t^e(\Omega_\square) = \varphi_t(\Omega^e) \subset \mathcal{S}$, and $f_\theta^e \overset{\text{def}}{=} f \circ \theta^e$. Moreover, let $\boldsymbol{t}$ be a spatial vector field defined on the boundary of $\varphi_t(\mathcal{B})$, and let $\boldsymbol{t}_\theta^e \overset{\text{def}}{=} \boldsymbol{t} \circ \theta^e$. Then,*

(i) the integral of f over $\varphi_t(\mathcal{B})$ can be approximated through

$$\int_{\varphi_t(\mathcal{B})} f \, \mathbf{d}\boldsymbol{v} \approx \int_{\varphi_t(\bar{\mathcal{B}})} f \, \mathbf{d}\boldsymbol{v} = \bigcup_{e=1}^{n_{\mathrm{el}}} \int_{\varphi_t(\Omega^e)} f \, \mathbf{d}\boldsymbol{v} = \bigcup_{e=1}^{n_{\mathrm{el}}} \int_{\Omega_\square} f_\theta^e J_\theta^e \, \mathbf{d}\square \, .$$

(ii) if $\boldsymbol{t}$ is read componentwise in Cartesian coordinates, then its integral over the boundary $\partial\varphi_t(\mathcal{B})$ can be approximated through

$$\int_{\partial\varphi_t(\mathcal{B})} \boldsymbol{t} \, \mathbf{d}\boldsymbol{a} \approx \bigcup_{e=1}^{n_{\mathrm{el}}} \int_{\bar{\partial}\varphi_t(\Omega^e)} \boldsymbol{t} \, \mathbf{d}\boldsymbol{a} = \bigcup_{e=1}^{b_{\mathrm{el}}} \int_{\bar{\partial}\Omega_\square} \boldsymbol{t}_\theta^e \, \|J_\theta^e (\boldsymbol{F}_\theta^e)^{-\mathrm{T}} \cdot \boldsymbol{n}^*\| \, \mathbf{d}(\partial\square) \, ,$$

where $\bar{\partial}$ denotes a part of the element boundary used for the spatial approximation of the boundary $\partial\varphi_t(\mathcal{B})$.

Proof. Both statements are consequences of Definition 5.3.1, (5.3.5), (5.3.6), and the similar basic result 3.2.1. ∎

Based on Proposition 5.3.7, the integrals over the current configuration of the body in space are approximated by the integrals over the parent elements. Integration on the parent element is defined with respect to the natural coordinates ξ^α. In general, the integration is carried out numerically. *Gauss quadrature* is usually applied to lines, quadrilaterals and hexahedra. It approximates the integral of a real function $f(\xi)$ over the interval $[-1, 1]$ through

$$\int_{-1}^{1} y(\xi) \, \mathrm{d}\xi \approx \sum_{q=1}^{n_{\mathrm{Q}}} w_q \, y(\xi_q) \, , \tag{5.3.8}$$

where n_{Q} is the number of *quadrature points* or *Gauss points* used for the approximation, and ξ_q and w_q are the natural coordinate and the weight associated with the q-th Gauss point, respectively. (5.3.8) integrates exactly if $y(\xi)$ is a polynomial of degree $m \leq 2n_{\mathrm{Q}} - 1$ [see Belytschko et al., 2000]. Tables that list the locations of the Gauss points and the related weights for different kinds of elements can be found in the standard FEM textbooks that have been already cited.

Isoparametric Finite Element Concept

Finite element methods determine the primary solution variables only at the *nodes* of the *finite element mesh*, that is, at discrete points. The solution between the nodes is obtained via interpolation. The isoparametric Lagrangian FE concept is commonly applied to engineering initial boundary value problems, in which the solution variables and the geometry are interpolated by the same shape functions. This concept is well-suited for geometrically nonlinear problems, because one can always fall back on the coordinate chart $(\Omega_\square, \xi)$ of the parent element [Wriggers, 2008].

Definition 5.3.9. The *isoparametric updated Lagrangian (UL) finite element concept* has two basic ingredients.

(i) The geometry of a single finite element in the current configuration is approximated through

$$x \overset{\text{def}}{=} \theta(\xi,t) \approx \sum_{I=1}^{n_{\text{nd}}} N^I(\xi)\, x_I(t) \overset{\text{def}}{=} N^I(\xi)\, x_I(t) \quad \text{resp.} \quad z^b \overset{\text{def}}{=} \theta_z^b(\xi^\alpha,t) \approx N^I(\xi^\alpha)\, z_I^b(t)\,,$$

where n_{nd} is the number of nodes of the element, and N^I is the *interpolation function* (also called *shape function* or *ansatz function*) for geometry and the node $I \in \{1,\dots,n_{\text{nd}}\}$. z^b are the Cartesian coordinates of $\mathbb{R}^m$, and θ and θ_z^b refer to the parent element as defined previously. The functions $z_I^b(t)$ are the spatial Cartesian coordinates of node I, which are functions of time t through $x \overset{\text{def}}{=} \theta(\xi,t)$. Time-dependency entirely resides in the nodal values, while the shape functions have no explicit time-dependency.

(ii) The spatial velocity $\boldsymbol{v}(x,t) \overset{\text{def}}{=} v_z^b(x,t)\,\boldsymbol{e}_b$ at every $x \in \varphi_t(\Omega^e) \subset \mathcal{S}$ and $t \in [0,T]$ is the primary solution variable, where $x = \theta(\xi,t)$. It is approximated within a finite element by using the same shape functions as for the geometry:

$$\boldsymbol{v}(\xi,t) \approx N^I(\xi)\,\boldsymbol{v}_I(t) \qquad \text{resp.} \qquad v_z^b(\xi,t) \approx N^I(\xi)\, v_{zI}^b(t)\ .$$

Similar holds for $\boldsymbol{\eta}_t$. ◇

Remark 5.3.10. It is emphasized that the finite element approximation 5.3.9 enforces the Einstein summation convention (A.0.1) due to notational brevity, despite the fact that $I, J, K, \dots$ label the element nodes, and not coordinates. △

Remark 5.3.11. Definition 5.3.9 clearly reflects the updated Lagrangian description introduced in Section 5.1. Note that $\boldsymbol{v}(\xi,t)$, for example, is actually $\boldsymbol{v}(\theta(\xi,t),t)$, where $\boldsymbol{v}(x,t)$ is the spatial velocity field and $x = \theta(\xi,t)$, so $\boldsymbol{v}(\xi,t)$ is in fact the "material" velocity field over θ_t, and $\dot{\boldsymbol{v}}(\xi,t)$ is the "material" acceleration. △

Using Definition 5.3.9, the components of $\boldsymbol{F}_{\theta t}$ given by (5.3.4) are approximated through

$$(\boldsymbol{F}_\theta)^b{}_\alpha(\xi,t) = \frac{\partial \theta_z^b}{\partial \xi^\alpha}(\xi,t) \approx \frac{\partial N^I}{\partial \xi^\alpha}(\xi)\, z_I^b(t)\ . \tag{5.3.12}$$

The matrix arrangement of these components is the so-called *Jacobian matrix of the map* θ_t. By this the components of $\boldsymbol{\nabla}\boldsymbol{\eta}_t$ with respect to the spatial Cartesian coordinates z^b can be computed from the chain rule (arguments are suppressed):

$$(\boldsymbol{\nabla}\boldsymbol{\eta}_t)^b{}_d = \frac{\partial \eta^b_{tz}}{\partial z^d} = \frac{\partial \eta^b_{tz}}{\partial \xi^\alpha}\,\frac{\partial (\theta_t^{-1})^\alpha_z}{\partial z^d} = \frac{\partial \eta^b_{tz}}{\partial \xi^\alpha}\,(\boldsymbol{F}_\theta^{-1})^\alpha{}_d = \eta^b_{zI}\frac{\partial N^I}{\partial z^d}\,, \tag{5.3.13}$$

where $\frac{\partial N^I}{\partial z^d} = \frac{\partial N^I}{\partial \xi^\alpha}\,(\boldsymbol{F}_\theta^{-1})^\alpha{}_d$ being understood.

Matrix Notation

Components of vectors and tensors with respect to the canonical basis $\{\boldsymbol{e}_1,\dots,\boldsymbol{e}_m\} \stackrel{\text{def}}{=} \{\boldsymbol{e}_a\} \in \mathbb{R}^m$ can be arranged in some suitable matrix format. As an example, consider the spatial velocity field in two dimensions. The representative $\boldsymbol{v} = v^b_z\,\boldsymbol{e}_b$ can then be identified with its column-matrix taken with respect to the basis $\{\boldsymbol{e}_b\}$, that is, $\boldsymbol{v} \stackrel{\text{def}}{=} (v^1_z, v^2_z)^{\mathrm{T}} \in \mathbb{R}^2$. The approximation of the spatial velocity in Definition 5.3.9(ii) can likewise be written as a matrix equation. Let the number of nodes in the element be $n_{\mathrm{nd}} = 2$, then, for example, define the matrix arrangement of the finite element approximation in 5.3.9 as

$$\begin{pmatrix} v^1_z(\xi,t) \\ v^2_z(\xi,t) \end{pmatrix} \approx \begin{pmatrix} N^1(\xi) & 0 & N^2(\xi) & 0 \\ 0 & N^1(\xi) & 0 & N^2(\xi) \end{pmatrix} \begin{pmatrix} v^1_1(t) \\ v^2_1(t) \\ v^1_2(t) \\ v^2_2(t) \end{pmatrix} \tag{5.3.14}$$

$$\boldsymbol{v}(\xi,t) \qquad \approx \qquad \boldsymbol{N}(\xi) \qquad\qquad \boldsymbol{v}_e(t)\,,$$

where $\boldsymbol{N}$ is called the *matrix of interpolation functions* and $\boldsymbol{v}_e$ is called the *element nodal velocity vector*. In case of n_{nd} element nodes in m dimensions, the latter is generalized as

$$\boldsymbol{v}_e \stackrel{\text{def}}{=} \begin{pmatrix} v^1_1 \\ \vdots \\ v^m_1 \\ \vdots \\ v^1_{n_{\mathrm{nd}}} \\ \vdots \\ v^m_{n_{\mathrm{nd}}} \end{pmatrix} = \begin{pmatrix} \boldsymbol{v}_1 \\ \vdots \\ \boldsymbol{v}_{n_{\mathrm{nd}}} \end{pmatrix} \stackrel{\text{def}}{=} \bigcup_{I=1}^{n_{\mathrm{nd}}} \boldsymbol{v}_I\,. \tag{5.3.15}$$

5.3.2 Semi-Discrete Weak Form of Balance of Momentum

The weak form of balance of momentum without contact constraints, (5.2.5), is solved with respect to the assembly of finite elements such that

$$\bigcup_{e=1}^{n_{\mathrm{el}}} \int_{\varphi_t(\Omega^e)} \rho(\dot{\boldsymbol{v}} - \bar{\boldsymbol{b}})\cdot\boldsymbol{\eta}_t\,\mathrm{d}\boldsymbol{v} + \bigcup_{e=1}^{n_{\mathrm{el}}} \int_{\varphi_t(\Omega^e)} \boldsymbol{\sigma} : \boldsymbol{\nabla}^{\mathrm{s}}\boldsymbol{\eta}_t\,\mathrm{d}\boldsymbol{v} - \bigcup_{e=1}^{t_{\mathrm{el}}} \int_{\partial_\tau\varphi_t(\Omega^e)} \bar{\boldsymbol{t}}\cdot\boldsymbol{\eta}_t\,\mathrm{d}\boldsymbol{a} = 0\,, \tag{5.3.16}$$

where $t_{\mathrm{el}} \leq b_{\mathrm{el}}$ is the number of elements with prescribed traction located at the boundary of $\varphi_t(\tilde{\mathcal{B}})$. (5.3.16) states that the integrals over the current configuration of the body resp. its boundary are approximated by the assembly of integrals over the current configuration of the finite elements. In adding all ingredients prepared in the previous section, the integrals in (5.2.5) resp. (5.3.16) become

$$\int_{\varphi_t(\mathcal{B})} \rho \dot{\boldsymbol{v}} \cdot \boldsymbol{\eta}_t \,\mathrm{d}\boldsymbol{v} \approx \bigcup_{e=1}^{n_{\mathrm{el}}} \boldsymbol{\eta}_{tI}^{\mathrm{T}} \boldsymbol{M}^{IJ} \dot{\boldsymbol{v}}_J \stackrel{\mathrm{def}}{=} \bigcup_{e=1}^{n_{\mathrm{el}}} \boldsymbol{\eta}_{te}^{\mathrm{T}} \boldsymbol{M}_e \dot{\boldsymbol{v}}_e = \boldsymbol{\eta}_{tg}^{\mathrm{T}} \boldsymbol{M}_g \dot{\boldsymbol{v}}_g = \boldsymbol{\eta}_{tg}^{\mathrm{T}} \boldsymbol{f}_g^{\mathrm{kin}} \,, \tag{5.3.17}$$

$$\int_{\varphi_t(\mathcal{B})} \rho \bar{\boldsymbol{b}} \cdot \boldsymbol{\eta}_t \,\mathrm{d}\boldsymbol{v} \approx \bigcup_{e=1}^{n_{\mathrm{el}}} \boldsymbol{\eta}_{tI}^{\mathrm{T}} \boldsymbol{p}_{\boldsymbol{b}}^I \stackrel{\mathrm{def}}{=} \bigcup_{e=1}^{n_{\mathrm{el}}} \boldsymbol{\eta}_{te}^{\mathrm{T}} \boldsymbol{f}_e^{\boldsymbol{b}} = \boldsymbol{\eta}_{tg}^{\mathrm{T}} \boldsymbol{f}_g^{\boldsymbol{b}} \,, \tag{5.3.18}$$

$$\int_{\partial_\tau \varphi_t(\mathcal{B})} \bar{\boldsymbol{t}} \cdot \boldsymbol{\eta}_t \,\mathrm{d}\boldsymbol{a} \approx \bigcup_{e=1}^{t_{\mathrm{el}}} \boldsymbol{\eta}_{tI}^{\mathrm{T}} \boldsymbol{p}_{\boldsymbol{t}}^I \stackrel{\mathrm{def}}{=} \bigcup_{e=1}^{t_{\mathrm{el}}} \boldsymbol{\eta}_{te}^{\mathrm{T}} \boldsymbol{f}_e^{\boldsymbol{t}} = \boldsymbol{\eta}_{tg}^{\mathrm{T}} \boldsymbol{f}_g^{\boldsymbol{t}} \,, \qquad \text{and} \tag{5.3.19}$$

$$\int_{\varphi_t(\mathcal{B})} \boldsymbol{\sigma} : \boldsymbol{\nabla}^{\mathrm{s}} \boldsymbol{\eta}_t \,\mathrm{d}\boldsymbol{v} \approx \bigcup_{e=1}^{n_{\mathrm{el}}} \boldsymbol{\eta}_{tI}^{\mathrm{T}} \boldsymbol{p}_{\boldsymbol{\sigma}}^I \stackrel{\mathrm{def}}{=} \bigcup_{e=1}^{n_{\mathrm{el}}} \boldsymbol{\eta}_{te}^{\mathrm{T}} \boldsymbol{f}_e^{\mathrm{int}} = \boldsymbol{\eta}_{tg}^{\mathrm{T}} \boldsymbol{f}_g^{\mathrm{int}} \,, \tag{5.3.20}$$

where

$$\boldsymbol{M}^{IJ} \stackrel{\mathrm{def}}{=} \Big(\int_{\Omega_\square} \rho N^I N^J J_\theta^e \,\mathrm{d}\square \Big) \boldsymbol{I} \,, \qquad \boldsymbol{p}_{\boldsymbol{b}}^I \stackrel{\mathrm{def}}{=} \int_{\Omega_\square} \rho N^I \,\bar{\boldsymbol{b}} J_\theta^e \,\mathrm{d}\square \,,$$
$$\boldsymbol{p}_{\boldsymbol{\sigma}}^I \stackrel{\mathrm{def}}{=} \int_{\Omega_\square} (\boldsymbol{B}_{\mathrm{s}}^I)^{\mathrm{T}} \boldsymbol{\sigma} J_\theta^e \,\mathrm{d}\square \,, \qquad \text{and} \qquad \boldsymbol{p}_{\boldsymbol{t}}^I \stackrel{\mathrm{def}}{=} \int_{\bar{\partial}\Omega_\square} N^I \bar{\boldsymbol{t}} \,\| J_\theta^e (\boldsymbol{F}_\theta^e)^{-\mathrm{T}} \cdot \boldsymbol{n}^* \| \,\mathrm{d}(\partial\square) \,.$$

Concerning the indices I and J, note that the Einstein summation convention (A.0.1) is forced. $\boldsymbol{I} \in \mathbb{R}^{m_{\mathrm{dim}}} \times \mathbb{R}^{m_{\mathrm{dim}}}$ is the unit matrix in m_{dim} spatial dimensions. $\boldsymbol{M}_g$ is called the *(consistent) global mass matrix*, which is constant because of conservation of mass in Lagrangian description. $\dot{\boldsymbol{v}}_g$ is the *global nodal acceleration vector*, and $\boldsymbol{M}_g \dot{\boldsymbol{v}}_g \stackrel{\mathrm{def}}{=} \boldsymbol{f}_g^{\mathrm{kin}}$ is referred to as the *global kinetic nodal force vector*. The sum $\boldsymbol{f}_g^{\mathrm{ext}} \stackrel{\mathrm{def}}{=} \boldsymbol{f}_g^{\boldsymbol{b}} + \boldsymbol{f}_g^{\boldsymbol{t}}$ is called the *global applied external nodal force vector*, and $\boldsymbol{f}_g^{\mathrm{int}}$ is referred to as the *global internal nodal force vector*.

For the stress term in the weak form of balance of momentum, $\int_{\varphi_t(\mathcal{B})} \boldsymbol{\sigma} : \boldsymbol{\nabla}^{\mathrm{s}} \boldsymbol{\eta}_t \,\mathrm{d}\boldsymbol{v}$, the components of the Cauchy stress in $\mathbb{R}^m$ are arranged in a column-matrix, which is also denoted by $\boldsymbol{\sigma}$. This column-matrix usually follows *Voigt's notation* [Belytschko et al., 2000, app. 1]. For example, in $\mathbb{R}^3$ the stress column-matrix is defined through

$$\boldsymbol{\sigma} \stackrel{\mathrm{def}}{=} \left(\sigma^{11}, \sigma^{22}, \sigma^{33}, \sigma^{12}, \sigma^{23}, \sigma^{13} \right)^{\mathrm{T}} \,. \tag{5.3.21}$$

Voigt's notation uses the fact that the Cauchy stress is symmetric, hence only one of the $\sigma^{ij} = \sigma^{ji}$ is stored. The compatible column-matrix $\boldsymbol{\nabla}^{\mathrm{s}} \boldsymbol{\eta}_t$ over the current configuration $\varphi_t(\Omega^e)$ of the element is then approximated by the matrix-vector product

$$\boldsymbol{\nabla}^{\mathrm{s}} \boldsymbol{\eta}_t |_{\varphi_t(\Omega^e)} \approx \boldsymbol{B}_{\mathrm{s}}^I \boldsymbol{\eta}_{tI} \stackrel{\mathrm{def}}{=} \boldsymbol{B}_{\mathrm{s}e}^{\mathrm{s}} \boldsymbol{\eta}_{te} \,, \tag{5.3.22}$$

in which $\boldsymbol{\eta}_{te} = \bigcup_{I=1}^{n_{\mathrm{nd}}} \boldsymbol{\eta}_{tI}$ by (5.3.15), and $\boldsymbol{B}_{\mathrm{s}}^I$ is called the *matrix of symmetrized derivatives of interpolation function* N^I. The order of the rows of $\boldsymbol{B}_{\mathrm{s}}^I$ must be compatible with the order of the rows of the column-matrix $\boldsymbol{\sigma}$, so that $(\boldsymbol{\sigma} : \boldsymbol{\nabla}^{\mathrm{s}} \boldsymbol{\eta}_t)|_{\varphi_t(\Omega^e)} = (\boldsymbol{B}_{\mathrm{s}}^I \boldsymbol{\eta}_{tI})^{\mathrm{T}} \boldsymbol{\sigma}$.

The assembly of the integrals in (5.3.16) over all elements, which is represented in (5.3.17) to (5.3.20) by scattering the element matrices into global matrices, is achieved by boolean *assembly matrices* defined for each element. These matrices extract the vector of a certain element (index "e") from the corresponding global vector (index "g"). Details are available in the cited FEM textbooks [e.g. Belytschko et al., 2000, sec. 2.5].

Substitution of (5.3.17) to (5.3.20) into (5.3.16), and dropping the index "g" for notational brevity, results in the *isoparametric semi-discrete updated Lagrangian weak form of balance of momentum*

$$\boldsymbol{\eta}_t^{\mathrm{T}} \left(\boldsymbol{M}\dot{\boldsymbol{v}} + \boldsymbol{f}^{\mathrm{int}} - \boldsymbol{f}^{\mathrm{ext}} \right) = \boldsymbol{0} \,. \tag{5.3.23}$$

Finally, as this equation must hold for arbitrary virtual velocities, one can make the following concluding definition.

Definition 5.3.24. The *isoparametric semi-discrete version of the weak form 5.2.6 of the IBVP 5.1.1 without contact constraints* is the problem of finding the velocity field $\boldsymbol{v}$, the stress field $\boldsymbol{\sigma}$, the mass density ρ, and the internal state variables $\boldsymbol{\alpha}$ such that conservation of mass and balance of momentum

$$\boldsymbol{M}\dot{\boldsymbol{v}} + \boldsymbol{f}^{\mathrm{int}} - \boldsymbol{f}^{\mathrm{ext}} = \boldsymbol{0}$$

hold in consideration of prescribed boundary and initial conditions. ◊

5.4 Temporal Discretization and Solution

The following section provides a rough introduction of the standard finite element procedures to advance the semi-discrete weak form of the generic mechanical initial boundary value problem without contact constraints (Definition 5.3.24) in time. These numerical procedures achieve *temporal discretization* of the governing equations. The focus is on implicit integration, as it generally is better suited for the quasi-static processes considered here. A required step in the derivation of implicit methods is the *linearization* of the equations, which is briefly addressed. More elaborated and comprehensive descriptions can be found in the textbooks about nonlinear finite element methods [Bathe, 1996; Belytschko et al., 2000; Wriggers, 2008; Zienkiewicz and Taylor, 2000a,b].

The weak form of the IBVP stated in Definition 5.2.6 and its semi-discrete counterpart 5.3.24 are highly nonlinear in the presence of large material deformations and path-dependent material behavior. Therefore, numerical analysis generally requires a step-by-step solution of incrementally linear problems. Let $[0, T]$ be the continuous time interval of interest, then a partition

$$[0, T] \overset{\mathrm{def}}{=} \bigcup_{n=0}^{N-1} [t_n, t_{n+1}] \tag{5.4.1}$$

motivates a sequence $(t_0 = 0, t_1 = t_0 + \Delta t_1, \ldots, t_{n+1} = t_n + \Delta t_{n+1}, \ldots, t_N = T)$. Therein, the additive split

$$t_{n+1} = t_n + \Delta t_{n+1} \tag{5.4.2}$$

is called an *incremental decomposition of time*, where $\Delta t_{n+1} \overset{\text{def}}{=} t_{n+1} - t_n$ is called the *time increment* associated with the sequence. The time increment is often regarded constant, so that $\Delta t_{n+1} \overset{\text{def}}{=} \Delta t$, and $t_{n+1} = (n+1)\Delta t$ for $t_0 = 0$.

5.4.1 Linearized Form of Weak Balance of Momentum

The traditional but inconsistent approach to obtain the linearized form of weak balance of momentum uses the associated rate form in conjunction with an artificial time increment. This approach, which is also implemented here, remains widely used in finite element codes (e.g. ANSYS®, ABAQUS®). A critical assessment is given by Nagtegaal [1982], and Simo and Hughes [1998, section 7.2.3]. According to these references, the use of the rate formulation will in fact lead to an *inconsistently linearized* weak balance of momentum. From a numerical viewpoint, this puts unnecessary constraints on the step size, and destroys the quadratic rate of asymptotic convergence of Newton's method in implicit integration methods.

In determining an expression for the rate form of the weak form of balance of momentum resp. of the principle of virtual power (5.2.5), denoted by $\dot{P}(\boldsymbol{v}_t, \boldsymbol{\sigma}_t, \boldsymbol{\alpha}_t, \rho_t; \boldsymbol{\eta}_t)$, it is assumed that the loads are deformation-independent. That is to say, loads are *dead loads* depending only on the material particle $X \in \mathcal{B}$ in the reference configuration. Consequently, the $\dot{P}$-terms involving these quantities vanish, so

$$\dot{P} = \frac{\mathrm{d}}{\mathrm{d}t} \int_{\varphi_t(\mathcal{B})} \boldsymbol{\sigma}_t : \boldsymbol{\nabla}^{\mathrm{s}} \boldsymbol{\eta}_t \, \mathrm{d}\boldsymbol{v} \,. \tag{5.4.3}$$

Equivalent formulations of the rate of weak balance of momentum have been derived e.g. by Hill [1959] and McMeeking and Rice [1975]; see also [Simo and Hughes, 1998, sec. 7.2.3]. The particular form of $\dot{P}$ proposed next is connected with Nagtegaal and Veldpaus [1984], who also provide a full proof.

Proposition 5.4.4. *Let the external loads be deformation-independent, then the rate form of the weak balance of momentum (5.2.5) reads*

$$\dot{P} = \int_{\varphi_t(\mathcal{B})} \left((\mathring{\boldsymbol{\sigma}}_t^{\mathrm{ZJ}} - 2\boldsymbol{d}_t \cdot \boldsymbol{\sigma}_t + \boldsymbol{\sigma}_t \operatorname{tr} \boldsymbol{d}_t) : \boldsymbol{\nabla}^{\mathrm{s}} \boldsymbol{\eta}_t + \boldsymbol{\sigma}_t : \boldsymbol{l}_t \cdot (\boldsymbol{\nabla} \boldsymbol{\eta}_t)^{\mathrm{T}} \right) \mathrm{d}\boldsymbol{v} \,.$$

The term that stems from the change of volume, $(\operatorname{tr} \boldsymbol{d}_t)\, \boldsymbol{\sigma}_t : \boldsymbol{\nabla}^{\mathrm{s}} \boldsymbol{\eta}_t$, will lead to a non-symmetric finite element stiffness matrix. It is usually neglected by assuming that the volume changes will be negligible for large strain conditions [Nagtegaal and Veldpaus, 1984; Cheng and Tsui, 1992; ANSYS, 2007a]. If, in addition, the rate constitutive equation can be written in the form $\mathring{\boldsymbol{\sigma}}^{\mathrm{ZJ}} = \boldsymbol{m} : \boldsymbol{d}$, where $\boldsymbol{m}$ is a material tangent tensor, then

$$\dot{P} = \int_{\varphi_t(\mathcal{B})} (\boldsymbol{\nabla}^{\mathrm{s}} \boldsymbol{\eta}_t : \boldsymbol{m}_t : \boldsymbol{d}_t + \boldsymbol{\sigma}_t : (\boldsymbol{\nabla} \boldsymbol{\eta}_t \cdot \boldsymbol{l}_t - 2\, \boldsymbol{\nabla}^{\mathrm{s}} \boldsymbol{\eta}_t \cdot \boldsymbol{d}_t)) \, \mathrm{d}\boldsymbol{v} \,. \tag{5.4.5}$$

This form is in agreement with Eq. (3-99) of the ANSYS® theory reference [ANSYS, 2007a], and it will be used later on.

Now, consider an incremental decomposition of time (5.4.2) with constant time increment, viz. $t_{n+1} = t_n + \Delta t$. Concerning the weak form of the mechanical IBVP, 5.2.6, it is assumed that the configuration $\varphi_n(\mathcal{B}) \stackrel{\text{def}}{=} \varphi(\mathcal{B}, t_n)$ is given data, as well as the spatial velocity $\boldsymbol{v}_n$, the Cauchy stress $\boldsymbol{\sigma}_n$, the material state variables $\boldsymbol{\alpha}_n \stackrel{\text{def}}{=} \{\alpha_1, \ldots, \alpha_k\}_n$, and the spatial mass density ρ_n associated with that configuration. Moreover, the material body $\mathcal{B}$ is assumed to be in a state of equilibrium at time $t = t_n$ such that the weak balance of momentum (5.2.5) holds for all admissible spatial variations of φ_n, i.e.

$$P(\varphi_n) = 0\,, \quad \text{for all } \boldsymbol{\eta}_n \in \mathcal{V}_n\,, \tag{5.4.6}$$

Here $P(\varphi_n) \stackrel{\text{def}}{=} P(\boldsymbol{v}_n, \boldsymbol{\sigma}_n, \boldsymbol{\alpha}_n, \rho_n; \boldsymbol{\eta}_n)$ has been introduced in order to shorten notation, and $\mathcal{V}_n$ is the space of admissible spatial variations of φ_n according to 5.2.1. The linearization of $P(\varphi_{n+1}) = 0$ about φ_n is then defined *conceptually* through

$$P(\varphi_{n+1}) = 0 \qquad \Leftrightarrow \qquad P(\varphi_n) + \Delta P(\varphi_n) \stackrel{\text{def}}{=} P(\varphi_n) + \dot{P}(\varphi_n)\,\Delta t = 0\,. \tag{5.4.7}$$

By noting that the actual spatial velocity field at fixed time t_n, $\boldsymbol{v}_n : \varphi_n(\mathcal{B}) \to T\mathcal{S}$, is an admissible spatial variation [Simo and Hughes, 1998, section 7.2.3], let

$$\boldsymbol{u}_n = \boldsymbol{U}_n \circ \varphi_n^{-1} \stackrel{\text{def}}{=} \boldsymbol{v}_n\,\Delta t \qquad \in \mathcal{V}_n \tag{5.4.8}$$

be the *incremental spatial displacement field* imposed on $\varphi_n(\mathcal{B})$. Define the *displacement gradient* through $\boldsymbol{\nabla}\boldsymbol{u}_n \stackrel{\text{def}}{=} \boldsymbol{\nabla}\boldsymbol{v}_n\,\Delta t = \boldsymbol{l}_n\,\Delta t$. Its symmetric part,

$$\boldsymbol{\nabla}^{\mathrm{s}}\boldsymbol{u}_n = \tfrac{1}{2}(\boldsymbol{\nabla}\boldsymbol{u}_n + (\boldsymbol{\nabla}\boldsymbol{u}_n)^{\mathrm{T}}) \stackrel{\text{def}}{=} \boldsymbol{d}_n\,\Delta t\,, \tag{5.4.9}$$

is referred to as the *strain increment*. These quantities are substituted into $\Delta P(\varphi_n) = \dot{P}(\varphi_n)\,\Delta t$, in which $\dot{P}$ is given by (5.4.5). In this way the (conceptual) linearization of the weak form of balance of momentum (5.2.5) about the state at time t_n is obtained:

$$P(\varphi_n) + \Delta P(\varphi_n) = 0\,, \quad \text{for all } \boldsymbol{\eta}_n \in \mathcal{V}_n\,, \tag{5.4.10}$$

where

$$\Delta P(\varphi_n) = \int_{\varphi_n(\mathcal{B})} (\boldsymbol{\nabla}^{\mathrm{s}}\boldsymbol{\eta}_n : \boldsymbol{m}_n : \boldsymbol{\nabla}^{\mathrm{s}}\boldsymbol{u}_n + \boldsymbol{\sigma}_n : (\boldsymbol{\nabla}\boldsymbol{\eta}_n \cdot \boldsymbol{\nabla}\boldsymbol{u}_n - 2\,\boldsymbol{\nabla}^{\mathrm{s}}\boldsymbol{\eta}_n \cdot \boldsymbol{\nabla}^{\mathrm{s}}\boldsymbol{u}_n))\,\mathbf{d}\boldsymbol{v}\,. \tag{5.4.11}$$

The first term of the integrand contributes to the *material stiffness*, while the other two terms are related to the *geometric stiffness* or *stress stiffness*. The product $\boldsymbol{m}_n : \boldsymbol{\nabla}^{\mathrm{s}}\boldsymbol{u}_n \stackrel{\text{def}}{=} \Delta\boldsymbol{\sigma}_n^{\mathrm{ZJ}}$ represents the *Zaremba-Jaumann stress increment*.

The semi-discrete weak form of $P(\varphi_n) = 0$ in the Euclidian point space $\mathcal{S} = \mathbb{R}^m$ is (5.3.23) taken with respect to time $t = t_n \in [0, T]$. By assumption, the external loads $\boldsymbol{f}_n^{\text{ext}}$ are deformation-independent, and the mass matrix $\boldsymbol{M}$ is constant. In order to obtain the semi-discrete form of ΔP given by (5.4.11), one proceeds as in Section 5.3. Within the isoparametric finite element concept, the displacement increment $\boldsymbol{u}$ and the

virtual velocity $\boldsymbol{\eta}_t$ on an element are approximated by using the same interpolation functions N^I. Hence,

$$\boldsymbol{u}(\xi,t) \approx N^I(\xi)\,\boldsymbol{u}_I(t) \qquad \text{resp.} \qquad u^b_z(\xi,t) \approx N^I(\xi)\,u^b_{zI}(t)\,. \tag{5.4.12}$$

For the approximation of the material stiffness term in (5.4.11), $\boldsymbol{\nabla}^{\mathrm{s}}\boldsymbol{\eta}_n : \boldsymbol{m}_n : \boldsymbol{\nabla}^{\mathrm{s}}\boldsymbol{u}_n$, it is assumed that the components of the Cauchy stress as well as of the stress increment are arranged in a column-matrix by using Voigt's notation (5.3.21). Voigt's notation is also applied to the strain increment $\boldsymbol{\nabla}^{\mathrm{s}}\boldsymbol{u}_n$. The incremental form of the rate constitutive equation $\mathring{\boldsymbol{\sigma}}^{\mathrm{ZJ}} = \boldsymbol{m} : \boldsymbol{d}$ is then represented by the matrix equation $\Delta\boldsymbol{\sigma}^{\mathrm{ZJ}}_n = \boldsymbol{m}_n(\boldsymbol{\nabla}^{\mathrm{s}}\boldsymbol{u}_n)$, where the same symbols have been used to denote the component matrices of the tensors $\Delta\boldsymbol{\sigma}^{\mathrm{ZJ}}_n$, $\boldsymbol{m}_n$, and $\boldsymbol{\nabla}^{\mathrm{s}}\boldsymbol{u}_n$. In three-dimensional space, $\Delta\boldsymbol{\sigma}^{\mathrm{ZJ}}_n, \boldsymbol{\nabla}^{\mathrm{s}}\boldsymbol{u}_n \in \mathbb{R}^6$ are column-matrices with six components, and $\boldsymbol{m}_n \in \mathbb{R}^{6\times 6}$ is a (6×6)-matrix.

The approximations of $\boldsymbol{\nabla}^{\mathrm{s}}\boldsymbol{\eta}_n$ and $\boldsymbol{\nabla}^{\mathrm{s}}\boldsymbol{u}_n$ within the material stiffness term in (5.4.11) are given by the readily defined matrix-vector product (5.3.22), e.g. $\boldsymbol{\nabla}^{\mathrm{s}}\boldsymbol{\eta}_t|_{\varphi_t(\Omega^e)} \approx \boldsymbol{B}^I_{\mathrm{s}}\boldsymbol{\eta}_{tI}$. The direct consequence of the isoparametric concept is that the approximation of $\boldsymbol{\nabla}^{\mathrm{s}}\boldsymbol{u}$ uses the same matrix $\boldsymbol{B}^I_{\mathrm{s}}$ of the derivatives of the N^I as $\boldsymbol{\nabla}^{\mathrm{s}}\boldsymbol{\eta}_t$ does. The components of $\boldsymbol{\nabla}^{\mathrm{s}}\boldsymbol{\eta}_t$ and $\boldsymbol{\nabla}^{\mathrm{s}}\boldsymbol{u}$ with respect to the spatial Cartesian coordinates z^b and time $t = t_n$ can be determined from (5.3.13). The matrix format of the approximation of the geometric stiffness terms in (5.4.11) is prepared most conveniently in the spatial Cartesian coordinate system z^b.

Without going into to much detail, it turns out that, by using the definitions and relations of Sections 5.3.1, the spatial discretization of the increment (5.4.11) of the weak balance of momentum can be written in the form

$$\begin{aligned}
\Delta P &\approx \bigcup_{e=1}^{n_{\mathrm{el}}} \int_{\varphi_n(\Omega^e)} (\boldsymbol{\nabla}^{\mathrm{s}}\boldsymbol{\eta}_n : \boldsymbol{m}_n : \boldsymbol{\nabla}^{\mathrm{s}}\boldsymbol{u}_n + \boldsymbol{\sigma}_n : (\boldsymbol{\nabla}\boldsymbol{\eta}_n \cdot \boldsymbol{\nabla}\boldsymbol{u}_n - 2\,\boldsymbol{\nabla}^{\mathrm{s}}\boldsymbol{\eta}_n \cdot \boldsymbol{\nabla}^{\mathrm{s}}\boldsymbol{u}_n))\,\mathrm{d}\boldsymbol{v} \\
&\approx \bigcup_{e=1}^{n_{\mathrm{el}}} (\boldsymbol{\eta}_I)^{\mathrm{T}}_n \left(\boldsymbol{K}^{IJ}_{\mathrm{mat}} + \boldsymbol{K}^{IJ}_{\mathrm{geo}}\right)_n (\boldsymbol{u}_J)_n \stackrel{\mathrm{def}}{=} \bigcup_{e=1}^{n_{\mathrm{el}}} (\boldsymbol{\eta}_e)^{\mathrm{T}}_n \left(\boldsymbol{K}^{\mathrm{mat}}_e + \boldsymbol{K}^{\mathrm{geo}}_e\right)_n (\boldsymbol{u}_e)_n \\
&\stackrel{\mathrm{def}}{=} \bigcup_{e=1}^{n_{\mathrm{el}}} (\boldsymbol{\eta}_e)^{\mathrm{T}}_n (\boldsymbol{K}_e)_n (\boldsymbol{u}_e)_n = \boldsymbol{\eta}^{\mathrm{T}}_n \boldsymbol{K}_n \boldsymbol{u}_n\ ,
\end{aligned} \tag{5.4.13}$$

in which

$$\begin{aligned}
(\boldsymbol{K}^{IJ}_{\mathrm{mat}})_n &\stackrel{\mathrm{def}}{=} \int_{\Omega^e_\square} B^I_{\mathrm{s}\,db}\, m^{bc}_n\, B^J_{\mathrm{s}\,ca}\, J_\theta\,\mathrm{d}\square = \int_{\Omega^e_\square} (\boldsymbol{B}^I_{\mathrm{s}})^{\mathrm{T}}\boldsymbol{m}_n\boldsymbol{B}^J_{\mathrm{s}}\,J_\theta\,\mathrm{d}\square\,, \qquad \text{and} \\
(\boldsymbol{K}^{IJ}_{\mathrm{geo}})_n &\stackrel{\mathrm{def}}{=} \int_{\Omega^e_\square} \left(\frac{\partial N^I}{\partial z^a}\sigma^{ac}_n \frac{\partial N^J}{\partial z^c}\delta_{bd} - 2\delta_{pq}\frac{\partial N^I}{\partial z^k}\mathsf{1}_{ba}{}^{pk}\,\sigma^{ac}_n\,\mathsf{1}_{dc}{}^{qr}\frac{\partial N^J}{\partial z^r}\right) J_\theta\,\mathrm{d}\square\,.
\end{aligned}$$

Herein, all components are taken with respect to the spatial Cartesian coordinates z^b. m^{bc}_n are the components of the material tangent matrix $\boldsymbol{m}_n$, σ^{ac}_n are the stress components at time t_n, and $\mathsf{1}_{ab}{}^{cd} \stackrel{\mathrm{def}}{=} \frac{1}{2}\left(\delta_a{}^c\,\delta_b{}^d + \delta_a{}^d\,\delta_b{}^c\right)$ are the components of the symmetrizer defined by (A.5.11). Moreover, $\boldsymbol{K}^{\mathrm{mat}}_e$ and $\boldsymbol{K}^{\mathrm{geo}}_e$ are called the *material* and *geometric element stiffness matrix*, and $\boldsymbol{K}_n$ is the *global stiffness matrix* at time $t = t_n$. The index g, which indicates global quantities in the matrix representation, has been omitted.

The semi-discrete version of (5.4.10), representing the linearized weak form of balance of momentum (5.2.5) about the state at time t_n in accordance with (5.4.7), can now be cast in the form

$$\boldsymbol{\eta}_n^{\mathrm{T}} \left(\boldsymbol{K}_n \boldsymbol{u}_n + \boldsymbol{M} \dot{\boldsymbol{v}}_n + \boldsymbol{f}_n^{\mathrm{int}} - \boldsymbol{f}_n^{\mathrm{ext}} \right) = \boldsymbol{0} \,. \tag{5.4.14}$$

This must hold for arbitrary $\boldsymbol{\eta}_n^{\mathrm{T}}$, hence

$$\boldsymbol{K}_n \boldsymbol{u}_n + \boldsymbol{M} \dot{\boldsymbol{v}}_n + \boldsymbol{f}_n^{\mathrm{int}} - \boldsymbol{f}_n^{\mathrm{ext}} = \boldsymbol{0} \,. \tag{5.4.15}$$

Remark 5.4.16. The notion of *consistent linearization*, as opposed to the employed traditional approach in terms of a rate form and an artificial time increment, has been introduced by Hughes and Pister [1978]. It requires the linearization of a quantity to be defined in terms of the directional derivative at a given point, which represents the best linear approximation of the function near that point. In a flat background space, the directional derivative is represented by the Gâteaux derivative (Definition A.2.4). Applications within the context of continuum mechanics and computational mechanics can be found in [Hughes and Pister, 1978; Simo and Taylor, 1985; Simo and Hughes, 1998; Wriggers, 2008]. However, in order to achieve an intrinsically geometric formalism of linearization which is valid on Riemannian manifolds and referred to as *covariant linearization*, the directional derivative must be represented by the covariant derivative [Marsden and Hughes, 1994; Simo, 1992; Yavari and Ozakin, 2008]. △

5.4.2 Implicit Time Integration of Finite Element Equations

Assuming that a state of equilibrium has been determined for time t_n, the time integration procedure has to determine the state at time $t_{n+1} = t_n + \Delta t$ by solving 5.3.24 as an initial value problem. In ANSYS® (Release 11.0 SP1) [cf. ANSYS, 2007a], the background code employed in the present work, the *Newmark-β method* is used in conjunction with Newton's method to advance the solution implicitly in time. This common method provides the following time integration rules of a quantity $\boldsymbol{y}$ and its first derivative $\dot{\boldsymbol{y}}$:

$$\begin{aligned} \dot{\boldsymbol{y}}_{n+1} &\overset{\mathrm{def}}{=} \dot{\boldsymbol{y}}_n + \Delta t \left((1-\gamma)\, \ddot{\boldsymbol{y}}_n + \gamma\, \ddot{\boldsymbol{y}}_{n+1} \right) , \qquad \text{and} \\ \boldsymbol{y}_{n+1} &\overset{\mathrm{def}}{=} \boldsymbol{y}_n + \Delta t\, \dot{\boldsymbol{y}}_n + \tfrac{1}{2} \Delta t^2 \left((1-2\beta)\, \ddot{\boldsymbol{y}}_n + 2\beta\, \ddot{\boldsymbol{y}}_{n+1} \right) . \end{aligned} \tag{5.4.17}$$

γ, β are the *Newmark parameters*, which determine the behavior of the integration method. The method is unconditionally stable for [Belytschko et al., 2000, p. 318]

$$\beta \geq \frac{\gamma}{2} \geq \frac{1}{4} \,. \tag{5.4.18}$$

If these conditions hold, there is no restriction of the time integrator on the size of the time step Δt.

To get 5.3.24 solved in time, it is assumed that the first unknown determined in every time step is the nodal displacement vector $\boldsymbol{u}_{n+1}$. Using (5.4.17) and defining

$$\begin{aligned} a_0 &\stackrel{\text{def}}{=} \frac{1}{\beta\Delta t^2}\,, \qquad a_1 \stackrel{\text{def}}{=} \frac{\gamma}{\beta\Delta t}\,, \qquad a_2 \stackrel{\text{def}}{=} \frac{1}{\beta\Delta t}\,, \qquad a_3 \stackrel{\text{def}}{=} \frac{1}{2\beta} - 1\,, \\ a_4 &\stackrel{\text{def}}{=} \frac{\gamma}{\beta} - 1\,, \qquad \text{and} \qquad a_5 \stackrel{\text{def}}{=} \frac{\Delta t}{2}\left(\frac{\gamma}{\beta} - 2\right)\,, \end{aligned} \tag{5.4.19}$$

then the nodal accelerations and velocities can be expressed by

$$\dot{\boldsymbol{v}}_{n+1} = \dot{\boldsymbol{v}}^*_{n+1} + a_0\boldsymbol{u}_{n+1} \qquad \text{and} \qquad \boldsymbol{v}_{n+1} = \boldsymbol{v}^*_{n+1} + a_1\boldsymbol{u}_{n+1}\,, \tag{5.4.20}$$

respectively, where

$$\dot{\boldsymbol{v}}^*_{n+1} \stackrel{\text{def}}{=} -a_0\boldsymbol{u}_n - a_2\boldsymbol{v}_n - a_3\dot{\boldsymbol{v}}_n \qquad \text{and} \qquad \boldsymbol{v}^*_{n+1} \stackrel{\text{def}}{=} -a_1\boldsymbol{u}_n - a_4\boldsymbol{v}_n - a_5\dot{\boldsymbol{v}}_n\,. \tag{5.4.21}$$

Both $\dot{\boldsymbol{v}}^*_{n+1}$ and $\boldsymbol{v}^*_{n+1}$ involve only known values. $\boldsymbol{u}_{n+1}$ is the only unknown. Therefore, the semi-discrete weak balance of momentum of the IBVP 5.3.24 at time t_{n+1} can be stated as the homogeneous system of nonlinear algebraic equations

$$\boldsymbol{\Psi}_{n+1} \stackrel{\text{def}}{=} \boldsymbol{\Psi}(\boldsymbol{u}_{n+1}) = \boldsymbol{M}\dot{\boldsymbol{v}}(\boldsymbol{u}_{n+1}) + \boldsymbol{C}\boldsymbol{v}(\boldsymbol{u}_{n+1}) + \boldsymbol{f}^{\text{int}}(\boldsymbol{u}_{n+1}) - \boldsymbol{f}^{\text{ext}}(\boldsymbol{u}_{n+1}) = \boldsymbol{0}\,, \tag{5.4.22}$$

in which $\dot{\boldsymbol{v}}(\boldsymbol{u}_{n+1}) \stackrel{\text{def}}{=} \dot{\boldsymbol{v}}_{n+1}$, $\boldsymbol{v}(\boldsymbol{u}_{n+1}) \stackrel{\text{def}}{=} \boldsymbol{v}_{n+1}$, $\boldsymbol{f}^{\text{int}}(\boldsymbol{u}_{n+1}) \stackrel{\text{def}}{=} \boldsymbol{f}^{\text{int}}_{n+1}$, and $\boldsymbol{f}^{\text{ext}}(\boldsymbol{u}_{n+1}) \stackrel{\text{def}}{=} \boldsymbol{f}^{\text{ext}}_{n+1}$. Substitution of (5.4.20) yields

$$\begin{aligned} \boldsymbol{\Psi}_{n+1} &= \boldsymbol{0} \\ &= a_0\boldsymbol{M}\boldsymbol{u}_{n+1} + a_1\boldsymbol{C}\boldsymbol{u}_{n+1} + \boldsymbol{f}^{\text{int}}(\boldsymbol{u}_{n+1}) - \boldsymbol{f}^{\text{ext}}(\boldsymbol{u}_{n+1}) \\ &\quad - \boldsymbol{M}(a_0\boldsymbol{u}_n + a_2\boldsymbol{v}_n + a_3\dot{\boldsymbol{v}}_n) - \boldsymbol{C}(a_1\boldsymbol{u}_n + a_4\boldsymbol{v}_n + a_5\dot{\boldsymbol{v}}_n)\,. \end{aligned} \tag{5.4.23}$$

For reasons of generality, a constant *global damping matrix* $\boldsymbol{C}$ has been included in the previous equations. If $\boldsymbol{C} = \boldsymbol{0}$, then damping is assumed to reside entirely in dissipative material behavior.

Newton's method, (A.3.10), is applied to (5.4.23) for iteration of the solution $\boldsymbol{u}_{n+1}$. Let $\boldsymbol{u}^i_{n+1}$ be the known solution at the i-th iteration, with $\boldsymbol{u}^{i=0}_{n+1} = \boldsymbol{u}_n$, then linearization about $\boldsymbol{u}^i_{n+1}$ results in

$$\boldsymbol{\Psi}^{i+1}_{n+1} \stackrel{\text{def}}{=} \boldsymbol{\Psi}(\boldsymbol{u}^{i+1}_{n+1}) \approx \boldsymbol{\Psi}(\boldsymbol{u}^i_{n+1}) + D\boldsymbol{\Psi}(\boldsymbol{u}^i_{n+1}) \cdot d\boldsymbol{u}^i_{n+1} = \boldsymbol{0}\,, \tag{5.4.24}$$

where

$$\boldsymbol{u}^{i+1}_{n+1} \stackrel{\text{def}}{=} \boldsymbol{u}^i_{n+1} + d\boldsymbol{u}^i_{n+1} = \boldsymbol{u}_n + \Delta\boldsymbol{u}^i_{n+1}\,, \qquad \text{and} \qquad \Delta\boldsymbol{u}^i_{n+1} \stackrel{\text{def}}{=} \sum_{k=0}^{i} d\boldsymbol{u}^k_{n+1}\,. \tag{5.4.25}$$

In updated Lagrangian FE methods one usually has $\boldsymbol{u}_n = \boldsymbol{0}$.

Remark 5.4.26. The *accumulated displacement increment* $\Delta\boldsymbol{u}^i_{n+1}$ in (5.4.25) starts form the converged solution at time t_n and is used to form the strain increment for stress integration in path-dependent materials; see Section 5.5. The *solution increment* $d\boldsymbol{u}^i_{n+1}$ must not be used for the stress update because it is taken with respect to a non-converged solution [see also Zienkiewicz and Taylor, 2000b, p. 56]. △

Assuming that the loads included in $\boldsymbol{f}^{\text{ext}}$ are deformation-independent, then (5.4.23) gives

$$D\boldsymbol{\Psi}^i_{n+1} = \frac{\partial \boldsymbol{\Psi}^i_{n+1}}{\partial \boldsymbol{u}^i_{n+1}} = a_0\boldsymbol{M} + a_1\boldsymbol{C} + \boldsymbol{K}^i_{n+1} \stackrel{\text{def}}{=} \hat{\boldsymbol{K}}^i_{n+1}\,, \tag{5.4.27}$$

in which $\hat{\boldsymbol{K}}^i_{n+1}$ is called the *effective stiffness matrix*, and $\boldsymbol{K}^i_{n+1} \stackrel{\text{def}}{=} D(\boldsymbol{f}^{\text{int}}(\boldsymbol{u}^i_{n+1})) = \frac{\partial(\boldsymbol{f}^{\text{int}}(\boldsymbol{u}^i_{n+1}))}{\partial \boldsymbol{u}^i_{n+1}}$ is the global stiffness matrix derived in (5.4.13), but which is now related to the i-th iteration of the solution at time t_{n+1}. By definition, $\boldsymbol{K}^{i=0}_{n+1} \stackrel{\text{def}}{=} \boldsymbol{K}_n$. Substitution of (5.4.23) and (5.4.27) into (5.4.24) finally yields

$$\hat{\boldsymbol{K}}^i_{n+1} d\boldsymbol{u}^i_{n+1} = \boldsymbol{r}^i_{n+1}\,, \tag{5.4.28}$$

where

$$\boldsymbol{r}^i_{n+1} \stackrel{\text{def}}{=} \hat{\boldsymbol{f}}^{\text{ext}}_{n+1} - (a_0\boldsymbol{M}\boldsymbol{u}^i_{n+1} + a_1\boldsymbol{C}\boldsymbol{u}^i_{n+1} + \boldsymbol{f}^{\text{int}}(\boldsymbol{u}^i_{n+1}))\,, \tag{5.4.29}$$

is called the *vector of residuals*, and

$$\hat{\boldsymbol{f}}^{\text{ext}}_{n+1} \stackrel{\text{def}}{=} \boldsymbol{f}^{\text{ext}}_{n+1} + \boldsymbol{M}(a_0\boldsymbol{u}_n + a_2\boldsymbol{v}_n + a_3\dot{\boldsymbol{v}}_n) + \boldsymbol{C}(a_1\boldsymbol{u}_n + a_4\boldsymbol{v}_n + a_5\dot{\boldsymbol{v}}_n)\,, \tag{5.4.30}$$

is called the *effective load vector*.

Effects due to inertia and damping, except for static acceleration fields (e.g. gravitational acceleration), are ignored in quasi-static analysis. In this case, $\hat{\boldsymbol{K}}^i_{n+1} = \boldsymbol{K}^i_{n+1}$ in (5.4.28), and the vector of residuals and the effective load vector become

$$\boldsymbol{r}^i_{n+1} = \hat{\boldsymbol{f}}^{\text{ext}}_{n+1} - \boldsymbol{f}^{\text{int}}(\boldsymbol{u}^i_{n+1}) \qquad \text{and} \qquad \hat{\boldsymbol{f}}^{\text{ext}}_{n+1} = \boldsymbol{f}^{\text{ext}}_{n+1} - \boldsymbol{M}\bar{\boldsymbol{a}}\,, \tag{5.4.31}$$

respectively. $\bar{\boldsymbol{a}}$ is the *global applied external nodal acceleration vector*.

The cardinal dependent variables to solve (5.4.22) are the nodal displacements $\boldsymbol{u}_{n+1}$ and the Cauchy stresses $\boldsymbol{\sigma}_{n+1}$ at the integration points. The internal state variables $\boldsymbol{\alpha}$ are updated along with the stress update. By Definition 5.1.1 of the IBVP in the updated Lagrangian formulation, initial conditions must be given to the velocities, the Cauchy stress, and all internal state variables. When using the implicit time integration method initial conditions must be also given to the displacements. Initial acceleration can be specified by the user (e.g. to simulate gravity) or is computed in an extra load step at the beginning of the transient analysis [ANSYS, 2007a, sec. 17.2] according to

$$\dot{\boldsymbol{v}}(t_0) = \boldsymbol{M}^{-1}(\boldsymbol{f}_0 - \boldsymbol{C}\boldsymbol{v}_0)\,, \qquad \text{where} \quad \boldsymbol{f}_0 = \boldsymbol{f}^{\text{ext}}(\boldsymbol{u}_0) - \boldsymbol{f}^{\text{int}}(\boldsymbol{u}_0)\,. \tag{5.4.32}$$

In both transient and quasi-static analysis, (5.4.28) must be solved for the displacement increments $d\boldsymbol{u}^i_{n+1}$ in every iteration step to perform the displacement update (5.4.25). The updated displacements are employed to compute the inertia and damping terms in transient analysis, and to update velocities and accelerations according to (5.4.20). Geometry is updated if iteration has converged, and convergence is checked by a *convergence criterion*. Alg. 5.1 provides the pseudocode of the implicit time integration scheme [cf. Belytschko et al., 2000, box 6.3].

Algorithm 5.1: Implicit time integration of the finite element equations by the Newmark-β method in conjunction with Newton's method. Fully transient analysis.

Input: initial geometry $\boldsymbol{x}(t_0) = \boldsymbol{x}_0$, initial conditions $\boldsymbol{u}(t_0) = \boldsymbol{u}_0$, $\boldsymbol{v}(t_0) = \boldsymbol{v}_0$, $\boldsymbol{\sigma}(t_0) = \boldsymbol{\sigma}_0$, $\boldsymbol{\alpha}(t_0) = \boldsymbol{\alpha}_0$, $\rho(t_0) = \rho_{\text{ref}}$
Output: displacement $\boldsymbol{u}$, Cauchy stress $\boldsymbol{\sigma}$, and material state $\boldsymbol{\alpha}$

initialize $n = 0$, $t = t_0$, $\boldsymbol{M}$, $\boldsymbol{C}$, and $\boldsymbol{K}$;
compute initial load vector $\boldsymbol{f}_0 = \boldsymbol{f}^{\text{ext}}(\boldsymbol{u}_0) - \boldsymbol{f}^{\text{int}}(\boldsymbol{u}_0)$ and $\boldsymbol{C}\boldsymbol{v}_0$;
initial accelerations: $\dot{\boldsymbol{v}}(t_0) = \boldsymbol{M}^{-1}(\boldsymbol{f}_0 - \boldsymbol{C}\boldsymbol{v}_0)$;
while *time step* $n \leq n_{\max}$ *resp. time* $t_n \leq T$ **do**
  compute external load vector $\boldsymbol{f}^{\text{ext}}_{n+1}$ and effective load vector $\hat{\boldsymbol{f}}^{\text{ext}}_{n+1}$ (5.4.30);
  estimate $\boldsymbol{u}^0_{n+1} = \boldsymbol{u}_n$, and set $\Delta\boldsymbol{u}^0_n = \boldsymbol{0}$;
  while *Newton iteration step* $i \leq i_{\max}$ **do**
    compute $\boldsymbol{v}^i_{n+1}$ and $\dot{\boldsymbol{v}}^i_{n+1}$ according to (5.4.20);
    integrate constitutive equation (Section 5.5);
    compute $\boldsymbol{f}^{\text{int}}(\boldsymbol{u}^i_{n+1})$ and form vector of residuals $\boldsymbol{r}^i_{n+1}$ (5.4.29);
    compute effective stiffness matrix $\hat{\boldsymbol{K}}^i_{n+1}$ (5.4.27);
    modify $\hat{\boldsymbol{K}}^i_{n+1}$ for essential boundary conditions;
    solve linearized equations $d\boldsymbol{u}^i_{n+1} = (\hat{\boldsymbol{K}}^i_{n+1})^{-1}\boldsymbol{r}^i_{n+1}$;
    update $\boldsymbol{u}^{i+1}_{n+1} = \boldsymbol{u}_n + \Delta\boldsymbol{u}^i_{n+1}$, with $\Delta\boldsymbol{u}^i_{n+1} = \Delta\boldsymbol{u}^{i-1}_{n+1} + d\boldsymbol{u}^i_{n+1}$;
    if *convergence criterion met* **then**
      exit;
    $i \leftarrow i + 1$;
  geometry update by adding displacement increments: $\boldsymbol{x}_{n+1} = \boldsymbol{x}_n + \Delta\boldsymbol{u}_{n+1}$;
  check energy balance;
  $n \leftarrow n + 1$ (time update $t_n \leftarrow t_n + \Delta t$);

5.5 Integration of Rate Constitutive Equations

Solution of the finite element system of equations requires evaluation of the actual internal nodal forces $\boldsymbol{f}^{\text{int}}$ in every time step or iteration. By (5.3.20), the basic ingredient of $\boldsymbol{f}^{\text{int}}$ is the stress at the quadrature points of the finite elements. Hence, rate constitutive equations require suitable *stress integration methods* (or *stress point algorithms*) which are generally applicable to finite deformation problems. These will be introduced next. Comprehensive treatises are Simo and Hughes [1998] and the related chapters in textbooks about nonlinear finite element methods.

Rate constitutive equations, as outlined in Section 4.1.3, relate an objective rate of the Cauchy stress to the rate of deformation and a set of material state variables. In small-strain elasto-plasticity, the objective rate is the ordinary material time derivative, and the rate of the infinitesimal strain tensor represents rate of deformation. The problem of integration of the set of evolution equations for the stress and the material state

variables constitutes an *initial value problem* that can be solved either by *explicit schemes* or *implicit schemes*; see Section A.3 for the general statements.

Explicit stress integration methods are formulations using known quantities associated with the beginning of the time step, like the forward Euler scheme (A.3.3). The procedure is straightforward and the resulting equations are almost identical to the analytical set up. However, the simplicity of the implementation fronts the error accumulation during calculation, since generally no yield condition is enforced. Accuracy can be increased by partitioning the time increment into a number of substeps, and to perform automatic error control [Sloan, 1987; Sloan et al., 2001]. This is why explicit stress integration methods are often called *substepping algorithms*.

Implicit stress integration methods are also referred to as *return mapping algorithms* [Simo and Taylor, 1985; Ortiz and Simo, 1986]. These are based on quantities taken with respect to the end of the time step, like the backward Euler scheme (A.3.5). Operator-split procedures are preferred to solve the coupled system of nonlinear equations. From a geometric standpoint, the implicit stress update with operator-split projects an elastically estimated trial state onto the yield surface, in which the plastic multiplier serves as the projection magnitude. The yield condition is naturally enforced at the end of the time increment. Therefore, at the same increment size, implicit algorithms can be more accurate than explicit algorithms.

The rotational terms of the stress rate at finite deformation render the integration of rate constitutive equations expensive compared to the infinitesimal case. In this context, the restrictions related to the axiom of material frame indifference, 4.1.10, have led to the notion of incremental objectivity of the integration method over finite time steps [Hughes and Winget, 1980].

Definition 5.5.1. *Incremental objectivity* requires that if the motion $\varphi : \mathcal{B} \to \mathcal{S}$ of the material body over time increment $\Delta t = t_{n+1} - t_n$ is rigid, that is, if its tangent $T\varphi \overset{\text{def}}{=} \boldsymbol{Q}$ is proper orthogonal ($\det \boldsymbol{Q} = +1$), then the stress is exactly updated by

$$\boldsymbol{\sigma}_{n+1} = \boldsymbol{Q}_\star \boldsymbol{\sigma}_n = \boldsymbol{Q} \cdot \boldsymbol{\sigma}_n \cdot \boldsymbol{Q}^{\mathrm{T}}$$

without generation of spurious stresses. The same is required for tensor-valued material state variables, if any. ♢

Subsequent to the work of Hughes and Winget [1980], several authors have developed or improved incrementally objective algorithms, e.g. Pinsky et al. [1983], Rubinstein and Atluri [1983], Hughes [1984], Flanagan and Taylor [1987], Rashid [1993], and Simo and Hughes [1998]. One basic methodology in formulating objective integration methods is to adopt a *corotated representation*. Within this approach, the basic quantities and evolution equations are locally transformed to a rotating coordinate system that remains unaffected by superposed rigid body motions. Then, the rate constitutive equations is integrated in the corotated representation and finally transformed (rotated) back to the current spatial configuration. The main advantage of algorithms based on a corotated description is that the integration of the rate constitutive equation can be carried out by the same methods at both infinitesimal and finite deformations.

The remainder of this section outlines the integration of rate constitutive equations for finite deformation problems. The main concern is the numerical method designed in such a way that the axiom of material frame indifference is identically satisfied on a discrete level. It is assumed that the reader is somewhat familiar with explicit and implicit stress integration methods at infinitesimal deformation. A detailed description is omitted by referring to the cited literature, particularly [Simo and Hughes, 1998; Belytschko et al., 2000]. The remainder of this chapter is largely based on [Simo and Hughes, 1998, ch. 8] and [Hughes, 1984].

5.5.1 General Setup for Objective Integration

Let $\varphi : \mathcal{B} \times [0,T] \to \mathcal{S} = \mathbb{R}^{m_{\dim}}$ be the sufficiently differentiable motion of the body, and $\boldsymbol{v}(x,t)$ be the spatial velocity field of φ, defined for every $x = \varphi(X,t) \in \mathcal{S}$ and time $t \in [0,T]$, with $X \in \mathcal{B}$. The updated Lagrangian description defined in Section 5.1 is employed throughout. According to this description, equations are formulated in terms of spatial quantities, but these are taken with respect to the points of the reference configuration of the material body. For example, the Cauchy stress tensor $\boldsymbol{\sigma}(x,t)$, given at spatial points $x = \varphi(X,t) \in \mathcal{S}$ and time $t \in [0,T]$, is viewed as $\boldsymbol{\sigma}(\varphi(X,t),t)$.

Definition 5.5.2. The spatial rate of deformation tensor field $\boldsymbol{d} = \frac{1}{2}(\boldsymbol{\nabla v} + (\boldsymbol{\nabla v})^{\mathrm{T}})$ is introduced as an *objective measure of strain rate*, and the *spatial finite strain tensor field* $\boldsymbol{e}$ at $x = \varphi(X,t)$ and $t \in [0,T]$ is defined *conceptually* through

$$\boldsymbol{e}(x,t) \stackrel{\text{def}}{=} \boldsymbol{e}(x,0) + \int_0^t \boldsymbol{d}(x,\tau)\,\mathrm{d}\tau\,,$$

where $\boldsymbol{e}(x,0)$ is given. ◊

By discretization in time, the basic variables are incrementally decomposed. For example, $\boldsymbol{\sigma}_{n+1} \stackrel{\text{def}}{=} \boldsymbol{\sigma}_n + \Delta\boldsymbol{\sigma}$, in which $\boldsymbol{\sigma}_{n+1} \stackrel{\text{def}}{=} \boldsymbol{\sigma}(t_{n+1})$, $\boldsymbol{\sigma}_n \stackrel{\text{def}}{=} \boldsymbol{\sigma}(t_n)$, and $t_{n+1} = t_n + \Delta t \in [0,T]$, with $t_0 = 0$ and $\Delta t > 0$. The stress increment $\Delta\boldsymbol{\sigma}$ is assumed constant in the interval $[t_n, t_{n+1}]$. Similar holds for the internal state variables. The configuration of $\mathcal{B}$ at time $t_n \in [t_n, t_{n+1}]$, i.e. the set

$$\varphi(\mathcal{B}, t_n) = \varphi_n(\mathcal{B}) \stackrel{\text{def}}{=} \{x_n = \varphi_n(X) \,|\, X \in \mathcal{B}\}\,, \tag{5.5.3}$$

as well as the internal state of the material (i.e. stress and history variables) with respect to the *converged* solution at time t_n, are regarded as *given data*. The configuration $\varphi(\mathcal{B}, t_{n+1})$ is also assumed to be known.

Let the spatial velocity field be constant over the time increment Δt such that

$$\boldsymbol{u} \stackrel{\text{def}}{=} \boldsymbol{v}\Delta t : \quad \varphi_n(\mathcal{B}) \to T\mathcal{S} \tag{5.5.4}$$

is an *incremental spatial displacement field imposed on* $\varphi_n(\mathcal{B})$; so $\boldsymbol{u}$ is likewise constant over $[t_n, t_{n+1}]$. The incremental displacement is assumed to be given by the global time integration of the weak balance of momentum. In case of implicit global time

integration by Alg. 5.1, the incremental displacement field equals the accumulated displacement increment of the i-th iteration defined by (5.4.25), i.e. $\boldsymbol{u} \stackrel{\text{def}}{=} \Delta\boldsymbol{u}^i_{n+1}$. Due to this fact, the problem of integrating a rate constitutive equation is also called a *strain-driven* problem.

The overall accuracy of the objective integration method will be affected by the approximate evaluation of the *finite strain increment* constant in the interval $[t_n, t_{n+1}]$,

$$\Delta\boldsymbol{e}(x) \stackrel{\text{def}}{=} \int_{t_n}^{t_{n+1}} \boldsymbol{d}(x,t)\,\mathrm{d}t\,. \tag{5.5.5}$$

To achieve the objectives, define a *one-parameter family of configurations* by

$$\varphi_{n+\theta} \stackrel{\text{def}}{=} \theta\varphi_{n+1} + (1-\theta)\varphi_n\,, \qquad \text{with} \quad \theta \in [0,1]\,, \tag{5.5.6}$$

which linearly interpolates φ_n and φ_{n+1}. Conceptually, the *intermediate configuration* $\varphi_{n+\theta}$ is related to an intermediate time $t_{n+\theta} = \theta t_{n+1} + (1-\theta)t_n = t_n + \theta\Delta t$. According to (5.5.6), the deformation gradient of $\varphi_{n+\theta}$ is given by the relationship

$$\boldsymbol{F}_{n+\theta} = T\varphi_{n+\theta} = \theta\boldsymbol{F}_{n+1} + (1-\theta)\boldsymbol{F}_n\,, \qquad \text{with} \quad \theta \in [0,1]\,. \tag{5.5.7}$$

Due to the updated Lagrangian description chosen for the stress update procedures, a *spatial metric related to the configuration* $\varphi_{n+\theta}$ is defined through

$$\boldsymbol{g}_{n+\theta} \stackrel{\text{def}}{=} \boldsymbol{g} \circ \varphi_{n+\theta} \qquad \text{resp.} \qquad \boldsymbol{g}_{n+\theta}(X) \stackrel{\text{def}}{=} \boldsymbol{g}(\varphi(X, t_{n+\theta}))\,, \tag{5.5.8}$$

where $\boldsymbol{g} \in \mathfrak{T}^0_2(\mathcal{S})$ is the ordinary spatial metric. Hence, $\boldsymbol{g}_{n+\theta}$ implicitly depends on time $t_{n+\theta} \in [t_n, t_{+1}]$ through $\varphi_{n+\theta}$. It proves convenient to add the following definitions.

Definition 5.5.9. The *relative incremental deformation gradient* of the configuration $\varphi_{n+\theta}(\mathcal{B})$ with respect to the configuration $\varphi_n(\mathcal{B})$ is defined through

$$\boldsymbol{f}_{n+\theta} \stackrel{\text{def}}{=} \boldsymbol{F}_{n+\theta} \cdot \boldsymbol{F}_n^{-1}\,, \qquad \text{with} \quad \theta \in [0,1]\,,$$

where $\boldsymbol{F}_{n+\theta}$ is given by (5.5.7). The *relative incremental displacement gradient* is the tensor field $\boldsymbol{\nabla}_{n+\theta}\boldsymbol{u} \in \mathfrak{T}^1_1(\mathcal{S})$ which has the local representative

$$(\boldsymbol{\nabla}_{n+\theta}\boldsymbol{u})(x_{n+\theta}) \stackrel{\text{def}}{=} \left(\frac{\partial u^i(x_{n+\theta})}{\partial x^k_{n+\theta}} + u^j(x_{n+\theta})\,\gamma_j{}^i{}_k(x_{n+\theta})\right) \mathbf{d}x^k_{n+\theta} \otimes \frac{\boldsymbol{\partial}}{\boldsymbol{\partial} x^i_{n+\theta}}\,.$$

at $x_{n+\theta} \stackrel{\text{def}}{=} \varphi_{n+\theta}(X)$, where $u^i(x_{n+\theta}) \stackrel{\text{def}}{=} U^I(X)|_{X=\varphi^{-1}_{n+\theta}(x_{n+\theta})}$ are the *components of the incremental displacements referred to the configuration* $\varphi_{n+\theta}(\mathcal{B})$. ◇

By these definitions and the basic relationships of Section 3.1.1, the next results are obtained; see Simo and Hughes [1998, secs. 8.1 and 8.3] for full proofs with respect to Cartesian frames.

Proposition 5.5.10. *Let* $[t_n, t_{n+1}]$ *be an incremental time interval, where* $t_{n+1} = t_n + \Delta t$, *and let* $\theta \in [0,1]$. *Then,*

(i) the relative incremental deformation and displacement gradients are equivalent to

$$\boldsymbol{f}_{n+\theta} = \boldsymbol{I} + \theta \boldsymbol{\nabla}_n \boldsymbol{u} \qquad \textit{and} \qquad \boldsymbol{\nabla}_{n+\theta} \boldsymbol{u} = \boldsymbol{\nabla}_n \boldsymbol{u} \cdot \boldsymbol{f}_{n+\theta}^{-1} ,$$

respectively, where $\boldsymbol{\nabla}_n \boldsymbol{u}(x_n) = \partial \boldsymbol{u}(x_n)/\partial \boldsymbol{x}_n$ *in Cartesian coordinates,*

(ii) an objective approximation to the spatial rate of deformation in $[t_n, t_{n+1}]$ *is*

$$\boldsymbol{d}_{n+\theta} = \frac{1}{2\Delta t} \left(\boldsymbol{\nabla}_{n+\theta} \boldsymbol{u} + (\boldsymbol{\nabla}_{n+\theta} \boldsymbol{u})^{\mathrm{T}} + (1-2\theta)(\boldsymbol{\nabla}_{n+\theta} \boldsymbol{u})^{\mathrm{T}} \cdot \boldsymbol{\nabla}_{n+\theta} \boldsymbol{u} \right) ,$$

(iii) an algorithmic approximation to the vorticity in $[t_n, t_{n+1}]$ *is*

$$\boldsymbol{\omega}_{n+\theta} = \frac{1}{2\Delta t} \left(\boldsymbol{\nabla}_{n+\theta} \boldsymbol{u} - (\boldsymbol{\nabla}_{n+\theta} \boldsymbol{u})^{\mathrm{T}} \right) .$$

Definition 5.5.11. The *algorithmic finite strain increment* or *incremental finite strain tensor* is defined by the formula

$$\Delta \tilde{\boldsymbol{e}}_{n+\theta} \stackrel{\text{def}}{=} \boldsymbol{d}_{n+\theta} \Delta t ,$$

where $\boldsymbol{d}_{n+\theta}$ is given by Proposition 5.5.10(ii). Hence, $\Delta \tilde{\boldsymbol{e}}_{n+\theta}$ is likewise incrementally objective. ♢

Hughes [1984] shows that 5.5.11 is a first-order approximation to (5.5.5) for all θ. If $\theta = \frac{1}{2}$, then the approximation is second-order accurate. Moreover, for $\theta = \frac{1}{2}$ the approximation is linear in $\boldsymbol{u}$; cf. Proposition 5.5.10(ii). Therefore,

$$\Delta \tilde{\boldsymbol{e}}_{n+1/2} = \frac{1}{2} \left(\boldsymbol{\nabla}_{n+1/2} \boldsymbol{u} + (\boldsymbol{\nabla}_{n+1/2} \boldsymbol{u})^{\mathrm{T}} \right) \tag{5.5.12}$$

is the most attractive expression for the finite strain increment (5.5.5) from the standpoint of implementation. It is referred to as the *midpoint strain increment.*

5.5.2 Algorithms Based on a Corotated Description

The class of algorithms discussed in the following section are ideally suited for *corotational rate constitutive equations.* Within this class the constitutive response function has the value of a corotational stress rate, which include the Zaremba-Jaumann and Green-Naghdi stress rates as typical examples. Algorithms based on a corotated description go at least back to Nagtegaal and Veldpaus [1984] and Hughes [1984], and are used in several finite element codes, e.g. NIKE2D [Engelmann and Hallquist, 1991], and ANSYS®, from version 6.0 on [XANSYS Mailing List, 2004]. The algorithm of Hughes and Winget [1980], which is widely used in the finite element community (e.g. ABAQUS/Standard® and early versions of ANSYS®), does not fall into this category.

In Section 4.1.2, it has been shown that any corotational rate of a spatial second-order tensor field $\boldsymbol{t}$ defined by the spin $\boldsymbol{\Lambda} = \dot{\mathfrak{R}} \cdot \mathfrak{R}^{\mathrm{T}}$ is related to the material time derivative of the field by

$$\mathring{\boldsymbol{t}} = \mathfrak{R}_{\star}\overline{\dot{\mathfrak{R}^{\star}\boldsymbol{t}}} = \mathfrak{R} \cdot \dot{\mathfrak{T}} \cdot \mathfrak{R}^{\mathrm{T}} , \tag{5.5.13}$$

where $\mathfrak{T} \overset{\text{def}}{=} \mathfrak{R}^{\star}\boldsymbol{t} = \mathfrak{R}^{\mathrm{T}} \cdot \boldsymbol{t} \cdot \mathfrak{R}$. This fundamental property forms the theoretical basis for algorithms based on a corotated description. Boldface Fraktur majuscules are used for variables in the corotating $\mathfrak{R}$-system in what follows.

Definition 5.5.14. Let the rate constitutive equation take the form

$$\mathring{\boldsymbol{\sigma}} \overset{\text{def}}{=} \boldsymbol{m}(\boldsymbol{\sigma}, \boldsymbol{g}, \boldsymbol{\alpha}) : \boldsymbol{d} ,$$

where $\mathring{\boldsymbol{\sigma}}$ denotes any corotational rate of $\boldsymbol{\sigma}$ defined by the spin $\boldsymbol{\Lambda} = \dot{\mathfrak{R}} \cdot \mathfrak{R}^{\mathrm{T}}$, and the fourth-order tensor $\boldsymbol{m}$ represents the material tangent. Then, by employing the generalized midpoint rule (A.3.6), the Cauchy stress is *objectively updated* by the general integration algorithm

$$\boldsymbol{\sigma}_{n+1} \overset{\text{def}}{=} \mathfrak{R}_{n+1} \cdot (\mathfrak{S}_n + \Delta\mathfrak{S}_{n+\theta}) \cdot \mathfrak{R}_{n+1}^{\mathrm{T}} , \qquad \text{with} \quad \theta \in [0,1] ,$$

and

$$\begin{aligned}
\mathfrak{S}_n &\overset{\text{def}}{=} \mathfrak{R}_n^{\mathrm{T}} \cdot \boldsymbol{\sigma}_n \cdot \mathfrak{R}_n , \qquad \Delta\mathfrak{S}_{n+\theta} \overset{\text{def}}{=} \mathfrak{f}_{n+\theta}(\mathfrak{S}_{n+\theta}, \mathfrak{G}_{n+\theta}, \mathfrak{A}_{n+\theta}, \Delta\mathfrak{E}_{n+\theta}) , \\
\Delta\mathfrak{E}_{n+\varepsilon} &\overset{\text{def}}{=} \mathfrak{R}_{n+\varepsilon}^{\mathrm{T}} \cdot \Delta\tilde{\boldsymbol{e}}_{n+\varepsilon} \cdot \mathfrak{R}_{n+\varepsilon} , \text{ with } \varepsilon \in [0,1] , \qquad \mathfrak{S}_{n+\theta} \overset{\text{def}}{=} \mathfrak{R}_{n+\theta}^{\mathrm{T}} \cdot \boldsymbol{\sigma}_{n+\theta} \cdot \mathfrak{R}_{n+\theta} , \\
\mathfrak{G}_{n+\theta} &\overset{\text{def}}{=} \mathfrak{R}_{n+\theta}^{\mathrm{T}} \cdot \boldsymbol{g}_{n+\theta} \cdot \mathfrak{R}_{n+\theta} , \qquad \text{and} \qquad \mathfrak{A}_{n+\theta} \overset{\text{def}}{=} \mathfrak{R}_{n+\theta}^{\star}\boldsymbol{\alpha}_{n+\theta} .
\end{aligned}$$

$\mathfrak{f}_{n+\theta}$ is a response function for the stress increment whose particular form is governed by the constitutive equation and the actual integration algorithm. $\Delta\tilde{\boldsymbol{e}}_{n+\varepsilon}$, with $\varepsilon \in [0,1]$, is the algorithmic finite strain increment defined through 5.5.11 and regarded as given. Finally, $\mathfrak{R}_{n+\theta}^{\star}$ denotes the pullback by $\mathfrak{R}_{n+\theta}$, the rotation associated with the configuration at time $t_{n+\theta}$. The algorithm is incrementally objective provided that $\mathfrak{R}_n$, $\mathfrak{R}_{n+\theta}$, and $\mathfrak{R}_{n+1}$ are properly determined:

Case (i): $\boldsymbol{\Lambda} = \boldsymbol{\Omega}$, $\mathfrak{R} = \boldsymbol{R}$. The rate constitutive equation is formulated in terms of the Green-Naghdi stress rate, i.e. $\mathring{\boldsymbol{\sigma}} = \mathring{\boldsymbol{\sigma}}^{\mathrm{GN}}$. $\boldsymbol{R}$ is the rotation tensor in the polar decomposition of the deformation gradient, and $\boldsymbol{\Omega} = \dot{\boldsymbol{R}} \cdot \boldsymbol{R}^{\mathrm{T}}$.

Case (ii): $\boldsymbol{\Lambda} = \boldsymbol{\omega}$, $\mathfrak{R} \neq \boldsymbol{R}$. In this case the rate constitutive equation is formulated in terms of the Zaremba-Jaumann stress rate, i.e. $\mathring{\boldsymbol{\sigma}} = \mathring{\boldsymbol{\sigma}}^{\mathrm{ZJ}}$, and $\dot{\mathfrak{R}} = \boldsymbol{\omega} \cdot \mathfrak{R}$, by (4.1.13), has to be integrated. ◇

The stress update $\mathfrak{S}_n + \Delta\mathfrak{S}_{n+\theta} = \mathfrak{R}_{n+1}^{\mathrm{T}} \cdot \boldsymbol{\sigma}_{n+1} \cdot \mathfrak{R}_{n+1}$ is carried out with respect to material points in the unrotated configuration of the material body. The stress increment $\Delta\mathfrak{S}_{n+\theta}$ is calculated with respect to the unrotated $\varphi_{n+\theta}(\mathcal{B})$-configuration using the response function $\mathfrak{f}_{n+\theta}$. The response function depends on the choice of $\theta \in [0,1]$ and basically represent an explicit or implicit stress-point algorithm for case of infinitesimal deformation.

Remark 5.5.15. The most obvious procedure to determine $\boldsymbol{R}_{n+1}$ and $\boldsymbol{R}_{n+\theta}$ in case (i) of 5.5.14 (Green-Naghdi rate) is the polar decomposition of the total deformation gradients $\boldsymbol{F}_{n+1}$ and $\boldsymbol{F}_{n+\theta}$, respectively. Alternative procedures that circumvent polar decomposition have been proposed by Flanagan and Taylor [1987] and Simo and Hughes [1998, sec. 8.3.2]. An algorithmic approximations to the vorticity tensor $\boldsymbol{\omega}$ in case of the Zaremba-Jaumann rate (case (ii) in 5.5.14) is provided by Proposition 5.5.10(iii). The rotation group can be approximately integrated, for example, by using the general algorithm of Simo and Hughes [1998, sec. 8.3.2], or by the particular procedure of Hughes and Winget [1980]; see also algorithm of Hughes [1984] below. △

The particular algorithm of Hughes [1984] can be obtained from the general objective integration algorithm 5.5.14 by making a particular approximation to the orthogonal group of rotations and by employing time-centering, i.e. $\varepsilon = \frac{1}{2}$, to the algorithmic finite strain increment. The time-centered approximation is employed in accordance with the incrementally objective algorithm developed by Hughes and Winget [1980].

A straightforward application of Proposition 5.5.10(i) using $\theta = \frac{1}{2}$ proves that

$$\boldsymbol{\nabla}_{n+1/2}\boldsymbol{u} = 2(\boldsymbol{f}_{n+1} - \boldsymbol{I})(\boldsymbol{f}_{n+1} + \boldsymbol{I})^{-1} . \tag{5.5.16}$$

Using Propositions 5.5.10(ii) and (iii), finite strain and rotation increments are then computed from

$$\begin{aligned} \Delta\tilde{\boldsymbol{e}}_{n+1/2} &\overset{\text{def}}{=} \boldsymbol{d}_{n+1/2}\Delta t = \tfrac{1}{2}\Big(\boldsymbol{\nabla}_{n+1/2}\boldsymbol{u} + (\boldsymbol{\nabla}_{n+1/2}\boldsymbol{u})^{\mathrm{T}}\Big) \qquad \text{and} \\ \Delta\tilde{\boldsymbol{r}}_{n+1/2} &\overset{\text{def}}{=} \boldsymbol{\omega}_{n+1/2}\Delta t = \tfrac{1}{2}\Big(\boldsymbol{\nabla}_{n+1/2}\boldsymbol{u} - (\boldsymbol{\nabla}_{n+1/2}\boldsymbol{u})^{\mathrm{T}}\Big) , \end{aligned} \tag{5.5.17}$$

respectively. $\Delta\tilde{\boldsymbol{e}}_{n+1/2}$ is the second-order accurate midpoint strain increment (5.5.12). The corotated algorithmic finite strain increment equals the *corotated midpoint strain increment*,

$$\Delta\mathfrak{E}_{n+1/2} \overset{\text{def}}{=} \mathfrak{R}^{\mathrm{T}}_{n+1/2} \cdot \Delta\tilde{\boldsymbol{e}}_{n+1/2} \cdot \mathfrak{R}_{n+1/2} , \tag{5.5.18}$$

which is regarded as input variable to the local stress integration procedure. Summation of $\Delta\mathfrak{E}_{n+1/2}$ over a time interval $[t_0, t_{n+1}]$ gives an excellent approximation to the Lagrangian logarithmic strain [Hughes, 1984; ANSYS, 2007a].

If integration is carried out explicitly ($\theta = 0$), implicitly ($\theta = 1$), or based on the midpoint rule ($\theta = \frac{1}{2}$), then the rotations $\mathfrak{R}_{n+1}$ and $\mathfrak{R}_{n+1/2}$ need to be determined in order to complete the algorithm 5.5.14. In case of $\mathring{\boldsymbol{\sigma}} = \mathring{\boldsymbol{\sigma}}^{\mathrm{GN}}$, where $\mathfrak{R} = \boldsymbol{R}$, Hughes [1984] suggests polar decomposition of the total deformation gradients $\boldsymbol{F}_{n+1}$ and $\boldsymbol{F}_{n+1/2}$, respectively. In case of $\mathring{\boldsymbol{\sigma}} = \mathring{\boldsymbol{\sigma}}^{\mathrm{ZJ}}$, where $\mathfrak{R} \neq \boldsymbol{R}$, the rotation and half-step rotation are defined through

$$\mathfrak{R}_{n+1} = \Delta\mathfrak{R} \cdot \mathfrak{R}_n \qquad \text{and} \qquad \mathfrak{R}_{n+1/2} = \Delta\mathfrak{R}^{1/2} \cdot \mathfrak{R}_n , \tag{5.5.19}$$

where

$$\begin{aligned} \Delta\mathfrak{R} &= (\boldsymbol{I} + (\boldsymbol{I} - \tfrac{1}{2}\Delta\tilde{\boldsymbol{r}}_{n+1/2})^{-1}\Delta\tilde{\boldsymbol{r}}_{n+1/2}) \\ &= (\boldsymbol{I} - \tfrac{1}{2}\Delta\tilde{\boldsymbol{r}}_{n+1/2})^{-1}(\boldsymbol{I} + \tfrac{1}{2}\Delta\tilde{\boldsymbol{r}}_{n+1/2}) \end{aligned} \tag{5.5.20}$$

is an approximation to the relative rotation of the configuration $\varphi_{n+1}(\mathcal{B})$ with respect to the configuration $\varphi_n(\mathcal{B})$, i.e. to the incremental rotation over the time increment $[t_n, t_{n+1}]$. It results from the generalized midpoint rule (A.3.6) applied to the generating equation $\dot{\mathfrak{R}} = \boldsymbol{\omega} \cdot \mathfrak{R}$ and setting $\theta = \frac{1}{2}$. This procedure has been originally proposed by Hughes and Winget [1980]. For computation of the proper orthogonal square root $\Delta\mathfrak{R}^{1/2}$, see [Hughes, 1984].

The complete integration procedure is summarized in Alg. 5.2. An example application of this algorithm will be presented in Section 6.3.2, which employs the hypoplastic model for sand derived in Section 4.3.

Algorithm 5.2: Objective integration method for rate constitutive equations based on a corotated description according to Hughes [1984].

Input: geometry $\boldsymbol{x}_n$, incremental displacements $\boldsymbol{u}$ of global time integration, Cauchy stress $\boldsymbol{\sigma}_n$, material state variables $\boldsymbol{\alpha}_n$, and rotation $\mathfrak{R}_n$

Output: $\boldsymbol{\sigma}_{n+1}$, $\boldsymbol{\alpha}_{n+1}$, and material tangent tensor $\boldsymbol{m}$

compute $\boldsymbol{f}_{n+1} = \mathbf{1} + \boldsymbol{\nabla}_n \boldsymbol{u}$, $\boldsymbol{f}_{n+1/2} = \mathbf{1} + \frac{1}{2}\boldsymbol{\nabla}_n \boldsymbol{u}$, and $\boldsymbol{\nabla}_{n+1/2}\boldsymbol{u} = \boldsymbol{\nabla}_n \boldsymbol{u} \cdot \boldsymbol{f}_{n+1/2}^{-1}$;

obtain midpoint strain increment $\Delta\tilde{\boldsymbol{e}}_{n+1/2}$ and rotation increment $\Delta\tilde{\boldsymbol{r}}_{n+1/2}$ (5.5.17);

switch *corotational rate* $\mathring{\boldsymbol{\sigma}}$ **do**

  case *Green-Naghdi rate* $\mathring{\boldsymbol{\sigma}}^{\mathrm{GN}}$ *(*$\mathfrak{R} = \boldsymbol{R}$*)*

    compute $\boldsymbol{F}_{n+1} = \boldsymbol{f}_{n+1} \cdot \boldsymbol{F}_n$ and $\boldsymbol{F}_{n+1/2} = \frac{1}{2}(\boldsymbol{F}_{n+1} + \boldsymbol{F}_n)$;

    perform polar decomposition to obtain $\mathfrak{R}_{n+1}$ and $\mathfrak{R}_{n+1/2}$;

  case *Zaremba-Jaumann rate* $\mathring{\boldsymbol{\sigma}}^{\mathrm{ZJ}}$ *(*$\mathfrak{R} \neq \boldsymbol{R}$*)*

    compute $\Delta\mathfrak{R} = (\boldsymbol{I} - \frac{1}{2}\Delta\tilde{\boldsymbol{r}}_{n+1/2})^{-1}(\boldsymbol{I} + \frac{1}{2}\Delta\tilde{\boldsymbol{r}}_{n+1/2})$ and $\Delta\mathfrak{R}^{1/2}$;

    update $\mathfrak{R}_{n+1} = \Delta\mathfrak{R} \cdot \mathfrak{R}_n$ and $\mathfrak{R}_{n+1/2} = \Delta\mathfrak{R}^{1/2} \cdot \mathfrak{R}_n$;

corotate midpoint strain increment: $\Delta\mathfrak{E}_{n+1/2} = \mathfrak{R}_{n+1/2}^{\mathrm{T}} \cdot \Delta\tilde{\boldsymbol{e}}_{n+1/2} \cdot \mathfrak{R}_{n+1/2}$;

corotate stress, state variables, and the spatial metric based on the actual integration method:
$\mathfrak{S}_{n+\theta} = \mathfrak{R}_{n+\theta}^{\mathrm{T}} \cdot \boldsymbol{\sigma}_{n+\theta} \cdot \mathfrak{R}_{n+\theta}$, $\mathfrak{A}_{n+\theta} = \mathfrak{R}_{n+\theta}^{\star} \boldsymbol{\alpha}_{n+\theta}$, and
$\mathfrak{G}_{n+\theta} = \mathfrak{R}_{n+\theta}^{\mathrm{T}} \cdot \boldsymbol{g}_{n+\theta} \cdot \mathfrak{R}_{n+\theta}$, with $\theta \in \{0, \frac{1}{2}, 1\}$;

integrate constitutive equation using $\Delta\mathfrak{E}_{n+1/2}$, $\mathfrak{S}_{n+\theta}$, $\mathfrak{A}_{n+\theta}$, and $\mathfrak{G}_{n+\theta}$;

compute material tangent tensor $\boldsymbol{m}$;

back-rotate updated corotated stress to the current configuration:
$\boldsymbol{\sigma}_{n+1} = \mathfrak{R}_{n+1} \cdot \mathfrak{S}_{n+1} \cdot \mathfrak{R}_{n+1}^{\mathrm{T}}$;

back-rotate updated corotated state variables, if needed, to the current configuration;

Remark 5.5.21. According to the basic Definition 5.5.9, the deformation gradient of the motion is updated by $\boldsymbol{F}_{n+1} = \boldsymbol{f}_{n+1} \cdot \boldsymbol{F}_n$, where $\boldsymbol{F}_n = \boldsymbol{R}_n \cdot \boldsymbol{U}_n$, and $\boldsymbol{R}_n$ is proper orthogonal. Now, suppose that the current configuration at time t_n is taken as the reference configuration, i.e. $\mathcal{B} = \varphi_n(\mathcal{B})$ as in the updated Lagrangian description, and no data is available of configurations prior to t_n such that $\boldsymbol{F}_n = \boldsymbol{R}_n = \mathfrak{R}_n = \boldsymbol{I}^{\varphi}$ and $\boldsymbol{U}_n = \boldsymbol{I}$. Then, by Remark 4.1.18, one has $\boldsymbol{\omega} = \boldsymbol{\Omega}$ and the Zaremba-Jaumann and Green-Naghdi stress rates are identical. △

Remark 5.5.22. Alg. 5.2 places a restriction to the magnitude of the rotation increment $\|\Delta\tilde{\boldsymbol{r}}_{n+1/2}\| = \|\boldsymbol{\omega}_{n+1/2}\|\Delta t$ for $\boldsymbol{\Lambda} = \boldsymbol{\omega}$. From the approximation $\frac{1}{2}\|\Delta\tilde{\boldsymbol{r}}_{n+1/2}\| \approx \tan\|\frac{1}{2}\Delta\tilde{\boldsymbol{r}}_{n+1/2}\|$, [cf. Simo and Hughes, 1998, eq. 8.3.24], it follows that if $\Delta\mathfrak{R}$ would be determined from (5.5.20), it will be defined only for $\|\frac{1}{2}\Delta\tilde{\boldsymbol{r}}_{n+1/2}\| < 180°$. This is called the "black hole" condition [Hughes, 1984]. △

Chapter 6

Arbitrary Lagrangian-Eulerian Procedures

In the chapter that follows, a detailed description of specific arbitrary Lagrangian-Eulerian (ALE) procedures and their implementation into an existing large deformation Lagrangian finite element code will be given. These procedures incorporate the theoretical background of the ALE framework (Chapter 3), constitutive theory (Chapter 4), as well as Lagrangian finite element technology (Chapter 5). The basic solution strategies to solve mechanical initial boundary value problems in ALE description are reviewed in Section 6.1. The overall solution procedure of the particular ALE finite element method developed by the author is presented in Section 6.2. It is based on an operator-split and a single-material element formulation, which is also called an SALE method [Benson, 1989]. Each solution step in time is subdivided into a Lagrangian step, a mesh motion step, and a transport step. The procedures related to these steps as well as their actual implementation will be presented in Sections 6.3 to 6.6.

6.1 Review of Basic Solution Strategies

From a continuum mechanical point of view, the ALE formulation of kinematics, balance principles, and initial boundary value problems includes the Lagrangian and Eulerian formulations as special cases (cf. Remark 3.1.38). Similarly, ALE methods can be run in both purely Lagrangian and purely Eulerian fashion. In Lagrangian methods, the convective velocity is set to zero so that no material flux occurs with respect to the mesh. A Eulerian method is either obtained by keeping the mesh spatially fixed or by remapping onto the original mesh at the end of a calculation step. The first Lagrangian and Eulerian codes were developed almost 60 years ago and initiated ramified code family trees [Hertel, 1997]. Generally spoken, the contemporary Lagrangian codes are based on a finite element method, whereas Eulerian codes use finite difference or finite volume solution techniques. ALE codes try to combine the best features of both approaches.

The earliest ALE methods were based on finite difference approximations and belong to the class of *hydrocodes* [Johnson and Anderson, 1987; Anderson, 1987; Benson, 1992; Hertel, 1997; Mair, 1999; Wilkins, 1999; Rider, 2005]. They were developed in the 1960-70's at US laboratories to compute transient fluid flow [Frank and Lazarus, 1964; Trulio, 1966; Hirt et al., 1974; Pracht, 1975; Chan, 1975; Amsden et al., 1980]. ALE finite element methods appear only a few years later and were primarily concerned with fluid-structure interaction, free surface flow, and metal forming problems [Belytschko and Kennedy, 1978; Donea et al., 1981; Hughes et al., 1981; Huétink, 1982].

6.1.1 ALE Setting of the Initial Boundary Value Problem

Recall the fundamental relations for continuum mechanics on arbitrarily moving reference domains presented in Chapter 3, as well as the initial boundary value problem in the updated Lagrangian description stated in Section 5.1. In particular, let $\varphi : \mathcal{B} \times [t_0, T] \to \mathcal{S}$ be the regular motion of a material body, and let $q_t : \varphi_t(\mathcal{B}) \to T^r_s(\mathcal{S})$ be the spatial representation of the time-dependent physical field under consideration, with $t \in [t_0, T]$, $q_t(x) = q(x,t)$, $x = \varphi(X,t) = \varphi_t(X) \in \mathcal{S}$, and $X \in \mathcal{B}$. Moreover, let the quantity $\hat{q}_t \overset{\text{def}}{=} q_t \circ \Phi_t$ be the referential picture of the physical field. The map $\Phi_t : \mathcal{R} \to \mathcal{S}$ is the relative motion of the reference domain $\mathcal{R} \subset \mathcal{S}$ with points $\chi \in \mathcal{R}$, and $\Psi_t : \mathcal{R} \to \mathcal{B}$ is the referential motion such that

$$\varphi_t = \Phi_t \circ \Psi_t^{-1} \,. \tag{6.1.1}$$

The Jacobian of φ is denoted by J, and J_Φ is the Jacobian of Φ. The spatial velocity of φ_t and the the referential velocity have been defined through $\boldsymbol{v}_t = (\frac{\partial \varphi_t}{\partial t} \circ \varphi_t^{-1}) \in \Gamma(T\mathcal{S})$ and $\boldsymbol{\vartheta}_t = (\frac{\partial \Psi_t^{-1}}{\partial t} \circ \Psi_t) \in \Gamma(T\mathcal{R})$, respectively. The spatial velocity of Φ_t, $\boldsymbol{w}_t = (\frac{\partial \Phi_t^i}{\partial t} \circ \Phi_t^{-1}) \in \Gamma(T\mathcal{S})$, is also referred to as the relative velocity or mesh velocity. The convective velocity is the difference

$$\boldsymbol{c}(x,t) = \boldsymbol{v}(x,t) - \boldsymbol{w}(x,t) \,, \tag{6.1.2}$$

with $\boldsymbol{c}_t = \Phi_{t\star} \boldsymbol{\vartheta}_t$ by Theorem 3.1.27.

In the arbitrary Lagrangian-Eulerian formulation of IBVP, one usually refers to the current configuration of the reference domain $\mathcal{R} \subset \mathcal{S}$ at time $t = s \in [t_0, T]$, i.e. $\Phi_s(\mathcal{R}) \overset{\text{def}}{=} \mathcal{R}$, because any previous configuration is generally not available. It is assumed that the material body and the reference domain instantaneously occupy the same region of space such that $\varphi_s(\mathcal{B}) = \Phi_s(\mathcal{R}) \subset \mathcal{S}$, where $\varphi_s = (\Phi_s \circ \Psi_s^{-1}) : \mathcal{B} \to \mathcal{S}$ denotes the physical configuration of the body at time $t = s$.

The statement of the IBVP involves the ALE balance principles in conservation form derived in Section 3.2.3, namely conservation of volume, mass, momentum, and energy. Due to the broad range of applications, several constitutive approaches are available. The split $\boldsymbol{\sigma} \overset{\text{def}}{=} \boldsymbol{\sigma}_{\text{dev}} - p\, \boldsymbol{g}^\sharp$ is common in fluid dynamics and hypervelocity impact calculations, with $\boldsymbol{\sigma}_{\text{dev}}$ usually calculated from a rate constitutive equation, and p calculated from an equation of state. Solid mechanical low-velocity applications, on the

other hand, favor rate constitutive equations mostly based on the objective Zaremba-Jaumann or Green-Naghdi rates for unsplit $\boldsymbol{\sigma}$. In this latter case, which applies to the ALE framework proposed in the present thesis, balance of energy needs not to be solved as a separate differential equation.

Definition 6.1.3. Let $\hat{\rho} = \rho \circ \Phi$, $\hat{\boldsymbol{v}} = \boldsymbol{v} \circ \Phi$, and $\hat{\boldsymbol{\sigma}} = \boldsymbol{\sigma} \circ \Phi$. An *IBVP for mechanics in the arbitrary Lagrangian-Eulerian description* is the problem of finding the spatial mass density ρ, the spatial velocity $\boldsymbol{v}$, the Cauchy stress $\boldsymbol{\sigma}$, and the internal material state on the current spatial domain $\Phi_t(\mathcal{R}) \subset \mathcal{S}$ for every $t \in [t_0, T]$ provided that for a body force $\bar{\boldsymbol{b}}$ given,

(i) conservation of volume $\partial J_\Phi / \partial t - J_\Phi \operatorname{div} \boldsymbol{w} = 0$,

(ii) conservation of mass $\partial(\hat{\rho} J_\Phi)/\partial t + J_\Phi \operatorname{div}(\rho \boldsymbol{c}) = 0$, and

(iii) conservation of momentum $\partial(\hat{\rho}\hat{\boldsymbol{v}} J_\Phi)/\partial t + J_\Phi \operatorname{div}(\rho \boldsymbol{v} \otimes \boldsymbol{c}) = J_\Phi \left(\rho \bar{\boldsymbol{b}} + \operatorname{div} \boldsymbol{\sigma}\right)$ hold,

(iv) the stress $\boldsymbol{\sigma} = \boldsymbol{\sigma}^{\mathrm{T}}$ is obtained through integration of a rate constitutive equation $\mathring{\boldsymbol{\sigma}}^{\star} = \boldsymbol{h}(\boldsymbol{\sigma}, \boldsymbol{d}, \ldots)$, and the evolution equations for the internal state variables are similar functions,

(v) for the boundary $\partial\Phi_t(\mathcal{R})$ of the reference domain in its current spatial configuration with unit outward normals $\boldsymbol{n}^*$ there are prescribed boundary conditions,

(vi) ρ, $\boldsymbol{v}$, $\boldsymbol{\sigma}$, and the internal state variables are given at $t = 0$ (*initial conditions*), and

(vii) the relative velocity $\boldsymbol{w}$ of Φ_t is prescribed for every $\chi \in \mathcal{R}$ and $t \in [0, T]$. ♢

6.1.2 Monolithic or Unsplit ALE Methods

Stated formally, the main objective of the present research is the numerical solution of the IBVP 6.1.3 subject to prescribed contact, boundary, and initial conditions associated with penetration into sand. The most natural choice would be to solve the coupled set of equations as they are written and without any further assumptions. This is called an *unsplit* or *monolithic ALE solution procedure*. It generally ensures consistency between the deformation state and the material response, and avoids accuracy losses and the generation of spurious forces due to a sequential solution. Monolithic ALE methods were developed e.g. by Belytschko and Kennedy [1978]; Hughes et al. [1981]; Huétink [1982]; Huétink et al. [1990]; Haber [1984]; Liu et al. [1986, 1988]; Ghosh and Kikuchi [1991]; Ghosh [1992]; Sarrate et al. [2001]; Bayoumi and Gadala [2004]. The papers of Huétink [1982]; Huétink et al. [1990] and Liu et al. [1986, 1988] include early applications to solid mechanical problems involving path-dependent material. Ghosh [1992] introduces contact of multiple flexible bodies to a monolithic ALE approach using implicit integration in time.

Convective terms appear in the governing equations of the IBVP 6.1.3 due to the relative motion between the material body and the reference domain, making the development of numerical methods for the monolithic problem difficult. In the semi-discrete equations the approximations of the convective terms include gradients of the shape

functions. For convection dominated problems, that is, if the convective velocity $\boldsymbol{c}$ is large, a standard Galerkin FE formulation can lead to numerical instabilities, and spurious spatial oscillations are exhibited in the variable fields to be advected [Benson, 1992; Belytschko et al., 2000]. The stability condition is a function of the element *Péclet number* defined as

$$Pe \stackrel{\text{def}}{=} \frac{h\|\boldsymbol{c}\|}{2k}\,, \tag{6.1.4}$$

where h is a characteristic element length and k is the diffusion coefficient.

The *streamline-upwind Petrov-Galerkin (SUPG)* finite element formulation is of particular interest to overcome the above mentioned problems associated with monolithic ALE methods. As Benson [1992, p. 328] notices, SUPG methods "[...] are the only higher order accurate finite element methods that have been applied to problems in solid mechanics." Example applications can be found in [Liu et al., 1986, 1988]. The SUPG formulation incorporates the streamline upwind concept devised by Brooks and Hughes [1982], which introduces an artificial diffusion acting only in the flow direction. The solution accuracy is governed by the amount of diffusion assigned. In addition, the Petrov-Galerkin discretization technique defines different sets of interpolation functions for the approximation of the basic variables and the associated test functions. This allows for more flexibility compared to a Galerkin discretization.

6.1.3 Operator-Split or Lagrange-plus-Remap ALE Methods

Complicated problems can be broken up into a series of less complicated problems through *operator-splitting* [Strang, 1963, 1964, 1968; Chorin et al., 1978]. If an operator-split is applied to the governing equations of the problem, the resulting equations are simpler and can be solved sequentially. The algorithms needed for solution are usually more robust and of lower implementation costs than for a monolithic approach. The main disadvantage of operator-splitting is its limitation on accuracy as physical phenomena are decoupled.

Operator-split ALE procedures, which are likewise called *Lagrange-plus-remap* or *fractional-step ALE procedures*, divide solution to the IBVP 6.1.3 into a Lagrangian step and a remap step. In the Lagrangian step the sources are taken into account but the convective terms are neglected. The subsequent remap step accounts for the relative motion between the body and the reference domain but leaves any source term unconsidered. In actual finite element implementations, the remap step is subdivided into a mesh motion step where nodes are relocated in order to smooth the mesh, and a transport step in which the convective terms are taken into account. A Eulerian method is obtained when the nodes are relocated to their original positions.

Finite element discretization and advancing the solution in time during the Lagrangian step of operator-split ALE methods is almost identical to the updated Lagrangian treatment outlined in Chapter 5. Therefore, the primary advantage of the operator-split over the the monolithic ALE solution procedure is that existing Lagrangian FE codes can be easily upgraded. The only difference is due to the non-Lagrangian view

of material deformations, by which conservation of mass is not automatically satisfied but must be treated as an additional equation.

ALE finite difference codes [Trulio, 1966; Hirt et al., 1974; Pracht, 1975; Chan, 1975; Amsden et al., 1980] as well as most of the Eulerian hydrocodes traditionally employ the operator-split strategy [cf. Benson, 1992]. Probably the earliest references in this context are [Evans and Harlow, 1957; Noh, 1964] concerned with the so-called *particle-in-cell (PIC)* and *coupled Eulerian-Lagrangian (CEL)* methods, respectively. These codes did pioneer work to the ALE finite element methods for fluid-structure interaction problems [Donea et al., 1981, 1982] and free surface flow [Ramaswamy and Kawahara, 1987; Ramaswamy, 1990]. With regard to solid mechanical problems, an operator-split ALE finite element method was first proposed by Benson [1989]. Operator-splitting is the proven technology in the development of ALE methods, particularly with regard to path-dependent material response of metals [Benson, 1995; Huerta and Casadei, 1994; Rodríguez-Ferran et al., 1998, 2002; Aymone et al., 2001; Aymone, 2004] and soils [Nazem, 2006; Nazem et al., 2006, 2008; Di et al., 2007; Sheng et al., 2009].

As time evolves during the Lagrangian step but is held fixed in the mesh motion and transport steps, operator-split ALE methods can be regarded as special remap strategies, called *advective remaps* [Benson, 1989]. The mesh topology does not change in advective remaps, hence elements have the same neighbors during the entire solution of the IBVP. This enables exact calculation of material in- and outflux between adjacent elements and the application of conservative advection algorithms provided by the computational fluid dynamics community. Therefore, operator-split ALE methods permit mechanically consistent transport of variables.

6.2 Proposed Operator-Split Solution Procedure

6.2.1 Split Initial Boundary Value Problem

The ALE method developed in this thesis is based on the operator-split solution strategy. According to the references [Benson, 1997, 2000; Benson and Okazawa, 2004; Vitali and Benson, 2008, 2009], this strategy is most easily illustrated by considering the conservation form of the generic ALE balance principle proposed in 3.2.41,

$$\frac{\partial \hat{q} J_{\Phi}}{\partial t} + J_{\Phi} \left(\operatorname{div} \boldsymbol{\psi}(q)\right) \circ \Phi = \hat{S} J_{\Phi} \,. \tag{6.2.1}$$

Recall that $\hat{q} = q \circ \Phi$, $\boldsymbol{\psi}(q)$ is the convective flux density of the generic quantity q, J_{Φ} is the Jacobian of the relative motion Φ_t, and $\hat{S} \overset{\text{def}}{=} S \circ \Phi \overset{\text{def}}{=} (b + \operatorname{div} \boldsymbol{u}) \circ \Phi$ accounts for the sources b and $\boldsymbol{u}$ given per unit spatial volume and per unit spatial area, respectively. The flux density is defined by $\boldsymbol{\psi}(q) \overset{\text{def}}{=} q\boldsymbol{c}$ for q being scalar-valued, and by $\boldsymbol{\psi}(q) \overset{\text{def}}{=} q \otimes \boldsymbol{c}$ for q being tensor-valued.

Definition 6.2.2. The *operator-split* applied to (6.2.1) results in the partial differential equations

$$\frac{\partial \hat{q} J_{\Phi}}{\partial t} = \hat{S} J_{\Phi} \qquad \text{and} \qquad \frac{\partial \hat{q} J_{\Phi}}{\partial t} + J_{\Phi} \left(\operatorname{div} \boldsymbol{\psi}(q)\right) \circ \Phi = 0 \; . \qquad \diamond$$

The first equation in Definition 6.2.2, which is called the *Lagrangian equation*, is a parabolic PDE that accounts for the source. Conceptually, it can be obtained from (6.2.1) by setting $\boldsymbol{c} = \boldsymbol{0}$ resp. $\boldsymbol{w} = \boldsymbol{v}$. This means that no convective terms are present. Moreover, the motion of the reference domain coincides with the material motion such that $\dot{q} = \frac{\partial \hat{q}_t}{\partial t} \circ \Phi_t^{-1}$ and the description of motion is Lagrangian.

Proposition 6.2.3. *The Lagrangian equation 6.2.2*$_1$ *is equivalent to the localized spatial master balance principle in its material form (cf. Definition 3.2.11)*

$$\dot{q} = S - q \operatorname{div} \boldsymbol{v} \; , \qquad \textit{with} \quad S = b + \operatorname{div} \boldsymbol{u} \; .$$

Proof. The assertion follows by the product rule, $(3.1.29)_1$, and switching the independent variables from (χ, t) to (x, t). ∎

The second equation in Definition 6.2.2, called the *transport equation*, represents the generic ALE conservation law 3.2.42. It formalizes the transport resp. advection of the physical quantity on the reference domain moving with convective velocity $\boldsymbol{c} \neq \boldsymbol{0}$. Any external source and material evolution that has been accounted for in the Lagrangian equation is not present in the transport step. Physical time elapses only during in the Lagrangian step. By the evolution equation $(3.1.29)_1$ for the Jacobian J_{Φ}, $6.2.2_2$ boils down to the *linear advection equation without a source* [LeVeque, 1992, 2002]

$$\frac{\partial \hat{q}}{\partial t} \circ \Phi^{-1} + \boldsymbol{\nabla}_{\boldsymbol{c}} q = 0 \; . \tag{6.2.4}$$

Now, consider the mechanical initial boundary value problem (IBVP) in ALE description defined through 6.1.3. Solution of the IBVP requires the conservation of volume, mass, and momentum in the ALE description (cf. Section 3.2.3) in time, as well as integration of the rate constitutive equations. The set of equations is revised in order to embody the particular conditions associated with the current work:

(i) Omission of geometric conservation laws. As a first particularization of the proposed ALE method, the geometric conservation laws proposed in 3.2.39 remain unconsidered for reasons of simplification. This is the common approach in solid mechanical ALE applications.

(ii) Specific form of conservation of mass. By Propositions 3.1.19 and 3.2.18, and by assuming that the reference configuration occurs at time $t = t_0$ such that

$\varphi_{t_0} = \mathrm{id}$ and $J(X, t_0) = 1$, conservation of mass in the Lagrangian form $\dot{\rho} = -\rho \operatorname{div} \boldsymbol{v}$ is equivalent to

$$\rho_{\mathrm{ref}} = \rho J \qquad \text{in conjunction with} \qquad \frac{\partial J}{\partial t} = J \operatorname{div} \boldsymbol{v} \,. \tag{6.2.5}$$

Compositions with the map φ have been dropped. The motivation for using the form (6.2.5) is that J rather than ρ is a fundamental solution variable in Lagrangian finite element methods [Rodríguez-Ferran et al., 2002].

(iii) Quasi-static analysis. Only quasi-static problems are considered in this thesis such that responses due to inertia and damping can be ignored, except for prescribed static spatial acceleration fields $\bar{\boldsymbol{a}} : \varphi_t(\mathcal{B}) \to T\mathcal{S}$. This means that no time derivative and hence no convective term is associated with balance of momentum. Therefore, the transport step in the operator-split ALE procedure is considerably simplified.

(iv) Considered class of rate constitutive equations. The present thesis considers material response described by a spatial rate constitutive equation of the form $\mathring{\boldsymbol{\sigma}}^{\mathrm{ZJ}} \stackrel{\mathrm{def}}{=} \boldsymbol{h}(\boldsymbol{\sigma}, \boldsymbol{g}, \boldsymbol{\alpha}, \boldsymbol{d})$, where $\mathring{\boldsymbol{\sigma}}^{\mathrm{ZJ}} = \dot{\boldsymbol{\sigma}} - \boldsymbol{\omega} \cdot \boldsymbol{\sigma} + \boldsymbol{\sigma} \cdot \boldsymbol{\omega}$, by (4.1.15), is the Zaremba-Jaumann rate of symmetric Cauchy stress, $\boldsymbol{\omega} = \frac{1}{2}(\boldsymbol{\nabla v} - (\boldsymbol{\nabla v})^{\mathrm{T}})$ is the vorticity of motion, $\boldsymbol{d} = \frac{1}{2}(\boldsymbol{\nabla v} + (\boldsymbol{\nabla v})^{\mathrm{T}})$ is the rate of deformation, $\boldsymbol{\alpha} = \{\alpha_1, \ldots, \alpha_m\} \stackrel{\mathrm{def}}{=} \{\alpha_k\}$ is a probably empty set of internal material state variables in addition to stress, and $\boldsymbol{g}$ is the spatial metric. Note that the constitutive rate equation takes the equivalent form

$$\dot{\boldsymbol{\sigma}} = \check{\boldsymbol{h}}(\boldsymbol{\sigma}, \boldsymbol{g}, \boldsymbol{\alpha}, \boldsymbol{\nabla v}) \stackrel{\mathrm{def}}{=} \boldsymbol{h}(\boldsymbol{\sigma}, \boldsymbol{g}, \boldsymbol{\alpha}, \boldsymbol{d}) + \boldsymbol{\omega} \cdot \boldsymbol{\sigma} - \boldsymbol{\sigma} \cdot \boldsymbol{\omega} \,. \tag{6.2.6}$$

In case where $\boldsymbol{\alpha} = \{\alpha_k\}$ is a non-empty set of internal state variables, its elements are assumed to have evolution equations comparable to (6.2.6). That is to say, for a generally tensor-valued state variable α_k one has $\mathring{\alpha}_k^{\mathrm{ZJ}} \stackrel{\mathrm{def}}{=} j_k(\boldsymbol{\sigma}, \boldsymbol{g}, \boldsymbol{\alpha}, \boldsymbol{d})$ resp. $\dot{\alpha}_k = \check{\jmath}_k(\boldsymbol{\sigma}, \boldsymbol{g}, \boldsymbol{\alpha}, \boldsymbol{\nabla v})$.

(v) Simplified ALE approach. The fact that the present thesis is concerned with a so-called *single-material* or *simplified ALE approach* [Benson, 1989, 1992; Mair, 1999] can be formalized as the *zero-flux constraint* [cf. Frank and Lazarus, 1964]

$$(\boldsymbol{v} - \boldsymbol{w}) \cdot \boldsymbol{n}^* = 0 \qquad \text{on} \quad \partial\varphi(\mathcal{B}, t) = \partial\Phi(\mathcal{R}, t) \,, \tag{6.2.7}$$

where $\boldsymbol{n}^*$ denotes the outward normal field. That is, material and mesh velocities coincide in the direction normal to the their boundaries, but may vary in tangential direction. The constraint thus phrases that no material may cross the boundary of the reference domain, i.e. material interfaces are explicitly resolved by element edges in the numerical solution. Multi-material ALE methods do not have this limitation [cf. Benson, 1992; Mair, 1999; Freßmann and Wriggers, 2007].

By the previous particularizations, the governing equations of the IBVP 6.1.3 read

$$\begin{aligned}
\frac{\partial \hat{J} J_\Phi}{\partial t} + J_\Phi \operatorname{div}(J\boldsymbol{c}) \circ \Phi &= 2\hat{J} J_\Phi \, (\operatorname{div} \boldsymbol{v}) \circ \Phi \,, \\
(\rho \bar{\boldsymbol{a}}) \circ \Phi &= (\rho \bar{\boldsymbol{b}} + \operatorname{div} \boldsymbol{\sigma}) \circ \Phi \,, \\
\frac{\partial \hat{\boldsymbol{\sigma}} J_\Phi}{\partial t} + J_\Phi \operatorname{div}(\boldsymbol{\sigma} \otimes \boldsymbol{c}) \circ \Phi &= J_\Phi \, (\check{\boldsymbol{h}}(\boldsymbol{\sigma}, \boldsymbol{g}, \boldsymbol{\alpha}, \boldsymbol{\nabla} \boldsymbol{v}) + \boldsymbol{\sigma} \operatorname{div} \boldsymbol{v}) \circ \Phi \,, \quad \text{and} \\
\frac{\partial \hat{\alpha}_k J_\Phi}{\partial t} + J_\Phi \operatorname{div}(\alpha_k \otimes \boldsymbol{c}) \circ \Phi &= J_\Phi \, (\check{\jmath}_k(\boldsymbol{\sigma}, \boldsymbol{g}, \boldsymbol{\alpha}, \boldsymbol{\nabla} \boldsymbol{v}) + \alpha_k \operatorname{div} \boldsymbol{v}) \circ \Phi \,,
\end{aligned} \tag{6.2.8}$$

where $\hat{J} \overset{\text{def}}{=} J \circ \Phi$ and $\hat{\boldsymbol{\sigma}} \overset{\text{def}}{=} \boldsymbol{\sigma} \circ \Phi$. The first, third, and fourth equations are the evolution equations $(6.2.5)_2$, (6.2.6), and $\dot{\alpha}_k = \check{\jmath}_k(\boldsymbol{\sigma}, \boldsymbol{g}, \boldsymbol{\alpha}, \boldsymbol{\nabla} \boldsymbol{v})$, respectively, in the ALE conservation form according to Proposition 3.2.44. Note that the first equation must be solved in conjunction with $\rho_{\text{ref}} = \rho J$ to represent conservation of mass. The relative velocity $\boldsymbol{w}$, the body force $\bar{\boldsymbol{b}}$, the static acceleration field $\bar{\boldsymbol{a}}$, and the reference mass density ρ_{ref} are assumed given.

The operator-split 6.2.2 applied to (6.2.8) results in the two sets of equations

$$\begin{aligned}
&\text{conservation of mass} && \frac{\partial \hat{J} J_\Phi}{\partial t} = 2\hat{J} J_\Phi \, (\operatorname{div} \boldsymbol{v}) \circ \Phi \qquad \text{i.c.w. } \rho_{\text{ref}} = \rho J \,, \\
&\text{balance of momentum} && (\rho \bar{\boldsymbol{a}}) \circ \Phi = (\rho \bar{\boldsymbol{b}} + \operatorname{div} \boldsymbol{\sigma}) \circ \Phi \,, \\
&\text{rate constitutive equation} && \frac{\partial \hat{\boldsymbol{\sigma}} J_\Phi}{\partial t} = J_\Phi \, (\check{\boldsymbol{h}}(\boldsymbol{\sigma}, \boldsymbol{g}, \boldsymbol{\alpha}, \boldsymbol{\nabla} \boldsymbol{v}) + \boldsymbol{\sigma} \operatorname{div} \boldsymbol{v}) \circ \Phi \,, \\
&\text{evolution equation} && \frac{\partial \hat{\alpha}_k J_\Phi}{\partial t} = J_\Phi \, (\check{\jmath}_k(\boldsymbol{\sigma}, \boldsymbol{g}, \boldsymbol{\alpha}, \boldsymbol{\nabla} \boldsymbol{v}) + \alpha_k \operatorname{div} \boldsymbol{v}) \circ \Phi \,,
\end{aligned} \tag{6.2.9}$$

and

$$\begin{aligned}
&\text{transport of Jacobian of } \varphi && \frac{\partial \hat{J} J_\Phi}{\partial t} + J_\Phi \operatorname{div}(J\boldsymbol{c}) \circ \Phi = 0 \,, \\
&\text{transport of stress} && \frac{\partial \hat{\boldsymbol{\sigma}} J_\Phi}{\partial t} + J_\Phi \operatorname{div}(\boldsymbol{\sigma} \otimes \boldsymbol{c}) \circ \Phi = \boldsymbol{0} \,, \\
&\text{transport of state variables} && \frac{\partial \hat{\alpha}_k J_\Phi}{\partial t} + J_\Phi \operatorname{div}(\alpha_k \otimes \boldsymbol{c}) \circ \Phi = \boldsymbol{0} \,.
\end{aligned} \tag{6.2.10}$$

By Proposition 6.2.3, (6.2.5), and (6.2.6) the set (6.2.9) is equivalent to

$$\dot{\rho} = -\rho \operatorname{div} \boldsymbol{v} \,, \quad \rho \bar{\boldsymbol{a}} = \rho \bar{\boldsymbol{b}} + \operatorname{div} \boldsymbol{\sigma} \,, \quad \mathring{\boldsymbol{\sigma}}^{\text{ZJ}} = \boldsymbol{h}(\boldsymbol{\sigma}, \boldsymbol{g}, \boldsymbol{\alpha}, \boldsymbol{d}) \,, \quad \mathring{\alpha}_k^{\text{ZJ}} = j_k(\boldsymbol{\sigma}, \boldsymbol{g}, \boldsymbol{\alpha}, \boldsymbol{d}) \,. \tag{6.2.11}$$

This set is form-identical to the governing equations of the initial boundary value problem in the updated Lagrangian description 5.1.1, so that operator-split ALE methods can be easily added to existing Lagrangian finite element codes.

Remark 6.2.12. The Zaremba-Jaumann stress rate $\mathring{\boldsymbol{\sigma}}^{\text{ZJ}}$ is the most attractive choice for both monolithic and operator-split ALE solution procedures because it is cheap, takes little storage, and does not add variables for transport. The Zaremba-Jaumann rate requires knowledge only of the instantaneous motion of the material body and

not of total deformation. If, on the other hand, the Green-Naghdi stress rate $\mathring{\boldsymbol{\sigma}}^{\mathrm{GN}}$ defined by (4.1.17) would be the underlying stress rate, then evolution equations for the deformation gradient or the rotation group must be added to the systems of equations; see also [Benson, 1992, sec. 2.6.2] and [Benson, 2000]. △

6.2.2 Overall ALE Finite Element Procedure

The crucial observation to be made is that the operator-split 6.2.2 leads to a set of Lagrangian equations (6.2.11) which is form-identical to the governing equations of the IBVP in the updated Lagrangian description defined by 5.1.1. Therefore, finite element discretization, advancing in time, and solution of (6.2.11) can be carried out identical to the classical updated Lagrangian approach described in Chapter 5 —except for the mass update; see below.

Assume that the ambient space is an m_{dim}-dimensional Euclidian point space, i.e. $\mathcal{S} = \mathbb{R}^{m_{\mathrm{dim}}}$. The reference configuration of the material body, $\mathcal{B} \subset \mathbb{R}^{m_{\mathrm{dim}}}$, as well as the reference domain $\mathcal{R} \subset \mathbb{R}^{m_{\mathrm{dim}}}$ are assumed to have the same dimensions. Arbitrary Lagrangian-Eulerian finite element methods approximate the reference domain $\mathcal{R}$ by an assembly of n_{elem} finite elements $\hat{\Omega}_e \subset \mathbb{R}^{m_{\mathrm{dim}}}$ appropriately connected by nodes,

$$\mathcal{R} \approx \tilde{\mathcal{R}} \stackrel{\mathrm{def}}{=} \bigcup_{e=1}^{n_{\mathrm{elem}}} \hat{\Omega}_e \,. \tag{6.2.13}$$

Here $\hat{\Omega}_e$ is the reference configuration of a parent element $\Omega_\square$ (Fig. 5.2 and Sec. 5.3.1). Besides spatial discretization by finite elements, the time interval of interest, $[t_0, T] \subset \mathbb{R}$, is approximated by the sequence $(t_0, t_1 = t_0 + \Delta t, \ldots, t_{n+1} = t_n + \Delta t, \ldots, T)$ of discrete time steps with probably variable time increment $\Delta t = t_{n+1} - t_n > 0$. In the context of operator-split ALE methods it proves convenient to add the following definition.

Definition 6.2.14. Let $[t_n, t_{n+1}[\subset \mathbb{R}$ be a conceptual right-open incremental time interval, then a small neighborhood of t_{n+1} is defined through

$$t_{n+1}^{\pm} \stackrel{\mathrm{def}}{=} \lim_{\varepsilon \to 0}(t_n + \Delta t \pm \varepsilon) \qquad \in [t_n, t_{n+1}[\,,$$

where $\pm$ means *either* $+$ *or* $-$, so that $t_{n+1}^{-} = \lim_{\varepsilon\to 0}(t_{n+1} - \varepsilon)$ and $t_{n+1}^{+} = \lim_{\varepsilon\to 0}(t_{n+1} + \varepsilon)$, respectively. ♢

The configurations of the reference domain $\mathcal{R} = \Psi_t^{-1}(\mathcal{B})$ and of the material body $\mathcal{B}$ in the ambient space at time $t = t_n$ are assumed coincident. Moreover, incremental ALE frameworks impose the requirement that $\mathcal{R}$ and $\mathcal{B}$ coincide with their current configurations at $t = t_n$, i.e. $\Phi_n = \varphi_n \stackrel{\mathrm{def}}{=} \mathrm{id}$, because prior configurations are not available. Therefore,

$$\mathcal{R} = \Phi_n(\mathcal{R}) = \varphi_n(\mathcal{B}) = \mathcal{B} \qquad \text{and} \qquad \Phi_n(\chi) = \varphi_n(X) \stackrel{\mathrm{def}}{=} x_n \,, \tag{6.2.15}$$

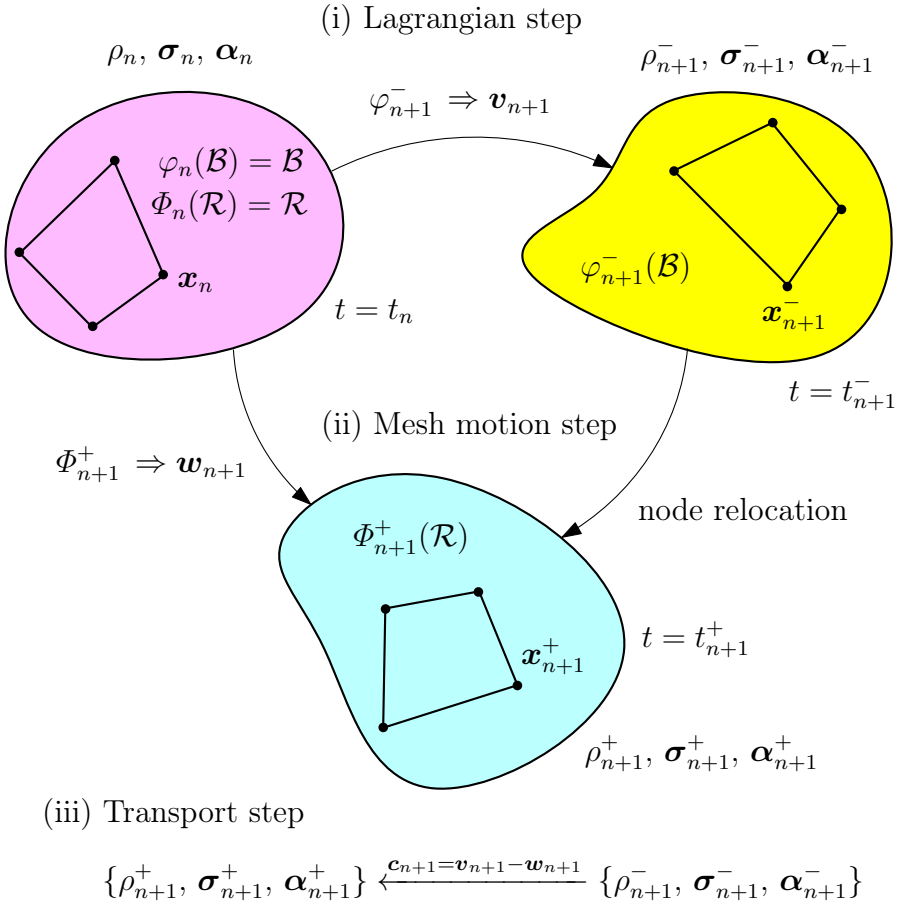

Figure 6.1: Schematic diagram of the proposed incremental operator-split ALE solution procedure.

for all $\chi \in \mathcal{R}$ and $X \in \mathcal{B}$, where $\Phi_n(\mathcal{R}) \overset{\text{def}}{=} \Phi(\mathcal{R}, t_n)$ and $\varphi_n(\mathcal{B}) \overset{\text{def}}{=} \varphi(\mathcal{B}, t_n)$. The points $x_n \overset{\text{def}}{=} \Phi_n(\chi) \overset{\text{def}}{=} \varphi_n(X)$, with position vectors $(o, \boldsymbol{x}_n) \overset{\text{def}}{=} (o, \overrightarrow{ox_n}) \in T\mathbb{R}^{m_{\text{dim}}}$, or just

$$\boldsymbol{x}_n = \overrightarrow{ox_n} \qquad \in \mathbb{R}^{m_{\text{dim}}}, \tag{6.2.16}$$

denotes both the locations of the reference points and the material particles in the ambient space at time t_n with respect to the origin $o \in \mathcal{S} = \mathbb{R}^{m_{\text{dim}}}$; see also Remark 3.1.4. The configurations $\Phi_n(\mathcal{R}) = \varphi_n(\mathcal{B})$ are regarded as given data, meaning that the position vectors $\boldsymbol{x}_n$ of all the mesh nodes are known. The situation is illustrated in Fig. 6.1.

Once the reference domain of interest has been spatially discretized by finite elements, the solution in time of the mechanical IBVP 6.1.3 using the particularizations of Section 6.2.1 is carried out in calculational cycles consisting of three steps: 1. a *Lagrangian step*, 2. a *mesh motion step*, and 3. a *transport step*. The time associated with the end of the Lagrangian step is t_{n+1}^-, whereas the time associated with the end of both the mesh motion step and the transport step is t_{n+1}^+. However, physical time elapses during in the Lagrangian step, but is held fixed during the mesh motion and transport steps. The time increment associated with the mesh motion and transport steps is a pseudo time interval.

Alg. 6.1 provides the pseudocode of the proposed incremental operator-split ALE finite element solution procedure for quasi-static problems, which will be summarized in what follows. The steps in Alg. 6.1 marked with "$*$" have been coded by the author during this research work, whereas the other are provided by the host application (currently ANSYS® Release 11.0 SP1).

Step 1: Implicit Updated Lagrangian Calculation

In the first solution step, the *Lagrangian step*, the set of equations (6.2.11) is solved. In particular, balance of momentum $(6.2.11)_2$ is solved in the updated Lagrangian isoparametric semi-discrete weak form. The time associated with the end of the converged Lagrangian step is t_{n+1}^-. The solution variables referring to that time are the approximations to the spatial velocity field $\boldsymbol{v}_{n+1}^- \overset{\text{def}}{=} \boldsymbol{v}_{n+1}$ resp. to the material displacement field over the time increment $\boldsymbol{u}_{n+1}^- \overset{\text{def}}{=} \boldsymbol{u}_{n+1}$, as well as the Cauchy stress $\boldsymbol{\sigma}_{n+1}^-$ and the material state variables $\boldsymbol{\alpha}_{n+1}^-$ (Fig. 6.1).

Only quasi-static problems are considered, and global time integration of the finite element equations is carried out implicitly. The Newmark-β method in conjunction with Newton's method is applied, which has been presented in Alg. 5.1 in Section 5.4.2. The resulting system of linearized equations is

$$\boldsymbol{K}_{n+1}^i d\boldsymbol{u}_{n+1}^i = \boldsymbol{r}_{n+1}^i \,, \qquad \text{where} \quad \boldsymbol{r}_{n+1}^i = \boldsymbol{f}_{n+1}^{\text{ext}} - \boldsymbol{M}\bar{\boldsymbol{a}} - \boldsymbol{f}^{\text{int}}(\boldsymbol{u}_{n+1}^i) \,, \tag{6.2.17}$$

$\boldsymbol{M}$ is the global mass matrix of the finite element assembly, $\boldsymbol{f}^{\text{int}}$ and $\boldsymbol{f}^{\text{ext}}$ are the global internal and external nodal force vectors, respectively, and $\boldsymbol{K}_{n+1}^i = D(\boldsymbol{f}^{\text{int}}(\boldsymbol{u}_{n+1}^i))$ is the global stiffness matrix given by (5.4.13) referring to the i-th iteration of the solution at time t_{n+1}^-. The external nodal acceleration vector $\bar{\boldsymbol{a}}$ is required to simulate gravity in quasi-static analysis.

Eq. (6.2.17) is solved for the solution increment of material displacements, $d\boldsymbol{u}_{n+1}^i$. The current accumulated incremental material displacements in the i-th iteration during the Lagrangian step, $\sum_{k=0}^i d\boldsymbol{u}_{n+1}^k$, are passed to the local stress integration method (Remark 5.4.26). The rate constitutive equation $(6.2.11)_3$ and the evolution equations $(6.2.11)_4$ are then integrated in a well-established way in order to provided the Cauchy stress $\boldsymbol{\sigma}_{n+1}^-$ and the material state variables $\boldsymbol{\alpha}_{n+1}^-$ at the integration points of the finite elements at time t_{n+1}^-. The general integration procedure has been outlined in Section 5.5.

If solution has converged after the i-th global Newton iteration, the Lagrangian step has completed and the incremental material displacements over the time increment $t_{n+1}^- - t_n$ are given by $\boldsymbol{u}_{n+1} = \sum_{k=0}^i d\boldsymbol{u}_{n+1}^k$. As time is a dummy parameter in quasi-static analysis, the spatial velocity constant over the time increment can be defined through

$$\boldsymbol{v}_{n+1} \overset{\text{def}}{=} \frac{\boldsymbol{x}_{n+1}^- - \boldsymbol{x}_n}{t_{n+1}^- - t_n} = \frac{\boldsymbol{u}_{n+1}}{\Delta t} \,, \tag{6.2.18}$$

which is a simple finite difference approximation. In fully transient analysis, $\boldsymbol{v}_{n+1}$ would be given by the global time integration scheme.

Algorithm 6.1: Overall incremental operator-split ALE finite element solution procedure with implicit global time integration for quasi-static problems.

Input: initial mesh, initial geometry $\boldsymbol{x}(t_0) = \boldsymbol{x}_0$, initial conditions $\boldsymbol{u}(t_0) = \boldsymbol{0}$, $\rho(t_0) = \rho_0$, $\boldsymbol{\sigma}(t_0) = \boldsymbol{\sigma}_0$, $\boldsymbol{\alpha}(t_0) = \boldsymbol{\alpha}_0$

Output: incremental displacement $\boldsymbol{u}$, mass density ρ, Cauchy stress $\boldsymbol{\sigma}$, material state $\boldsymbol{\alpha}$

∗ initialize $n = 0$ and $t = t_0$;
∗ collect topological data required for mesh motion and transport;
while *number of time steps* $n \leq n_{\max}$ *resp. time* $t_n \leq T$ **do**
  begin Lagrangian Step – Section 6.3, Chapter 5, and Alg. 5.1
    re-initialize mass matrix $\boldsymbol{M}$ and stiffness matrix $\boldsymbol{K}$;
    compute effective loads $\boldsymbol{f}^{\text{ext}}_{n+1} - \boldsymbol{M}\bar{\boldsymbol{a}}$;
    set $\boldsymbol{u}^0_{n+1} = \boldsymbol{0}$;
    while *number of Newton iteration steps* $i \leq i_{\max}$ **do**
      begin *objective integration* – Sections 6.3.2 and 5.5, and Alg. 5.2
        compute corotated strain increment using $\boldsymbol{u}^i_{n+1}$;
        corotate stress $\boldsymbol{\sigma}^i_{n+1}$ and state variables $\boldsymbol{\alpha}_n$;
        ∗ integrate constitutive equation and compute material tangent;
        ∗ obtain $\boldsymbol{\sigma}^{i+1}_{n+1}$, $\boldsymbol{\alpha}_{n+1}$ by back-rotation to current configuration;
      compute $\boldsymbol{f}^{\text{int}}(\boldsymbol{u}^i_{n+1})$ and form vector of residuals $\boldsymbol{r}^i_{n+1}$ $(6.2.17)_2$;
      compute effective stiffness matrix $\boldsymbol{K}^i_{n+1} = \hat{\boldsymbol{K}}^i_{n+1}$ (5.4.27);
      solve $d\boldsymbol{u}^i_{n+1} = (\boldsymbol{K}^i_{n+1})^{-1}\boldsymbol{r}^i_{n+1}$ and update $\boldsymbol{u}^{i+1}_{n+1} = \boldsymbol{u}^i_{n+1} + d\boldsymbol{u}^i_{n+1}$;
      if *convergence criterion met* **then**
        exit;
      $i \leftarrow i + 1$;
    ∗ update mass density at quadrature points (Section 6.3.1);
    ∗ store ρ^-_{n+1}, $\boldsymbol{\sigma}^-_{n+1}$, $\boldsymbol{\alpha}^-_{n+1}$;
    ∗ update and store geometry $\boldsymbol{x}^-_{n+1} = \boldsymbol{x}_n + \boldsymbol{u}_{n+1}$;
    ∗ time update $t^-_{n+1} = t_n + \Delta t$;
  begin Mesh Motion Step – Section 6.4
    ∗ fix corner nodes and relocate boundary nodes (Alg. 6.3);
    ∗ loop mesh elements and evaluate element quality Q;
    ∗ **if** $Q < Q_{\min}$ **then** flag nodes of the element;
    ∗ relocate flagged internal nodes (Section 6.4.3 and Alg. 6.5);
    ∗ obtain and store smoothed geometry $\boldsymbol{x}^+_{n+1}$;
  begin Transport Step – Section 6.5
    ∗ gather elements affected by mesh motion step;
    ∗ advect ρ^-_{n+1}, $\boldsymbol{\sigma}^-_{n+1}$, $\boldsymbol{\alpha}^-_{n+1}$ by finite volume scheme (Alg. 6.6);
    ∗ obtain and store ρ^+_{n+1}, $\boldsymbol{\sigma}^+_{n+1}$, $\boldsymbol{\alpha}^+_{n+1}$;
  ∗ $n \leftarrow n + 1$ (time update $t_n \leftarrow t^+_{n+1}$);

The mass density is an additional variable in ALE methods. The mass matrix $\boldsymbol{M}$ is computed based on the mass density stored at the quadrature points and the geometry of the finite element model at time t_n associated with the beginning of the Lagrangian step. As no mass flux occurs during the interval $[t_n, t_{n+1}^-]$, the mass density is constant over that interval, that is, $\rho_{n+1}^- = \rho_n$.

Step 2: Smoothing of the Distorted Mesh

In the second solution step, referred to as the *mesh motion step*, the selected nodes of the finite element mesh are relocated with the intention to reduce the amount of element distortion occurred in the Lagrangian step. Suitable mesh smoothing or optimization techniques are applied that do not change the mesh topology. Basically, the mesh motion step provides the mesh velocity resp. relative velocity $\boldsymbol{w}$, which is the spatial velocity of the relative map $\Phi_t : \mathcal{R} \to \mathcal{S}$. The mesh velocity thus generates the time-dependent flow $\Phi_t \circ \Phi_s^{-1} : \Phi_s(\mathcal{R}) \to \Phi_t(\mathcal{R}) \subset \mathcal{S}$, for all $t, s \in [t_0, T]$; see Section 3.1.

Definition 6.2.19. In ordinary $\mathbb{R}^{m_{\text{dim}}}$, the *mesh flow* or *incremental mesh motion over the time step* $\Delta t = t_{n+1}^+ - t_n$ is defined through

$$\Phi_{n+1}^+ \circ \Phi_n^{-1} : \quad \Phi_n(\mathcal{R}) \to \Phi_{n+1}^+(\mathcal{R}) \subset \mathbb{R}^{m_{\text{dim}}}$$
$$\boldsymbol{x}_n \mapsto \boldsymbol{x}_{n+1}^+ = \boldsymbol{x}_n + \int_{t_n}^{t_{n+1}^+} \boldsymbol{w} \, \mathrm{d}t \, ,$$

in which $\Phi_{n+1}^+(\mathcal{R}) \stackrel{\text{def}}{=} \Phi(\mathcal{R}, t_{n+1}^+)$ is the mesh configuration at time t_{n+1}^+, and $\Phi_n(\mathcal{R}) = \mathcal{R}$ is the configuration of the mesh at time t_n, the beginning of the Lagrangian step (Fig. 6.1). The incremental mesh flow is required to be a homeomorphism, that is, a bijective and continuous map between $\Phi_n(\mathcal{R})$ and $\Phi_{n+1}^+(\mathcal{R})$ which preserves topology of the mesh. $\boldsymbol{x}_{n+1}^+$ is the position vector of the point $x_{n+1}^+ \stackrel{\text{def}}{=} \Phi_{n+1}^+(\Phi_n^{-1}(x_n))$. In the ALE finite element treatment, $\boldsymbol{x}_{n+1}^+$ denotes the location of a node at time t_{n+1}^+, and the totality of all $\boldsymbol{x}_{n+1}^+$ represents the mesh configuration after the mesh motion step.$\diamond$

The calculation of the discrete mesh velocity $\boldsymbol{w}$ over Δt from $\int_{t_n}^{t_{n+1}^+} \boldsymbol{w} \, \mathrm{d}t = \boldsymbol{x}_{n+1}^+ - \boldsymbol{x}_n$ is not obvious. The intuitive definition, which has been naturally used by several investigators, employs a finite difference approximation:

$$\boldsymbol{w}_{n+1} \stackrel{\text{def}}{=} \frac{\boldsymbol{x}_{n+1}^+ - \boldsymbol{x}_n}{\Delta t} \, . \tag{6.2.20}$$

Step 3: Remap Onto the Updated Mesh

In the *transport step*, which is the last step of each calculational cycle of the operator-split ALE solution procedure, the mass density, momentum, Cauchy stress, and the material state variables obtained after the Lagrangian step are remapped onto the updated mesh according to the equations (6.2.10). Momentum transport is not necessary because only quasi-static problems are considered. Since no physical time is associated with the transport step, the transport constitutes an instantaneous projection

(remap) of the solution variables from the old mesh $\Phi(\mathcal{R}, t^-_{n+1})$ onto the modified mesh $\Phi(\mathcal{R}, t^+_{n+1})$:

$$\{J^-_{n+1},\, \boldsymbol{\sigma}^-_{n+1},\, \boldsymbol{\alpha}^-_{n+1}\}\Big|_{\Phi(\mathcal{R},t^-_{n+1})} \longrightarrow \{J^+_{n+1},\, \boldsymbol{\sigma}^+_{n+1},\, \boldsymbol{\alpha}^+_{n+1}\}\Big|_{\Phi(\mathcal{R},t^+_{n+1})} , \tag{6.2.21}$$

in which the Jacobian J is related to the mass density ρ by Proposition 3.2.18(i), that is, $\rho = \rho_{\text{ref}} J^{-1}$. The remap (6.2.21) is generally a function of the two mesh configurations $\Phi^-_{n+1}(\mathcal{R})$ and $\Phi^+_{n+1}(\mathcal{R})$ before and after the mesh motion step. However, time and geometry are kept fixed during the transport step. Therefore, the transport step can be regarded a pseudo-Eulerian calculation using the convective velocity $\boldsymbol{c}$.

Proposition 6.2.22. *In quasi-static analysis the convective velocity over the time step* $\Delta t = t_{n+1} - t_n$ *is*

$$\boldsymbol{c}_{n+1} = \frac{\boldsymbol{x}^-_{n+1} - \boldsymbol{x}^+_{n+1}}{\Delta t} .$$

Proof. By (6.2.18) and (6.2.20) in conjunction with (6.1.2). ∎

The construction of the projection (6.2.21) governed by the set of equations (6.2.10) can be based on the fact that the mesh topology does not change, and that elements have the same neighbors during the entire solution process. In this case, methods proposed by the computational fluid dynamics community can be employed in order to implement projections with highly desirable properties.

Remark 6.2.23. Equilibrium of the finite element system iterated during the Lagrangian step will be somewhat disrupted depending on the accuracy of the transport step. However, investigations showed that the spurious residual forces related to the transport step are small and practically do not affect solution quality [Rodríguez-Ferran et al., 1998]. Moreover, any discrepancy present is naturally resolved during the next Lagrangian step. △

Remark 6.2.24. If the convective velocity is computed from 6.2.22, it can likewise be interpreted as the negative mesh velocity over the pseudo time interval $[t^-_{n+1}, t^+_{n+1}]$ elapsing during the transport step. On occasion this viewpoint would be more convenient. △

6.3 Lagrangian Step

Without any additional storage, the material motion is known only for the short time duration of the Lagrangian step in an operator-split ALE method. That is, even though the operator-split defines a purely Lagrangian step, in which mass conservation is automatically satisfied, this step relies on the current and not on a past configuration. Therefore, once balance of momentum $(6.2.11)_2$ resp. (6.2.17) has been solved for the incremental displacements, incremental procedures must update the stress, the material state, the mass density, and any other variable associated with material motion that needs to be known. The specific definitions and results of Section 5.5 are employed. The time associated with the end of the Lagrangian step is t^-_{n+1} defined through 6.2.14. However, in order to ease notation the superscripted "$-$" will be suppressed.

6.3.1 Evolution of Mass Density

While changes in mass density along with deformation of metals and other materials are often regarded negligible, they play a crucial role in soil mechanics and the mechanics of granular material. The mass density of a sand specimen, for example, is closely related to its void ratio (cf. Section 4.2). The void ratio, on the other hand, constitutes an essential internal state variable when it comes to realistic modeling of the mechanical behavior of sand. In cases where the mesh and material motions are uncoupled, as in the Eulerian and ALE finite element methods, mass of the system in generally not conserved. Hence, $(6.2.9)_1$ or equivalently (6.2.5) must be integrated over the time increment $[t_n, t_{n+1}]$ in the Lagrangian step. Clearly, a solution is required to the initial value problem

$$\dot{J}(x,t) = J(x,t)\,\mathrm{tr}\,\boldsymbol{d}(x,t)\,, \qquad \text{subject to} \quad J(x,t_n) = J_n(x) \tag{6.3.1}$$

for all $t \in [t_n, t_{n+1}]$. Recall that $\mathrm{tr}\,\boldsymbol{d} = \mathrm{div}\,\boldsymbol{v}$. In order to simplify the notation, $J(x,t)$ is written here in place of the correct $(J \circ \varphi^{-1})(\Phi(\chi,t),t) = (J \circ \Psi)(\chi,t)$, with $x = \Phi(\chi,t)$, and $\chi \in \mathcal{R}$ denoting the reference points.

Different procedures have been implemented into the ALE method in order to integrate the rate of the Jacobian over the time increment $[t_n, t_{n+1}]$. Consider an approximation to the solution at time t_{n+1} by the generalized midpoint rule (A.3.6):

$$J_{n+1} \overset{\text{def}}{=} J_n + \Delta J_{n+\theta}\,, \qquad \text{with} \quad \theta \in [0,1]\,. \tag{6.3.2}$$

The increment $\Delta J_{n+\theta}$ generally depends on variables taken with respect to a configuration

$$\varphi_{n+\theta}(\mathcal{B}) = \theta\varphi_{n+1}(\mathcal{B}) + (1-\theta)\varphi_n(\mathcal{B})\,, \tag{6.3.3}$$

which linearly interpolates $\varphi_n(\mathcal{B})$ and $\varphi_{n+1}(\mathcal{B})$, see Section 5.5.1. By the evolution equation $(6.3.1)_1$ and Definition 5.5.11, the increment of the Jacobian over the time step can be approximated through

$$\Delta J_{n+\theta} = J_{n+\theta}\,\mathrm{tr}(\boldsymbol{d}_{n+\theta}\Delta t) = J_{n+\theta}\,\mathrm{tr}\Delta\tilde{\boldsymbol{e}}_{n+\theta}\,, \tag{6.3.4}$$

where $\Delta\tilde{\boldsymbol{e}}_{n+\theta}$ denotes the algorithmic finite strain increment, and

$$J_{n+\theta} = \theta J_{n+1} + (1-\theta)J_n\,, \tag{6.3.5}$$

in accordance with (6.3.3). Substitution into (6.3.2) then gives

$$J_{n+1} = J_n\,(1 - \theta\,\mathrm{tr}\Delta\tilde{\boldsymbol{e}}_{n+\theta})^{-1}(1 + (1-\theta)\mathrm{tr}\Delta\tilde{\boldsymbol{e}}_{n+\theta})\,. \tag{6.3.6}$$

The purely explicit ($\theta = 0$) and implicit ($\theta = 1$) procedures are special cases of (6.3.6), but they result in a first-order approximation to the Jacobian at time t_{n+1}. Therefore, if displacement increments grow larger, the quality of the approximation deteriorates. A formally second-order approximation can be achieved by the midpoint rule, i.e. by setting $\theta = \frac{1}{2}$ in (6.3.6), so that

$$J_{n+1} = J_n\,(1 - \tfrac{1}{2}\,\mathrm{tr}\Delta\tilde{\boldsymbol{e}}_{n+1/2})^{-1}(1 + \tfrac{1}{2}\,\mathrm{tr}\Delta\tilde{\boldsymbol{e}}_{n+1/2})\,. \tag{6.3.7}$$

Here $\Delta\tilde{\boldsymbol{e}}_{n+1/2}$ is the midpoint strain increment determined from (5.5.12), which is a second-order approximation to the finite strain increment (5.5.5). A proof can be found in [Hughes, 1984, p. 49].

Recall that for any proper orthogonal transformation $\mathfrak{R}$, the principle invariants of the corotated rate of deformation tensor, $\mathfrak{R}^{\star}\boldsymbol{d}$, are identical to those of $\boldsymbol{d}$. In particular, $\operatorname{tr}\boldsymbol{d} = \operatorname{tr}(\mathfrak{R}^{\star}\boldsymbol{d})$ holds. Therefore, by noting that the Jacobian likewise is an honest scalar not affected by rotations, the formulas above apply without changes if the rate of the Jacobian is to be integrated in a corotated description (Alg. 5.2). In this case, (6.3.7) is replaced with the equivalent formula

$$J_{n+1} = J_n \left(1 - \tfrac{1}{2}\operatorname{tr}\Delta\mathfrak{E}_{n+1/2}\right)^{-1}\left(1 + \tfrac{1}{2}\operatorname{tr}\Delta\mathfrak{E}_{n+1/2}\right), \tag{6.3.8}$$

where $\Delta\mathfrak{E}_{n+1/2}$ is the corotated midpoint strain increment.

6.3.2 Evolution of Stress and Material State

The evaluation of the new stress and material state within the Lagrangian step is carried out by integrating $(6.2.11)_3$ over the time step $[t_n, t_{n+1}]$, where $t_{n+1} = t_n + \Delta t$. While Section 5.5 describes the stress and material state update rather generally, the present section provides more details on the integration of the hypoplastic model for sand (Section 4.3). Concerning integration of the hypoelastic model of grade zero (4.1.23) and the hypoelasto-J_2-plastic model with linear isotropic hardening (Section 4.1.3), which have also been implemented by the author into the ALE framework, the reader is referred to [Hughes, 1984] for details.

As the ALE framework was intended to be added to the commercial FE code ANSYS®, the stress and material state update must fit to the objective integration algorithm 5.2 [XANSYS Mailing List, 2004]. According to this algorithm, all variables are transformed to the virtually corotated (or unrotated) configuration of the material body, i.e. to the $\mathfrak{R}$-system associated with the corotational stress rate used. After rotation, the rate constitutive equation is integrated in the corotating system by common methods, and then rotated back to the current configuration of the body.

Hypoplastic Model for Isotropic Sand

The current ALE finite element framework can account for isotropic sand response at large deformations under monotonic and cyclic loading by providing the hypoplastic model with the intergranular strain concept introduced in Section 4.3. This spatial rate constitutive equation specifies the Cauchy stress $\boldsymbol{\sigma}$, the void ratio e, and the a so-called intergranular strain $\boldsymbol{\delta}$ as internal state variables, and prescribes response functions for their objective rates. In the Lagrangian step of the operator-split ALE solution procedure (cf. Section 6.1), these evolution equations are given by

$$\mathring{\boldsymbol{\sigma}}^{\mathrm{ZJ}} = \boldsymbol{m}(\boldsymbol{\sigma}, \boldsymbol{g}, e, \boldsymbol{\delta}) : \boldsymbol{d}\,, \qquad \dot{e} = (1+e)\operatorname{tr}\boldsymbol{d}\,, \qquad \text{and} \quad \mathring{\boldsymbol{\delta}}^{\mathrm{ZJ}} = \boldsymbol{j}(\boldsymbol{\delta}, \boldsymbol{g}, \boldsymbol{d})\,, \tag{6.3.9}$$

respectively, where values of $\boldsymbol{m}(\boldsymbol{\sigma}, \boldsymbol{g}, e, \boldsymbol{\delta})$ represent the material tangent tensor prescribed by (4.3.22), and $\boldsymbol{j}(\boldsymbol{\delta}, \boldsymbol{g}, \boldsymbol{d})$ takes the form of (4.3.18). Indeed, Cauchy stress associated with sand is the effective stress in terms of (4.2.6), thus $\boldsymbol{\sigma} \stackrel{\text{def}}{=} \boldsymbol{\sigma}'$ being understood in this section. Moreover, $\boldsymbol{\sigma} \stackrel{\text{def}}{=} \boldsymbol{\sigma}^\sharp$, $\boldsymbol{d} \stackrel{\text{def}}{=} \boldsymbol{d}^\flat$, and $\boldsymbol{\delta} \stackrel{\text{def}}{=} \boldsymbol{\delta}^\flat$ as usual.

Eq. (6.3.9) subject to the initial condition $\{\boldsymbol{\sigma}, e, \boldsymbol{\delta}\}|_{t=t_n} = \{\boldsymbol{\sigma}_n, e_n, \boldsymbol{\delta}_n\}$ phrases an initial value problem. The evolution equations of the stress and the state variables have to be integrated over the incremental time interval $[t_n, t_{n+1}]$ both simultaneously and objectively. Let time be discretized such that $t_{n+1} = t_n + \Delta t$. Application of the general objective integration algorithm 5.2 in combination with the generalized midpoint rule (A.3.6) then results in the following set of equations:

$$\begin{aligned} \boldsymbol{\sigma}_{n+1} &= \boldsymbol{\mathfrak{R}}_{n+1} \cdot (\boldsymbol{\mathfrak{S}}_n + \Delta\boldsymbol{\mathfrak{S}}_{n+\theta}) \cdot \boldsymbol{\mathfrak{R}}_{n+1}^{\mathrm{T}} \,, \\ e_{n+1} &= e_n + \Delta e_{n+\theta} \,, \\ \boldsymbol{\delta}_{n+1} &= \boldsymbol{\mathfrak{R}}_{n+1} \cdot (\boldsymbol{\mathfrak{H}}_n + \Delta\boldsymbol{\mathfrak{H}}_{n+\theta}) \cdot \boldsymbol{\mathfrak{R}}_{n+1}^{\mathrm{T}} \,. \end{aligned} \tag{6.3.10}$$

The input variables to the integration algorithm include the corotated stress $\boldsymbol{\mathfrak{S}}_{n+\theta} = \boldsymbol{\mathfrak{R}}_{n+\theta}^{\mathrm{T}} \cdot \boldsymbol{\sigma}_{n+\theta} \cdot \boldsymbol{\mathfrak{R}}_{n+\theta}$, the corotated intergranular strain $\boldsymbol{\mathfrak{H}}_n \stackrel{\text{def}}{=} \boldsymbol{\mathfrak{R}}_n^\star \boldsymbol{\delta}_n = \boldsymbol{\mathfrak{R}}_n^{\mathrm{T}} \cdot \boldsymbol{\delta}_n \cdot \boldsymbol{\mathfrak{R}}_n$, and the void ratio e_n, all at time $t = t_n$, as well as the corotated midpoint strain increment given by (5.5.18). Recall that, since the void ratio is an honest scalar, rotation does not affect e_{n+1}. The procedures implemented in the ALE framework to evaluate $\boldsymbol{\mathfrak{S}}_{n+1}$, e_{n+1}, and $\boldsymbol{\mathfrak{H}}_{n+1}$ are presented next.

The forward Euler method is currently used for the explicit stress update [cf. Nübel and Niemunis, 1999], so $\theta = 0$ in $(6.3.10)_1$ being understood. In order to retain stability of the algorithm, the time increment is divided into constant subincrements defined through $dt \stackrel{\text{def}}{=} \Delta t / m_{\text{sub}}$, $m_{\text{sub}} \geq 1$. Estimates for m_{sub} resp. dt are presented below. The corotated midpoint strain increment is constant in time over the increment and assumed to be given. Therefore, it can be expressed as the sum

$$\Delta\boldsymbol{\mathfrak{E}}_{n+1/2} = \sum_{m_{\text{sub}}} d\boldsymbol{\mathfrak{E}}_{n+1/2} \,, \qquad \text{where} \quad d\boldsymbol{\mathfrak{E}}_{n+1/2} \stackrel{\text{def}}{=} m_{\text{sub}}^{-1} \, \Delta\boldsymbol{\mathfrak{E}}_{n+1/2} \,. \tag{6.3.11}$$

The stress at the $(i+1)$-th subincrement in $[t_n, t_{n+1}]$ is given by

$$\boldsymbol{\mathfrak{S}}_{n+1}^{i+1} = \boldsymbol{\mathfrak{S}}_{n+1}^{i} + d\boldsymbol{\mathfrak{S}}_{n+1}^{i} = \boldsymbol{\mathfrak{S}}_n + \Delta\boldsymbol{\mathfrak{S}}_n^i \,, \qquad \text{in which} \quad \Delta\boldsymbol{\mathfrak{S}}_n^i \stackrel{\text{def}}{=} \sum_{k=0}^{i} d\boldsymbol{\mathfrak{S}}_{n+1}^k \,, \tag{6.3.12}$$

and $i \in \{0, \ldots, m_{\text{sub}} - 1\} \subset \mathbb{N}$. The substepping procedure is initialized by $\boldsymbol{\mathfrak{S}}_{n+1}^{i=0} = \boldsymbol{\mathfrak{S}}_n$ and it closes by setting $\boldsymbol{\mathfrak{S}}_{n+1} = \boldsymbol{\mathfrak{S}}_{n+1}^{m_{\text{sub}}}$. Since stress update is explicit, the hypoplastic stress subincrement can be determined from

$$d\boldsymbol{\mathfrak{S}}_{n+1}^i = \boldsymbol{m}(\boldsymbol{\mathfrak{S}}_{n+1}^i, \boldsymbol{\mathfrak{G}}_{n+1}^i, e_{n+1}^i, \boldsymbol{\mathfrak{H}}_{n+1}^i) : d\boldsymbol{\mathfrak{E}}_{n+1/2} \,. \tag{6.3.13}$$

By isotropy of the function $\boldsymbol{m}$, the particular expression (4.3.22) of $\boldsymbol{m}(\boldsymbol{\sigma}, \boldsymbol{g}, e, \boldsymbol{\delta})$ is functionally identical to that of $\boldsymbol{m}(\boldsymbol{\mathfrak{S}}_{n+1}^i, \boldsymbol{\mathfrak{G}}_{n+1}^i, e_{n+1}^i, \boldsymbol{\mathfrak{H}}_{n+1}^i)$. A small amount of artificial capillary pressure p_{c} can be subtracted from the stress state $\boldsymbol{\mathfrak{S}}_{n+1}^i$ in order to improve

the stability of stress integration at very low mean effective stress levels. In this case, (6.3.13) becomes

$$d\mathfrak{S}^i_{n+1} = \boldsymbol{m}(\bar{\mathfrak{S}}^i_{n+1}, \mathfrak{G}^i_{n+1}, e^i_{n+1}, \mathfrak{H}^i_{n+1}) : d\mathfrak{E}_{n+1/2}\,, \tag{6.3.14}$$

where $\bar{\mathfrak{S}}^i_{n+1} \overset{\text{def}}{=} \mathfrak{S}^i_{n+1} - p_{\text{c}}\boldsymbol{I}$.

It can be seen from (6.3.13) resp. (6.3.14) that evaluation of the hypoplastic stress subincrement $d\mathfrak{S}^i_{n+1}$ requires not only the current corotated stress state $\mathfrak{S}^i_{n+1}$ but also the corotated spatial metric, $\mathfrak{G}_{n+\theta}$, the void ratio e^i_{n+1}, as well as the corotated intergranular strain $\mathfrak{H}^i_{n+1}$ of the i-th subincrement. The corotated spatial metric must be passed to the integration algorithm in case where tensor invariants or vector norms need to be computed with respect to curvilinear coordinate systems. However, evaluation of the metric is trivial if global Cartesian coordinates would be used because then, $\mathfrak{G}^i_{n+1} = \boldsymbol{I}$.

As discussed in Section 4.2, the void ratio constitutes an essential internal state variable of sand and granular material when it comes to realistic modeling of its mechanical behavior. Hence, the accuracy of the numerical procedure that integrates the initial value problem

$$\dot{e}(x,t) = (1 + e(x,t))\,\mathrm{tr}\,\boldsymbol{d}(x,t)\,, \qquad \text{subject to} \quad e(x,t_n) = e_n(x) \tag{6.3.15}$$

for all $t \in [t_n, t_{n+1}]$, where $x = \Phi(\chi, t)$ are the current locations of the reference points $\chi \in \mathcal{R}$, plays an important role.

Consider a subincremental decomposition of the the void ratio which is again compatible with stress substepping (6.3.12). Then, application of the generalized midpoint rule yields

$$e^{i+1}_{n+1} \overset{\text{def}}{=} e^i_{n+1} + de^{i+\theta}_{n+1} = e_n + \Delta e^i_{n+\theta}\,, \qquad \text{where} \quad \Delta e^i_{n+\theta} \overset{\text{def}}{=} \sum_{k=0}^{i} de^{k+\theta}_{n+1}\,, \tag{6.3.16}$$

$i \in \{0, \ldots, m_{\text{sub}} - 1\}$, and $\theta \in [0, 1]$. In order to reduce the amount of symbols, the superscript indicating the subincrement is suppressed in the following. The increment $\Delta e_{n+\theta}$ generally depends on variables taken with respect to an intermediate configuration of the body, as defined in Section 5.5.1. By the evolution equation of the void ratio $(6.3.15)_1$, the increment of the void ratio constant over the time step can be approximated through

$$\Delta e_{n+\theta} = (1 + e_{n+\theta})\,\mathrm{tr}\Delta\tilde{\boldsymbol{e}}_{n+1/2} = (1 + e_{n+\theta})\,\mathrm{tr}\Delta\mathfrak{E}_{n+1/2}\,, \tag{6.3.17}$$

where $e_{n+\theta} = \theta e_{n+1} + (1-\theta)e_n$ by the generalized midpoint rule. Choosing $\theta = \frac{1}{2}$ represents the midpoint rule which, after some algebraic manipulation, yields the second-order formula

$$e_{n+1} = (1 - \tfrac{1}{2}\,\mathrm{tr}\Delta\mathfrak{E}_{n+1/2})^{-1}((1 + \tfrac{1}{2}\,\mathrm{tr}\Delta\mathfrak{E}_{n+1/2})\,e_n + \mathrm{tr}\Delta\mathfrak{E}_{n+1/2})\,. \tag{6.3.18}$$

The update of integranular strain is governed by $(6.3.10)_3$. Explicit and implicit procedures are available to integrate intergranular strain in the corotated description. The

local integration procedures split the time increment $\Delta t = t_{n+1} - t_n$ of global time integration into m_{sub} equal subincrements $dt = \Delta t / m_{\text{sub}}$. The time at the end of the i-th subincrement, where $i \in \{0, \dots, m_{\text{sub}} - 1\} \subset \mathbb{N}$, is then defined through

$$t^i_{n+1} \overset{\text{def}}{=} t_n + \tfrac{i}{m_{\text{sub}}} \Delta t = t_n + i\, dt\,, \tag{6.3.19}$$

with $t^{i=0}_{n+1} = t_n$ and $t_{n+1} = t^{m_{\text{sub}}}_{n+1}$. Subincrements of corotated intergranular strain, stress, and void ratio are required to be compatible. By the generalized midpoint rule, then, the corotated intergranular strain at the $(i+1)$-th subincrement can be expressed as

$$\mathfrak{H}^{i+1}_{n+1} \overset{\text{def}}{=} \mathfrak{H}^i_{n+1} + d\mathfrak{H}^{i+\theta}_{n+1} = \mathfrak{H}_n + \Delta\mathfrak{H}^i_{n+\theta}\,, \qquad \text{in which} \quad \Delta\mathfrak{H}^i_{n+\theta} \overset{\text{def}}{=} \sum_{k=0}^{i} d\mathfrak{H}^{k+\theta}_{n+1}\,. \tag{6.3.20}$$

The subincrement $d\mathfrak{H}^{i+\theta}_{n+1}$ generally depends on variables taken with respect to the configuration of the body at a conceptual intermediate time

$$t^{i+\theta}_{n+1} \overset{\text{def}}{=} \theta t^{i+1}_{n+1} + (1-\theta) t^i_{n+1} = t_n + (i+\theta) dt = t_n + \tfrac{i+\theta}{m_{\text{sub}}} \Delta t\,, \tag{6.3.21}$$

where $\theta \in [0, 1]$. Recall that configurations of the body have been determined only at times t_n and $t_{n+1} = t_n + \Delta t$ through time integration of the global initial boundary value problem; cf. Section 5.4.2. Therefore, the intermediate configuration at time $t^{i+\theta}_{n+1} \in [t_n, t_{n+1}]$ is defined by the linear interpolation

$$\varphi^{i+\theta}_{n+1}(\mathcal{B}) \overset{\text{def}}{=} \tfrac{i+\theta}{m_{\text{sub}}}\, \varphi_{n+1}(\mathcal{B}) + \left(1 - \tfrac{i+\theta}{m_{\text{sub}}}\right) \varphi_n(\mathcal{B})\,. \tag{6.3.22}$$

For the choice $\theta = 0$, integration over subincrements is carried out explicitly, whereas $\theta = 1$ gives an implicit integration algorithm. At $i = 0$ and $i + 1 = m_{\text{sub}}$ one sets $\mathfrak{H}^{i=0}_{n+1} = \mathfrak{H}_n$ and $\mathfrak{H}_{n+1} = \mathfrak{H}^{m_{\text{sub}}}_{n+1}$, respectively.

The explicit integration algorithm for intergranular strain, which stipulates $\theta = 0$ in (6.3.20), is based on a forward Euler approximation of its rate according to (A.3.3). This is similar to the explicit stress update algorithm, in which the hypoplastic stress subincrement is determined from (6.3.13). Therefore, by considering the evolution equation for intergranular strain, $(6.3.9)_2$, and noting that the function $\boldsymbol{j}$, by (4.3.18), is isotropic in all arguments, one has

$$d\mathfrak{H}^i_{n+1} = \boldsymbol{j}(\mathfrak{H}^i_{n+1}, \mathfrak{G}^i_{n+1}, \mathfrak{D}_{n+1/2})\, dt \overset{\text{def}}{=} \tilde{\boldsymbol{j}}(\mathfrak{H}^i_{n+1}, \mathfrak{G}^i_{n+1}, d\mathfrak{E}_{n+1/2})\,, \tag{6.3.23}$$

where $d\mathfrak{E}_{n+1/2} = \mathfrak{D}_{n+1/2}\, dt$, and $\mathfrak{D}_{n+1/2} = \mathfrak{R}^{\mathrm{T}}_{n+1/2} \cdot \boldsymbol{d}_{n+1/2} \cdot \mathfrak{R}_{n+1/2}$ is the corotated rate of deformation tensor associated with the midpoint configuration. An explicit procedure is also employed for sudden changes in loading direction, at which $\tilde{\boldsymbol{\delta}}^\sharp : \boldsymbol{d} \leq 0$ holds and $(4.3.18)_2$ applies:

$$\mathfrak{H}^{i+1}_{n+1} = \mathfrak{H}^i_{n+1} + d\mathfrak{H}^i_{n+1}\,, \qquad \text{with} \quad d\mathfrak{H}^i_{n+1} = d\mathfrak{E}_{n+1/2}\,. \tag{6.3.24}$$

Because of the strong nonlinearity of the response function of integranular strain rate, (4.3.18), and due to the fact that the forward Euler method is only conditionally stable,

an implicit integration procedure has been developed for the case where $\tilde{\boldsymbol{\delta}}^{\sharp} : \boldsymbol{d} > 0$, with $\tilde{\boldsymbol{\delta}} = \boldsymbol{\delta}/\|\boldsymbol{\delta}\|$ [cf. Niemunis, 2003, p. 106]. The type of loading associated with this condition is handled by Eq. $(4.3.18)_1$, which can be written as

$$\mathring{\boldsymbol{\delta}}^{\mathrm{ZJ}} = \boldsymbol{j}(\boldsymbol{\delta}, \boldsymbol{g}, \boldsymbol{d}) = \left(\mathbf{1} - \rho^{\beta_\mathrm{r}}\, \tilde{\boldsymbol{\delta}} \otimes \tilde{\boldsymbol{\delta}}\right) : \boldsymbol{d} \tag{6.3.25}$$

where $\mathbf{1}$ is the fourth-order symmetric identity tensor, $\rho = \|\boldsymbol{\delta}\|/R$, and both β_r and R are material constants. The operators indicating tensor index raising and lowering have been suppressed for brevity. In consideration of (6.3.20) and $\theta = 1$, which corresponds to the backward Euler scheme (A.3.5), the incrementally objective approximation to (6.3.25) in the corotated description takes the form

$$d\mathfrak{H}^{i+1}_{n+1} = \left(\mathbf{1} - \frac{\rho^{\beta_\mathrm{r}}}{\|\mathfrak{H}^{i+1}_{n+1}\|^2}\, \mathfrak{H}^{i+1}_{n+1} \otimes \mathfrak{H}^{i+1}_{n+1}\right) : d\mathfrak{E}_{n+1/2}\ , \tag{6.3.26}$$

where $\rho^{\beta_\mathrm{r}} = f(\mathfrak{H}^{i+1}_{n+1}, \mathfrak{E}^{i+1}_{n+1})$, and $\mathfrak{H}^{i+1}_{n+1}$ being the only unknown. Accordingly, (6.3.26) can be written as

$$d\mathfrak{H}^{i+1}_{n+1} = \boldsymbol{f}(\mathfrak{H}^{i+1}_{n+1}) : d\mathfrak{E}_{n+1/2}\ , \tag{6.3.27}$$

in which

$$\boldsymbol{f}(\mathfrak{H}^{i+1}_{n+1}) \overset{\mathrm{def}}{=} \mathbf{1} - \frac{\rho^{\beta_\mathrm{r}}}{\|\mathfrak{H}^{i+1}_{n+1}\|^2}\, \mathfrak{H}^{i+1}_{n+1} \otimes \mathfrak{H}^{i+1}_{n+1}\ . \tag{6.3.28}$$

The function $\boldsymbol{f}$ is fourth-order tensor-valued, symmetric, isotropic and nonlinear in $\mathfrak{H}$.

Note that (6.3.27) cannot be solved in closed-form because $\boldsymbol{f}(\mathfrak{H}^{i+1}_{n+1})$ implicitly depends on $d\mathfrak{H}^{i+1}_{n+1}$ through $\mathfrak{H}^{i+1}_{n+1} = \mathfrak{H}^{i}_{n+1} + d\mathfrak{H}^{i+1}_{n+1}$. Let $\boldsymbol{f}$ be Fréchet-differentiable at $\mathfrak{H}^{i}_{n+1}$, then the linearization of $\boldsymbol{f}(\mathfrak{H}^{i+1}_{n+1})$ about $\mathfrak{H}^{i}_{n+1}$ results in

$$\boldsymbol{f}(\mathfrak{H}^{i+1}_{n+1}) \approx \boldsymbol{f}(\mathfrak{H}^{i}_{n+1}) + D\boldsymbol{f}^{i}_{n+1} : d\mathfrak{H}^{i+1}_{n+1}\,, \qquad \text{where} \quad D\boldsymbol{f}^{i}_{n+1} = \frac{\partial \boldsymbol{f}(\mathfrak{H}^{i}_{n+1})}{\partial \mathfrak{H}^{i}_{n+1}}\,. \tag{6.3.29}$$

Substitution in (6.3.27) and rearrangement then yields the closed-form expression

$$d\mathfrak{H}^{i+1}_{n+1} = \left(\mathbf{1} - D\boldsymbol{f}^{i}_{n+1} : d\mathfrak{E}_{n+1/2}\right)^{-1} : \boldsymbol{f}(\mathfrak{H}^{i}_{n+1}) : d\mathfrak{E}_{n+1/2}\ . \tag{6.3.30}$$

It remains to estimate the number of subincrements, $m_{\mathrm{sub}} = \Delta t/dt$, used for substepping integration of the hypoplastic model. Two cases are distinguished, depending on whether the intergranular strain extension (see Section 4.3.2) is activated or not [Nübel and Niemunis, 1999]. If intergranular strain is inactive, the hypoplastic rate constitutive equation reduces to the reference model introduced in Section 4.3.1. In this case, the number of subincrements is defined as a function of the norm of the strain increment through

$$m_{\mathrm{sub}} = \mathrm{sub}_1\,, \qquad \text{where} \quad \mathrm{sub}_1 \overset{\mathrm{def}}{=} \max\left(\mathrm{nint}\left(\frac{\|\Delta\mathfrak{E}_{n+1/2}\|}{a}\right), 1\right), \tag{6.3.31}$$

and $a > 0$; $a = 0.0001$ as been chosen for the numerical examples in Chapter 8. The function $\mathrm{nint}(\cdot)$ returns the nearest integer to its argument, and $\max(\cdot,\cdot)$ returns the maximum of the two arguments.

Special estimates of the number of subincrements are used in the second case where intergranular strain, $\boldsymbol{\delta}$, is activated, i.e. when the fully-fledged hypoplastic rate constitutive equation introduced in Section 4.3.2 is employed; cf. [Niemunis, 2003, pp. 105–106] and [Nübel and Niemunis, 1999]. The estimates depend on the norm of intergranular strain, on the relative loading direction $\boldsymbol{\delta} : \boldsymbol{d} = \mathfrak{H} : \mathfrak{D}$, and on the material constants R and β_{r}. In particular, define

$$\mathrm{sub}_2 \overset{\mathrm{def}}{=} \begin{cases} \max\left(\mathrm{sub}_1\,,\ \mathrm{nint}\left(\left|\frac{1-\rho^{\beta_{\mathrm{r}}}}{0.1R}\right| \|\Delta\mathfrak{E}_{n+1/2}\|\right)\right) & \text{for } \mathfrak{H} : \mathfrak{D} > 0 \text{ and } \rho < 1\,, \\ \mathrm{sub}_1 & \text{for } \mathfrak{H} : \mathfrak{D} > 0 \text{ and } \rho \geq 1\,, \\ \mathrm{sub}_{\max} \overset{\mathrm{def}}{=} \mathrm{nint}\left(\frac{1}{\mu R}\|\Delta\mathfrak{E}_{n+1/2}\|\right)\,,\ 0 < \mu < 1 & \text{for } \mathfrak{H} : \mathfrak{D} \leq 0\,. \end{cases} \tag{6.3.32}$$

Note that the condition $\mathfrak{H} : \mathfrak{D} > 0$ (resp. $\mathfrak{H} : \mathfrak{D} \leq 0$) is equivalent to the condition employed in (4.3.18), $\tilde{\boldsymbol{\delta}} : \boldsymbol{d} > 0$ (resp. $\tilde{\boldsymbol{\delta}} : \boldsymbol{d} \leq 0$), with $\tilde{\boldsymbol{\delta}} = \boldsymbol{\delta}/\|\boldsymbol{\delta}\|$. The meaning of these and the conditions $\rho < 1$ and $\rho \geq 1$ is illustrated in Section 4.3.2. Recall from Section 4.3.2 that the scalar $\rho = \|\boldsymbol{\delta}\|/R = \|\mathfrak{H}\|/R$ denotes the normalized magnitude of intergranular strain, R represents the norm of maximum intergranular strain, and β_{r} is an exponent that controls the rate of $\boldsymbol{\delta}$. The choice $\mu = 0.1$ to the parameter in $(6.3.32)_3$ is used throughout, but $\mu = 0.2$ also worked fine [Niemunis, 2003, p. 106].

The estimate sub_2 is a function only of ρ, R and β_{r}, but not of the relative loading direction $\mathfrak{H} : \mathfrak{D}$. In order to modify the number of substeps with respect to the relative loading direction, let

$$\mathrm{sub}_3 \overset{\mathrm{def}}{=} \mathrm{nint}\left(\frac{\Delta t}{dt'}\right)\,, \tag{6.3.33}$$

and define dt', representing an estimate of substep size, through

$$dt' \overset{\mathrm{def}}{=} \begin{cases} \frac{\Delta t}{\mathrm{sub}_{\max}} + \frac{\mathrm{sub}_{\max} - \mathrm{sub}_2}{\mathrm{sub}_2\,\mathrm{sub}_{\max}\|\mathfrak{H}_n\|\,\|\Delta\mathfrak{E}_{n+1/2}\|}\mathfrak{H}_n : \Delta\mathfrak{E}_{n+1/2} & \text{for } \mathfrak{H} : \mathfrak{D} \geq 0 \text{ and } \rho > 0\,, \\ \frac{\Delta t}{\mathrm{sub}_2} & \text{else.} \end{cases} \tag{6.3.34}$$

Then finally, $m_{\mathrm{sub}} = \mathrm{sub}_3$ is set for the case where intergranular strain is active.

Rotation Required for the Corotated Description

If integration of the stress and material state variables at finite deformations is carried out in a corotated description according to Section 5.5, then at each time a rotation tensor $\mathfrak{R}$ must be determined. In the incremental ALE framework proposed in this thesis, the vorticity of motion $\boldsymbol{\omega}$ is taken as the spin tensor and the current configuration at time t_n serves as the reference configuration, i.e. $\mathcal{B} = \varphi_n(\mathcal{B})$. By this, (4.1.13) takes the particular form

$$\dot{\mathfrak{R}} = \boldsymbol{\omega} \cdot \mathfrak{R}\,, \qquad \text{with} \qquad \mathfrak{R}|_{t=t_n} = \boldsymbol{I}\,. \tag{6.3.35}$$

Due to the non-Lagrangian view of material deformation, any data of configurations prior to t_n is getting lost if not stored and transported properly. In particular, the deformation gradient $\boldsymbol{F}_n = \boldsymbol{R}_n \cdot \boldsymbol{U}_n$ and the rotation $\mathfrak{R}_n$ related to the configuration

at time t_n boil down to the identity map. Based on this observation, two methods have been implemented to determine the rotation $\mathfrak{R}_{n+1} = \Delta\mathfrak{R}$ associated with the Zaremba-Jaumann rate. The first method computes the incremental rotation according to Hughes and Winget [1980], whereas the second is the polar decomposition algorithm of Simo and Hughes [1998, p. 244]. That is, the user can choose from either

$$\mathfrak{R}_{n+1} = (\boldsymbol{I} - \tfrac{1}{2}\Delta\tilde{\boldsymbol{r}}_{n+1/2})^{-1}(\boldsymbol{I} + \tfrac{1}{2}\Delta\tilde{\boldsymbol{r}}_{n+1/2}) \qquad \text{or} \qquad \mathfrak{R}_{n+1} = \boldsymbol{R}_{n+1}\,, \tag{6.3.36}$$

where $\Delta\tilde{\boldsymbol{r}}_{n+1/2}$ is the rotation increment according to $(5.5.17)_2$, and $\boldsymbol{R}_{n+1}$ is obtained from the polar decomposition of the incremental deformation gradient, $\boldsymbol{f}_{n+1}$.

6.4 Mesh Motion Step

In the operator-split ALE finite element solution procedure, the deformed geometry at the beginning of the mesh motion step is represented by the position vectors of the nodes $\boldsymbol{x}^-_{n+1} \overset{\text{def}}{=} \boldsymbol{x}^-$ at the end of the Lagrangian step. Thereafter, a motion can be prescribed to the element mesh in order to improve mesh quality. This mesh motion step, which will be established in the following section, provides the geometry at time $t^+_{n+1} \overset{\text{def}}{=} t^+$ represented by the position vectors of the (probably relocated) nodes $\boldsymbol{x}^+_{n+1} \overset{\text{def}}{=} \boldsymbol{x}^+$. The mesh motion step leaves mesh connectivity unchanged.

In the following section, some basic terminology and tools concerning mesh improvement will be introduced, and the smoothing algorithms for triangle meshes currently implemented in the ALE framework will be outlined. For the related topic of mesh generation methods and mesh postprocessing the interested reader is referred to the literature [e.g. Ho-Le, 1988; Thompson et al., 1999; Frey and George, 2000; George et al., 2004]. The terminology of Section A.1 is employed and the two-dimensional case will be considered in applications. The underlying finite element mesh is assumed to be composed of 3-node triangles (simplicial mesh). Concerning the evaluation of geometric primitives for triangles in $\mathbb{R}^2$, the reader is referred to Appendix B.

6.4.1 General Remarks and Mesh Improvement Procedure

The main objective of the mesh motion step is the improvement of the underlying finite element mesh. *Mesh improvement* becomes necessary in all mesh-based methods, at least in postprocessing the originally generated mesh. This is because the kernel of mesh generators generally does not produce meshes that meet all users' requirements. The generic mesh improvement procedure is summarized in Alg. 6.2.

Mesh improvement is usually initiated if a quality measure drops below a certain value which could have been specified by the user. Typical quality measures are defined locally and are based on either *geometric* (resp. *a priori*) or *physical* (resp. *a posteriori*) criteria. Physical quality measures are employed in the adaptive versions of FEM, which will not be discussed here. Geometric quality measures, on the other hand, can be evaluated independently of the finite element solution and usually at lower

Algorithm 6.2: Generic mesh improvement procedure.

Input: nodal locations and connectivity of the mesh
Output: improved mesh

```
initialize i = 0, choose quality measure, specify Q_min;
while global iteration step i ≤ i_max do
    loop mesh entities and evaluate quality Q;
    if Q < Q_min then flag mesh entity;
    foreach flagged mesh entity do
        apply local improvement tool;
    i ← i + 1;
```

computational costs. Theoretical background related to these measures and examples for different kinds of elements can be found in [e.g. Liu and Joe, 1994; Field, 2000; Frey and George, 2000; Knupp, 2001, 2003; Erhart, 2004]. Stated loosely, a geometrically high quality mesh is made up of more or less equal-sized elements with low distortion.

The mesh motion step of the current ALE method adopts the generic mesh improvement procedure (Alg. 6.2). By assuming a 3-node triangle mesh (cf. Appendix B), the elements in the mesh are looped and then a quality check is carried out for each element. The nodes of poor elements that should be moved are flagged.

Definition 6.4.1. Let $\mathcal{N}(\mathcal{M})$ be the set of all nodes in a mesh $\mathcal{M}$ and $P \in \mathcal{N}(\mathcal{M})$. Moreover, let Q_Ω be the geometric quality of element $\Omega \in \mathcal{M}$ and $Q_{\min}$ a minimal acceptable quality which could have been specified by the user. Then, the *set of flagged nodes intended for relocation* is defined through

$$\mathcal{N}' \stackrel{\text{def}}{=} \{P \in \mathcal{N}(\mathcal{M}) \,|\, P \in \mathcal{N}(\Omega) \text{ and } \Omega \in \mathcal{M} \text{ and } Q_\Omega < Q_{\min}\} \qquad \subset \mathcal{N}\,. \qquad \diamond$$

The implemented element quality measure is the weighted average of two normalized element quality measures:

$$\bar{Q} \stackrel{\text{def}}{=} \tfrac{1}{2}(Q_1 + Q_2) \qquad \in [0,1]\,, \tag{6.4.2}$$

where [cf. Field, 2000, eq. (3)]

$$Q_1(\boldsymbol{x}_0, \boldsymbol{x}_1, \boldsymbol{x}_2) \stackrel{\text{def}}{=} \frac{2r}{R} \qquad \in [0,1] \tag{6.4.3}$$

and [cf. Erhart, 2004, eq. (4.9)]

$$Q_2(\boldsymbol{x}_0, \boldsymbol{x}_1, \boldsymbol{x}_2) \stackrel{\text{def}}{=} 1 - \max_{k\in\{0,1,2\}} \begin{cases} \frac{60^\circ - \alpha_k}{60^\circ} & \text{for } 0^\circ \le \alpha_k \le 60^\circ \\ \frac{1}{2}\frac{\alpha_k - 60^\circ}{60^\circ} & \text{for } 60^\circ < \alpha_k \le 180^\circ \end{cases} \qquad \in [0,1]\,. \tag{6.4.4}$$

Here r and R are the unique incircle and circumcircle of the associated simplex, respectively, α_k, with $k \in \{0,1,2\}$, are the internal angles, and $\boldsymbol{x}_0, \boldsymbol{x}_1, \boldsymbol{x}_2 \in \mathbb{R}^m$ being

the positions of the element nodes. Both quality measures, Q_1 and Q_2, incorporate an explicit comparison with the optimal equilateral triangle (i.e. $\bar{Q} \stackrel{\text{def}}{=} 1$), for which

$$R = 2r \qquad \text{and} \qquad \alpha_k = 60^\circ, \text{ for all } k \in \{0, 1, 2\}\,. \tag{6.4.5}$$

Note that Q_1 is directly applicable to tetrahedra (3-simplices). The formulas to evaluate R, r, and α_k are listed in Appendix B.

The quality improvement of a mesh can be governed by quality evolution and is done by repeated application of appropriate tools. The choice of a tool is crucial for the success of the overall procedure. Most of the improvement tools process the mesh only locally, by modifying either the connectivity (topology) or the node positions of a mesh entity (edge, element, or ball). Attention must be also drawn to the strategy in order to globally improve the mesh. Any improved mesh entity may deteriorate the quality of neighboring entities. It might thus be more effective to process randomly picked mesh entities instead of all starting from the first and going to the last.

Definition 6.4.6. Let $\mathcal{N}$ denote the set of nodes in a two-dimensional mesh $\mathcal{M}$. The set of nodes included in the interior of the mesh, $\text{int}(\mathcal{M})$, is denoted by $\mathcal{N}_{\text{int}}$, and the elements of $\mathcal{N}_{\text{int}}$ are referred to as the *internal nodes* of the mesh. The nodes contained in the mesh boundary $\partial\mathcal{M}$ are called *boundary nodes*, and the set of all boundary nodes in $\mathcal{M}$ is written $\mathcal{N}_\partial$. Obviously, $\mathcal{N} = \mathcal{N}_{\text{int}} \cup \mathcal{N}_\partial$. Boundary nodes that essentially define the shape of the meshed domain are called *corner nodes*, and are contained in the set $\mathcal{N}_{\partial\partial} \subset \mathcal{N}_\partial$. Corner nodes divide the boundary into a number of distinct *mesh edges* consisting of *edge nodes* lying in the interior of the mesh edges. The set of all edge nodes in $\mathcal{M}$, denoted by $\mathcal{N}_{\text{edg}}$, is then defined through

$$\mathcal{N}_{\partial\partial} \stackrel{\text{def}}{=} \mathcal{N}_\partial \backslash \mathcal{N}_{\text{edg}}\,.$$

If the boundary of a mesh $\mathcal{M}$ is given as the disjoint union $\partial\mathcal{M} = \bigcup_{j=1}^{n_{\text{bnd}}} \partial_j\mathcal{M}$ of $n_{\text{bnd}} \in \mathbb{N}$ sub-boundaries $\partial_j\mathcal{M}$, then the definitions of the boundary, corner, and edges nodes carry over to every sub-boundary: $\mathcal{N}^j_{\partial\partial} = \mathcal{N}^j_\partial \backslash \mathcal{N}^j_{\text{edg}}$. ♢

Definition 6.4.7. The *ball* or *cluster* of elements associated with some node $P_0 \in \mathcal{N}$, with $\mathcal{N} = \mathcal{N}_{\text{int}} \cup \mathcal{N}_\partial$, is the disjoint union $\mathcal{B}_0 \stackrel{\text{def}}{=} \bigcup_{n_{\text{el}}} \Omega$ of all elements Ω in a mesh sharing P_0 as a node, and then that node is referred to as the *vertex of the ball*. A ball is called *closed* if $P_0 \in \mathcal{N}_{\text{int}}$, and *open* if $P_0 \in \mathcal{N}_\partial$. ♢

Smoothing is intended to improve overall mesh quality by node relocation. It represents a class of homeomorphic (i.e. bijective and continuous) maps between meshes which keep the local connectivity of elements and nodes, as well as the global topology of the original mesh unchanged. Smoothing that achieves a quality mesh in terms of geometric measures is also referred to as *mesh regularization*, whereas the incorporation of physical solution error estimates leads to the notion of *adaptive smoothing*. Adaptive smoothing is the central issue of r-adaptive finite element and finite difference methods, but is left unconsidered in the current arbitrary Lagrangian-Eulerian method. The success of this method is primarily determined by the smoothing procedure, hence it can be regarded as the most important task in the development.

Automatic mesh regularization methods which are not governed by quality evolution are called *direct* or *heuristic smoothing algorithms*. Examples include *Laplacian smoothing* [Buell and Bush, 1973; Field, 1988; Freitag, 1997; Knupp, 1999; Frey and George, 2000], *smoothing by weighted averaging* [Aymone et al., 2001; Aymone, 2004] and *Giuliani's method* [Giuliani, 1982]. These methods provide closed-form expressions for the new node location which is supposed to smooth the associated ball of elements. Even though these methods are numerically attractive, they cannot ensure quality improvement for general cases. As will be shown in Chapter 8, the heuristic smoothing algorithms proposed by Aymone et al. [2001] and Giuliani [1982], for example, fail on a non-convexly distorted mesh.

Another class of smoothing algorithms is referred to as *physically-based smoothing*. In these algorithms, physical properties are assigned to the mesh entities, and then a specific initial boundary value problem is solved over a dummy time step in order to determine the nodal displacements. Examples of physically-based smoothing methods are proposed by Löhner et al. [1986], Belytschko et al. [2000, sec. 7.10.6], and Nazem et al. [2006, 2008]. The success of such a procedure, however, is by pure chance. It cannot be ensured that any mesh processed is not worse than before.

The drawbacks of heuristic and physically-based smoothing methods when dealing with non-convex meshes can be avoided if the appropriate new node positions are determined from optimization. In contrast to the other two approaches, *optimization-based smoothing algorithms* are governed by geometric quality evolution [see, for example, Kennon and Dulikravich, 1986; Dari and Buscaglia, 1993; Zavattieri et al., 1996; Joun and Lee, 1997; Braess, 2000; Braess and Wriggers, 2000; Knupp et al., 2002; Dyadechko et al., 2005]. A single quality measure or combinations are the basic ingredients in the definition of an *objective function* whose minimum is associated with a properly smoothed mesh, or a part of it.

The distinction between the internal nodes and the boundary nodes of a mesh is crucial for the development of an overall smoothing procedure. It is generally recommended to process the boundary nodes before the internal nodes, like in initial mesh generation. Unfortunately, the algorithms intended to smooth the interior of a mesh are generally not directly applicable to the boundary mesh, and vice versa. One reason for this is the constraint (6.2.7), which requires boundary nodes to remain on the boundary of the computational domain. The algorithms to smooth the boundaries should force this constraint, at least approximately. Simple averaging or weighted averaging is sufficient in most cases.

6.4.2 Smoothing of the Boundary Mesh

The profit of appropriate smoothing schemes for internal nodes is limited if the boundaries remain distorted. In many cases it would be even more effective to smooth the boundaries prior to the interior of a mesh. The boundary smoother, however, must leave the positions of corner nodes unchanged, because they define the shape of the computational domain (cf. Definition 6.4.6). The boundaries of two-dimensional meshes

can simply be smoothed by heuristic procedures in order to improve the quality of the complete mesh considerably. Such a procedure can be found in [Aymone et al., 2001], which is outlined next.

The open ball $\mathcal{B}_0$ of a boundary node $P_0 \in (\mathcal{N}' \cap \mathcal{N}_{\text{edg}})$ intended for relocation in a two-dimensional mesh consists of a one-dimensional boundary curve formed by two element edges and at least three nodes, depending on the order of interpolation. The boundary node P_0 intended for relocation has two neighbors, P_1 and P_2, which lie on the boundary. The boundary curve through (P_1, P_0, P_2) is piecewise linear. However, to smooth the boundary curve, assume that the three points lie on a sufficiently smooth curve

$$\begin{aligned} c: \ \mathbb{R} \supset [-1,1] \ &\rightarrow \ \mathcal{S} = \mathbb{R}^2 \\ \xi \ &\mapsto \ c(\xi)\,, \ \exists c^{-1}\,, \end{aligned} \tag{6.4.8}$$

in which the inverse c^{-1} gives the natural coordinate ξ of a point on the curve. Let $O \in \mathcal{S}$ be an arbitrary point, and $(\mathcal{S}, \mathbb{R}^2)$ be the standard 2-dimensional Euclidian point space associated with $\mathcal{S}$. Then the curve (6.4.8) on $\mathcal{S}$ defines the *one-parameter family of position vectors*

$$\left(O, \overrightarrow{Oc(\xi)}\right) \stackrel{\text{def}}{=} (O, \boldsymbol{x}(\xi)) \stackrel{\text{def}}{=} \begin{pmatrix} x(\xi) \\ y(\xi) \end{pmatrix}_O \qquad \in T\mathbb{R}^2\,, \tag{6.4.9}$$

with $\xi \in [-1,1]$ and $\boldsymbol{x}(\xi) = (x(\xi), y(\xi))^{\mathrm{T}} \in \mathbb{R}^2$.

A straightforward quality measure for the distortion of the boundary curve through (P_1, P_0, P_2) is

$$Q_{\text{bnd}} \stackrel{\text{def}}{=} \frac{\min(d_1, d_2)}{\max(d_1, d_2)} \qquad \in [0,1]\,, \tag{6.4.10}$$

which involves the distances d_1 and d_2 defined through

$$\begin{aligned} d_1 &\stackrel{\text{def}}{=} d(P_0, P_1) = \|\boldsymbol{x}_1 - \boldsymbol{x}_0\| = \sqrt{(x_1 - x_0)^2 + (y_1 - y_0)^2} \qquad \text{and} \\ d_2 &\stackrel{\text{def}}{=} d(P_0, P_2) = \|\boldsymbol{x}_2 - \boldsymbol{x}_0\| = \sqrt{(x_2 - x_0)^2 + (y_2 - y_0)^2}\,, \end{aligned} \tag{6.4.11}$$

respectively. $\boldsymbol{x}_I$ is the position vector of the node P_I, $I \in \{0,1,2\}$, with respect to O. On a good quality resp. smoothed boundary, the location of the node P_0 equalizes the distances, so that $Q_{\text{bnd}} = 1$.

If the smooth curve (6.4.8) is a polynomial of degree two through (P_1, P_0, P_2), with $c(-1) = P_1$, $c(0) = P_0$, and $c(1) = P_2$, then the one-parameter family (6.4.9) has the exact representation (the base point O is suppressed)

$$\boldsymbol{x}(\xi) = \sum_{I=0}^{2} N^I(\xi)\, \boldsymbol{x}_I\,, \tag{6.4.12}$$

where N^I are quadratic interpolation functions for $\boldsymbol{x}$ and node P_I, having the particular form

$$N^0(\xi) \stackrel{\text{def}}{=} 1 - \xi^2\,, \qquad N^1(\xi) \stackrel{\text{def}}{=} \tfrac{1}{2}(\xi^2 - \xi)\,, \qquad \text{and} \qquad N^2(\xi) \stackrel{\text{def}}{=} \tfrac{1}{2}(\xi^2 + \xi)\,. \tag{6.4.13}$$

Aymone et al. [2001] apply weighted averaging to determine a natural coordinate $\xi_0' \in [-1,1]$ of the node P_0 that smoothes the boundary curve through (P_1, P_0, P_2). By using the distances d_1, d_2 in (6.4.11) as the weights associated with P_I he arrives at

$$\xi_0' = \frac{\sum_{I=0}^{2} \|\boldsymbol{x}_I - \boldsymbol{x}_0\| \, \xi(P_I)}{\sum_{I=0}^{2} \|\boldsymbol{x}_I - \boldsymbol{x}_0\|} = \frac{\|\boldsymbol{x}_2 - \boldsymbol{x}_0\| - \|\boldsymbol{x}_1 - \boldsymbol{x}_0\|}{\|\boldsymbol{x}_1 - \boldsymbol{x}_0\| + \|\boldsymbol{x}_2 - \boldsymbol{x}_0\|} \,. \tag{6.4.14}$$

Here $\xi(P_I) \equiv c^{-1}(P_I)$ is the natural coordinate $\xi \in [-1,1]$ of the node P_I. Finally, the new position vector of P_0 that smoothes the boundary curve in the open ball $\mathcal{B}_0$ can be obtained from (6.4.12) by using the coordinate $\xi = \xi_0'$, so $\boldsymbol{x}_0' = \boldsymbol{x}(\xi_0')$. The procedure is summarized in Alg. 6.3. Because the total number of boundary nodes is not very large in two-dimensional meshes, it would be adequate to relocate all boundary nodes except for the corner nodes without any prior quality check.

Algorithm 6.3: Smoothing of the boundaries of a two-dimensional mesh according to the averaging procedure of Aymone et al. [2001].

Input: distorted mesh geometry $\boldsymbol{x}^-$, number of sub-boundaries n_{bnd}, set of edge nodes $\mathcal{N}_{\text{edg}}^j$, $j \leq n_{\text{bnd}}$, for each sub-boundary, neighboring nodes P_1, P_2 of every $P_0 \in \mathcal{N}_{\text{edg}}^j$

Output: smoothed geometry $\boldsymbol{x}^+$ of mesh boundary

```
initialize i = 0 and j = 0;
while global iteration step i ≤ i_max do
    while sub-boundary j ≤ n_bnd do
        foreach P_0 ∈ N_edg^j do
            read locations of nodes x_0, x_1, and x_2;
            compute distances ||x_1 − x_0|| and ||x_2 − x_0|| (6.4.11);
            natural coordinate to equalize distances ξ_0' = (||x_2−x_0||−||x_1−x_0||)/(||x_1−x_0||+||x_2−x_0||);
            location of P_0 smoothing the boundary curve is
            x_0' = Σ_{I=0}^{2} N^I(ξ_0') x_I, with N^I given by (6.4.13);
        j ← j + 1;
    i ← i + 1;
totality of (new) locations of all the nodes in the mesh is x^+;
```

6.4.3 Smoothing of the Internal Mesh

Finding the best location of a node in the associated ball of elements in terms of geometric quality constitutes an optimization problem. In contrast to optimization-based methods the results produced by heuristic and physically-based methods are rarely optimal. Some basic definitions and results concerning optimization theory are addressed next before presenting the particular optimization-based local mesh smoothing algorithm that has been developed during the present research. Recommended textbooks for further studies are [Sun and Yuan, 2006; Luenberger and Ye, 2008; Nocedal and Wright, 2006; Press et al., 2007].

Fundamentals of Optimization Theory

Definition 6.4.15. Let $\mathcal{X} \subset \mathbb{R}^m$ be a feasible region, $\boldsymbol{x} \in \mathcal{X}$, and $f : \mathcal{X} \to \mathbb{R}$ a function. The general *optimization problem* can be defined as follows:

$$\text{minimize } f(\boldsymbol{x}) \qquad \text{subject to} \quad \boldsymbol{x} \in \mathcal{X}\,.$$

The function f is then called the *objective function*, and $\boldsymbol{x}$ is called the *decision variable*. The optimization problem is *unconstrained* if $\mathcal{X} = \mathbb{R}^m$. The *constrained optimization problem* can be cast in the form

$$\text{minimize } f(\boldsymbol{x}) \qquad \text{subject to} \quad c_i(\boldsymbol{x}) = 0,\ i \in \mathcal{I},\ c_j(\boldsymbol{x}) \geq 0,\ j \in \mathcal{J}\,,$$

where $\mathcal{I} \subset \mathbb{N}$ is an index set of equality constraints, and $\mathcal{J} \subset \mathbb{N}$ is an index set of inequality constraints. $c_i(\boldsymbol{x})$ and $c_j(\boldsymbol{x})$ are referred to as the *constraint functions*. When all the objective function and constraint functions are linear functions of $\boldsymbol{x}$, then the process of optimization is called *linear programming*, otherwise *nonlinear programming*. ♢

Definition 6.4.16. Let $f : \mathbb{R}^m \to \mathbb{R}$ be the objective function in an unconstrained optimization problem.

(i) A point resp. a component column $\boldsymbol{x}' \in \mathbb{R}^m$ is called a *local minimizer of* f if there exists some $\varepsilon > 0$ such that $f(\boldsymbol{x}') \leq f(\boldsymbol{x})$ for all $\boldsymbol{x} \in \mathbb{R}^m$ satisfying $\|\boldsymbol{x} - \boldsymbol{x}'\| < \varepsilon$. A point $\boldsymbol{x}' \in \mathbb{R}^m$ is called a *strict local minimizer of* f if there exists $\varepsilon > 0$ such that $f(\boldsymbol{x}') < f(\boldsymbol{x})$ for all $\boldsymbol{x} \in \mathbb{R}^m$ with $\boldsymbol{x} \neq \boldsymbol{x}'$ and $\|\boldsymbol{x} - \boldsymbol{x}'\| < \varepsilon$.

(ii) A point $\boldsymbol{x}' \in \mathbb{R}^m$ is referred to as a *global minimizer of* f if $f(\boldsymbol{x}') \leq f(\boldsymbol{x})$ holds for all $\boldsymbol{x} \in \mathbb{R}^m$. A point $\boldsymbol{x}' \in \mathbb{R}^m$ is a *strict global minimizer of* f if $f(\boldsymbol{x}') < f(\boldsymbol{x})$ for all $\boldsymbol{x} \in \mathcal{X}$ with $\boldsymbol{x} \neq \boldsymbol{x}'$. ♢

Definition 6.4.17. The *set of minimizers of* $f : \mathcal{X} \to \mathbb{R}$ *on* $\mathcal{X} \subset \mathbb{R}^m$ is defined by

$$\arg\min_{\boldsymbol{x} \in \mathcal{X}} f(\boldsymbol{x}) \stackrel{\text{def}}{=} \{\boldsymbol{x} \in \mathcal{X} \mid f(\boldsymbol{x}) \text{ minimal}\}\,.$$

A *minimizer of* $f : \mathcal{X} \to \mathbb{R}$ is a point $\boldsymbol{x}' \in \arg\min_{\boldsymbol{x} \in \mathcal{X}} f(\boldsymbol{x})$ on $\mathcal{X}$. By abuse of notation, a *strict minimizer of* $f : \mathcal{X} \to \mathbb{R}$ *on* $\mathcal{X} \subset \mathbb{R}^m$ is usually written

$$\boldsymbol{x}' = \arg\min_{\boldsymbol{x} \in \mathcal{X}} f(\boldsymbol{x})\,.$$ ♢

Global minimizers necessarily are local minimizers, but not conversely. Determination of the global minimizers is challenging and has grown a science of its own, referred to as *global optimization*. In practice, however, it is often sufficient to find a local minimizer and to iterate the global minimum.

Definition 6.4.18. Let $\{z^1, \ldots, z^m\} \stackrel{\text{def}}{=} \{z^b\} \in \mathbb{R}^m$ be the standard Cartesian coordinate system on the space $\mathcal{S} = \mathbb{R}^m$. Let $f : \mathbb{R}^m \to \mathbb{R}$ be a C^2-function in the Fréchet-sense and $\boldsymbol{x} \in \mathbb{R}^m$ a column matrix.

(i) The matrix arrangement of the components of the *gradient* $\boldsymbol{\nabla} f$ at $\boldsymbol{x}$ with respect to the coordinates z^b is the column given by

$$\boldsymbol{\nabla} f(\boldsymbol{x}) \stackrel{\text{def}}{=} \begin{pmatrix} \frac{\partial f(\boldsymbol{x})}{\partial z^1} \\ \vdots \\ \frac{\partial f(\boldsymbol{x})}{\partial z^m} \end{pmatrix} \qquad \in \mathbb{R}^m \,.$$

The gradient of f at point $\boldsymbol{x}$ is the steepest ascent direction at that point, with the steepness given by $\|\boldsymbol{\nabla} f(\boldsymbol{x})\|$. By abuse of language, $\boldsymbol{\nabla} f$ should represent both the gradient of f, which is a vector, as well as the matrix arrangement of its components in $\mathbb{R}^m$.

(ii) The *Hessian matrix*, or just the *Hessian* of the function f at $\boldsymbol{x}$ with respect to the coordinates z^b is the matrix arrangement of second-order partial derivatives of f, viz.

$$\boldsymbol{H}_f(\boldsymbol{x}) \stackrel{\text{def}}{=} \begin{pmatrix} \frac{\partial^2 f(\boldsymbol{x})}{\partial z^1 \partial z^1} & \cdots & \frac{\partial^2 f(\boldsymbol{x})}{\partial z^1 \partial z^m} \\ \vdots & \ddots & \vdots \\ \frac{\partial^2 f(\boldsymbol{x})}{\partial z^m \partial z^1} & \cdots & \frac{\partial^2 f(\boldsymbol{x})}{\partial z^m \partial z^m} \end{pmatrix} \qquad \in \mathbb{R}^{m \times m} \,.$$

Since $\frac{\partial^2 f(\boldsymbol{x})}{\partial z^j \partial z^k} = \frac{\partial^2 f(\boldsymbol{x})}{\partial z^k \partial z^j}$, for $j, k \in \{1, \ldots, m\}$, the Hessian is symmetric. It represents the transposed gradient of the gradient of f. ♢

Definition 6.4.19. Let the objective function $f : \mathbb{R}^m \to \mathbb{R}$ be differentiable at $\boldsymbol{x} \in \mathbb{R}^m$. A *descent direction of f at $\boldsymbol{x}$* is a vector $\boldsymbol{d} \in \mathbb{R}^m$ satisfying

$$\langle \boldsymbol{\nabla} f(\boldsymbol{x}), \boldsymbol{d} \rangle < 0 \,,$$

in which $\langle \cdot, \cdot \rangle : \mathbb{R}^m \times \mathbb{R}^m \to \mathbb{R}$ denotes the standard inner product in $\mathbb{R}^m$. In matrix notation, write $(\boldsymbol{\nabla} f)^{\mathrm{T}} \boldsymbol{d} < 0$, evaluation at $\boldsymbol{x} \in \mathbb{R}^m$ being understood. ♢

It directly follows from the definition that $\boldsymbol{d}$ is a descent direction of f at $\boldsymbol{x}$ if and only if the angle θ between $-\boldsymbol{\nabla} f(\boldsymbol{x})$ and $\boldsymbol{d}$ less than 90°, that is, if

$$\cos\theta \stackrel{\text{def}}{=} -\frac{\langle \boldsymbol{\nabla} f(\boldsymbol{x}), \boldsymbol{d} \rangle}{\|\boldsymbol{\nabla} f(\boldsymbol{x})\| \|\boldsymbol{d}\|} > 0 \,. \tag{6.4.20}$$

The following first- and second-order conditions for local minimizers of a function $f : \mathcal{X} \to \mathbb{R}$ on open $\mathcal{X} \subset \mathbb{R}^m$ are of fundamental importance. Proofs can be found in [Sun and Yuan, 2006, sec. 1.4].

Theorem 6.4.21. *(i) If $f : \mathcal{X} \to \mathbb{R}$ is continuously differentiable on $\mathcal{X} \subset \mathbb{R}^m$ and $\boldsymbol{x}' \in \mathcal{X}$ is a local minimizer of f, then*

$$\boldsymbol{\nabla} f(\boldsymbol{x}') = \boldsymbol{0} \,.$$

(ii) If $\boldsymbol{x}' \in \mathcal{X}$ is a local minimizer of f and f is twice continuously differentiable on $\mathcal{X}$, i.e. f is of class C^2, then $\boldsymbol{\nabla} f(\boldsymbol{x}') = \boldsymbol{0}$ and the Hessian $\boldsymbol{H}_f(\boldsymbol{x}')$ is positive semidefinite, i.e. $\boldsymbol{x}^{\mathrm{T}} \boldsymbol{H}_f \, \boldsymbol{x} \geq 0$ for every $\boldsymbol{x} \in \mathbb{R}^m$ with $\boldsymbol{x} \neq \boldsymbol{0}$.

(iii) Let f be C^2 on $\mathcal{X}$, $\boldsymbol{x}' \in \mathcal{X}$, $\boldsymbol{\nabla} f(\boldsymbol{x}') = \boldsymbol{0}$, and let $\boldsymbol{H}_f(\boldsymbol{x}')$ be positive definite such that $\boldsymbol{x}^{\mathrm{T}} \boldsymbol{H}_f \, \boldsymbol{x} > 0$ for every $\boldsymbol{x} \in \mathbb{R}^m$ with $\boldsymbol{x} \neq \boldsymbol{0}$, then $\boldsymbol{x}'$ is a strict local minimizer.

Finding a solution of the optimization problem 6.4.15 usually is an iterative procedure [cf. Sun and Yuan, 2006, sec. 1.5]. Let $\mathcal{J} \in \mathbb{N}$ be an index set and $j, j+1 \in \mathcal{J}$. For a given $\boldsymbol{x}^j$, the iterative procedure takes the form

$$\boldsymbol{x}^{j+1} = \boldsymbol{x}^j + \lambda^j \boldsymbol{d}^j \,. \tag{6.4.22}$$

Once a starting point $\boldsymbol{x}^{j=0}$, a step size $\lambda^{j=0} > 0$, and a tolerance $\varepsilon > 0$ have been specified, a termination criterion of the form

$$\|\boldsymbol{\nabla} f(\boldsymbol{x}^j)\| < \varepsilon \tag{6.4.23}$$

is checked. If this criterion is met, then $\boldsymbol{x}^j \approx \boldsymbol{x}'$ is an approximate minimizer of f. If the criterion is not met, the descent direction $\boldsymbol{d}^j$ supposed to point to the minimum of the objective function is determined by some method. Thereafter, a so-called *line search* is carried out in order to find the step size λ^j satisfying

$$f(\boldsymbol{x}^j + \lambda^j \boldsymbol{d}^j) < f(\boldsymbol{x}^j) \,. \tag{6.4.24}$$

The iterative procedure continues with the repeated evaluation of the termination criterion using $\boldsymbol{x}^{j+1} = \boldsymbol{x}^j + \lambda^j \boldsymbol{d}^j$. Alg. 6.4 shows the basic scheme of optimization procedures.

Algorithm 6.4: Generic optimization procedure; according to Sun and Yuan [2006].

Input: objective function f, gradient $\boldsymbol{\nabla} f$, point $\bar{\boldsymbol{x}}$
Output: minimizer of f

initialize $j = 0$, point $\boldsymbol{x}^{j=0} = \bar{\boldsymbol{x}}$, step size $\lambda^{j=0} > 0$, and tolerance $\varepsilon > 0$;
while *iteration step* $j \leq j_{\max}$ **do**
  if $\|\boldsymbol{\nabla} f(\boldsymbol{x}^j)\| < \varepsilon$ **then**
    exit;
  else
    find descent direction $\boldsymbol{d}^j$ according to some method;
    line search: determine step size λ^j such that $f(\boldsymbol{x}^j + \lambda^j \boldsymbol{d}^j) < f(\boldsymbol{x}^j)$;
    update $\boldsymbol{x}^{j+1} = \boldsymbol{x}^j + \lambda^j \boldsymbol{d}^j$;
  $j \leftarrow j + 1$;

The overall accuracy of the iterative procedure (6.4.22) is affected by the descent direction $\boldsymbol{d}^j$ and the step size λ^j. Particular optimization procedures vary in the methods to determine them. The following paragraphs describe the application of *Newton's method* and *backtracking line search* using Armijo's rule for step size control. The handling of non-positive definite Hessian will be also discussed.

Theorem 6.4.21(i) defines a homogeneous system of generally nonlinear algebraic equations, $\boldsymbol{\nabla} f(\boldsymbol{x}') = \boldsymbol{0}$, whose solution is $\boldsymbol{x}' \in \mathcal{X}$, the local minimizer of f. The solution can be approximated by Newton's method introduced in Section A.3.2. In the present

case, let $\boldsymbol{x}^j$ be a close-enough guess of the local minimizer. For $f : \mathcal{X} \to \mathbb{R}$ being twice Fréchet-differentiable at $\boldsymbol{x}^j$, the linearization of $\boldsymbol{\nabla} f(\boldsymbol{x}') = Df(\boldsymbol{x}') = \boldsymbol{0}$ about $\boldsymbol{x}^j$ is

$$\boldsymbol{\nabla} f(\boldsymbol{x}^j) + \boldsymbol{H}_f(\boldsymbol{x}^j) \cdot (\boldsymbol{x}' - \boldsymbol{x}^j) \approx \boldsymbol{0}\,. \tag{6.4.25}$$

Provided that the gradient $\boldsymbol{\nabla} f$ is a sufficiently smooth function, then any guess $\boldsymbol{x}^{j+1}$ for which $\boldsymbol{\nabla} f(\boldsymbol{x}^j) + \boldsymbol{H}_f(\boldsymbol{x}^j) \cdot (\boldsymbol{x}^{j+1} - \boldsymbol{x}^j) = \boldsymbol{0}$ is a better approximation than $\boldsymbol{x}^j$. If $\boldsymbol{H}_f$ is regular on $\mathcal{X}$, this latter condition results in

$$\boldsymbol{x}^{j+1} = \boldsymbol{x}^j - (\boldsymbol{H}_f^{-1}\boldsymbol{\nabla} f)(\boldsymbol{x}^j)\,, \qquad \text{and} \quad \lim_{j\to\infty} \boldsymbol{x}^{j+1} = \boldsymbol{x}'\,. \tag{6.4.26}$$

The term $-(\boldsymbol{H}_f^{-1}\boldsymbol{\nabla} f)(\boldsymbol{x}^j)$ is a *Newton's direction*. By Definition 6.4.19, Newton's direction is a descent direction provided that, in matrix notation,

$$(\boldsymbol{\nabla} f)^{\mathrm{T}} \boldsymbol{H}_f^{-1} \boldsymbol{\nabla} f > 0 \tag{6.4.27}$$

holds at $\boldsymbol{x}^j \in \mathcal{X}$, that is, provided that $\boldsymbol{H}_f(\boldsymbol{x}^j)$ is regular and positive definite. Quadratic rate of convergence of the iteration is only achieved if the Hessian is evaluated in every iteration step (full Newton's method).

Some difficulties are encountered with Newton's method (6.4.26) and require careful intervention at certain points in the implementation. First, the partial derivatives of f have to be evaluated. The numerical differentiation by finite differences can be employed whenever analytical (i.e. closed-form) expressions are not available or the straightforward derivation of f is too expensive. Moreover, the iterative scheme for the solution $\boldsymbol{x}'$ converges only if the starting point $\boldsymbol{x}^{j=0}$ is a close-enough guess of the solution. This is why Newton's method is called a local method. When the starting point is far away from the solution, it is not guaranteed that the Hessian $\boldsymbol{H}_f$ is invertible and positive definite at each $\boldsymbol{x}^j \in \mathcal{X}$, with $j \in \mathcal{J}$, and that Newton's direction is indeed a descent direction. In these cases solution may diverge. Even if the starting point is close to solution, there may still be non-positive definite Hessians so that the objective function may not have local minimizers (cf. Theorem 6.4.21(iii)).

In order to ensure convergence at non-positive definite Hessians, a modified Newton's method should be employed. The method suggested by Goldstein and Price [1967], for example, substitutes the steepest descent direction $-\boldsymbol{\nabla} f(\boldsymbol{x}^j)$ instead of $-(\boldsymbol{H}_f^{-1}\boldsymbol{\nabla} f)(\boldsymbol{x}^j)$ for $\boldsymbol{d}^j$ in (6.4.22) in cases where $\boldsymbol{H}_f$ is not regular or positive definite at $\boldsymbol{x}^j$. The check for positive definiteness can be done by the angle criterion (6.4.20) [see also Sun and Yuan, 2006, pp. 135–136]. To this end, define, in matrix notation,

$$\cos\theta^j \stackrel{\text{def}}{=} -\frac{(\boldsymbol{\nabla} f(\boldsymbol{x}^j))^{\mathrm{T}} \boldsymbol{d}^j}{\|\boldsymbol{\nabla} f(\boldsymbol{x}^j)\| \|\boldsymbol{d}^j\|} \tag{6.4.28}$$

at the j-th iteration. If $\cos\theta^j > 0$ for $\boldsymbol{d}^j = -(\boldsymbol{H}_f^{-1}\boldsymbol{\nabla} f)(\boldsymbol{x}^j)$, then Newton's direction is indeed a descent direction resp. $\boldsymbol{H}_f$ is positive definite, and the iterative scheme converges; by a basic theorem of linear algebra, every positive definite matrix is also regular, so $\boldsymbol{H}_f^{-1}(\boldsymbol{x}^j)$ will indeed exist if $\cos\theta^j > 0$. If, on the other hand, $\cos\theta^j \leq 0$ for $\boldsymbol{d}^j = -(\boldsymbol{H}_f^{-1}\boldsymbol{\nabla} f)(\boldsymbol{x}^j)$, then $\boldsymbol{d}^j = -\boldsymbol{\nabla} f(\boldsymbol{x}^j)$ is used as the descent direction, satisfying

$\cos\theta^j > 0$ when substituted into (6.4.28) as long as $\boldsymbol{x}^j$ is not a minimizer of f. This can be summarized as follows:

$$\boldsymbol{d}^j \stackrel{\text{def}}{=} \begin{cases} -\boldsymbol{\nabla} f(\boldsymbol{x}^j), & \text{if } \boldsymbol{H}_f(\boldsymbol{x}^j) \text{ is singular, or if } \cos\theta^j \leq 0, \\ -(\boldsymbol{H}_f^{-1}\boldsymbol{\nabla} f)(\boldsymbol{x}^j), & \text{otherwise.} \end{cases} \tag{6.4.29}$$

Due to round-off errors in actual numerical implementations of the method, $\cos\theta^j$ should be compared with a reasonable tolerance $\eta > 0$, i.e. $\cos\theta^j \leq \eta$ is used as the criterion in (6.4.29).

It remains to determine the size of the steps with which the minimum of the objective function is approached in an optimization process. The step size must not be too large so as not to overshoot the minimum. On the other hand, tiny step sizes would decelerate the overall procedure. It is, therefore, a mandatory goal to let the programm determine an appropriate size for every step at little user intervention, which is then called a line search.

Definition 6.4.30. A *line search* automatically determines an acceptable step size λ^j in optimization procedures from the condition $f(\boldsymbol{x}^j + \lambda^j \boldsymbol{d}^j) < f(\boldsymbol{x}^j)$. If the step size satisfies

$$f(\boldsymbol{x}^j + \lambda^j \boldsymbol{d}^j) = \min_{\lambda > 0} f(\boldsymbol{x}^j + \lambda \boldsymbol{d}^j)\,,$$

then it is called the *optimal step size* and the line search is called *exact*. If an *inexact line search* is applied, a *step size rule* ensures that the decrease of the objective function, i.e. the value of the difference

$$f(\boldsymbol{x}^j) - f(\boldsymbol{x}^j + \lambda^j \boldsymbol{d}^j) > 0\,,$$

remains acceptable. ◊

Exact line search generally requires more computational effort than inexact line search and, in practice, the convergence rate of many optimization procedures does not depend on exact line search [Sun and Yuan, 2006, p. 102]. Inexact line search hence is preferable provided that there is an effective step size rule which gives a sufficient decrease in the objective function. One of such rules is the widely-used *Armijo rule* [Armijo, 1966]:

$$f(\boldsymbol{x}^j + \lambda^j \boldsymbol{d}^j) - f(\boldsymbol{x}^j) \leq \tfrac{1}{2}\lambda^j (\boldsymbol{\nabla} f(\boldsymbol{x}^j))^{\mathrm{T}} \boldsymbol{d}^j\,. \tag{6.4.31}$$

An inexact line search using the Armijo rule is called a *backtracking line search* [cf. Sun and Yuan, 2006, alg. 2.5.2]. In a backtracking line search, for given f, $\boldsymbol{\nabla} f$, $\boldsymbol{d}^j$, $\boldsymbol{x}^j$, and $\lambda^{j=0} = 1.0$, the condition (6.4.31) is checked. If it is satisfied, then $\lambda^{j+1} = \lambda^j$ and $\boldsymbol{x}^{j+1} = \boldsymbol{x}^j + \lambda^j \boldsymbol{d}^j$ is set. If the condition is not satisfied, the current guess of the minimizer is used in the next iteration and the step size is bisected, that is,

$$\boldsymbol{x}^{j+1} = \boldsymbol{x}^j \qquad \text{and} \qquad \lambda^{j+1} = \frac{\lambda^j}{2}\,, \tag{6.4.32}$$

respectively.

It can be concluded that damped Newton's method combined with backtracking line search and the Goldstein-Price method constitutes a fast and robust optimization procedure which is applicable to mesh smoothing. Newton's method alone is a local method, meaning that it is convergent only for starting points close enough to the solution. Combination with line search guarantees the global convergence Newton's method. The Goldstein-Price method handles Hessians that are not positive definite.

OSMOT – An Optimization-Based Mesh Smoothing Algorithm

Several algorithms are reported in the literature which achieve mesh quality improvement based on node relocation and optimization theory. Early references are the papers of Barfield [1970] and Brackbill and Saltzman [1982], which are concerned with the global optimization of two-dimensional structured grids. Kennon and Dulikravich [1986] developed one of the first mesh smoothing algorithms that use principles of local optimization resp. nonlinear programming. The local objective function involves geometric quality measures for the ball of four quadrilateral elements surrounding a single internal node.

Dari and Buscaglia [1993] and Zavattieri et al. [1996], among others, provide several refinements of the local approach and generalize it to unstructured three-dimensional meshes. Steps towards an efficient algorithmic treatment in two dimensions by using generalized linear programming are presented in [Amenta et al., 1999]. Development of optimization-based smoothing algorithms continued up to the present, with focuses on unstructured quadrilateral meshes [Joun and Lee, 1997], unstructured triangle meshes [Braess, 2000; Braess and Wriggers, 2000], structured quadrilateral meshes [Knupp et al., 2002], and general unstructured polyhedral meshes [Dyadechko et al., 2005]. The generic optimization scheme, Alg. 6.4, is incorporated into all these algorithms. They differ in the methods to determine the descent direction and step size, and particularly in the objective function.

The choice of an objective function is crucial to the success of optimization-based mesh smoothing. The objective function has to be formulated in terms of some quality measure, so that the optimization is governed by quality evolution. To meet the requirement of a local algorithm, it is reasonable to start with an objective function for a single mesh element. Presuming that the mesh is made up of 3-node triangles, the class of local objective functions envisaged here takes the form [Braess, 2000; Braess and Wriggers, 2000]

$$\bar{w}(\boldsymbol{x}_0, \boldsymbol{x}_1, \boldsymbol{x}_2) \stackrel{\text{def}}{=} \left(\frac{R(\boldsymbol{x}_0, \boldsymbol{x}_1, \boldsymbol{x}_2)}{R_{\text{ref}}} \right)^{\beta} \left(\frac{R(\boldsymbol{x}_0, \boldsymbol{x}_1, \boldsymbol{x}_2)}{r(\boldsymbol{x}_0, \boldsymbol{x}_1, \boldsymbol{x}_2)} \right)^{\gamma} \qquad \in [0, \infty[\,, \tag{6.4.33}$$

in which $\boldsymbol{x}_0, \boldsymbol{x}_1, \boldsymbol{x}_2 \in \mathbb{R}^2$ are the position vectors of the three triangle nodes $0, 1, 2$ with respect to some origin in the ambient space $\mathcal{S} = \mathbb{R}^2$, β and γ are constant positive weighting exponents, and $R_{\text{ref}} > 0$ is a constant reference radius.

The class of local objective functions defined through (6.4.33) takes into account the element radius ratio of the incircle and circumcircle, as well as the radius ratio of a

reference radius and the circumcircle. Both measures are well known geometric quality measures for simplicial element types (triangle or tetrahedron). Every particular function included in (6.4.33) approaches its minimum value when the triangle is equilateral (i.e. $R = 2r$) and when $R \ll R_{\text{ref}}$.

Now, let $\mathcal{N}'$ be the set of flagged nodes intended for relocation in a mesh $\mathcal{M}$ according to Definition 6.4.1. Let m_{el} be the number of those elements in $\mathcal{M}$ which contain at least one $P \in \mathcal{N}'$. A possible class of objective functions for the whole mesh then reads

$$\bar{W} \stackrel{\text{def}}{=} \sum_{m_{\text{el}}} \bar{w} = \sum_{m_{\text{el}}} \left(\frac{R}{R_{\text{ref}}} \right)^{\beta} \left(\frac{R}{r} \right)^{\gamma} , \tag{6.4.34}$$

in which the list of arguments $(\boldsymbol{x}_0, \boldsymbol{x}_1, \boldsymbol{x}_2)$ has been suppressed. The weighting exponents in (6.4.34) control the domination of the worst element. For example, if γ is large and β is moderate, then the most distorted element contributes more to the sum than a too large element or any of the remaining elements.

The reference radius is an attribute assigned to every element and defines its maximum acceptable size in the mesh. Specifying appropriate R_{ref} thus controls mesh grading during the optimization process. If the value of the reference radius is not specified by the user *a priori*, but *a posteriori* by element quality measures based on the finite element solution, then an optimization algorithm based on (6.4.34) would lead to r-adaptive mesh improvement. Whenever R_{ref} is constant and takes the same value in all elements, the mesh smoothing algorithm produces a uniform mesh.

It proves convenient to add the following general definitions.

Definition 6.4.35. Let $P_0 \in \mathcal{N}'$ be a flagged node, and let n_{el} be the *number of elements in the mesh sharing* P_0 *as a node* such that the ball associated with P_0 is the disjoint union $\mathcal{B}_0 \stackrel{\text{def}}{=} \bigcup_{n_{\text{el}}} \Omega$, where $\Omega \in \mathcal{M}$. $\mathcal{B}_0$ is closed if $P_0 \in (\mathcal{N}' \cap \mathcal{N}_{\text{int}})$, and open if $P_0 \in (\mathcal{N}' \cap \mathcal{N}_{\text{edg}})$ (corner nodes are not moved; cf. Definition 6.4.6). The *nodes in* $\mathcal{B}_0$ *other than* P_0 will be denoted by P_k, with $k \in \{1, \ldots, n_{\text{nd}}\}$, and n_{nd} being the *number of nodes in the ball except for* P_0. ◇

Definition 6.4.36. Let $\mathcal{B}_0$ be the ball associated with $P_0 \in \mathcal{N}'$. The *position vectors of the nodes* $P_0, P_1, \ldots, P_k, \ldots, P_{n_{\text{nd}}} \in \mathcal{S}$ *in the ball* $\mathcal{B}_0$ *with respect to an arbitrary origin* $O \in \mathcal{S}$ are defined through $\boldsymbol{x}_0, \boldsymbol{x}_1, \ldots, \boldsymbol{x}_k, \ldots, \boldsymbol{x}_{n_{\text{nd}}} \in \mathbb{R}^2$, respectively. Locally, the numbering of the nodes $0, 1, \ldots, N-1 \in \Omega$ in each element of the ball is chosen such that the orientation of the element with respect to the canonical basis in $\mathbb{R}^2$ is positive (cf. Definition B.1), and such that the location of the node $0 \in \Omega$ in $\mathcal{S}$ coincides with that of $P_0 \in \mathcal{N}'$. The position vectors of the element nodes with respect to $O \in \mathcal{S}$ are denoted by $\boldsymbol{x}_I \stackrel{\text{def}}{=} (x_I, y_I)^{\text{T}}$, where $I \in \{0, 1, \ldots, N-1\}$, and, by the previous convention, $\overrightarrow{O0} \stackrel{\text{def}}{=} \overrightarrow{OP_0} \stackrel{\text{def}}{=} \boldsymbol{x}_0$ concerning a single element. ◇

For the purposes of the present work, the class of objective functions defined through (6.4.34) is further specialized. The values $\beta = 1.0$, $\gamma = 3.0$, and $R_{\text{ref}} = 1.0$ are assigned to all elements in the mesh [cf. Braess, 2000; Braess and Wriggers, 2000]. Moreover, in order to render the resulting smoothing algorithm more effective, the sum in (6.4.34)

is taken only over the n_{el} triangles in the ball $\mathcal{B}_0(P_0) = \bigcup_{n_{\text{el}}} \triangle(P_0)$ associated with a single internal node $P_0 \in \mathcal{N}'$. The location of P_0 that smoothes the ball is regarded as the basic unknown, and the nodes $0, 1, 2 \in \triangle$ in each triangle of the ball are re-ordered in accordance with Definition 6.4.36.

Definition 6.4.37. Let $\mathcal{X} \subset \mathbb{R}^2$ and $\boldsymbol{x}_0 \in \mathcal{X}$. By the conventions above, the objective function $W : \mathcal{X} \to \mathbb{R}$ employed in the present work reads

$$W(\boldsymbol{x}_0) \stackrel{\text{def}}{=} \sum_{n_{\text{el}}} w(\boldsymbol{x}_0)\,, \qquad \text{with} \quad w(\boldsymbol{x}_0) \stackrel{\text{def}}{=} \frac{R(\boldsymbol{x}_0)}{R_{\text{ref}}} \left(\frac{R(\boldsymbol{x}_0)}{r(\boldsymbol{x}_0)} \right)^3 ,$$

and R and r being the circumcircle radius and incircle radius of the triangle, respectively, which can be computed according to (B.7) resp. (B.8). ♢

Only the closed balls in the sense of Definition 6.4.35 will be handled by 6.4.37, that is, $\boldsymbol{x}_0$ is the variable location of a flagged internal mesh node intended for relocation, and $\mathcal{X}$ is the domain in $\mathcal{S} = \mathbb{R}^2$ covered by the closed ball. Flagged boundary nodes, on the other hand, will not be handled by 6.4.37 but will be efficiently smoothed by the weighted averaging procedure summarized in Alg. 6.3.

Recall that if $\boldsymbol{x}_0' \in \arg\min_{\boldsymbol{x}_0 \in \mathcal{X}} W(\boldsymbol{x}_0)$ is a local minimizer of $W : \mathcal{X} \to \mathbb{R}$ on $\mathcal{X}$, then

$$\boldsymbol{\nabla} W(\boldsymbol{x}_0') = \boldsymbol{0} \tag{6.4.38}$$

by Theorem 6.4.21(i). By (iii) of the same theorem, $\boldsymbol{x}_0'$ is a strict local minimizer if the Hessian $\boldsymbol{H}_W(\boldsymbol{x}_0')$ is positive definite. To locally minimize W resp. to locally smooth the interior of the considered two-dimensional triangle mesh, the definitions in 6.4.37 are substituted into the iterative scheme (6.4.26) of Newton's method:

$$\boldsymbol{x}_0^{j+1} = \boldsymbol{x}_0^j - (\boldsymbol{H}_W^{-1} \boldsymbol{\nabla} W)(\boldsymbol{x}_0^j)\,, \qquad \text{and} \quad \lim_{j \to \infty} \boldsymbol{x}_0^{j+1} = \boldsymbol{x}_0'\,. \tag{6.4.39}$$

By linearity, then,

$$\boldsymbol{\nabla} W(\boldsymbol{x}_0^j) = \sum_{n_{\text{el}}} \boldsymbol{\nabla} w(\boldsymbol{x}_0^j) \qquad \text{and} \qquad \boldsymbol{H}_W(\boldsymbol{x}_0^j) = \sum_{n_{\text{el}}} \boldsymbol{H}_w(\boldsymbol{x}_0^j)\,. \tag{6.4.40}$$

Closed-form expressions for the components of $\boldsymbol{\nabla} w(\boldsymbol{x}_0^j)$ and $\boldsymbol{H}_w(\boldsymbol{x}_0^j)$, i.e. the first- and second-order partial derivatives of w, are available through (B.5)-(B.8); see Appendix C for a straightforward calculation.

Exact Newton's method in the form (6.4.39) is combined with backtracking line search using Armijo's rule (6.4.31), and with the Goldstein-Price method (6.4.29) that handles non-positive definite Hessians. The globally optimized mesh is approximated by looping over the flagged internal nodes of the mesh repeatedly. Hence, smoothing of the whole interior mesh is achieved in an iterative fashion. The entire procedure is provided by Alg. 6.5, which shall be referred to as the OSMOT (Optimization-based SMOothing of Triangle meshes) algorithm. The included tolerances have been chosen to $\varepsilon = 10^{-8}$, $\delta = 10^{-6}$, and $\eta = 0.05$ for all the numerical examples of Chapter 8. The resulting algorithm is both efficient and robust and works excellently on unstructured and structured meshes, as well as on convex and non-convex meshes (cf. Chapter 8).

Algorithm 6.5: OSMOT – Optimization-based mesh smoothing by damped Newton's method using the Armijo rule and the Goldstein-Price method.

Input: distorted mesh geometry $\boldsymbol{x}^-$, set $\mathcal{N}' \cap \mathcal{N}_{\text{int}}$ of internal nodes intended for relocation, closed ball $\mathcal{B}_0$ associated with every $P_0 \in (\mathcal{N}' \cap \mathcal{N}_{\text{int}})$

Output: smoothed interior mesh geometry $\boldsymbol{x}^+$

initialize $i = 0$, tolerances ε, δ, and η;
while *global iteration step* $i \leq i_{\max}$ **do**
  foreach $P_0 \in (\mathcal{N}' \cap \mathcal{N}_{\text{int}})$ **do**
    initialize $j = 0$, $\boldsymbol{x}_0^{j=0} = \boldsymbol{x}^-(P_0)$, and $\lambda^{j=0} = 1.0$;
    while *damped Newton iteration step* $j \leq j_{\max}$ **do**
      initialize $W(\boldsymbol{x}_0^j)=0$, $W(\boldsymbol{x}_0^j + \lambda^j \boldsymbol{d}^j)=0$, $\boldsymbol{\nabla} W(\boldsymbol{x}_0^j)=\boldsymbol{0}$, $\boldsymbol{H}_W(\boldsymbol{x}_0^j)=\boldsymbol{0}$;
      while *element in the ball* $e \leq n_{\text{el}}$ **do**
        read and store locations of nodes $\boldsymbol{x}_0^j$, $\boldsymbol{x}_1$, and $\boldsymbol{x}_2$;
        compute element objective function $w(\boldsymbol{x}_0^j)$ by 6.4.37;
        compute gradient $\boldsymbol{\nabla} w(\boldsymbol{x}_0^j)$ and Hessian $\boldsymbol{H}_w(\boldsymbol{x}_0^j)$ (Appendix C);
        $W(\boldsymbol{x}_0^j) \leftarrow W(\boldsymbol{x}_0^j) + w(\boldsymbol{x}_0^j)$;
        $\boldsymbol{\nabla} W(\boldsymbol{x}_0^j) \leftarrow \boldsymbol{\nabla} W(\boldsymbol{x}_0^j) + \boldsymbol{\nabla} w(\boldsymbol{x}_0^j)$;
        $\boldsymbol{H}_W(\boldsymbol{x}_0^j) \leftarrow \boldsymbol{H}_W(\boldsymbol{x}_0^j) + \boldsymbol{H}_w(\boldsymbol{x}_0^j)$;
      if $\|\boldsymbol{\nabla} W(\boldsymbol{x}_0^j)\| < \varepsilon$ **then**
        exit (location of P_0 is optimal);
      else
        Descent Direction (Goldstein-Price Method):
        if $\det \boldsymbol{H}_W(\boldsymbol{x}_0^j) < \delta$ **then**
          steepest descent $\boldsymbol{d}^j = -\boldsymbol{\nabla} W(\boldsymbol{x}_0^j)$;
        else
          Newton's direction $\boldsymbol{d}^j = -(\boldsymbol{H}_W^{-1} \boldsymbol{\nabla} W)(\boldsymbol{x}_0^j)$;
          compute $\cos\theta^j = -(\boldsymbol{\nabla} W(\boldsymbol{x}_0^j))^{\mathrm{T}} \boldsymbol{d}^j / \|\boldsymbol{\nabla} W(\boldsymbol{x}_0^j)\| \|\boldsymbol{d}^j\|$;
          if $\cos\theta^j < \eta$ **then**
            steepest descent $\boldsymbol{d}^j = -\boldsymbol{\nabla} W(\boldsymbol{x}_0^j)$;
        Line Search (Armijo Rule):
        while *element in the ball* $e \leq n_{\text{el}}$ **do**
          compute element objective function $w(\boldsymbol{x}_0^j + \lambda^j \boldsymbol{d}^j)$ by 6.4.37;
          $W(\boldsymbol{x}_0^j + \lambda^j \boldsymbol{d}^j) \leftarrow W(\boldsymbol{x}_0^j + \lambda^j \boldsymbol{d}^j) + w(\boldsymbol{x}_0^j + \lambda^j \boldsymbol{d}^j)$;
        if $W(\boldsymbol{x}_0^j + \lambda^j \boldsymbol{d}^j) - W(\boldsymbol{x}_0^j) \leq \frac{1}{2} \lambda^j (\boldsymbol{\nabla} W(\boldsymbol{x}_0^j))^{\mathrm{T}} \boldsymbol{d}^j$ **then**
          update nodal location $\boldsymbol{x}_0^{j+1} = \boldsymbol{x}_0^j + \lambda^j \boldsymbol{d}^j$, whereas $\lambda^{j+1} = \lambda^j$;
        else
          update step size $\lambda^{j+1} = \frac{1}{2} \lambda^j$, whereas $\boldsymbol{x}_0^{j+1} = \boldsymbol{x}_0^j$;
      $j \leftarrow j + 1$;
    location of P_0 smoothing the ball is $\boldsymbol{x}_0' = \boldsymbol{x}_0^j$;
  $i \leftarrow i + 1$;
totality of (new) locations of all the nodes in the mesh is $\boldsymbol{x}^+$;

6.5 Transport Step

The mesh motion assigned in the previous step biases the solution state obtained after the Lagrangian step. This is because the variables had been stored at the nodes resp. at the integration points of the finite elements, which have been relocated during the mesh motion step. Therefore, a correcting remap of the solution variables onto the updated mesh becomes necessary. Because the mesh motion step preserves all the topological properties of the mesh by definition, this remap can be carried out in a conservative manner, that is, as an advective remap.

6.5.1 Advection Problem Associated with the Transport Step

The governing equations of the transport step at the end of a time step in the overall operator-split ALE solution procedure (Alg. 6.1) are the advection equations included in the set (6.2.10). This set can be equivalently expressed in form of the generic ALE conservation law 3.2.42, viz.

$$\frac{\partial \hat{q} J_{\Phi}}{\partial t} + J_{\Phi} \left(\operatorname{div} \boldsymbol{\psi}(q) \right) \circ \Phi = 0 \,. \tag{6.5.1}$$

Here $q_t : \Phi_t(\mathcal{W}) \to T^s_r(\mathcal{S})$, with $q_t(x) = q(x,t)$, is an honest spatial $\binom{r}{s}$-tensor field on the current configuration $\Phi_t(\mathcal{W}) \subset \mathcal{S}$ of a nice (i.e. with piecewise C^1-continuous boundaries) subset $\mathcal{W} \subset \mathcal{R}$ of the reference domain. The referential picture of the field, $\hat{q} \stackrel{\text{def}}{=} q \circ \Phi$, is a tensor field over Φ, and $\boldsymbol{\psi}(q) \stackrel{\text{def}}{=} q \otimes \boldsymbol{c}$ is the linear flux density of q along the convective velocity (Definition 3.2.8).

The general multi-dimensional advection problem including discontinuities and non-linearities can only be solved approximatively because no exact solution is available. Concerning numerical solution of the advection problem, the definitions made in Section 6.2 are used throughout. The transport step takes place in the pseudo time interval $[t^-_{n+1}, t^+_{n+1}] \stackrel{\text{def}}{=} [t^-, t^+]$ whose magnitude, by abuse of notation, is denoted by Δt as in other sections. Clearly,

$$\Delta t \stackrel{\text{def}}{=} t^+ - t^- \,. \tag{6.5.2}$$

The generic quantity q in (6.5.1) probably has evolved during the Lagrangian step, but it actually is time-independent during the transport step. The configuration of the material body in space is frozen. Therefore, the transport step in operator-split ALE method is characterized by

$$\boldsymbol{v}(x,t) \equiv \boldsymbol{0} \quad \text{and} \quad \frac{\partial q(x,t)}{\partial t} \equiv 0 \,, \qquad \text{for all } \; t \in [t^-, t^+] \,, \tag{6.5.3}$$

so that $\dot{q}(x,t) = 0$ also holds, but $\boldsymbol{\nabla} q(x,t) \neq \boldsymbol{0}$ in general. Therefore, time-dependency of the transported variable is solely implicit, i.e. $q(x,t) \equiv q(x) = q(\Phi(\chi,t)) = \hat{q}(\chi,t)$ during the transport step, with $t \in [t^-, t^+]$.

Data assumed to be given in the transport step includes both the distorted and smoothed geometry $\Phi(\mathcal{R}, t^-)$ and $\Phi(\mathcal{R}, t^+)$, represented by the totality of nodal positions $\boldsymbol{x}^-$ and $\boldsymbol{x}^+$, respectively, as well as the Jacobian J^-, the Cauchy stress $\boldsymbol{\sigma}^-$, and the set of material state variables $\boldsymbol{\alpha}^- = \{\alpha_k^-\}$ given at the quadrature points at time $t = t^-$. The convective velocity $\boldsymbol{c}$ is given at the nodes. Recall that $\boldsymbol{x}^\pm$, where $\pm$ means *either* $+$ *or* $-$, is the position vector (with respect to some origin) of the spatial point $x^\pm \stackrel{\text{def}}{=} \Phi(\chi, t^\pm)$ occupied by the reference point $\chi \in \mathcal{R}$ at time $t = t^\pm$. Since no physical time is associated with the transport step, the transport boils down to the instantaneous projection or remap (6.2.21). In shorthand notation, this remap reads $q^- \to q^+$, where $q \in \{J, \boldsymbol{\sigma}, \boldsymbol{\alpha}\}$ and

$$q^\pm \stackrel{\text{def}}{=} \{q(x, t^\pm) \equiv q(x) \,|\, x \in \Phi(\mathcal{R}, t^\pm)\}\,. \tag{6.5.4}$$

That is, $q^\pm(\chi) \stackrel{\text{def}}{=} q(\Phi(\chi, t^\pm)) = \hat{q}(\chi, t^\pm)$. Owing to (6.5.1), however, the remap in the transport step takes the form of an *advection problem*, which is a particular initial value problem subject to the initial condition

$$\{J,\, \boldsymbol{\sigma},\, \boldsymbol{\alpha}\}|_{t=t^-} = \{J^-,\, \boldsymbol{\sigma}^-,\, \boldsymbol{\alpha}^-\} \qquad \text{resp.} \qquad q|_{t=t^-} = q^-\,. \tag{6.5.5}$$

As the standard Euclidian point space has been chosen as the background space, the variable q should represent a scalar (e.g. J) or a tensor component (e.g. σ^{ab}) in the global Cartesian coordinate system.

The next section is concerned with the numerical solution of the advection problem. Any appropriate solution method should fulfil some basic requirements like conservativity, accuracy, and stability. These and other requirements have been the matter of intense research and will be addressed in the text as needed. The reader is referred to [Benson, 1989; Ortiz and Quigley, 1991; LeVeque, 1992, 2002; Ganzha and Vorozhtsov, 1996; Toro, 1999; Donea and Huerta, 2003; Freßmann, 2004; Freßmann and Wriggers, 2007; Barth and Ohlberger, 2004] for further reading.

6.5.2 Solution Approaches to the Advection Problem

The common approaches to treat the convective terms present in the ALE transport step are based on either *direct solution* employing C^0-continuous data or *advection algorithms*.

Direct solution of (6.5.1) resp. of its convective form (6.2.4), which is nothing but the linear advection equation without a source, is widely-used in the context of operator-split ALE finite element methods for solid mechanical applications [e.g. Huétink, 1982; Huétink et al., 1990; Aymone et al., 2001; Aymone, 2004; Nazem, 2006; Nazem et al., 2006, 2008; Sheng et al., 2009; Freßmann, 2004; Freßmann and Wriggers, 2007]. Finite element interpolation functions are used to approximate the field and to compute the convective term on a spatially discrete level. The problem to be faced, then, is that the Jacobian, the stress components, and the state variables are stored at the integration points, thus are generally discontinuous across the element edges. Therefore, the crucial

step in direct advection equation solution is the construction of at least C^0-continuous fields which are equivalent to the discontinuous distribution of the variables.

Some of the drawbacks associated with the direct finite element solution of the advection equation can be avoided by using *finite difference methods (FDM)* or *finite volume methods (FVM)*. These strategies have been traditionally pursued by the computational fluid dynamics (CFD) community [cf. Vinokur, 1989; LeVeque, 1992, 2002; Toro, 1999; Ferziger and Perić, 2002; Hirsch, 2007; Barth and Ohlberger, 2004], and have earned broad recognition in the history of development of ALE and related methods [e.g. Amsden and Hirt, 1973; Hirt et al., 1974; Amsden et al., 1980; Benson, 1989, 1992, 1995, 2008; Huerta and Casadei, 1994; Rodríguez-Ferran et al., 1998, 2002; Askes et al., 1998; van Haaren et al., 2000; Di et al., 2007; Freßmann, 2004; Freßmann and Wriggers, 2007]. In operator-split ALE methods, and as done in the present work, FV methods are used to conservatively remap all the variables of the problem from the distorted Lagrangian mesh onto the smoothed mesh despite the fact that some variables, like stress, do not obey a conservation law [cf. Benson, 1992, p. 330].

Finite volume methods originated from the finite difference methods in one dimension [Courant et al., 1952; Godunov, 1959; Lax and Wendroff, 1960], but they are better suited for multi-dimensional problems on irregular domains involving discontinuities in the solution variables [cf. LeVeque, 2002; Barth and Ohlberger, 2004; Hirsch, 2007; Toro, 1999; Ferziger and Perić, 2002; Vinokur, 1989]. They *per se* fulfill the requirement of conservativity, because they solve the integral form of (6.5.1) and are applicable to unstructured computational meshes in two and three dimensions. One of the first FV methods proposed for a structured mesh is that of MacCormack and Paullay [1972], which has been extended shortly after by Rizzi and Inouye [1973]. An early reference concerned with the development of FVM on unstructured meshes is [Barth and Jespersen, 1989].

Inevitably connected with FV methods is the computation of the flux of a solution variable across the boundary of the control volumes. Depending on the accuracy of the computational algorithm, finite volume methods are divided into first-order, second-order, and higher-order accurate methods. The property refers to the accuracy of the spatial approximation used for the flux calculation. Despite this, most finite volume and finite difference advection schemes in ALE methods apply explicit first- or second-order accurate methods to advance solution in time.

The following sections introduce finite volume methods for generally time-dependent control volumes by providing some basic definitions and results. Strategies to determine the numerical flux will be presented, as well as the particular donor-cell (or Godunov-type) advection scheme that has been implemented by the author into the current operator-split ALE method.

Definitions and Conventions Related to Finite Volume Methods

Let $[0, \tau] \subset \mathbb{R}$ denote a continuous time interval, which can be, for example, the pseudo time interval $[t^-, t^+]$ associated with the transport step, and let $\mathcal{D} \stackrel{\text{def}}{=} \Phi(\mathcal{R}, t) \subset \mathcal{S}$,

with $t \in [0,\tau]$, be the spatial domain of the physical problem considered. By the usual conventions, $\varphi_t \stackrel{\text{def}}{=} (\Phi_t \circ \Psi_t^{-1}) : \mathcal{B} \to \mathcal{S}$ is the physical motion of the material body $\mathcal{B}$ in the ambient space $\mathcal{S} = \mathbb{R}^{m_{\text{dim}}}$, whose spatial velocity is $\boldsymbol{v}_t \stackrel{\text{def}}{=} (\frac{\partial}{\partial t}\varphi_t) \circ \varphi_t^{-1}$. Moreover, $\Phi_t : \mathcal{R} \to \mathcal{S}$ is the relative motion of the reference domain $\mathcal{R}$, $\boldsymbol{w}_t \stackrel{\text{def}}{=} (\frac{\partial}{\partial t}\Phi_t) \circ \Phi_t^{-1}$ is its velocity, referred to as the mesh velocity, and $\boldsymbol{c}_t = \Phi_{t\star}\left((\frac{\partial}{\partial t}\Psi_t^{-1}) \circ \Psi_t\right)$ is the convective velocity.

The following definitions concerning finite volume methods consolidate those given in [Barth and Ohlberger, 2004; LeVeque, 2002; Freßmann, 2004; Freßmann and Wriggers, 2007; Lesoinne and Farhat, 1996; Farhat et al., 2001; Barth and Jespersen, 1989; Vinokur, 1989; Hirsch, 2007].

Definition 6.5.6. *Finite volume methods* can be characterized as follows:

(i) They operate on a *control volume tessellation* $\mathcal{T}$, which is established by a finite disjoint union $\mathcal{D}_\mathcal{T} = \bigcup_{j=1}^{n_{\text{cv}}} \mathcal{V}_j$ of $n_{\text{cv}} \in \mathbb{N}$ *control volumes* $\mathcal{V}_j$ that approximately covers the computational domain $\mathcal{D}$. Accordingly, $\mathcal{V}_j \subset \mathcal{D}_\mathcal{T}$ if and only if $\mathcal{V}_j \in \mathcal{T}$. Each control volume $\mathcal{V}_j$ is a probably non-convex polytope having a characteristic length h_j. The control volume is fixed in the Eulerian description, whereas it is a time-dependent image $\mathcal{V}_j \stackrel{\text{def}}{=} \Phi_t(\mathcal{W}_j) = \Phi(\mathcal{W}_j, t)$ in the ALE description, with $\mathcal{W}_j \subset \mathcal{R}$ and $t \in [0,\tau] \subset \mathbb{R}$. The boundary $\partial\mathcal{V}_j$ of every control volume $\mathcal{V}_j$ is piecewise oriented and C^1-continuous by definition. It is throughout assumed that the orientation of the boundary $\partial\mathcal{V}_j$ is compatible with the orientation of $\mathcal{V}_j$ such that the unit normals to $\partial\mathcal{V}_j$, denoted by $\boldsymbol{n}^* \in \Gamma(T^*\mathcal{V}_j)$, point outwards.

(ii) Since overlaps and gaps are precluded, the intersection $\mathcal{V}_j \cap \mathcal{V}_k$ of every pair of control volumes $(\mathcal{V}_j, \mathcal{V}_k)$, with $\mathcal{V}_j, \mathcal{V}_k \in \mathcal{T}$, $j,k \in \{1,\dots,n_{\text{cv}}\}$ and $k \neq j$, equals either $\emptyset$, a vertex, an edge, or a face (only for $m_{\text{dim}} = 3$). Accordingly, the control volume boundary is represented by the disjoint union

$$\partial\mathcal{V}_j = \bigcup_{k\neq j} \mathcal{V}_j \cap \mathcal{V}_k \,.$$

If a vertex, an edge, or a face of $\mathcal{V}_j$ is aligned with the boundary $\partial\mathcal{D}_\mathcal{T}$, a fictive control volume $\mathcal{V}_k$ is added to the tessellation $\mathcal{T}$ as a so-called *ghost cell* such that the intersection $\mathcal{V}_j \cap \mathcal{V}_k$ is non-zero. Those control volume intersections which form an $(m_{\text{dim}}-1)$-face, that is, a *facet* of $\mathcal{V}_j$ are denoted by

$$\Gamma_{j,k} \stackrel{\text{def}}{=} \mathcal{V}_j \cap \mathcal{V}_k \neq \emptyset \,, \qquad \text{with } \mathcal{V}_j, \mathcal{V}_k \in \mathcal{T} \text{ and } k \neq j \,.$$

Note that $\Gamma_{j,k}$ denotes a vertex in 1d, an edge in 2d, and a face in 3d, and that an approximation to the control volume boundary is $\partial\mathcal{V}_j \approx \bigcup_{k=1}^{n_{\text{fac}}} \Gamma_{j,k} \stackrel{\text{def}}{=} \bigcup_{k\neq j} \Gamma_{j,k}$, where n_{fac} is the number of facets of $\mathcal{V}_j$. Here and in what follows, the union $\bigcup_{k\neq j} \stackrel{\text{def}}{=} \bigcup_{\mathcal{V}_j\cap\mathcal{V}_k=\Gamma_{j,k}}$ and the sum $\sum_{k\neq j} \stackrel{\text{def}}{=} \sum_{\mathcal{V}_j\cap\mathcal{V}_k=\Gamma_{j,k}}$ take only into account the $(m_{\text{dim}}-1)$-faces $\Gamma_{j,k} = \mathcal{V}_j \cap \mathcal{V}_k \neq \emptyset$, with $k \neq j$. Intersections $\mathcal{V}_j \cap \mathcal{V}_k$ that define a vertex in 2d and 3d, or an edge in 3d will not be considered.

(iii) Let $q_t : \mathcal{D} \to \mathbb{R}$ be a time-dependent scalar-valued spatial field, with $q_t(x) = q(x,t)$ and $x = \Phi(\chi,t) \in \mathcal{S}$. Supposing that the relative motion Φ_t and the convective velocity

$\boldsymbol{c}_t$ are given, the *transport of the field q on a moving mesh* based on a finite volume method is concerned with the approximate solution to the integral form of the generic ALE conservation law (6.5.1) with respect to each control volume and subject to the initial condition $q(x,t)|_{t=0} = q_0(x)$:

$$\frac{\mathrm{d}}{\mathrm{d}t}\int_{\mathcal{V}_j} q\,\mathbf{d}\boldsymbol{v} + \int_{\partial\mathcal{V}_j} q\boldsymbol{c}\cdot\boldsymbol{n}^*\,\mathbf{d}\boldsymbol{a} = 0\,, \qquad \text{where} \quad \mathcal{V}_j = \Phi(\mathcal{W}_j,t)\,.$$

This equation is a general conservation law (Section 3.2). Recall that $(q\boldsymbol{c})(x,t) \stackrel{\text{def}}{=} \boldsymbol{\psi}(q(x,t))$ is the flux density of q per unit area per unit time along the convective velocity, being linear in q in the present case.

(iv) In solving the problem defined through (iii), finite volume methods approximate the evolution of the *control volume average*

$$\bar{q}_j(x,t) \stackrel{\text{def}}{=} \frac{1}{V_j}\int_{\mathcal{V}_j} q(x,t)\,\mathbf{d}\boldsymbol{v}\,, \qquad \text{with} \quad V_j \stackrel{\text{def}}{=} \int_{\mathcal{V}_j}\mathbf{d}\boldsymbol{v} \quad \text{and} \quad \lim_{V_j\to 0}\bar{q}_j(x,t) = q(x,t)\,,$$

for the considered variable q and each control volume $\mathcal{V}_j$ over the time interval $[0,\tau]$, with $j \in \{1,\ldots,n_{\mathrm{cv}}\}$. Accordingly, the field $\bar{q}$ on the tessellated domain $\mathcal{D}_{\mathcal{T}} \approx \mathcal{D}$ is a piecewise constant representation of q. It is assumed that the control volumes are regular and that the underlying vector basis in $\mathcal{S} = \mathbb{R}^{m_{\mathrm{dim}}}$ used for the subsequent computations is positively oriented with respect to the volume form $\mathbf{d}\boldsymbol{v}$, so that $V_j > 0$ always and for all $\mathcal{V}_j \in \mathcal{T}$ (otherwise, $|V_j|$ has to be used to define $\bar{q}_j$). The measure V_j is a volume if $m_{\mathrm{dim}} = 3$, an area if $m_{\mathrm{dim}} = 2$, and a length if $m_{\mathrm{dim}} = 1$, but the term *volume* is used in all cases for reasons of convenience.

(v) The *averaged convective volume flux density* across the moving and deforming control volume facet $\Gamma_{j,k} = \mathcal{V}_j \cap \mathcal{V}_k$, with $\mathcal{V}_j = \Phi(\mathcal{W}_j,t)$, $j,k \in \{1,\ldots,n_{\mathrm{cv}}\}$, and $k \neq j$, is defined by

$$F^V_{j,k}(x,t) \stackrel{\text{def}}{=} \frac{1}{S_{j,k}}\int_{\Gamma_{j,k}} \boldsymbol{c}(x,t)\cdot\boldsymbol{n}^*(x)\,\mathbf{d}\boldsymbol{a}\,, \qquad \text{where} \quad S_{j,k} \stackrel{\text{def}}{=} \int_{\Gamma_{j,k}}\mathbf{d}\boldsymbol{a}\,.$$

The total convective volume flux across the control volume boundary $\partial\mathcal{V}_j \approx \bigcup_{k\neq j}\Gamma_{j,k}$ is then given by $\sum_{k\neq j} S_{j,k}F^V_{j,k}$. Moreover, if $\boldsymbol{y} : \mathcal{S} \to T\mathcal{S}$ is a constant vector field, the *averaged outward normal field $\boldsymbol{n}_{j,k}(x)$ on $\Gamma_{j,k}$* is defined through

$$\boldsymbol{y}\cdot\boldsymbol{n}_{j,k} \stackrel{\text{def}}{=} \frac{1}{S_{j,k}}\int_{\Gamma_{j,k}} \boldsymbol{y}\cdot\boldsymbol{n}^*\,\mathbf{d}\boldsymbol{a}\,.$$

Accordingly, there is a unique *averaged convective velocity field $\boldsymbol{c}_{j,k}$ on $\Gamma_{j,k}$* defined by $F^V_{j,k}(x,t) \stackrel{\text{def}}{=} \boldsymbol{c}_{j,k}(x,t)\cdot\boldsymbol{n}_{j,k}(x)$. Note that volume flux is positive if material leaves the moving control volume $\mathcal{V}_j = \Phi_t(\mathcal{W}_j)$ through the moving boundary. For convenience, the measure $S_{j,k} > 0$ is called *area* for all $m_{\mathrm{dim}} \in \{1,2,3\}$, although it would be a length in 2d, and a point in 1d.

(vi) For every pair of control volumes $(\mathcal{V}_j, \mathcal{V}_k)$, the true averaged convective flux density of the field q across the facet $\Gamma_{j,k} = \mathcal{V}_j \cap \mathcal{V}_k \neq \emptyset$ is replaced by a *numerical averaged convective flux density* $F^q_{j,k}$:

$$F^q_{j,k}(x,t) \approx \frac{1}{S_{j,k}} \int_{\Gamma_{j,k}} q(x,t)\, \boldsymbol{c}(x,t) \cdot \boldsymbol{n}^*(x)\, \mathbf{d}\boldsymbol{a}\,, \qquad \text{for all } \Gamma_{j,k} = \mathcal{V}_j \cap \mathcal{V}_k \neq \emptyset,\ k \neq j\,.$$

The numerical averaged convective flux density is regarded as a Lipschitz-continuous function $\mathfrak{F} : \mathbb{R}\times\mathbb{R}\times\mathbb{R} \to \mathbb{R}$ of the averaged convective volume flux $F^V_{j,k}$ defined through (v) as well as of the two states $\bar{q}_j, \bar{q}_k$ of the averaged field $\bar{q} : \mathcal{D}_\mathcal{T} \to \mathbb{R}$ at $\Gamma_{j,k}$. That is,

$$F^q_{j,k} \stackrel{\text{def}}{=} \mathfrak{F}(\bar{q}_j, \bar{q}_k, F^V_{j,k})\,.$$

Accordingly, $\sum_{k\neq j} S_{j,k} F^q_{j,k}$ is an approximation to the total convective flux of q across the control volume boundary $\partial\mathcal{V}_j \approx \bigcup_{k\neq j} \Gamma_{j,k}$.

(vii) The numerical flux function $\mathfrak{F}$ defined in (vi) should be *consistent* with the averaged convective volume flux density defined in (v) in such a way that

$$\mathfrak{F}(1, 1, F^V_{j,k}) = F^V_{j,k}\,. \qquad \diamond$$

Remark 6.5.7. The initial value problem associated with the transport step constitutes an *advective remap* rather than an advection problem in its classical sense. This is because of the property (6.5.3). The data $q(x,t^-) = q(x,t^+)$ is regarded stationary in space during the transport step, by which $q(x,t) \equiv q(x) = q(\Phi(\chi,t))$ can be set. Therefore, time-dependency is only implicit by the relative map Φ_t. A method that determines $q(x,t)$ on a fixed mesh likewise determines $q(\Phi(\chi,t))$ on a non-stationary mesh because the viewpoints are dual. In the definitions above, the arguments (x,t) have been used for reasons of generality, and to be in accordance with the majority of literature in this area. However, the average for a moving control volume defined in (iv) remains a function of time, even if the field is stationary in space. $\triangle$

Spatial and Temporal Discretization, Integration in Time

Along with spatial discretization of the problem phrased in Definition 6.5.6(iii) using a control volume tessellation $\mathcal{T}$, the scalar field $q_t(x) = q(x,t)$ under consideration is approximated by some field $q_t^\blacksquare : \mathcal{D}_\mathcal{T} \to \mathbb{R}$ which is piecewise constant in space. Hence, the control volume average defined through 6.5.6(iv) is generally approximated as

$$\bar{q}_j(x,t) \approx q_j(x,t) \stackrel{\text{def}}{=} \frac{1}{V_j} \int_{\mathcal{V}_j} q^\blacksquare(x,t)\, \mathbf{d}\boldsymbol{v}\,. \tag{6.5.8}$$

In the present work, the control volume tessellation has to be constructed based on the background finite element mesh $\mathcal{M}$ that is used in the overall ALE solution procedure. The different ways to obtain the tessellation are illustrated in Fig. 6.2. For historical reasons, the influence domain of a single storage point within a finite element is called the *cell* associated with that point. The totality of discrete values of the variable at

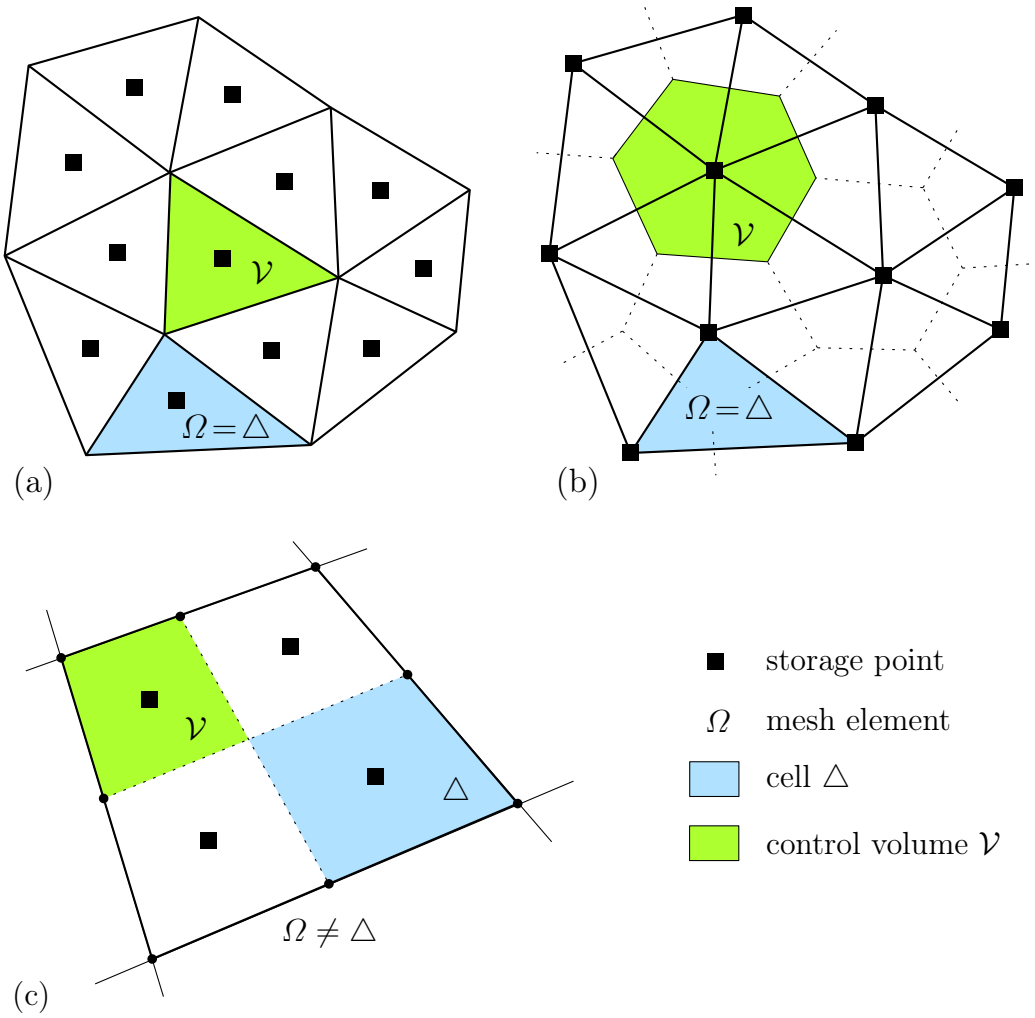

Figure 6.2: Variants of control volume definition used in finite volume-based solution methods. (a) cell-centered, (b) vertex-centered, (c) cell-centered in elements with multiple quadrature points. See also [Barth and Ohlberger, 2004; Rodríguez-Ferran et al., 1998].

all storage points of the mesh represents the desired piecewise constant field $q^{\blacksquare}$ with respect to the cell complex. The influence domains of the element's quadrature points can be employed in order to set up cell-centered control volumes. In this case, the control volume average of the variable approximately equals the discrete value at the storage point:

$$\bar{q}_j(x,t) \approx q_j(x,t) = q^{\blacksquare}(x,t)|_{\mathcal{V}_j} = \text{const.} \qquad \text{for every } j \in \{1,\ldots,n_{\text{cv}}\}\,. \tag{6.5.9}$$

In summarizing the preceding considerations, the semi-discrete (discrete in space, continuous in time) form of the problem phrased in Definition 6.5.6(iii) is concerned with the solution of

$$\frac{\mathrm{d}}{\mathrm{d}t}\,(q_j V_j) = -\sum_{k\neq j} S_{j,k} F^q_{j,k}\,, \qquad \text{with} \quad F^q_{j,k} = \mathfrak{F}(q_j, q_k, F^V_{j,k})\,, \tag{6.5.10}$$

for all $\mathcal{V}_j \in \mathcal{T}$ and subject to prescribed initial conditions. q_k is the approximation to the averaged field in the control volume $\mathcal{V}_k$ contiguous to the control volume $\mathcal{V}_j$ sharing the facet $\Gamma_{j,k} = \mathcal{V}_j \cap \mathcal{V}_k \neq \emptyset$, where $j, k \in \{1, \ldots, n_{\text{cv}}\}$ and $k \neq j$.

In addition to the spatial discretization of the computational domain by control volumes, the continuous time interval $[0, \tau] \subset \mathbb{R}$ is approximated by a sequence $(0, \ldots, t_n, t_{n+1} = t_n + \Delta t, \ldots, \tau)$ of discrete time steps with step length $\Delta t = t_{n+1} - t_n > 0$. In case of the ALE transport step taking place over the pseudo time interval $[t^-, t^+]$, the pseudo time increment associated with that step is defined through $\Delta t = t^+ - t^-$; see (6.5.2). Variables associated with the configurations at time t^- and t^+ (i.e. before and after the remap) are superscripted with $-$ and $+$, respectively. For example, the *volume measures* of $\Phi(\mathcal{W}_j, t^-)$ and $\Phi(\mathcal{W}_j, t^+)$ in $\mathcal{S}$, with $j \in \{1, \ldots, n_{\text{cv}}\}$, are respectively defined through

$$V_j^- \stackrel{\text{def}}{=} \int_{\Phi(\mathcal{W}_j, t^-)} \mathbf{d}\boldsymbol{v} \qquad \text{and} \qquad V_j^+ \stackrel{\text{def}}{=} \int_{\Phi(\mathcal{W}_j, t^+)} \mathbf{d}\boldsymbol{v} \,. \tag{6.5.11}$$

Their difference, the *total transported volume* or *fluxing volume*, is defined through $\Delta V_j \stackrel{\text{def}}{=} V_j^- - V_j^+$, which is positive if the amount of gained material over the time step Δt is outbalanced by the amount of material leaving the moving control volume. The evaluation of ΔV_j will be discussed later.

First-order accurate explicit methods to integrate (6.5.10) in time are the common choice in operator-split ALE methods for solid mechanical applications, and the issues arising from the geometric conservation laws 3.2.39 (volume and surface conservation) are usually ignored (see Section 6.2.1). In following this guideline, one arrives at

Proposition 6.5.12. *Explicit integration of the semi-discrete initial value problem (6.5.10) over the pseudo time interval $[t^-, t^+]$ by the forward Euler method (A.3.3) results in the finite volume transport algorithm*

$$q_j^+ = \frac{q_j^- V_j^- - \Delta t \sum_{k \neq j} S_{j,k}^- F_{j,k}^{q-}}{V_j^+} \,, \qquad \textit{with} \quad V_j^+ = V_j^- - \Delta V_j \,,$$

and all flux densities $F_{j,k}^V$ and $F_{j,k}^q = \mathfrak{F}(q_j, q_k, F_{j,k}^V)$ across the facet $\Gamma_{j,k} = \mathcal{V}_j \cap \mathcal{V}_k \neq \emptyset$ with $k \neq j$ being calculated with respect to the mesh configuration and associated data at time t^-.

Proof. The forward Euler method approximates the time derivative in (6.5.10) by

$$\frac{\mathrm{d}}{\mathrm{d}t}(q_j V_j) \approx \frac{q_j^+ V_j^+ - q_j^- V_j^-}{\Delta t} \,,$$

yielding an update formula for the control volume average of the variable. The explicit nature of the forward Euler method now requires the flux densities $F_{j,k}^V$ and $F_{j,k}^q$ to be evaluated with data given at time t^-, which finally proves the assertion. ∎

Proposition 6.5.13. *For $V_j^+ = V_j^- - \Delta t \sum_{k \neq j} S_{j,k} F_{j,k}^V$, algorithm 6.5.12 is equivalent to*

$$q_j^+ = q_j^- - \frac{\Delta t}{V_j^+} \sum_{k \neq j} S_{j,k}^- (F_{j,k}^{q-} - q_j^- F_{j,k}^{V-}) \,.$$

Explicit advection algorithms give rise to stability issues. Stability of a numerical algorithm ensures that the local errors introduced by the approximate solution are not amplified and that the global error produced by the algorithm after several time steps is bounded. A necessary stability condition for any transport algorithm (explicit or implicit) is the well-known *Courant-Friedrichs-Lewy (CFL) condition* [Courant et al., 1928], which can be formalized as [cf. Freßmann and Wriggers, 2007]

$$0 \leq \quad Co \stackrel{\text{def}}{=} \frac{\|\boldsymbol{c}\,\Delta t\|}{h} \quad \leq 1\,. \tag{6.5.14}$$

Here $\boldsymbol{c}$ is the convective velocity, Δt is the time increment, $h > 0$ is a characteristic element length, and Co is called the *Courant number* or *CFL number*. The CFL condition phrases that a material particle must not pass an element within one step. Concerning the transport step of implicit operator-split ALE methods for quasi-static problems, the condition (6.5.14) applied to the discrete convective velocity 6.2.22 constrains the difference of nodal positions before and after the mesh motion step:

$$\|\boldsymbol{x}^- - \boldsymbol{x}^+\| \leq h\,. \tag{6.5.15}$$

While integration of (6.5.10) over the time increment Δt is commonly carried out explicitly by the forward Euler method, the ALE advection algorithms essentially differ in the numerical scheme to determine the flux term on the right hand sides of 6.5.12. This will be investigated next, by starting with the one-dimensional case.

Determination of the Fluxes in One Dimension

The classical procedures to determine the numerical flux function in 6.5.12 in accordance with Definition 6.5.6(vi) are based on one-dimensional finite difference schemes. To this end, consider a one-dimensional finite volume setup defining the j-th time-dependent control volume by $\mathcal{V}_j \stackrel{\text{def}}{=} [x_{j-1/2}, x_{j+1/2}] \subset \mathbb{R}$, with $j \in \{1, \ldots, n_{\text{cv}}\}$ and $x_{j-1/2} < x_{j+1/2}$, and the time-dependency of $x_{j-1/2} = \Phi(\chi_{j-1/2}, t) \stackrel{\text{def}}{=} x_{j-1/2}(t)$ and $x_{j+1/2} = \Phi(\chi_{j+1/2}, t) \stackrel{\text{def}}{=} x_{j+1/2}(t)$ being understood. The volume measure of the j-th control volume is the distance $\Delta x_j \stackrel{\text{def}}{=} x_{j+1/2} - x_{j-1/2} = V_j$. Finite difference notation [Benson, 1992] has been employed such that the two-point set $\{x_{j-1/2}, x_{j+1/2}\}$, with $x_{j\pm1/2} = \Gamma_{j,j\pm1} = \mathcal{V}_j \cap \mathcal{V}_{j\pm1}$ and $j \in \{1, \ldots, n_{\text{cv}}\}$, denotes the control volume boundary. The unit outward normals at the two boundary vertices are $n(x_{j-1/2}) = -1$ and $n(x_{j+1/2}) = +1$, respectively. The notations $(\cdot)_{j\pm1/2}$ and $(\cdot)_{j,j\pm1}$ for quantities specified at the boundary vertices are interchangeable.

The generic ALE integral conservation law of 6.5.6(iii) over the one-dimensional control volume reads

$$\frac{\mathrm{d}}{\mathrm{d}t} \int_{x_{j-1/2}}^{x_{j+1/2}} q(x,t)\,\mathrm{d}x = -\Big((qc)(x_{j+1/2},t) - (qc)(x_{j-1/2},t)\Big)\,, \tag{6.5.16}$$

in which $c(x,t)$ is the one-component convective velocity. Finite volume discretization in space and first-order accurate integration in time results in

$$q_j^+ \Delta x_j^+ - q_j^- \Delta x_j^- = -(F^q_{j+1/2} + F^q_{j-1/2})\Delta t\,, \tag{6.5.17}$$

in which $F^q_{j\pm1/2} \overset{\text{def}}{=} \mathfrak{F}(q_j, q_{j\pm1}, F^V_{j\pm1/2}) \approx \pm(qc)(x_{j\pm1/2}, t)$ and $F^q_{j\pm1/2} \overset{\text{def}}{=} F^q_{j,j\pm1}$. The negative sign at $x = x_{j-1/2}$ is due to the unit outward normal $n(x_{j-1/2})$ pointing in the negative x-direction. If integration in time is carried out explicitly by the forward Euler method, then (6.5.17) is the one-dimensional counterpart of algorithm 6.5.12.

Recall that since no physical time is associated with the transport step, the convective velocity plays the role of a negative mesh velocity over the pseudo time increment $\Delta t = t^+ - t^-$ (cf. Remark 6.2.24). By this and the procedure outlined in [Lesoinne and Farhat, 1996, sec. 2.3], it can be shown that the convective volume flux $F^V_j = F^V_{j+1/2} + F^V_{j-1/2}$ satisfies the volume conservation law 3.2.39(i) in one dimension over Δt provided that

$$F^V_{j\pm1/2} = \pm\, c_{j\pm1/2}\,, \qquad \text{with} \quad c_{j\pm1/2} = (x^-_{j\pm1/2} - x^+_{j\pm1/2})/\Delta t\,. \tag{6.5.18}$$

The formula for the convective velocity at the nodes, $c_{j\pm1/2}$, corresponds to that of Proposition 6.2.22. Note that if $c(x,t) > 0$ for all $x \in [x_{j-1/2}, x_{j+1/2}]$, then $F^V_{j-1/2} = -c_{j-1/2} < 0$ is a flux *into* the control volume, whereas $F^V_{j+1/2} = c_{j+1/2} > 0$ is an *outflux*. If on the other hand $c < 0$, then $F^V_{j-1/2} > 0$ is an outflux and $F^V_{j+1/2} < 0$ is an influx. Clearly, the general characterization of the flux is

$$\operatorname{sgn}(F^V_{j\pm1/2}) = \begin{cases} +1 & \text{outflux} \\ 0 & \text{no flux} \\ -1 & \text{influx}\,. \end{cases} \tag{6.5.19}$$

$\operatorname{sgn} : \mathbb{R} \to \{-1, 0, +1\}$ is the sign function, with properties $a = |a| \operatorname{sgn} a$ and $|a| = a \operatorname{sgn} a$ for all $a \in \mathbb{R}$, and $\operatorname{sgn} a = a/|a|$ for $a \neq 0$. The property (6.5.19) of the volume flux will be utilized to define reasonable numerical flux functions for the variable q.

In order to complete the transport algorithm 6.5.17, the numerical convective flux $F^q_{j\pm1/2}$ resp. $F^q_{j,j\pm1}$ of the field q across the control volume boundary has to be determined. The numerical flux should possess some important properties so that the algorithm fulfills some basic requirements. Among these requirements, four should be stated more clearly [cf. LeVeque, 2002; Barth and Ohlberger, 2004; Margolin and Shashkov, 2006]:

Definition 6.5.20. A transport algorithm of the form (6.5.17) is called

(i) *conservative* if

$$F^q_{j,j\pm1} = -F^q_{j\pm1,j}\,.$$

(ii) *consistent* if it is exact for all functions q satisfying (6.5.16) as $\Delta t \to 0$, and if

$$F^q_{j,j\pm1} \equiv 0 \qquad \text{unless} \quad c \neq 0\,.$$

(iii) *monotonicity-preserving* if

$$q^-_j \geq q^-_{j+1}, \ \forall j \text{ and } Co \in [0,1] \qquad \text{implies that} \qquad q^+_j \geq q^+_{j+1}, \ \forall j\,.$$

(iv) *sign-preserving* if

$$q_j^- \geq 0, \ \forall j \text{ and } Co \in [0,1] \qquad \text{implies that} \qquad q_j^+ \geq 0, \ \forall j \,. \qquad \diamond$$

In a conservative transport algorithm, every contribution, say $F^q_{j,j+1}\Delta t$, that is subtracted from (added to) the control volume $\mathcal{V}_j$ is added to (subtracted from) the control volume $\mathcal{V}_{j+1}$ sharing the facet $\Gamma_{j,j+1} = \mathcal{V}_j \cap \mathcal{V}_{j+1}$. Monotonicity is a stronger property than sign-preservation because the latter is independent of the convective velocity distribution in space [Margolin and Shashkov, 2006]. Consistency, as defined by 6.5.20(ii), refers to the local error produced at any one time step. If the algorithm is also stable, then the global error after several time steps is bounded, and so the algorithm is convergent as $\Delta t \to 0$.

Since the flux density of q in the advection equation (6.5.1) is linear in $\boldsymbol{c}$, the simplest numerical flux for a consistent finite volume algorithm in the ALE transport step would be of the form

$$F^q_{j\pm1/2} = q^\star_{j\pm1/2} F^V_{j\pm1/2} \,. \tag{6.5.21}$$

Here $q^\star_{j\pm1/2}$ represents the variable at the control volume boundaries defined by an appropriate one-dimensional flux scheme. A numerical flux of the form (6.5.21) will be developed in the following. It is important to note that, according to Godunov's theorem [LeVeque, 1992, ch. 16], linearity of the numerical flux will limit the maximum accuracy of a monotonicity-preserving transport algorithm to first order.

Weighted Donor-Cell (Godunov-Type) Advection Scheme

Finite volume methods generally approximate the variable intended for advection by the piecewise constant function q_j defined through (6.5.8), thus flux calculation is not straightforward. The piecewise constant initial data in conjunction with the governing conservation law define a so-called *Riemann problem* [LeVeque, 1992, 2002; Toro, 1999]. The situation is illustrated in Fig. 6.3 for the j-th control volume in a one-dimensional transport step with nodal convective velocity of $c_{j\pm1/2} > 0$.

As shown in Fig. 6.3 above, the integral average of the variable q over the j-th control volume at the end of the Lagrangian step at time t^- is given by $q_j^- \Delta x_j^-$, which is highlighted by the blue area. Thereafter, the mesh motion step relocates the boundary nodes from $x^-_{j\pm1/2}$ to $x^+_{j\pm1/2}$ at time t^+, respectively. The convective velocity at these nodes is then calculated from $c_{j\pm1/2} = (x^-_{j\pm1/2} - x^+_{j\pm1/2})/\Delta t > 0$, in accordance with Proposition 6.2.22, and the new volume measure of the control volume is Δx_j^+. The updated integral average of the variable q after the transport step is $q_j^+ \Delta x_j^+$, which is the hatched area in Fig. 6.3 below. Since the field $q(x)$, with $x = \Phi(\chi, t)$, does not evolve during the transport step, the value of $q_j^+ \Delta x_j^+$ (hatched area in Fig. 6.3 below) can be exactly computed based on the piecewise constant contribution of q at time t^- and the updated control volume (blue area in Fig. 6.3 below):

$$\begin{aligned} q_j^+ \Delta x_j^+ &= q_j^- (\Delta x_j^- - |c_{j+1/2}\Delta t|) + q_{j-1}^- |c_{j-1/2}\Delta t| \\ &= q_j^- \Delta x_j^- + q_{j-1}^- c_{j-1/2}\Delta t - q_j^- c_{j+1/2}\Delta t \,. \end{aligned} \tag{6.5.22}$$

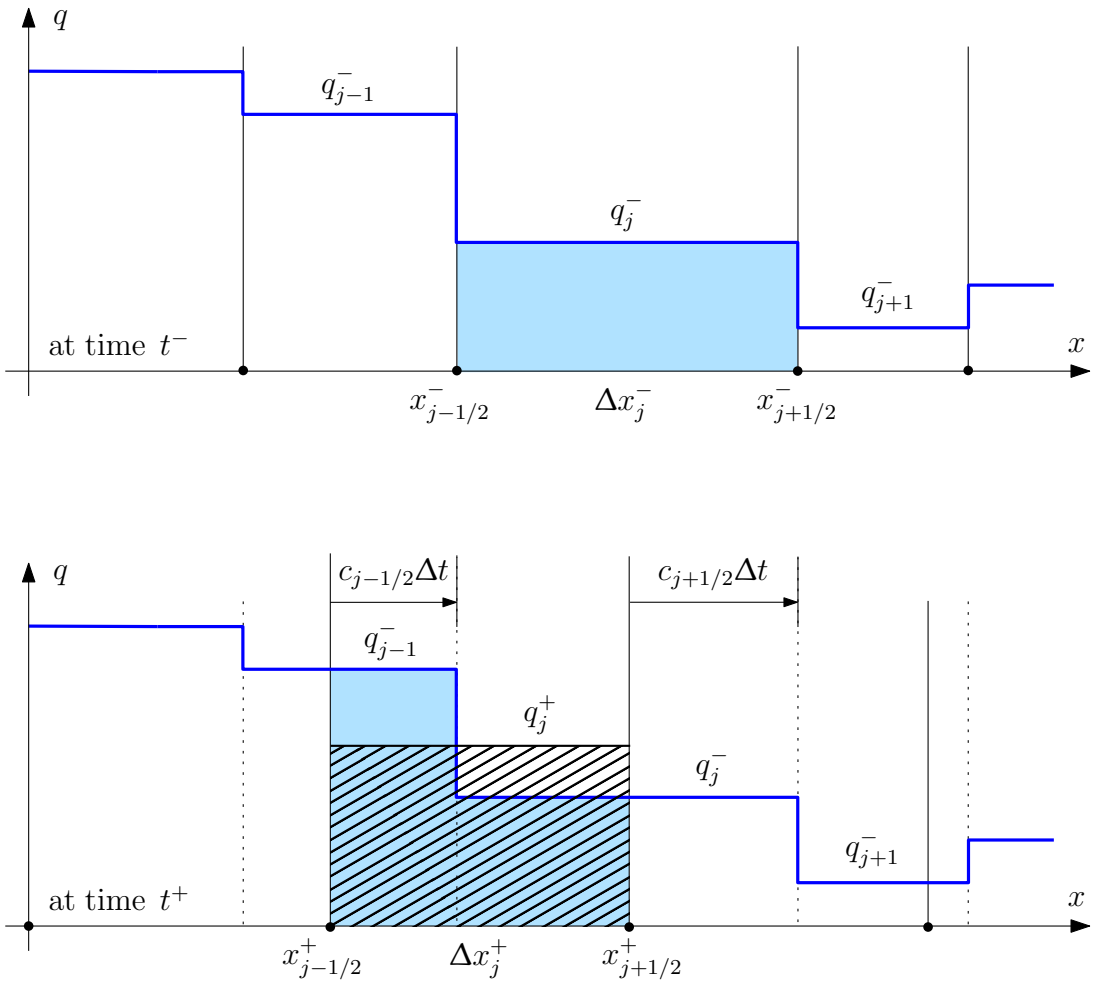

Figure 6.3: One-dimensional transport of the piecewise constant field q by the finite volume method in the operator-split ALE method (representing the first-order donor-cell resp. Godunov-type advection scheme; see Definition 6.5.28). The situations after the Lagrangian step (above) and at the end of the transport step (below) are shown for the j-th control volume. The blue areas indicate the contributions of q to the control volume, and the hatched area represents the updated integral average $q^+_j \Delta x^+_j$.

Comparison with (6.5.17) using (6.5.18) shows that the numerical convective flux function at the two boundary nodes takes the values

$$F^q_{j-1/2} = q^-_{j-1} F^V_{j-1/2} \qquad \text{and} \qquad F^q_{j+1/2} = q^-_j F^V_{j+1/2} \,. \tag{6.5.23}$$

If the flow in the example depicted in Fig. 6.3 would be oriented in the opposite direction, that is, $c_{j\pm1/2} < 0$, then the nodal flux values were

$$F^q_{j-1/2} = q^-_j F^V_{j-1/2} \qquad \text{and} \qquad F^q_{j+1/2} = q^-_{j+1} F^V_{j+1/2} \,. \tag{6.5.24}$$

Combination of both results (6.5.23) and (6.5.24) yields

$$F^q_{j\pm1/2} = q^\star_{j\pm1/2} F^V_{j\pm1/2} \,, \qquad \text{with} \quad q^\star_{j\pm1/2} = \begin{cases} q^-_j & \text{for } F^V_{j\pm1/2} > 0 \text{ (outflux)} \\ q^-_{j\pm1} & \text{for } F^V_{j\pm1/2} < 0 \text{ (influx)} \end{cases} , \tag{6.5.25}$$

and $F^V_{j\pm1/2}$ being calculated according to (6.5.18). Branching can be avoided since

$$q^\star_{j\pm1/2} = \frac{1+\operatorname{sgn}(F^V_{j\pm1/2})}{2}\, q^-_j + \frac{1-\operatorname{sgn}(F^V_{j\pm1/2})}{2}\, q^-_{j\pm1} \tag{6.5.26}$$

by the property (6.5.19) of the volume flux. Manipulation using identities of the sign function finally results in

$$\begin{aligned} F^q_{j\pm1/2} &= q^\star_{j\pm1/2} F^V_{j\pm1/2} \\ &= \frac{1}{2} F^V_{j\pm1/2}(q^-_j + q^-_{j\pm1}) + \frac{1}{2}|F^V_{j\pm1/2}|(q^-_j - q^-_{j\pm1})\,. \end{aligned} \tag{6.5.27}$$

The values $q^\star_{j-1/2}$ and $q^\star_{j+1/2}$ are the exact solutions to the Riemann problems associated with the discontinuities of q^- at the boundaries $x^-_{j-1/2}$ and $x^-_{j+1/2}$, respectively. For that reason the numerical convective flux function (6.5.27) is called a *Godunov flux* [LeVeque, 1992, 2002; Toro, 1999; Barth and Ohlberger, 2004]. Moreover, the numerical flux function uses information of cells lying in the upstream direction of the flow with respect to the particular cell considered. An advection algorithm employing flux functions of this form is called an *upwind scheme*, and the adjacent cells on the upwind side are called the *donor cells* with respect to the considered cell.

The update formula (6.5.17) using the particular Godunov flux (6.5.27) results in a conservative first-order upwind transport algorithm which corresponds to the classical *first-order upwind scheme* or *donor-cell difference scheme* [LeVeque, 1992; Toro, 1999].

Definition 6.5.28. The one-dimensional method given by

$$q^+_j = \frac{q^-_j \Delta x^-_j - (F^q_{j+1/2} + F^q_{j-1/2})\Delta t}{\Delta x^+_j}\,,$$

where

$$F^q_{j\pm1/2} \stackrel{\text{def}}{=} \tfrac{1}{2} F^V_{j\pm1/2}(q^-_j + q^-_{j\pm1}) + \tfrac{1}{2}|F^V_{j\pm1/2}|(q^-_j - q^-_{j\pm1}) \qquad \text{and} \qquad F^V_{j\pm1/2} = \pm\, c_{j\pm1/2}\,,$$

is referred to as the *donor-cell transport algorithm* or *Godunov-type advection scheme*. $F^q_{j\pm1/2}$ so defined is called the *donor-cell convective flux density*. ◊

Proposition 6.5.29. *An equivalent formulation of the donor-cell transport algorithm 6.5.28 is*

$$\begin{aligned} q^+_j = q^-_j &- \frac{\Delta t}{2\Delta x^+_j} F^V_{j+1/2}(q^-_{j+1} - q^-_j)(1 - \operatorname{sgn}(F^V_{j+1/2})) \\ &- \frac{\Delta t}{2\Delta x^+_j} F^V_{j-1/2}(q^-_{j-1} - q^-_j)(1 - \operatorname{sgn}(F^V_{j-1/2}))\,. \end{aligned}$$

Proof. By Proposition 6.5.13,

$$\begin{aligned} q^+_j &= \frac{q^-_j \Delta x^-_j - (F^q_{j+1/2} + F^q_{j-1/2})\Delta t}{\Delta x^+_j} \\ &= q^-_j - \frac{\Delta t}{\Delta x^+_j}(F^q_{j+1/2} + F^q_{j-1/2} - q^-_j F^V_{j+1/2} - q^-_j F^V_{j-1/2})\,. \end{aligned}$$

The assertion then follows by substitution of the donor-cell flux (6.5.27) and using the identity $|F^V_{j\pm1/2}| = F^V_{j\pm1/2}\,\mathrm{sgn}(F^V_{j\pm1/2})$. ∎

Remark 6.5.30. Donor-cell advection is used in many ALE codes because it is simple, stable, conservative, and monotonicity-preserving [Hirt et al., 1974; Peery and Carroll, 2000; Rodríguez-Ferran et al., 1998, 2002; Askes et al., 1998; Di et al., 2007; Freßmann, 2004; Freßmann and Wriggers, 2007]. The donor-cell convective flux defined in 6.5.28 is in correspondence with [Benson, 1992, eq. (3.3.1.1)] and [Freßmann and Wriggers, 2007, eq. (53)], whereas donor-cell advection in the form of Proposition 6.5.29 is connected with [Rodríguez-Ferran et al., 1998, eq. (26)], [Askes et al., 1998, eq. (35)], and [Di et al., 2007, eq. (44)]. △

A weighting factor $\alpha \in [0,1]$ is introduced in order to generalize the numerical flux function (6.5.27):

$$F^q_{j\pm1/2} = \tfrac{1}{2}F^V_{j\pm1/2}(q^-_j + q^-_{j\pm1}) + \tfrac{1}{2}\alpha|F^V_{j\pm1/2}|(q^-_j - q^-_{j\pm1})\,. \tag{6.5.31}$$

The corresponding transport algorithm then reads

$$\begin{aligned} q^+_j = q^-_j &- \frac{\Delta t}{2\Delta x^+_j}F^V_{j+1/2}(q^-_{j+1} - q^-_j)(1 - \alpha\,\mathrm{sgn}(F^V_{j+1/2})) \\ &- \frac{\Delta t}{2\Delta x^+_j}F^V_{j-1/2}(q^-_{j-1} - q^-_j)(1 - \alpha\,\mathrm{sgn}(F^V_{j-1/2}))\,. \end{aligned} \tag{6.5.32}$$

Setting $\alpha = 1$ results in a full donor-cell upwind scheme, whereas $\alpha = 0$ results in a flux approximation centered in space [Hirt et al., 1974; Askes et al., 1998]. Recall that for $\alpha = 0$ the scheme is unconditionally unstable [Toro, 1999, p. 167]. The best choice for α is discussed in [Hirt et al., 1974, pp. 247-248].

Extensions to Multiple Dimensions

In two and three space dimensions, material may arbitrarily flow through the mesh in directions specified by the convective velocity field. The majority of flux schemes for multidimensional advection algorithms have been derived from one-dimensional finite difference schemes and many of them use a logically regular mesh. The difficulty in extending one-dimensional methods to 2d or 3d and to unstructured meshes mainly lies in the proper determination of the amount of information ("material") entering or leaving the control volume during a time step. A related problem is the proper evaluation of flux across edges (in 3d) and vertices (in 2d and 3d) because finite volume methods usually approximate the control volume boundary by the disjoint union of its facets (cf. Definition 6.5.6).

Finite volume methods that account for all flux contributions in a single step are called *unsplit* or *fully multidimensional*. Simpler strategies for achieving the multidimensional extension apply one-dimensional advection schemes directly by either a *spatially isotropic approach* or *dimensional splitting*. The interested reader should consult [Zalesak, 1979; Colella, 1990; Benson, 1989, 1992, 2008; LeVeque, 1992, 2002;

Toro, 1999; Ferziger and Perić, 2002; Freßmann, 2004; Freßmann and Wriggers, 2007] for examples and further discussion. The spatially isotropic approach is applied in the present work because of its simplicity and due to the fact that proper dimensional splitting is limited to orthogonal meshes. All flow components with respect to the coordinate axes are treated simultaneously. This means that in the generic explicit algorithm 6.5.12, the full advection volumes $S_{j,k}F^q_{j,k}\Delta t$ across all facets $\Gamma_{j,k} = \mathcal{V}_j \cap \mathcal{V}_k$ of the control volume $\mathcal{V}_j$ are evaluated in a single step.

Determination of the Transport Volumes and Volume Flux

Determination of the convective volume fluxes $F^V_{j,k}$ and of the total transport volume $\Delta V_j \stackrel{\text{def}}{=} V_j^- - V_j^+$ for all control volumes $\mathcal{V}_j = \Phi(\mathcal{W}_j, t)$, with $j, k \in \{1, \ldots, n_{\text{cv}}\}$ and $k \neq j$, is an important part in advection algorithms for ALE methods. The total transport volume can be exactly determined by clipping the old control volume against the new tessellation. However, other choices are more common [cf. Benson, 2008], and these define the total transport volume as the sum of signed volumes transported across the control volume facets (edges in 2d, faces in 3d).

In the present work, the definition of the transport volume across the control volume facet $\Gamma_{j,k}$ is defined through $\Delta V_{j,k} \stackrel{\text{def}}{=} S_{j,k}F^V_{j,k}\,\Delta t$, where $S_{j,k}$ is the facet area and $F^V_{j,k}$ is the averaged convective volume flux density defined by 6.5.6(v). This results in transport volumes given by the average normal face displacements multiplied by the face areas. Once $S_{j,k}$ and $F^V_{j,k}$ have been determined for all facets $\Gamma_{j,k}$ of the control volume $\mathcal{V}_j \in \mathcal{T}$, the total transport volume can be computed. In full agreement with the advection algorithm 6.5.12 for the field q, first-order accurate explicit integration in time by the forward Euler method is used to update the control volume measure V_j. That is, the formula applied in the present work is

$$V_j^+ = V_j^- - \Delta t \sum_{k \neq j} S^-_{j,k} F^{V-}_{j,k} \,, \tag{6.5.33}$$

with the fluxes and facet areas being calculated with respect to the deformed (i.e. unsmoothed) configuration after the Lagrangian step resp. at the beginning of the transport step at time t^-. The evaluation of $S_{j,k}$ and the determination of $F^V_{j,k}$ for plane and axisymmetric problems is shown below.

Plane and Axisymmetric Problems

Plane and axisymmetric initial boundary value problems are three-dimensional in nature, thus are located in the Euclidian space $\mathcal{S} = \mathbb{R}^3$. However, in both plane and axisymmetric problems, all the variables can be expressed as functions of only two coordinates in a Euclidian subspace $\mathcal{S}' = \mathbb{R}^2$. The following section addresses to the unified description of these problems in the context of finite volume methods.

Definition 6.5.34. According to Addessio et al. [1990] and Maire [2009], the description of plane and axisymmetric problems can be combined as follows:

(i) A *pseudo-Cartesian frame* $(o, \boldsymbol{e}_1, \boldsymbol{e}_2)$ that spans the subspace $\mathcal{S}' \stackrel{\text{def}}{=} \mathbb{R}^2$ is introduced in conjunction with a *pseudo-radius* R defined for all $x \in \mathcal{S}'$ through

$$R(x) \stackrel{\text{def}}{=} 1 - \beta + \beta z^1(x) = (z^1(x))^\beta \,, \qquad \text{where } \beta \in \{0, 1\} \,.$$

$\overrightarrow{ox} \stackrel{\text{def}}{=} z^1(x)\, \boldsymbol{e}_1 + z^2(x)\, \boldsymbol{e}_2 \stackrel{\text{def}}{=} z^b(x)\, \boldsymbol{e}_b \in \mathbb{R}^2$ is the position vector of x with respect to the frame. The plane case, $R = 1$, is recovered if $\beta = 0$, for which the definitions $z^1 \stackrel{\text{def}}{=} x$ and $z^2 \stackrel{\text{def}}{=} y$ would be convenient. On the other hand, by setting $\beta = 1$ one recovers the axisymmetric case $R = z^1$, with z^1 now corresponding to the radial coordinate. Therefore, $z^1 \stackrel{\text{def}}{=} r$ and $z^2 \stackrel{\text{def}}{=} z$ for $\beta = 1$, by referring to the standard cylindrical coordinates.

(ii) Volume and area integrals in $\mathcal{S} = \mathbb{R}^3$ related to plane and axisymmetric problems are defined *per unit thickness* in the x-y-plane ($\beta = 0$) and *per unit radian* in the r-z-plane ($\beta = 1$). By recalling that in three dimensions the Jacobian determinant of the transformation $(x, y, z) \mapsto (r, z, \phi)$ equals r, the Riemannian volume form and area form on $\mathcal{S}' = \mathbb{R}^2$ are respectively introduced as

$$\mathbf{d}\boldsymbol{v}_{\mathcal{S}'}(x) \stackrel{\text{def}}{=} R(x)\, \mathbf{d}\boldsymbol{a}(x) \qquad \text{and} \qquad \mathbf{d}\boldsymbol{a}_{\mathcal{S}'}(x) \stackrel{\text{def}}{=} R(x)\, \mathrm{d}l(x) \,,$$

where $\mathbf{d}\boldsymbol{a}(x) \stackrel{\text{def}}{=} \mathbf{d}z^1 \wedge \mathbf{d}z^2$ and $x \in \mathcal{S}'$. ♢

In the context of finite volume methods, the j-th control volume of the tessellation in $\mathcal{S} = \mathbb{R}^3$ is defined through $\mathcal{V}_j \stackrel{\text{def}}{=} \mathcal{A}_j \times \mathcal{I}$, where $\mathcal{A}_j \subset \mathcal{S}'$ is the cross-sectional area of the control volume in the two-dimensional subspace, with $\mathcal{I} \stackrel{\text{def}}{=} \mathbb{R}$ in plane conditions and $\mathcal{I} \stackrel{\text{def}}{=} [0, 2\pi]$ in axisymmetric conditions. The cross section is a time-dependent image $\mathcal{A}_j \stackrel{\text{def}}{=} \Phi(\mathcal{Y}_j, t)$ in arbitrary Lagrangian-Eulerian methods, with $\mathcal{Y}_j \subset \mathcal{S}'$. Moreover, a control volume face $\Gamma_{j,k}$ in 3d is represented by the straight edge $\mathcal{L}_{j,k} \subset \mathcal{S}'$ given by

$$\Gamma_{j,k} = \mathcal{V}_j \cap \mathcal{V}_k = (\mathcal{A}_j \times \mathcal{I}) \cap (\mathcal{A}_k \times \mathcal{I}) = (\mathcal{A}_j \cap \mathcal{A}_k) \times \mathcal{I} \stackrel{\text{def}}{=} \mathcal{L}_{j,k} \times \mathcal{I} \,, \tag{6.5.35}$$

with $j, k \in \{1, \ldots, n_{\text{cv}}\}$ and $k \neq j$. The area of $\mathcal{A}_j$ and the length of $\mathcal{L}_{j,k}$ are computed from

$$A_j \stackrel{\text{def}}{=} \int_{\mathcal{A}_j} \mathbf{d}\boldsymbol{a} \qquad \text{and} \qquad L_{j,k} \stackrel{\text{def}}{=} \int_{\mathcal{L}_{j,k}} \mathrm{d}l \,, \tag{6.5.36}$$

respectively. It is assumed that the orientation of $\mathcal{A}_j$ and $\partial\mathcal{A}_j$ is positive with respect to the canonical basis in $\mathbb{R}^2$ such that $A_j > 0$ and $L_{j,k} > 0$. On the other hand, the volume of the j-th control volume and the area of its faces per unit thickness resp. per unit radian are given by

$$V_j \stackrel{\text{def}}{=} \int_{\mathcal{A}_j} R\, \mathbf{d}\boldsymbol{a} \qquad \text{and} \qquad S_{j,k} \stackrel{\text{def}}{=} \int_{\mathcal{L}_{j,k}} R\, \mathrm{d}l \,, \tag{6.5.37}$$

respectively. $R(x)$ is the pseudo radius by Definition 6.5.34(i). Again, it is assumed that $V_j > 0$ and $S_{j,k} > 0$. By using (6.5.36) and (6.5.37), *averaged pseudo radii* associated with $\mathcal{A}_j$ and $\mathcal{L}_{j,k}$ can be defined through

$$R_j \stackrel{\text{def}}{=} \frac{1}{A_j} \int_{\mathcal{A}_j} R\, \mathbf{d}\boldsymbol{a} = \frac{V_j}{A_j} \qquad \text{and} \qquad R_{j,k} \stackrel{\text{def}}{=} \frac{1}{L_{j,k}} \int_{\mathcal{L}_{j,k}} R\, \mathrm{d}l = \frac{S_{j,k}}{L_{j,k}} \,, \tag{6.5.38}$$

so that $V_j = R_j A_j$ and $S_{j,k} = R_{j,k} L_{j,k}$. According to Pappus's theorems [Thomas and Finney, 1996], R_j and $R_{j,k}$ are the centroids of $\mathcal{A}_j$ and $\mathcal{L}_{j,k}$, respectively, in the pseudo-Cartesian frame. In plane conditions, however, $R_j = 1$ and $R_{j,k} = 1$, leading to the identities $V_j = A_j$ and $S_{j,k} = L_{j,k}$.

Having prepared for the unified description of plane and axisymmetric problems, Definition 6.5.6 concerning finite volume-based advection algorithms can now be revised. According to Definition 6.5.34(ii), all volume and area integrals in three dimensions are defined per unit thickness in plane conditions, and per unit radian in axisymmetric conditions. For example, the integral form of the generic ALE conservation law (6.5.1) written for the j-th control volume takes the form

$$\frac{\mathrm{d}}{\mathrm{d}t} \int_{\mathcal{A}_j} qR \, \mathbf{d}\boldsymbol{a} + \int_{\partial \mathcal{A}_j} q\boldsymbol{c} \cdot \boldsymbol{n}^* R \, \mathrm{d}l = 0 \,, \qquad \text{where } \mathcal{A}_j = \Phi(\mathcal{Y}_j, t) \subset \mathcal{S}' = \mathbb{R}^2. \tag{6.5.39}$$

The control volume average and the averaged convective volume flux density are respectively defined through

$$\bar{q}_j \stackrel{\text{def}}{=} \frac{1}{R_j A_j} \int_{\mathcal{A}_j} qR \, \mathbf{d}\boldsymbol{a} \qquad \text{and} \qquad F^V_{j,k} \stackrel{\text{def}}{=} \frac{1}{R_{j,k} L_{j,k}} \int_{\mathcal{L}_{j,k}} \boldsymbol{c} \cdot \boldsymbol{n}^* R \, \mathrm{d}l \,. \tag{6.5.40}$$

Other definitions made for general m_{dim}-dimensional advection problems can be easily adjusted to the combined plane and axisymmetric formulation.

Let the control volumes have non-self-intersecting closed polygonal cross sections $\mathcal{A}_j$ defined by N vertices in counter-clockwise order along the perimeter of $\mathcal{A}_j$, and let the vertices I and $I+1$ define the edge $\mathcal{L}_{j,k}$, with $I \in \{0, \ldots, N-1\}$. Moreover, the vertex N, with position vector $\boldsymbol{x}_N = (z^1_N, z^2_N)^{\mathrm{T}}$, is assumed to coincide with vertex 0. Note that in this case, Proposition B.2 and Definition B.1(ii) do apply. Accordingly, A_j, R_j, $L_{j,k}$, and $R_{j,k}$ can be computed from

$$A_j = \frac{1}{2} \sum_{I=0}^{N-1} (z^1_I z^2_{I+1} - z^1_{I+1} z^2_I) \,, \tag{6.5.41}$$

$$R_j = 1 - \beta + \frac{\beta}{6A_j} \sum_{I=0}^{N-1} (z^1_I + z^1_{I+1})(z^1_I z^2_{I+1} - z^1_{I+1} z^2_I) \,, \tag{6.5.42}$$

$$L_{j,k} = \sqrt{(z^1_{I+1} - z^1_I)^2 + (z^2_{I+1} - z^2_I)^2} \,, \qquad \text{and} \tag{6.5.43}$$

$$R_{j,k} = 1 - \beta + \frac{\beta}{2}(z^1_I + z^1_{I+1}) \,, \tag{6.5.44}$$

respectively, where $\beta \in \{0, 1\}$. The (averaged) unit outward normals $\boldsymbol{n}_{j,k}$ to the edges $\mathcal{L}_{j,k}$ are obtained from Definition B.1(iii), that is,

$$\boldsymbol{n}_{j,k} \stackrel{\text{def}}{=} \frac{\tilde{\boldsymbol{n}}_{j,k}}{\|\tilde{\boldsymbol{n}}_{j,k}\|} \,, \qquad \text{with} \quad \tilde{\boldsymbol{n}}_{j,k} \stackrel{\text{def}}{=} \left(\begin{array}{c} n_1 \\ n_2 \end{array} \right) \Bigg|_{\mathcal{L}_{j,k}} = \left(\begin{array}{c} z^2_{I+1} - z^2_I \\ z^1_I - z^1_{I+1} \end{array} \right) \Bigg|_{\mathcal{L}_{j,k}} . \tag{6.5.45}$$

Moreover, the averaged convective velocity field $\boldsymbol{c}_{j,k}$ defined through 6.5.6(v) has the local representative

$$\boldsymbol{c}_{j,k} = \frac{1}{2} \left(\begin{array}{c} c^1_I + c^1_{I+1} \\ c^2_I + c^2_{I+1} \end{array} \right) \Bigg|_{\mathcal{L}_{j,k}} . \tag{6.5.46}$$

The convective volume flux densities $F^V_{j,k}$ across $\mathcal{L}_{j,k}$ can then be obtained from

$$F^V_{j,k} = \boldsymbol{c}_{j,k} \cdot \boldsymbol{n}_{j,k} = \frac{c^b_I n_b + c^b_{I+1} n_b}{2} = \text{const.}\,, \qquad \text{with} \quad b = 1, 2\,. \tag{6.5.47}$$

6.5.3 Transport Algorithm Based on Finite Volumes

The variety of definitions and concepts presented in the previous sections perhaps obscure what exactly has been implemented into the developed operator-split ALE method for plane strain and axisymmetric penetration into sand. Therefore, a brief summary of the transport step is given here. Its pseudocode is provided by Alg. 6.6. As before, the quantities calculated with respect to the mesh configurations before and after the mesh motion step are superscripted with $-$ and $+$, respectively.

The transport algorithm falls into the category of so-called advective remaps and achieves consistency as well as conservativity because it is based on the finite volume method. In the full donor-cell limit ($\alpha = 1$), the algorithm is extremely robust, sign-preserving for arbitrary convective velocities $\boldsymbol{c}$, and monotonicity-preserving for $\boldsymbol{c} = \text{const}$ [Margolin and Shashkov, 2006]. The transport algorithm is conditionally stable for all $\alpha \in [0, 1[$, with stability condition (6.5.14). There is only one cell-centered control volume tessellation associated with the transport step, and this coincides with the finite element mesh because the developed ALE method is based on constant strain triangles having a single storage point. Moreover, no ghost cells are added to the tessellation at physical boundaries because the relocation of boundary nodes during the mesh motion step approximately meets the zero-flux constraint (6.2.7).

The general form of the spatially isotropic algorithm has been proposed in 6.5.13. It advances the j-th control volume average of the considered data $q \in \{J, \boldsymbol{\sigma}, \boldsymbol{\alpha}\}$ in the pseudo time interval $[t^-, t^+]$ by using the first-order accurate explicit forward Euler method. The data includes the element Jacobian J, $\boldsymbol{\sigma}$ contains the (effective) stress components, and $\boldsymbol{\alpha}$ is a possibly empty array of generally tensor-valued material state variables, depending on the constitutive equation employed. Transport must be carried out for each tensor component separately, so that a total of 10 variables have to be advected in plain strain resp. axisymmetric analysis when using the hypoplastic model for sand (Section 4.3): 4 stress components, 1 void ratio, 4 intergranular strain components, 1 element Jacobian.

As described in the previous section, the volume and the area appearing in Proposition 6.5.13 are defined per unit thickness (per unit radian) in plane (axisymmetric) geometries, respectively: $V^+_j = R^+_j A^+_j$ and $S^-_{j,k} = R^-_{j,k} L^-_{j,k}$. Note that $L^-_{j,k}$ and $R^-_{j,k}$ require the geometry $\boldsymbol{x}^-$, and A^+_j and R^+_j the geometry $\boldsymbol{x}^+$. In the present work, the numerical flux function substituted for the averaged convective flux density $F^{q-}_{j,k}$ is the donor-cell flux density weighted by a factor $\alpha \in [0, 1]$. The one-dimensional version of this flux density is given by (6.5.31), and its isotropic multidimensional extension takes the form

$$F^q_{j,k} = \tfrac{1}{2} F^V_{j,k} (q^-_j + q^-_k) + \tfrac{1}{2} \alpha |F^V_{j,k}| (q^-_j - q^-_k)\,, \tag{6.5.48}$$

Algorithm 6.6: Finite volume-based transport of the field q in two dimensions by using the weighted donor-cell (Godunov-type) advection scheme.

Input: solution data q^- at storage points, distorted mesh geometry $\boldsymbol{x}^-$, smoothed mesh geometry $\boldsymbol{x}^+$, set $\mathcal{C}$ of all control volumes in the tessellation, set $\mathcal{C}'$ of all control volumes affected by mesh motion, facets $\mathcal{F}(\mathcal{V}_j)$ and neighbors $\mathcal{N}(\mathcal{V}_j)$ of every $\mathcal{V}_j \in \mathcal{C}'$, problem type $\beta \in \{0, 1\}$ (plane: $\beta = 0$, axisymmetric: $\beta = 1$)

Output: transported solution data q^+ at storage points

compute convective velocity $\boldsymbol{c} = (\boldsymbol{x}^- - \boldsymbol{x}^+)/\Delta t$ at all nodes;
specify donor-cell weighting factor $\alpha \in [0, 1]$ (full: $\alpha = 1$, centered: $\alpha = 0$);
forall the $\mathcal{V}_j \in \mathcal{C}$ **do** determine q_j^- from q^-;
begin Determination of Flux Contributions
  foreach $\mathcal{V}_j = (\mathcal{A}_j \times \mathcal{I}) \in \mathcal{C}'$ **do**
    compute cross sectional area A_j^+ (6.5.41);
    compute averaged pseudo radius R_j^+ (6.5.42);
    read data q_j^- and initialize $\Delta q_j = 0$;
    foreach $\Gamma_{j,k} = (\mathcal{L}_{j,k} \times \mathcal{I}) \in \mathcal{F}(\mathcal{V}_j)$ **do**
      determine $\mathcal{V}_k \in \mathcal{N}(\mathcal{V}_j)$ such that $\Gamma_{j,k} = \mathcal{V}_j \cap \mathcal{V}_k \neq \emptyset$;
      read data q_k^-;
      compute cross sectional length $L_{j,k}^-$ (6.5.43);
      compute averaged pseudo radius $R_{j,k}^-$ (6.5.44);
      compute averaged unit outward normals $\boldsymbol{n}_{j,k}^-$ (6.5.45);
      obtain convective volume flux density $F_{j,k}^{V-}$ (6.5.47);
      $\Delta q_j \leftarrow \Delta q_j + \Delta t R_{j,k}^- L_{j,k}^- F_{j,k}^{V-}(q_k^- - q_j^-)(1 - \alpha \operatorname{sgn}(F_{j,k}^{V-}))$;
    $\Delta q_j \leftarrow \Delta q_j / (2 R_j^+ A_j^+)$;
begin Update of Control Volume Data
  foreach $\mathcal{V}_j \in \mathcal{C}$ **do**
    if $\mathcal{V}_j \in \mathcal{C}'$ **then**
      $q_j^+ = q_j^- - \Delta q_j$;
    else
      $q_j^+ = q_j^-$;
forall the $\mathcal{V}_j \in \mathcal{C}$ **do** determine transported data $q^+ \stackrel{\text{def}}{=} q_{n+1}$ from q_j^+;

which completes the algorithm. Substitution into 6.5.13 and rearrangement yields the final form

$$\begin{aligned} q_j^+ &= q_j^- - \Delta q_j \\ &= q_j^- - \frac{\Delta t}{2R_j^+ A_j^+} \sum_{k \neq j} R_{j,k}^- L_{j,k}^- F_{j,k}^{V^-} (q_k^- - q_j^-)(1 - \alpha \operatorname{sgn}(F_{j,k}^{V^-})) \end{aligned} \tag{6.5.49}$$

having been implemented. Note that (6.5.49) is the isotropic multidimensional extension of the transport algorithm (6.5.32) for both plane and axisymmetric initial boundary value problems. A full donor-cell upwind scheme is obtained by setting $\alpha = 1$, whereas $\alpha = 0$ results in a scheme second-order centered in space. For $\alpha \neq 1$, however, the scheme is not sign-preserving, and hence not monotonicity-preserving.

Input to the transport algorithm (Alg. 6.6) is the problem type $\beta \in \{0, 1\}$ defined by 6.5.34(i), the solution data q^- at the quadrature points, the distorted (i.e. upstream) mesh geometry $\boldsymbol{x}^-$ after the Lagrangian step, the smoothed mesh geometry $\boldsymbol{x}^+$ after the mesh motion step, as well as the set $\mathcal{C} \stackrel{\text{def}}{=} \{\mathcal{V}_1, \ldots, \mathcal{V}_{n_{\text{cv}}}\}$ of all control volumes in the tessellation and the set $\mathcal{C}' \stackrel{\text{def}}{=} \{\mathcal{V}_1, \ldots, \mathcal{V}_j, \ldots, \mathcal{V}_{n'_{\text{cv}}}\}$ comprising all the control volumes which contain vertices affected by the mesh motion step. In addition, the transport algorithm requires the facets $\mathcal{F}(\mathcal{V}_j) \stackrel{\text{def}}{=} \bigcup_{k \neq j} \Gamma_{j,k}$ and the neighboring control volumes $\mathcal{N}(\mathcal{V}_j) \stackrel{\text{def}}{=} \bigcup_{k \neq j} \mathcal{V}_k$ that share a common facet $\Gamma_{j,k}$, where $\mathcal{V}_j \in \mathcal{C}'$, $\mathcal{V}_k \in \mathcal{C}$, $j \in \{1, \ldots, n'_{\text{cv}}\}$, $k \in \{1, \ldots, n_{\text{cv}}\}$, $n'_{\text{cv}} \leq n_{\text{cv}}$, and $k \neq j$.

6.6 Numerical Implementation

The following section briefly describes the numerical implementation of the Lagrangian step (Section 6.3), the mesh motion step (Section 6.4), and the transport step (Section 6.5) of the ALE method self-developed by the author. The method has not been implemented as a stand-alone code but adds specific capabilities to the proprietary finite element code system ANSYS® (Release 11.0 SP1) via programming interfaces. This strategy has been chosen in order to profit from the powerful solvers, pre- and postprocessors of the host application. Since only a few interfaces are required, the present approach will certainly be compatible with other Lagrangian FE codes providing user-programmable features (e.g. ABAQUS®).

6.6.1 Authorship

The complete ANSYS® ALE capabilities presented here have been designed and coded by the author. Although ANSYS AUTODYN® and ANSYS LS-DYNA® provide ALE solvers for explicit dynamical analysis on a short time scale, no ALE capability has been available so far in ANSYS® Mechanical™ (currently Release 14.5), which solves structural mechanical problems by using implicit integration in time. An implicit ALE solver is, however, necessary to analyze quasi-static penetration into sand.

Concerning the Lagrangian step of the ALE method, the Fortran source code of the hypoplastic model for sand (Sections 4.3 and 6.3.2) was made available by Nübel and Niemunis [1999], which has been adapted to meet specific requirements. The source code of the hypoelasto-J_2-plastic model with linear isotropic hardening (isotropic von Mises plasticity; Sections 4.1.3 and 6.3.2) is identical with that in the distributed ANSYS® user material subroutine usermat [ANSYS, 1999], which uses the same constitutive equation for demonstration.

The entire OSMOT algorithm (Section 6.4.3; Alg. 6.5) in the mesh motion step has been designed and coded by the author. The objective function of this optimization-based mesh smoothing algorithm has been proposed by Braess [2000] and Braess and Wriggers [2000]. The smoothing procedures for internal nodes and boundary nodes proposed by Aymone et al. [2001], see also Section 6.4.2 and Alg. 6.3, as well as the method of Giuliani [1982] have also been programmed by the author during the present research.

The finite volume-based advection algorithm (Section 6.5.3 and Alg. 6.6) used in the transport step of the developed ALE method has been coded by the author. In this algorithm, numerical advection is carried out by applying Godunov's scheme [Godunov, 1959] to the linear conservation laws governing the transport step. The method corresponds to a conservative formulation of the first-order upwind advection scheme of Courant et al. [1952]. The donor-cell weighting factor has been introduced according to Hirt et al. [1974]. The final formula (6.5.49), which has been implemented, corresponds to those found in [Rodríguez-Ferran et al., 1998; Askes et al., 1998; Di et al., 2007].

6.6.2 Interfacing with ANSYS®

General Remarks

Since ANSYS® is not open source the developed incremental operator-split ALE finite element method, whose overall solution procedure is expressed in Alg. 6.1, had to be fitted to the interfaces provided by the software. However, ANSYS® does not provide any interface designated to add ALE capabilities or to modify a given mesh. According to the programmer's manual [ANSYS, 2007b] and the scripting language guide [ANSYS, 2007c], interaction with the main program can be realized by using

1. Utilities and Fortran 90 routines to directly access the database and the binary files written or used by ANSYS®.
2. User programmable features (UPF), which comprise Fortran 90 user subroutines and functions that can be modified, as well as include decks, database access routines, and subroutines for user's convenience.
3. ANSYS® Parametric Design Language (APDL), which is a fast and highly productive scripting language similar to Fortran 90.

A combination of UPF and APDL is used in the present work. APDL macros are written for all the initial boundary value problems to be presented in Chapter 8. The

parameters of the specific problem, the geometry and mesh definitions, solution options, and output of the results are set therein. The consecutive Lagrangian, mesh motion, and transport steps of the ALE method are initiated and controlled via both conventional and user-programmed commands.

The UPF functions and routines are written in Fortran 90 [ANSYS, 2007b]. In contrast to older versions, Fortran 90 allows e.g. for dynamic memory allocation, modular programming, ability to operate on arrays or array sections as a whole, composite (derived) data types, pointer assignment, and multi-way selection. By employing these capabilities, a somewhat *object-oriented programming* can be achieved, which greatly facilitated implementation of the mesh motion and transport steps of the ALE method.

Implementation of Necessary Steps

In order to extend the host application by the desired features, the "$*$"-steps in Alg. 6.1 had to be implemented. The following UPF subroutines and functions have been coded for this purpose: user01, user07, user09, usermat, and ustress. The first three are functions for accessing data on the ANSYS® command line or in an APDL macro (user command), usermat allows to implement user-defined material constitutive models, and ustress gets the user-supplied stress state for initial stress analysis. A couple of additional Fortran 90 subroutines and modules containing data structures have been written by the author in order to accomplish the implementation.

usermat in conjunction with user01 contains the implementations of the rate constitutive equations applied in the Lagrangian step, which are the grade-zero hypoelastic model and the hypoelasto-J_2-plastic model (Secs. 4.1.3 and 6.3.2), as well as the hypoplastic model for sand (Secs. 4.3 and 6.3.2). usermat is called in every iteration step of the implicit global time integration procedure, and it operates on the level of the element's quadrature points and in the corotated material frame [XANSYS Mailing List, 2004]. Clearly, usermat implements step 12 of Alg. 6.1 based on the strain increment, the Cauchy stress, and the material state variables (all in the corotated frame).

user09 function has been coded to collect some primary information concerning the connectivity of the finite element mesh required for mesh motion (Section 6.4). For two-dimensional meshes, required information addressed by user09 includes the list of all internal nodes, the list of all the nodes belonging to a certain boundary edge of the computational domain (sub-boundary), and the list of those nodes belonging to a certain boundary edge that might be moved.

Derived topological information, like the neighboring elements of an internal node, are assembled in user07. This function also implements the mesh smoothing procedures the user can choose from: smoothing by weighted averaging [Aymone et al., 2001] resp. (Sec. 6.4.2; Alg. 6.3), Giuliani's method [Giuliani, 1982], and optimization-based smoothing using the OSMOT algorithm (Sec. 6.4.3; Alg. 6.5). The particular method that should be employed must be specified by the user command related to user07.

Most of the ALE capabilities are accessed via user07. Besides mesh smoothing, this function is responsible e.g. for initialization of ALE, time incrementing, allocation and

deallocation of user defined arrays, as well as for the transport step (Section 6.5). The latter involves the weighted donor-cell advection scheme (Alg. 6.6), which requires the list of elements adjacent to each element sharing a common facet, and a list of all the elements whose nodes were relocated during the mesh motion step. The former list is generated in user07 only once during the initialization phase, whereas the elements affected by mesh motion are gathered at the beginning of each transport step.

Restart Procedure in Each Calculational Cycle

Implementation was strongly influenced by the fact that one must temporarily exit the solution processor and enter the preprocessor when nodes should be relocated. Reentering the solution processor, which becomes necessary before the next Lagrangian step, generally resets the material and load histories unless analysis is properly restarted. ANSYS® is capable of restarting an analysis by writing a load history file and additional result files [cf. ANSYS, 2007d, sec. 3.9]. Unfortunately, these files are neither accessible nor can the restart process be modified by the user, hence advancing ALE solution in time had to be squeezed into the interfaces provided. The author is thoroughly convinced that user programmable features for rezoning would have greatly facilitated implementation of the ALE method.

ANSYS® in fact starts a new calculation when normally reentering the solution processor. Therefore, if ALE solution should be continued, the variables of the problem (mass density, stress, material state variables) have to be overwritten with the values obtained at the end of the most recent transport step; this generally is a non-trivial task in proprietary codes because of the limitation on access. Supplied stress must be balanced by the nodal reaction forces from the most recent solution step to avoid unphysical deformation. Spurious residual forces caused by the transport step are usually small and will be balanced during the next solution (cf. Remark 6.2.23). Loads and boundary conditions applied to the old model have to be reapplied or transferred to the new model. After the application of additional loads and boundary conditions, the load step counter is increased and the time level is updated. The finite element system of equation is solved, and then the next mesh motion and transport steps are issued.

In summary, the *restart procedure* in each calculational cycle of the operator-split ALE method consists of the steps listed in Alg. 6.7.

Algorithm 6.7: Restart procedure in each calculational cycle of the operator-split ALE method.

1 Overwrite solution variables with previously saved values;
2 Apply nodal reaction forces of the previous solution step as loads;
3 Transfer or reapply loads and boundary conditions;
4 Apply additional loads and boundary conditions;
5 Increase cycle counter and update time;
6 Continue the solution and balance residual forces;
7 Permanently save the evolved solution variables;

Remarks on the Element Type

The current ALE method has been customized for the 3-node triangle element with 1-point integration (constant strain triangle) because it is both very simple and extremely robust. The well-known locking phenomenon associated with this element type at the incompressible limit can be handled by using problem-specific mesh patterns. Creation of a new element type via UserElem subroutine could be avoided by using the outlined approach in conjunction with the PLANE182 element type provided by distributed ANSYS®. PLANE182 generally is a two-dimensional 4-node quadrilateral solid element but has a triangular option in addition to the plane strain and axisymmetric options.

6.6.3 Summary of Code Features and Capabilities

Table 6.1: ALE code features and capabilities chart.

	Capability[a]	Coded UPF routine[b]
Analysis type	quasi-static mechanical	(none)[c]
Problem type	plane strain axisymmetric	user07[d]
Mesh type	unstructured structured	(none)
Element type	3-node triangle	(none – PLANE182)
Material type	single-phase solid granular solid; dry or drained	(none)
Material model	hypoelastic (Secs. 4.1.3, 6.3.2) hypoelasto-plastic (Secs. 4.1.3, 6.3.2) hypoplastic (Secs. 4.3, 6.3.2)	usermat; user01
Contact behavior	zero friction no sliding	(none)
Mesh motion	weighted averaging [1]; (Sec. 6.4.2) Giuliani's method [2] optimization-based (Sec. 6.4.3) Eulerian (initial mesh)	user07; user09
Transport	weighted donor-cell FVM (Sec. 6.5.3)	user07; usermat; ustress[e]

[1]=[Aymone et al., 2001]; [2]=[Giuliani, 1982]

[a]Only those capabilities are listed which have been implemented or tested in conjunction with the ALE method. Additional distributed ANSYS® capabilities might be compatible with the ALE method.

[b]ANSYS® Release 11.0 SP1.

[c]Capabilities that have not been coded are distributed ANSYS® capabilities.

[d]Coded in order to adapt the transport step in ALE calculations. Plane strain and axisymmetric problems are supported by distributed ANSYS®.

[e]Subroutine ustress is no longer supported as of ANSYS® Release 12.0.

Chapter 7

Experimental Model Tests

The following chapter is concerned with the experimental model tests that have been designed and carried out in order to observe the flow field during penetration into sand and to investigate the load-displacement response of the penetrator. The main purpose of these tests is the validation of the developed ALE method, whose main features include an advanced rate constitutive equation to model the mechanical behavior of sand. Determination of the full set of material constants associated with this constitutive equation requires a sufficiently detailed description of the properties of the test sand, which generally disqualifies experimental tests reported in the literature.

The tests addressed here involve the quasi-static penetration of a model foundation and model piles with different pile tips in chambers filled with air-dried sand at different initial densities. The foundation and the piles are pressed into the sand along an observing window so that the generated flow field in that plane can be digitally photographed by means of a charge-coupled device (CCD) camera. A method based on particle image velocimetry (PIV) is then applied to measure incremental deformation (instantaneous velocity) and incremental strains by cross-correlating the image sequences recorded. On-sample instrumentation for deformation measurement does not become necessary when using the PIV method.

Preliminary work for this chapter was done by Eichstädt [2006], Vierhaus [2007], and Carow [2009] at Technische Universität Berlin (TU Berlin) within the scope of their theses. White [2002] reports on pile penetration model tests which he carried out at the University of Cambridge; see also Chapter 2. That thesis includes many helpful suggestions and served as a general guideline for the experimental investigations reported here. Prof. White, now based at the University of Western Australia, also co-developed and kindly provided the GeoPIV particle image velocimetry software which has been used for deformation measurement in the present work [White, 2009]. GeoPIV is a MATLAB® toolbox used at many research institutes worldwide.

Some remarks regarding the conceptual design of the tests will be made in the following section. Thereafter, the test equipment will be described and the experimental program will be outlined. The PIV measurement will be addressed subsequently, and test results will be presented at the end.

7.1 Conceptual Design

7.1.1 Requirements Specification

The main objective of the model tests is to provide experimental data at a reasonable effort and sufficiently detailed for back-analysis by using the self-developed ALE method. Accordingly, the tests are carried out in chambers whose dimensions must be small compared to the dimensions of piles and foundations in the field, so that each test can be set up by a single person in one or two working days. The testing devices should be designed in such a way that they carry over the relevant capabilities of the ALE method (cf. Tab. 6.1) to an experimental level, which is important for method validation. In particular, the testing devices should allow for the displacement-controlled plane strain or axisymmetric quasi-static penetration at least into dry sand. Since contact behavior in the computational models can be either smooth (zero friction) or perfectly rough (no sliding), the model penetrators should likewise exhibit low or high surface roughness.

If penetration tests are carried out in a chamber, there must be a sufficiently large separation S of the walls and the model penetrator in order to avoid side boundary effects. Equivalently, given a chamber with specific dimensions the diameter or breadth of the penetrator should be small enough. The minimum separation has been investigated by different authors and depends, amongst others, on the grain material and the relative density of the sand. For example, Linder [1977] performed penetration tests in dense sand at container to pile diameter ratios of 10, 12.5, and 16.67. In the centrifuge tests conducted by de Nicola and Randolph [1997], the distance to the nearest boundary was chosen to 4.8 respectively 6. Larger ratios showed insignificant variations in the cone resistance profile. De Nicola and Randolph used silica flour to scale down the particle size of a typical sand. Bolton et al. [1999] extensively studied the influence of the container to pile diameter ratio as well as of the distance to the nearest boundary during cone penetration in dense and medium dense uniform silica sand carried out in a centrifuge. They concluded that in any container with hard boundaries the boundary distance should be at least ten times the cone diameter to avoid significant interference.

Contrary to the aforementioned requirement, a large diameter D or breadth B of the penetrator and a large mean grain size d_{50} of the sand are desirable to increase the resolution of the PIV-based deformation measurement. Beyond that, the pile diameter to grain size ratio should have a large value, at least twenty [Bolton et al., 1999], to reduce grain size effects and to comply with the assumption of a soil continuum. However, content of fines should be as small as possible to ensure a good image texture for PIV evaluation and to prevent any ingress of sand between the penetrator and the observing window. The latter will cause the penetrator to gradually deviate from the desired direction, so that its motion can be no longer observed through the window.

The minimal boundary distance to foundation breadth ratio in the conducted shallow penetration tests is $S/B = 3.34$, and the minimal boundary distance to pile diameter ratio in the pile penetration tests is $S/D = 5$. The test sand used was washed to eliminate the content of fines and has a mean grain size of $d_{50} = 1.37\,\text{mm}$, which

results in a foundation breadth (resp. pile diameter) to grain size ratio of $B/d_{50} = 109.5$ (resp. $D/d_{50} = 36.5$). Investigation of the influence of these ratio on the results were not undertaken during the present research.

7.1.2 Similitude and Scale Effects

No attempts have been made during the experimental investigations to reproduce penetration processes associated with foundations, piles, or sounding tools in the field, or to correlate the obtained results with these; examples of such attempts can be found elsewhere [e.g. Linder, 1977; de Nicola and Randolph, 1997; Bolton et al., 1993, 1999; Gui and Bolton, 1998; Klotz and Coop, 2001]. As a consequence, no scale models or other similitude theoretical issues to achieve field-scale equivalence needed to be considered. This has greatly simplified the design of the experimental tests. For example, tests could be conducted at $1g$ and without the use of a surcharge weight at the ground surface. Moreover, the use of special test sand respecting the law of similitude could be avoided. The absence of scale effects will also facilitate the validation process without placing any further restrictions on the applicability of the ALE method. Along with this validation carried out in a subsequent chapter, ALE computational models will be built to back-calculate selected experimental tests "as is", i.e. without any scaling and with slight geometrical modifications only (see Chapter 8).

7.1.3 Measurement Concept

Attention is payed mainly to the qualitative rather than quantitative experimental analysis of penetration into sand. The latter is extensively studied in [Linder, 1977; White, 2002; White et al., 2003] and would require proper calibration of the preparation and measurement technology. Concerning the PIV method used for displacement and strain measurement, for example, the camera must be calibrated in order to properly transform the pixel coordinates of the image space into the spatial coordinates of the object space. The assumption that a single scale factor can be used to transform pixel coordinates into object space coordinates is invalid in case of short focal length digital photography. The calibration process must instead respect the sources of image distortion, which are the non-parallelism of the camera's CCD and the object plane, lens distortion, CCD pixel non-squareness, and refraction through the observing window [White, 2002; White et al., 2003]. Close range photogrammetry can then be used to formalize the coordinate transformation.

Without thorough calibration the soil deformation measurement in this work using PIV remained solely qualitative. It can be assumed that the soil deformation observed at the window is not biased by interface friction because the friction angle between the soil and the glass panel is significantly lower than the internal friction angle of the soil. In contrast to the qualitative soil deformation measurement, the total penetration force was measured by using a calibrated load cell, and the pile displacements were obtained from the specifications of the jack-in device or measured by dial gauge displacement sensors.

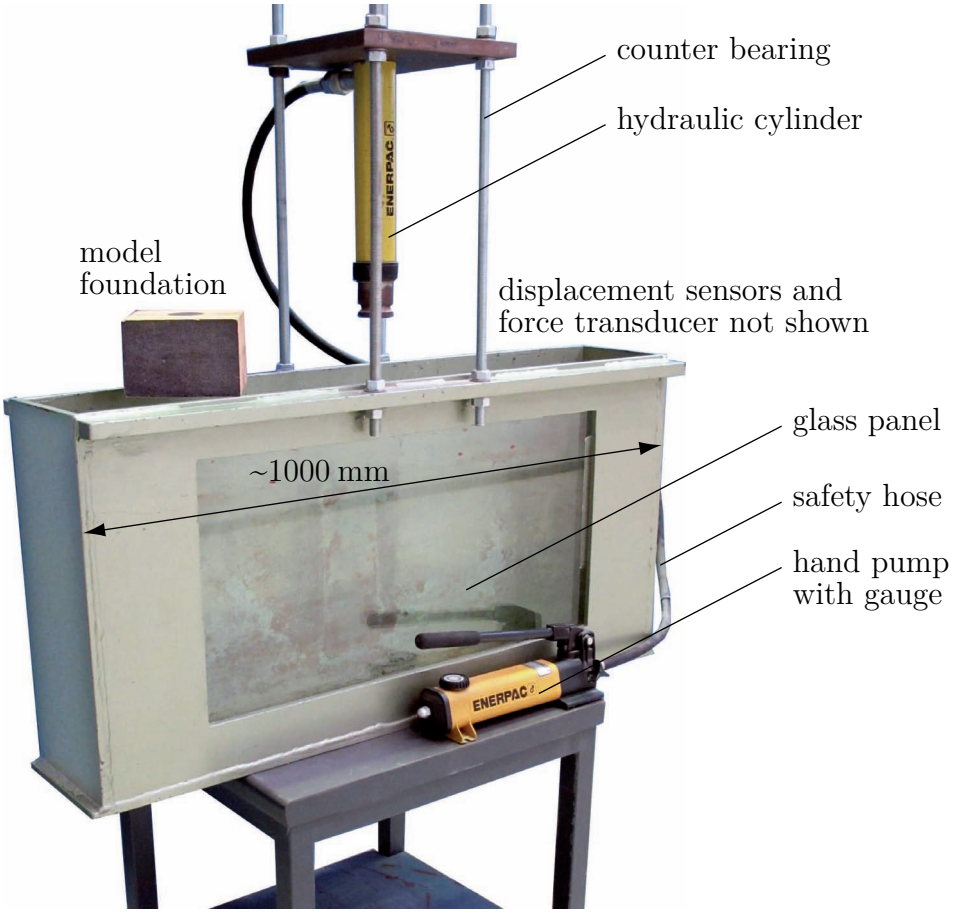

Figure 7.1: Experimental set-up for the shallow penetration into sand (SP tests).

7.2 Test Equipment Overview

Two different experimental set-ups have been used: one for the shallow penetration of a model foundation (abbreviated as "SP") and another for the penetration of model piles ("PP") with flat, conical, and hemispherical pile tip. The equipment of both set-ups will be described next. The camera equipment is the same for all SP and PP tests.

7.2.1 Set-up for Shallow Penetration (SP) Tests

The penetration of foundation test chamber shown in Fig. 7.1 had traditionally been used to demonstrate base failure for educational purposes at the author's affiliation. In the present study, the chamber has been employed without any modification for shallow penetration (SP) tests to supplement the conducted pile penetration (PP) tests. The characteristic width of the model foundation is about three times larger than the diameter of model piles used in the PP tests, hence allows for a higher displacement measurement resolution at otherwise equal conditions.

The test chamber has internal dimensions of 1003 mm × 502 mm × 152 mm and is a welded assembly of steel plates with a thickness of 10 mm. The front and rear panels

have reinforcing straps at the brim of the chamber which also carry the counter bearing for the jack-in device. In order to observe the flow field within the soil caused by the penetration process, the front plate is equipped with a centered 700 mm × 350 mm viewing window whose structural element is a 15 mm thick tempered safety glass panel. In the conducted tests, the sand filling had a height of about 400 mm.

A wooden rectangular cuboid with dimensions 150 mm × 100 mm × 150 mm (breadth $B = 150$ mm) serves as a model foundation and approximately ensures plane strain conditions in the filling of the chamber. The maximum separation of 2 mm in thickness direction between the foundation and the chamber walls minimizes spurious penetration forces provided there is no sand ingress and the foundation is vertically pressed into the sand along the glass panel. The jack-in device for the foundation is an ENERPAC® RC-108 hydraulic cylinder in conjunction with a two-speed hand pump and a connecting safety hose. The cylinder has a capacity of 1000 kg (101 kN) and a stroke of 203 mm.

Mechanical dial gauge displacement sensors were mounted onto the chamber to measure the vertical displacement of two opposite corners on the top face of the model foundation. Moreover, a force transducer measured the force between the hydraulic cylinder and the foundation. In order to achieve a somewhat displacement controlled test, pairs of force and displacement values were simply written down by hand every 2 mm of average incremental displacement.

7.2.2 Set-up for Pile Penetration (PP) Tests

A completely new test equipment has been developed during the course of the present research for the investigation of the penetration of model piles into sand. The main components are a chamber with glass walls, a half-cylindrical pile prototype with different pile tips, and a jack-in piling device. The complete set-up is shown in Fig. 7.2. The major parts of the chamber, the model piles, and the pile guide were manufactured in-house by Mr. Rüdiger von König and Mr. Harald Lorenz at the laboratory of the Chair of Soil Mechanics and Geotechnical Engineering, TU Berlin.

Chamber

A welded steel frame made from 50 mm × 50 mm × 3 mm S235 square tubes forms the chamber structure (Fig. 7.2). The front and rear walls are 1050 mm × 891 mm panels of laminated sheet glass (LSG) with a thickness of 2 × 12 mm = 24 mm each. Four 452 mm × 823 mm viewing windows, i.e. two for the glass panels on each side, are left open by the steel frame. Under test conditions, each glass panel acts like an all-round simply supported plate with an additional line support that bisects the span in horizontal direction. The side walls and the bottom slab of the chamber are 27 mm thick film coated plywood. The glass panels rest on hard rubber strips placed on the slab, whereas hard PVC strips between the glass and the steel frame should keep unwanted plate bending to a minimum. In total, the test chamber has internal dimensions of 1000 mm × 891 mm × 388 mm.

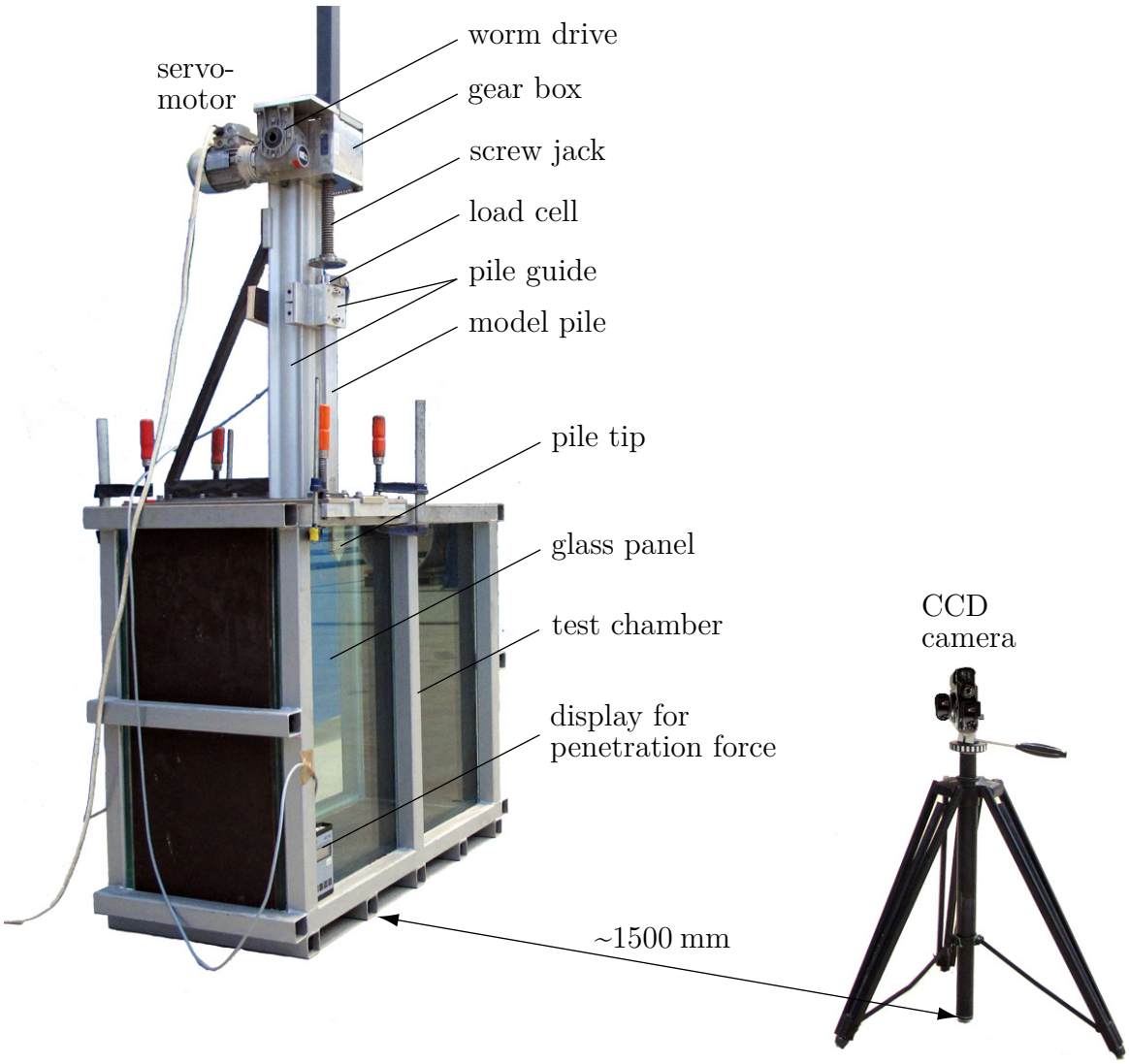

Figure 7.2: Experimental set-up for the penetration of model piles into sand (PP tests).

Model Piles

A half-cylindrical pile prototype with exchangeable tips was manufactured in order to model axisymmetric pile penetration with one glass panel serving as a plane of symmetry. The parts were molded by machining from solid round aluminium bars with a diameter of $D = 50\,\text{mm}$ (Fig. 7.3). Aluminium has been chosen because it constitutes a compromise between machinability, large stiffness, and low surface roughness. Note that a large stiffness is necessary to prevent deviation of the pile from the vertical, and a smooth pile is the least problematic when it comes to back-analysis of the experimental tests. The pile prototype is 500 mm long and the pile tip segments have a length of 150 mm. Both are connected by a countersunk butt strap joint made of steel, so that a maximum relative penetration depth of the pile of $z_{\max}/D \approx 9.0$ can be achieved if the chamber is completely filled with sand. Three different pile tip shapes are available to investigate the influence of the tip geometry on the penetration process and the load-displacement response: conical, flat, and hemispherical.

The conical shape is the one most intensively studied in literature because of its relevance to the cone penetration test (CPT), which is widely-used for the characterization of soils in-situ. Flat penetrators are the most challenging in numerical simulations as they cause drastic changes of the computational domain's initial shape. During penetration into sand, several researchers observed a hemispherical core zone under a flat-ended pile (cf. Chapter 2). This is also investigated in the present studies. The hemispherical pile tip was manufactured for purely academic purposes. It anticipates the core zone and reduces the difficulties associated with the flat tip in the computational models used for back-analysis.

Jack-in Device

The jack-in piling device is shown in detail in Fig. 7.3 below. It consists of a pile guide with sliding carriage and press-in jig, a worm gear screw jack combined with a worm drive, and a servo motor. The driving parts were purchased from T.E.A. Technische Antriebselemente GmbH, Hamburg. The SEO25-L work gear spindle of the screw jack is 700 mm long and allows for a maximum force of 25 kN. It has a gear reduction of 24 : 1 and a stroke of 0.25 mm per unit input cycle. The spindle runs through a MI-40 worm drive with gear reduction 80 : 1 which is connected to a 3-phase servo motor. The chosen combination of the screw jack, the worm drive, and the motor results in a penetration velocity of $4.6\,\text{mm}\,\text{min}^{-1}$, which can be regarded constant during the penetration tests because the driving parts are overdesigned.

Keeping the half-cylindrical pile penetrating into the sand strictly along the glass panel is the main task of the pile guide. To achieve this, the guide was manufactured from high-tensile aluminium profiles and accessories from a professional building kit system. A press-in jig for the pile, which is set into the base plate of the guide, was cut in a piece of hard PVC.

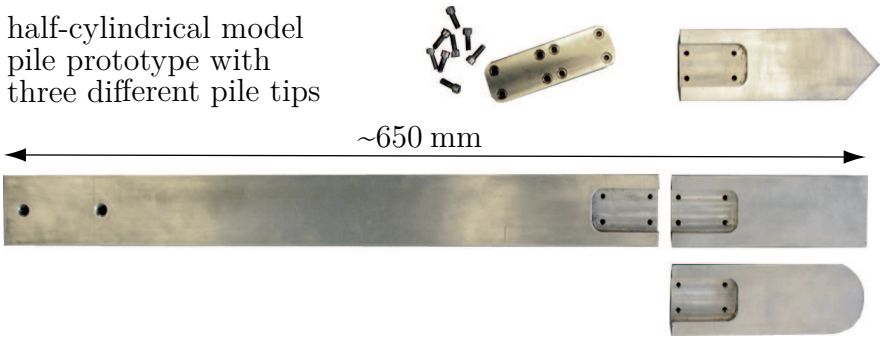

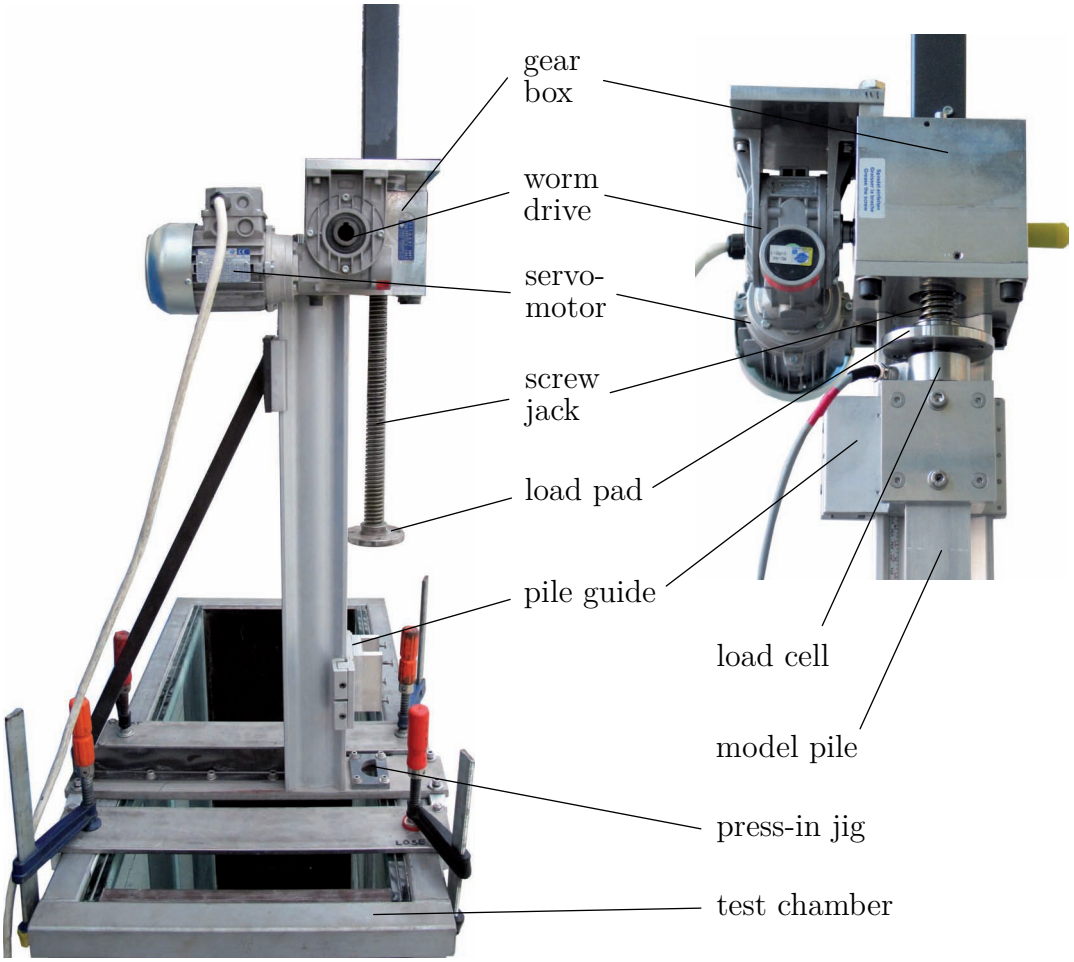

Figure 7.3: Detailed view of the model piles, the pile guide, and the jack-in device.

Instrumentation

The instrumentation used in the pile penetration set-up is quite simple. A reference scale is attached to the pile guide for pile displacement measurement purposes, and a load cell is placed between the pile head and the load pad of the screw jack (Fig. 7.2). The load cell has a portable display which is attached to the chamber. By this, the total penetration force can be read on every image captured of the process. However, no attempts have been made to differentiate between base resistance and shaft friction of a pile.

7.2.3 Camera Equipment

The experimental set-ups for the SP and PP tests are supplemented by camera equipment. A Canon® PowerShot G5 digital still camera mounted on a tripod was used throughout the present research. This camera is equipped with a CCD chip providing a maximum resolution of 2592×1944 pixels. In order to allow for remote shutter triggering or automatic capturing after a specified period of time, the camera is connected to a PC where Canon® RemoteCapture software has been installed. Images captured with the camera via the software are automatically converted, JPEG-compressed, and downloaded to the computer. Concerning the shallow penetration tests, images are captured every 2 mm of incremental displacement of the model foundation. In case of the pile penetration tests, the shutter is triggered automatically every 30 s, so that, owing to the specifications of the jack-in device, the pile has moved by a further 2.3 mm between two consecutive images. Higher frame rates at maximum image resolution are not supported when the camera is run in remote capture mode.

The distance between the camera and the viewing window in the final arrangement is approximately 1500 mm. Two 500 W halogen floodlights are used to illuminate the soil through the window. They will strongly heat the neighborhood, thus should be placed in a large enough distance to the camera and instrumentation. In order to avoid reflections on the viewing window mainly caused by natural light, the complete test set-up is encased in a party tent with additional webs.

7.3 Experimental Program

7.3.1 Model Test Sand and Preparation

The sand employed in the experimental model tests has been purchased from Heidelberger Sand und Kies GmbH as "gravel sand 1 to 3 mm". It is a quartz sand with well-rounded to angular grains identified as *fine-gravelly coarse Sand (fgrCSa)* according to DIN EN ISO 14688-1. Fig. 7.4 reproduces an optical microscope photograph of a specimen. Quartz sands have a grain mass density of about $\rho_s = 2.65\,\mathrm{g/cm^3}$ [cf. Herle and Gudehus, 1999; Rackwitz, 2003]. Grain form, angularity and uniformity of

Figure 7.4: Optical microscope photograph of a model test sand specimen.

the test sand are comparable with Berlin sand [cf. Rackwitz, 2003; Herle and Mayer, 1999; Mayer, 2000]; see also Section 4.3.3.

The limit void ratios of the test sand are $e_{\min} = 0.482$ and $e_{\max} = 0.779$ according to the procedure specified in DIN 18126. Its grain size distribution curve has been determined based on DIN 18123 and is drawn in Fig. 7.5. From this, one obtains $d_{10} = 0.61\,\mathrm{mm}$, $d_{30} = 1.07\,\mathrm{mm}$, $d_{50} = 1.37\,\mathrm{mm}$, and $d_{60} = 1.58\,\mathrm{mm}$, where d_i is a characteristic grain size defined by the size of the sieve opening passed by $i\,\%$ of the total weight of grains. By DIN EN ISO 14688-2, then, the coefficient of non-uniformity is $C_\mathrm{u} \overset{\mathrm{def}}{=} d_{60}/d_{10} = 2.59$ and the coefficient of curvature is $C_\mathrm{c} \overset{\mathrm{def}}{=} d_{30}^2/(d_{10}\,d_{60}) = 1.19$. The granulometric properties of the model test sand are listed in Tab. 7.1.

In the conducted tests, the chambers were filled with air-dried test sand by either dry sieve pluviation or dry deposition using a shovel. Each sand model was prepared in several layers of equal thickness in order to achieve a homogeneous distribution of initial density. The steel container used for dry sieve pluviation by hand has an inner diameter of 350 mm and a height of 500 mm, resulting in a usable volume of $0.0481\,\mathrm{m}^3$. Sieve opening is infinitely adjustable from 0 mm to 8 mm. The container had been employed for other types of model tests using fine sand and has not been adapted to the present situations.

Unfortunately, the intended range of initial densities could not be achieved by way of the container because the minimum height of pluviation for the first layer of sand is restricted by the inner height of the chamber. The initial mean relative densities of the pluviated sand model were always larger than 75 % in the shallow penetration tests and above 80 % in the pile penetration tests (cf. Tabs. 7.2 and 7.3). Therefore, a dry deposition technique has been employed in order to prepare a sand model in a loose state. The sand is placed in thin layers of less than 30 mm in a low-energy state

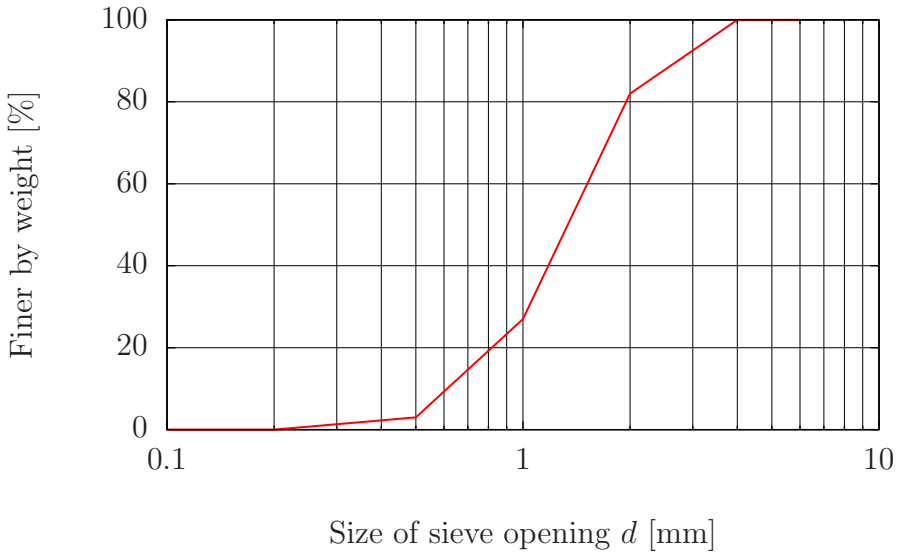

Figure 7.5: Grain size distribution curve of the model test sand.

Table 7.1: Granulometric properties of the model test sand.

Property	Unit	Value	Determination method resp. definition
angularity	–	rounded to subangular	DIN EN ISO 14688-1
form	–	cubic to elongate	DIN EN ISO 14688-1
grain mass density ρ_s	g/cm^3	2.65[a]	(estimated)
min. void ratio e_{min}	–	0.482	DIN 18126
max. void ratio e_{max}	–	0.779	DIN 18126
char. grain size d_{10}	mm	0.61	DIN 18123
char. grain size d_{30}	mm	1.07	DIN 18123
mean grain size d_{50}	mm	1.37	DIN 18123
char. grain size d_{60}	mm	1.58	DIN 18123
non-uniformity C_u	–	2.59	DIN EN ISO 14688-2
curvature C_c	–	1.19	DIN EN ISO 14688-2

[a]typical value for quartz sand [cf. Herle and Gudehus, 1999; Rackwitz, 2003]

without any drop height by using a shovel. By using this technique, the lowest initial mean relative density achieved was $D_{r0} = 21\,\%$ ($e_0 = 0.718$).

Relative density is defined by DIN 18126 resp. Definition 4.2.9. In the present work, the mean relative density of the sand model in the chambers is calculated from

$$D_r = \frac{e_{max} - e}{e_{max} - e_{min}}\,, \qquad \text{with} \quad e = \frac{\rho_s}{\rho_d} - 1 \quad \text{and} \quad \rho_d \approx \frac{F_g}{gV}\,, \tag{7.3.1}$$

where F_g and V are the weight and volume of the sand filling, respectively, and $g \stackrel{\text{def}}{=} 9.81\,\mathrm{m/s^2}$ is the Earth's standard acceleration due to gravity. Any water content of the air-dried sand is not taken into account.

7.3.2 Test Procedure

The procedure traced during each of the shallow penetration and pile penetration tests consists of the following steps:

1. Preparation
   (a) Adjust pile and jack-in device if necessary, then remove from chamber.
   (b) Prepare air-dried sand filling by either pluviation or deposition.
   (c) Mount jack-in device and penetrator.
   (d) Install instrumentation and camera equipment.
   (e) Launch camera software and check settings.
2. Test
   (a) Mark filling level on the glass panel.
   (b) Start penetration and recording, and monitor.
   (c) When finished, retract hydraulic cylinder resp. screw jack.
3. Postprocessing
   (a) Remove instrumentation, penetrator, and jack-in device.
   (b) Vacuum chamber parts.
   (c) Weigh filled chamber.
   (d) Remove (vacuum) sand filling.
   (e) Weigh empty chamber.
   (f) Determine initial mean relative density of sand filling.
   (g) Apply GeoPIV software to recorded images.

7.3.3 Details of SP and PP Tests

Series of shallow penetration (Tab. 7.2) and pile penetration (Tab. 7.3) model tests have been undertaken with a total of 3 and 28 tests, respectively. Parameters varied during the test series were the initial sample density and the pile tip geometry (only PP tests). The sand samples in tests SP-1 and PP-21 to PP-28 initially were in different loose or medium dense states, whereas they were in different dense or very dense states in tests SP-3 and PP-1 to PP-20. In the tables, z denotes the penetration depth respectively the distance between the pile base and the initial ground surface, $B = 150\,\text{mm}$ is the breadth of the model foundation, and $D = 50\,\text{mm}$ is the model pile diameter.

7.4 Particle Image Velocimetry

7.4.1 Overview

Particle image velocimetry (PIV) is a two-dimensional measuring technique for the whole instantaneous spatial velocity field resp. incremental displacement field of a moving and deforming material sample. It was originally developed in the area of experimental fluid mechanics [Pickering and Halliwell, 1984; Adrian, 1984, 1991, 2005], and has more recently been applied in experimental soil mechanics [White, 2002; White et al., 2003; Nübel and Weitbrecht, 2002; Hauser and Walz, 2004]. PIV is based on image analysis and can be used for measurement purposes ranging between simple visualization and accurate quantification of the flow field. The following section outlines the basic concepts and briefly introduces capabilities provided by GeoPIV [White and Take, 2002; White, 2009], the software that has been employed in this research for qualitative measurement.

The term "particle image velocimetry" was coined independently by Adrian [1984] and Pickering and Halliwell [1984]. In contrast to other imaging techniques to visualize or measure flows, PIV works with *particulate markers* at moderate concentrations [Adrian, 1991]. Visible, i.e. illuminated markers act as sources of scattered light which generates spatial variation of luminance (*texture*) on a photographic film or on the CCD chip of a digital still camera. PIV operates by tracking the texture within areas of an image through a sequence of images. While gas and fluid flows must be seeded with marker particles to carry a sufficiently large number of light sources, the grains in a body of sand usually entail adequate image texture and may exclusively serve as markers.

The particle concentration or *source density* measures the probability of encountering image overlaps of markers contained in the visible volume (light sheet of finite thickness), e.g. because one particle lies behind another. A large source density implies the formation of *speckle patterns* in the image plane, making identification of individual particles impossible. *Laser speckle velocimetry (LSV)* is preferable over PIV in this case. The probability of detecting more than one individual marker in a small region in the visible volume, on the other hand, is measured by the so-called *image density*.

Table 7.2: Details of conducted shallow penetration (SP) tests in air-dried sand.

Test ID	Date	e_0 [−]	D_{r0} [%]	Preparation method	Comment
SP-1[a]	05-02-2010	0.678	34	deposition	$z_{max}/B = 0.53$
SP-2	10-02-2010	*no data available*			
SP-3[a]	18-02-2010	0.546	78	pluviation	$z_{max}/B = 0.55$

Table 7.3: Details of conducted pile penetration (PP) tests in air-dried sand.

Test ID	Date	Pile tip	e_0 [−]	D_{r0} [%]	Preparation method	Comment
PP-1-C	2007	C	0.522	87	pluviation	$z_{max}/D = 8.0$
PP-2-F		F				stopped at $z/D = 4.0$[b]
PP-3-F		F	0.529	84		stopped at $z/D = 2.7$[b]
PP-4-H		H				$z_{max}/D > 8.0$
PP-5-F[a]		F	0.504	93		stopped at $z/D = 3.8$[b]
PP-6-C		C				$z_{max}/D > 8.0$
PP-7-H[a]		H	0.506	92		$z_{max}/D > 9.0$
PP-8-F		F				stopped at $z/D = 3.1$[b]
PP-9-F		F	0.497	95		stopped at $z/D = 4.0$[b]
PP-10-C[a]		C				$z_{max}/D > 9.0$
PP-11-C		C	0.518	88		stopped at $z/D = 4.2$[b]
PP-12-H		H				$z_{max}/D > 8.0$
PP-13-C	28-05-08	C	0.490	97	pluviation[c]	$z_{max}/D > 8.0$
PP-14-F	05-06-08	F				stopped at $z/D = 0.4$[b]
PP-15-C	18-06-08	C	0.473	103		stopped at $z/D = 1.2$[b]
PP-16-H	01-07-08	H				stopped at $z/D = 0.8$[b]
PP-17-?	*loss of data*					
PP-18-?						
PP-19-H	16-10-08	H	*loss of data*		pluviation	$z_{max}/D > 8.0$
PP-20-F	22-10-08	F				stopped at $z/D = 0.8$[b]
PP-21-F	13-05-09	F	0.678	34	deposition	stopped at $z/D = 3.0$[b]
PP-22-H	15-05-09	H				$z_{max}/D > 8.0$
PP-23-F	14-07-09	F	*without sand filling*[d]			
PP-24-F	21-07-09	F				
PP-25-F	23-07-09	F	0.678	34	deposition	$z_{max}/D > 8.0$
PP-26-H[a]	30-07-09	H				
PP-27-F[a]	06-08-09	F	0.718	21		
PP-28-C[a]	07-08-09	C				

C – conical; F – flat; H – hemispherical

[a] analyzed by using particle image velocimetry; see Appendix D
[b] due to severe ingress of sand between the pile and the viewing window
[c] additionally compacted by vibration
[d] in order to estimate the restraining force inherent to the system

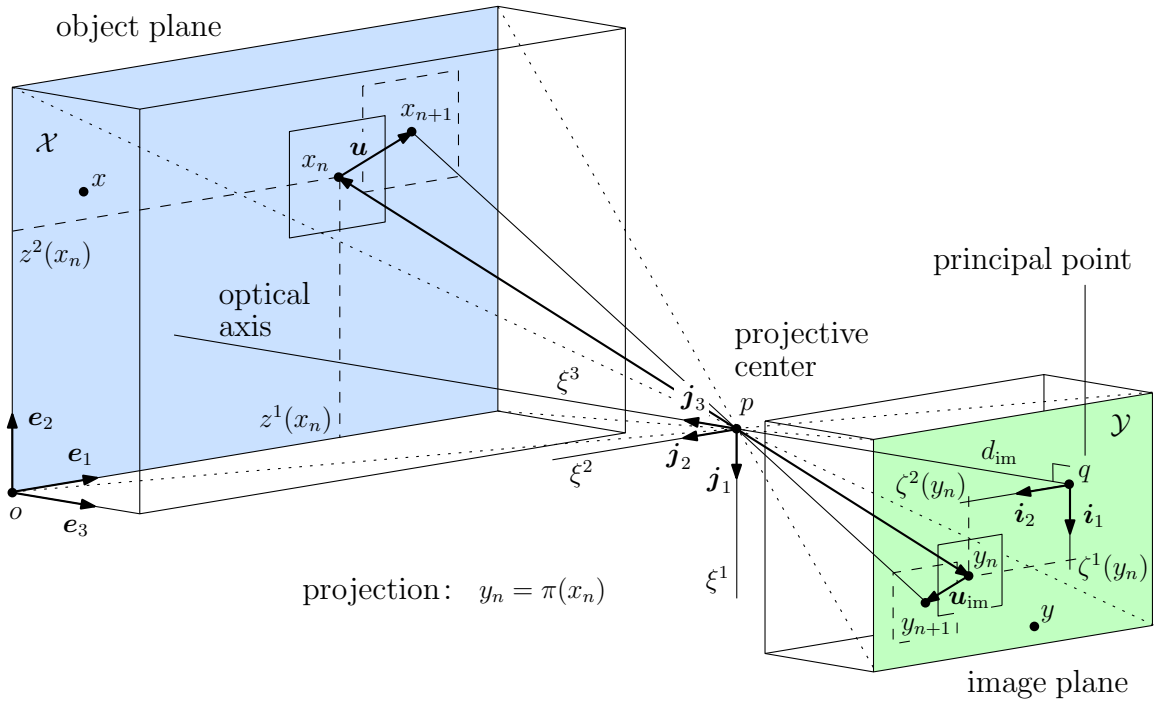

Figure 7.6: Geometry of the optical system of the planar particle image velocimeter applied in the present work (pinhole camera model).

Image density can be used to define different modes of the PIV method [Adrian, 1991]. In the low-image-density mode of particle image velocimetry, which is also referred to as *particle tracking velocimetry (PTV)*, images of individual particles in the interrogation cells dominate, so that individual images can be easily identified. The high-image-density mode of PIV is the technique applied in the present study [cf. White, 2002]. In this mode, the instantaneous velocity field is obtained by measuring the incremental displacement over a time step of groups of particles contained in small patches, called *interrogation cells* or *test patches*, within the image.

7.4.2 Basic Definitions and Relations

The optical system of the planar particle image velocimeter applied in this work is depicted in Fig. 7.6 and consists of an *object plane* represented by the field of view, the *camera aperture*, and the camera's CCD defining the *image plane*. The so-called *pinhole camera model* is applied, by which the camera aperture is described as a point. This idealized concept does neither account for aberrations related to finite-sized apertures and distorted lenses nor respects the discrete image coordinates (pixels) provided by the CCD. The basic definitions follow.

Definition 7.4.1. Let $\mathcal{S}$ be a set and $\mathcal{Y} \subset \mathcal{S}$. A *projection* is an idempotent map

$$\begin{aligned} \pi: \ & \mathcal{S} \to \mathcal{Y} \\ & x \mapsto y = \pi(x) \end{aligned}$$

such that $\pi \circ \pi = \pi$ and the restriction on the subset is the identity map, that is, $\pi(y) = y$ for all $y \in \mathcal{Y}$. $\diamond$

The class of three-dimensional projections considered here map visible *object points* $x \in \mathcal{S} = \mathbb{R}^3$ of the Euclidian *object space* or *world* onto *image points* $y \in \mathcal{Y} \subset \mathcal{S}$. The *image plane* $\mathcal{Y}$ thus contains the object's projected image. The spaces considered here are *Euclidian point spaces* within the meaning of Section A.1.

Definition 7.4.2. Based on the *pinhole camera model*, which is the technical interpretation of a *central projection*, the *geometry of the PIV optical system* is specified as follows (cf. Fig. 7.6):

(i) The test object under consideration is located in the three-dimensional Euclidian *object space* $\mathcal{S} = \mathbb{R}^3$ equipped with a global Cartesian frame $(o, \boldsymbol{e}_1, \boldsymbol{e}_2, \boldsymbol{e}_3) \stackrel{\text{def}}{=} (o, \boldsymbol{e}_b)$ called *object frame of reference*, where $b \in \{1, 2, 3\}$, $o \in \mathcal{S}$ is an arbitrary point and $\{\boldsymbol{e}_b\} \in \mathbb{R}^3$ is an ortho-normalized basis. The position vector $\overrightarrow{ox} \in \mathbb{R}^3$ of a generic *object point* $x \in \mathbb{R}^3$ has a local representative $\overrightarrow{ox} \stackrel{\text{def}}{=} z^b(x)\, \boldsymbol{e}_b$ with respect to the frame, and z^b being Cartesian coordinates.

(ii) A second Cartesian frame $(p, \boldsymbol{j}_1, \boldsymbol{j}_2, \boldsymbol{j}_3) \stackrel{\text{def}}{=} (p, \boldsymbol{j}_\alpha)$, $\alpha \in \{1, 2, 3\}$, called *camera frame of reference*, is associated with the three-dimensional *camera space*. The *projective center* $p \in \mathcal{S}$ represents the camera aperture (pinhole), and $\boldsymbol{j}_3 \in \mathbb{R}^3$, referred to as the *optical axis*, is pointing in the viewing direction of the camera. The coordinate tuple of some object point $x \in \mathcal{S}$ with respect to that frame is denoted by $(\xi^1(x), \xi^2(x), \xi^3(x))^{\mathrm{T}} \in \mathbb{R}^3$, so that $\overrightarrow{px} \stackrel{\text{def}}{=} \xi^\alpha(x)\, \boldsymbol{j}_\alpha$. By noting that

$$\overrightarrow{px} = \overrightarrow{po} + \overrightarrow{ox} \qquad \in \mathbb{R}^3\,,$$

the *change of framing* $(o, \boldsymbol{e}_b) \mapsto (p, \boldsymbol{j}_\alpha)$ defines a transformation of affine coordinates for the point x, which involves the orientation of the camera relative to the object (so-called *exterior orientation*).

(iii) The *image plane* is represented by the camera's CCD chip and is regarded a two-dimensional bounded subset $\mathcal{Y} \subset \mathcal{S} = \mathbb{R}^3$ spanned by the basis vectors $\{\boldsymbol{j}_1, \boldsymbol{j}_2\}$ of the camera frame at point $q = (p - d_{\mathrm{im}}\, \boldsymbol{j}_3)$. Hence, $\boldsymbol{j}_3$ is the unit normal to the image plane in $\mathbb{R}^3$. The point $q \in \mathcal{S}$ is called the *principal point*, and the *focal length* or *image distance* $d_{\mathrm{im}} \stackrel{\text{def}}{=} \|\overrightarrow{pq}\|$ measures the shortest distance of the projective center p from the image plane. As a consequence, $\xi^3(y) = -d_{\mathrm{im}}$ for all image points $y \in \mathcal{Y}$ such that

$$\overrightarrow{py} = \xi^\nu(y)\, \boldsymbol{j}_\nu - d_{\mathrm{im}} \boldsymbol{j}_3 \stackrel{\text{def}}{=} \begin{pmatrix} \xi^1(y) \\ \xi^2(y) \\ -d_{\mathrm{im}} \end{pmatrix} \quad \in \mathbb{R}^3\,, \qquad \text{with} \quad \nu \in \{1, 2\}\,.$$

(iv) Let $(q, \boldsymbol{i}_1, \boldsymbol{i}_2)$ denote the *image frame of reference* whose ortho-normalized basis vectors are respectively aligned with $\boldsymbol{j}_1, \boldsymbol{j}_2 \in \mathbb{R}^2 \times \{0\} \subset \mathbb{R}^3$. This frame parameterizes the two-dimensional image plane by the *image coordinates* ζ^1, ζ^2 defined through the local representative

$$\overrightarrow{qy} \stackrel{\text{def}}{=} \zeta^\nu(y)\, \boldsymbol{i}_\nu \qquad \in \mathbb{R}^2\,,$$

where $y \in \mathcal{Y}$ and $\nu \in \{1,2\}$. Note that $\zeta^\nu(y) = \xi^\nu(y)$ for each $\nu \in \{1,2\}$ and all $y \in \mathcal{Y}$ by definition of the image frame. ◊

For the present studies, it is assumed that rays of visible object points are near the optical axis (referring to *paraxial photography*) and that the relative distance along the optical axis of any two visible points is small compared to their average distance to the projective center d_{ob}, called *object distance*. As a consequence of these assumptions, out-of-plane motion cannot be measured and all visible object points approximately lie on a bounded *visible object plane* $\mathcal{X} \subset \mathcal{S}$, which is associated with the back side of the glass panel of the test chamber. Moreover, the object and image planes are parallel, resulting in

$$\xi^3(x) = d_{\text{ob}} \quad \text{for all } x \in \mathcal{X} \qquad \text{and} \qquad M = -\frac{d_{\text{im}}}{d_{\text{ob}}} = \text{const.} \tag{7.4.3}$$

M is called the *magnification* of the camera model. The image of a vector $\boldsymbol{u} \in \mathbb{R}^2$ lying in the object plane is then given by the simple transformation rule [cf. Adrian, 1991]

$$\boldsymbol{u}_{\text{im}} = M\boldsymbol{u} \qquad \text{resp.} \qquad \begin{pmatrix} u^1_{\text{im}}(y) \\ u^2_{\text{im}}(y) \end{pmatrix}_{|\boldsymbol{i}_\nu} = M \begin{pmatrix} u^1(x) \\ u^2(x) \end{pmatrix}_{|\boldsymbol{j}_\alpha} \in \mathbb{R}^2\,, \tag{7.4.4}$$

where $y = \pi(x)$, $\boldsymbol{u}_{\text{im}} \overset{\text{def}}{=} u^\nu_{\text{im}}(y)\,\boldsymbol{i}_\nu$, and $\boldsymbol{u} \overset{\text{def}}{=} u^\alpha(x)\,\boldsymbol{j}_\alpha = u^b(x)\,\boldsymbol{e}_b$, with $u^3(x) = 0$.

In order to determine the flow field of a material body contained in the object space, object points are regarded as places of material points parameterized by time $t \in [0,T] \subset \mathbb{R}$. Recall that material points are represented by individual marker particles or by the reference points of small groups of particles in PIV methods. However, object points are fixed throughout the PIV evaluation. This means that PIV naturally results in an Eulerian description of motion with independent coordinates $\zeta^1(\pi(x))$ and $\zeta^2(\pi(x))$ on the image plane; see also Sections 3.1.3 and 5.1, and [Nübel and Weitbrecht, 2002].

Consider two images captured at times $t = t_n$ and $t = t_{n+1}$ in the time interval of interest. These images respectively show configurations $\varphi(\mathcal{B}, t_n) \overset{\text{def}}{=} \varphi_n(\mathcal{B}) \subset \mathcal{S}$ and $\varphi(\mathcal{B}, t_{n+1}) \overset{\text{def}}{=} \varphi_{n+1}(\mathcal{B}) \subset \mathcal{S}$ of the material body $\mathcal{B}$ in the ambient space $\mathcal{S}$; see also Section 3.1. A single material point $X \in \mathcal{B}$ located at $x = x_n \overset{\text{def}}{=} \varphi_n(X) \in \mathcal{S}$ in the first configuration will move to

$$x_{n+1} \overset{\text{def}}{=} \varphi_{n+1}(X) = \varphi_n(X) + \boldsymbol{u}(\varphi_n(X)) \qquad \in \varphi_{n+1}(\mathcal{B}) \subset \mathcal{S}\,, \tag{7.4.5}$$

in the second configuration. The vector field $\boldsymbol{u} : \varphi_n(\mathcal{B}) \to T\mathcal{S}$ defined pointwise through $\boldsymbol{u}(x) \overset{\text{def}}{=} (x, \overrightarrow{x_n x_{n+1}})$, with $x = x_n$ is called the *incremental spatial displacement field imposed on* $\varphi_n(\mathcal{B}) \subset \mathcal{S}$ (Fig. 7.6). It is determined based on (7.4.4) and the image analysis procedure outlined in the following section. The flow field, that is, the *spatial velocity field* of the material (Definition 3.1.5) is then approximated by

$$\boldsymbol{v}(x)\,\Delta t \approx \boldsymbol{u}(x) = M^{-1}\boldsymbol{u}_{\text{im}}(y)\,, \tag{7.4.6}$$

where $y = \pi(x) = \pi(\varphi_n(X)) \in \mathcal{Y}$ is the image of $x = \varphi_n(X)$ in the image plane. Both $\boldsymbol{u}$ and $\boldsymbol{v}$ are constant in the incremental time interval $[t_n, t_{n+1}]$.

7.4.3 Image Analysis Procedure and Postprocessing

The incremental spatial displacement field $\boldsymbol{u}$ imposed on the configuration $\varphi_n(\mathcal{B})$ at time $t = t_n$ must be determined from *image vectors*

$$\boldsymbol{s}(y) \stackrel{\text{def}}{=} s^\nu(y)\, \boldsymbol{i}_\nu \qquad \in \mathbb{R}^2\,, \tag{7.4.7}$$

with $\nu \in \{1, 2\}$. The particular image vector which is the image of $\boldsymbol{u}(x)$ by (7.4.4) resp. (7.4.6) is denoted by $\boldsymbol{u}_{\text{im}}(y) \stackrel{\text{def}}{=} u^\nu_{\text{im}}(y)\, \boldsymbol{i}_\nu \in \mathbb{R}^2$.

The primary objective of the PIV method is the determination of $\boldsymbol{u}_{\text{im}}$, usually on a part $\mathcal{A} \subset \mathcal{Y}$ of the image plane called an *area of interest (AOI)*. The field, however, is determined at discrete image points $y \in \mathcal{A}$ owing to the working principle of the method. In case of this research, a multi-frame high-image-density PIV software for soil mechanics [White, 2002; White and Take, 2002; White et al., 2003; White, 2009], called GeoPIV, has been applied. Its workflow is illustrated in Fig. 7.7 and Alg. 7.1, and will be outlined next.

Let $(\mathcal{I}_0, \mathcal{I}_1, \ldots, \mathcal{I}_n, \ldots, \mathcal{I}_N)$, with $\mathcal{I}_n = \mathcal{Y}$ for all $n \in \{0, 1, \ldots, N\}$, be a series of consecutive still images recorded at equally spaced time stations $t_0, t_1, \ldots, t_n, \ldots, t_N$, respectively, by using a steady light source. For the first image of an image pair $(\mathcal{I}_n, \mathcal{I}_{n+1})$ in this series, with $0 \leq n < N$, a regular grid of small *first interrogation windows* or *test patches* is generated (Figs. 7.7a) —it is assumed that the whole image is an AOI for reasons of notational brevity. All test patches in the grid are squares with equal edge length l, the *patch size*, such that each test patch $\mathcal{P} \subset \mathcal{Y}$ is uniquely defined by its centroid y_{c}. Its (fixed) position in both images $\mathcal{I}_n$ and $\mathcal{I}_{n+1}$ is specified by the coordinates $\zeta^1(y_{\text{c}}), \zeta^2(y_{\text{c}})$, which are the components of $\overrightarrow{qy_{\text{c}}}$ with respect to the image frame (Definition 7.4.2(iv) and Fig. 7.7b). Shifted coordinates

$$\zeta^{\nu'}(y) \stackrel{\text{def}}{=} \zeta^\nu(y) - \zeta^\nu(y_{\text{c}})\,, \qquad \text{with} \quad \nu \in \{1, 2\} \quad \text{and} \quad y \in \mathcal{P}\,, \tag{7.4.8}$$

are introduced for each test patch domain $\mathcal{P}$ to locate points relative to the patch centroid. In the next step, a larger *second interrogation window* or *search patch* is assigned to each test patch in the second image $\mathcal{I}_{n+1}$. The search patch is a square with edge length $l + 2s_{\max}$ and centered at y_{c}, the centroid of the test patch.

Typical values for l range between 5 and 50 pixels concerning soil mechanical applications. The resolution of the measured displacement field increases with decreasing patch size, but the standard error also does. On the other hand, precision is improved when using large patches, but this will reduce the density of data points in an image. The *search range* $s_{\max} \stackrel{\text{def}}{=} \|\boldsymbol{u}_{\text{im}}\|_{\max}$ represents the length of the largest incremental displacement vector image that can be detected by the method. A larger search range generally requires more computing time. In order to produce reliable results, however, the test patch and the search patch must overlap in consecutive images, that is, $s_{\max} < l$.

The image of the incremental spatial displacement vector, $\boldsymbol{u}_{\text{im}}(y_{\text{c}})$, is determined for each test patch by means of a cross-correlation of the image intensities in the test

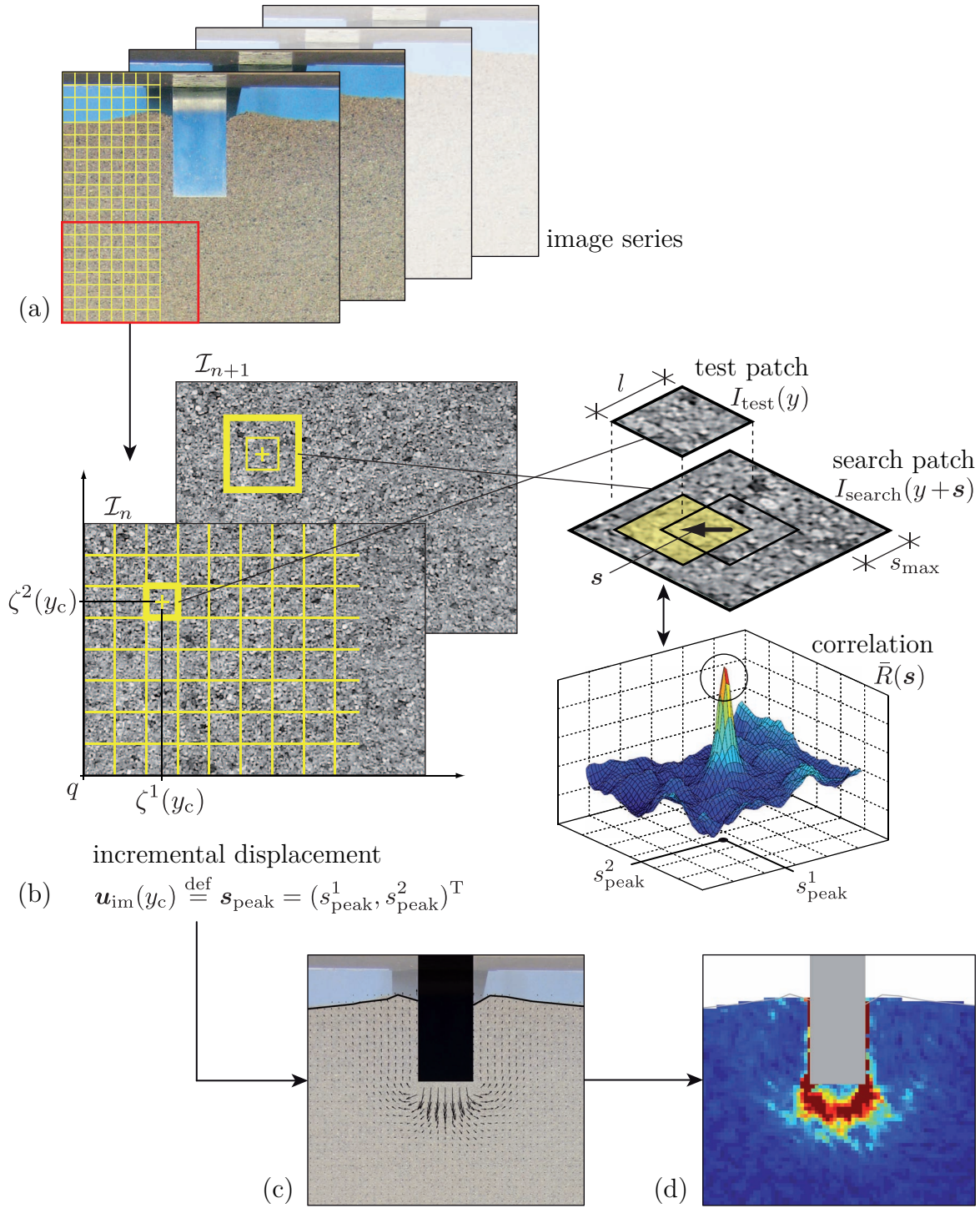

Figure 7.7: Workflow of multi-frame high-image-density PIV software for soil mechanical applications. Two images from consecutive configurations of the granular body are subdivided into patches (a), and then the pixel intensity (luminance) of each pair of patches are cross-correlated (b). From the field of local incremental displacement vectors obtained (c), the equivalent shear strain rate (d) can be derived; based on White [2002, fig. 3.6].

patch of image $\mathcal{I}_n$ and in the associated search patch of image $\mathcal{I}_{n+1}$ (Fig. 7.7b). *Image intensity* or *luminance* is a scalar field $I : \mathbb{R}^2 \supset \mathcal{Y} \to \mathbb{R}$, and the particular intensity fields associated with the test patch and the search patch are denoted by I_{test} and I_{search}, respectively; it should be noted that these are in fact intensity *matrices* by means of discrete pixel coordinates. *Cross-correlation* is generally used in signal processing to measure the similarity of two waveforms. If $f(t), g(t)$ are two continuous waveforms, their cross-correlation is defined through

$$(f \star g)(t) \stackrel{\text{def}}{=} \int_{-\infty}^{+\infty} f(\tau)\, g(\tau + t)\, \mathrm{d}\tau\,, \tag{7.4.9}$$

where $\tau \in \mathbb{R}$ is the *cross-correlation lag*. Cross-correlation of $f(t)$ and $g(t)$ is equivalent to the *convolution* of $f(t)$ and $g(-t)$, which is written $f * g$.

Definition 7.4.10. The *cross-correlation of* I_{test} *and* I_{search} is defined through

$$R(\boldsymbol{s}) \stackrel{\text{def}}{=} (I_{\text{test}} \star I_{\text{search}})(\boldsymbol{s}) = \int_{-\frac{l}{2}}^{+\frac{l}{2}} \int_{-\frac{l}{2}}^{+\frac{l}{2}} I_{\text{test}}(y)\, I_{\text{search}}(y + \boldsymbol{s})\, \mathrm{d}\zeta^{1'} \mathrm{d}\zeta^{2'}\,,$$

where $y \in \mathcal{P} \subset \mathcal{Y}$ and $\boldsymbol{s} \stackrel{\text{def}}{=} (s^1, s^2)^{\mathrm{T}} \in \mathbb{R}^2$ with respect to the ortho-normalized vector basis $\{\boldsymbol{i}_1, \boldsymbol{i}_2\}$ of the image plane. ♢

In GeoPIV software, $R(\boldsymbol{s})$ is normalized according to [cf. White, 2002]

$$\bar{R}(\boldsymbol{s}) \stackrel{\text{def}}{=} \frac{R(\boldsymbol{s})}{N(\boldsymbol{s})} \qquad \in [0, 1]\,, \tag{7.4.11}$$

where

$$N(\boldsymbol{s}) \stackrel{\text{def}}{=} \int_{-\frac{l}{2}}^{+\frac{l}{2}} \int_{-\frac{l}{2}}^{+\frac{l}{2}} H(y)\, (I_{\text{search}}(y + \boldsymbol{s})\, I_{\text{search}}(y + \boldsymbol{s}))\, \mathrm{d}\zeta^{1'} \mathrm{d}\zeta^{2'}\,, \tag{7.4.12}$$

and

$$H(y) \stackrel{\text{def}}{=} \begin{cases} 1 & \text{if } y \in \mathcal{P} \\ 0 & \text{else} \end{cases} \tag{7.4.13}$$

being a uniform non-zero masking intensity field on the test patch. In order to reduce the computational costs, the correlation operations 7.4.10 and (7.4.12) are carried out in the frequency domain by making use of the *convolution theorem* and taking the *fast Fourier transform (FFT)* of each intensity field [White et al., 2003].

Now, the *fundamental assumption underlying the PIV method* is that the highest correlation of the test patch and search patch intensities occurs when the image vector $\boldsymbol{s}$ coincides with the image $\boldsymbol{u}_{\text{im}}(y_{\text{c}})$ of the averaged incremental displacement of the group of particles captured on the test patch (Fig. 7.7b). The next definition states this more precisely.

Definition 7.4.14. Let $\boldsymbol{s} \in \mathbb{R}^2$ be the argument of the cross-correlation $\bar{R}(\boldsymbol{s})$, and let $\max_{\boldsymbol{s} \in \mathbb{R}^2} \bar{R}(\boldsymbol{s})$ be the unique correlation peak. The image $\boldsymbol{u}_{\text{im}}$ of the incremental spatial displacement $\boldsymbol{u}$ is then defined through

$$\boldsymbol{u}_{\text{im}}(y_{\text{c}}) \stackrel{\text{def}}{=} \boldsymbol{s}_{\text{peak}} = \begin{pmatrix} s^1_{\text{peak}} \\ s^2_{\text{peak}} \end{pmatrix}, \qquad \text{with} \quad \boldsymbol{s}_{\text{peak}} \stackrel{\text{def}}{=} \arg\max_{\boldsymbol{s} \in \mathbb{R}^2} \bar{R}(\boldsymbol{s})\,. \qquad \diamondsuit$$

The measured displacement increment has single pixel resolution due to the integer coordinates imposed by the camera's CCD. Sub-pixel resolution of the components $s^1_{\text{peak}}, s^2_{\text{peak}}$ is established in GeoPIV by a bicubic interpolation in the vicinity of the integer peak [White, 2002].

The correlation procedure is repeated for all test patches in image $\mathcal{I}_n$ in order to determine the discrete incremental displacement field of the material sample (Fig. 7.7c), and then the subsequent images in the series are processed in the same manner; see Alg. 7.1.

Algorithm 7.1: GeoPIV analysis procedure according to White and Take [2002].

Input: image series $(\mathcal{I}_0, \mathcal{I}_1, \ldots, \mathcal{I}_N)$, magnification M
Output: incremental displacement field for each image $\mathcal{I}_n$, with $0 \leq n < N$

```
specify patch size l and search range s_max;
foreach image I_n with 0 ≤ n < N do
    foreach test patch P ⊂ I_n do
        determine test patch intensity field;
        determine associated search patch intensity field in image I_{n+1};
        evaluate cross-correlation R(s) by 7.4.10;
        evaluate N(s) by (7.4.12);
        compute normalization R̄(s) = R(s)/N(s);
        determine incremental displacement u_im = arg max_{s∈ℝ²} R̄(s);
        establish sub-pixel resolution of u_im using bicubic interpolation;
    totality of u = M^{-1} u_im for all patches is incremental displacement field;
```

Each incremental image displacement vector $\boldsymbol{u}_{\text{im}}$ is attached to a single test patch centroid $y_{\text{c}} \in \mathcal{P}$. Therefore, the set of all test patch centroids can be defined as the nodes of a finite element mesh in order to postprocess the PIV results. The finite element approach (Chapter 5) together with the relation (7.4.6) allows the computation of object strains or deformation history from image displacements (Fig. 7.7d). In GeoPIV, the test patch centroids form the nodes of a two-dimensional mesh made up of 3-node triangles with 1-point integration, and the Lagrangian logarithmic strain $\boldsymbol{\varepsilon}$ defined by (3.1.13) is employed as the finite deformation strain measure [White, 2002]. The eigenvalues of $\boldsymbol{\varepsilon}$ can be directly obtained from *Mohr's circle for plane strain*:

$$\varepsilon_{1,2} = \frac{\varepsilon_{11} + \varepsilon_{22}}{2} \pm \sqrt{\left(\frac{\varepsilon_{11} - \varepsilon_{22}}{2}\right)^2 + \varepsilon_{12}^2}\,. \tag{7.4.15}$$

ε_{11}, ε_{22}, and $\varepsilon_{12} = \varepsilon_{21}$ are the components of $\boldsymbol{\varepsilon}$ with respect to the camera frame or image frame. The *total volumetric strain* and the *total maximum shear strain* are then defined through

$$\varepsilon_{\text{vol}} \overset{\text{def}}{=} \varepsilon_1 + \varepsilon_2 = \varepsilon_{11} + \varepsilon_{22} \quad \text{and} \quad \gamma_{\text{max}} \overset{\text{def}}{=} \varepsilon_1 - \varepsilon_2 = 2\sqrt{\left(\frac{\varepsilon_{11} - \varepsilon_{22}}{2}\right)^2 + \varepsilon_{12}^2}\,, \tag{7.4.16}$$

Note that in GeoPIV, volumetric strain is taken positive if it is compressive. The incremental strains are readily available by analyzing only an image pair $(\mathcal{I}_n, \mathcal{I}_{n+1})$ and not a series of images.

7.5 Discussion of Test Results

Before closing this chapter with a discussion of the test results, it should be noted that PIV analysis may produce incorrect displacement and strain data in some situations [cf. White and Take, 2002]. For example, if the camera frame rate is too low, particles have moved a long distance between two images. A group of particles captured on one image then might be hardly identified on the second image. Consequently, there might be no single distinct peak in the correlation plane and the displacement detected by the program might be the wrong one. Such vectors are called *wild vectors* and should be removed along with postprocessing the results.

Another pitfall that may lead to incorrect measurement is the occurrence of *stuck patches*. These are patches with stationary image content caused by visible objects other than the non-stationary test object, e.g. scratches on the glass panel or structural elements of the chamber. Stuck patches may locally corrupt the displacement and strain fields, hence should be removed, too. Further difficulties during PIV analysis may arise from material interfaces, which are present between the pile and the soil or at the ground surface during soil penetration. In order to completely avoid these errors, interfaces should be masked at the beginning of the analysis.

Concerning the results discussed next, focus is placed on those penetration tests which have been analyzed by using particle image velocimetry; see Tabs. 7.2 and 7.3 above for details. Wild vectors and many but not all stuck patches have been deleted. The results are compiled with additional comments in Appendix D.

7.5.1 Shallow Penetration Tests

One shallow penetration test in relatively loose sand (SP-1, $D_{\mathrm{r0}} = 34\,\%$) and one in relatively dense sand (SP-3, $D_{\mathrm{r0}} = 78\,\%$) have been analyzed. As can be seen from the PIV results in Figs. D.1b and D.3b, respectively, shearing of the sand model in both tests is initiated below the outer edges the model foundation immediately after penetration has begun. It is related to a sudden change in moving direction indicated by the incremental displacement vectors (Figs. D.1a and D.3a). At continued penetration, shearing localizes and primarily propagates along distinct slip surfaces which encapsulate a wedge-shaped zone immediately below the model foundation.

The situation at a relative penetration depth of about $z/B = 0.3$ is depicted in Fig. D.2 for the loose sand and in Fig. D.4 for the dense sand. Three characteristic zones highlighted in Fig. 7.8 become apparent from the incremental strain fields, and they are comparable with the zones that appear during *general shear failure* of the supporting soil immediately below and adjacent to a loaded strip footing [Terzaghi, 1943; Craig,

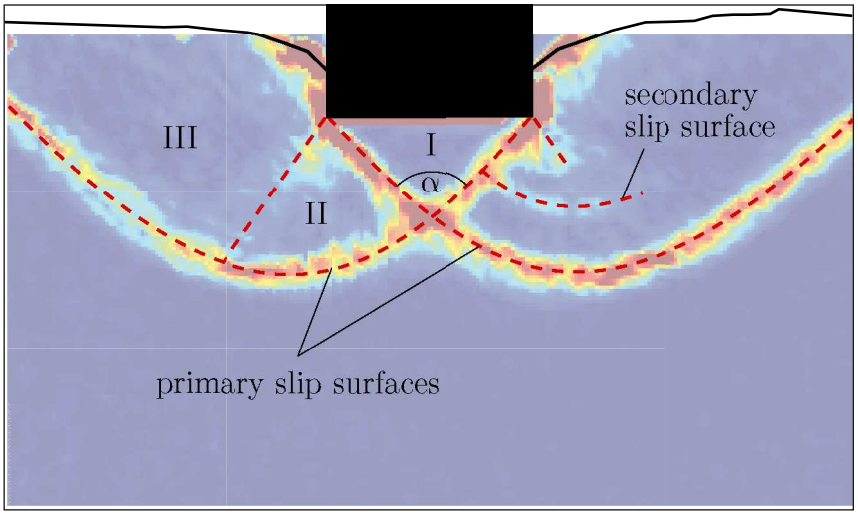

Figure 7.8: PIV results with overlaid failure mechanism for shallow penetration test SP-1 after shear failure of the supporting soil.

2007]. In particular, zones I and III are comparable with the *active* and *passive Rankine zones*, respectively. Their lower boundaries are formed by the primary slip surfaces of the shear failure mechanism. The transition zone II, which is also called *Prandtl zone*, is associated with radial shear and contains secondary slip surfaces (or slip fans). However, the measured load-displacement curve plotted in Fig. D.5 indicates that the dense sand model of test SP-3 is in a state of post-failure at $z/B = 0.3$, so the classical theory is not directly applicable.

From Figs. D.2 and D.4, it can be concluded that the wedge-shaped zone I behaves almost monolithically because no significant shear strain and volumetric strain have been measured. This so-called *dead zone* or *core*, as reviewed in Chapter 2, was also observed by other researchers [e.g. Heinz, 1970; Linder, 1977; White, 2002]. The angle α at the apex of the core zone (cf. Fig. 7.8) increases along with increasing initial relative density, which corresponds to previous test results [Heinz, 1970, sec. 8.3].

Shearing of sand is accompanied by grain rearrangement and changes in bulk volume resp. in relative density. Recall from Section 4.2 that the density change due to shearing is governed by the void ratio and the mean effective stress of the grain skeleton. At very low mean effective stress levels, e.g. near the unloaded ground surface, even a loose sand can be in a relatively dense state and then behaves dilative. This behavior is also reflected in the spatial distribution of incremental volumetric strain shown in Figs. D.1c to D.4c. Sand loosens at small penetration depths primarily next to the outer edges of the shallow foundation at the ground surface and adjacent to the slip surfaces within the soil. The core zone being about to be formed under the foundation is surrounded by areas of severe loosening, as in comparable tests reported by Heinz [1970]; see also Fig. 2.1 in Chapter 2. Local compression of the sand model is not significant.

At continued penetration of the shallow foundation, incremental volumetric strain adjacent to the slip surfaces is not monotonic but varies between compressive and expansive

(Figs. D.2c and D.4c). Compression of the soil dominates in the vicinity of the core zone, but no attempts have been made to measure the density of the sand models before and after the SP-1 and SP-3 tests. However, the results suggest that the rate of bulk volume change during shallow penetration in both loose and dense sand is always negative (i.e. expansive) and non-decreasing at increasing penetration depth.

The fluctuations in the measured incremental volumetric strain distribution is most likely due to the heterogeneity of sand on the micro scale. The finite element mesh employed for strain calculation, which is constructed from the grid of interrogation patches used for PIV analysis, is not coarse enough to smooth out these fluctuations. This fundamental observation renders soil strains obtained from PIV results generally questionable.

7.5.2 Pile Penetration Tests

The PIV analysis results of a subset of conducted pile penetration tests in sand are are shown in Figs. D.6 to D.21. Wild vectors have been completely removed, but potential stuck patches located at the ground surface and at the interface between the pile and the soil have been kept because they may carry physical information. The selection of test results covers the full range of initial relative densities and pile tip geometries that have been investigated. The sand model prepared for tests PP-5-F, PP-7-H, and PP-10-C initially was very dense ($D_{r0} > 90\,\%$), whereas it was initially loose ($D_{r0} < 35\,\%$) in case of PP-26-H, PP-27-F, and PP-28-C; see also Tab. 7.3.

The beginning of a pile penetration is a shallow penetration, hence it was expected that incremental displacement and strains generated within the soil in both test series are comparable in respective depths. Indeed, the PIV results of all three PP tests in dense sand indicate a general shear failure turning into another mode of failure at relative penetration depths of about $z/D \approx 1.5$ (Figs. D.6 to D.12). This is independent of the geometry of the pile tip and becomes particularly apparent from the distribution of incremental maximum shear strain. Figs. D.6b, D.8a, and D.11a indicate slip surfaces in the vicinity of the pile tip which do not reach the ground surface. The phenomenon corresponds exactly to that referred to in the literature as *local shear failure* [cf. Terzaghi, 1943; Vesic, 1963, 1973; Craig, 2007]. The slip surfaces were formed at the beginning of a general shear failure and will fade in larger depths. Compared to the results of SP tests presented in the previous section, compression of the soil under the pile has become more significant at $z/D \approx 1.5$ (Figs. D.6c, D.9a, D.12a).

From Figs. D.8b and D.11b, it can be concluded that local shear failure in dense sand is about to pass into a *punching shear failure* at relative penetration depths of $z/D \approx 5$. Punching shear failure is characterized by a vanishing soil motion on the sides of a foundation and vertical shearing around the perimeter of the foundation at continued penetration [Vesic, 1963, 1973]. Moreover, compression of the soil is underneath a foundation (Figs. D.9b and D.12b). The incremental motion and deformation of the test sand is slightly modified once more until the final relative penetration depths of $z/D \approx 8.5$ has been reached (Figs. D.7c to D.12c). At that point, punching shear failure

is clearly noticeable. During the whole penetration process, tests PP-7-H and PP-10-C were accompanied by sand loosening at the shoulders of the pile base (Figs. D.9 and D.12).

Concerning the conducted pile penetration tests in loose sand (Figs. D.13 to D.21), the incremental displacement and incremental strains at relative penetration depths of $z/D \approx 1.5$ already correspond to those of dense sand at $z/D \approx 5$. Neither global nor local shear failure can be identified. Instead, the penetration process is controlled by punching shear failure in all three depths that have been analyzed. Soil motion is located almost exclusively underneath the pile, and is directed vertically or normal to the boundary of the pile tip or of the core zone formed.

The variation of the geometry of the pile tip does not significantly change the qualitative deformation behavior of sand, except for the core zone generated immediately under a pile. This is true for both initially dense sand (tests PP-5-F, PP-7-H, and PP-10-C) as well as initially loose sand (tests PP-26-H, PP-27-F, and PP-28-C). However, quantitative differences have not been studied and would require further investigations. As can be seen from the incremental maximum shear strain distributions, the typical core zone is formed during shallow penetration and is present at all depths shown. In case of the flat-ended pile, the core is obtuse in dense sand (Fig. D.6b) and acute in loose sand (Fig. D.17), which agrees with results from shallow penetration tests. Using the hemispherical tip (Figs. D.8 and D.14) results in a much smaller core zone, and it is practically not present when using the conical tip (Figs. D.11 and D.20). One may conclude that both shapes of the pile tip anticipate the core zone to a certain degree.

The measured load-displacement curves of the tests that have been analyzed by using the PIV method are plotted in Fig. D.22; note that Fig. D.22b zooms in the force range $0 \leq F \leq 0.5$ of Fig. D.22a. The load-displacement curve of the PP-25-F test has been added to the diagram for reasons of comparison. By assuming that the force due to sliding friction between the glass panel and the cut face of the aluminium pile is negligibly small compared to the force due to shaft friction and base resistance, the force values of a full pile would be two times the force values of the half pile plotted in Fig. D.22.

The tests indicate that the penetration resistance of a pile is related to the relative density of sand. The vertical forces required for penetration in very dense sand were between six and eight times larger than those for penetration in loose sand using the same geometry of the pile tip. On the other hand, a relationship between penetration resistance and the pile tip shape is not obvious. Penetration forces associated with the conical and the hemispherically-shaped pile tip are comparable, though the conical tip causes slightly smaller forces. At relative penetration depths of $z/D < 6$, the flat-ended pile bears the largest force irrespective of the initial relative density of the sand model. One possible explanation could be the core zone generated under a flat-ended pile, which is usually smaller under tapered pile tips. Beyond this depth, however, the values for the flat-ended pile in loose sand (PP-25-F and PP-27-F) drop below the values of the piles having a hemispherical (PP-26-H) or conical (PP-28-C) tip.

Roughly speaking, all four curves obtained for loose sand share a common inflection point located at $z/D \approx 6$. Another inflection point of each of these curves lies within the range of $0 < z/D < 2.5$. Despite the fact that the utilized instrumentation does not differentiate between base resistance and shaft friction, the shape of the obtained load-displacement curves for loose sand is comparable with the enveloping base resistance-displacement curve for dense sand deduced by Linder [1977, p. 171] up to the vicinity of the second inflection point. This latter curve has been reprinted with English translations in Fig. 2.6.

In summarizing the previous discussion, it can be concluded that the results of the penetration tests carried out in dense sand are comparable to those obtained by Linder [1977], which have been discussed in Chapter 2. The observed phenomena can be associated with Linder's phases I and II in a pile penetration process. The wedge-shaped core zone is characteristic of flat-ended piles, and its breadth is approximately equal to the breadth of the flat side. The apex angle of the core will increase with increasing relative density of sand, in accordance with the observations of Heinz [1970, sec. 8.3]. Moreover, in quoting Vesic [1963, p. 136] it can be concluded that there "[..] is a critical relative depth below which only punching shear failure occurs." Such a critical relative depth has been observed irrespective of the relative density of sand and irrespective of the geometry of the pile tip. The critical relative depth is generally larger for higher initial relative densities.

Chapter 8

Numerical Examples and Validation

The numerical examples that will be presented in the following chapter have been designed for *verification and validation (V&V)*[1] purposes with the intention to control and ensure quality of the ALE method developed in this work. Two different groups of examples will be analyzed. The main objective when solving problems of the first group is the verification of particular algorithms of the method, namely the mesh smoothing algorithms (Section 6.4) and the transport scheme (Section 6.5). Test cases include patch tests and basic initial boundary value problems. Elements of the second group of numerical examples are large deformation solid mechanical and soil mechanical initial boundary value problems. Among these are some of the experimental model tests carried out in Chapter 7 as well as example problems from literature for which analytical or numerical data is available. The back-analysis of these results by using ALE computational models will enable validation of the ALE method.

8.1 Verification of Mesh Smoothing Algorithms

Maintaining the quality of the finite element mesh throughout the calculation is one of the principal tasks of any ALE method. Recall from Section 6.4 that the current ALE method addresses this in an iterative fashion by repeatedly looping over balls of affected triangle elements and relocating the associated nodes. The node relocation schemes that have been implemented by the author are based on geometric criteria only, i.e. they are smoothing algorithms. Their applicability to different types of meshes and mesh configurations will be investigated in what follows.

[1] According to the definitions in [DoDI 5000.61], which are adopted here, *verification* is the "[..] process of determining that a model or simulation implementation and its associated data accurately represent the developer's conceptual description and specifications", whereas *validation* is the "[..] process of determining the degree to which a model or simulation and its associated data are an accurate representation of the real world from the perspective of the intended uses of the model."

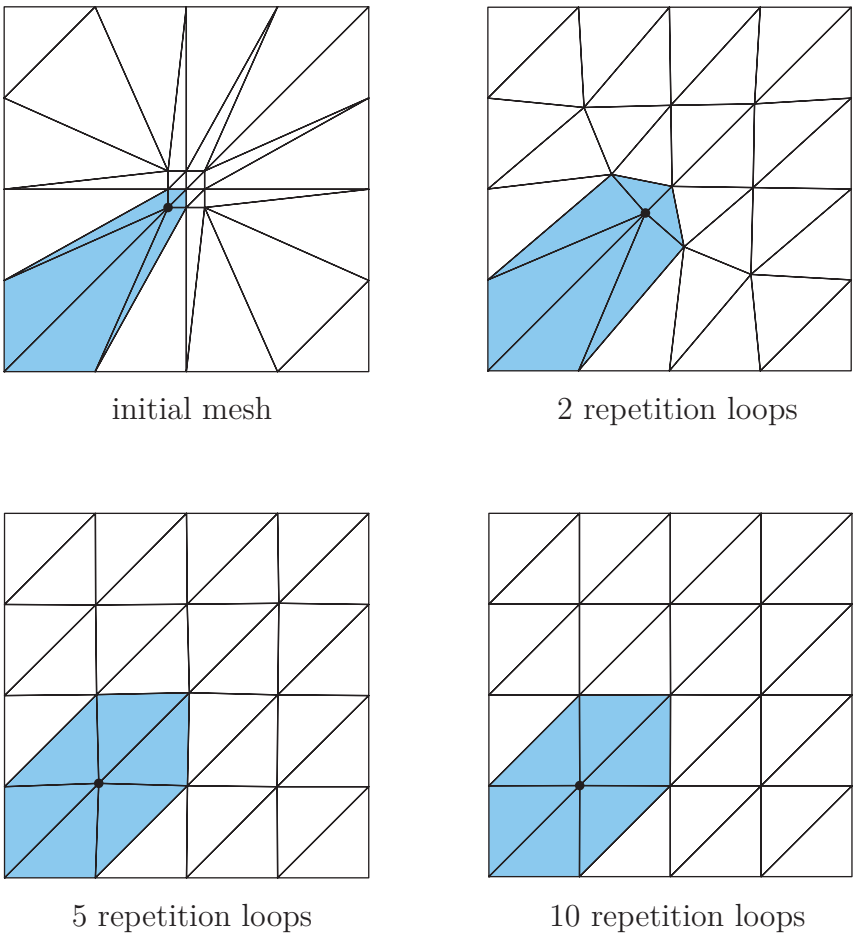

Figure 8.1: Investigation of the number of repetition loops required to globally improve the mesh. The blue zone indicates the ball of elements sharing the lower left internal node.

8.1.1 Patch Tests

The first example shown in Fig. 8.1 is a structured square patch consisting of 32 triangle elements. The best quality of the given mesh is obtained if the elements were arranged in a rising diagonals triangle pattern. In the initial configuration, however, elements are severely distorted. Merely the placement of the boundary nodes is optimal. Due to locality of the implemented smoothing algorithms, an acceptable mesh quality cannot be achieved in one step but requires several repetition loops over the balls of elements sharing a common internal node. However, five to ten loops are sufficient to produce an almost optimal mesh. This is independent of the particular smoothing algorithm having been used.

In the example, the quality improvement of the ball associated with the lower left internal node (blue zone in Fig. 8.1) lags behind the other after two iterations. This is a consequence of the current strategy that globally improves the mesh: all balls in the mesh are processed in a fixed order in every repetition loop. It might be more effective to process randomly picked groups of elements, but this has not been implemented yet.

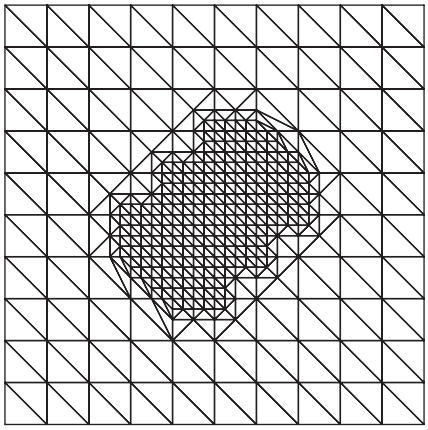

(a) initial mesh

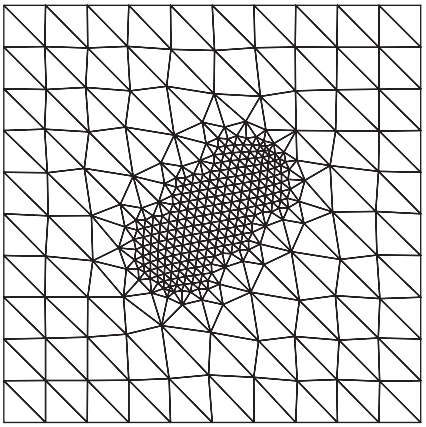

(b) optimization-based smoothing (OSMOT)

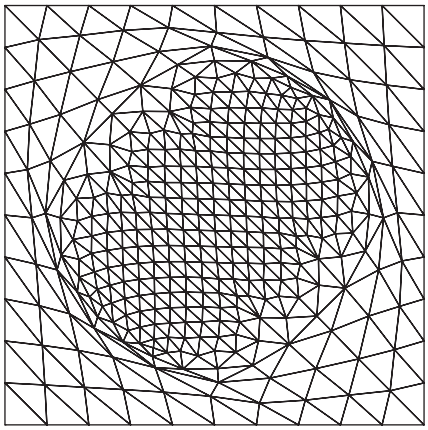

(c) Giuliani's smoothing method

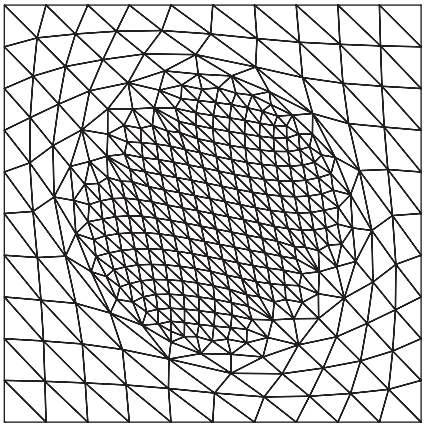

(d) smoothing by averaging

Figure 8.2: Influence of the smoothing algorithm on mesh grading after 1000 repetition loops.

The influence of the smoothing algorithm on mesh grading is investigated in the second example. Graded or anisotropic meshes made up of elements of prescribed size are often present in finite element analysis, e.g. in h-adaptive strategies or when the computational model contains regions of secondary interest. In these cases it is important to preserve the prescribed element size. Fig. 8.2a shows a structured triangle mesh zone with constant density interlaced with a coarser structured mesh. The small interface zone is unstructured and distorted, whereas the structured parts of the mixed mesh are of best quality. An appropriate smoothing algorithm hence would improve the interface zone and would leave the structured zones unchanged.

It can be seen from Fig. 8.2 that after 1000 loops running over the internal nodes the optimization-based algorithm derived in Section 6.4.3 results in the mesh with the highest quality. Structure is disturbed only slightly, and the node density distribution resp. the size of elements is largely preserved. In contrast to that, Giuliani's method as

well as smoothing by weighted averaging fail the test (Fig. 8.2c and d). Both heuristic procedures blow up the finer mesh zone, leading to a mesh with equal-sized elements at repeated application. The quality of elements at the interface deteriorated, Giuliani's method even caused degenerate elements. The tendency to equalize the size of elements is an undesirable feature which arises from the use of averaged geometric measures in the governing equations.

Note that the smoothing algorithm for the boundary nodes implemented in the ALE method, Alg. 6.3, is a simple averaging of node distances, taking into account the two neighbors of every boundary (in 2d). Graded boundaries, if present, would be smoothed faster than the nodes enclosed by the boundaries, which may worsen the quality of the mesh instead of improving it. In order to circumvent this problem, the boundary can be partitioned in a set of ungraded edges and defining the connecting node to be a corner of the boundary which is not to be moved.

8.1.2 Non-Convexly Distorted Meshes

During the numerical simulation of penetration starting by simplified ALE methods, one is inevitably faced with non-convexly distorted meshes or mesh regions. A *non-convexly distorted mesh* is a mesh that contains stretched and/or skewed elements in the vicinity of the indented boundary, which probably has a high curvature. The automatic regularization of such a mesh at fixed connectivity is very challenging. At the same time, problems associated with non-convexly distorted meshes constitute important benchmark problems for the implemented smoothing algorithms.

Backward extrusion is a common numerical example where non-convex regions are created when large material deformation occurs. In this initial boundary value problem a billet is loaded into a heavy walled container and then a die is moved towards the billet, so that the material is pushed through the die. Provided that the die and the container are rigid and their surfaces are rough respectively smooth, it suffices to discretize only the billet by finite elements (Fig. 8.3). Nodes aligned with the lower horizontal boundary are fixed in vertical direction, whereas nodes at the wall of the container are fixed in horizontal direction. The nodes located directly below the die are horizontally fixed and will be displaced in vertical direction to model the die moving downward.

Fig. 8.3 top shows the edges of the undeformed billet together with the deformed mesh at 30 % height reduction. The left hand side illustrates the results of the calculation using a heuristic scheme for mesh smoothing, whereas the mesh on the right hand side results from the optimization-based smoothing algorithm. Giuliani's heuristic method has been employed in the example, but smoothing by weighted averaging would yield similar results. The mesh quality of regions immediately under the die is comparable at this stage. Near the lower boundary, the optimization-based algorithm produces a slightly smoother mesh. At 50 % reduction, the heavy squeezing of elements around the corner of the die cannot be avoided when using the heuristic method. The area

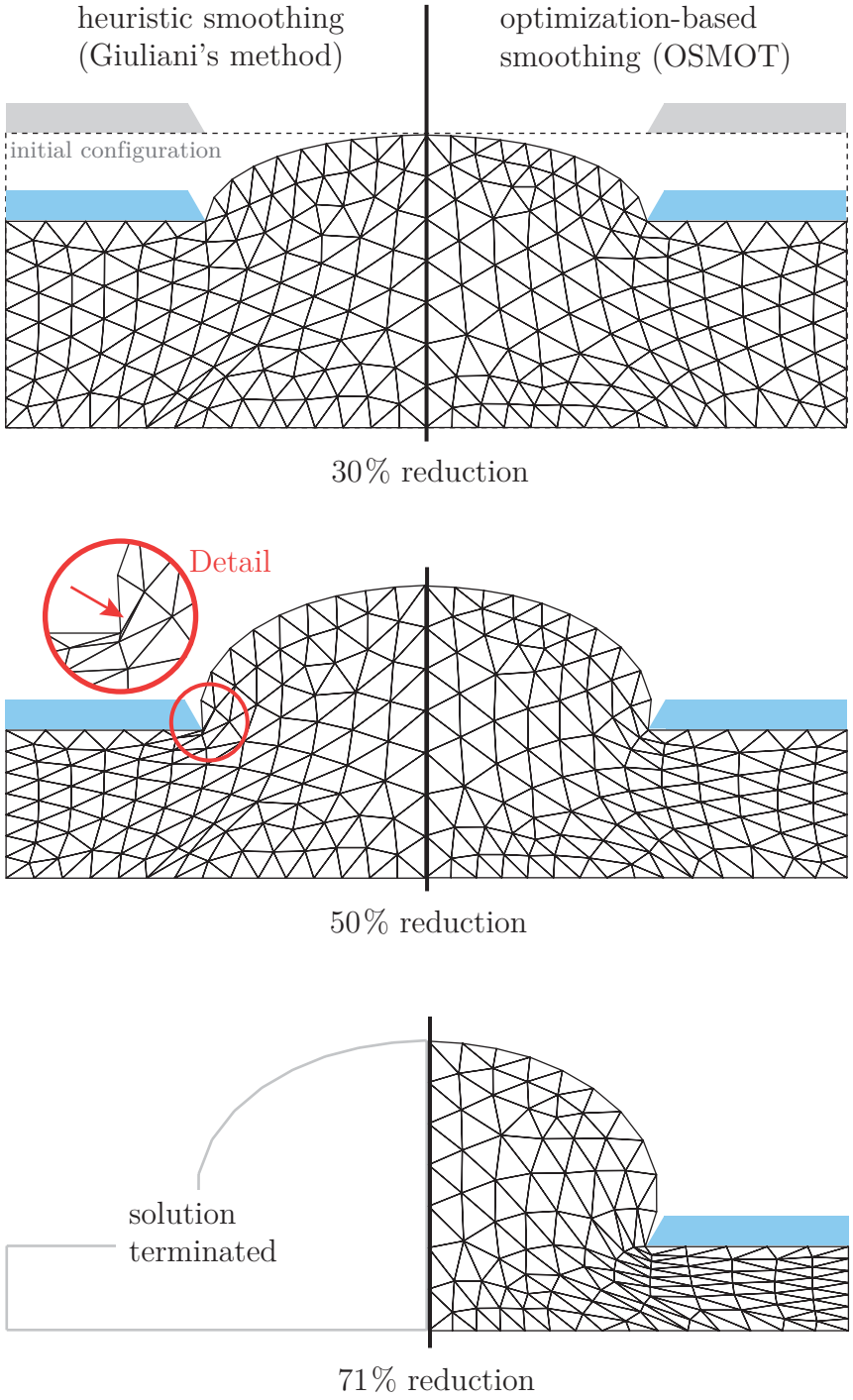

Figure 8.3: Comparison of an heuristic smoothing method and the developed optimization-based algorithm OSMOT when applied to the numerical simulation of backward extrusion.

of one element even vanishes, which inhibits convergence of the solution at continued extrusion.

Compared to the heuristic method, optimization-based smoothing achieves an excellent mesh regularization. At 50 % height reduction, element squeezing is moderate, even in the non-convexly distorted region at the corner of the die. However, at continued extrusion the fixed mesh connectivity associated with smoothing algorithms limits gains of mesh quality. Calculation terminates at height reductions of more than 71 %. Only a complete remeshing would eliminate degenerate elements so as to continue solution.

It should be noted that Fig. 8.3 shows results of ALE simulations. In these and the ALE simulations that follow, the simple averaging procedure summarized in Alg. 6.3 has been chosen to smooth the boundary nodes.

8.2 Verification of the Transport Algorithm

An example problem towards verification of an advective transport algorithm in two dimensions is the so-called *Molenkamp test* [Molenkamp, 1968], or variants of it. This class of numerical tests uses fixed (Eulerian) meshes and prescribes a steady velocity field of the material in conjunction with an initial distribution of a scalar field. The latter is referred to as a *color function* or *signal* in this context. The signal usually has the form of a pulse and has no specific physical meaning but represents the quantity being advected through the mesh. The steady velocity field either describes a rigid rotation or rigid translation of the material, so that an analytical solution is possible. The original Molenkamp test rotates a conical pulse about an axis perpendicular to the plane through a point lying outside the cone.

When variants of the Molenkamp test are applied to the advection algorithm in the transport step of the developed operator-split ALE method, the latter is run in the purely Eulerian mode such that the convective velocity equals the spatial velocity of the material, i.e. $\boldsymbol{c} = \boldsymbol{v}$ (see Section 6.2). The initial signal being advected can be associated with the solution obtained at the end of the Lagrangian step, e.g. a stress component or the void ratio concerning the problem of penetration into sand.

Fig. 8.4a shows the unstructured mesh used in the first example calculation. It is almost uniform and consists of 5516 triangle elements. The initial signal (Fig. 8.4b) is a cylindrical pulse implemented as follows. The color function is set to zero at the center (i.e. the quadrature point) of all elements except for the circular zone highlighted in Fig. 8.4a, where the color function is set to 100. For visualization the element-centered values are copied to the nodes and then averaged. In the next step, a steady velocity field is prescribed in such a way that the material performs a full 360° clockwise rigid rotation about the center of the square domain in 720 advection steps. This means that the analytical solution at the final state and the initial cylindrical pulse are identical.

The results of the implemented weighted donor-cell algorithm 6.6 after one half rotation and after a full rotation, respectively, are plotted in Figs. 8.4c and 8.4d. The dashed circle represents the analytical solution. It can be seen from the figures that the

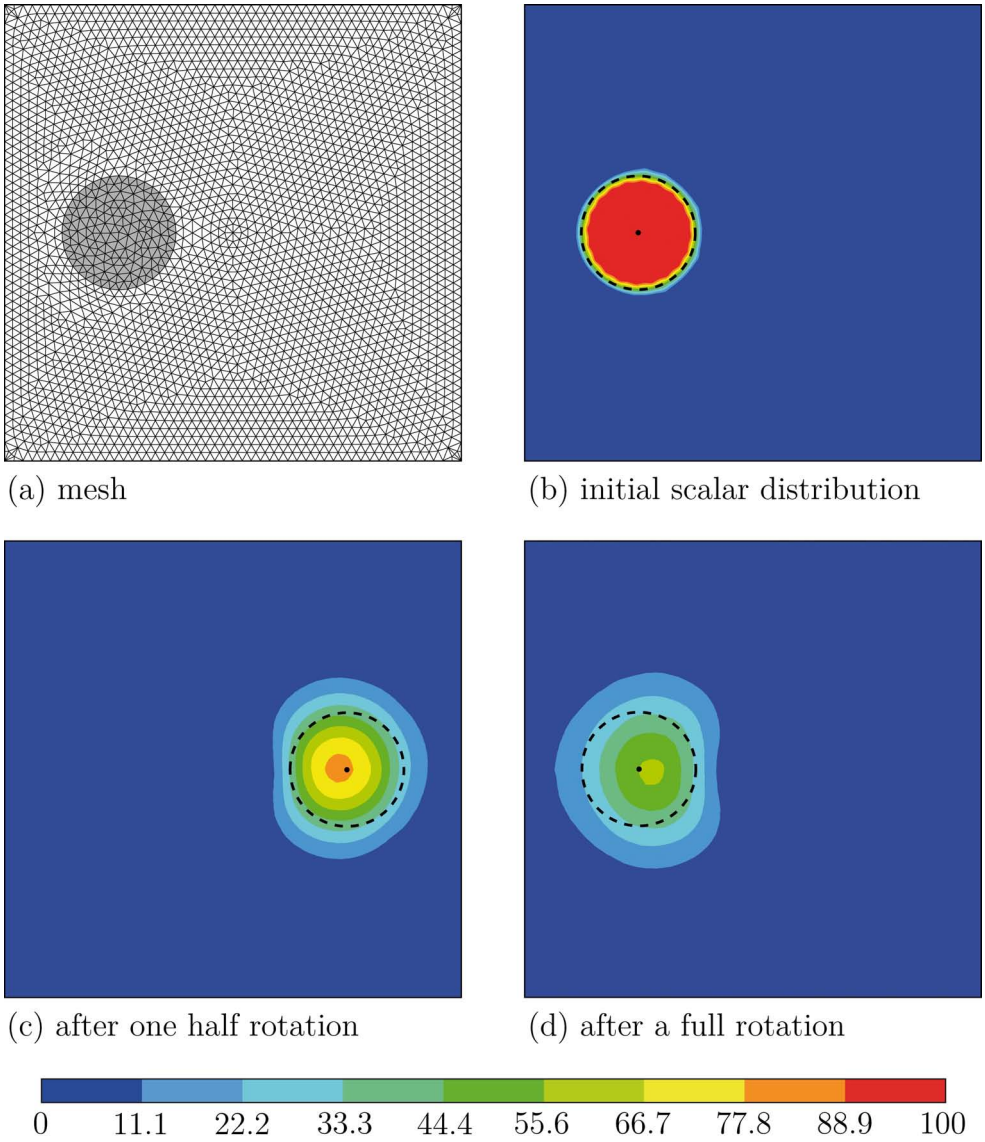

Figure 8.4: Rotational advection of a cylindrical pulse by the donor-cell transport algorithm (Molenkamp test). The analytical solution is indicated by the dashed circle.

implemented ALE method can indeed transport material through the mesh in a purely Eulerian fashion, though the upgraded finite element code is purely Lagrangian. The gradual increase of the area were the color function has values greater than zero indicates numerical diffusion introduced by the finite volume approximation. Numerical diffusion dominates in the direction of the flow because the isolines are elongated. This means that crosswind diffusion perpendicular to the streamlines is not significant in the present example, despite the absence of corner coupling in the transport algorithm. The plateau erodes and the steep gradients present in the initial signal are getting smeared during the course of rotation. Moreover, the peak moves radially inward, and its maximum value after a full rotation is reduced to only 57 % of its initial value.

Results are comparable to those of the spatially first-order accurate *Upstream N* scheme reported by Molenkamp [1968, fig. 1] which, in one dimension, corresponds to the donor-cell method currently implemented. In contrast to second- or higher-order methods, first-order advective transport algorithms are overly diffusive. It has to be noted, however, that rotation of a cylindrical pulse constitutes an academic extreme example. The solution variables in practical soil mechanical problems often have smaller gradients, leading to less apparent numerical diffusion. Moreover, in the operator-split ALE method, every transport step is followed by a Lagrangian step that should bring back the solution variables to an admissible state. Hence, the detail resolution of these variables is predominantly determined by the node density in the mesh, and not by the transport algorithm.

The second test problem for the weighted donor-cell transport algorithm 6.6 is a variant of the Molenkamp test. In this test a cylindrical pulse is advected along the diagonal of a square domain by a steady uniform flow field. The Courant number defined through 6.5.14 as well as the coarseness of the mesh were varied. The initial scalar distribution together with the meshes used are shown in Fig. 8.5. Results of three calculations are plotted in Fig. 8.6, in which the left column assembles the initial states and the right column the final states after transport. In Fig. 8.6 the values assigned to the element centers have again been averaged to the nodes for reasons of visualization.

The results on the coarse mesh (Figs. 8.6a and 8.6b) indicate that the amount of numerical diffusion generally decreases with increasing Courant numbers $Co \in [0, 1]$. The maximum value of the pulse is reduced to only 38 % of its initial value for $Co = 0.21$, and to 56 % for $Co = 0.42$; here Co is calculated from the travelled distance of a material particle relative to the mesh in one advection sweep divided by the element size specified during mesh generation. In contrast to that, numerical crosswind diffusion is less pronounced if Courant numbers are small. Elongation of the isolines in the direction transverse to the propagation of the pulse is more significant at $Co = 0.42$ than at $Co = 0.21$. Recall that the overall amount of crosswind diffusion can be reduced if the implemented isotropic advection in two dimensions would be replaced by the alternating direction approach; see Section 6.5.2.

At a Courant number of $Co = 0.33$ numerical diffusion is also present with the fine mesh (Fig. 8.6c) but not as severe as with the coarse mesh. Still 89 % of the maximum value of the signal at the initial state remain at the final state. This is remarkable

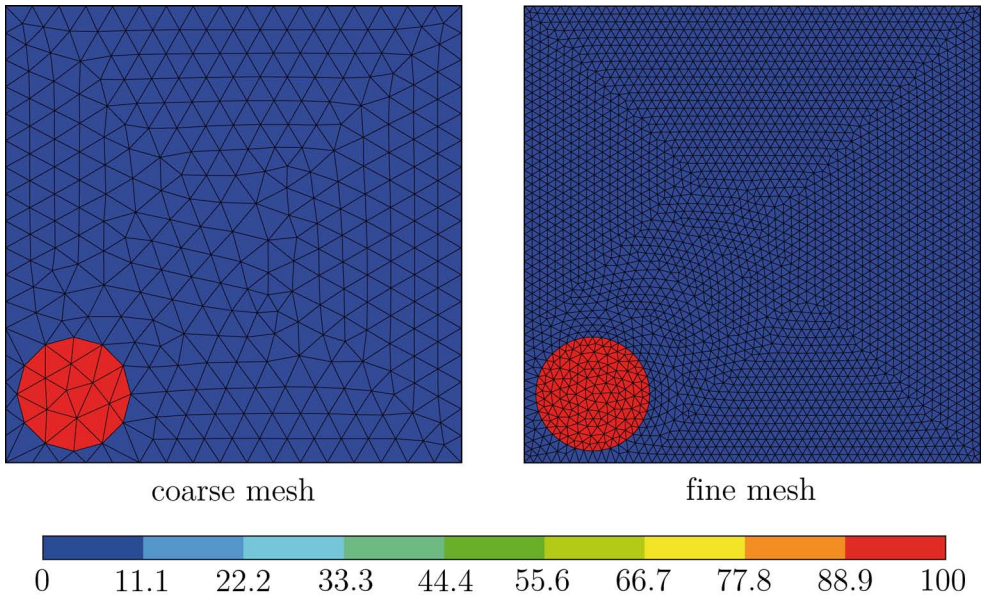

Figure 8.5: Initial scalar distribution and meshes for the diagonal advection of a cylindrical pulse.

because the number of advection sweeps taken for diagonal transport on the fine mesh is about two resp. four times larger than on the coarse mesh.

In all the calculations presented in this section and the sections that follow, the donor-cell weighting factor has been chosen to $\alpha = 1.0$, which results in a full donor-cell advection scheme (first-order upwind scheme); see Section 6.5 for details.

8.3 Coining Test

The remaining example problems that will be presented are useful applications of the developed ALE method because (i) they demonstrate the capability and versatility of the method and (ii) there is data available for comparison. The examples include large material deformations and non-convexly distorted domains resulting from the indentation or penetration of blunt bodies. This renders purely Lagrangian methods and the majority of ALE mesh smoothing algorithms inapplicable. Hence, the optimization-based algorithm (Alg. 6.5) was applied to internal nodes in all the subsequent ALE simulations, and boundary nodes were smoothed by applying the averaging procedure (Alg. 6.3).

The quasi-static coining test is a sheet-metal forming manufacturing process. In this initial boundary value problem, a punch is stamped on a metallic disk lying on a die. The section that follows is concerned with the back-calculation of the particular example presented in [Rodríguez-Ferran et al., 1998, sec. 4.2] and [Rodríguez-Ferran et al., 2002, sec. 5.2]. The problem statement including the axisymmetric model and one of the several 3-node triangle meshes that have been analyzed are depicted in Fig. 8.7.

(a) $Co = 0.21$, coarse mesh, 80 advection sweeps

(b) $Co = 0.42$, coarse mesh, 40 advection sweeps

(c) $Co = 0.33$, fine mesh, 150 advection sweeps

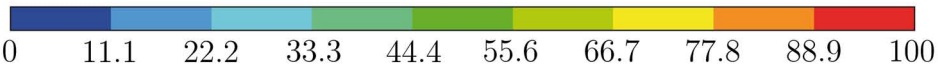

Figure 8.6: Initial states (left) and final states (right) of a cylindrical pulse after diagonal advection by the donor-cell transport algorithm.

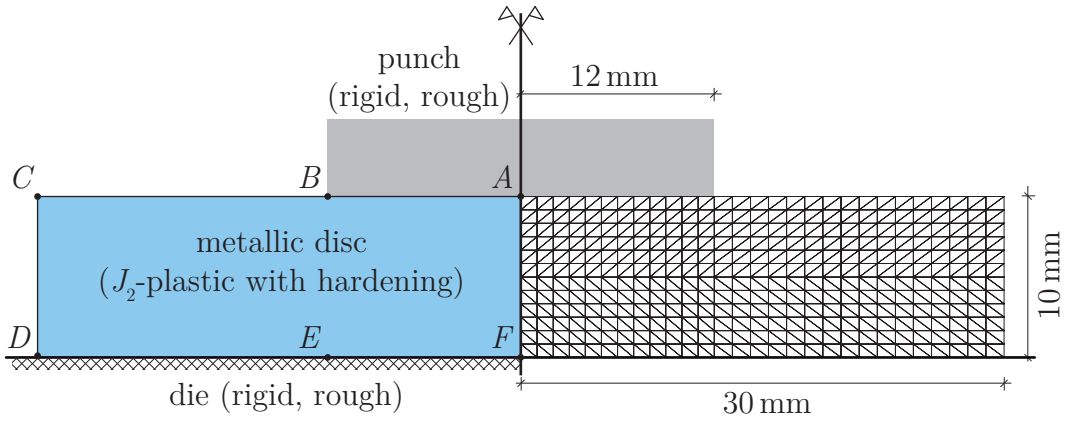

Figure 8.7: Coining of a metallic disk. Problem statement and initial mesh (here: coarse structured mesh).

The workpiece is a metallic disk with a radius of 30 mm and a height of 10 mm. The disk is placed with its entire base area on a die and its height is deformed by a vertically displaced plane punch 12 mm in radius. The punch is monotonically stamped onto the disk until a height reduction of 60 % has been achieved. Constitutive behavior of the disk is modeled by hypoelastic-J_2-plasticity (Secs. 4.1.3, 6.3.2), with the material constants chosen as follows: Young's modulus $E = 200\,\mathrm{GPa}$, Poisson's ratio $\nu = 0.3$, initial yield stress $\sigma^{\mathrm{y}0} = 250\,\mathrm{MPa}$, and plastic modulus $E^{\mathrm{p}} = 1\,\mathrm{GPa}$.

Only the workpiece needs to be discretized by finite elements because both the die and the punch are assumed rigid, and the contact conditions in the punch-disk and disk-die interfaces are assumed perfectly rough (stick). Under these assumptions loading is reduced to a simple vertical displacement of the interface nodes located on the line between A and B. The model outlined in Fig. 8.7 right takes advantage of axial symmetry, that is, the nodes lying on the line between A and F are fixed in horizontal direction. To simulate uplift due to coining, the surface of the workpiece is covered with contact elements between points C, D, and E (Fig. 8.7), and the die is discretized using complementary target elements.

Both purely Lagrangian and ALE simulations have been carried out. The computed yield stress distribution at different height reductions are plotted in Fig. 8.8. In both formulations, the plastic zone is initiated under the corner of the punch, particularly where the disk is in contact with the die. The central part of the workpiece between the punch and the die begins to yield and flows outward, which leads to an elongation of initially horizontal material lines. Plastic hardening occurs in the zone of high yield stress at the lower boundary and causes the flowed out material next to the punch to lift up. From the yield stress distribution at 12 %, 24 %, and 36 % reduction, it can be seen that the Lagrangian formulation involves shear localization along specific mesh lines. This is probably due to the low-order approximation in the formulation of the constant strain triangle. However, no such shear localization is present at all when using the ALE formulation.

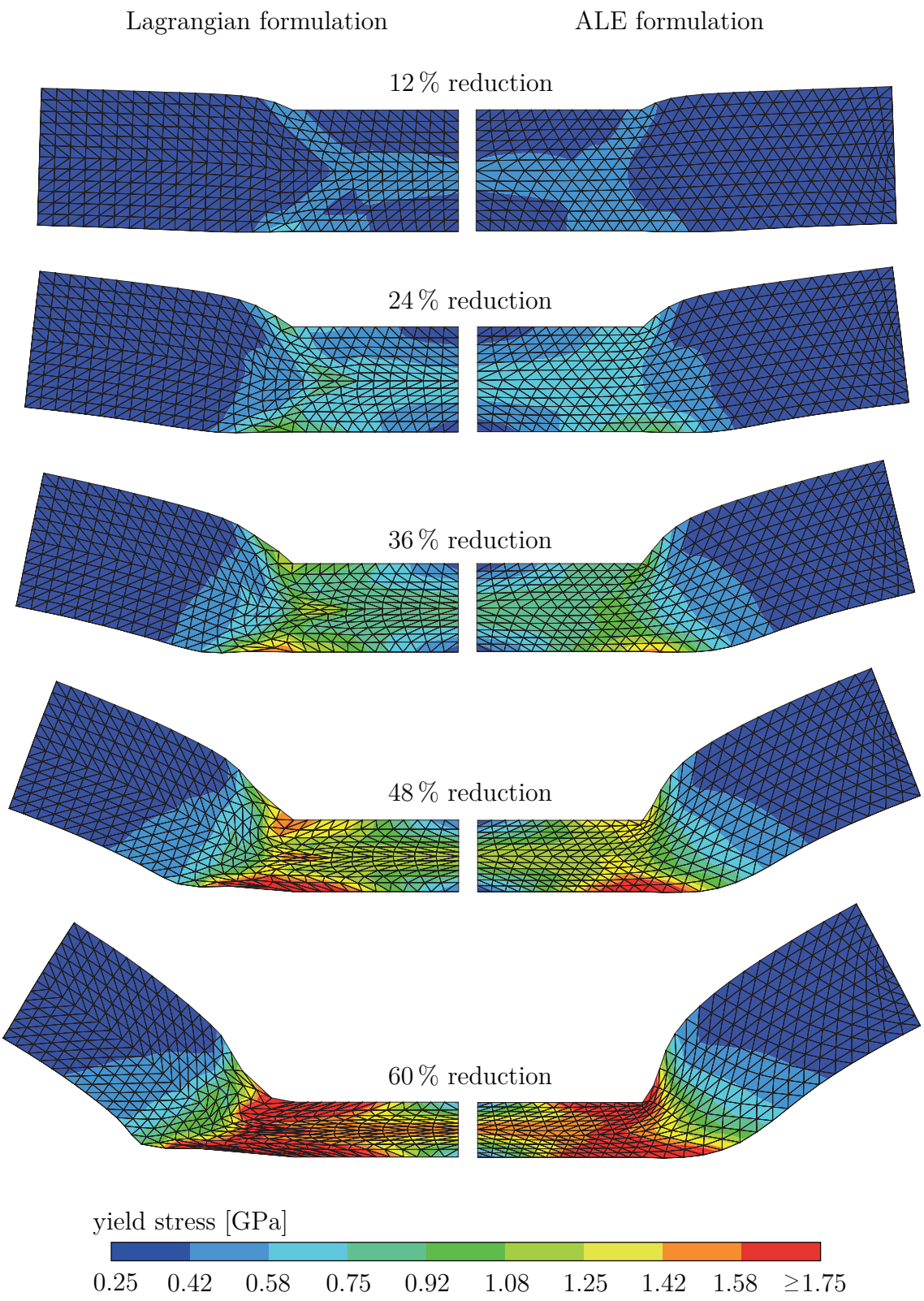

Figure 8.8: Coining of a metallic disk. Simulated yield stress distribution at different height reductions by using the Lagrangian formulation (left) and the ALE formulation (right).

Element distortion in the Lagrangian analysis (Fig. 8.8 left) keeps within an acceptable range up to 36 % height reduction. At higher indentations, the quality of elements immediately below the corner of the punch is almost maintained, but elements in the vicinity of point E on the lower boundary of the workpiece are heavily squeezed and stretched. Moreover, elements next to the punch at the free surface are stretched, which reduces the resolution of the variables in that region. Analysis did not terminate solely because element shape checking had been switched off and convergence tolerances were given very large values. Mesh distortion present in the Lagrangian analysis is greatly reduced by mesh regularization in the ALE analysis (Fig. 8.8 right). Smoothing of the boundary nodes naturally prevents the associated elements from being excessively stretched, hence maintains the initial density of nodes lateral to the punch. All internal nodes and all boundary nodes except for the nodes associated with points A to F were relocated with the respective algorithms of Section 6.4 during each mesh motion step.

Rodríguez-Ferran et al. [1998, sec. 4.2] and Rodríguez-Ferran et al. [2002, sec. 5.2] analyze the same quasi-static coining process by using an ALE method which is, in this regard, comparable to the current one. However, the finite element models reported in these two references employ eight-noded quadrilateral elements with 2×2 Gauss points. Moreover, the hypoelastic part of the J_2-plasticity model used in [Rodríguez-Ferran et al., 1998] is replaced with a hyperelastic formulation in [Rodríguez-Ferran et al., 2002]. The direct comparison of the results in Fig. 8.9 shows excellent agreement in all stages of the forming process. Note that the results of the hyperelastic and hypoelastic approaches are very similar because elastic strains are small compared to the plastic strains for this numerical example.

8.4 Piercing Test

Piercing is another test problem borrowed from the metal forming community which can be employed to validate the ALE method in conjunction with the J_2-plasticity model. In this quasi-static process a billet is held in a heavy walled container and hollowed out by a flat punch (Fig. 8.10). The example is a plane strain problem and assumes the punch to be rigid and perfectly rough (no sliding). The vertical and horizontal walls of the container are smooth to ensure sliding contact conditions in the container-billet interface. Moreover, the initial boundary value problem is modeled as one of plain strain. For the case of plastic-rigid material and a container to punch breadth ratio of $S/B = 0.5$, then, Hill [1998, pp. 186–188] provides the following analytical solution of the maximum punch pressure (or penetration pressure) in a steady piercing process:

$$p = (2 + \pi)\, \tau^{\mathrm{y}}\,, \qquad \text{where} \quad \tau^{\mathrm{y}} = \sigma^{\mathrm{y}}/\sqrt{3}\,. \tag{8.4.1}$$

σ^{y} is the stress at the yielding point in uniaxial tension. Eq. (8.4.1) is the same relation as for the ultimate bearing capacity of a strip footing on the plane surface of a weightless and frictionless cohesive soil; cf. Prandtl [1920, eq. (14a)], Hill [1998, sec. IX 5(i)], and [Craig, 2007, eq. (8.1)].

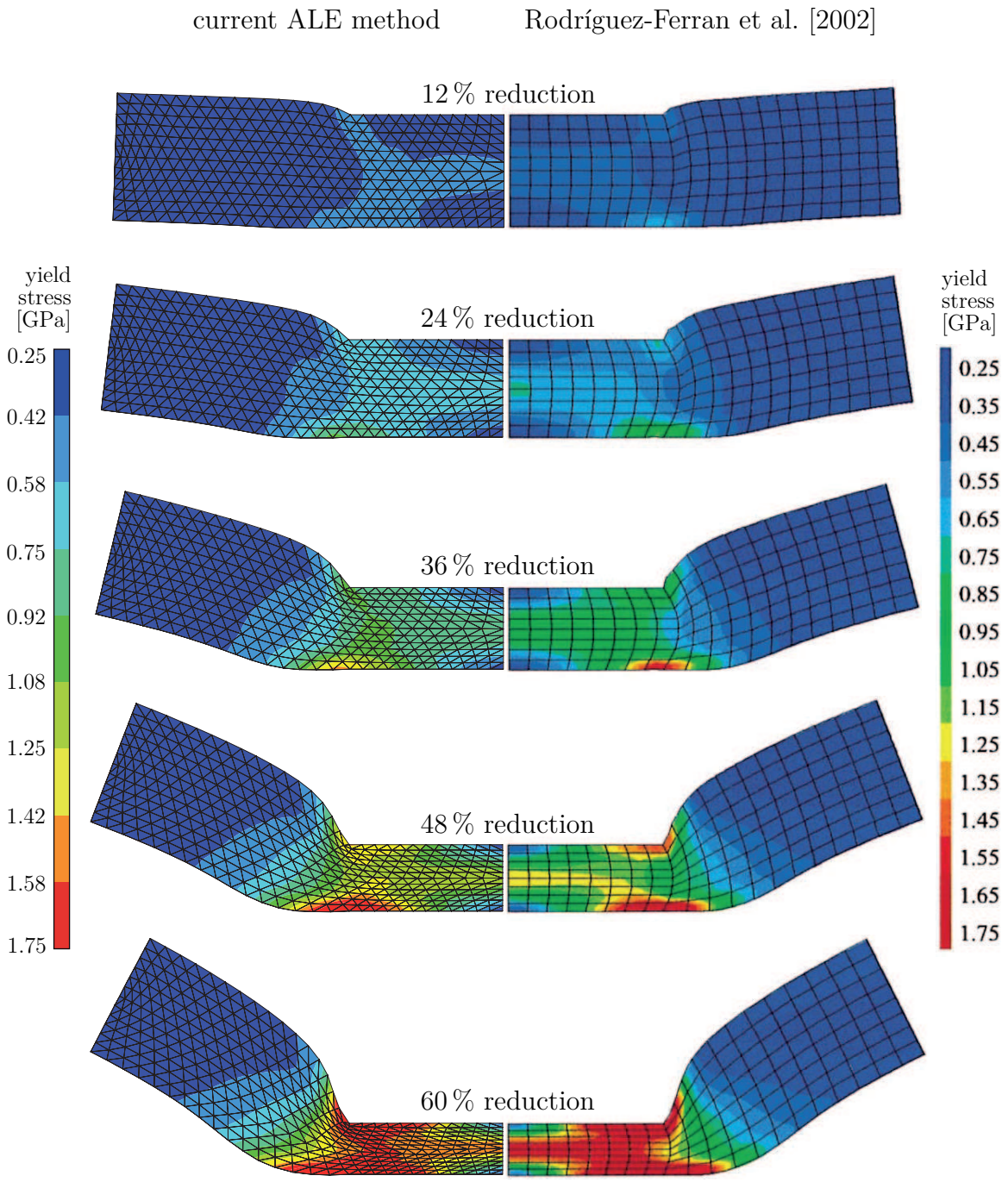

Figure 8.9: Coining of a metallic disk. Comparison of the results obtained using the current ALE method (left) with those of Rodríguez-Ferran et al. [2002, plate 3] (right).

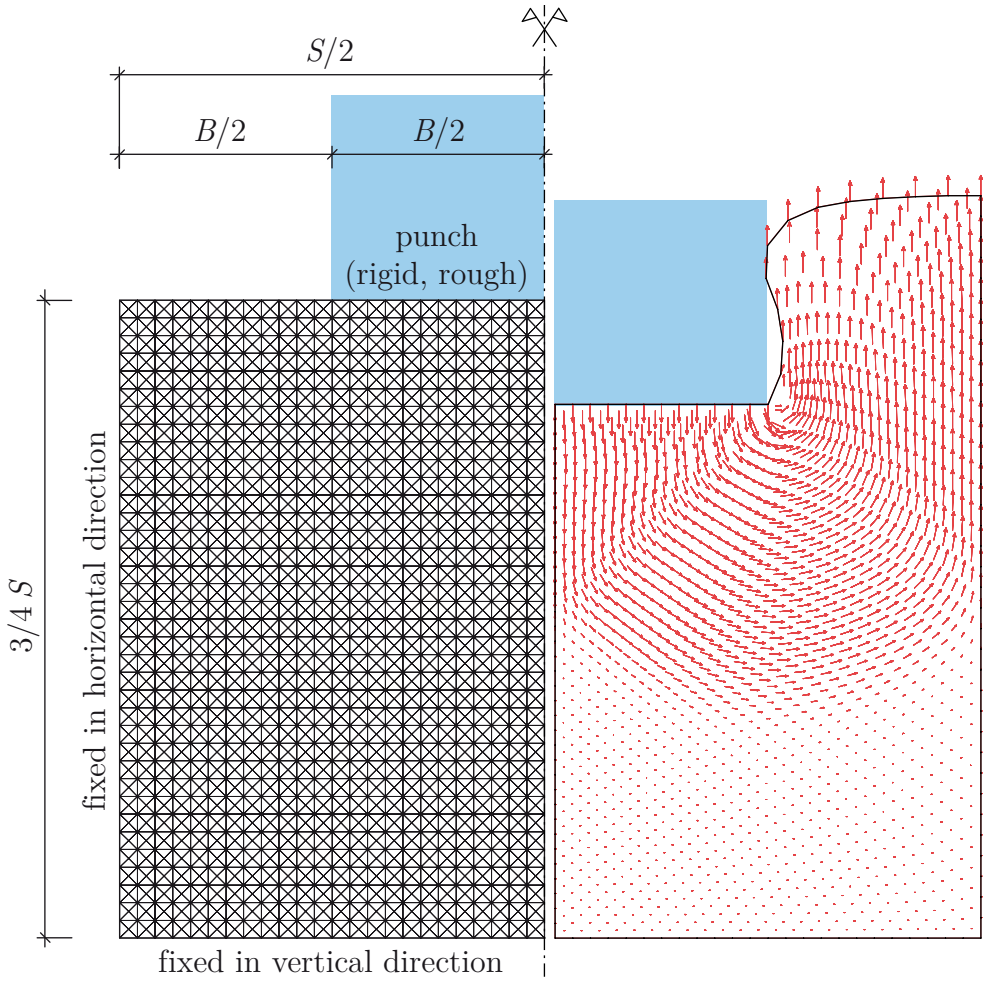

Figure 8.10: Simulation of a piercing process. Problem statement and coarse structured mesh (left), deformed domain and velocity field at $z/B = 0.25$ (right).

The two finite element models used for back-calculation of the analytical solution take advantage of symmetry and differ only in the coarseness of the mesh. The model and the coarse mesh are shown in Fig. 8.10 left. No contact elements were used. In both models, the cross-diagonal mesh pattern [Nagtegaal et al., 1974] is applied to prevent overconstrained (locked) constant strain triangles. This results in uniform structured meshes composed of quadrilateral macroelements which are formed by four triangles. The edge length of the macroelements is $S/48$ in the coarse mesh and $S/100$ in the fine mesh, where S is the breadth of the container. The plastic-rigid material of the billet is modeled by the hypoelasto-J_2-plastic rate constitutive equation already employed for the coining test. The set of material constants chosen for the simulations consists of Young's modulus $E = 2600\,\mathrm{kPa}$, Poisson's ratio $\nu = 0.3$, initial yield stress $\sigma^{\mathrm{y}0} = 20\,\mathrm{kPa}$, and plastic modulus $E^{\mathrm{p}} = 0\,\mathrm{kPa}$ (ideal plastic response).

Fig. 8.10 on the right plots the deformed computational domain at a relative penetration depth of $z/B = 0.25$ together with the velocity field on the billet obtained with the coarse mesh. The sudden change in flow direction below the punch is related to a slip line that intersects the axis of symmetry at 45°. A second, less apparent slip line intersects the wall of the container at 45°. The velocity field is in a fairly good agreement with that of a coupled Eulerian-Lagrangian (CEL) analysis reported by Henke et al. [2010]. However, the results also indicate that numerical methods allowing material boundaries to flow through the mesh (like Eulerian, CEL, or MMALE methods) are better suited for such large deformation problems than SALE or other single-material methods. The unrealistic deformation of the unconstrained material boundary lateral to the punch (Fig. 8.10 right) is partly due to this simplified treatment in the developed ALE method, but the problem could be resolved in this example by using a finer mesh.

The calculated load-displacement curves and the analytical solution are plotted in Fig. 8.11. In contrast to the plastic-rigid material behavior assumed in [Hill, 1998, pp. 186–188], the rate equation governing hypoelastic response in the ALE simulation results in a gradual increase of the punch pressure along with increasing indentation. The relative pressure $p/\sigma^{\mathrm{y}} = 2.97$ of the analytical solution is, however, reached at relative penetration depths of less than $z/B = 0.05$ in all calculations. Beyond that point, the simulated pressure is always larger than the plastic-rigid solution, but the difference decreases with decreasing element size. The maximum relative error after intersecting the analytical solution is 23 % for the coarse mesh and 10 % for the fine mesh.

8.5 Shallow Penetration into Sand

Complexity of the numerical examples is further increased by considering the penetration of blunt bodies into sand. The first example in this context is concerned with shallow penetration, and it constitutes one test case to examine the capability of the fully-fledged ALE method developed and implemented during this research.

Fig. 8.12a shows the computational model that has been designed with the intention to back-calculate the results of the experimental penetration test SP-3; cf. Chapter 7

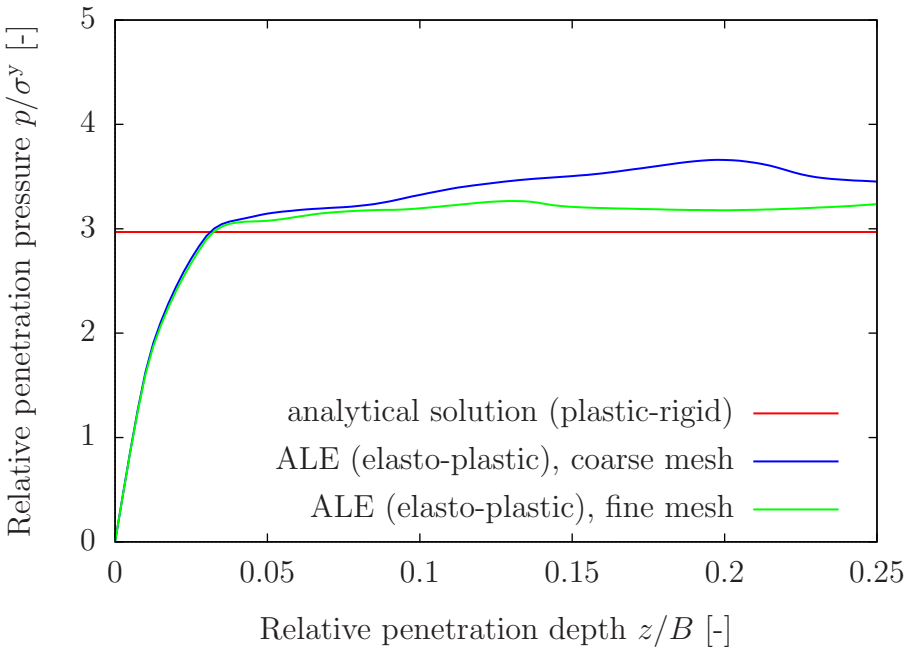

Figure 8.11: Simulation of a piercing process. Analytical solution $p/\sigma^y = (2+\pi)/\sqrt{3}$ for plastic-rigid material [Hill, 1998, pp. 186-188] and results of an ALE simulation using the hypoelasto-J_2-plastic model (von Mises plasticity).

and Appendix D. The model assumes plain strain conditions and takes advantage of symmetry. The flat-ended penetrator, representing a strip footing in the present case, is rigid and perfectly rough (no sliding), except for its sides which are assumed perfectly smooth (zero friction). The sides of the penetrator and the ground surface lateral to the penetrator form a rigid-to-flexible contact pair and are discretized as such. All nodes at the lower boundary of the computational domain are fixed in vertical direction, and the nodes at the vertical boundaries are fixed in horizontal direction. The penetration process starts at the unloaded ground surface and is displacement controlled, and the initial relative density of the sand is $D_{r0} = 78\,\%$ (initial void ratio $e_0 = 0.546$), as in the experimental test.

The assumed initial stress state within the sand is the so-called K_0-*state*. It is calculated in an isotropically elastic dummy load step based on the bulk mass density and the following estimate of Poisson's ratio:

$$\nu = \frac{K_0}{1+K_0} = \frac{1-\sin\phi'}{2-\sin\phi'} \,. \tag{8.5.1}$$

Here K_0 is the coefficient of earth pressure at-rest and ϕ' is the angle of internal friction. The first equality can be derived from elasticity theory and by assuming that $\sigma_{ab} = 0$ for all $a \neq b$, $\sigma_{11} = \sigma_{22} = K_0\sigma_{33}$, and $\varepsilon_{11} = \varepsilon_{22} = 0$; note that the third coordinate axis is aligned with the vertical. Under these assumptions,

$$0 = \sigma_{11} - \nu\,(\sigma_{22}+\sigma_{33}) = \sigma_{33}\,(K_0 - \nu\,(1+K_0)) \,. \tag{8.5.2}$$

The right hand side of (8.5.1) employs Jaky's formula [cf. Craig, 2007, eq. (6.15a)] for the coefficient of earth pressure at-rest. It should be noted, however, that soil

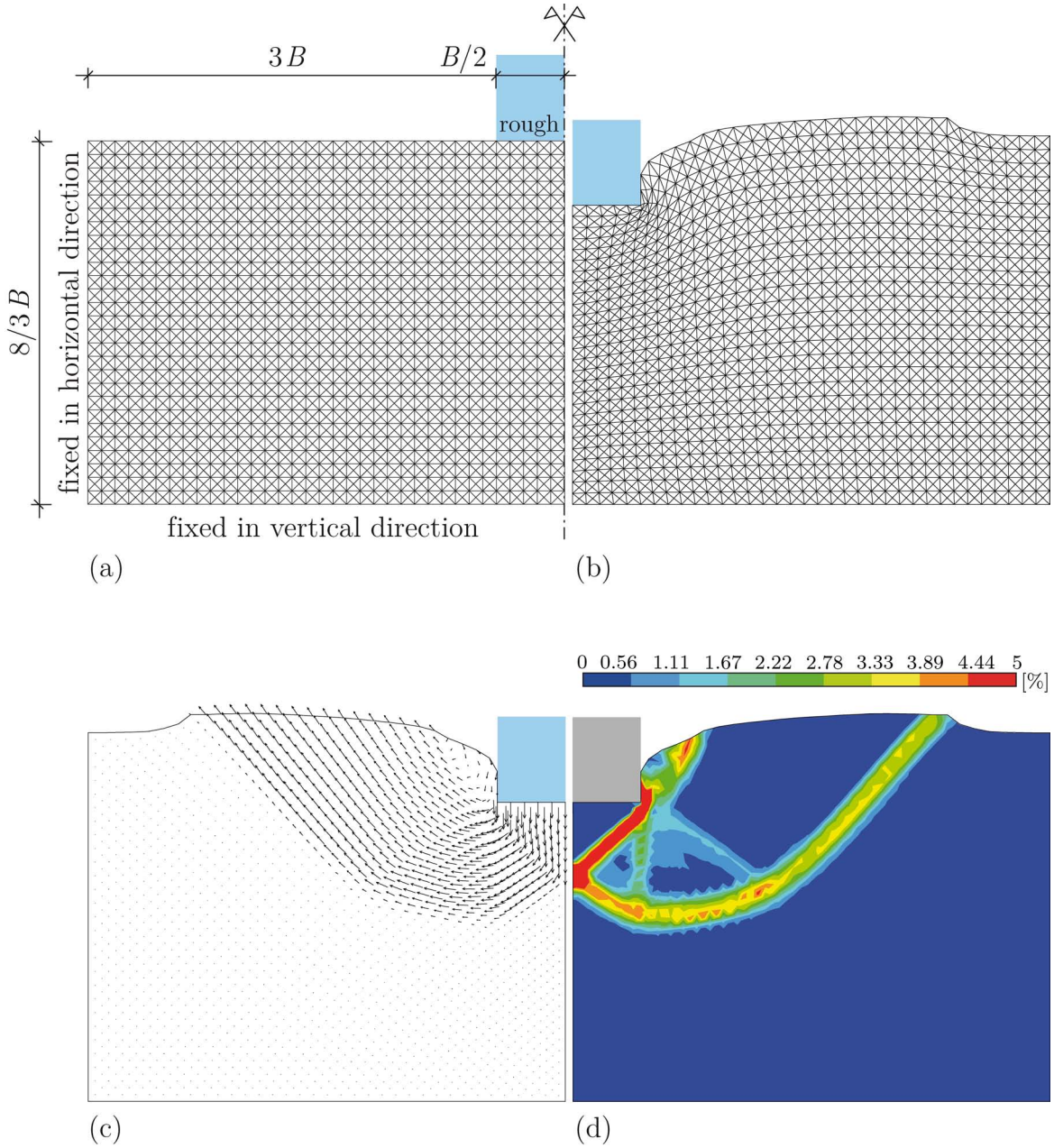

Figure 8.12: ALE simulation of shallow penetration into sand. (a) Problem statement and mesh, (b) deformed and smoothed mesh at a relative penetration depth of $z/B = 0.55$, (c) incremental displacement, (d) incremental maximum shear strain.

in-situ generally possesses values of K_0 which may not comply with Jaky's formula. $\phi' = 30° \approx \phi_c$ is assumed for the present example, resulting in $K_0 = 0.5$ resp. $\nu = 1/3$.

The hypoplastic rate constitutive equation using the intergranular strain extension (Section 4.3) is employed to model the behavior of the test sand. Determination resp. estimation of the material constants has been outlined in Section 4.3.3, and the complete set of constants for the model test sand is in Tab. 4.2. Recall that there is a subtlety in the proper determination of the constant h_s, referred to as granulate hardness, for very small values of mean effective stress. The conventional procedures to determine the granulate hardness are valid only if the mean effective stress is larger than 20 kPa. For a mean effective stress that tends toward zero near the unloaded ground surface, the conventionally determined h_s is divided by a sufficiently large number such that $h_s < 1000\,\mathrm{MPa}$. The best choice for that number will be discussed later.

For a relative penetration of $z/B = 0.55$, the deformed mesh after smoothing, the calculated incremental displacement field, and the incremental maximum shear strain field are depicted in Figs. 8.12b, c, and d, respectively. A direct comparison of Figs. 8.12a and b reveals that the node density at the corner of the strip footing is considerably increased by the applied mesh smoothing procedure but the mesh has a good quality in terms of the shape of elements. It has already been mentioned that the optimization-based algorithm 6.5 was used to optimized the locations of the internal nodes. It is also remarked that neither the purely Lagrangian mode of the ALE method nor the two heuristic smoothing algorithms led to a convergent solution for this example. None of these approaches could prevent elements to invert along with penetration, particularly at the indented mesh corner.

The advanced constitutive equation provides valuable insight into the mechanical behavior of sand. Consider, for example, the simulated void ratio distribution at $z/B = 0.55$, which is plotted in Fig. 8.13. The minimum void ratio, the maximum void ratio, and the initial void ratio of the test sand are also listed. The results indicate that sand locally undergoes severe density changes during the process of penetration. The initially dense sand loosens due to shearing lateral to the strip footing and along the slip surfaces; see also Fig. 8.12d. At the foundation corner, the reached void ratio of $e = 0.81$ even lies above the maximum void ratio of $e_{max} = 0.779$ determined through a laboratory test. In the wedge-shaped zone immediately below the foundation, on the other hand, the sand densifies along with penetration and reaches its minimum void ratio of $e_{min} = 0.482$. It can be concluded that the development of the void ratio agrees with that of the relative density reported in the literature (cf. Chapter 2); relative density is proportional to the negative of the void ratio by Definition 4.2.9.

The numerical simulations likewise are in good agreement with the results of the experimental model test SP-3, as can be seen from the comparative view in Fig. 8.14. Results of the PIV analysis are depicted on the left (see also Fig. D.4) and the results of the ALE back-calculation are on the right. The incremental displacement and the zones of maximum shear strain measured within the sand can be fairly reproduced; in fact, the incremental penetration leading to the incremental displacement and strain fields was $\Delta z_{exp} = 2\,\mathrm{mm}$ in case of the SP tests but only $\Delta z_{num} = 1.2\,\mathrm{mm}$ in the numerical simulation. The measured and the predicted ground heaving also match very well.

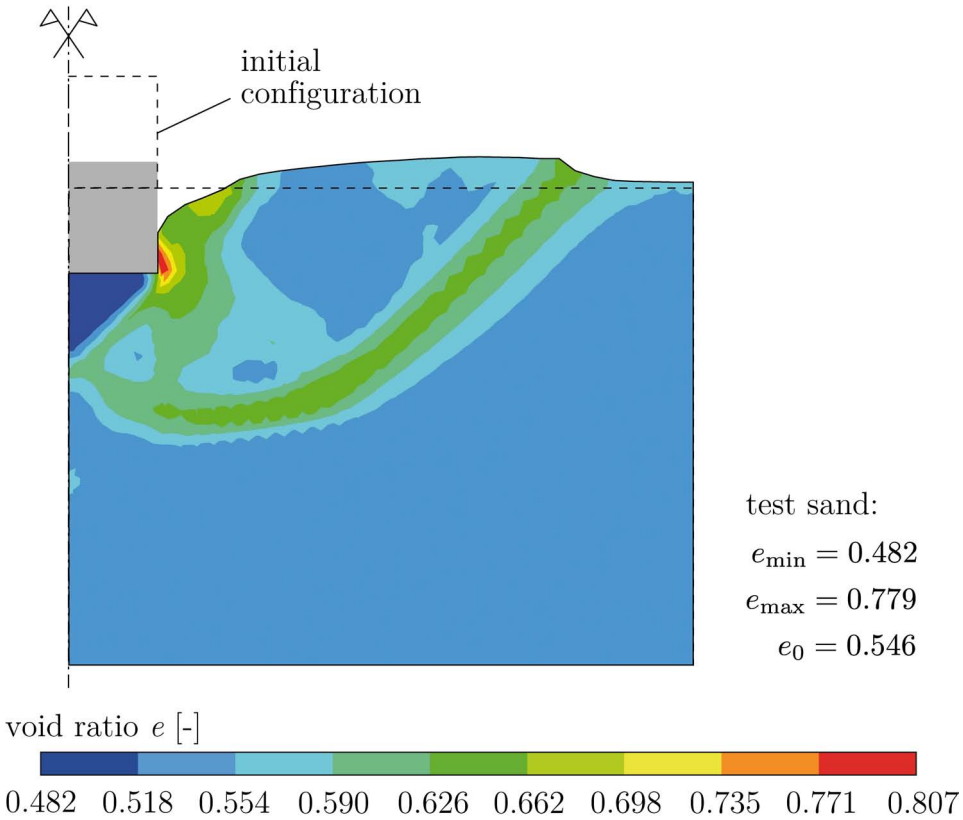

Figure 8.13: ALE simulation of shallow penetration into sand. Predicted distribution of the void ratio at a relative penetration depth of $z/B = 0.55$.

Differences are found, however, in the shape of wedge underneath the pile base. The angle at the apex of this zone is exactly 90° in the simulation, whereas the experimental investigations indicate much larger angles.

It is emphasized that the accurate prediction of ground heaving in sand is related to the capability of the constitutive equation to model dilatancy. Concerning the hypoplastic rate constitutive equation used here, dilatancy is strongly influenced by the value of the granulate hardness. In the present example, $h_s/1000$ has been set to obtain the results shown in Figs. 8.12, 8.13, and 8.14, where $h_s = 76\,500\,\mathrm{MPa}$ denotes the value of granulate hardness for the test sand determined by using the conventional procedure (cf. Section 4.3.3). Dilatancy resp. ground heaving was overestimated when assigning the value $h_s/100$ instead. However, in this case the predicted load-displacement curve is very close to the experimental data (Fig. 8.15). The choice $h_s/1000$ led to a curve whose peak is located in a larger penetration depth and has a much higher value.

8.6 Pile Penetration into Sand

The last section of this chapter is concerned with the numerical simulation of deep quasi-static penetration into sand that starts from the ground surface. In particular, this section presents back-calculations of some of the conducted pile penetration tests (Chapter 7 and Appendix D) and discusses the applicability of different finite element models.

Difficulties encountered with the rigorous modeling of penetration into sand have been introduced in Chapter 1 and include the strong nonlinearities due to complex material behavior, large deformations, and contact constraints. A related challenge is the large variation of the soil stiffness at the unloaded ground surface and underneath the penetrator, which may lead to an ill-conditioned matrix. Owing to these difficulties, stable and robust simulations are usually hard to achieve. Design of a set of appropriate time steps and the adjustment of the contact parameters only at the beginning of the simulation is a science of its own. The author emphasizes that the sensitivity to the time step is connected with the Lagrangian phase of the solution, and is generally independent of the specific capabilities of ALE methods. As a matter of fact, the ALE approach can improve convergence of the solution and addresses problems where purely Lagrangian methods will fail.

8.6.1 Back-Calculation of PP-27-F Test

Test PP-27-F involved the penetration of a flat-ended pile into initially loose sand (initial relative density $D_{r0} = 21\,\%$ resp. initial void ratio $e_0 = 0.718$). The obvious way to design a finite element model for back-calculation is to take a model for shallow penetration and to scale up the soil domain and penetration depth. The axisymmetric model depicted in Fig. 8.16a falls into this category.

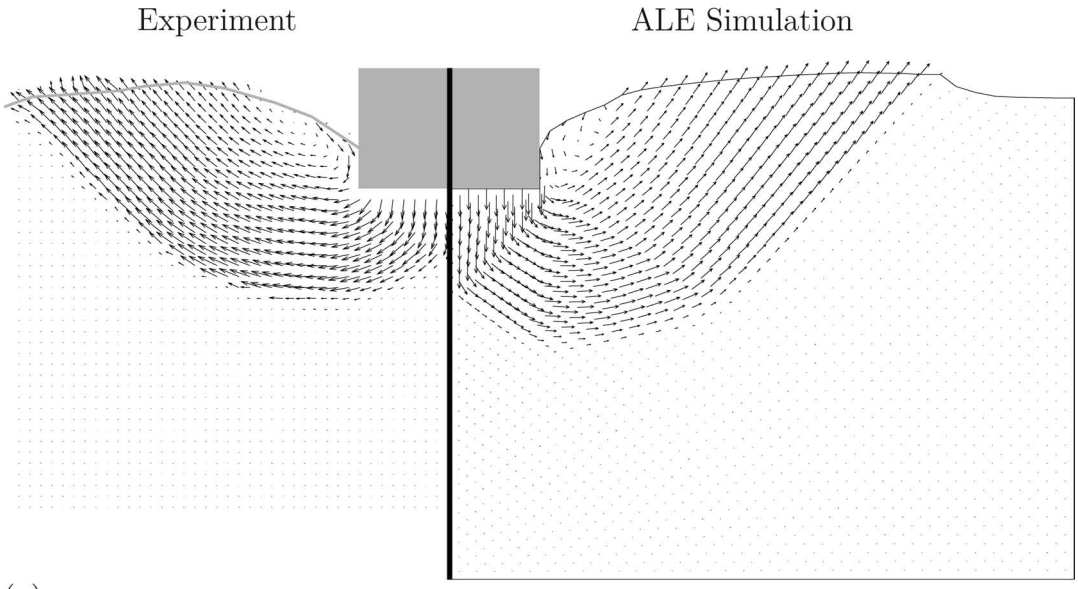

(a)

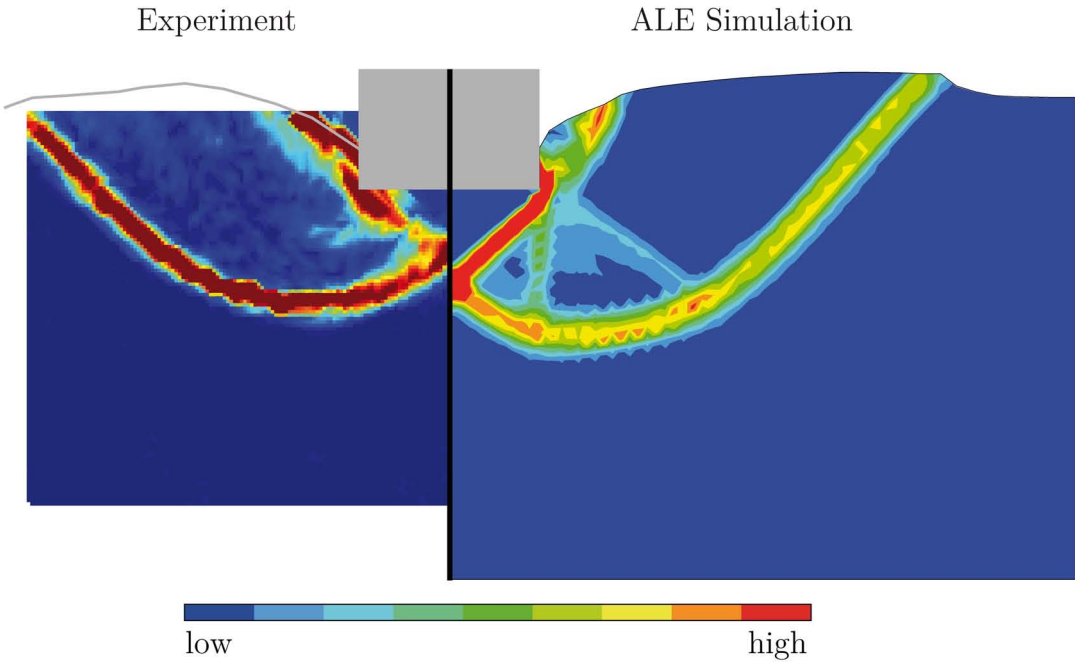

(b)

Figure 8.14: Comparison of the results of experimental test SP-3 and of the ALE back-calculation at $z/B = 0.55$. (a) Incremental displacement, (b) incremental maximum shear strain.

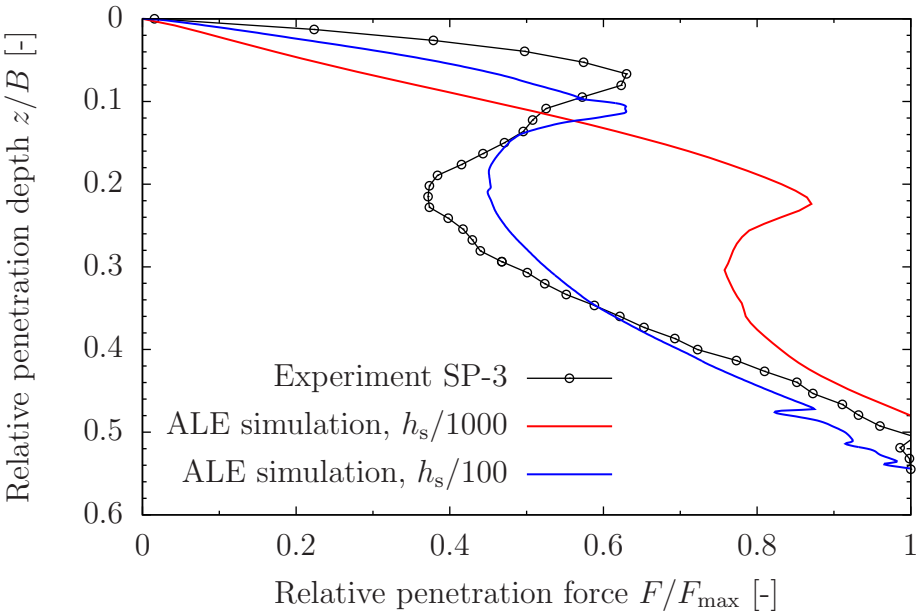

Figure 8.15: Comparison of the measured and predicted load-displacement curves of shallow penetration test SP-3.

As penetration starts from the soil surface, the initial configuration has a simple geometry. The pile is assumed rigid and its surface is assumed perfectly smooth. The entire pile skin and the ground surface are modeled as a contact pair using straight segments for the slave surface and accounting for large deformation of the interface. A Lagrange multiplier contact algorithm enforces zero penetration of the pile elements when contact is closed. In order to smooth the interface geometry and to ease solution of the contact problem, the corner of the pile tip was rounded. The prescribed boundary conditions and initial conditions, including the initial stress state, are the same as for the finite element model used for the simulation of shallow penetration (Section 8.5).

For a relative penetration depth of $z/D = 5.0$, the deformed mesh together with the void ratio distribution are shown in Fig. 8.16b. The figure indicates that the distance between the densified zone under the pile base and the lower boundary is too small to avoid boundary effects. Sand located in that region is compressed in vertical direction but then is forced to move radially, leading to an increase of pore volume resp. void ratio relative to the initial state through shearing. The gaps between the mesh and the pile are caused by the poor discretization of the interface in conjunction with the small amount of artificial capillary pressure added to the soil material for numerical reasons. It is remarkable that purely Lagrangian calculations as well as ALE calculations terminated at an early stage. Only the ALE calculation which employed optimization-based mesh smoothing after every Lagrangian step has led to a convergent solution.

The results, though they are plausible, reveal the drawbacks of the "geometrically exact" modeling of axisymmetric pile penetration starting from the ground surface. The

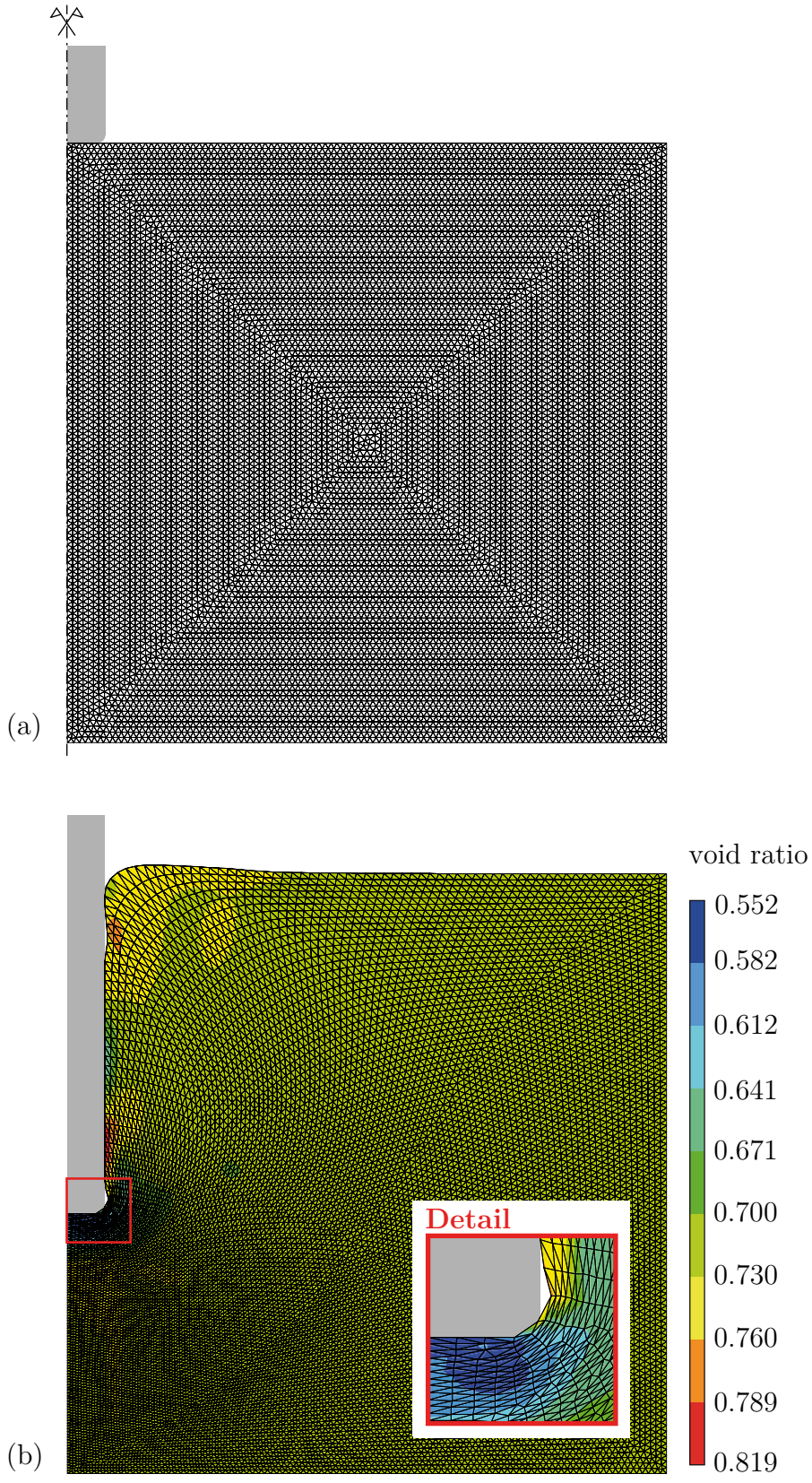

Figure 8.16: ALE simulation of penetration of a flat-ended pile into sand. (a) Problem statement and mesh, (b) predicted distribution of the void ratio overlaid by the deformed and smoothed mesh at a relative penetration depth of $z/D = 5.0$.

initially square computational domain is severely deformed by indentation, resulting in a drastic increase of the perimeter-to-area ratio. Elements at the elongated boundary are stretched, i.e. the density of nodes is reduced. On the other hand, the local reduction in height of the domain below the pile base comes along with squeezing of elements which has negative effects on finite element solution. Smoothing has indeed improved mesh quality in this example, but could not completely avoid element distortion because the mesh topology is fixed. To say it in the words of Mair [1999, p. 89], the mesh that defines the soil material underneath the pile "[...] cannot simply 'get out of the way' [...]", even if the soil material itself could. Unless the computational domain would be completely remeshed the numerical model must contain a larger "stockpile" of less deformed mesh in order to achieve a higher mesh quality. This, however, renders the present modeling technique inefficient.

8.6.2 Back-Calculation of PP-26-H Test

A class of finite element models for pile penetration problems which is entirely different from the previous one is established by the pilot-hole or zipper-type modeling technique. This technique was originally developed to limit mesh distortion in purely Lagrangian calculations and became widely-used, as indicated by the literature review in Chapter 2. In the axisymmetric models set up here (Fig. 8.17), the "pile" is designed as a segment of a rigid and perfectly smooth slideline supporting the soil in the direction normal to the slideline throughout the calculation. To put it more clearly, the slideline models the pile as well as a pilot hole of small diameter ($D/250$; pile diameter $D = 50\,\text{mm}$) guiding the pile as it moves downward the axis of penetration. A fillet line guarantees a smooth transition between the two line segments defining the pile and the pilot hole, respectively. The slideline and the pile of each finite element model are highlighted in Fig. 8.17 by the red line and light blue area, respectively.

The three numerical models used for the ALE back-calculation of the test PP-26-H only differ in the meshes defining the body of sand. The dimensions of the computational domain in all three models are $250\,\text{mm} \times 700\,\text{mm} = 5D \times 14D$, which complies with the configuration of the experimental test. One unstructured and two structured finite element meshes were generated (Fig. 8.17). The structured meshes are based on the cross-diagonal triangle pattern [Nagtegaal et al., 1974] and define different sizes of the elements. All three meshes are uniform, and the number of degrees of freedom is approximately 26 000 for the unstructured mesh and 30 000 resp. 65 000 for the structured meshes. The slideline is defined as the master of the surface-to-surface contact problem modeled, and its counterpart is formed by the left vertical boundary and the upper boundary (ground surface) of the mesh. For contact elements that are nearly or actually in contact, a Lagrange multiplier contact algorithm enforces zero penetration.

The prescribed boundary conditions are as follows. All nodes at the lower boundary of the mesh are fixed in vertical direction, and the nodes at the right vertical boundary are fixed in radial direction. A K_0 initial stress state within the sand is assumed in accordance with the shallow penetration test; see Section 8.5. The remaining initial

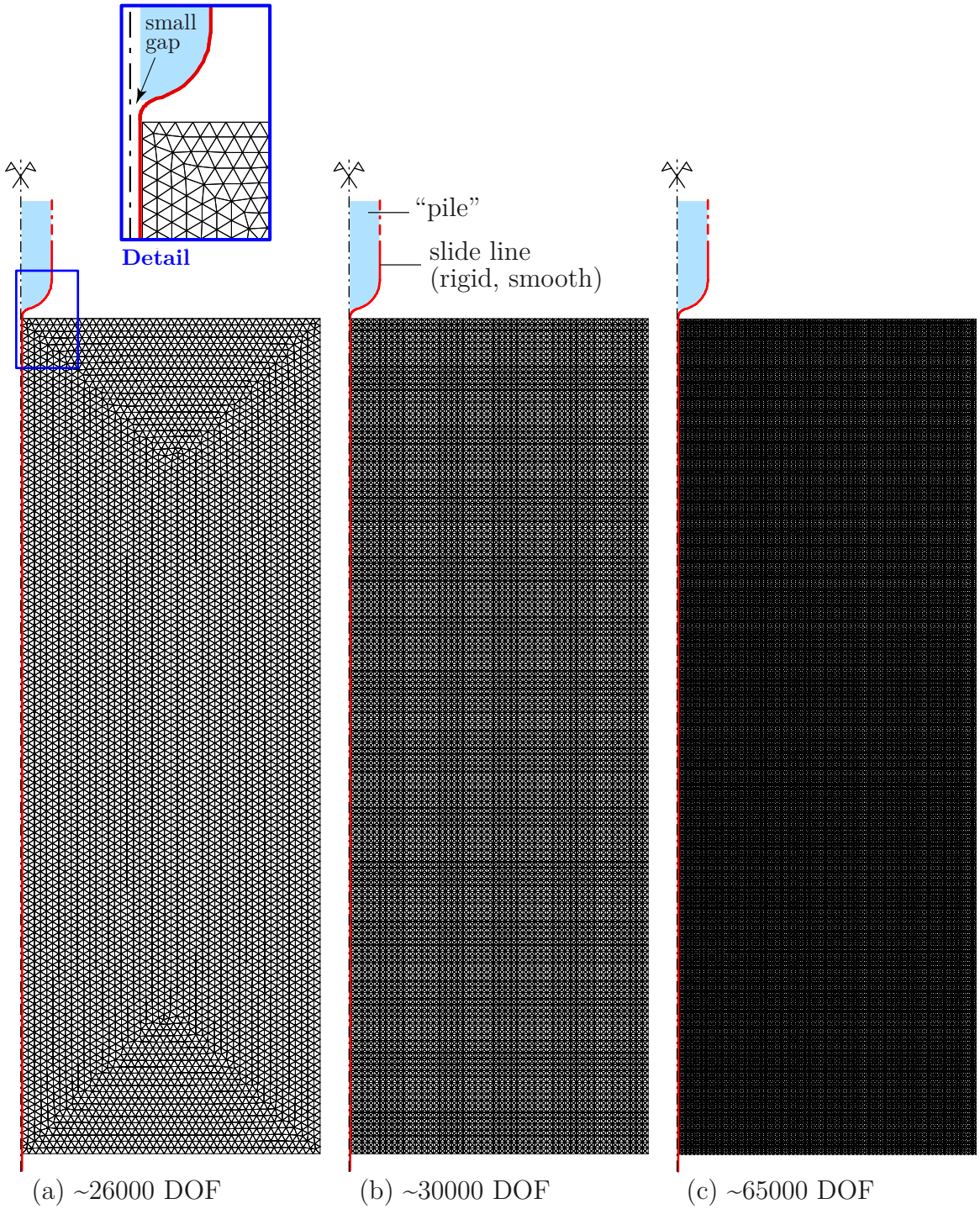

Figure 8.17: ALE simulation of pile penetration test PP-26-H. Problem statement and (a) initial unstructured coarse mesh, (b) initial structured coarse mesh, (c) initial structured fine mesh.

conditions are fitted to the experiment reported in Chapter 7. That is to say, the initial relative density of the sand is $D_{r0} = 34\,\%$ (initial void ratio $e_0 = 0.678$), and the penetration process starts at the unloaded ground surface and is displacement controlled. Again, artificial capillary pressure of 0.1 kPa was subtracted from the normal effective stress components during the integration of the hypoplastic rate constitutive equation in order to improve its stability at very low mean effective stress levels. The granulate hardness material constant for the test sand was chosen to $76.5\,\mathrm{MPa} = h_s/1000$ in all three numerical models, where h_s is the value of granulate hardness determined for a mean effective stress lying between 20 kPa and 2 MPa (cf. Section 4.3.3)

Numerical results of the succeeded ALE simulation on the structured fine mesh are plotted in Figs. 8.18 and 8.19. Results are plottet for the same three penetration depths that have been analyzed in the experimental test using particle image velocimetry (cf. Chapter 7 and Appendix D). As an example, consider the simulated distribution of the void ratio at different stages of the process (Fig. 8.18b). Recall that void ratio is a material state variable in the formulation of the hypoplastic model for sand, hence its spatial distribution is generally affected by advection during the ALE transport step. Also recall that the minimum and maximum void ratio of the test sand determined through laboratory tests are $e_{min} = 0.482$ and $e_{max} = 0.779$, respectively.

Fig. 8.18b indicates a significant densification of the sand immediately underneath the pile base at all stages of penetration. At a relative penetration depth of $z/D = 8.5$, the maximum relative density reaches $D_r = 68\,\%$. The hemispherical shape and the smooth skin of the pile prevents soil from being trapped in a core zone ahead of the pile base. The sand instead leaves the compression zone and continuously expands through shearing once the pile base has passed. As a consequence of this, the pile shaft is surrounded by a zone of severe loosening during the course of penetration. The zone of maximum loosening possesses a void ratio of about $e = 0.81 > e_{max}$ and is located between $0.5D$ and $1.0D$ below the ground surface irrespective of the penetration depth. Mahutka and Henke [2009, p. 482] observed a fairly comparable evolution of the void ratio in a purely Lagrangian simulation employing the same hypoplastic rate constitutive equation for sand.

The spatial distributions of the radial normal component σ^{11} and of the vertical normal component σ^{22} of the Cauchy stress are depicted in Figs. 8.19a and b, respectively. In the initial K_0-state, the stress components vary linearly from $\sigma^{11} = \sigma^{22} = 0\,\mathrm{kPa}$ at the ground surface, and $\sigma^{11} = -5.41\,\mathrm{kPa}$ and $\sigma^{22} = -10.82\,\mathrm{kPa}$ at the lower boundary of the model, with $K_0 = \sigma^{11}/\sigma^{22} = 0.5 = \text{const}$. It can be seen from Fig. 8.19 that the maximum compressive stress in the sand is concentrated in the immediate vicinity of the pile base and continuously increases with increasing penetration depth. With regard to the shown penetration depths, the increase in stress is approximately linear.

In Fig. 8.19, the radius of the bulb of isolines obtained for the vertical stress component is smaller than for the radial stress component, but the vertical stress bulb is larger in vertical direction. This corresponds to the simulation results of Sheng et al. [2005] plotted for $z/D = 8$. As a consequence, the value of the stress ratio σ^{11}/σ^{22} ahead of the pile base is smaller than in radial direction. Moreover, at the pile base the stress ratio is nearly stationary between $z/D = 1.4$ and 8.5, which also means that the shape

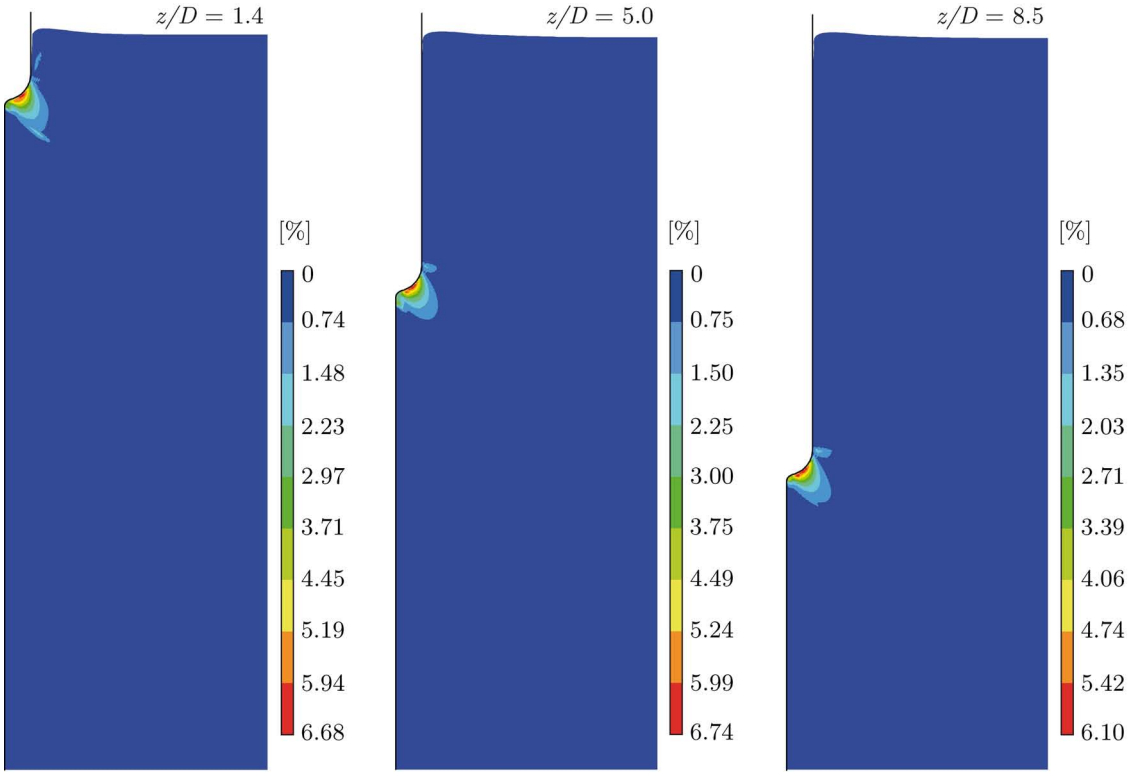

(a) incremental maximum shear strain

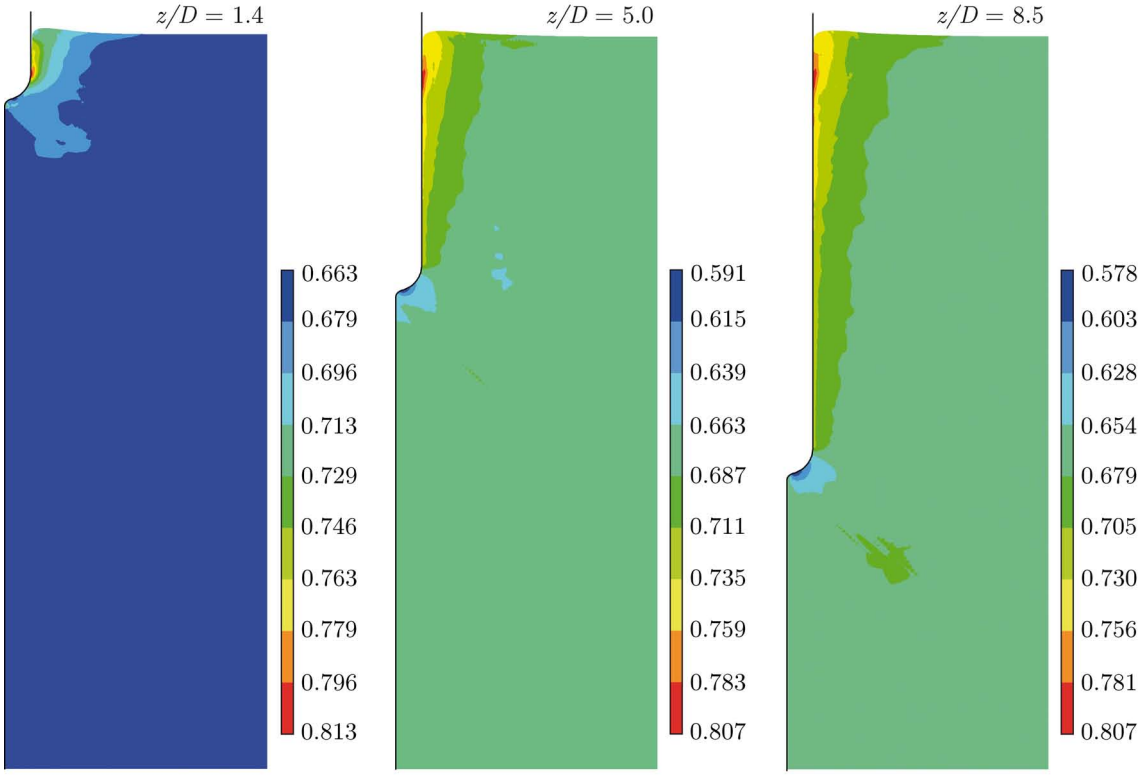

(b) void ratio ($e_0 = 0.678$)

Figure 8.18: ALE simulation of pile penetration test PP-26-H. Incremental maximum shear strain and void ratio distributions at different penetration depths.

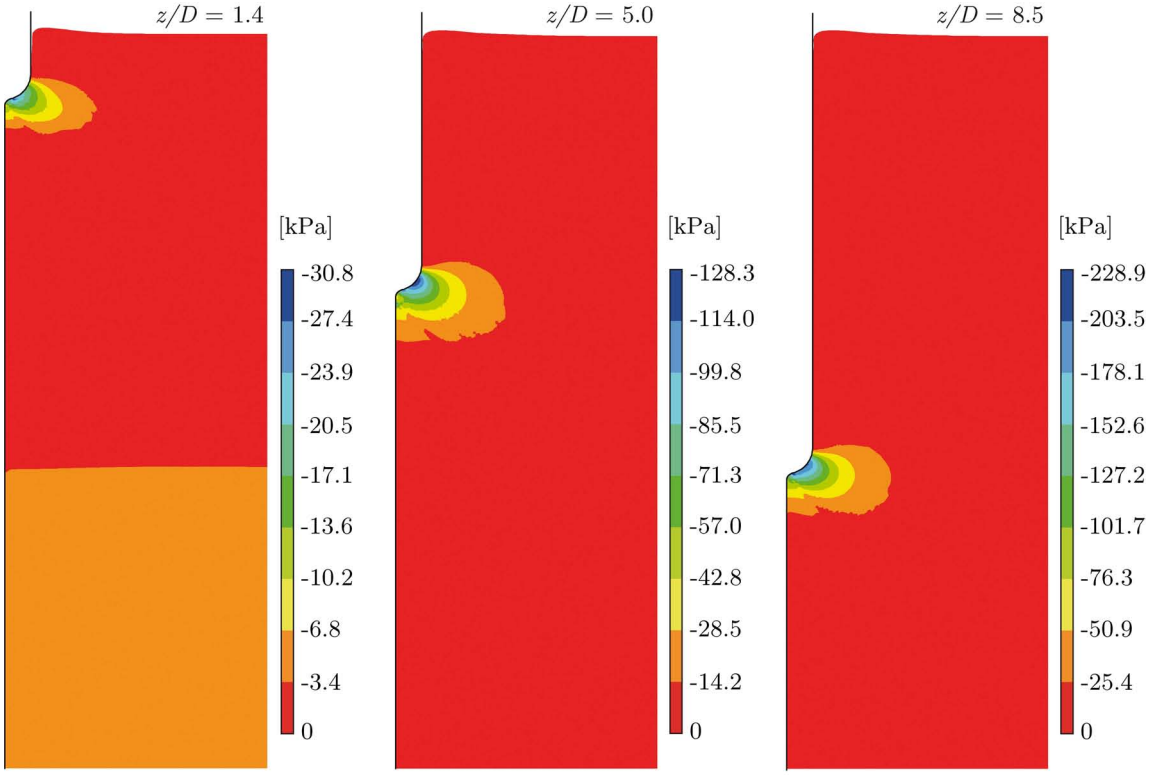

(a) radial normal stress component σ^{11}

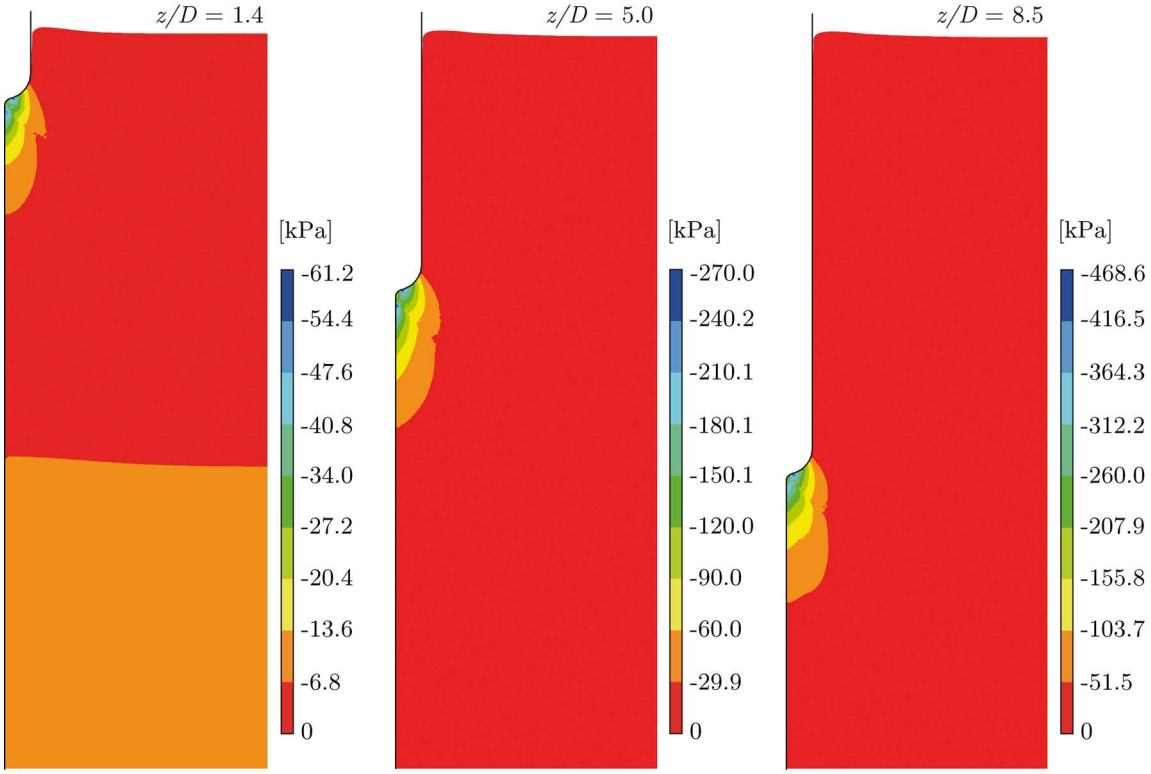

(b) vertical normal stress component σ^{22}

Figure 8.19: ALE simulation of pile penetration test PP-26-H. Vertical and radial stress distributions at different penetration depths.

of the isolines does not change very much. The color resolution in the figures is not sufficient to reveal the isolines for low stress levels. However, investigations carried out by the author indicate that during the penetration process, the magnitude of the vertical soil stress drops below its initial value in the observed cone of loosening around the pile shaft.

Results of the ALE simulation are now compared with results of the experimental test PP-26-H. Fig. 8.20 shows the measured and simulated incremental maximum shear strain at different penetration depths. The field obtained by PIV analysis of the images recorded during the experiment is on the left (cf. Figs. D.14), whereas the right hand side provides detailed views of Fig. 8.18a. Comparison is only qualitative because the plotted incremental strain fields resulted from different incremental displacement of the penetrator, which was $\Delta z_{\text{exp}} = 2.3\,\text{mm}$ in the test but only $\Delta z_{\text{num}} = 0.5\,\text{mm}$ in the numerical simulation.

At $z/D = 1.4$, the measured and the predicted ground heaving match very well. Moreover, in all three depth shown the ALE simulation reproduces the peak of incremental maximum shear strain located where the sand is flowing around the hemispherical pile tip. The small wedge-shaped dead zone formed underneath the pile base in the experiment, however, is not present in the back-calculation. Such a zone is a manifestation of arching effects and becomes even more apparent when the penetrator is flat and rough, like in the example of shallow penetration presented in Section 8.5. Hence, the comparison in Fig. 8.20 suggests that the assumption of a perfectly smooth surface of the pile tip in the numerical model does not correspond to reality.

The measured and predicted load-displacement curves of pile penetration test PP-26-H are in a reasonably good agreement (Fig. 8.21). However, the curves considerably differ in relative penetration depths of $z/D < 1$ and $z/D > 5$. The difference at small penetration depths is related to the undesired restraining forces in the experimental set-up not accounted for in the numerical model as well as to the problem of modeling the behavior of sand at very low effective stress levels. The latter has been discussed within the context of shallow penetration into sand (Section 8.5). In larger depths, the predicted load-displacement curves show a characteristic *zig-zag* form depending on the spatial approximation of the pile-soil contact interface. This problem is well-known, as reviewed in Chapter 2. For the unstructured coarse mesh, which corresponds to the worst interface discretizazion (cf. Figs 8.17a), the frequency of spurious oscillation is very low but its mean amplitude is the largest of all three meshes considered. The structured fine mesh, on the other hand, yields oscillations with the highest frequency and the smallest mean amplitude.

8.6.3 Back-Calculation of PP-28-C Test

The final application of the developed ALE method is a back-calculation of the pile penetration test PP-28-C. The finite element model is the same as in the previous section when using the structured coarse mesh (cf. Fig. 8.17b), except that the pile tip now has a conical shape and the initial void ratio of the sand is $e_0 = 0.718$ (initial

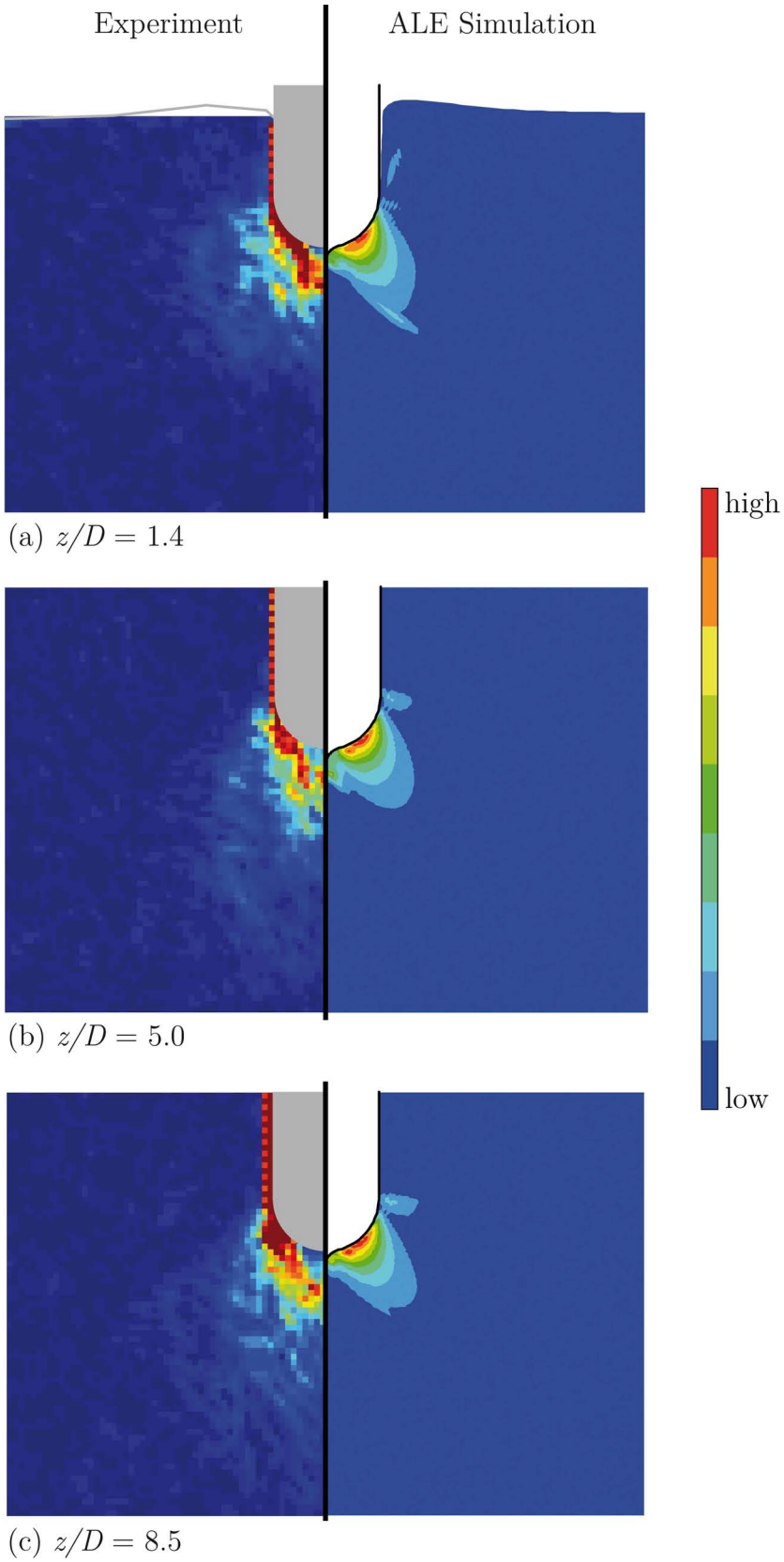

(a) $z/D = 1.4$

(b) $z/D = 5.0$

(c) $z/D = 8.5$

Figure 8.20: Comparison of the measured (left) and simulated (right) incremental maximum shear strain at different penetration depths during test PP-26-H.

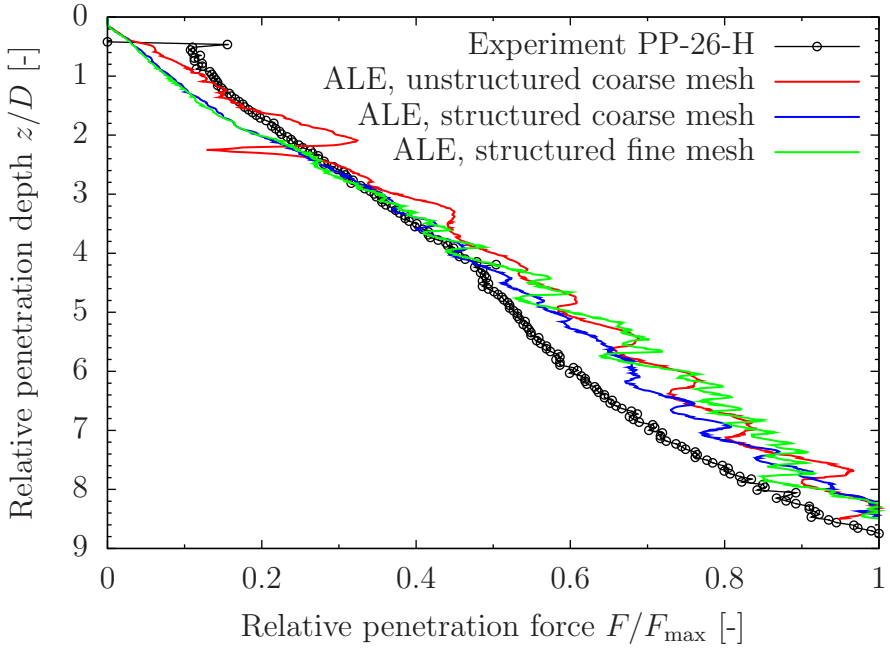

Figure 8.21: Comparison of the measured and predicted load-displacement curves of pile penetration test PP-26-H.

relative density $D_{r0} = 21\,\%$; cf. Tab. 7.3). The beneficial "dagger-like" geometry of the smooth pile in conjunction with the zipper-type modeling technique does not generate indented mesh regions with high curvature and prevents the soil from being excessively distorted along with penetration. This considerably improved stability and convergence of the solution. It might also enable the application of heuristic algorithms in the ALE mesh motion step. This, however, has not been investigated here.

The calculated incremental maximum shear strain and the void ratio distributions are depicted in Fig. 8.22a and b, respectively, for different penetration depths. The results indicate that the change from a hemispherical to a conical geometry of the tip leads to a different behavior of the void ratio in the vicinity of the penetrating pile. In contrast to the results for the PP-26-H test shown in Fig. 8.18b, the conical pile tip causes densification not only underneath the pile base but also along the lower part of the pile shaft (Fig. 8.22b). The radius of the densified zone in a relative penetration depth of $z/D = 8.5$ is larger than $5D$, the breadth of the computational model. Loosening of the sand occurs in a small triangular zone lateral to the pile at the ground surface.

Fig. 8.23 plots the relative load-displacement curves measured during the experiment and predicted by the ALE simulation, respectively. The agreement is fairly good, even though the simulated curve possesses spurious oscillation in larger depths, like in previous calculations (cf. Fig. 8.21). Due to this the zig-zag form only the first of the two inflection points at $z/D \approx 2.5$ and $z/D \approx 6$ in the measured load-displacement curve is reproduced by the back-calculation.

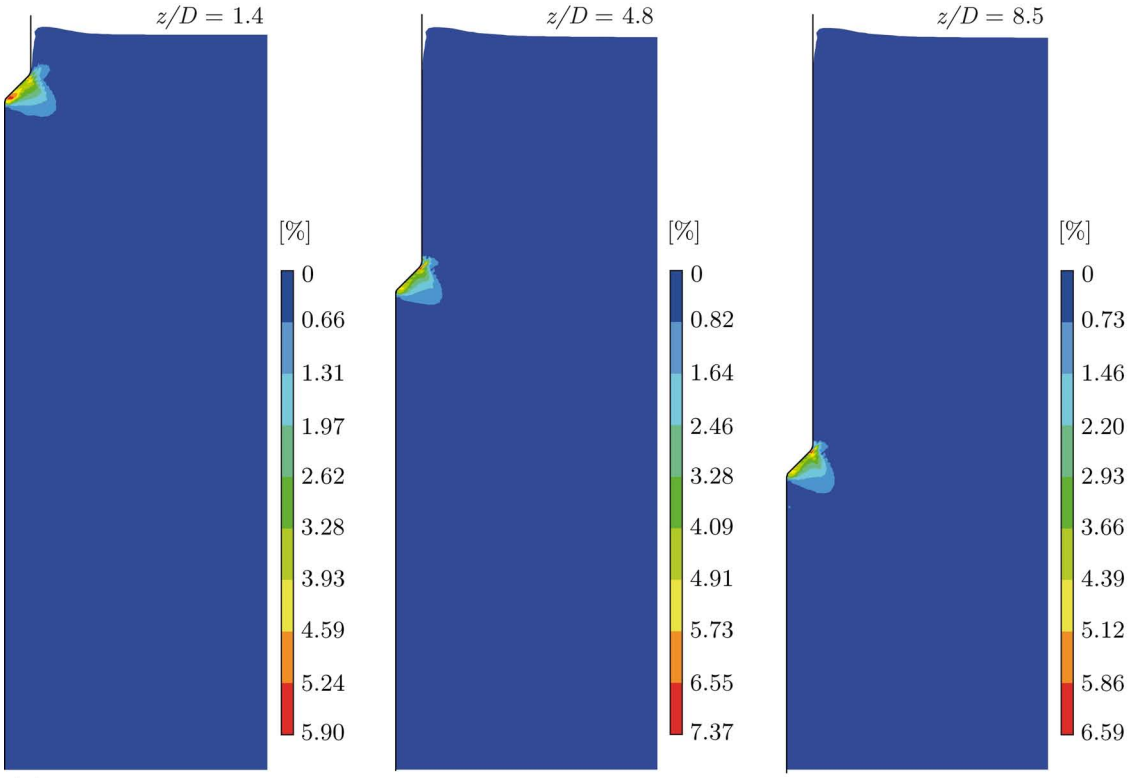

(a) incremental maximum shear strain

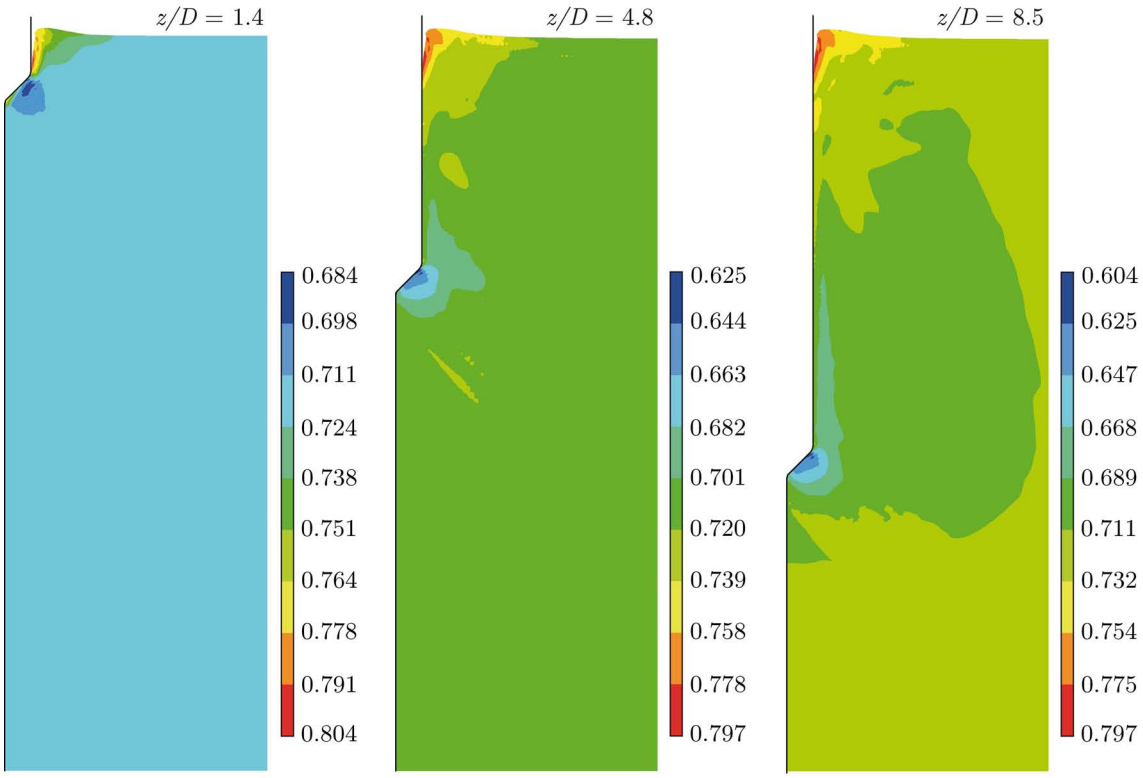

(b) void ratio ($e_0 = 0.718$)

Figure 8.22: ALE simulation of pile penetration test PP-28-C. Incremental maximum shear strain and void ratio distributions at different penetration depths.

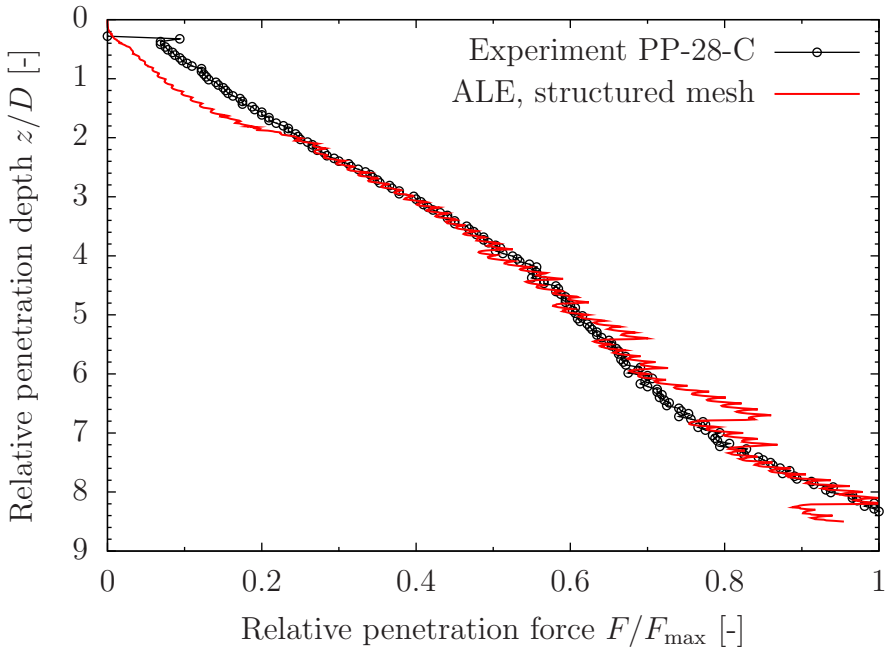

Figure 8.23: Comparison of the measured and predicted load-displacement curves of pile penetration test PP-28-C.

Chapter 9

Conclusions and Outlook

9.1 Conclusions

A comprehensive arbitrary Lagrangian-Eulerian framework for the numerical simulation of large deformation problems with special consideration of plane strain and axisymmetric quasi-static penetration into sand has been presented. The requisite fundamentals of continuum mechanics were derived *ab initio* based on a modern differential geometrical approach which has gained deeper insight into the Lagrangian, Eulerian, and ALE descriptions. Concerning the geometrical treatment of the continuum mechanical basis, the present work has partly ventured into uncharted scientific terrain. The overall operator-split ALE solution procedure that divides each solution increment into a Lagrangian step, a mesh motion step, and a transport step has enabled the straightforward upgrade of a Lagrangian finite element program. By using ANSYS® as an example, it has been shown that the limited number of user-programmable interfaces of proprietary codes is sufficient for successful implementation.

The class of ALE numerical methods has been advanced during the present work in the direction of soil mechanics and geotechnical engineering. More precisely, an implicit ALE method has been combined for the first time with an advanced hypoplastic rate constitutive equation which predicts the mechanical behavior of sand quite realistically. It is an incrementally nonlinear model that incorporates the stress, the void ratio, and a tensor-valued measure carrying information about the material history as internal state variables. Such complex constitutive equations are unusual in the traditional application areas of arbitrary Lagrangian-Eulerian codes (industrial forming processes, fluid-structure interaction, etc.). Moreover, an efficient optimization technique has been developed and implemented into the ALE method which smoothes out the non-convexly distorted mesh regions that occur along with penetration.

In the Lagrangian step of the method, the solution of the updated Lagrangian form of weak balance of momentum is advanced implicitly in time subject to prescribed boundary conditions, initial conditions, and contact constraints. 3-node triangles with 1-point integration (constant strain triangles) are used for the spatial discretization. The stress and the state variables of the hypoplastic rate constitutive equation for

sand, and those of the other material models that have also been implemented, are integrated over the time step by using a common incrementally objective algorithm. The integration algorithm takes into account finite deformation effects. Due to the non-Lagrangian view of material deformations the mass density constitutes an additional variable. Conservation of mass is not implicitly satisfied as in the Lagrangian methods, hence it must be solved as an additional governing equation. Unlike metals or many other materials for which density changes are negligible, the dilatancy of sand may cause significant density changes which have to be accounted for. The midpoint rule has been implemented to integrate the rate of mass density resp. the rate of the element Jacobian with a formal accuracy of second order on the element level during the Lagrangian step.

After the Lagrangian step, the finite element mesh is smoothed by node relocation at fixed mesh connectivity. This can be interpreted as mesh motion over a pseudo-time step. Mesh quality was intended to be improved solely based on geometric criteria. The mesh smoothing procedure operates locally in terms of the ball of elements enclosing a single node. It is initiated if the quality measure based on the triangle's radius ratio and skew drops below a certain value specified by the user. A globally smoothed mesh is pursued by loops repeatedly running over the nodes of elements that fail the quality check. To begin with, two heuristic smoothing algorithms reported in the literature have been implemented and tested. Although they are simple and fast, these methods are inapplicable if the meshed domain becomes non-convex with high curvature, e.g during penetration of a blunt body. Therefore, a third optimization-based algorithm has been developed during the course of the research presented. This extremely robust method, referred to as the OSMOT algorithm, works iteratively on a local level and delivers excellent results for both structured and unstructured triangle meshes over arbitrarily shaped domains.

In the final solution step, the stress components, the material state variables, and the mass density (resp. element Jacobian) are transported through the smoothed mesh by solving the advection problem that resulted from the operator-split. The integral conservation form of the advection equations is treated by the finite volume method, a numerical tool widely used in the field of computational fluid dynamics. The weighted donor-cell (Godunov-type) advection scheme which has been implemented into the ALE method for this purpose solves the Riemann problem associated with the piece-wise constant distribution of the variables in the finite volume mesh. Donor-cell advection has been chosen because it is the simplest transport algorithm which is both conservative and monotonicity-preserving. It is explicit in time and has a maximum accuracy of first order in space. The author is aware of the fact that first-order advection schemes tend to excessive numerical diffusion in comparison to second- and higher-order methods. However, many other ALE methods proposed in the literature even employ non-conservative interpolative techniques to remap the variables form the old onto the modified mesh. Moreover, most of the algorithms that integrate the rate constitutive equations in the Lagrangian step are also first-order accurate as it is the case in virtually all purely Lagrangian finite element methods published.

Experimental model tests concerned with the quasi-static penetration of model foundations and model piles into sand at different initial densities have been successfully

conducted. Based on the image sequences recorded during these tests, application of the particle image velocimetry method has enabled indirect measurement of the time histories of the incremental soil displacement. The increments of volumetric strain and shear strain have been subsequently derived from the discrete incremental displacement field by using the PIV software. Although PIV methods can reach a high accuracy of measurement if calibrated properly and performing an analysis of error, this option has been abandoned and attention has been given to qualitative analysis of the penetration processes. Despite the lack of a thorough quantification, the experimental model tests have revealed interesting details of the phenomenology related to penetration into sand. The test results have been successfully compared with results from the literature.

The numerical examples and back-calculations of selected experimental tests by using the self-developed ALE method has proven to be computationally intensive, although the numerical models had a moderate number of degrees of freedom ($< 70\,000$). Some pile penetration simulations took about one week on a workstation (CPU: 2x Dual-Core AMD Opteron 2222; RAM: 32 GB). This primarily arose from the strong nonlinearities inherent to the Lagrangian step and not from the mesh motion or transport steps of the ALE method. In most cases, the computational effort needed for mesh smoothing and advection was outbalanced by the implicit Lagrangian calculation because of the path-dependent material response (physical nonlinearity), finite deformation effects (geometrical nonlinearity), and contact constraints (nonlinearity due to boundary conditions) which required very small time steps with ten to hundreds of global equilibrium iterations per step. Purely Lagrangian calculations that did not utilize ALE capabilities slowed down or even terminated due to severe element distortion, as it was expected.

Generally speaking, the experimental results and the results obtained through ALE finite element simulations are in good agreement. Shear zones observed within the sand can be fairly reproduced. The measured and predicted load-displacement curves, however, differ considerably in depths of less than one and more than five times the diameter of the penetrator. It has been found that the difference at small penetration depths is closely related to the modeled material behavior resp. to the applied set of material constants. From the viewpoint of constitutive modeling, simulation of penetration into sand starting at the unloaded ground surface poses a great challenge. This is because at the unloaded ground surface next to the penetrator, the mean effective stress tends to zero so that the shear strength of a granular solid likewise vanishes. Under such conditions the shear parameters of a sand specimen can be hardly determined in geotechnical laboratory tests. As a result, it was possible to adjust the set of material constants of the hypoplastic rate constitutive equation such that either the load-displacement curve of the penetrator or the soil heaving matched the experimental results at small penetration depth, but not both.

At penetration depths larger than five times the pile diameter, on the other hand, the numerical model of the contact interface between the pile and the soil became more and more important and it strongly influenced the predicted load-displacement curves. In such large depths, the curves have a characteristic *zig-zag* form which is also reported in literature. This manifestation of spurious oscillation is governed by

the quality of geometry representation at the interfaces in the finite element model as well as by mesh coarseness and the contact algorithm applied in the discrete interface model. The more inaccurate the spatial approximation of the interface becomes the lower the frequency of spurious oscillation and the larger its mean amplitude under otherwise equal conditions will be.

During penetration into sand starting from the ground surface, the initially convex computational domain necessarily becomes indented resp. non-convex with high curvature because material boundaries are explicitly resolved by element edges. At drastic changes of the domain's shape due to large penetration distances mesh quality improvement by smoothing can only be achieved if there is a sufficiently large "stockpile" of less deformed mesh. This generally calls for numerical models in which the number of finite elements becoming additionally necessary increases disproportionately with the desired penetration distance. The pilot-hole resp. zipper-type modeling technique for the pile can reduce the size of the finite element model but it succeeds only if the pile tip geometry is sufficiently smooth and predominantly causes soil motion in normal direction to the pile axis. In other words, the zipper-type technique fails if flat-ended piles or blunt bodies penetrate a large distance.

Highlights

- Applied a modern differential geometrical approach to derive the fundamentals of continuum mechanics in the Lagrangian, Eulerian, and ALE descriptions.
- Developed an ALE method particularly suitable for plane strain and axisymmetric quasi-static penetration into sand.
- Developed an optimization-based mesh regularization algorithm which works excellent on unstructured and structured, convex and non-convex meshes.
- Implemented the ALE method into an existing Lagrangian finite element code by programming only a few user interfaces.
- Conducted experimental penetration tests in sand using particle image velocimetry to validate the ALE method.
- Unique features of the new ALE method are (i) the advanced hypoplastic rate constitutive equation for sand and (ii) the efficient and robust optimization-based mesh regularization algorithm.

9.2 Outlook

The assumptions and restrictions associated with the present work (cf. Chapter 1) give motivation to further research. For example, the incorporation of inertia effects in the developed ALE method is of great practical importance because displacement piles are usually driven by hammering or vibration. The inertia term that would be

present in the balance of momentum then will necessitate momentum transport across element boundaries. In contrast to the mass density, stress components, and history variables, which are stored at the integration points of the finite elements, the velocity components are stored at the nodes. Momentum transport in the ALE method would therefore require a different algorithm. Simulation of transient penetration in semi-infinite media by using a finite model also brings about the problem of wave reflection at the artificial boundaries, which needs to be resolved.

Further improvement of the presented ALE method would be the provision for surface roughness in the contact model at the soil-penetrator interface. This would introduce contact history variables that must be properly remapped onto the somehow smoothed mesh during the transport step of the method. It should be noted that tangential contact and roughness are of little importance in traditional ALE applications (e.g. hypervelocity impact, free surface flow), but they are omnipresent in soil mechanics and geotechnical engineering. Hence, further research into this topic would not be wasted effort.

Another relevant aspect of research in the area of soil mechanical ALE methods is the interaction of the solid phase with one or more pore fluids. Contrary to the assumptions inherent to the current method, sand *in situ* is rarely dry in its strict sense or fully saturated and locally drained. Therefore, many important phenomena cannot be reproduced. Taking into account the soil as a two-phase or even three-phase medium would enable a large deformation analysis of problems involving liquefaction-prone and/or partially saturated soils under cyclic loading, for example slopes and dams under earthquake excitation and driving of piles into saturated sand by vibration.

Since the operator-split ALE method designed for plane strain and axisymmetric penetration is based on a simplicial element type, it has a natural extension to three dimensions if the 3-node triangles are replaced by 4-node tetrahedra. The Lagrangian step of the overall ALE algorithm would basically remain unchanged by the 3d extension. The optimization algorithm running in the mesh motion step has a three dimensional analog, though exact evaluation of the gradient and Hessian of the related objective function would yield awfully lengthy expressions. The extension of the donor-cell algorithm in the transport step is trivial, but it probably would be too diffusive because the current multi-dimensional scheme only accounts for neighboring elements that share a facet and ignores any flux across edges and vertices. While in 2d, one half of the neighboring triangles are taken into account, there would be ten of fourteen neighbors left unconsidered in 3d tetrahedral meshes. Sufficient improvement might be achieved simply by replacing the spatially isotropic advection with one-dimensional, alternating advection sweeps carried out dimension by dimension.

Extension to non-simplicial and higher-order elements would generally require completely different algorithms in the mesh motion and transport steps. Higher-order or fully integrated elements are rarely used in ALE methods. Most methods advance solution explicitly in time, for which reduced integration with hourglass control is the proven technology on the element level. Concerning the mesh motion step, it would be difficult to construct a local smoothing procedure for unstructured meshes, like the present optimization-based scheme, which properly accounts for the nodes lying inside

an edge or a facet. In the transport step, the finite volume scheme that has been implemented assumes a piecewise constant distribution of the variables in each control volume. For variables stored at the Gauss points (quadrature points) of the finite element mesh, a control volume is represented by the influence domain of a single Gauss point. Higher-order elements would then require element subdivision in order to take multiple quadrature points into account. A cheaper but probably inadequate approach would be to relocate only the corner nodes in the mesh motion step and to interpolate the midside and interior nodes of each affected element. In the transport step, computational cost can be reduced by abandoning element subdivision and computing an element average of the Gauss point values.

None of the previous improvements and extensions of the current simplified arbitrary Lagrangian-Eulerian (SALE) method compares to the complexity associated with the change to a multi-material ALE (MMALE) approach. However, the present work suggests that such an extension would be worthwhile. Although the numerical examples have proven the general applicability of the ALE method to problems of deep penetration into sand starting at the ground surface, they have also pointed out the shortcomings of the SALE approach. It turned out that the simplified approach cannot completely avoid mesh distortion because mesh motion is almost Lagrangian, so SALE methods can handle only a few problems more than purely Lagrangian methods. In MMALE methods on the other hand, elements potentially contain two or more materials because material boundaries are allowed to flow across element edges. Most of the increase in complexity and computational cost is related to the continuum mechanical and numerical treatment of these multi-material elements: mixture theory, closure models, material interface tracking, etc. Since typical MMALE methods apply an incremental operator-split solution approach as well, the SALE method that has been developed in the present work forms an excellent basis for subsequent research going in this direction.

The range of problems that MMALE methods will compute makes them particularly attractive for soil mechanical and geotechnical applications involving large deformations and post-failure behavior, e.g. slope stability, landslide, phase transition phenomena and liquefaction, penetration, soil mixing, water jetting, and grouting. All existing codes possessing multi-material capabilities, however, address other classes of problems and do not adequately model the complex soil behavior under low-velocity monotonic and cyclic loads, possibly with pore water coupling. Therefore, a geomechanical MMALE method would currently be unique on a national as well as international scale.

A P P E N D I X

(This page intentionally left blank)

Appendix A

Mathematical Prerequisites

Central to the problems in soil mechanics and geotechnical engineering are the soil stress and density distributions. The availability of stress and density fields is closely related to the continuum assumption, and the tensorial nature of stress additionally requires the continuum to have a differentiable structure. Systematically, the notion of a differentiable continuum is part of the mathematic branch of differential geometry [Abraham et al., 1983; Bishop and Goldberg, 1968; Spivak, 1965, 1999; Synge and Schild, 1978; Misner et al., 1973; Raschewski, 1995]. Therefore, it seems to be advantageous to analyze and to discuss the topics of soil continuum mechanics by applying the geometric terminology. Although most authors use the well-known Euclidian three-dimensional space $\mathbb{R}^3$ as a background [e.g. Truesdell and Toupin, 1960; Truesdell and Noll, 2004; Ciarlet, 1988], differential geometry on manifolds has been found to be the most natural way in formulating continuum mechanics [e.g. Kondo, 1955–1968; Marsden and Hughes, 1994; Abraham et al., 1983; Romano and Baretta, 2009; Aubram, 2009; Segev, 2013].

The following appendix should briefly introduce the topics of differential geometry needed for the continuum mechanics on manifolds presented in Chapter 3. Linear geometry, Banach spaces, differential calculus, and basic numerical methods frequently used in computational mechanics are reviewed first. More details on tensor analysis and differential geometry can be found in the cited literature.

The *Einstein summation convention* [Einstein, 1916] is forced in the present thesis. By this convention, the sum is taken over all possible values of a coordinate index variable whenever it appears twice, and as both a subscript and a superscript, in a single term. For example, the local representative of a vector $\boldsymbol{v}$ with respect to a basis $\{\boldsymbol{g}_1, \dots, \boldsymbol{g}_n\}$ reads

$$\boldsymbol{v} = \sum_{i=1}^{n} v^i \boldsymbol{g}_i \stackrel{\text{def}}{=} v^i \boldsymbol{g}_i \,. \tag{A.0.1}$$

The summation convention is also adopted in the context of finite element interpolation outlined in Chapter 5. If summation should be inhibited, this will be explicitly stated.

A.1 Vector Spaces and Affine Point Spaces

A.1.1 Vector Spaces

A set $\mathcal{V} \stackrel{\text{def}}{=} \{\boldsymbol{u}, \boldsymbol{v}, \ldots\}$ together with an addition $(\boldsymbol{u}, \boldsymbol{v}) \mapsto \boldsymbol{u} + \boldsymbol{v} = \boldsymbol{v} + \boldsymbol{u}$ and a scalar multiplication $(\lambda, \boldsymbol{u}) \mapsto \lambda\boldsymbol{u} = \boldsymbol{u}\lambda$ for all $\lambda \in \mathbb{R}$, is called a *real vector space*, and the elements of $\mathcal{V}$ are called *vectors*. The co-vector space $\mathcal{V}^*$ dual to $\mathcal{V}$ comprehends the *linear forms* $\boldsymbol{a}^* : \mathcal{V} \to \mathbb{R}$, $\boldsymbol{v} \mapsto \boldsymbol{a}^*(\boldsymbol{v}) \stackrel{\text{def}}{=} \boldsymbol{a}^* \cdot \boldsymbol{v}$ that, when applied to a vector, will yield a real number.

An *inner product* on the vector space $\mathcal{V}$ is defined through $\langle \boldsymbol{a}, \boldsymbol{b} \rangle = \langle \boldsymbol{b}, \boldsymbol{a} \rangle \in \mathbb{R}_+$, with $\boldsymbol{u}, \boldsymbol{v} \in \mathcal{V}$, making $\mathcal{V}$ resp. the pair $(\mathcal{V}, \langle \cdot \rangle)$ to an *inner product space* or *Euclidian vector space*. Inner product spaces are special *normed spaces* . A normed space is a vector space $\mathcal{V}$ together with a *norm* $\| \cdot \| : \mathcal{V} \to \mathbb{R}$ that has the following properties: 1. $\|\boldsymbol{v}\| \geq 0$ for all $\boldsymbol{v} \in \mathcal{V}$, and $\|\boldsymbol{v}\| = 0$ if and only if $\|\boldsymbol{v}\| = \boldsymbol{0}$ (positive definiteness), 2. $\|\lambda\boldsymbol{v}\| = |\lambda| \, \|\boldsymbol{v}\|$ for all $\boldsymbol{v} \in \mathcal{V}$ and $\lambda \in \mathbb{R}$ (homogeneity), 3. $\|\boldsymbol{u} + \boldsymbol{v}\| \leq \|\boldsymbol{u}\| + \|\boldsymbol{v}\|$ for all $\boldsymbol{u}, \boldsymbol{v} \in \mathcal{V}$ (triangle inequality). In inner product spaces, the norm can be defined through $\|\boldsymbol{v}\| \stackrel{\text{def}}{=} \sqrt{\langle \boldsymbol{v}, \boldsymbol{v} \rangle}$, the *Euclidian norm*.

Considering the hierarchy of generality, it should be mentioned that normed spaces require a *metric* $d : \mathcal{V} \times \mathcal{V} \to \mathbb{R}$ on the set $\mathcal{V}$. The metric can be defined through $d(\boldsymbol{u}, \boldsymbol{v}) \stackrel{\text{def}}{=} \|\boldsymbol{u} - \boldsymbol{v}\|$, making the pair $(\mathcal{V}, d)$ to a *metric space*; this concept will be generalized in Section A.4.

Remark A.1.1. The given definition of a vector space is general enough to include, as a special case, the vector spaces of real functions $\mathcal{F}(t) \stackrel{\text{def}}{=} \{f(t), g(t), \ldots\}$ over a set $\mathcal{T}$, where $t \in \mathcal{T}$. For the functions $f, g, \ldots$ of this *function space*, the vector space operations are defined pointwise, that is, $f + g \stackrel{\text{def}}{=} (f + g)(t) = f(t) + g(t)$, for all $t \in \mathcal{T}$, and $\lambda\, f \stackrel{\text{def}}{=} (\lambda\, f)(t) = \lambda\, f(t)$, for all $t \in \mathcal{T}$ and $\lambda \in \mathbb{R}$. △

Let n be the *dimension* of $\mathcal{V} \stackrel{\text{def}}{=} \mathcal{V}_n$, then a *basis of* $\mathcal{V}$ is the set $\{\boldsymbol{g}_1, \boldsymbol{g}_2, \ldots, \boldsymbol{g}_n\}$ of linearly independent vectors $\boldsymbol{g}_i$, with $i \in \{1, \ldots, n\}$. By abuse of notation, $\{\boldsymbol{g}_i\} \in \mathcal{V}$ is written if $\{\boldsymbol{g}_1, \boldsymbol{g}_2, \ldots, \boldsymbol{g}_n\}$ is a basis of $\mathcal{V}$. Provided such a basis is given, then every vector $\boldsymbol{v} \in \mathcal{V}$ can be represented by

$$\boldsymbol{v} = v^1 \boldsymbol{g}_1 + v^2 \boldsymbol{g}_2 + \ldots + v^n \boldsymbol{g}_n = v^i \boldsymbol{g}_i \,, \tag{A.1.2}$$

in which the components of $\boldsymbol{v} \neq \boldsymbol{0}$ with respect to the basis $\{\boldsymbol{g}_i\}$, i.e. $v^1, v^2, \ldots, v^n \in \mathbb{R}$, are not all zero. Note that duality of the spaces $\mathcal{V}$ and $\mathcal{V}^*$ requires that $\boldsymbol{g}^i \cdot \boldsymbol{g}_j = \delta^i{}_j$, where $\{\boldsymbol{g}^i\}$ is the *dual basis*, and $\delta^i{}_j$ is the *Kronecker delta*. Accordingly, the component of $\boldsymbol{v}$ with respect to $\boldsymbol{g}_i$ can be calculated from $\boldsymbol{g}^i \cdot \boldsymbol{v} = v^i$, and a linear form $\boldsymbol{a}^* \in \mathcal{V}^*$ has the local representative $\boldsymbol{a}^* = a_i \boldsymbol{g}^i$.

Let $\mathcal{V}$ be an n-dimensional Euclidian vector space and $\mathcal{V}^*$ its dual space, and let the *metric coefficients* be defined through $g_{ij} \stackrel{\text{def}}{=} \langle \boldsymbol{g}_i, \boldsymbol{g}_j \rangle \geq 0$. Then one is allowed to set $\boldsymbol{g}_i = g_{ij} \boldsymbol{g}^j$, and to write

$$\boldsymbol{a}^* \cdot \boldsymbol{b} = a_i b^j \, \boldsymbol{g}^i \cdot \boldsymbol{g}_j = a_i b^j \delta^i{}_j = a_i b^i = g_{ij} a^i b^j = a^i b^j \langle \boldsymbol{g}_i, \boldsymbol{g}_j \rangle = \langle \boldsymbol{a}, \boldsymbol{b} \rangle \,, \tag{A.1.3}$$

where $a_i = g_{ij}\, a^j$. The linear form $\boldsymbol{a}^*$ and the vector $\boldsymbol{a}$ thus correspond by so-called *index-lowering* resp. *index-raising* operations. Note that in n-dimensional Euclidian vector spaces there exists a basis $\{\boldsymbol{e}_a\}$ with

$$\langle \boldsymbol{e}_a, \boldsymbol{e}_b \rangle = \delta_{ab}\,, \qquad \text{for every } a, b \in \{1, \ldots, n\}\,, \tag{A.1.4}$$

so that the index-lowering resp. index-raising operations become trivial, viz. $\boldsymbol{e}_a = \delta_{ab}\boldsymbol{e}^b = \delta^a{}_b\boldsymbol{e}^b = \boldsymbol{e}^a$. Such a vector basis is then called *ortho-normalized*. δ_{ab} is the *Kronecker delta*

From linear algebra, it is well known that the set of ordered *n-tuples* (which are also called $(n \times 1)$-*matrices* or *columns*),

$$\mathbb{R}^n \stackrel{\text{def}}{=} \{\boldsymbol{u} = \begin{pmatrix} u^1 \\ \vdots \\ u^n \end{pmatrix} \mid u^1, \ldots, u^n \in \mathbb{R}\}\,, \tag{A.1.5}$$

forms an n-dimensional Euclidian vector space. An ortho-normalized basis $\{\boldsymbol{e}_a\} \in \mathbb{R}^n$ with

$$\begin{pmatrix} 1 \\ 0 \\ \vdots \\ 0 \end{pmatrix} \stackrel{\text{def}}{=} \boldsymbol{e}_1, \quad \begin{pmatrix} 0 \\ 1 \\ \vdots \\ 0 \end{pmatrix} \stackrel{\text{def}}{=} \boldsymbol{e}_2, \quad \ldots, \quad \begin{pmatrix} 0 \\ 0 \\ \vdots \\ 1 \end{pmatrix} \stackrel{\text{def}}{=} \boldsymbol{e}_n \quad \in \mathbb{R}^n \tag{A.1.6}$$

is referred to as the *canonical* or *standard basis* in $\mathbb{R}^n$. It follows from (A.1.2) that the local representative of n-tuples is just $\boldsymbol{u} = u^a\boldsymbol{e}_a \in \mathbb{R}^n$. The inner product on $\mathbb{R}^n$, $\langle \boldsymbol{u}, \boldsymbol{v} \rangle = \delta_{ab}u^a v^b$, where $\boldsymbol{u}, \boldsymbol{v} \in \mathbb{R}^n$ and $1 \leq a, b \leq n$, is called the *standard inner product*. Index placement in $\mathbb{R}^n$ is of no relevance because of (A.1.4).

A.1.2 Linear Transformations and Matrix Representation

A *linear transformation* $\boldsymbol{A} : \mathcal{V} \to \mathcal{W}$ (also called a *linear map* or *homomorphism*) maps a vector $\boldsymbol{v} \in \mathcal{V}$ onto $\boldsymbol{A}\boldsymbol{v} \stackrel{\text{def}}{=} \boldsymbol{A}(\boldsymbol{v}) \in \mathcal{W}$. If $\boldsymbol{A}$ is an *isomorphism*, it has an *inverse* $\boldsymbol{A}^{-1}$. Linear transformations $\boldsymbol{A} : \mathcal{V} \to \mathcal{V}$ are called *endomorphisms*, and isomorphisms with $\mathcal{V}{=}\mathcal{W}$ are called *automorphisms*. The *identity map* $\boldsymbol{I}$ *on* $\mathcal{V}$ is defined through $\boldsymbol{I}\boldsymbol{v} = \boldsymbol{v}$, $\forall \boldsymbol{v} \in \mathcal{V}$, and $\boldsymbol{I} = \boldsymbol{A}^{-1}\boldsymbol{A} = \boldsymbol{A}\boldsymbol{A}^{-1}$ provided that $\boldsymbol{A}$ is an automorphism on $\mathcal{V}$. A linear transformation $\boldsymbol{A} : \mathcal{V} \to \mathcal{W}$ is called a *linear form* if $\mathcal{W} = \mathbb{R}$; in this case one writes $\boldsymbol{A}(\boldsymbol{v}) \stackrel{\text{def}}{=} \boldsymbol{a}^* \cdot \boldsymbol{v}$.

By (A.1.2), every linear transformation has a local representative. For example, let $\{\boldsymbol{g}_i\} \in \mathcal{V}$ and $\{\boldsymbol{h}_\alpha\} \in \mathcal{W}$ be vector bases, then the linear transformation $\boldsymbol{A} : \mathcal{V} \to \mathcal{W}$ can be expressed by

$$\boldsymbol{A}\boldsymbol{g}_i = A^\alpha{}_i \boldsymbol{h}_\alpha \tag{A.1.7}$$

with respect to $\{\boldsymbol{g}_i\}$ and $\{\boldsymbol{h}_\alpha\}$. Note that the basis vectors $\boldsymbol{h}_\alpha$ themselves have an expression in the basis $\{\boldsymbol{g}_i\}$ by (A.1.2), hence the right hand side of (A.1.7) also has.

Every linear transformation has a matrix representation. The unique *matrix* $(A^\alpha{}_i)|_{\boldsymbol{g}_i, \boldsymbol{h}_\alpha}$ *of a linear transformation* $\boldsymbol{A} : \mathcal{V}_n \to \mathcal{W}_m$ *with respect to the bases* $\{\boldsymbol{g}_i\} \in \mathcal{V}_n$ *and*

$\{\boldsymbol{h}_\alpha\} \in \mathcal{W}_m$ is obtained through the matrix arrangement of the $(m \times n)$ numbers $A^\alpha{}_i$ of its local representative (A.1.7) with respect to that bases:

$$(A^\alpha{}_i)|_{\boldsymbol{g}_i,\boldsymbol{h}_\alpha} \stackrel{\text{def}}{=} \begin{pmatrix} A^1{}_1 & \dots & A^1{}_n \\ \vdots & \ddots & \vdots \\ A^m{}_1 & \dots & A^m{}_n \end{pmatrix}_{|\boldsymbol{g}_i,\boldsymbol{h}_\alpha} \in \mathbb{R}^{m\times n}\,. \tag{A.1.8}$$

As usual in matrix calculus, the first index is taken as the *row index*, and the second index is the *column index*, and the transpose of a matrix is obtained by interchanging the indices. Provided that the bases are set, a linear transformation can be identified with its matrix with respect to that bases. The matrix representation in (A.1.8) is regarded as a map $(A^\alpha{}_i)|_{\boldsymbol{g}_i,\boldsymbol{h}_\alpha} : \mathbb{R}^n \to \mathbb{R}^m$, where $\mathbb{R}^n$ resp. $\mathbb{R}^m$ denote the sets of columns that have n resp. m elements. Conversely, any matrix $(A^a{}_b) \in \mathbb{R}^{m\times n}$ represents a linear transformation $\boldsymbol{A} : \mathbb{R}^n \to \mathbb{R}^m$.

The matrix of the identity map $\boldsymbol{I} : \mathcal{V} \to \mathcal{V}$, with $\boldsymbol{I}\boldsymbol{g}_i \stackrel{\text{def}}{=} B^{i'}_i \boldsymbol{g}_{i'}$, is the *inverse matrix of the change of basis*. That is to say, $(B^{i'}_i)^{-1} \stackrel{\text{def}}{=} (B^i_{i'})$ arranges the components of the change of basis: $\boldsymbol{g}_{i'} = B^i{}_{i'}\boldsymbol{g}_i$. Then $\boldsymbol{I}\boldsymbol{g}_j = \delta^i{}_j \boldsymbol{g}_i$ follows immediately. Now since every vector $\boldsymbol{v} = v^i\boldsymbol{g}_i = v^{i'}\boldsymbol{g}_{i'} = \boldsymbol{I}\boldsymbol{v}$ is independent of the basis by definition, a change of basis transforms the components of $\boldsymbol{v}$ according to the fundamental *tensorial transformation rule*

$$v^{i'} = B^{i'}_i\, v^i\,. \tag{A.1.9}$$

In Euclidian vector spaces $\mathcal{V}$ and $\mathcal{W}$, a map $\boldsymbol{A} : \mathcal{V} \to \mathcal{W}$ is called an *isometry* provided that

$$\langle \boldsymbol{A}\boldsymbol{a}, \boldsymbol{A}\boldsymbol{b}\rangle_{\mathcal{W}} = \langle \boldsymbol{a}, \boldsymbol{b}\rangle_{\mathcal{V}}\,, \tag{A.1.10}$$

for all $\boldsymbol{a}, \boldsymbol{b} \in \mathcal{V}$. An isometry $\boldsymbol{A} : \mathcal{V} \to \mathcal{V}$ is called an *orthogonal map*, having the properties $\det \boldsymbol{A} = \pm 1$ and $\boldsymbol{A}^{-1} = \boldsymbol{A}^{\mathrm{T}}$. If a linear transformation is orthogonal, then its matrix with respect to an ortho-normalized basis also is.

A.1.3 Point Spaces and Coordinates

Points do not exist in abstract vector spaces. In continuum mechanics, however, vectors attached to points are chief ingredients, so the *affine point spaces* need to be defined. A more general version of these spaces are the differentiable manifolds introduced later.

Definition A.1.11. An *affine point space* $(\mathcal{S}, \mathcal{V})$, or just $\mathcal{S}$ if the meaning is clear from the context, consists of a set of points $\mathcal{S} \stackrel{\text{def}}{=} \{A, B, C, \dots\}$, a vector space $\mathcal{V}$, and a map $\mathcal{S} \times \mathcal{S} \to \mathcal{V}$. Moreover, the following two axioms must hold: 1. For every $A \in \mathcal{S}$ and every $\boldsymbol{v} \in \mathcal{V}$ there is a unique $A + \boldsymbol{v} = B \in \mathcal{S}$, so that $\boldsymbol{v} = \overrightarrow{AB}$. 2. If $\overrightarrow{AB} = \overrightarrow{CD}$, then $\overrightarrow{AC} = \overrightarrow{BD}$. ♢

The second claim is known as the parallelogram axiom. This axiom is equivalent in saying that $\boldsymbol{v}(A) = \boldsymbol{v}(C)$ resp. $(A, \boldsymbol{v}) = (C, \boldsymbol{v}) \in (\mathcal{S}, \mathcal{V})$, proving that affine point spaces are *flat*.

If the vector space $\mathcal{V}$ is Euclidian, an affine point space $(\mathcal{S}, \mathcal{V})$ is called a *Euclidian point space*. In Euclidian point spaces, the *distance of the points* $P, Q \in \mathcal{S}$ is defined through the metric $d(P,Q) \stackrel{\text{def}}{=} \sqrt{\langle \boldsymbol{v}, \boldsymbol{v} \rangle} = \|\boldsymbol{v}\|$, where $\boldsymbol{v} = \overrightarrow{PQ}$.

Definition A.1.12. A *frame of reference* $(O, \boldsymbol{g}_1, \boldsymbol{g}_2, \ldots, \boldsymbol{g}_{n_{\text{dim}}}) \stackrel{\text{def}}{=} (O, \boldsymbol{g}_i)$ in an affine point space $(\mathcal{S}, \mathcal{V})$ is a vector basis $\{\boldsymbol{g}_i\} \in \mathcal{V}$ attached to a point $O \in \mathcal{S}$. Every point $P \in \mathcal{S}$ has a *position vector* $\boldsymbol{x} \stackrel{\text{def}}{=} \overrightarrow{OP} \in \mathcal{V}$ with respect to the frame $(O, \boldsymbol{g}_i)$. Since $\boldsymbol{x}$ emanates from $O \in \mathcal{S}$ and not from any other point, the position vector is properly denoted by the pair

$$(O, \boldsymbol{x}) = (O, \overrightarrow{OP}) \stackrel{\text{def}}{=} \boldsymbol{x}_O \stackrel{\text{def}}{=} \boldsymbol{x}(O) \qquad \in \mathcal{S} \times \mathcal{V} \,.$$

Note that $\overrightarrow{OP}$ would be an ordinary vector if it is viewed from another frame $(O', \boldsymbol{g}_{i'})$, hence the base point is important for distinction in affine point spaces. The local representative of $\boldsymbol{x}_O$, with $\boldsymbol{x} = x^i(P)\, \boldsymbol{g}_i$, gives the *affine coordinates* $\{x^1, x^2, \ldots, x^{n_{\text{dim}}}\}_P \stackrel{\text{def}}{=} \{x^i\}_P$ of P in the frame $(O, \boldsymbol{g}_i)$. For any frame given, every P can be identified with the n_{dim}-tuple of its coordinates with respect to that frame. The totality of affine coordinates is called the *affine coordinate system* $(\mathcal{S}, x)$ and defines a global chart for $\mathcal{S}$. Continuity and smoothness of the coordinate system is closely related to the continuity and smoothness of the coordinate lines x^i embedded in $\mathbb{R}^{n_{\text{dim}}}$. ♢

In Euclidian point spaces $(\mathcal{S}, \mathcal{V})$, a special frame of reference can be constructed from an ortho-normalized basis $\{\boldsymbol{e}_a\} \in \mathcal{V}$. The local representative $\overrightarrow{OP} = z^a(P)\, \boldsymbol{e}_a$ of the position vector of $P \in \mathcal{S}$ with respect to the frame $(O, \boldsymbol{e}_a)$ gives the so-called *Cartesian coordinates* $\{z^1, \ldots, z^{n_{\text{dim}}}\}_P \stackrel{\text{def}}{=} \{z^a\}_P$ of P in that frame. The totality of Cartesian coordinates in $\mathcal{S}$ is called a *Cartesian coordinate system*. In a Cartesian coordinate system with fixed frame $(O, \boldsymbol{e}_a)$, points can be globally identified with their coordinate n_{dim}-tuple $(z^1, \ldots, z^{n_{\text{dim}}})$. Therefore, Euclidian point spaces are often denoted by $(\mathbb{R}^{n_{\text{dim}}}, \mathbb{R}^{n_{\text{dim}}})$, $\mathcal{S} = \mathbb{R}^{n_{\text{dim}}}$, or just $\mathbb{R}^{n_{\text{dim}}}$. The global Cartesian coordinate system (global chart) is denoted by $(\mathcal{S}, z = \text{id})$ or $(\mathbb{R}^{n_{\text{dim}}}, \text{id})$.

Let $(\mathcal{S}, x)$ and $(\mathcal{S}, x')$ be affine coordinate systems associated with the two frames $(O, \boldsymbol{g}_i)$ and $(O', \boldsymbol{g}_{i'})$ in $\mathcal{S}$, respectively. Then under a *change of framing* $(O, \boldsymbol{g}_i) \mapsto (O', \boldsymbol{g}_{i'})$, the coordinate functions transform linearly with

$$x^{i'} = B^{i'}_{\ i}\, x^i + c^{i'} \,, \tag{A.1.13}$$

where the $B^{i'}_{\ i}$ are the components of the inverse change of basis $\{\boldsymbol{g}_{i'}\} \mapsto \{\boldsymbol{g}_i\}$, and the $c^{i'}$ are the components of the translation vector $\overrightarrow{O'O}$. In other words, the functions $\chi^{i'}$ involved in $x^{i'} \stackrel{\text{def}}{=} \chi^{i'}(x^1, \ldots, x^{n_{\text{dim}}})$ are linear in x, and the partial derivatives of the change of affine coordinates are just $\frac{\partial \chi^{i'}}{\partial x^j} = B^{i'}_{\ i}$, the components of the inverse change of basis.

Assume that $\mathcal{A} \subset \mathcal{S}$ is an n-dimensional surface embedded in the m-dimensional affine point space $\mathcal{S}$, where $n \leq m$ —for example, $\mathcal{A}$ could be a shell in $\mathcal{S} = \mathbb{R}^3$. Let $(\mathcal{S}, y)$ and $(\mathcal{A}, x)$ be the coordinate systems on $\mathcal{S}$ and $\mathcal{A}$, respectively. From the theory of

parametric surfaces it is known that a *curvilinear coordinate system* on $\mathcal{S}$ is determined by the map $\mathbb{R}^n \supset \Omega \to \mathbb{R}^m$, in which the coordinates y^a restricted to $\mathcal{A} \subset \mathcal{S}$ are given by m nonlinear and continuously differentiable functions f^a. Clearly,

$$y^a \stackrel{\text{def}}{=} f^a(x^1, \ldots, x^n)\,, \qquad \text{with} \quad a = 1, \ldots, m\,, \tag{A.1.14}$$

and the lines x^i are generally *curvilinear* in $\mathcal{S}$. By (A.1.14), the simple transformation rule (A.1.13) thus changes to $y^{a'} = (\chi^{a'} \circ f^a)(x^1, \ldots, x^n)$. The inverse functions $x^i = (f^{-1})^i(y^1, \ldots, y^m)$, with $i = 1, \ldots, n$, provided that they do exist at every $P \in \mathcal{A} \subset \mathcal{S}$, are referred to as the *convected coordinates* on $\mathcal{A}$ in $\mathcal{S}$.

If the y^a are Cartesian coordinates relative to the frame $(O, \boldsymbol{e}_a)$ in $\mathcal{S} = \mathbb{R}^3$, then the vector basis $\{\boldsymbol{g}_i\}_P$ that spans the *tangent space* attached to $P \in \mathcal{A}$ is given by the partial derivatives of the position vector $\overrightarrow{OP} \stackrel{\text{def}}{=} \boldsymbol{y}(y^a(P)) = y^a(P)\boldsymbol{e}_a \stackrel{\text{def}}{=} \boldsymbol{f}((f^{-1})^i(y^a(P)))$ in $\mathcal{S}$ with respect to the convected coordinates. That is, $\boldsymbol{g}_i(P) \stackrel{\text{def}}{=} \frac{\partial \boldsymbol{y}}{\partial (f^{-1})^i}(P) = \frac{\partial \boldsymbol{f}}{\partial x^i}(P)$, by abuse of notation. $\{\boldsymbol{g}_i\}_P$ is called the *covariant basis* at P.

The transformation rule (A.1.13) specifies the coordinates of an affine point space under a change of framing within that space (passive transformation), whereas an affine transformation changes the affine point space itself (active transformation).

Definition A.1.15. Let $(\mathcal{S}, \mathcal{V})$, $(\mathcal{T}, \mathcal{W})$ be affine point spaces, $\boldsymbol{A} : \mathcal{V} \to \mathcal{W}$ a linear map, and $O, P \in \mathcal{S}$. Then under an *affine transformation* $\theta : \mathcal{S} \to \mathcal{T}$ the point $P = O + \overrightarrow{OP}$ changes to

$$\theta(P) = \theta(O) + \boldsymbol{A}(\overrightarrow{OP}) \quad \in \mathcal{T}\,.$$

The vector $\overrightarrow{OP}$ is said to be *pushed forward* by θ. An affine transformation is an *affine isometry* if the distance of every two points $P, Q \in \mathcal{S}$ remains unaltered, that is, $d_{\mathcal{T}}(\theta(P), \theta(Q)) = d_{\mathcal{S}}(P, Q)$. ◊

Affine isometries play a fundamental role in continuum mechanics as they form a group of transformations. If the affine isometry

$$\begin{aligned} \theta :\ \mathcal{S} &\ \to\ \mathcal{S} \\ O + \overrightarrow{OP} &\ \mapsto\ \theta(O) + \boldsymbol{Q}(\overrightarrow{OP}) \end{aligned} \tag{A.1.16}$$

preserves orientation, then the *rotation* $\boldsymbol{Q}$ is proper orthogonal ($\det \boldsymbol{Q} = +1$) and θ is called a *rigid motion*. Rigid motions $\theta : \mathcal{S} \to \mathcal{S}$ belong to the special Euclidian group $\mathrm{SE}(\mathcal{S})$, and rotations $\boldsymbol{Q} : \mathcal{V} \to \mathcal{V}$ belong to the special orthogonal group $\mathrm{SO}(\mathcal{V})$. Note that every vector $\boldsymbol{v}$ transforms under a rigid motion according to $\boldsymbol{v}' = \boldsymbol{Q}\boldsymbol{v}$, which is referred to as its *objective transformation*.

To get a coordinate description of (A.1.16) with respect to a frame $(O, \boldsymbol{g}_i)$, define $\boldsymbol{x} \stackrel{\text{def}}{=} \overrightarrow{OP} = x^i \boldsymbol{g}_i$, $\boldsymbol{x}' \stackrel{\text{def}}{=} \overrightarrow{O\theta(P)} = x^{i'} \boldsymbol{g}_{i'}$, and $\boldsymbol{c} \stackrel{\text{def}}{=} \overrightarrow{O\theta(O)} = c^{i'} \boldsymbol{g}_{i'}$, so that $\boldsymbol{x}' = \boldsymbol{Q}\boldsymbol{x} + \boldsymbol{c}$. Let the basis $\{\boldsymbol{g}_{i'}\}$ be given by $\boldsymbol{Q}\boldsymbol{g}_i = Q^{i'}{}_i \boldsymbol{g}_{i'}$, then

$$x^{i'} = Q^{i'}{}_i\, x^i + c^{i'}\,. \tag{A.1.17}$$

A.2 Banach Spaces and Differential Calculus

The key facts presented in this section are basic ingredients of constitutive theory and of the numerical treatment of initial boundary value problems.

Let $\mathcal{V}$ be a vector space with metric d, and $\boldsymbol{v}_1, \boldsymbol{v}_2, \ldots \in \mathcal{V}$, then a sequence $(\boldsymbol{v}_1, \boldsymbol{v}_2, \ldots)$ is called a *Cauchy sequence* if for all real numbers $\varepsilon > 0$ there is an integer N such that $m, n \geq N$ implies $d(\boldsymbol{v}_m, \boldsymbol{v}_n) < \varepsilon$. The metric space $(\mathcal{V}, d)$ is called *complete* if every Cauchy sequence converges. A complete normed space $(\mathcal{V}, \|\cdot\|)$, or just $\mathcal{V}$ if the meaning is clear, with corresponding metric d defined through $d(\boldsymbol{v}_1, \boldsymbol{v}_2) \stackrel{\text{def}}{=} \|\boldsymbol{v}_1 - \boldsymbol{v}_2\|$ is then called a *Banach space*. The vector spaces of real functions (see Remark A.1.1) can be made into Banach spaces provided that suitable norms exist on these spaces.

Let $\mathcal{V}, \mathcal{W}$ be Banach spaces with norms $\|\cdot\|_{\mathcal{V}}$ and $\|\cdot\|_{\mathcal{W}}$, respectively, then a linear map $\boldsymbol{A} : \mathcal{V} \to \mathcal{W}$ is called an *linear operator*. $\boldsymbol{A}$ is called *bounded* if there is some constant $\lambda > 0$ such that for all $\boldsymbol{v} \in \mathcal{V}$,

$$\|\boldsymbol{A}\boldsymbol{v}\|_{\mathcal{W}} \leq \lambda \|\boldsymbol{v}\|_{\mathcal{V}} \,. \tag{A.2.1}$$

The set of all bounded linear operators of $\mathcal{V}$ to $\mathcal{W}$ is denoted by $B(\mathcal{V}, \mathcal{W})$.

Definition A.2.2. Let $\mathcal{V}, \mathcal{W}$ be Banach spaces, and $\mathcal{U} \subset \mathcal{V}$ a subset. An operator $f : \mathcal{U} \to \mathcal{W}$ is called *Fréchet-differentiable* at $\bar{\boldsymbol{u}} \in \mathcal{U}$ if there is a bounded linear operator $Df(\bar{\boldsymbol{u}}) \in B(\mathcal{V}, \mathcal{W})$ such that for every $\boldsymbol{u} \stackrel{\text{def}}{=} (\bar{\boldsymbol{u}} + t\boldsymbol{v}) \in \mathcal{U}$, with $\boldsymbol{v} \in \mathcal{V}$ and $t \in \mathbb{R}$,

$$\lim_{\|\boldsymbol{h}\| \to 0} \frac{\|f(\boldsymbol{u}) - f(\bar{\boldsymbol{u}}) - Df(\bar{\boldsymbol{u}}) \cdot \boldsymbol{h}\|_{\mathcal{W}}}{\|\boldsymbol{h}\|_{\mathcal{V}}} = 0 \,,$$

where $\boldsymbol{h} \stackrel{\text{def}}{=} \boldsymbol{u} - \bar{\boldsymbol{u}}$. If f is Fréchet-differentiable at each $\bar{\boldsymbol{u}} \in \mathcal{U}$, the map $Df : \mathcal{U} \to B(\mathcal{V}, \mathcal{W})$, $\boldsymbol{u} \mapsto Df(\boldsymbol{u})$ is called the *Fréchet derivative of* f. If Df is differentiable as well, then $D^2 f : \mathcal{U} \to B(\mathcal{V}, B(\mathcal{V}, \mathcal{W}))$ is called the *second derivative* of f. ♢

Remark A.2.3. For the differentiable maps $f : \mathbb{R}^m \to \mathbb{R}^n$, $Df(\boldsymbol{x})$ is just the matrix of partial derivatives of f evaluated at $\boldsymbol{x} = (x^1, \ldots, x^m) \in \mathbb{R}^m$, i.e. its $n \times m$ Jacobian matrix. △

Definition A.2.4. Let $f : \mathcal{V} \supset \mathcal{U} \to \mathcal{W}$, and $\bar{\boldsymbol{u}} \in \mathcal{U}$. Then f is called *Gâteaux-differentiable* if a weak differential

$$\frac{\mathrm{d}}{\mathrm{d}t} f(\bar{\boldsymbol{u}} + t\boldsymbol{v})|_{t=0}$$

does exist for all directions $\boldsymbol{v} \in \mathcal{V}$. ♢

If f is Fréchet-differentiable at $\bar{\boldsymbol{u}}$, then it is also Gâteaux-differentiable at $\bar{\boldsymbol{u}}$, because the derivatives in the direction of $\boldsymbol{v}$ exist:

$$\frac{\mathrm{d}}{\mathrm{d}t} f(\bar{\boldsymbol{u}} + t\boldsymbol{v})|_{t=0} = \left[\frac{\partial f(\bar{\boldsymbol{u}} + t\boldsymbol{v})}{\partial \boldsymbol{u}} \frac{\partial(\bar{\boldsymbol{u}} + t\boldsymbol{v})}{\partial t}\right]_{t=0} = Df(\bar{\boldsymbol{u}}) \cdot \boldsymbol{v} \,. \tag{A.2.5}$$

where $Df(\bar{\boldsymbol{u}}) \cdot \boldsymbol{v}$ means $Df(\bar{\boldsymbol{u}})$ applied to $\boldsymbol{v}$ as a linear map at $\bar{\boldsymbol{u}}$.

In addition to the previous definitions, let $\mathcal{Y} \subset \mathcal{W}$ and $f(\mathcal{U}) \subset \mathcal{Y}$. Let $\mathcal{Z}$ be another Banach space and let $g : \mathcal{W} \supset \mathcal{Y} \to \mathcal{Z}$ be Fréchet-differentiable at $\boldsymbol{y} = f(\boldsymbol{u}) \in \mathcal{Y}$, then the composite map $g \circ f : \mathcal{U} \to \mathcal{Z}$ is Fréchet differentiable at $\boldsymbol{u}$ and the chain rule

$$D(g \circ f)(\boldsymbol{u}) = Dg(f(\boldsymbol{u})) \cdot Df(\boldsymbol{u}) = Dg(\boldsymbol{y}) \cdot Df(\boldsymbol{u}) \tag{A.2.6}$$

resp. $D(g \circ f)(\boldsymbol{u}) \cdot \boldsymbol{v} = Dg(f(\boldsymbol{u})) \cdot ((Df(\boldsymbol{u}) \cdot \boldsymbol{v})$ does apply.

As an example application of the chain rule, let $f : \mathcal{I} \to \mathcal{W}$, with $\mathcal{I} \subset \mathbb{R}$, be a curve in $\mathcal{W}$ and differentiable at $t \in \mathcal{I}$. Then define $\frac{\mathrm{d}f}{\mathrm{d}t}(t) = Df(t) \cdot 1$, where $1 \in \mathbb{R}$ is the real number "one". Let $g : \mathcal{W} \supset \mathcal{Y} \to \mathbb{R}$ be differentiable at $\boldsymbol{y} = f(t) \in \mathcal{Y}$, then by the chain rule,

$$\frac{\mathrm{d}(g \circ f)}{\mathrm{d}t}(t) = Dg(\boldsymbol{y}) \cdot \frac{\mathrm{d}f}{\mathrm{d}t}(t)\,. \tag{A.2.7}$$

Definition A.2.8. Let $\mathcal{V}, \mathcal{W}$ be Banach spaces, $\mathcal{U} \subset \mathcal{V}$ a subset, and let $f : \mathcal{U} \to \mathcal{W}$ be C^1-differentiable at $\bar{\boldsymbol{u}} \in \mathcal{U}$ in the Fréchet-sense. Let $\boldsymbol{u} \stackrel{\text{def}}{=} (\bar{\boldsymbol{u}} + t\boldsymbol{v}) \in \mathcal{U}$, with $\boldsymbol{v} \in \mathcal{V}$ and $t \in \mathbb{R}$, then the *linearization* of the equations $f(\boldsymbol{u}) = 0$ about $\bar{\boldsymbol{u}}$ in the direction of $\boldsymbol{v}$ is defined through

$$\mathrm{LIN}_{\bar{\boldsymbol{u}}}(f; \boldsymbol{v}) \stackrel{\text{def}}{=} f(\bar{\boldsymbol{u}}) + \frac{\mathrm{d}}{\mathrm{d}t}\, f(\bar{\boldsymbol{u}} + t\boldsymbol{v})|_{t=0} = f(\bar{\boldsymbol{u}}) + Df(\bar{\boldsymbol{u}}) \cdot \boldsymbol{v} = 0\,. \qquad \diamond$$

Here $f(\boldsymbol{u}) = 0$ shall denote the abstraction of a given set of equations. For $\mathrm{LIN}_{\bar{\boldsymbol{u}}}(f; \boldsymbol{v}) = 0$, the vector $\boldsymbol{u} = \bar{\boldsymbol{u}} + t\boldsymbol{v}$ satisfies $f(\boldsymbol{u}) = 0$ to first order in t. Thus $\mathrm{LIN}_{\bar{\boldsymbol{u}}}(f; \boldsymbol{v})$, with $\bar{\boldsymbol{u}}$ fixed, are the first two terms in a *Taylor series expansion* of $f(\bar{\boldsymbol{u}} + t\boldsymbol{v})$, so $f(\boldsymbol{u}) \approx \mathrm{LIN}_{\bar{\boldsymbol{u}}}(f; \boldsymbol{v})$.

A.3 Basic Numerical Methods

A.3.1 Solution of Initial Value Problems

Definition A.3.1. Let $\mathcal{V}$ be a Banach space, $[t_0, T] \times \Omega \subset \mathbb{R} \times \mathcal{V}$, and $\boldsymbol{f} : [t_0, T] \times \Omega \to \mathcal{V}$, then an *initial value problem (IVP)* is an ordinary differential equation

$$\dot{\boldsymbol{y}}(t) = \boldsymbol{f}(t, \boldsymbol{y}(t))$$

together with a so-called *initial condition* $(t_0, \boldsymbol{y}_0) \in [t_0, T] \times \Omega$. A *solution to the IVP* is a function $\boldsymbol{y}$ that is a solution to the differential equation for all $t \in [t_0, T]$, and that satisfies $\boldsymbol{y}(t_0) = \boldsymbol{y}_0$. $\diamond$

By abuse of notation, $\boldsymbol{y}(t_0) = \boldsymbol{y}_0$ is identified with the initial condition. If $\boldsymbol{f}$ is continuous on a domain containing $(t_0, \boldsymbol{y}_0)$, and if $t_0 \in [0, T]$, then *Picard-Lindelöf's theorem* guarantees uniqueness of the solution.

Numerical time integration methods to determine the solution $\boldsymbol{y}(t)$ can be divided into first-order (e.g. Euler methods), second-order (e.g. Newmark-β, central difference), and higher-order accurate methods (e.g. Runge-Kutta), as well as into explicit (e.g. forward Euler, forward difference, central difference) and implicit methods (e.g. backward Euler, Newmark-β, Crank-Nicolson). Euler methods are often implemented in finite element codes to integrate rate constitutive equations on the local integration point level, while the central difference and Newmark-β methods are employed for global time integration of the FE system of equations.

The difference between explicit and implicit time integrators is outlined based on Euler methods. The continuous time interval $[t_0, T]$ is approximated by the sequence $(t_0, t_1 = t_0 + \Delta t, \ldots, t_{n+1} = t_n + \Delta t, \ldots, T)$ with constant time increment or step size Δt, i.e. time is incrementally decomposed. With the *forward Euler method*, the rate $\dot{\boldsymbol{y}}(t)$ in Definition A.3.1 is approximated through

$$\dot{\boldsymbol{y}}(t) \approx \frac{\boldsymbol{y}(t_n + \Delta t) - \boldsymbol{y}(t_n)}{\Delta t} \,. \tag{A.3.2}$$

Note that the right hand side is a function of time t_n. By setting $\boldsymbol{y}(t_n) \stackrel{\text{def}}{=} \boldsymbol{y}_n$ and noting that $\dot{\boldsymbol{y}}(t_n) = \boldsymbol{f}(t_n, \boldsymbol{y}(t_n))$ by definition, one obtains

$$\boldsymbol{y}_{n+1} = \boldsymbol{y}_n + \Delta t \, \boldsymbol{f}(t_n, \boldsymbol{y}_n) \,. \tag{A.3.3}$$

The *backward Euler method* uses the approximation

$$\dot{\boldsymbol{y}}(t) \approx \frac{\boldsymbol{y}(t_{n+1}) - \boldsymbol{y}(t_{n+1} - \Delta t)}{\Delta t} \,, \tag{A.3.4}$$

which yields

$$\boldsymbol{y}_{n+1} = \boldsymbol{y}_n + \Delta t \, \boldsymbol{f}(t_{n+1}, \boldsymbol{y}_{n+1}) \,. \tag{A.3.5}$$

Both equations (A.3.3) and (A.3.5) can be combined to obtain the so-called *generalized midpoint rule*

$$\boldsymbol{y}_{n+1} = \boldsymbol{y}_n + \Delta t \, \boldsymbol{f}_{n+\theta} \,, \tag{A.3.6}$$

where

$$\boldsymbol{f}_{n+\theta} \stackrel{\text{def}}{=} \theta \boldsymbol{f}(t_{n+1}, \boldsymbol{y}_{n+1}) + (1 - \theta) \boldsymbol{f}(t_n, \boldsymbol{y}_n) \,, \qquad \theta \in [0, 1] \,. \tag{A.3.7}$$

The *Crank-Nicolson method*, which possesses accuracy of second order, is recovered from the generalized midpoint rule by setting $\theta = \frac{1}{2}$.

In the forward Euler method ($\theta = 0$), the solution $\boldsymbol{y}_{n+1}$ at time t_{n+1} is determined from the value $\boldsymbol{f}(t_n, \boldsymbol{y}_n)$ at time t_n, whereas $\boldsymbol{y}_{n+1}$ is determined from the value $\boldsymbol{f}(t_{n+1}, \boldsymbol{y}_{n+1})$ at time t_{n+1} in the backward Euler method ($\theta = 1$). Since $\boldsymbol{f}$ generally is a nonlinear function, and the value $\boldsymbol{f}(t_{n+1}, \boldsymbol{y}_{n+1})$ at a time prior to t_{n+1} is an unknown, an iteration must be carried out. This can be done, for example, by employing Newton's method.

A.3.2 Newton's Method

Let $\mathcal{V}, \mathcal{W}$ be Banach spaces. *Newton's method*, which is also known as the *Newton-Raphson method*, approximates the solution $\hat{\boldsymbol{x}} \in \mathcal{V}$ of a homogeneous system of nonlinear algebraic equations

$$\boldsymbol{f}(\hat{\boldsymbol{x}}) = \boldsymbol{0} \qquad \in \mathcal{W}\,. \tag{A.3.8}$$

Let $\boldsymbol{x}^i$, with $i \in \mathbb{N}$, be a close-enough guess of the solution, and let $\boldsymbol{f}$ be Fréchet-differentiable at $\boldsymbol{x}^i$. Then, according to Definition A.2.8 the linearization of $\boldsymbol{f}(\hat{\boldsymbol{x}})$ about $\boldsymbol{x}^i$ is

$$\mathrm{LIN}_{\boldsymbol{x}^i}(\boldsymbol{f}; \hat{\boldsymbol{x}} - \boldsymbol{x}^i) = \boldsymbol{f}(\boldsymbol{x}^i) + D\boldsymbol{f}(\boldsymbol{x}^i) \cdot (\hat{\boldsymbol{x}} - \boldsymbol{x}^i) \approx \boldsymbol{0}\,. \tag{A.3.9}$$

$\hat{\boldsymbol{x}}$ is unknown. However, provided that the function $\boldsymbol{f}$ is reasonably well-behaved, any guess $\boldsymbol{x}^{i+1}$ for which $\boldsymbol{f}(\boldsymbol{x}^i) + D\boldsymbol{f}(\boldsymbol{x}^i) \cdot (\boldsymbol{x}^{i+1} - \boldsymbol{x}^i) = \boldsymbol{0}$ is a better approximation than $\boldsymbol{x}^i$. From this condition one obtains

$$\boldsymbol{x}^{i+1} = \boldsymbol{x}^i + \boldsymbol{d}(\boldsymbol{x}^i) = \boldsymbol{x}^i - ((D\boldsymbol{f})^{-1} \cdot \boldsymbol{f})(\boldsymbol{x}^i)\,, \qquad \text{and} \quad \lim_{i\to\infty} \boldsymbol{x}^{i+1} = \hat{\boldsymbol{x}}\,, \tag{A.3.10}$$

where $\boldsymbol{d}(\boldsymbol{x}^i)$ is called the *descent direction of* $\boldsymbol{f}$ *at* $\boldsymbol{x}^i$. Newton's method (A.3.10) is a convergent iteration scheme for the solution $\hat{\boldsymbol{x}}$ only if $D\boldsymbol{f}$ is invertible and the starting value $\boldsymbol{x}^{i=0}$ is a close-enough guess of the solution. Iteration can be terminated if $\|\boldsymbol{f}(\boldsymbol{x}^{i+1})\| < \varepsilon$.

Definition A.3.11. Newton's method, (A.3.10), is called a *full Newton's method* if $D\boldsymbol{f} \stackrel{\text{def}}{=} D\boldsymbol{f}^i$ is determined in every iteration step i. A full Newton's method has a quadratic rate of convergence. *Quasi-Newton methods*, in contrast to *exact Newton methods*, do not exactly determine $D\boldsymbol{f}$ but use approximations. In a *damped Newton's method* the descent direction $\boldsymbol{d}(\boldsymbol{x}^i)$ is multiplied by a *step size* $0 \le \lambda^i \le 1$ determined by a so-called *line search*, which is supposed to guarantee $\|\boldsymbol{f}(\boldsymbol{x}^i + \lambda^i \boldsymbol{d}(\boldsymbol{x}^i))\| < \|\boldsymbol{f}(\boldsymbol{x}^i)\|$. If $D\boldsymbol{f}$ is not positive definite, the descent direction $\boldsymbol{d}$ should not be determined from *Newton's direction*, $\boldsymbol{d} \stackrel{\text{def}}{=} -(D\boldsymbol{f})^{-1} \cdot \boldsymbol{f}$ because solution may diverge. In this case the descent direction has to be modified, leading to the class of *modified Newton's methods*.$\diamond$

Definition A.3.12. The so-called *secant Newton's method* is obtained from (A.3.10) by referring to the starting value (or a converged solution) $\boldsymbol{x}^0$ instead of $\boldsymbol{x}^i$, and by replacing the continuous tangent $D\boldsymbol{f}$ with an *algorithmic tangent* $D\boldsymbol{f}^{\mathrm{al}}(\boldsymbol{x}^0, \boldsymbol{x}^{i+1})$ taking into account the finite step size $\Delta\boldsymbol{x}^{i+1} = \boldsymbol{x}^{i+1} - \boldsymbol{x}^0$ in the algorithmic treatment:

$$\boldsymbol{x}^{i+1} = \boldsymbol{x}^0 - (D\boldsymbol{f}^{\mathrm{al}})^{-1}(\boldsymbol{x}^0, \boldsymbol{x}^{i+1}) \cdot \boldsymbol{f}(\boldsymbol{x}^0)\,. \qquad \diamond$$

A.4 Differentiable Manifolds

Riemann [1868, 1873] has introduced the local or intrinsic description of geometric objects without the need of a linear background space. However, in the intrinsic description by using differentiable manifolds position vectors do not exist and every coordinate system is necessarily curvilinear. Furthermore, as the parallelogram axiom

exists no longer, and vectors and tensors must be defined point by point. Equations of the kind $\boldsymbol{v}(P) = \boldsymbol{v}(Q)$ are not permitted, because the vectors at different points cannot be compared. This makes differential geometry and continuum mechanics on manifolds generally hard to challenge. The large investment of effort, however, is rewarded with unifying and aesthetically satisfying basic notions and notation which gain insight and facilitate a deep understanding even of the complex issues.

If one drops all the affine properties of a point space studied in the previous section, one is left with a topological space constituted by a set of points. Descriptively, a topological space is a set together with a topology that carries the relations or interconnections between elements of the set.

Definition A.4.1. A *topological space* is the pair $(\mathcal{S}, \mathscr{T})$ comprising a set $\mathcal{S}$ and a collection $\mathscr{T}$ of subsets called *open sets* such that

1. $\emptyset \in \mathscr{T}$ and $\mathcal{S} \in \mathscr{T}$.
2. If $\mathcal{A}, \mathcal{B} \in \mathscr{T}$, then $\mathcal{A} \cap \mathcal{B} \in \mathscr{T}$ also holds.
3. Let $\mathcal{I} \subset \mathbb{N}$ be a set of indices. If $\mathcal{A}_i \in \mathscr{T}$, $\forall\, i \in \mathcal{I}$, then $\bigcup_{i\in\mathcal{I}} \mathcal{A}_i \in \mathscr{T}$ also holds.

$\mathscr{T}$ is called the *topology*. Usually $\mathcal{S}$ is written instead of $(\mathcal{S}, \mathscr{T})$ if the meaning is clear. ♢

A subsets $\mathcal{M} \subset \mathcal{S}$ is called *closed*, if the complement $\mathcal{S}\backslash\mathcal{M}$ is open. The *interior* $\mathrm{int}(\mathcal{M})$ is the union of all open sets that completely lie in $\mathcal{M}$, and the *closure* $\mathrm{cl}(\mathcal{M})$ is the smallest closed set which completely includes $\mathcal{M}$. The difference $\mathrm{cl}(\mathcal{M})\backslash\mathrm{int}(\mathcal{M}) \stackrel{\mathrm{def}}{=} \partial\mathcal{M}$, resp. the intersection $\mathrm{cl}(\mathcal{M}) \cap \mathrm{cl}(\mathcal{S}\backslash\mathcal{M}) \stackrel{\mathrm{def}}{=} \partial\mathcal{M}$, which is the same set, is called the *boundary* of $\mathcal{M}$ and is closed. A *neighborhood* of a point $X \in \mathcal{M}$ is an open set $\mathcal{U}$ such that $X \in \mathcal{U}$. A topological space $\mathcal{M}$ is referred to as a *Hausdorff space*, if every two points $X, Y \in \mathcal{M}$, $X \neq Y$, can be separated by neighborhoods $\mathcal{U}(X) \subset \mathcal{M}$ and $\mathcal{V}(Y) \subset \mathcal{M}$ such that $\mathcal{U} \cap \mathcal{V} = \emptyset$. In a Hausdorff space $\mathcal{M}$ the singleton sets $\{X\}$, with $X \in \mathcal{M}$, are closed.

Let $\mathcal{S}$ be a topological space and $X, Y, O \in \mathcal{S}$. A *metric* on $\mathcal{S}$ is a map $d : \mathcal{S} \times \mathcal{S} \to \mathbb{R}$ such that 1. $d(X, Y) = 0$ if and only if $X = Y$ (definiteness). 2. $d(X, Y) = d(Y, X)$ (symmetry), and 3. $d(O, Y) \leq d(O, X) + d(X, Y)$ (triangle inequality). The pair $(\mathcal{S}, d)$, or just $\mathcal{S}$ if there is no danger of confusion, is called a *metric space*. Inner product spaces and normed spaces are specialized metric spaces.

A continuous bijective mapping $\varphi : \mathcal{M} \to \mathcal{N}$ between topological spaces $\mathcal{M}$ and $\mathcal{N}$ which has a continuous inverse preserves the topology of a topological space $\mathcal{M}$ and is referred to as an *homeomorphism*. Let $\mathcal{U}(X) \subset \mathcal{M}$ be an open neighborhood of the point $X \in \mathcal{M}$, then the pair $(\mathcal{U}, \beta)$ including the homeomorphism

$$\begin{aligned} \beta :\ \mathcal{M} \supset \mathcal{U} \ &\to\ \mathcal{X} \subset \mathbb{R}^{n_{\mathrm{dim}}} \\ X \ &\mapsto\ \beta(X) = \{x^1, x^2, \ldots, x^{n_{\mathrm{dim}}}\}_X \stackrel{\mathrm{def}}{=} \{x^i\}_X,\ \exists\, \beta^{-1}\,, \end{aligned} \tag{A.4.2}$$

is called a *chart* or *local coordinate system* on $\mathcal{M}$ and the x^i are *coordinate functions*. The tuple $\{x^i\}_X$ is called the *coordinates of X in the chart* $(\mathcal{U}, \beta)$. An *atlas* of $\mathcal{M} \stackrel{\mathrm{def}}{=}$

$\bigcup_{i\in\mathcal{I}\subset\mathbb{N}}\mathcal{U}_i$ is a collection $\mathfrak{A}(\mathcal{M}) \stackrel{\text{def}}{=} \{(\mathcal{U}_i,\beta_i)\}_{i\in\mathcal{I}\subset\mathbb{N}}$ of a finite number of charts that covers $\mathcal{M}$. Charts provide a one-to-one relation between points and coordinates, and the homeomorphism onto the $\mathbb{R}^n$-continuum expresses the continuity of $\mathcal{M}$ (at least locally).

A *chart transition* or *change of coordinates* can be described by

$$\beta'\circ\beta^{-1}\Big|_{\beta(\mathcal{U}\cap\mathcal{U}')} : \beta\left(\mathcal{U}\cap\mathcal{U}'\right)\to\beta'\left(\mathcal{U}\cap\mathcal{U}'\right)\,, \tag{A.4.3}$$

in which $(\mathcal{U},\beta)$, $(\mathcal{U}',\beta')$ are charts on $\mathcal{M}$, and $\mathcal{U}\cap\mathcal{U}'\neq\emptyset$. If the chart transition is at least C^1, i.e. 1-fold continuously differentiable, then for a point $X\in\mathcal{U}\cap\mathcal{U}'$ having coordinates $\{x^i\}_X\in\beta(\mathcal{U})$ and $\{x^{i'}\}_X\in\beta'(\mathcal{U}')$ in each chart the *Jacobian matrix* of the coordinate functions at X is given by

$$\mathrm{d}x^{i'} = \left(\frac{\partial(x^{i'}\circ\beta^{-1})}{\partial x^i}\right)(\beta(X))\;\mathrm{d}x^i\,.$$

The point argument indicates that $x^{i'}\circ\beta^{-1}$ is generally non-linear in x^i. An atlas is called *differentiable*, if for every two charts the chart transition is differentiable. A differentiable atlas generates a global differentiable structure on the manifold, which would be important in what follows.

Definition A.4.4. An *differentiable manifold* $\mathcal{M}$ is a Hausdorff space together with a differentiable atlas. ♢

Probably the simplest example of a differentiable manifold is $\mathbb{R}^{n_{\mathrm{dim}}}$ which has the one-chart atlas $(\mathbb{R}^{n_{\mathrm{dim}}},\mathrm{id})$.

Obviously, there is a difference between a point and its picture in a chart. One should also distinguish a continuous map $\varphi:\mathcal{M}\to\mathcal{N}$ between manifolds from its *local representative* or *localization*. Let $\mathcal{U}(X)\subset\mathcal{M}$ and $\mathcal{V}(x)\subset\mathcal{N}$ be neighborhoods of $X\in\mathcal{M}$ and $x\in\mathcal{N}$, respectively, and let $(\mathcal{U},\beta)$, $(\mathcal{V},\sigma)$ be charts. Then for non-empty $\varphi^{-1}(\mathcal{V})\cap\mathcal{U}$, the localization $\sigma\circ\varphi\circ\beta^{-1}$ describes the chart transition concerning φ with respect to β and σ:

$$\sigma\circ\varphi\circ\beta^{-1}\Big|_{\beta(\varphi^{-1}(\mathcal{V})\cap\mathcal{U})} : \quad \beta\left(\varphi^{-1}(\mathcal{V})\cap\mathcal{U}\right)\to\sigma\left(\mathcal{V}\cap\varphi(\mathcal{U})\right)\,. \tag{A.4.5}$$

For $\varphi=\mathrm{id}$ (the identity map), (A.4.5) reduces to (A.4.3). If x^i are the coordinate functions of $(\mathcal{V},\sigma)$ and X^I are those of $(\mathcal{U},\beta)$, then it would be convenient to define

$$\varphi^i \stackrel{\text{def}}{=} x^i\circ\varphi\circ\beta^{-1} \qquad \text{resp.} \qquad \varphi^i(X^I)\stackrel{\text{def}}{=}(x^i\circ\varphi\circ\beta^{-1})(X^I)\,. \tag{A.4.6}$$

The map φ is called *differentiable at* $X\in\varphi^{-1}(\mathcal{V})\cap\mathcal{U}$, if $\sigma\circ\varphi\circ\beta^{-1}$ is differentiable at $\beta(X)$. A bijective differentiable map $\varphi:\mathcal{M}\to\mathcal{N}$ is referred to as a *diffeomorphism*, if both φ and φ^{-1} are continuous differentiable. A map $\varphi:\mathcal{M}\to\mathcal{N}$ is called an *embedding*, if $\varphi(\mathcal{M})\subset\mathcal{N}$ is a submanifold in $\mathcal{N}$ and $\mathcal{M}\to\varphi(\mathcal{M})$ is a diffeomorphism. For example, a simple surface is a two-dimensional manifold embedded in three-dimensional space.

Vectors and linear forms in the traditional sense (see Section A.1) do not exist on manifolds. Fortunately there are objects on differentiable manifolds whose components obey the tensorial transformation rules

$$t^{i'} = \frac{\partial x^{i'}}{\partial x^i}\, t^i \qquad \text{and} \qquad t_{i'} = \frac{\partial x^i}{\partial x^{i'}}\, t_i \tag{A.4.7}$$

in a local chart. From these a local vector space and local co-vector space can be constructed.

Let $[-\tau, \tau] \subset \mathbb{R}$ be an interval and $s : [-\tau, \tau] \to \mathcal{M}$ a curve on an n-dimensional differentiable manifold $\mathcal{M}$. In an appropriate chart on $\mathcal{M}$ with coordinate x^i, the functions $s^i(t) = x^i \circ s(t) \subset \mathbb{R}^n$ define coordinates parameterized by $t \in [-\tau, \tau]$. Let $f : \mathcal{M} \to \mathbb{R}$ be a C^1 real function, then the *directional derivative of f along the curve $s(t) \subset \mathcal{M}$ at point $X = s(0) \in \mathcal{U} \subset \mathcal{M}$* is defined through

$$\left.\frac{\mathrm{d}f}{\mathrm{d}t}\right|_X = \left.\frac{\mathrm{d}f}{\mathrm{d}t}\right|_{t=0} \stackrel{\text{def}}{=} \left.\frac{\partial (f \circ \beta^{-1})}{\partial x^i}\right|_{\xi(X)} \left.\frac{\mathrm{d}s^i}{\mathrm{d}t}\right|_{t=0} = \left.\frac{\partial (f \circ \beta^{-1})}{\partial x^i}\right|_{\xi(X)} w^i\,, \tag{A.4.8}$$

where $(f \circ \beta^{-1}) : \mathbb{R}^n \to \mathbb{R}$ is the picture of f in the chart $(\mathcal{U}, \beta)$, and $w^i \stackrel{\text{def}}{=} \left.\frac{\mathrm{d}s^i}{\mathrm{d}t}\right|_{t=0}$. In other words, the derivative of a function f at X on the manifold is understood as the derivative of $f \circ \beta^{-1}$ at $\beta(X)$ in a chart.

Under a chart transition resp. coordinate transformation $x^i \mapsto x^{i'}$ one has

$$\frac{\partial f}{\partial x^{i'}} w^{i'} = \left(\frac{\partial x^i}{\partial x^{i'}} \frac{\partial f}{\partial x^i}\right) \left(\frac{\partial x^{i'}}{\partial x^i} w^i\right) = \frac{\partial x^{i'}}{\partial x^i} \frac{\partial x^i}{\partial x^{i'}} \frac{\partial f}{\partial x^i} w^i = \frac{\partial f}{\partial x^i} w^i\,. \tag{A.4.9}$$

Compositions with the inverse chart map β^{-1} has been omitted. Therefore, the directional derivative is a coordinate-invariant object, and $w^i \frac{\partial}{\partial x^i}$ also is. $\left\{\frac{\partial}{\partial x^i}\right\} \stackrel{\text{def}}{=} \left\{\frac{\boldsymbol{\partial}}{\boldsymbol{\partial} x^i}\right\}$ is a vector basis, called the *Gaussian basis* or *holonomic basis* [Misner et al., 1973], hence $\boldsymbol{w}(X) = w^i(X) \frac{\boldsymbol{\partial}}{\boldsymbol{\partial} x^i}(X)$ is an honest vector at $X \in \mathcal{M}$. Hence, one may define the following:

Definition A.4.10. Let $\mathcal{M}$ be an n-dimensional differentiable manifold, $\mathcal{U} \subset \mathcal{M}$ a subset, and $(\mathcal{U}, \beta)$ a chart with coordinate functions $\beta(X) = \{x^i\}_X$ for every $X \in \mathcal{U}$. The *tangent space* $T_X\mathcal{M}$ at X is a local vector space $\mathcal{V}_n$ that is spanned by the basis vectors $\left\{\frac{\boldsymbol{\partial}}{\boldsymbol{\partial} x^i}\right\}_X$ at X. Conceptually,

$$T_X\mathcal{M} \stackrel{\text{def}}{=} \{X\} \times \mathcal{V}_n\,.$$

The disjoint union $T\mathcal{M} \stackrel{\text{def}}{=} \bigcup_{X \in \mathcal{M}} T_X\mathcal{M}$ of all tangent spaces at all points of the manifold is called the *tangent bundle* of $\mathcal{M}$. An element $(X, \boldsymbol{w}) \in T\mathcal{M}$, called a *tangent vector*, will often be denoted by $\boldsymbol{w}_X$, or just $\boldsymbol{w}$ if the base point X is clear from the context. ♢

Remark A.4.11. For Euclidian $\mathcal{M} = \mathbb{R}^n$, the tangent bundle is trivial: $T\mathbb{R}^n = \mathbb{R}^n \times \mathbb{R}^n$. It represents the set of all vectors $\boldsymbol{v} = (v^1, \ldots, v^n) \in \mathbb{R}^n$ at all points $X = (z^1, \ldots, z^n) \in \mathbb{R}^n$, that is, the set of all pairs $(X, \boldsymbol{v})$. △

Now having a local vector space at every point $X \in \mathcal{M}$ of a differentiable manifold $\mathcal{M}$, one is able to translate linear geometry into the "manifold language" by providing a local definition for the property under consideration. In doing so, the duality relation $\boldsymbol{g}^i \cdot \boldsymbol{g}_j = \delta^i{}_j$ of linear geometry is replaced with $\mathbf{d}x^i(X) \cdot \frac{\boldsymbol{\partial}}{\boldsymbol{\partial} x^j}(X) = \frac{\partial x^i}{\partial x^j}(X) = \delta^i{}_j(X)$, so the coordinate differentials $\{\mathrm{d}x^i\}_X \stackrel{\text{def}}{=} \{\mathbf{d}x^i\}_X$ form a dual basis at X. The co-vector space dual to the tangent space $T_X\mathcal{M}$ is called the *cotangent space* $T_X^*\mathcal{M} \stackrel{\text{def}}{=} \{X\} \times \mathcal{V}_n^*$, and elements of $T_X^*\mathcal{M}$ are called *covectors*, *differential 1-forms*, or just *1-forms*. The union $T^*\mathcal{M} \stackrel{\text{def}}{=} \bigcup_{X\in\mathcal{M}} T_X^*\mathcal{M}$ is referred to as the *cotangent bundle of* $\mathcal{M}$.

It has been shown in (A.4.9) that the directional derivative of the function f along the tangent vector $\boldsymbol{w}$ does not depend on the coordinate system resp. chart on $\mathcal{M}$. Indeed, by defining the 1-form-valued *differential of* f through $\mathbf{d}f \stackrel{\text{def}}{=} \frac{\partial f}{\partial x^i}\,\mathbf{d}x^i$ one obtains

$$\frac{\partial f}{\partial x^i} w^i = \left(\frac{\partial f}{\partial x^i}\mathbf{d}x^i\right) \cdot \left(w^j \frac{\boldsymbol{\partial}}{\boldsymbol{\partial} x^j}\right) = \mathbf{d}f \cdot \boldsymbol{w} \tag{A.4.12}$$

at $X = s(0) \in \mathcal{M}$.

A.5 Tensor Algebra

Some algebraic properties and relations of tensors and two-point tensors which are frequently used in this thesis are investigated in the following section. Many of the formulas will be presented in absolute notation, as well as in component and local notation.

Definition A.5.1. A $\binom{p}{q}$*-tensor* $\boldsymbol{T}(X)$ at point X of a differentiable manifold $\mathcal{M}$ is a multilinear mapping

$$\boldsymbol{T}(X) : \underbrace{T_X^*\mathcal{M} \times \ldots \times T_X^*\mathcal{M}}_{p-\text{fold}} \times \underbrace{T_X\mathcal{M} \times \ldots \times T_X\mathcal{M}}_{q-\text{fold}} \to \mathbb{R}\,.$$

The space of all $\binom{p}{q}$-tensors at all points $X \in \mathcal{M}$ is denoted by $T_q^p(\mathcal{M})$. If $\mathcal{N}$ is another differentiable manifold, a $\binom{p\ r}{q\ s}$*-two-point tensor* over a map $\varphi : \mathcal{M} \to \mathcal{N}$ is a multilinear mapping

$$\begin{aligned}\boldsymbol{T}(X) : \underbrace{T_{\varphi(X)}^*\mathcal{N} \times \ldots \times T_{\varphi(X)}^*\mathcal{N}}_{p-\text{fold}} \times \underbrace{T_{\varphi(X)}\mathcal{N} \times \ldots \times T_{\varphi(X)}\mathcal{N}}_{q-\text{fold}} \\ \times \underbrace{T_X^*\mathcal{M} \times \ldots \times T_X^*\mathcal{M}}_{r-\text{fold}} \times \underbrace{T_X\mathcal{M} \times \ldots \times T_X\mathcal{M}}_{s-\text{fold}} \to \mathbb{R}\,.\end{aligned} \qquad \diamond$$

Multilinearity of a $\binom{p}{q}$-tensor phrases that at $X \in \mathcal{M}$,

$$\boldsymbol{T}\left(\boldsymbol{a}_1^*, \ldots, \boldsymbol{a}_p^*, \boldsymbol{v}_1, \ldots, \lambda\,\boldsymbol{x}, \ldots, \boldsymbol{v}_q\right) = \lambda\,\boldsymbol{T}\left(\boldsymbol{a}_1^*, \ldots, \boldsymbol{a}_p^*, \boldsymbol{v}_1, \ldots, \boldsymbol{x}, \ldots, \boldsymbol{v}_q\right)\,, \tag{A.5.2}$$

for some $\lambda \in \mathbb{R}$, and

$$\begin{aligned}\boldsymbol{T}\left(\boldsymbol{a}_1^*,\ldots,\boldsymbol{a}_p^*,\boldsymbol{v}_1,\ldots,\boldsymbol{x}+\boldsymbol{y},\ldots,\boldsymbol{v}_q\right)\\ =\boldsymbol{T}\left(\boldsymbol{a}_1^*,\ldots,\boldsymbol{a}_p^*,\boldsymbol{v}_1,\ldots,\boldsymbol{x},\ldots,\boldsymbol{v}_q\right)+\boldsymbol{T}\left(\boldsymbol{a}_1^*,\ldots,\boldsymbol{a}_p^*,\boldsymbol{v}_1,\ldots,\boldsymbol{y},\ldots,\boldsymbol{v}_q\right),\end{aligned} \tag{A.5.3}$$

where $\boldsymbol{a}_1^*,\ldots,\boldsymbol{a}_p^* \in T_X^*\mathcal{M}$ and $\boldsymbol{x},\boldsymbol{y},\boldsymbol{v}_1,\ldots,\boldsymbol{v}_q \in T_X\mathcal{M}$. Addition of two tensors on general differentiable manifolds requires that both are of the same order $\binom{p\ \ r}{q\ \ s}$ and evaluated at the same point X.

Let $(\mathcal{U},\beta)$, where $\mathcal{U}\subset\mathcal{M}$, be a local chart on $\mathcal{M}$ such that $\left\{\frac{\partial}{\partial x^i}\right\} \in T_X\mathcal{M}$ is a local basis at $X\in\mathcal{U}$, and $\{\mathbf{d}x^i\} \in T_X^*\mathcal{M}$ is its dual. The *components of a* $\binom{p}{q}$*-tensor in the chart* $(\mathcal{U},\beta)$ are then defined through

$$T^{i_1\ldots i_p}{}_{j_1\ldots j_q} \overset{\text{def}}{=} \boldsymbol{T}\left(\mathbf{d}x^{i_1},\ldots,\mathbf{d}x^{i_p},\frac{\boldsymbol{\partial}}{\boldsymbol{\partial}x^{j_1}},\ldots,\frac{\boldsymbol{\partial}}{\boldsymbol{\partial}x^{j_q}}\right), \tag{A.5.4}$$

and based on the index placements one says that $\boldsymbol{T}$ is *contravariant of order* p *and covariant of order* q. In (A.5.4), lower case Greek denotes the coordinate indices, whereas lower case Latin denote labels; this nested indication becomes necessary since each of the $p+q$ index slots pass through the numbers $1,\ldots,n_{\text{dim}}$. Under a chart transition with Jacobian matrix $\frac{\partial x^{i'}}{\partial x^i}$ and its inverse $\frac{\partial x^i}{\partial x^{i'}}$ the tensorial transformation rule (A.4.7) yields

$$T^{i'_1\ldots i'_p}{}_{j'_1\ldots j'_q} = \frac{\partial x^{i'_1}}{\partial x^{i_1}}\cdots\frac{\partial x^{i'_p}}{\partial x^{i_p}}\,\frac{\partial x^{j_1}}{\partial x^{j'_1}}\cdots\frac{\partial x^{j_q}}{\partial x^{j'_q}}\,T^{i_1\ldots i_p}{}_{j_1\ldots j_q}\,. \tag{A.5.5}$$

From the definition of a tensor it should be clear that every 1-form $\boldsymbol{a}^* = a_i\mathbf{d}x^i$ is a $\binom{0}{1}$-tensor, and every vector $\boldsymbol{v} = v^i\frac{\boldsymbol{\partial}}{\boldsymbol{\partial}x^i}$ is a $\binom{1}{0}$-tensor by setting $\boldsymbol{a}^*(\boldsymbol{v}) = a_iv^i \in \mathbb{R}$. The operation $\boldsymbol{a}^*(\boldsymbol{v}) \overset{\text{def}}{=} \boldsymbol{a}^*\cdot\boldsymbol{v}$ is then called the *contraction* of the tensors $\boldsymbol{a}^*$ and $\boldsymbol{v}$. Contraction reduces the order of tensors. The covariant slot of a $\binom{1}{1}$-tensor $\boldsymbol{T}$ contracted with $\boldsymbol{v}$, for example, would result in the $\binom{1}{0}$-tensor

$$\boldsymbol{T}\cdot\boldsymbol{v} = v^i\,\boldsymbol{T}\left(\frac{\boldsymbol{\partial}}{\boldsymbol{\partial}x^i}\right), \qquad \text{in components,} \qquad T^i{}_j\,v^j\,. \tag{A.5.6}$$

In general, the contraction two tensors $\boldsymbol{T}$ and $\boldsymbol{S}$ in the i-th covariant slot of $\boldsymbol{T}$ and the j-th contravariant slot of $\boldsymbol{S}$ is defined as if the covariant slot is a 1-form and the contravariant slot is a vector. If the slots are not specified, and T^{abcd} and S_{ijkl} are the components of $\boldsymbol{T}$ and $\boldsymbol{S}$, respectively, then the (single) contraction $\boldsymbol{T}\cdot\boldsymbol{S}$ simply means $T^{abcd}S_{ijkd}$ in components. *Double contraction* condenses the last two slots of $\boldsymbol{T}$ and $\boldsymbol{S}$:

$$\boldsymbol{T}:\boldsymbol{S}\,, \qquad \text{in components,} \qquad T^{abcd}S_{ijcd}\,. \tag{A.5.7}$$

Recall that the contraction of a $\binom{1}{1}$-tensor $\boldsymbol{T}$ is called its *trace*, written $\operatorname{tr}\boldsymbol{T} = T^i_{\ i}$. It should be borne in mind that a tensor $\boldsymbol{T}$ is an operator acting on some other tensor $\boldsymbol{S}$, so that $\boldsymbol{T}(\boldsymbol{S}) \neq \boldsymbol{S}(\boldsymbol{T})$ resp. $\boldsymbol{T}\cdot\boldsymbol{S} \neq \boldsymbol{S}\cdot\boldsymbol{T}$ in general.

Definition A.5.8. Let $\boldsymbol{T} \in T^p_q(\mathcal{M})$ and $\boldsymbol{S} \in T^r_s(\mathcal{M})$ at a point $X \in \mathcal{M}$, then the *tensor product* $\boldsymbol{T} \otimes \boldsymbol{S}$ is the $\binom{p+r}{q+s}$-tensor defined by

$$(\boldsymbol{T} \otimes \boldsymbol{S}) \left(\boldsymbol{a}^*_1, \ldots, \boldsymbol{a}^*_p, \boldsymbol{v}_1, \ldots, \boldsymbol{v}_q, \boldsymbol{b}^*_1, \ldots, \boldsymbol{b}^*_r, \boldsymbol{w}_1, \ldots, \boldsymbol{w}_s\right) \\ \stackrel{\text{def}}{=} \boldsymbol{T}\left(\boldsymbol{a}^*_1, \ldots, \boldsymbol{a}^*_p, \boldsymbol{v}_1, \ldots, \boldsymbol{v}_q\right) \boldsymbol{S}\left(\boldsymbol{b}^*_1, \ldots, \boldsymbol{b}^*_r, \boldsymbol{w}_1, \ldots, \boldsymbol{w}_s\right) ,$$

where $\boldsymbol{v}_1, \ldots, \boldsymbol{v}_q, \boldsymbol{w}_1, \ldots, \boldsymbol{w}_s \in T_X\mathcal{M}$ and $\boldsymbol{a}^*_1, \ldots, \boldsymbol{a}^*_p, \boldsymbol{b}^*_1, \ldots, \boldsymbol{b}^*_r \in T^*_X\mathcal{M}$. ♢

By (A.5.4), (A.5.6), and Definition A.5.8, every $\binom{p}{q}$-tensor $\boldsymbol{T}$ has the local representative

$$\boldsymbol{T}(X) = T^{i_1 \ldots i_p}{}_{j_1 \ldots j_q}(X)\, \frac{\boldsymbol{\partial}}{\boldsymbol{\partial} x^{i_1}} \otimes \ldots \otimes \frac{\boldsymbol{\partial}}{\boldsymbol{\partial} x^{i_p}} \otimes \mathbf{d}x^{j_1} \otimes \ldots \otimes \mathbf{d}x^{j_q} . \tag{A.5.9}$$

and $T^p_q(\mathcal{M}) = \underbrace{T\mathcal{M} \otimes \ldots \otimes T\mathcal{M}}_{p-\text{fold}} \otimes \underbrace{T^*\mathcal{M} \otimes \ldots \otimes T^*\mathcal{M}}_{q-\text{fold}}$.

A manifold $\mathcal{M}$ with an inner product defined on its tangent bundle has metric coefficients $g_{ij}(X) \stackrel{\text{def}}{=} \left\langle \frac{\boldsymbol{\partial}}{\boldsymbol{\partial} x^i}, \frac{\boldsymbol{\partial}}{\boldsymbol{\partial} x^j} \right\rangle_X \geq 0$ at every point $X \in \mathcal{M}$. From those the *metric* $\boldsymbol{g} \stackrel{\text{def}}{=} g_{ij}\, \mathbf{d}x^i \otimes \mathbf{d}x^j$ can be defined, and the pair $(\mathcal{M}, \boldsymbol{g})$ is then called a *Riemannian manifold*. Contracting the metric tensor with the *inverse metric* $\boldsymbol{g}^{-1} = g^{ij}\, \frac{\boldsymbol{\partial}}{\boldsymbol{\partial} x^i} \otimes \frac{\boldsymbol{\partial}}{\boldsymbol{\partial} x^j}$, where $g_{ik}\, g^{kj} = \delta_i{}^j$, gives the *second-order identity tensor on* $\mathcal{M}$,

$$\boldsymbol{I}_{\mathcal{M}} \stackrel{\text{def}}{=} \boldsymbol{g} \cdot \boldsymbol{g}^{-1} = \delta_i{}^j\, \mathbf{d}x^i \otimes \frac{\boldsymbol{\partial}}{\boldsymbol{\partial} x^j} = \mathbf{d}x^i \otimes \frac{\boldsymbol{\partial}}{\boldsymbol{\partial} x^i} . \tag{A.5.10}$$

The *fourth-order symmetric identity tensor* or *symmetrizer* $\mathbf{1}_{\mathcal{M}}$, with components

$$\mathbf{1}_{ij}{}^{kl} \stackrel{\text{def}}{=} \frac{1}{2}\left(\delta_i{}^k\, \delta_j{}^l + \delta_i{}^l\, \delta_j{}^k\right) , \tag{A.5.11}$$

is often used in constitutive theory. It yields the symmetric part $\operatorname{Sym}(\boldsymbol{T}) \stackrel{\text{def}}{=} \mathbf{1}_{\mathcal{M}} : \boldsymbol{T}$ of a compatible second-order tensor $\boldsymbol{T} \in T^1_1(\mathcal{M})$. Obviously, $\mathbf{1}_{\mathcal{M}} \neq \boldsymbol{I}_{\mathcal{M}} \otimes \boldsymbol{I}_{\mathcal{M}}$. The *second-order identity two-point tensor over a map* φ is denoted by $\boldsymbol{I}^{\varphi}$.

Tensor indices can be raised by the inverse metric coefficients, and lowered by the metric coefficients. For example, let $\boldsymbol{T} = T^i{}_j \frac{\boldsymbol{\partial}}{\boldsymbol{\partial} x^i} \otimes \mathbf{d}x^j \in T^1_1(\mathcal{M})$, then the *associated tensors of* $\boldsymbol{T}$ are

$$\boldsymbol{T}^{\flat} \stackrel{\text{def}}{=} \boldsymbol{g} \cdot \boldsymbol{T} = g_{ik} T^k{}_j\, \mathbf{d}x^i \otimes \mathbf{d}x^j \qquad \text{and} \qquad \boldsymbol{T}^{\sharp} \stackrel{\text{def}}{=} \boldsymbol{T} \cdot \boldsymbol{g}^{-1} = T^i{}_k g^{kj} \frac{\boldsymbol{\partial}}{\boldsymbol{\partial} x^i} \otimes \frac{\boldsymbol{\partial}}{\boldsymbol{\partial} x^j} . \tag{A.5.12}$$

$^{\flat}$ is called the *index lowering operator*, and $^{\sharp}$ is the *index raising operator*. Note that $\boldsymbol{g} \stackrel{\text{def}}{=} \boldsymbol{g}^{\flat} = (\boldsymbol{I}_{\mathcal{M}})^{\flat}$ and $\boldsymbol{g}^{-1} \stackrel{\text{def}}{=} \boldsymbol{g}^{\sharp} = (\boldsymbol{I}_{\mathcal{M}})^{\sharp}$. The squared tensor $\boldsymbol{T}^2 \in T^1_1(\mathcal{M})$ can be defined through $\boldsymbol{T}^2 \stackrel{\text{def}}{=} \boldsymbol{T}^{\sharp} \cdot \boldsymbol{T}^{\flat}$, its *Frobenius norm* is $\|\boldsymbol{T}\| \stackrel{\text{def}}{=} \sqrt{\operatorname{tr}(\boldsymbol{T}^2)}$, and the trace of $\boldsymbol{T}$ can be written $\operatorname{tr}\boldsymbol{T} \stackrel{\text{def}}{=} \boldsymbol{T}^{\sharp} : \boldsymbol{g}$. Let $\boldsymbol{S} \in T^p_q(\mathcal{M})$, then $\boldsymbol{S}^{\flat} \in T^0_{p+q}(\mathcal{M})$ is the tensor with all indices lowered, and $\boldsymbol{S}^{\sharp} \in T^{p+q}_0(\mathcal{M})$ has all indices raised. Let $f : \mathcal{M} \to \mathbb{R}$ be a real function with differential $\mathbf{d}f$ according to (A.4.12), then

$$\boldsymbol{\nabla} f \stackrel{\text{def}}{=} (\mathbf{d}f)^{\sharp} \tag{A.5.13}$$

is called the *gradient of* f.

Remark A.5.14. Although there is a fundamental difference between the second-order tensors with components $T^i{}_j$ and $T_j{}^i$, respectively, both are regarded as elements $\boldsymbol{T} \in T^1_1(\mathcal{M})$ throughout the text, due to notational brevity. It is usually clear from the context which one of these associated tensors is meant. In the literature, the tensors with components $T^i{}_j$ are sometimes denoted by $\boldsymbol{T}^{\backslash} \in T^1_{\cdot 1}(\mathcal{M})$, and those with components $T_j{}^i$ are regarded as elements $\boldsymbol{T}^{/} \in T^{\cdot 1}_1(\mathcal{M})$. △

Remark A.5.15. As $g_{ij} = \delta_{ij}$ in Cartesian spaces, the distinction of $\boldsymbol{T}$, $\boldsymbol{T}^\sharp$ and $\boldsymbol{T}^\flat$ would be unnecessary. △

The transpose and inverse of a linear transformation have counterparts on differentiable manifolds. The formulas listed next apply for general two-point tensors $\boldsymbol{T}(X) : T_X\mathcal{M} \to T_{\varphi(X)}\mathcal{N}$ over diffeomorphisms $\varphi : \mathcal{M} \to \mathcal{N}$. However, setting $X = \varphi(X)$ and $\mathcal{N} = \mathcal{M}$ would give the transpose and inverse for ordinary (one-point) tensors. Now let $\boldsymbol{U} \in T_X\mathcal{M}$ and $\boldsymbol{v} \in T_x\mathcal{N}$ be vectors on $\mathcal{M}$ and $\mathcal{N}$, respectively, with $x = \varphi(X)$. The *transpose* of $\boldsymbol{T}$ is the linear map $\boldsymbol{T}^{\mathrm{T}}(x) : T_x(\varphi(\mathcal{M})) \to T_{\varphi^{-1}(x)}\mathcal{M}$ defined through

$$\langle \boldsymbol{v}, \boldsymbol{T}(\boldsymbol{U}) \rangle_x \stackrel{\text{def}}{=} \left\langle \boldsymbol{T}^{\mathrm{T}}(\boldsymbol{v}), \boldsymbol{U} \right\rangle_X . \tag{A.5.16}$$

The components of $\boldsymbol{T}^{\mathrm{T}}$ at $x \in \mathcal{N}$ with respect to the bases $\left\{\frac{\partial}{\partial X^I}\right\} \in T_X\mathcal{M}$ and $\left\{\frac{\partial}{\partial x^i}\right\} \in T_x\mathcal{N}$ are

$$(\boldsymbol{T}^{\mathrm{T}})_i{}^I(x) = g_{ij}(x)\, T^j{}_J(\varphi^{-1}(x))\, G^{IJ}(\varphi^{-1}(x)) , \tag{A.5.17}$$

where $g_{ij}(x)$ are the metric coefficients —provided that they exist— on $\mathcal{N}$, and $G^{IJ}(X)$ are the coefficients of the inverse metric on $\mathcal{M}$ (see [Marsden and Hughes, 1994] or [Aubram, 2009] for a proof). With $\boldsymbol{T}$, $\boldsymbol{U}$, and $\boldsymbol{v}$ be as before, the operations

$$\boldsymbol{T}^{-1} \cdot \boldsymbol{T}(\boldsymbol{U}) = \boldsymbol{U} \qquad \text{and} \qquad \boldsymbol{T}^{-\mathrm{T}} \cdot \boldsymbol{T}^{\mathrm{T}}(\boldsymbol{v}) = \boldsymbol{v} \tag{A.5.18}$$

involve the *inverse* $\boldsymbol{T}^{-1}(X)$ and the *inverse transpose* $\boldsymbol{T}^{-\mathrm{T}}(x)$. A two-point tensor $\boldsymbol{T}(X) : T_X\mathcal{M} \to T_{\varphi(X)}\mathcal{N}$ is called *orthogonal* provided that $\boldsymbol{T}^{\mathrm{T}} \cdot \boldsymbol{T} = \boldsymbol{I}_{\mathcal{M}}$ and $\boldsymbol{T} \cdot \boldsymbol{T}^{\mathrm{T}} = \boldsymbol{I}_{\mathcal{N}}$ [cf. Marsden and Hughes, 1994, p. 51]. If $\boldsymbol{T}$ is orthogonal and $\det \boldsymbol{T} = +1$, then $\boldsymbol{T}$ is called *proper orthogonal*.

Recall that a tensor $\boldsymbol{S}(X) : T_X\mathcal{M} \to T_X\mathcal{M}$ is called *symmetric*, if $\boldsymbol{S} = \boldsymbol{S}^{\mathrm{T}}$. Its *deviator* can then be defined through $\boldsymbol{S}_{\mathrm{dev}} \stackrel{\text{def}}{=} \boldsymbol{S} - \frac{1}{3}(\operatorname{tr} \boldsymbol{S})\boldsymbol{I}_{\mathcal{M}}$. For $\dim(\mathcal{N}) = 3$, Cayley-Hamilton's theorem yields

$$\boldsymbol{S}^3 - I_1(\boldsymbol{S})\boldsymbol{S}^2 + I_2(\boldsymbol{S})\boldsymbol{S} - I_3(\boldsymbol{S})\boldsymbol{I}_{\mathcal{M}} = \boldsymbol{0} , \tag{A.5.19}$$

where I_1, I_2, and I_3 are the *principal invariants of* $\boldsymbol{S}$ given by

$$\begin{aligned} I_1(\boldsymbol{S}) &\stackrel{\text{def}}{=} \operatorname{tr} \boldsymbol{S} , \\ I_2(\boldsymbol{S}) &\stackrel{\text{def}}{=} \det \boldsymbol{S}\, (\operatorname{tr} \boldsymbol{S}^{-1}) = \frac{1}{2}\left((\operatorname{tr} \boldsymbol{S})^2 - \operatorname{tr}(\boldsymbol{S}^2) \right) , \text{ and} \\ I_3(\boldsymbol{S}) &\stackrel{\text{def}}{=} \det \boldsymbol{S} , \end{aligned} \tag{A.5.20}$$

respectively. In fact, $I_1(\boldsymbol{S}) = \tilde{I}_1(\boldsymbol{S}, \boldsymbol{g})$ and $I_2(\boldsymbol{S}) = \tilde{I}_2(\boldsymbol{S}, \boldsymbol{g})$, but the dependency on the metric $\boldsymbol{g}$ on $\mathcal{M}$ has been omitted for notational convenience. $\det(\cdot)$ denotes the determinant operator on $\mathcal{M}$; a geometric definition will be given in Section A.8.

A.6 Tensor Fields and Action of Maps

While the previous section was about tensors at single points, the following is dedicated to distributed tensors on manifolds in order to carry out tensor analysis.

The tangent bundle of $\mathcal{M}$, with $\dim(\mathcal{M}) = n$, has been denoted by $T\mathcal{M}$ but in a more rigorous definition it should be the triplet $(T\mathcal{M}, \tau_{\mathcal{M}}, \mathcal{M})$ including the *projection* $\tau_{\mathcal{M}} : T\mathcal{M} \to \mathcal{M}$. At $X \in \mathcal{M}$ the tangent space $\tau_{\mathcal{M}}^{-1}(X) = T_X\mathcal{M} = \{X\} \times \mathcal{V}_n$ is called *fibre over* X, and the vector space $\mathcal{V}_n$ spanned by the tangent vectors is the *fibre space*. If $(T\mathcal{N}, \tau_{\mathcal{N}}, \mathcal{N})$ is another tangent bundle, then a continuous map $\varphi : \mathcal{M} \to \mathcal{N}$ induces the bundle $\tau'_{\mathcal{N}} : \varphi^\star T\mathcal{N} \to \mathcal{M}$. The restriction of $\varphi^\star T\mathcal{N}$ to $x = \varphi(X) \in \mathcal{N}$ is the tangent space $T_{\varphi(X)}\mathcal{N}$. A *vector field* $\boldsymbol{v}$ *on* $\mathcal{M}$ is identified with a so-called *tangent bundle section*

$$\boldsymbol{v} : \mathcal{M} \to T\mathcal{M}\,, \tag{A.6.1}$$

with $\tau_{\mathcal{M}}(\boldsymbol{v}(X)) = X$, $\forall X \in \mathcal{M}$. A *1-form field* is a section of the cotangent bundle: $\boldsymbol{a}^* : \mathcal{M} \to T^*\mathcal{M}$. The sets of all sections of $T\mathcal{M}$ and $T^*\mathcal{M}$ are denoted by $\Gamma(T\mathcal{M})$ and $\Gamma(T^*\mathcal{M})$, respectively. If some manifold $\mathcal{N}$ has the tangent bundle $T\mathcal{N}$, $\boldsymbol{u} \in \Gamma(T\mathcal{N})$ is a vector field, and $\varphi : \mathcal{M} \to \mathcal{N}$ is continuous, then the related *vector field over* φ is the *induced section* $\varphi^\star\boldsymbol{u} : \mathcal{M} \to T\mathcal{N}$ defined through $(\varphi^\star\boldsymbol{u})(X) \stackrel{\text{def}}{=} \boldsymbol{u}(\varphi(X))$.

To get a local representative of vector fields, choose a chart $(\mathcal{U}, \beta)$ with coordinate functions x^i for a subset $\mathcal{U} \subset \mathcal{M}$. Then

$$\left\{\frac{\boldsymbol{\partial}}{\boldsymbol{\partial} x^1}, \ldots, \frac{\boldsymbol{\partial}}{\boldsymbol{\partial} x^n}\right\} : \quad \mathcal{U} \to T\mathcal{M}|_{\mathcal{U}} \tag{A.6.2}$$

defines the *local basis sections* of $T\mathcal{M}$ restricted to $\mathcal{U}$, and $\{\mathbf{d}x^1, \ldots, \mathbf{d}x^n\} : \mathcal{U} \to T^*\mathcal{M}|_{\mathcal{U}}$ are their duals. Hence, for every fibre $\tau_{\mathcal{M}}^{-1}(X)$ at $X \in \mathcal{U}$, $\boldsymbol{v}(X) = v^i(X)\frac{\boldsymbol{\partial}}{\boldsymbol{\partial} x^i}(X)$ and $\boldsymbol{a}^*(X) = a_i(X)\,\mathbf{d}x^i(X)$, respectively. Continuous differentiability of the vector and 1-form fields requires the mappings $x^i \to v^j(x^i)$ and $x^i \to a_j(x^i)$ on $\beta(\mathcal{U}) \subset \mathbb{R}^n$ to be continuously differentiable.

One may construct tensor fields of any order by tensor-multiplying vector and 1-form fields pointwisely (see Definition A.5.8). For example, if $\boldsymbol{w} \in \Gamma(T\mathcal{M})$ and $\boldsymbol{b}^* \in \Gamma(T^*\mathcal{M})$, a $\binom{1}{1}$-tensor field $\boldsymbol{T}$ would be

$$\boldsymbol{T} \stackrel{\text{def}}{=} (\boldsymbol{w} \otimes \boldsymbol{b}^*) \in \Gamma(T\mathcal{M} \otimes T^*\mathcal{M})\,, \tag{A.6.3}$$

and $(\boldsymbol{w} \otimes \boldsymbol{b}^*)(X) \stackrel{\text{def}}{=} \boldsymbol{w}(X) \otimes \boldsymbol{b}^*(X)$. Thus $\boldsymbol{T}$ is a section of the $\binom{1}{1}$-tensor bundle $T^1_1(\mathcal{M}) = T\mathcal{M} \otimes T^*\mathcal{M} \to \mathcal{M}$. Two-point tensor fields over maps $\varphi : \mathcal{M} \to \mathcal{N}$ are defined analogously by taking into account the sections induced by φ. The set $\Gamma(T^p_q(\mathcal{M}))$ of all continuously differentiable sections of $T^p_q(\mathcal{M})$ is usually written $\mathfrak{T}^p_q(\mathcal{M})$.

For the rest of this section, $\mathcal{M}$ and $\mathcal{N}$ are continuously differentiable manifolds, and $\varphi : \mathcal{M} \to \mathcal{N}$ is a diffeomorphism. Moreover, $(\mathcal{U}, \beta)$ and $(\mathcal{V}, \sigma)$ are charts of $\mathcal{U} \subset \mathcal{M}$ and $\mathcal{V} \subset \mathcal{N}$, respectively, and $\varphi^i(X^I) \stackrel{\text{def}}{=} (x^i \circ \varphi \circ \beta^{-1})(X^I)$ are the coordinates x^i on

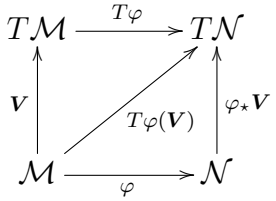

Figure A.1: A differentiable map $\varphi : \mathcal{M} \to \mathcal{N}$ acting on a vector field $\boldsymbol{V} \in \Gamma(T\mathcal{M})$; according to Aubram [2009, fig. 3.4].

$\mathcal{N}$ arising from the coordinates X^I on $\mathcal{U}$ via localization of φ. The differential of φ, given by $T\varphi : T\mathcal{M} \to T\mathcal{N}$, is called the *tangent map over* φ or just the *tangent of* φ. If $\boldsymbol{V} = V^I \frac{\boldsymbol{\partial}}{\boldsymbol{\partial} X^I} \in T_X\mathcal{M}$ is a vector at $X \in \mathcal{M}$, then

$$T\varphi\,(\boldsymbol{V}) = V^I \frac{\partial \varphi^i}{\partial X^I} \frac{\boldsymbol{\partial}}{\boldsymbol{\partial} x^i} = V^I \underbrace{\left(\frac{\partial \varphi^i}{\partial X^J} \frac{\boldsymbol{\partial}}{\boldsymbol{\partial} x^i} \otimes \mathbf{d}X^J \right)}_{\stackrel{\text{def}}{=} \boldsymbol{F}} \cdot \frac{\boldsymbol{\partial}}{\boldsymbol{\partial} X^I} \stackrel{\text{def}}{=} \boldsymbol{F} \cdot \boldsymbol{V} \ \in T_{\varphi(X)}\mathcal{N}\,, \quad \text{(A.6.4)}$$

evaluation at $X \in \mathcal{M}$ being understood. Here $\boldsymbol{F}(X) \in T_{\varphi(X)}\mathcal{N} \otimes T^*_X\mathcal{M}$ is the two-point tensor associated with $T\varphi$.

If $\boldsymbol{V} : \mathcal{M} \to T\mathcal{M}$ is a vector field and not just a vector, then $T\varphi(\boldsymbol{V})$ is a vector field over φ (Fig. A.1). $T\varphi(\boldsymbol{V})$ becomes an honest vector field on $\mathcal{N}$ when the base points are switched. One then refers to

$$\varphi_\star \boldsymbol{V} \stackrel{\text{def}}{=} T\varphi \circ \boldsymbol{V} \circ \varphi^{-1} \quad \text{(A.6.5)}$$

as the *pushforward of* $\boldsymbol{V}$ *by* φ. For a vector field $\boldsymbol{w}$ on $\mathcal{N}$, the *pullback of* $\boldsymbol{w}$ *by* φ is a vector field on $\mathcal{M}$ defined through $\varphi^\star \boldsymbol{w} \stackrel{\text{def}}{=} T(\varphi^{-1}) \circ \boldsymbol{w} \circ \varphi$.

Let $f : \mathcal{M} \to \mathbb{R}$ be a real function resp. scalar field on $\mathcal{M}$, then the pushforward $\varphi_\star f \stackrel{\text{def}}{=} f \circ \varphi^{-1}$ is a scalar field on $\mathcal{N}$, and $\varphi_\star = (\varphi^{-1})^\star$ defines the pullback of a scalar field as the inverse operation. Note that f has the same values at $X \in \mathcal{M}$ as $\varphi_\star f$ has at $x = \varphi(X) \in \mathcal{N}$. For a composition of maps φ and ψ, the chain rule gives

$$(\psi \circ \varphi)^\star = \varphi^\star \circ \psi^\star \qquad \text{and} \qquad (\psi \circ \varphi)_\star = \psi_\star \circ \varphi_\star\,. \quad \text{(A.6.6)}$$

The pullback and pushforward of fields of 1-forms $\boldsymbol{a}^* \in \Gamma(T^*\mathcal{N})$ and $\boldsymbol{B}^* \in \Gamma(T^*\mathcal{M})$ on $\mathcal{N}$ and $\mathcal{M}$, respectively, are being defined according to their action on vector fields:

$$\varphi^\star \boldsymbol{a}^* \stackrel{\text{def}}{=} (\boldsymbol{a}^* \circ \varphi) \cdot T\varphi \qquad \text{and} \qquad \varphi_\star \boldsymbol{B}^* \stackrel{\text{def}}{=} (\boldsymbol{B}^* \circ \varphi^{-1}) \cdot T(\varphi^{-1})\,. \quad \text{(A.6.7)}$$

For arbitrary tensor fields, pushforward and pullback is realized by applying the pushforward and the pullback of vector fields and fields of 1-forms, respectively, to all index slots of the tensor.

Definition A.6.8. Let $\boldsymbol{T} \in \mathfrak{T}^p_q(\mathcal{M})$ and $\boldsymbol{t} \in \mathfrak{T}^p_q(\mathcal{N})$, then

$$\begin{aligned}(\varphi_\star \boldsymbol{T})(x) &\left(\boldsymbol{a}^*_1, \ldots, \boldsymbol{a}^*_p, \boldsymbol{w}_1, \ldots, \boldsymbol{w}_q\right) \\ &\stackrel{\text{def}}{=} \boldsymbol{T}(X)\left((\varphi^\star \boldsymbol{a}^*_1), \ldots, (\varphi^\star \boldsymbol{a}^*_p), (\varphi^\star \boldsymbol{w}_1), \ldots, (\varphi^\star \boldsymbol{w}_q)\right)\,,\end{aligned}$$

and

$$(\varphi^\star \boldsymbol{t})(X)\left(\boldsymbol{B}_1^*,\ldots,\boldsymbol{B}_p^*,\boldsymbol{V}_1,\ldots,\boldsymbol{V}_q\right) \\ \stackrel{\text{def}}{=} \boldsymbol{t}(x)\left((\varphi_\star \boldsymbol{B}_1^*),\ldots,(\varphi_\star \boldsymbol{B}_p^*),(\varphi_\star \boldsymbol{V}_1),\ldots,(\varphi_\star \boldsymbol{V}_q)\right) ,$$

where $X \in \mathcal{M}$ and $x = \varphi(X)$. ◊

Since $\varphi : \mathcal{M} \to \mathcal{N}$ was presumed to be a diffeomorphism one has $\varphi^\star(\boldsymbol{s}\otimes\boldsymbol{t}) = \varphi^\star\boldsymbol{s}\otimes\varphi^\star\boldsymbol{t}$, where $\boldsymbol{s} \in \mathfrak{T}_q^p(\mathcal{N})$ and $\boldsymbol{t} \in \mathfrak{T}_s^r(\mathcal{N})$. Also note that in general pushforward and pullback do not commute with index raising and lowering, i.e. $\varphi_\star(\boldsymbol{T}^\flat) \neq (\varphi_\star \boldsymbol{T})^\flat$ in general.

The objective transformation of vectors defined in Section A.1 can now be generalized as follows:

Definition A.6.9. Let $\mathcal{N}$, $\mathcal{N}'$ be differentiable manifolds, $\boldsymbol{t} \in \mathfrak{T}_q^p(\mathcal{N})$ a tensor field, and $\varphi : \mathcal{N} \to \mathcal{N}'$ a diffeomorphism, then

$$\boldsymbol{t}' \stackrel{\text{def}}{=} \varphi_\star \boldsymbol{t}$$

is called the *objective transformation* of $\boldsymbol{t}$ under the map φ. The tensor $\boldsymbol{t}$ is called *(generally) covariant* under the map φ if $\boldsymbol{t}$ transform objectively under the map φ. ◊

For $\varphi = \mathrm{id}_\mathcal{N}$ one obtains the tensorial transformation law (A.5.5). That is, every tensor field is generally covariant with respect to coordinate transformations resp. *coordinate invariant*.

A.7 Differentiation on Manifolds

Continuum mechanics calls for tensor analysis, as the involved tensor fields generally depend on time and location. However, the ordinary differentials of tensor components do not transform as tensor components, hence avoiding invariant results. Various kinds of differential calculi are available on manifolds which lead to proper, coordinate invariant tensor fields, and each kind is appropriate for special problems. The following section briefly introduces the covariant differentiation and the Lie differentiation.

Definition A.7.1. Let $\mathcal{N}$ be a manifold, $\mathcal{V} \subset \mathcal{N}$, and let $(\mathcal{V},\sigma)$ be a chart with coordinate functions $\sigma(x) = \{x^i\}_x$ at $x \in \mathcal{V}$. Moreover, define the local representatives of a vector field $\boldsymbol{v} \in \Gamma(T\mathcal{N})$ and a 1-form field $\boldsymbol{a}^* \in \Gamma(T^*\mathcal{N})$ at $x \in \mathcal{V}$ through $\boldsymbol{v}(x) \stackrel{\text{def}}{=} v^i(x)\frac{\boldsymbol{\partial}}{\boldsymbol{\partial} x^i}(x)$ and $\boldsymbol{a}^*(x) \stackrel{\text{def}}{=} a_i(x)\,\mathbf{d}x^i(x)$, respectively.

(i) Let $\boldsymbol{v},\boldsymbol{w} \in \Gamma(T\mathcal{N})$ be vector fields, and $\boldsymbol{v}$ continuously differentiable, then $\boldsymbol{\nabla}_{\boldsymbol{w}}\boldsymbol{v} \stackrel{\text{def}}{=} \boldsymbol{\nabla}\boldsymbol{v}(\boldsymbol{w}) \stackrel{\text{def}}{=} \boldsymbol{w}\cdot\boldsymbol{\nabla}\boldsymbol{v} \in \Gamma(T\mathcal{N})$ is called the *covariant derivative* of $\boldsymbol{v}$ along $\boldsymbol{w}$, and $\boldsymbol{\nabla}\boldsymbol{v}$ is called the *covariant derivative* or *gradient* of $\boldsymbol{v}$. In the chart,

$$\boldsymbol{\nabla}_{\boldsymbol{w}}\boldsymbol{v} = \nabla_j v^i w^j \frac{\boldsymbol{\partial}}{\boldsymbol{\partial} x^i} \stackrel{\text{def}}{=} \left(\frac{\partial v^i}{\partial x^j}w^j + v^k w^j \gamma_k{}^i{}_j\right)\frac{\boldsymbol{\partial}}{\boldsymbol{\partial} x^i} .$$

(ii) For $\boldsymbol{a}^* \in \Gamma(T^*\mathcal{N})$ being continuously differentiable the covariant derivative is defined through

$$\boldsymbol{\nabla a}^* \stackrel{\text{def}}{=} \left(\frac{\partial a_i}{\partial x^j} - a_k \gamma_i{}^k{}_j \right) \mathbf{d}x^i \otimes \mathbf{d}x^j \qquad \in \mathfrak{T}_2^0(\mathcal{N}) \; .$$

(iii) The operator $\boldsymbol{\nabla} : \Gamma(T\mathcal{N}) \times \Gamma(T\mathcal{N}) \to \Gamma(T\mathcal{N})$ is referred to as the *connection* on $\mathcal{N}$. The *connection coefficients* $\gamma_k{}^j{}_i$ are called *Christoffel symbols of the second kind* if $\mathcal{N}$ has a metric. If g_{ij} and g^{ij} denote the metric coefficients and the inverse metric coefficients, respectively, then

$$\gamma_i{}^k{}_j = \frac{1}{2} g^{kl} \left(\frac{\partial g_{jl}}{\partial x^i} + \frac{\partial g_{il}}{\partial x^j} - \frac{\partial g_{ij}}{\partial x^l} \right) .$$

Hence, $\gamma_k{}^j{}_i = \gamma_i{}^j{}_k$ and the connection is called *torsion-free*. ◊

Based on the Definitions A.7.1(i) and (ii), the covariant derivative of ordinary $\binom{p}{q}$-tensor fields on $\mathcal{N}$ can be easily constructed. The following fundamental result is due to Bishop and Goldberg [1968, p. 223]. It can be employed to define covariant differentiation for two-point tensor fields and to derive the general ALE operator.

Theorem A.7.2 (Induced Connection). *Let $\mathcal{M}$, $\mathcal{N}$ be differentiable manifolds, $\varphi : \mathcal{M} \to \mathcal{N}$ a diffeomorphism, and $\boldsymbol{w} : \mathcal{N} \to T\mathcal{N}$ differentiable. If $\boldsymbol{\nabla}$ is the connection on $\mathcal{N}$ and $\boldsymbol{V} \in T_X\mathcal{M}$ is a vector at $X \in \mathcal{M}$, then there exists a unique connection $\boldsymbol{\nabla}^\star$ on $\mathcal{M}$ given by*

$$\boldsymbol{\nabla}^\star_{\boldsymbol{V}}(\boldsymbol{w} \circ \varphi) = \boldsymbol{\nabla}_{T\varphi(\boldsymbol{V})} \boldsymbol{w}$$

at every $X \in \mathcal{M}$.

Proof. The theorem involves the vector field over φ that corresponds to $\boldsymbol{w}$, i.e. $(\boldsymbol{w} \circ \varphi) : \mathcal{M} \to T\mathcal{N}$, so one has to take care of the reference points. A down-to-earth proof in local coordinates is carried out here. To this end, let $\mathcal{U}$ be a neighborhood of X, and $x \in \mathcal{V} \subset \mathcal{N}$. In the charts $(\mathcal{U}, \beta)$ and $(\mathcal{V}, \sigma)$, let $\boldsymbol{V}(X) = V^I \frac{\boldsymbol{\partial}}{\boldsymbol{\partial} X^I}$ and $\boldsymbol{w}(x) = w^i \frac{\boldsymbol{\partial}}{\boldsymbol{\partial} x^i}$ be the local representatives of $\boldsymbol{V}$ and $\boldsymbol{w}$, respectively, and let $F^i{}_I(X) = \frac{\partial \varphi^i}{\partial X^I}(X)$ be the components of the tangent map $T\varphi : T\mathcal{M} \to T\mathcal{N}$ at X according to (A.6.4). If $\gamma_j{}^i{}_k(x)$ are the coefficients of $\boldsymbol{\nabla}$, and $x = \varphi(X)$, then by Definition A.7.1 one has

$$\begin{aligned}
\boldsymbol{\nabla}_{T\varphi(\boldsymbol{V})} \boldsymbol{w} &= V^I F^k{}_I \left(\frac{\partial w^i}{\partial x^k} + w^j \gamma_j{}^i{}_k \right) \frac{\boldsymbol{\partial}}{\boldsymbol{\partial} x^i} \\
&= \left(\left(\frac{\partial w^i}{\partial x^k} \circ \varphi \right) F^k{}_I V^I + \left(w^j \circ \varphi \right) V^I \left(\gamma_j{}^i{}_k \circ \varphi \right) F^k{}_I \right) \frac{\boldsymbol{\partial}}{\boldsymbol{\partial} x^i} \\
&= \left(\frac{\partial \left(w^i \circ \varphi \right)}{\partial X^I} V^I + \left(w^j \circ \varphi \right) V^I \gamma_j{}^i{}_I \right) \frac{\boldsymbol{\partial}}{\boldsymbol{\partial} x^i} = \boldsymbol{\nabla}^\star_{\boldsymbol{V}} (\boldsymbol{w} \circ \varphi) \, .
\end{aligned}$$

The coefficients of $\boldsymbol{\nabla}^\star$ are thus given by $\gamma_j{}^i{}_I = (\gamma_j{}^i{}_k \circ \varphi) \, F^k{}_I$ on $\mathcal{M}$. ■

In other words, if $\boldsymbol{\nabla}$ is the connection for honest vector fields on $\mathcal{N}$, then the induced connection $\boldsymbol{\nabla}^\star$ is for the corresponding vector fields over maps $\varphi : \mathcal{M} \to \mathcal{N}$.

The *divergence* of a tensor field $\boldsymbol{t} \in \mathfrak{T}^p_q(\mathcal{N})$ is defined as the contraction of $\boldsymbol{\nabla t}$ on the last contravariant leg. Abstractly, one has

$$\operatorname{div} \boldsymbol{t} \stackrel{\text{def}}{=} \boldsymbol{t} \cdot \boldsymbol{\nabla} \,. \tag{A.7.3}$$

To give some examples, let $\varphi : \mathcal{M} \to \mathcal{N}$ be a diffeomorphism, $\boldsymbol{t}$ be a $\binom{3}{0}$-tensor field, and $\boldsymbol{T}$ a $\left(\begin{smallmatrix}1 & 2\\ 0 & 0\end{smallmatrix}\right)$-two-point tensor field over φ, then

$$(\operatorname{div} \boldsymbol{t})^{ij} \stackrel{\text{def}}{=} \nabla_k \, t^{ijk} \qquad \text{and} \qquad (\operatorname{DIV} \boldsymbol{T})^{iI} \stackrel{\text{def}}{=} \widetilde{\nabla}_J \, T^{iIJ} \,, \tag{A.7.4}$$

where div and DIV denote the divergence operators on $\mathcal{N}$ and $\mathcal{M}$, respectively.

Let $\boldsymbol{t}$ be a tensor field on $\mathcal{N}$ of any order and $\boldsymbol{v} \in \Gamma(T\mathcal{N})$, then the product rule yields

$$\operatorname{div}(\boldsymbol{t} \otimes \boldsymbol{v}) = \boldsymbol{v} \cdot \boldsymbol{\nabla t} + \boldsymbol{t} \operatorname{div} \boldsymbol{v} \,. \tag{A.7.5}$$

For a scalar field $f : \mathbb{R} \to \mathcal{N}$ the formula boils down to

$$\operatorname{div}(f \boldsymbol{v}) = \mathbf{d}f \cdot \boldsymbol{v} + f \operatorname{div} \boldsymbol{v} \,. \tag{A.7.6}$$

A tensor field may change under the action of differentiable maps, e.g. if the manifold $\mathcal{M}$ evolves in time, and the Lie derivative establishes a measure for that change. The evolution of $\mathcal{M}$ can be described by a mapping $\psi_{t,s} : \mathcal{M} \to \mathcal{M}$, where t, s are points in a "time" interval $\mathcal{I} \subset \mathbb{R}$. $\psi_{t,s}$ is also called a *time-dependent flow on* $\mathcal{M}$ provided that

$$\psi_{t,s} \circ \psi_{s,r} = \psi_{t,r} \qquad \text{and} \qquad \psi_{t,t} = \mathrm{id}_{\mathcal{M}} \,. \tag{A.7.7}$$

If $X_s = \psi_{s,s}(X_s) \in \mathcal{M}$ is the starting point at starting time $t = s$, then $X = c(t) = \psi_{t,s}(X_s) = \psi(X_s, s, t)$ is the point at $t = t$, for s, t fixed. Hence, $c : \mathcal{I} \to \mathcal{M}$ is a curve on $\mathcal{M}$ with the initial condition $c(s) = X_s$. Since every curve constitutes a field of tangent vectors (see Sec. A.4), $\psi_{t,s}$ constitutes the time-dependent vector field $\boldsymbol{u} : \mathcal{M} \times \mathcal{I} \to T\mathcal{M}$ through $\boldsymbol{u}(\psi_{t,s}(X_s), t) = \dot{c}(t)$, with $c(s) = X_s$. Conversely, $c(t)$ is called the *unique integral curve* of $\boldsymbol{u}$ starting at X_s at time $t = s$; thus $\boldsymbol{u}$ generates the flow, so $\psi_{t,s}$ needs not to be given explicitly.

Definition A.7.8. The *Lie derivative* of a time-dependent tensor field $\boldsymbol{T}_t \in \mathfrak{T}^p_q(\mathcal{M})$ along a time-dependent vector field $\boldsymbol{u}_t$ on $\mathcal{M}$ is defined by

$$\mathrm{L}_{\boldsymbol{u}} \boldsymbol{T} \stackrel{\text{def}}{=} \psi_{\star t,s} \frac{\mathrm{d}}{\mathrm{d}t} (\psi^\star_{t,s} \boldsymbol{T}_t) \,,$$

where $\psi_{\star t,s}$ and $\psi^\star_{t,s}$ denote the pushforward and pullback concerning the flow $\psi_{t,s}$ associated with $\boldsymbol{u}_t$, respectively. The so-called *autonomous Lie derivative* is then defined by $\pounds_{\boldsymbol{u}} \boldsymbol{T} \stackrel{\text{def}}{=} \mathrm{L}_{\boldsymbol{u}} \boldsymbol{T} - \frac{\partial \boldsymbol{T}}{\partial t}$. Fig. A.2 illustrates the concept. ◊

Important properties of the Lie derivative are $\pounds_{\boldsymbol{u}+\boldsymbol{v}} = \pounds_{\boldsymbol{u}} + \pounds_{\boldsymbol{v}}$, and $\varphi^\star(\pounds_{\boldsymbol{u}} \boldsymbol{T}) = \pounds_{\varphi^\star \boldsymbol{u}} \varphi^\star \boldsymbol{T}$ provided that φ is a diffeomorphism. As pushforward and pullback do not commute with index raising and lowering, the Lie derivative also does not commute with these operations in general, that is, for example, $\mathrm{L}_{\boldsymbol{u}}(\boldsymbol{T}^\flat) \neq (\mathrm{L}_{\boldsymbol{u}} \boldsymbol{T})^\flat$.

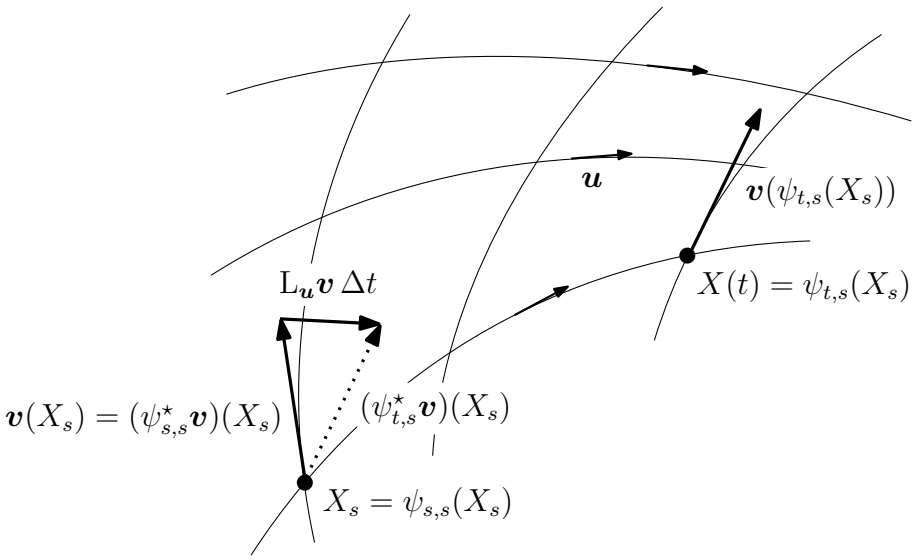

Figure A.2: Lie derivative $\mathrm{L}_{\boldsymbol{u}}\boldsymbol{v}$ of a time-independent vector field $\boldsymbol{v}$ along a time-dependent vector field $\boldsymbol{u}$ generating the flow $\psi_{t,s}$; according to Aubram [2009, fig. 3.5].

A.8 Exterior Calculus and Integration

A.8.1 Differential Forms

From an engineer's viewpoint, probably one of the most exotic fields of modern differential geometry is that of exterior algebra and the related calculus. It is a very complex machinery utilized to get, for example, coordinate-invariant definitions of determinants and integrals. This section gives a rough introduction of those topics frequently applied in continuum mechanics. If not stated otherwise, lower case Greek is used for coordinate indices, and lower case Latin is used for labels.

In exterior calculus, permutation plays a fundamental role. A *permutation* π changes the order of the numbers in a set $\{1, \dots, k\} \subset \mathbb{N}$. The set $\mathit{\Pi}_k$ of all permutations $\{\pi(1), \dots, \pi(k)\}$ has $k!$ elements. Every permutation is composed of even or odd numbers of *transpositions* that interchange only two numbers. The *signature* of the permutation is $\operatorname{sgn}\pi = +1$ for even permutations, and $\operatorname{sgn}\pi = -1$ for odd permutations, so that $\operatorname{sgn}\pi = (-1)^{\nu}$, where ν is the number of transpositions.

Definition A.8.1. Let $\boldsymbol{T}(X) \in T^0_k(\mathcal{M})$ be a $\binom{0}{k}$-tensor at $X \in \mathcal{M}$, then the *alternation mapping* $\operatorname{alt} : T^0_k(\mathcal{M}) \to \bigwedge^k T^*\mathcal{M}$ is defined through

$$\operatorname{alt} \boldsymbol{T}(\boldsymbol{v}_1, \dots, \boldsymbol{v}_k) \stackrel{\text{def}}{=} \frac{1}{k!} \sum_{\pi \in \mathit{\Pi}_k} (\operatorname{sgn}\pi)\, \boldsymbol{T}(\boldsymbol{v}_{\pi(1)}, \dots, \boldsymbol{v}_{\pi(k)})\,,$$

for every $X \in \mathcal{M}$ and $\boldsymbol{v}_1, \dots, \boldsymbol{v}_k \in T_X\mathcal{M}$. Hence, $\bigwedge^k T^*\mathcal{M}$ is a subspace of $T^0_k(\mathcal{M})$, where $\bigwedge^k$ denotes the *k-th exterior power*. The factor $1/k!$ is a convention to avoid double counts. ♢

If $\boldsymbol{S}(X) \in T^0_l(\mathcal{M})$ is another tensor, then define the *wedge product* $(\boldsymbol{T} \wedge \boldsymbol{S}) \in \bigwedge^{k+l} T^*_X\mathcal{M}$ by

$$\boldsymbol{T} \wedge \boldsymbol{S} \stackrel{\text{def}}{=} \frac{(k+l)!}{k!\,l!} \operatorname{alt}(\boldsymbol{T} \otimes \boldsymbol{S}) . \tag{A.8.2}$$

For example, if $\boldsymbol{a}^*, \boldsymbol{b}^* \in T^*_X\mathcal{M}$ are 1-forms, then $\boldsymbol{a}^* \wedge \boldsymbol{b}^* = \boldsymbol{a}^* \otimes \boldsymbol{b}^* - \boldsymbol{b}^* \otimes \boldsymbol{a}^* = -(\boldsymbol{b}^* \otimes \boldsymbol{a}^* - \boldsymbol{a}^* \otimes \boldsymbol{b}^*) = -\boldsymbol{b}^* \wedge \boldsymbol{a}^*$, and $\boldsymbol{a}^* \wedge \boldsymbol{a}^* = 0$.

Definition A.8.3. A *differential k-form* at $X \in \mathcal{M}$, or just *k-form*, is a $\binom{0}{k}$-tensor $\boldsymbol{\omega}(X) \in \bigwedge^k T^*_X\mathcal{M}$ such that $\operatorname{alt} \boldsymbol{\omega} = \boldsymbol{\omega}$. ♢

For a k-form $\boldsymbol{\omega}$ and an l-form $\boldsymbol{\beta}$ the wedge product has the properties $a(\boldsymbol{\omega} \wedge \boldsymbol{\beta}) = a\boldsymbol{\omega} \wedge \boldsymbol{\beta} = \boldsymbol{\omega} \wedge a\boldsymbol{\beta}$, $\forall a \in \mathbb{R}$, and $\boldsymbol{\omega} \wedge \boldsymbol{\beta} = (-1)^{kl}\boldsymbol{\beta} \wedge \boldsymbol{\omega}$.

Let $\mathcal{M}$ be n-dimensional, $X \in \mathcal{U} \subset \mathcal{M}$ a point, and $(\mathcal{U}, \beta)$ a chart with coordinate functions given by $\beta(X) = \{x^\nu\}_X$. Since $\bigwedge^k T^*\mathcal{M} \subset T^0_k(\mathcal{M})$, where $k \leq n$, every k-form $\boldsymbol{\omega}(P)$ is a $\binom{0}{k}$-tensor that has components $\omega_{\nu_1\ldots\nu_k}(X) = \boldsymbol{\omega}\left(\frac{\boldsymbol{\partial}}{\boldsymbol{\partial} x^{\nu_1}}, \ldots, \frac{\boldsymbol{\partial}}{\boldsymbol{\partial} x^{\nu_k}}\right)$ by (A.5.4), and a local representative $\boldsymbol{\omega} = \omega_{\nu_1\ldots\nu_k} \mathbf{d}x^{\nu_1} \otimes \ldots \otimes \mathbf{d}x^{\nu_k}$ by (A.5.9). Note that $\omega_{\nu_1\ldots\nu_k} = 0$ if not all indices are distinct. Therefore,

$$\boldsymbol{\omega}(X) = \sum_{\nu_1 < \ldots < \nu_k} \omega_{\nu_1\ldots\nu_k}(X)\, \mathbf{d}x^{\nu_1} \wedge \ldots \wedge \mathbf{d}x^{\nu_k} , \tag{A.8.4}$$

and $\{\mathbf{d}x^{\nu_1} \wedge \ldots \wedge \mathbf{d}x^{\nu_k}\}$, with $1 \leq \nu_1 < \ldots < \nu_k \leq n$, is a basis of $\bigwedge^k T^*_X\mathcal{M}$.

A field of k-forms is defined as follows. Let $\boldsymbol{\sigma}^* : \mathcal{M} \to T^*\mathcal{M}$ denote the sections of the cotangent bundle $T^*\mathcal{M}$, i.e. the 1-form fields on $\mathcal{M}$, then a *k-form field* is a section of the k-th exterior power of $T^*\mathcal{M}$; clearly,

$$\boldsymbol{\omega} \stackrel{\text{def}}{=} \operatorname{alt}(\boldsymbol{\sigma}^*_1 \otimes \ldots \otimes \boldsymbol{\sigma}^*_k) \in \Gamma(\textstyle\bigwedge^k T^*\mathcal{M}) . \tag{A.8.5}$$

The set of all sections $\Gamma(\bigwedge^k T^*\mathcal{M})$ is denoted by $\Omega^k(\mathcal{M})$. By abuse of language, the term "k-form" will be used for both elements of $\bigwedge^k T^*\mathcal{M}$ and $\Omega^k(\mathcal{M})$.

Let $\boldsymbol{u} \in \Gamma(T\mathcal{M})$ be a vector field and $\boldsymbol{\omega} \in \Omega^k(\mathcal{M})$ a k-form, then the *interior product* is a map $\boldsymbol{i}_{\boldsymbol{u}} : \Omega^k(\mathcal{M}) \to \Omega^{k-1}(\mathcal{M})$ defined through the contraction of $\boldsymbol{u}$ with the first index slot of $\boldsymbol{\omega}$. Hence in local coordinates x^ν,

$$\boldsymbol{i}_{\boldsymbol{u}}\boldsymbol{\omega} \stackrel{\text{def}}{=} \frac{1}{(k-1)!}\, u^\alpha \omega_{\alpha\nu_2\ldots\nu_k} \mathbf{d}x^{\nu_2} \wedge \ldots \wedge \mathbf{d}x^{\nu_k} , \tag{A.8.6}$$

and for $\boldsymbol{v}_2, \ldots, \boldsymbol{v}_k \in \Gamma(T\mathcal{M})$, an alternative definition is $\boldsymbol{i}_{\boldsymbol{u}}\boldsymbol{\omega}(\boldsymbol{v}_2, \ldots, \boldsymbol{v}_k) \stackrel{\text{def}}{=} \boldsymbol{\omega}(\boldsymbol{u}, \boldsymbol{v}_2, \ldots, \boldsymbol{v}_k)$. By Definition A.6.8, it is then easily verified that for a diffeomorphism φ, one has $\varphi^\star(\boldsymbol{i}_{\boldsymbol{u}}\boldsymbol{\omega}) = \boldsymbol{i}_{\varphi^\star \boldsymbol{u}}\varphi^\star\boldsymbol{\omega}$. Also, note that if $\boldsymbol{\omega}$ is a k-form and $\boldsymbol{\beta}$ an l-form, then

$$\boldsymbol{i}_{\boldsymbol{u}}(\boldsymbol{\omega} \wedge \boldsymbol{\beta}) = \boldsymbol{i}_{\boldsymbol{u}}\boldsymbol{\omega} \wedge \boldsymbol{\beta} + (-1)^k \boldsymbol{\omega} \wedge \boldsymbol{i}_{\boldsymbol{u}}\boldsymbol{\beta} . \tag{A.8.7}$$

There is a third type of a calculus of differentiation on manifolds involving the *exterior derivative* $\mathbf{d}$, which is restricted to differential forms. If $\boldsymbol{\omega} \in \Omega^k(\mathcal{M})$ is a k-form, then $\mathbf{d}\boldsymbol{\omega} \in \Omega^{k+1}(\mathcal{M})$ is the $(k+1)$-form given by

$$\mathbf{d}\boldsymbol{\omega} \stackrel{\text{def}}{=} \mathbf{d} \wedge \boldsymbol{\omega} = \frac{1}{k!} \frac{\partial \omega_{\mu_1\ldots\mu_k}}{\partial x^\nu}\, \mathbf{d}x^\nu \wedge \mathbf{d}x^{\mu_1} \wedge \ldots \wedge \mathbf{d}x^{\mu_k} . \tag{A.8.8}$$

The exterior derivative of a 0-form resp. scalar field is its differential, defined in (A.4.12). A k-form $\boldsymbol{\omega}$ is called *exact*, if there exists a $(k-1)$-form $\boldsymbol{\alpha}$ such that $\mathbf{d}\boldsymbol{\alpha} = \boldsymbol{\omega}$, and $\boldsymbol{\omega}$ is called *closed*, if $\mathbf{d}\boldsymbol{\omega} = \mathbf{0}$. By (A.8.4), and the properties of the wedge product, every $(k = n_{\dim})$-form is closed, and for diffeomorphisms φ, one has $\varphi^\star(\mathbf{d}\boldsymbol{\omega}) = \mathbf{d}(\varphi^\star\boldsymbol{\omega})$. Finally, the exterior derivative, the interior product, and the Lie derivative are connected through *Cartan's formula*:

$$\pounds_{\boldsymbol{u}}\boldsymbol{\omega} = \boldsymbol{i}_{\boldsymbol{u}}\mathbf{d}\boldsymbol{\omega} + \mathbf{d}\boldsymbol{i}_{\boldsymbol{u}}\boldsymbol{\omega}\,. \tag{A.8.9}$$

A.8.2 Orientation and Determinants

To define the integral on differentiable manifolds, it needs a more detailed study of the differential n-forms on n-dimensional manifolds $\mathcal{M}$. By (A.8.4), n-forms have a single component. An n-form $\boldsymbol{\mu} \in \Omega^n(\mathcal{M})$ for which $\boldsymbol{\mu}(X) \neq \mathbf{0}$ for all $X \in \mathcal{M}$ is called a *volume form*, and the set of all volume forms on $\mathcal{M}$ is the *volume bundle*. Manifolds with a volume bundle are called *orientable*. Two volume forms $\boldsymbol{\mu}', \boldsymbol{\mu}$ are *equivalent*, if there is some $f(X) > 0$ for all $X \in \mathcal{M}$ such that $\boldsymbol{\mu}' = f\boldsymbol{\mu}$, and the equivalence classes $[\boldsymbol{\mu}]$ and $[-\boldsymbol{\mu}]$ are called the *orientation* and *reverse orientation* on $\mathcal{M}$, respectively. An orientable manifold is an *oriented manifold*, if it has an orientation $[\boldsymbol{\mu}]$ or $[-\boldsymbol{\mu}]$.

Let $(\mathcal{U}, \beta)$ be a chart defining coordinates x^ν, then at $X \in \mathcal{U} \subset \mathcal{M}$, a local representative of $\boldsymbol{\mu} \in \Omega^n(\mathcal{M})$ would be

$$\boldsymbol{\mu}(X) = \mu(X)\,\mathbf{d}x^{\nu_1} \wedge \ldots \wedge \mathbf{d}x^{\nu_n} = f(X)\,\mu(X)\,\mathbf{d}x^1 \wedge \ldots \wedge \mathbf{d}x^n\,. \tag{A.8.10}$$

This follows directly from (A.8.4) and the definition of the equivalence of forms. If $\mathcal{M}$ has the orientation $[\boldsymbol{\mu}]$, then a basis $\left\{\frac{\boldsymbol{\partial}}{\boldsymbol{\partial}x^\nu}\right\} \in T_X\mathcal{M}$ is called *positively* (resp. *negatively*) *oriented* relative to the volume form $\boldsymbol{\mu}$ provided that $\boldsymbol{\mu}(X)\left(\frac{\boldsymbol{\partial}}{\boldsymbol{\partial}x^1}, \ldots, \frac{\boldsymbol{\partial}}{\boldsymbol{\partial}x^n}\right) > 0$ (resp. $<$ 0) for all $X \in \mathcal{U}$. The chart $(\mathcal{U}, \beta)$ is called *positively oriented*, if $f\mu\,\mathbf{d}x^1 \wedge \ldots \wedge \mathbf{d}x^n$ in (A.8.10) is equivalent to the *standard volume form* $\mathrm{d}x^1 \wedge \ldots \wedge \mathrm{d}x^n \in \Omega^n(x(\mathcal{U}))$ on $\mathbb{R}^n$.

The following theorem is a fundamental result that is needed later on; a proof can be found in [Aubram, 2009, p. 56], or in some of the other textbooks already cited.

Theorem A.8.11 (Transformation of n-Forms). *In a chart $(\mathcal{U}, \beta)$ on n-dimensional $\mathcal{M}$, let $\boldsymbol{a}_1(X), \ldots, \boldsymbol{a}_n(X) \in T_X\mathcal{M}$ be a set of vectors with $\boldsymbol{a}_i(X) = a^\nu{}_i(X)\frac{\boldsymbol{\partial}}{\boldsymbol{\partial}x^\nu}$, where $X \in \mathcal{U}$ and $\nu, i \in \{1, \ldots, n\}$. Let $\boldsymbol{\mu} \in \Omega^n(\mathcal{M})$, then*

$$\boldsymbol{\mu}\,(\boldsymbol{a}_1, \ldots, \boldsymbol{a}_n) = \det(a^\nu{}_i)\,\boldsymbol{\mu}\left(\frac{\boldsymbol{\partial}}{\boldsymbol{\partial}x^1}, \ldots, \frac{\boldsymbol{\partial}}{\boldsymbol{\partial}x^n}\right)\,,$$

where $(a^\nu{}_i)$ is the $(n \times n)$-matrix whose columns arrange the components of $\boldsymbol{a}_i$.

By using the theorem, one can obtain a transformation rule for n-forms over diffeomorphisms $\varphi : \mathcal{M} \to \mathcal{N}$. To this end, let $(\mathcal{U}, \beta)$ and $(\mathcal{V}, \sigma)$ be charts on $\mathcal{M}$ and $\mathcal{N}$,

respectively, such that $\varphi^\nu(X^\alpha) \stackrel{\text{def}}{=} (x^\nu \circ \varphi \circ \beta^{-1})(X^\alpha)$ defines the coordinate functions of the localization of φ. If $\boldsymbol{\mu}_\mathcal{N} = \mu\, \mathbf{d}x^1 \wedge \ldots \wedge \mathbf{d}x^n$ is an n-form on $\mathcal{N}$, then

$$\varphi^\star(\mu\, \mathbf{d}x^1 \wedge \ldots \wedge \mathbf{d}x^n) = \det\left(\frac{\partial \varphi^\nu}{\partial X^\alpha}\right)(\mu \circ \varphi)\, \mathbf{d}X^1 \wedge \ldots \wedge \mathbf{d}X^n \tag{A.8.12}$$

at $X \in \varphi^{-1}(\mathcal{V}) \cap \mathcal{U} \subset \mathcal{M}$ with $\beta(X) = \{X^\alpha\}_X$, where $\left(\frac{\partial \varphi^\nu}{\partial X^\alpha}\right)$ is the Jacobian matrix of φ with respect to σ and β. Note that $\det(\frac{\partial \varphi^\nu}{\partial X^\alpha})$ generally does not transform as a proper scalar under coordinate transformations, that is, it is not coordinate-invariant. Eq. (A.8.12) has an expression in absolute notation which enables a coordinate-independent definition of the determinant on manifolds:

Definition A.8.13. Let $\mathcal{M}$ and $\mathcal{N}$ have the volume forms $\boldsymbol{\mu}_\mathcal{M}$ and $\boldsymbol{\mu}_\mathcal{N}$, respectively, and let $\varphi : \mathcal{M} \to \mathcal{N}$ be a diffeomorphism, then $J_{\boldsymbol{\mu}_\mathcal{M}, \boldsymbol{\mu}_\mathcal{N}}\varphi$, defined through

$$\varphi^\star \boldsymbol{\mu}_\mathcal{N} \stackrel{\text{def}}{=} (J_{\boldsymbol{\mu}_\mathcal{M}, \boldsymbol{\mu}_\mathcal{N}}\varphi)\, \boldsymbol{\mu}_\mathcal{M}\,,$$

is called the *Jacobian determinant* of φ with respect to $\boldsymbol{\mu}_\mathcal{M}$ and $\boldsymbol{\mu}_\mathcal{N}$. ♢

A.8.3 Stokes' Theorem and Volume Measures

As n-forms on n-dimensional manifolds have a single component by (A.8.4), they can be integrated over oriented domains. The integral of an n-form $f\, \mathrm{d}x^1 \wedge \ldots \wedge \mathrm{d}x^n \in \Omega^n(\mathcal{X})$ on an open subset $\mathcal{X}$ of $\mathbb{R}^n$ is defined as the ordinary Riemann integral of f; clearly,

$$\int_\mathcal{X} f\, \mathrm{d}x^1 \wedge \ldots \wedge \mathrm{d}x^n \stackrel{\text{def}}{=} \int_\mathcal{X} f\, \mathrm{d}x^1 \ldots \mathrm{d}x^n \stackrel{\text{def}}{=} \int_\mathcal{X} f\,, \tag{A.8.14}$$

where it is understood that $f \stackrel{\text{def}}{=} f(x^1 \ldots x^n)$. Under a coordinate transformation $x^\nu \mapsto x^{\nu'}$ that preserves the orientation, formula (A.8.12) yields $\int_{\mathcal{X}'} f(x')\, \mathrm{d}x^{1'} \ldots \mathrm{d}x^{n'} = \int_\mathcal{X} f(x) \det\left(\frac{\partial x^{\nu'}}{\partial x^\nu}\right) \mathrm{d}x^1 \ldots \mathrm{d}x^n$, but this is a well-known result from the analysis of real functions. On manifolds it can be generalized as follows.

Theorem A.8.15 (Change of Variables). *Let $\mathcal{M}$ be oriented, $\varphi : \mathcal{M} \to \mathcal{N}$ orientation preserving, and $\boldsymbol{\omega} \in \Omega^n(\varphi(\mathcal{M}))$, then*

$$\int \varphi^\star \boldsymbol{\omega} = \int_\varphi \boldsymbol{\omega}\,.$$

Now let $(\mathcal{U}, \beta)$ be a positively oriented chart on $\mathcal{M}$, then by applying the theorem the integral of an n-form $\boldsymbol{\omega} \in \Omega^n(\mathcal{M})$ over $\mathcal{U}$ is computed in coordinates by $\int_\mathcal{U} \boldsymbol{\omega} = \int_{\xi(\mathcal{U})} \omega \circ \beta^{-1}$, where $\omega \circ \beta^{-1}$ represents the component of $\boldsymbol{\omega}$ in the chart.

Stokes's theorem is a fundamental ingredient for balance equations in continuum mechanics. It requires the manifold boundary $\partial\mathcal{M}$ to have an orientation compatible to the orientation of $\mathcal{M}$; a detailed discussion on Stokes's theorem, and a full proof can be found in the references already cited.

Theorem A.8.16 (Stokes' Theorem). *Let $\mathcal{N}$ be oriented with an oriented boundary $\partial\mathcal{N}$, and let $\boldsymbol{\omega}$ be an $(n-1)$-form on $\mathcal{N}$, then*

$$\int_{\mathcal{N}} \mathbf{d}\boldsymbol{\omega} = \int_{\partial\mathcal{N}} \boldsymbol{\omega}\,.$$

A combination of Stokes' theorem, the change of variables formula, and the property $\varphi^\star(\mathbf{d}\boldsymbol{\omega}) = \mathbf{d}(\varphi^\star\boldsymbol{\omega})$ shows that for $\boldsymbol{\omega} \in \Omega^{n-1}(\mathcal{N})$, and an orientation preserving diffeomorphism $\varphi : \mathcal{M} \to \mathcal{N}$,

$$\int_{\varphi(\mathcal{M})} \mathbf{d}\boldsymbol{\omega} = \int_{\mathcal{M}} \varphi^\star(\mathbf{d}\boldsymbol{\omega}) = \int_{\mathcal{M}} \mathbf{d}(\varphi^\star\boldsymbol{\omega}) = \int_{\partial\mathcal{M}} \varphi^\star\boldsymbol{\omega} = \int_{\varphi(\partial\mathcal{M})} \boldsymbol{\omega} = \int_{\partial\varphi(\mathcal{M})} \boldsymbol{\omega}\,, \quad \text{(A.8.17)}$$

that is, $\partial\varphi(\mathcal{M}) = \varphi(\partial\mathcal{M})$.

Note that if $\mathcal{N}$ has a volume form $\boldsymbol{\mu}$, then any n-form $\boldsymbol{\omega} \in \Omega^n(\mathcal{N})$ can be written $\boldsymbol{\omega} = g\,\boldsymbol{\mu}$, where $g : \mathcal{N} \to \mathbb{R}$. Therefore, $m_{\boldsymbol{\mu}}(\mathcal{V}) = \int_{\mathcal{V}} \boldsymbol{\mu}$ defines a *measure* on every open subset $\mathcal{V} \subset \mathcal{N}$. On manifolds having a metric, which are then called Riemannian, volume forms enable volume measurement.

Definition A.8.18. Let $\mathcal{N}$ be an n-dimensional Riemannian manifold with orientation $[\boldsymbol{\mu}]$, and the set $\boldsymbol{w}_1, \ldots, \boldsymbol{w}_n \in \Gamma(T\mathcal{N})$ be positively oriented with respect to $\boldsymbol{\mu}$, then the *Riemannian volume form* or *volume element* $\mathbf{d}\boldsymbol{v} \in \Omega^n(\mathcal{N})$ is defined through $\mathbf{d}\boldsymbol{v}(\boldsymbol{w}_1, \ldots, \boldsymbol{w}_n) \stackrel{\text{def}}{=} \sqrt{\det \langle \boldsymbol{w}_\mu, \boldsymbol{w}_\nu \rangle}$, where $\det\langle \boldsymbol{w}_\mu, \boldsymbol{w}_\nu \rangle$ is the determinant of the matrix $(W_{\mu\nu})$, whose elements are given by the inner products $W_{\mu\nu} \stackrel{\text{def}}{=} \langle \boldsymbol{w}_\mu, \boldsymbol{w}_\nu \rangle$. Therefore, $\mathbf{d}\boldsymbol{v}$ works out the volume of the parallelepiped spanned by the vectors $\boldsymbol{w}_1, \ldots, \boldsymbol{w}_n$. If $\{\boldsymbol{e}_1, \ldots, \boldsymbol{e}_n\}$ is a positively oriented ortho-normalized basis in $T\mathcal{N}$, note that $\mathbf{d}\boldsymbol{v}(\boldsymbol{e}_1, \ldots, \boldsymbol{e}_n) = 1$. ♢

If $\left\{\frac{\partial}{\partial x^1}, \ldots, \frac{\partial}{\partial x^n}\right\} \in T_x\mathcal{N}$ is a positively oriented basis at $x \in \mathcal{V}$, and $g_{\mu\nu}$ the metric coefficients on $\mathcal{N}$, then a local representative of $\mathbf{d}\boldsymbol{v}$ is

$$\mathbf{d}\boldsymbol{v}(x) = \sqrt{\det\, g_{\mu\nu}}\; \mathbf{d}x^1 \wedge \ldots \wedge \mathbf{d}x^n\,. \quad \text{(A.8.19)}$$

Additionally, let $\mathcal{M}$ be orientable, with metric coefficients $G_{\alpha\beta}$, and let $\varphi : \mathcal{M} \to \mathcal{N}$ be a diffeomorphism. If $\mathbf{d}\boldsymbol{V}$ and $\mathbf{d}\boldsymbol{v}$ are the Riemannian volume forms on $\mathcal{M}$ and $\mathcal{N}$, respectively, then

$$\varphi^\star\mathbf{d}\boldsymbol{v} = J_\varphi\, \mathbf{d}\boldsymbol{V}\,. \quad \text{(A.8.20)}$$

J_φ is the Jacobian determinant of φ with respect to $\mathbf{d}\boldsymbol{V}$ and $\mathbf{d}\boldsymbol{v}$ according to the more general definition A.8.13; because of its broad use J_φ is often just called the *Jacobian of* φ. For a positively oriented chart $(\mathcal{U}, \beta)$ on $\mathcal{M}$, with non-empty $\varphi^{-1}(\mathcal{V}) \cap \mathcal{U} \subset \mathcal{M}$, and $\varphi^\nu(X^\alpha) \stackrel{\text{def}}{=} (x^\nu \circ \varphi \circ \beta^{-1})(X^\alpha)$ denoting the coordinate functions associated with the chart $(\mathcal{V}, \sigma)$ concerning φ with respect to the chart map β, one has

$$J_\varphi(X) = \det\left(\frac{\partial\varphi^\nu}{\partial X^\alpha}\right) \frac{\left(\sqrt{\det\, g_{\mu\nu}}\right) \circ \varphi}{\sqrt{\det\, G_{\alpha\beta}}} \quad \text{(A.8.21)}$$

for every $X \in \varphi^{-1}(\mathcal{V}) \cap \mathcal{U}$. Indeed, J_φ transforms under (orientation-preserving) chart transitions as a proper scalar, and $\mathbf{d}\boldsymbol{v}$ and $\mathbf{d}\boldsymbol{V}$ also do, thus (A.8.20) can be reduced to $\mathbf{d}\boldsymbol{v} \circ \varphi = J_\varphi \, \mathbf{d}\boldsymbol{V}$.

Proposition A.8.22. *(Without proof.) If $\boldsymbol{\mu}$ is an n-form on an n-dimensional manifold, e.g. $\boldsymbol{\mu} = \mathbf{d}\boldsymbol{v}$, then $\pounds_{\boldsymbol{u}}\boldsymbol{\mu} = \mathbf{d}(\boldsymbol{i}_{\boldsymbol{u}}\boldsymbol{\mu}) = (\operatorname{div} \boldsymbol{u})\, \boldsymbol{\mu}$.*

Proposition A.8.23. *Let $\mathcal{N}$ be an oriented n-dimensional manifold with compatible oriented boundary $\partial\mathcal{N}$ such that the normals to $\partial\mathcal{N}$, $\boldsymbol{n}^* \in \Gamma(T^*\mathcal{N})$, point outwards. Then for a vector field $\boldsymbol{w} \in \Gamma(T\mathcal{N})$, on $\partial\mathcal{N}$ there is*

$$\boldsymbol{i}_{\boldsymbol{w}}\mathbf{d}\boldsymbol{v} = \boldsymbol{w} \cdot \boldsymbol{n}^* \, \mathbf{d}\boldsymbol{a} \qquad \textit{resp.} \qquad \boldsymbol{i}_{\boldsymbol{w}}\boldsymbol{\mu}_{\mathcal{N}} = \boldsymbol{w} \cdot \boldsymbol{n}^* \, \boldsymbol{\mu}_{\partial\mathcal{N}} \,,$$

where $\mathbf{d}\boldsymbol{a} \stackrel{\text{def}}{=} \mathbf{d}\boldsymbol{v}_{\partial\mathcal{N}}$, called the area form, is the volume form on $(n-1)$-dimensional $\partial\mathcal{N}$ induced by the volume form $\mathbf{d}\boldsymbol{v}$ on $\mathcal{N}$, with $\boldsymbol{n}^* \wedge \mathbf{d}\boldsymbol{a} = \mathbf{d}\boldsymbol{v}$.

Proof. Let $\{x^\nu\}$ be the coordinate system on $\mathcal{N}$ and choose $\partial\mathcal{N}$ to be the plane where $x^1 = 0$, and $\boldsymbol{n}^* = \mathbf{d}x^1$, then $\mathbf{d}\boldsymbol{a} = \sqrt{\det\, g_{ab}}\, \mathbf{d}x^2 \wedge \ldots \wedge \mathbf{d}x^n$, where $a, b = 2, \ldots, n$. Apply (A.8.6) and (A.8.7) to get

$$\begin{aligned} \boldsymbol{i}_{\boldsymbol{w}}\mathbf{d}\boldsymbol{v} &= \boldsymbol{i}_{\boldsymbol{w}}\,(\boldsymbol{n}^* \wedge \mathbf{d}\boldsymbol{a}) = \boldsymbol{i}_{\boldsymbol{w}}\boldsymbol{n}^* \wedge \mathbf{d}\boldsymbol{a} - \boldsymbol{n}^* \wedge \boldsymbol{i}_{\boldsymbol{w}}\mathbf{d}\boldsymbol{a} \\ &= w^1\sqrt{\det\, g_{ab}}\, \mathbf{d}x^2 \wedge \ldots \wedge \mathbf{d}x^n - \mathbf{d}x^1 \wedge \boldsymbol{i}_{\boldsymbol{w}}\sqrt{\det\, g_{ab}}\, \mathbf{d}x^2 \wedge \ldots \wedge \mathbf{d}x^n \,. \end{aligned}$$

Evaluated on $\partial\mathcal{M}$, i.e. at $x^1 = 0 = \text{const.}$, the second term vanishes. Hence, $\boldsymbol{i}_{\boldsymbol{w}}\mathbf{d}\boldsymbol{v} = w^1\sqrt{\det\, g_{ab}}\, \mathbf{d}x^2 \wedge \ldots \wedge \mathbf{d}x^n = (\boldsymbol{w} \cdot \boldsymbol{n}^*)\, \mathbf{d}\boldsymbol{a}$. ∎

Conversely, the boundary $\partial\mathcal{N}$ has an orientation compatible to the orientation of $\mathcal{N}$ provided that $\boldsymbol{i}_{\boldsymbol{w}}\mathbf{d}\boldsymbol{v} = (\boldsymbol{w} \cdot \boldsymbol{n}^*)\, \mathbf{d}\boldsymbol{a}$. By using the previous relations together with Stokes' theorem, the following is proved to hold.

Theorem A.8.24 (Divergence Theorem).

$$\int_{\mathcal{N}} (\operatorname{div} \boldsymbol{w})\, \mathbf{d}\boldsymbol{v} = \int_{\partial\mathcal{N}} \boldsymbol{w} \cdot \boldsymbol{n}^* \, \mathbf{d}\boldsymbol{a} \,.$$

A.8.4 Piola Transform

The chapter closes with two geometric concepts that are of fundamental importance in continuum mechanics: the transformation of area elements and the Piola identity.

Proposition A.8.25 (Nanson's Formula). *Let $\mathcal{M}$ be oriented, and $\varphi : \mathcal{M} \to \mathcal{N}$ an orientation preserving diffeomorphism with tangent $\boldsymbol{F} = T\varphi$. Let $\mathbf{d}\boldsymbol{A}$ and $\mathbf{d}\boldsymbol{a}$ be the volume forms on $\partial\mathcal{M}$ and $\partial(\varphi(\mathcal{M}))$, respectively. Then $\mathbf{d}\boldsymbol{a} = \varphi_\star\mathbf{d}\boldsymbol{A} = \mathbf{d}\boldsymbol{A} \circ \varphi^{-1}$ if and only if the outward normals on $\partial(\varphi(\mathcal{M}))$ and $\partial\mathcal{M}$ are related by*

$$\boldsymbol{n}^* = \varphi_\star(J_\varphi \boldsymbol{N}^*) = (J_\varphi \circ \varphi^{-1})\boldsymbol{F}^{-\mathrm{T}} \cdot (\boldsymbol{N}^* \circ \varphi^{-1}) \,,$$

where J_φ is the Jacobian of φ, and $J_\varphi \boldsymbol{F}^{-\mathrm{T}} \stackrel{\text{def}}{=} \operatorname{cof} \boldsymbol{F}$ is called the cofactor of $\boldsymbol{F}$.

PROOF. The outward normals on $\partial(\varphi(\mathcal{M}))$ are defined as the 1-forms $\boldsymbol{n}^*$ that define the Riemannian volume form on $\varphi(\mathcal{M}) \subset \mathcal{N}$ through $\mathbf{d}\boldsymbol{v} \stackrel{\text{def}}{=} \boldsymbol{n}^* \wedge \mathbf{d}\boldsymbol{a}$, and $\mathbf{d}\boldsymbol{V} \stackrel{\text{def}}{=} \boldsymbol{N}^* \wedge \mathbf{d}\boldsymbol{A}$ on $\mathcal{M}$. By (A.8.20) and the properties of the wedge product,

$$\mathbf{d}\boldsymbol{v} = \varphi_\star(J_\varphi \, \mathbf{d}\boldsymbol{V}) = \varphi_\star(J_\varphi \boldsymbol{N}^*) \wedge \varphi_\star \mathbf{d}\boldsymbol{A} \, .$$

Application of (A.6.7) in conjunction with (A.5.16), and $\mathbf{d}\boldsymbol{a} = \varphi_\star \mathbf{d}\boldsymbol{A}$ presumed then proofs the assertion. ∎

The original statement and proof was prepared in coordinates and is due to Nanson [1878].

Theorem A.8.26 (Transformation of Area Forms). *Let φ, $\mathbf{d}\boldsymbol{a}$, etc., be as before, and let $\boldsymbol{g}^\sharp = \boldsymbol{g}^{-1}$ be the inverse metric tensor on $\mathcal{N}$, with coefficients $g^{\mu\nu}$. If the outward normals $\boldsymbol{n}^*$ on $\partial(\varphi(\mathcal{M}))$ have unit length, then*

$$\varphi^\star \mathbf{d}\boldsymbol{a} = |J_\varphi| \sqrt{\boldsymbol{N}^* \cdot \varphi^\star(\boldsymbol{g}^\sharp) \cdot \boldsymbol{N}^*} \, \mathbf{d}\boldsymbol{A} \, .$$

PROOF. For unit 1-forms $\boldsymbol{n}^*$, Proposition A.8.25 yields $\boldsymbol{n}^* = (J_\varphi \boldsymbol{F}^{-\mathrm{T}} \cdot \boldsymbol{N}^*)/\|J_\varphi \boldsymbol{F}^{-\mathrm{T}} \cdot \boldsymbol{N}^*\|$, and the transformation formula [see also Ciarlet, 1988, p. 39]

$$\varphi^\star \mathbf{d}\boldsymbol{a} = \mathbf{d}\boldsymbol{a} \circ \varphi = \|J_\varphi \boldsymbol{F}^{-\mathrm{T}} \cdot \boldsymbol{N}^*\| \, \mathbf{d}\boldsymbol{A} \, .$$

Now the norm of the spatial 1-form $\boldsymbol{F}^{-\mathrm{T}} \cdot \boldsymbol{N}^*$ complies with the relation

$$\|\boldsymbol{F}^{-\mathrm{T}} \cdot \boldsymbol{N}^*\|^2 = g^{\mu\nu} (\boldsymbol{F}^{-1})_\mu{}^\alpha (\boldsymbol{F}^{-1})_\nu{}^\beta N_\alpha N_\beta = (\boldsymbol{C}^{-1})^{\alpha\beta} N_\alpha N_\beta = \boldsymbol{N}^* \cdot \boldsymbol{C}^{-1} \cdot \boldsymbol{N}^* \, ,$$

where $\boldsymbol{C}$ is the so-called *convected metric tensor*. Then, a consequence of Definition A.6.8 is $(\boldsymbol{C}^{-1})^\sharp = \varphi^\star(\boldsymbol{g}^\sharp)$ [see also Marsden and Hughes, 1994, p. 57], which completes the proof. ∎

Definition A.8.27. Let $\mathcal{M}$, φ etc. be as in proposition A.8.25, then the *Piola transform* of a spatial vector field $\boldsymbol{y} \in \Gamma(T\mathcal{N})$ is the vector field on $\mathcal{M}$ given by $\boldsymbol{Y} \stackrel{\text{def}}{=} J_\varphi \varphi^\star \boldsymbol{y} = J_\varphi \boldsymbol{F}^{-1} \cdot (\boldsymbol{y} \circ \varphi)$. ◇

Note that $\boldsymbol{Y}$ is the Piola transform of $\boldsymbol{y}$ if and only if $\varphi^\star(\boldsymbol{i}_{\boldsymbol{y}} \mathbf{d}\boldsymbol{v}) = \boldsymbol{i}_{\boldsymbol{Y}} \mathbf{d}\boldsymbol{V}$. Moreover, the divergence operators DIV on $\mathcal{M}$, and div on $\mathcal{N}$ are related by the *Piola identity*

$$\mathrm{DIV}\, \boldsymbol{Y} = (\mathrm{div}\, \boldsymbol{y} \circ \varphi) \, J_\varphi \, . \tag{A.8.28}$$

From this, together with the change of variables formula and the divergence theorem, one obtains the next statement on boundary integrals.

Proposition A.8.29. *Let $\boldsymbol{Y}$ be the Piola transform of $\boldsymbol{y}$, then*

$$\int_{\partial\varphi(\mathcal{M})} \boldsymbol{y} \cdot \boldsymbol{n}^* \, \mathbf{d}\boldsymbol{a} = \int_{\varphi(\mathcal{M})} (\mathrm{div}\, \boldsymbol{y}) \, \mathbf{d}\boldsymbol{v} = \int_{\mathcal{M}} (\mathrm{DIV}\, \boldsymbol{Y}) \, \mathbf{d}\boldsymbol{V} = \int_{\partial\mathcal{M}} \boldsymbol{Y} \cdot \boldsymbol{N}^* \, \mathbf{d}\boldsymbol{A}$$

respectively $(\boldsymbol{y} \cdot \boldsymbol{n}^* \, \mathbf{d}\boldsymbol{a}) \circ \varphi = \boldsymbol{Y} \cdot \boldsymbol{N}^* \, \mathbf{d}\boldsymbol{A}$.

Appendix B

Geometric Primitives of Triangles

Definition B.1. Consider a single triangle embedded in the two-dimensional Euclidian space, that is, a 2-simplex $\triangle \subset \mathcal{S} = \mathbb{R}^2$. The local nodes (resp. vertices) of the 2-simplex, $0, 1, 2 \in \triangle$, occupy points in the ambient space, say $P_0, P_1, P_2 \in \mathcal{S}$. In the predefined local connectivity, once the first node 0 has been chosen, the numbers of the other two nodes 1 and 2 are assigned in a counter-clockwise manner, as shown in Fig. B.1.

(i) The *position vectors of the nodes* with respect to the arbitrary origin $O \in \mathcal{S}$ are denoted by the pairs $(O, \boldsymbol{x}_k) \stackrel{\text{def}}{=} (O, \overrightarrow{OP_k}) \in T_O\mathbb{R}^2$, with $k \in \{0, 1, 2\}$. The origin will not be indicated in what follows, so that simply

$$\boldsymbol{x}_k \stackrel{\text{def}}{=} \begin{pmatrix} x_k \\ y_k \end{pmatrix} = x_k\, \boldsymbol{e}_x + y_k\, \boldsymbol{e}_y \quad \in \mathbb{R}^2\,, \qquad \text{for all } k \in \{0, 1, 2\}\,,$$

is the position vector of node k in the ambient space.

(ii) The vectors along the edges of $\triangle$ in $\mathcal{S}$ are given by $\boldsymbol{l}_{jk} = \overrightarrow{P_jP_k} = \boldsymbol{x}_k - \boldsymbol{x}_j$, with $j, k \in \{0, 1, 2\}$. The orientation of these vectors can be chosen such that the boundary path $\partial\triangle$ also runs counter-clockwise (Fig. B.1). The *edge vectors* so defined are

$$\boldsymbol{l}_{01} \stackrel{\text{def}}{=} \boldsymbol{x}_1 - \boldsymbol{x}_0\,, \qquad \boldsymbol{l}_{12} \stackrel{\text{def}}{=} \boldsymbol{x}_2 - \boldsymbol{x}_1\,, \qquad \text{and} \qquad \boldsymbol{l}_{20} \stackrel{\text{def}}{=} \boldsymbol{x}_0 - \boldsymbol{x}_2\,,$$

and the *edge lengths* are

$$a \stackrel{\text{def}}{=} \|\boldsymbol{l}_{01}\| = \|\boldsymbol{l}_{10}\|\,, \qquad b \stackrel{\text{def}}{=} \|\boldsymbol{l}_{12}\| = \|\boldsymbol{l}_{21}\|\,, \qquad \text{and} \qquad c \stackrel{\text{def}}{=} \|\boldsymbol{l}_{20}\| = \|\boldsymbol{l}_{02}\|\,,$$

with

$$\|\boldsymbol{l}_{jk}\| = \sqrt{(x_k - x_j)^2 + (y_k - y_j)^2}\,, \qquad j, k \in \{0, 1, 2\}\,.$$

The lengths of the shortest edge and longest edge are readily available through $l \stackrel{\text{def}}{=} \min(a, b, c)$ and $L \stackrel{\text{def}}{=} \max(a, b, c)$, respectively.

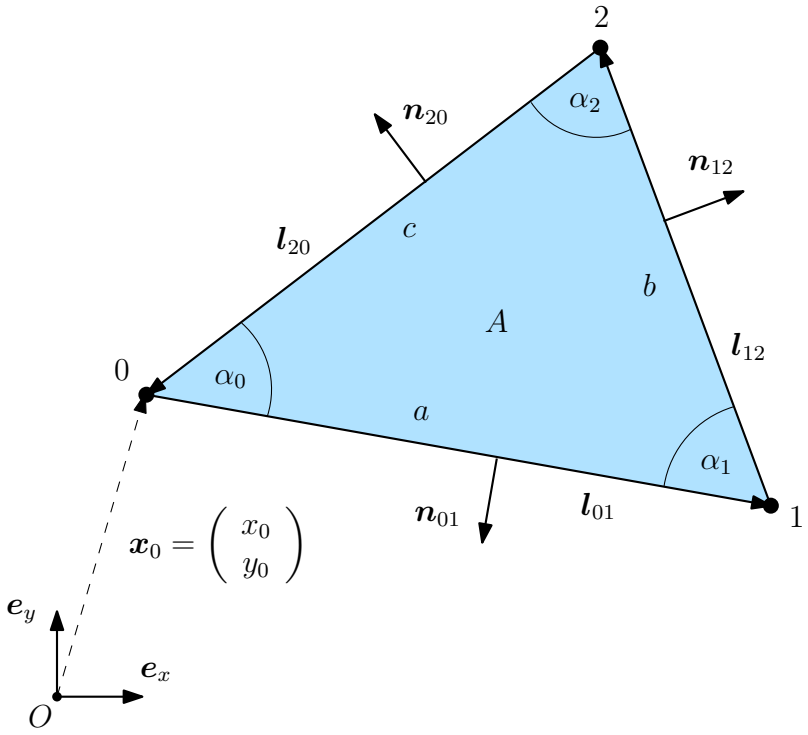

Figure B.1: Triangle element with three nodes in $\mathcal{S} = \mathbb{R}^2$ (2-simplex). Predefined local connectivity and definition of geometric primitives.

(iii) The *outward normals* to the edges $\boldsymbol{l}_{01}$, $\boldsymbol{l}_{12}$, and $\boldsymbol{l}_{20}$ are given by

$$\tilde{\boldsymbol{n}}_{01} = \begin{pmatrix} y_1 - y_0 \\ x_0 - x_1 \end{pmatrix}, \qquad \tilde{\boldsymbol{n}}_{12} = \begin{pmatrix} y_2 - y_1 \\ x_1 - x_2 \end{pmatrix}, \qquad \text{and} \qquad \tilde{\boldsymbol{n}}_{20} = \begin{pmatrix} y_0 - y_2 \\ x_2 - x_0 \end{pmatrix},$$

respectively. The *unit outward normals* are then defined through

$$\boldsymbol{n}_{01} \stackrel{\text{def}}{=} \tilde{\boldsymbol{n}}_{01}/\|\tilde{\boldsymbol{n}}_{01}\|, \qquad \boldsymbol{n}_{12} \stackrel{\text{def}}{=} \tilde{\boldsymbol{n}}_{12}/\|\tilde{\boldsymbol{n}}_{12}\|, \qquad \text{and} \qquad \boldsymbol{n}_{20} \stackrel{\text{def}}{=} \tilde{\boldsymbol{n}}_{20}/\|\tilde{\boldsymbol{n}}_{20}\|.$$

(iv) The *internal angles* α_0, α_1, and α_2 at local nodes 0, 1, and 2, respectively, are defined through

$$\alpha_0 \stackrel{\text{def}}{=} \cos^{-1}\left(\frac{\langle \boldsymbol{l}_{01}, \boldsymbol{l}_{02}\rangle}{ac}\right), \quad \alpha_1 \stackrel{\text{def}}{=} \cos^{-1}\left(\frac{\langle \boldsymbol{l}_{10}, \boldsymbol{l}_{12}\rangle}{ab}\right), \quad \text{and} \quad \alpha_2 \stackrel{\text{def}}{=} \cos^{-1}\left(\frac{\langle \boldsymbol{l}_{21}, \boldsymbol{l}_{20}\rangle}{bc}\right),$$

where $\langle \cdot, \cdot \rangle$ denotes the inner product in $\mathbb{R}^2$. ♢

When using the local connectivity defined above, with $0, 1, 2$ placed counter-clockwise, then the so-called *signed area* of a 2-simplex is positive, otherwise negative. In this context, the following general results are useful.

Proposition B.2. *For a simple (non-self-intersecting) closed convex or non-convex polygon defined by N vertices numbered in order of their occurrence along the polygon's perimeter,*

(i) the signed area A can be calculated from [cf. Barzel, 2005; Akenine-Möller et al., 2008; Schneider and Eberly, 2003; Foley et al., 1995; O'Rourke, 1998; Bronstein et al., 2007]

$$A = \frac{1}{2}\sum_{k=0}^{N-1}(x_k y_{k+1} - x_{k+1}y_k) = \frac{1}{2}\sum_{k=0}^{N-1} x_k(y_{k+1} - y_{k-1})\,.$$

(ii) the centroid (x_c, y_c) is given by [cf. Bashein and Detmer, 1994]

$$x_c = \frac{1}{6A}\sum_{k=0}^{N-1}(x_k + x_{k+1})(x_k y_{k+1} - x_{k+1}y_k) \qquad \textit{and}$$
$$y_c = \frac{1}{6A}\sum_{k=0}^{N-1}(y_k + y_{k+1})(x_k y_{k+1} - x_{k+1}y_k)\,,$$

respectively, where the vertex (x_N, y_N) is assumed to coincide with (x_0, y_0); so $y_{-1} = y_{N-1}$.

These relations are frequently used in finite element methods and ALE methods. In case of a 2-simplex, where $N = 3$, there are equivalent formulas for the area which are well-known from undergraduate texts in geometry [see also Bronstein et al., 2007]:

Proposition B.3. *(i) The signed area of a 2-simplex can be computed from*

$$A = \frac{1}{2!}\det\begin{pmatrix} x_1 - x_0 & x_2 - x_0 \\ y_1 - y_0 & y_2 - y_0 \end{pmatrix}.$$

(ii) The absolute value of the area is given by the absolute value of (i), or by

$$|A| = \frac{1}{2}\|\boldsymbol{l}_{01} \times \boldsymbol{l}_{02}\| = \frac{1}{2}\sum_{k=0}^{2}\|\boldsymbol{x}_k \times \boldsymbol{x}_{k+1}\|\,, \qquad \textit{with} \quad \boldsymbol{x}_3 \stackrel{\text{def}}{=} \boldsymbol{x}_0\,.$$

Let $2A_0 \stackrel{\text{def}}{=} \boldsymbol{l}_{01} \times \boldsymbol{l}_{02}$, $2A_1 \stackrel{\text{def}}{=} \boldsymbol{l}_{10} \times \boldsymbol{l}_{12}$, and $2A_2 \stackrel{\text{def}}{=} \boldsymbol{l}_{21} \times \boldsymbol{l}_{20}$ be different definitions of the same signed area of a triangle, then the sines of the internal angles follow from [cf. Benson, 1989]

$$\sin\alpha_0 = \frac{2A_0}{\|\boldsymbol{l}_{01}\|\|\boldsymbol{l}_{02}\|}\,, \quad \sin\alpha_1 = \frac{2A_1}{\|\boldsymbol{l}_{10}\|\|\boldsymbol{l}_{12}\|}\,, \quad \text{and} \quad \sin\alpha_2 = \frac{2A_2}{\|\boldsymbol{l}_{21}\|\|\boldsymbol{l}_{20}\|}\,. \tag{B.4}$$

The following relations for triangles are valid for any connectivity of the nodes [cf. Bronstein et al., 2007; Harris and Stöcker, 2006; Bronstein et al., 2001]:

$$\text{semiperimeter:} \qquad s = \tfrac{1}{2}(a + b + c)\,, \tag{B.5}$$
$$\text{Heron's formula:} \qquad |A| = \sqrt{s(s-a)(s-b)(s-c)}\,, \tag{B.6}$$
$$\text{incircle radius:} \qquad r = \frac{|A|}{s}\,, \tag{B.7}$$
$$\text{circumcircle radius:} \qquad R = \frac{abc}{4|A|}\,, \tag{B.8}$$
$$\text{altitude on side } b\text{:} \qquad h = \frac{2|A|}{b}\,. \tag{B.9}$$

Appendix C

Gradient and Hessian for Mesh Optimization

C.1 General Remarks

The optimization-based iterative mesh smoothing algorithm OSMOT developed in Section 6.4.3 requires frequent evaluation of the gradient and Hessian of the element objective function w defined through 6.4.37. These depend on the locations $\boldsymbol{x}_0, \boldsymbol{x}_1, \boldsymbol{x}_2 \in \mathbb{R}^2$ of the triangle nodes $0, 1, 2 \in \triangle$, respectively, where $\boldsymbol{x}_I \stackrel{\text{def}}{=} (x_I, y_I)^{\mathrm{T}}$ for $I \in \{0, 1, 2\}$. By assuming that the numbering of the local nodes meets the requirements of Definition 6.4.36, and assuming that $\boldsymbol{x}_1, \boldsymbol{x}_2$ are constant during the iteration process, the element objective function in the j-th iteration takes the form

$$w(\boldsymbol{x}_0^j) = \frac{R}{R_{\text{ref}}} \left(\frac{R}{r}\right)^3 = \frac{(abc)^4 s^3}{4^4 R_{\text{ref}} A^7} \,, \tag{C.1.1}$$

where (B.7) and (B.8) have been used, and the functional dependence of a, b, c, s, A, r, R on $(\boldsymbol{x}_0^j, \boldsymbol{x}_1, \boldsymbol{x}_2)$ is being understood. By dropping the superscribed j indicating the iteration step in what follows, the gradient and Hessian of $w(\boldsymbol{x}_0)$ in $\mathbb{R}^2$ are the component matrices given by

$$\boldsymbol{\nabla} w(\boldsymbol{x}_0) = \begin{pmatrix} \frac{\partial w}{\partial x_0} \\ \frac{\partial w}{\partial y_0} \end{pmatrix} \qquad \text{and} \qquad \boldsymbol{H}_w(\boldsymbol{x}_0) = \begin{pmatrix} \frac{\partial^2 w}{\partial x_0^2} & \frac{\partial^2 w}{\partial x_0 \partial y_0} \\ \frac{\partial^2 w}{\partial y_0 \partial x_0} & \frac{\partial^2 w}{\partial y_0^2} \end{pmatrix} , \tag{C.1.2}$$

respectively. The geometric primitives of 2-simplices provided in Appendix B enable the straightforward calculation of the components of $\boldsymbol{\nabla} w(\boldsymbol{x}_0)$ and $\boldsymbol{H}_w(\boldsymbol{x}_0)$, which is presented next. Note that the derivatives of $b = \sqrt{(x_2 - x_1)^2 + (y_2 - y_1)^2}$ with respect to $\boldsymbol{x}_0$, that is, $\frac{\partial b}{\partial x_0}$, $\frac{\partial b}{\partial y_0}$, $\frac{\partial^2 b}{\partial x_0 \partial y_0}$, etc., identically vanish.

C.2 First Derivatives of Objective Function

$$\frac{\partial w}{\partial x_0} = \frac{1}{4^4 R_{\text{ref}}} \left(\frac{s^3}{A^7} \frac{\partial}{\partial x_0} (abc)^4 + \frac{(abc)^4}{A^7} \frac{\partial}{\partial x_0} s^3 + (abc)^4 s^3 \frac{\partial}{\partial x_0} A^{-7} \right) \tag{C.2.1}$$

$$\frac{\partial w}{\partial y_0} = \frac{1}{4^4 R_{\text{ref}}} \left(\frac{s^3}{A^7} \frac{\partial}{\partial y_0} (abc)^4 + \frac{(abc)^4}{A^7} \frac{\partial}{\partial y_0} s^3 + (abc)^4 s^3 \frac{\partial}{\partial y_0} A^{-7} \right) \tag{C.2.2}$$

C.2.1 Extensions

$$\frac{\partial}{\partial x_0} (abc)^4 = 4b(abc)^3 (cC_{1x} + aC_{2x}) \tag{C.2.3}$$

$$\frac{\partial}{\partial y_0} (abc)^4 = 4b(abc)^3 (cC_{1y} + aC_{2y}) \tag{C.2.4}$$

$$\frac{\partial}{\partial x_0} s^3 = 3s^2 C_{3x} \tag{C.2.5}$$

$$\frac{\partial}{\partial y_0} s^3 = 3s^2 C_{3y} \tag{C.2.6}$$

$$\begin{aligned} \frac{\partial}{\partial x_0} A^{-7} = & -\frac{7}{2A^9} \Big[(2s-b)(s-a)(s-c)C_{3x} \\ & + s(s-b)(s-c)C_{4x} + s(s-a)(s-b)C_{5x} \Big] \end{aligned} \tag{C.2.7}$$

$$\begin{aligned} \frac{\partial}{\partial y_0} A^{-7} = & -\frac{7}{2A^9} \Big[(2s-b)(s-a)(s-c)C_{3y} \\ & + s(s-b)(s-c)C_{4y} + s(s-a)(s-b)C_{5y} \Big] \end{aligned} \tag{C.2.8}$$

$$\frac{\partial A}{\partial x_0} = -\frac{A^8}{7} \frac{\partial}{\partial x_0} A^{-7} \tag{C.2.9}$$

$$\frac{\partial A}{\partial y_0} = -\frac{A^8}{7} \frac{\partial}{\partial y_0} A^{-7} \tag{C.2.10}$$

C.2.2 Abbreviations

$$C_{1x} \stackrel{\text{def}}{=} \frac{\partial a}{\partial x_0} = \frac{\partial}{\partial x_0} \left((x_1 - x_0)^2 + (y_1 - y_0)^2 \right)^{\frac{1}{2}} = -\frac{x_1 - x_0}{a} \tag{C.2.11}$$

$$C_{1y} \stackrel{\text{def}}{=} \frac{\partial a}{\partial y_0} = \frac{\partial}{\partial y_0} \left((x_1 - x_0)^2 + (y_1 - y_0)^2 \right)^{\frac{1}{2}} = -\frac{y_1 - y_0}{a} \tag{C.2.12}$$

$$C_{2x} \stackrel{\text{def}}{=} \frac{\partial c}{\partial x_0} = \frac{\partial}{\partial x_0} \left((x_0 - x_2)^2 + (y_0 - y_2)^2 \right)^{\frac{1}{2}} = \frac{x_0 - x_2}{c} \tag{C.2.13}$$

$$C_{2y} \stackrel{\text{def}}{=} \frac{\partial c}{\partial y_0} = \frac{\partial}{\partial y_0} \left((x_0 - x_2)^2 + (y_0 - y_2)^2 \right)^{\frac{1}{2}} = \frac{y_0 - y_2}{c} \tag{C.2.14}$$

$$C_{3x} \stackrel{\text{def}}{=} \frac{\partial s}{\partial x_0} = \frac{1}{2}\left(\frac{\partial a}{\partial x_0} + \frac{\partial b}{\partial x_0} + \frac{\partial c}{\partial x_0}\right) = \frac{1}{2}(C_{1x} + C_{2x}) \tag{C.2.15}$$

$$C_{3y} \stackrel{\text{def}}{=} \frac{\partial s}{\partial y_0} = \frac{1}{2}\left(\frac{\partial a}{\partial y_0} + \frac{\partial b}{\partial y_0} + \frac{\partial c}{\partial y_0}\right) = \frac{1}{2}(C_{1y} + C_{2y}) \tag{C.2.16}$$

$$C_{4x} \stackrel{\text{def}}{=} \frac{\partial (s-a)}{\partial x_0} = \frac{\partial s}{\partial x_0} - \frac{\partial a}{\partial x_0} = C_{3x} - C_{1x} \tag{C.2.17}$$

$$C_{4y} \stackrel{\text{def}}{=} \frac{\partial (s-a)}{\partial y_0} = \frac{\partial s}{\partial y_0} - \frac{\partial a}{\partial y_0} = C_{3y} - C_{1y} \tag{C.2.18}$$

$$C_{5x} \stackrel{\text{def}}{=} \frac{\partial (s-c)}{\partial x_0} = \frac{\partial s}{\partial x_0} - \frac{\partial c}{\partial x_0} = C_{3x} - C_{2x} \tag{C.2.19}$$

$$C_{5y} \stackrel{\text{def}}{=} \frac{\partial (s-c)}{\partial y_0} = \frac{\partial s}{\partial y_0} - \frac{\partial c}{\partial y_0} = C_{3y} - C_{2y} \tag{C.2.20}$$

C.3 Second Derivatives of Objective Function

$$\begin{aligned}\frac{\partial^2 w}{\partial x_0^2} = \frac{1}{4^4 R_{\text{ref}}}\Bigg(&\frac{s^3}{A^7}\frac{\partial^2}{\partial x_0^2}(abc)^4 + \frac{(abc)^4}{A^7}\frac{\partial^2}{\partial x_0^2}s^3 + s^3(abc)^4\frac{\partial^2}{\partial x_0^2}A^{-7} \\ &+ \frac{2}{A^7}\frac{\partial}{\partial x_0}(abc)^4\frac{\partial}{\partial x_0}s^3 + 2s^3\frac{\partial}{\partial x_0}(abc)^4\frac{\partial}{\partial x_0}A^{-7} \\ &+2(abc)^4\frac{\partial}{\partial x_0}s^3\frac{\partial}{\partial x_0}A^{-7}\Bigg)\end{aligned} \tag{C.3.1}$$

$$\begin{aligned}\frac{\partial^2 w}{\partial y_0^2} = \frac{1}{4^4 R_{\text{ref}}}\Bigg(&\frac{s^3}{A^7}\frac{\partial^2}{\partial y_0^2}(abc)^4 + \frac{(abc)^4}{A^7}\frac{\partial^2}{\partial y_0^2}s^3 + s^3(abc)^4\frac{\partial^2}{\partial y_0^2}A^{-7} \\ &+ \frac{2}{A^7}\frac{\partial}{\partial y_0}(abc)^4\frac{\partial}{\partial y_0}s^3 + 2s^3\frac{\partial}{\partial y_0}(abc)^4\frac{\partial}{\partial y_0}A^{-7} \\ &+2(abc)^4\frac{\partial}{\partial y_0}s^3\frac{\partial}{\partial y_0}A^{-7}\Bigg)\end{aligned} \tag{C.3.2}$$

$$\begin{aligned}\frac{\partial^2 w}{\partial x_0 \partial y_0} = \frac{1}{4^4}\Bigg(&\frac{s^3}{A^7}\frac{\partial^2}{\partial x_0 \partial y_0}(abc)^4 + \frac{1}{A^7}\frac{\partial}{\partial x_0}(abc)^4\frac{\partial}{\partial y_0}s^3 \\ &+ s^3\frac{\partial}{\partial x_0}(abc)^4\frac{\partial}{\partial y_0}A^{-7} + \frac{1}{A^7}\frac{\partial}{\partial y_0}(abc)^4\frac{\partial}{\partial x_0}s^3 \\ &+ \frac{(abc)^4}{A^7}\frac{\partial^2}{\partial x_0 \partial y_0}s^3 + (abc)^4\frac{\partial}{\partial x_0}s^3\frac{\partial}{\partial y_0}A^{-7} \\ &+ s^3\frac{\partial}{\partial y_0}(abc)^4\frac{\partial}{\partial x_0}A^{-7} + (abc)^4\frac{\partial}{\partial y_0}s^3\frac{\partial}{\partial x_0}A^{-7} \\ &+s^3(abc)^4\frac{\partial^2}{\partial x_0 \partial y_0}A^{-7}\Bigg) = \frac{\partial^2 w}{\partial y_0 \partial x_0}\end{aligned} \tag{C.3.3}$$

C.3.1 Extensions

$$\frac{\partial^2}{\partial^2 x_0}(abc)^4 = 12b(abc)^2(cC_{1x} + aC_{2x})^2 + 4b(abc)^3(cD_{1x} + aD_{2x} + 2C_{1x}C_{2x}) \tag{C.3.4}$$

$$\frac{\partial^2}{\partial^2 y_0}(abc)^4 = 12b(abc)^2(cC_{1y} + aC_{2y})^2 + 4b(abc)^3(cD_{1y} + aD_{2y} + 2C_{1y}C_{2y}) \tag{C.3.5}$$

$$\frac{\partial^2}{\partial x_0 \partial y_0}(abc)^4 = 12b(abc)^2(cC_{1x} + aC_{2x})(cC_{1y} + aC_{2y}) + 4b(abc)^3(cE_1 + C_{1x}C_{2y} + C_{1y}C_{2x} + aE_2) \tag{C.3.6}$$

$$\frac{\partial^2}{\partial x_0^2}s^3 = 6sC_{3x}^2 + 3s^2D_{3x} \tag{C.3.7}$$

$$\frac{\partial^2}{\partial y_0^2}s^3 = 6sC_{3y}^2 + 3s^2D_{3y} \tag{C.3.8}$$

$$\frac{\partial^2}{\partial x_0 \partial y_0}s^3 = 6sC_{3x}C_{3y} + 3s^2E_3 \tag{C.3.9}$$

$$\begin{aligned}\frac{\partial^2}{\partial x_0^2}A^{-7} = {} & \frac{63}{A^9}\left(\frac{\partial A}{\partial x_0}\right)^2 \\ & - \frac{7}{2A^9}\Big[(s-a)\{(s-b)(sD_{5x} + (s-c)D_{3x} + 2C_{3x}C_{5x}) \\ & + (s-c)(sD_{3x} + 2C_{3x}^2) + 2sC_{3x}C_{5x}\} \\ & + (s-b)\{(s-c)(sD_{4x} + 2C_{3x}C_{4x}) + 2sC_{4x}C_{5x}\} \\ & + 2s(s-c)C_{3x}C_{4x}\Big]\end{aligned} \tag{C.3.10}$$

$$\begin{aligned}\frac{\partial^2}{\partial y_0^2}A^{-7} = {} & \frac{63}{A^9}\left(\frac{\partial A}{\partial y_0}\right)^2 \\ & - \frac{7}{2A^9}\Big[(s-a)\{(s-b)(sD_{5y} + (s-c)D_{3y} + 2C_{3y}C_{5y}) \\ & + (s-c)(sD_{3y} + 2C_{3y}^2) + 2sC_{3y}C_{5y}\} \\ & + (s-b)\{(s-c)(sD_{4y} + 2C_{3y}C_{4y}) + 2sC_{4y}C_{5y}\} \\ & + 2s(s-c)C_{3y}C_{4y}\Big]\end{aligned} \tag{C.3.11}$$

$$\begin{aligned}\frac{\partial^2}{\partial x_0 \partial y_0}A^{-7} = {} & \frac{63}{A^9}\frac{\partial A}{\partial y_0}\frac{\partial A}{\partial x_0} \\ & - \frac{7}{2A^9}\Big[(s-a)\{(s-b)(C_{3x}C_{5y} + (s-c)E_3 + C_{5x}C_{3y} + sE_5) \\ & + (s-c)(2C_{3x}C_{3y} + sE_3) + s(C_{5x}C_{3y} + C_{3x}C_{5y})\} \\ & + s(s-c)(C_{3x}C_{4y} + C_{4x}C_{3y}) + (s-b)\{s(C_{4x}C_{5y} + C_{5x}C_{4y}) \\ & + (s-c)(C_{3x}C_{4y} + C_{4x}C_{3y} + sE_4)\}\Big]\end{aligned} \tag{C.3.12}$$

C.3.2 Abbreviations

$$D_{1x} \stackrel{\text{def}}{=} \frac{\partial^2 a}{\partial x_0^2} = \frac{\partial}{\partial x_0}\left(-\frac{x_1 - x_0}{a}\right) = \frac{x_1 - x_0}{a^2} C_{1x} + \frac{1}{a} \tag{C.3.13}$$

$$D_{1y} \stackrel{\text{def}}{=} \frac{\partial^2 a}{\partial y_0^2} = \frac{\partial}{\partial y_0}\left(-\frac{y_1 - y_0}{a}\right) = \frac{y_1 - y_0}{a^2} C_{1y} + \frac{1}{a} \tag{C.3.14}$$

$$D_{2x} \stackrel{\text{def}}{=} \frac{\partial^2 c}{\partial x_0^2} = -\frac{x_0 - x_2}{c^2} C_{2x} + \frac{1}{c} \tag{C.3.15}$$

$$D_{2y} \stackrel{\text{def}}{=} \frac{\partial^2 c}{\partial y_0^2} = -\frac{y_0 - y_2}{c^2} C_{2y} + \frac{1}{c} \tag{C.3.16}$$

$$D_{3x} \stackrel{\text{def}}{=} \frac{\partial^2 s}{\partial x_0^2} = \frac{\partial}{\partial x_0}\left(\frac{\partial}{\partial x_0}\frac{a+b+c}{2}\right) = \frac{1}{2}(D_{1x} + D_{2x}) \tag{C.3.17}$$

$$D_{3y} \stackrel{\text{def}}{=} \frac{\partial^2 s}{\partial y_0^2} = \frac{\partial}{\partial y_0}\left(\frac{\partial}{\partial y_0}\frac{a+b+c}{2}\right) = \frac{1}{2}(D_{1y} + D_{2y}) \tag{C.3.18}$$

$$D_{4x} \stackrel{\text{def}}{=} \frac{\partial^2 (s-a)}{\partial x_0^2} = \frac{\partial^2 s}{\partial x_0^2} - \frac{\partial^2 a}{\partial x_0^2} = D_{3x} - D_{1x} \tag{C.3.19}$$

$$D_{4y} \stackrel{\text{def}}{=} \frac{\partial^2 (s-a)}{\partial y_0^2} = \frac{\partial^2 s}{\partial y_0^2} - \frac{\partial^2 a}{\partial y_0^2} = D_{3y} - D_{1y} \tag{C.3.20}$$

$$D_{5x} \stackrel{\text{def}}{=} \frac{\partial^2 (s-c)}{\partial x_0^2} = \frac{\partial^2 s}{\partial x_0^2} - \frac{\partial^2 c}{\partial x_0^2} = D_{3x} - D_{2x} \tag{C.3.21}$$

$$D_{5y} \stackrel{\text{def}}{=} \frac{\partial^2 (s-c)}{\partial y_0^2} = \frac{\partial^2 s}{\partial y_0^2} - \frac{\partial^2 c}{\partial y_0^2} = D_{3y} - D_{2y} \tag{C.3.22}$$

$$E_1 \stackrel{\text{def}}{=} \frac{\partial^2 a}{\partial x_0 \partial y_0} = -\frac{\partial}{\partial y_0}\left(\frac{x_1 - x_0}{a}\right) = -\frac{(x_1 - x_0)(y_1 - y_0)}{a^3} \tag{C.3.23}$$

$$E_2 \stackrel{\text{def}}{=} \frac{\partial^2 c}{\partial x_0 \partial y_0} = \frac{\partial}{\partial y_0}\left(\frac{x_0 - x_2}{c}\right) = -\frac{(x_0 - x_2)(y_0 - y_2)}{c^3} \tag{C.3.24}$$

$$E_3 \stackrel{\text{def}}{=} \frac{\partial^2 s}{\partial x_0 \partial y_0} = \frac{1}{2}\left(\frac{\partial^2 a}{\partial x_0 \partial y_0} + \frac{\partial^2 b}{\partial x_0 \partial y_0} + \frac{\partial^2 c}{\partial x_0 \partial y_0}\right) = \frac{1}{2}(E_1 + E_2) \tag{C.3.25}$$

$$E_4 \stackrel{\text{def}}{=} \frac{\partial^2 (s-a)}{\partial x_0 \partial y_0} = \frac{\partial^2 s}{\partial x_0 \partial y_0} - \frac{\partial^2 a}{\partial x_0 \partial y_0} = E_3 - E_1 \tag{C.3.26}$$

$$E_5 \stackrel{\text{def}}{=} \frac{\partial^2 (s-c)}{\partial x_0 \partial y_0} = \frac{\partial^2 s}{\partial x_0 \partial y_0} - \frac{\partial^2 c}{\partial x_0 \partial y_0} = E_3 - E_2 \tag{C.3.27}$$

Appendix D

Results of Experimental Tests

This appendix provides results of the conducted experimental model tests which have been described in detail in Chapter 7. The results contain conventionally measured load-displacement data as well as incremental soil displacement and strain data for different penetration depths obtained from particle image velocimetry analysis. GeoPIV software has been used for this analysis. The analyzed tests particularly include the shallow penetration tests SP-1 and SP-3 (cf. Tab. 7.2), and the pile penetration tests PP-5-F, PP-7-H, PP-10-C, PP-26-H, PP-27-F, and PP-28-C (cf. Tab. 7.3). Discussion of the test results is in the final section of Chapter 7.

In what follows, z denotes the penetration depth respectively the coordinate of the pile tip on the vertical axis, being zero at the ground surface, B is the breadth of the foundation in case of shallow penetration, and D is the pile diameter. The incremental penetration which causes the incremental displacement and strain fields in the sand shown in the figures, that is, the displacement of the penetrator between two consecutive images, was $\Delta z = 2\,\text{mm}$ in case of the SP tests and $\Delta z = 2.3\,\text{mm}$ in case of the PP tests. The patch size for PIV analysis has been chosen to $32 \times 32\,\text{pixels}$ for the SP tests and to $20 \times 20\,\text{pixels}$ for the PP tests.

Readers should be aware of the sign convention used in GeoPIV. In the figures, volumetric strain is taken positive if it is compressive, which is contrary to the convention used in the rest of this work.

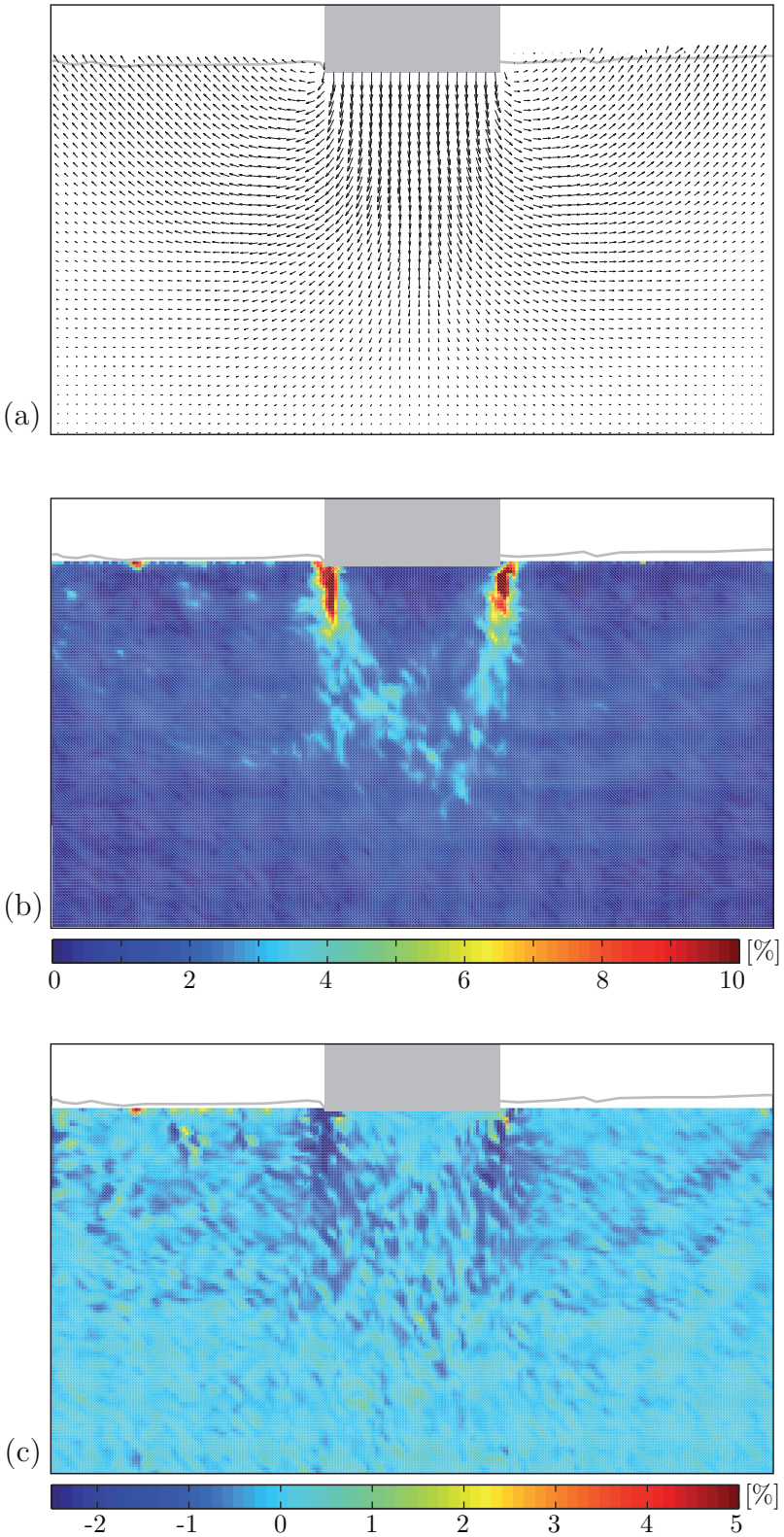

Figure D.1: PIV results for shallow penetration test SP-1 in loose sand ($D_{r0} = 34\,\%$) at $z/B = 0.06$. (a) Incremental displacement scaled up by a factor of 8, (b) incremental maximum shear strain, (c) incremental volumetric strain (positive if compressive).

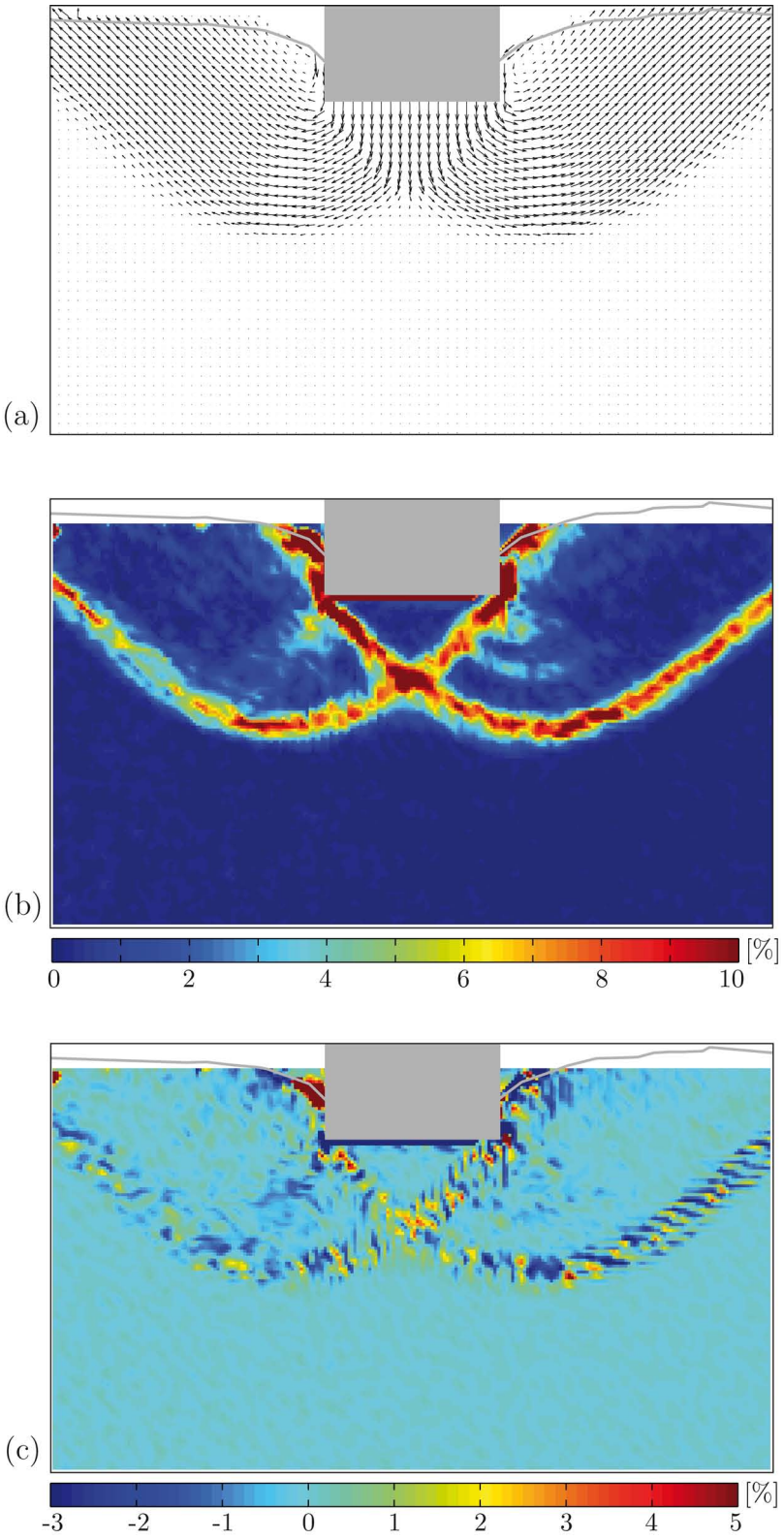

Figure D.2: PIV results for shallow penetration test SP-1 in loose sand ($D_{r0} = 34\,\%$) at $z/B = 0.33$. (a) Incremental displacement scaled up by a factor of 8, (b) incremental maximum shear strain, (c) incremental volumetric strain (positive if compressive).

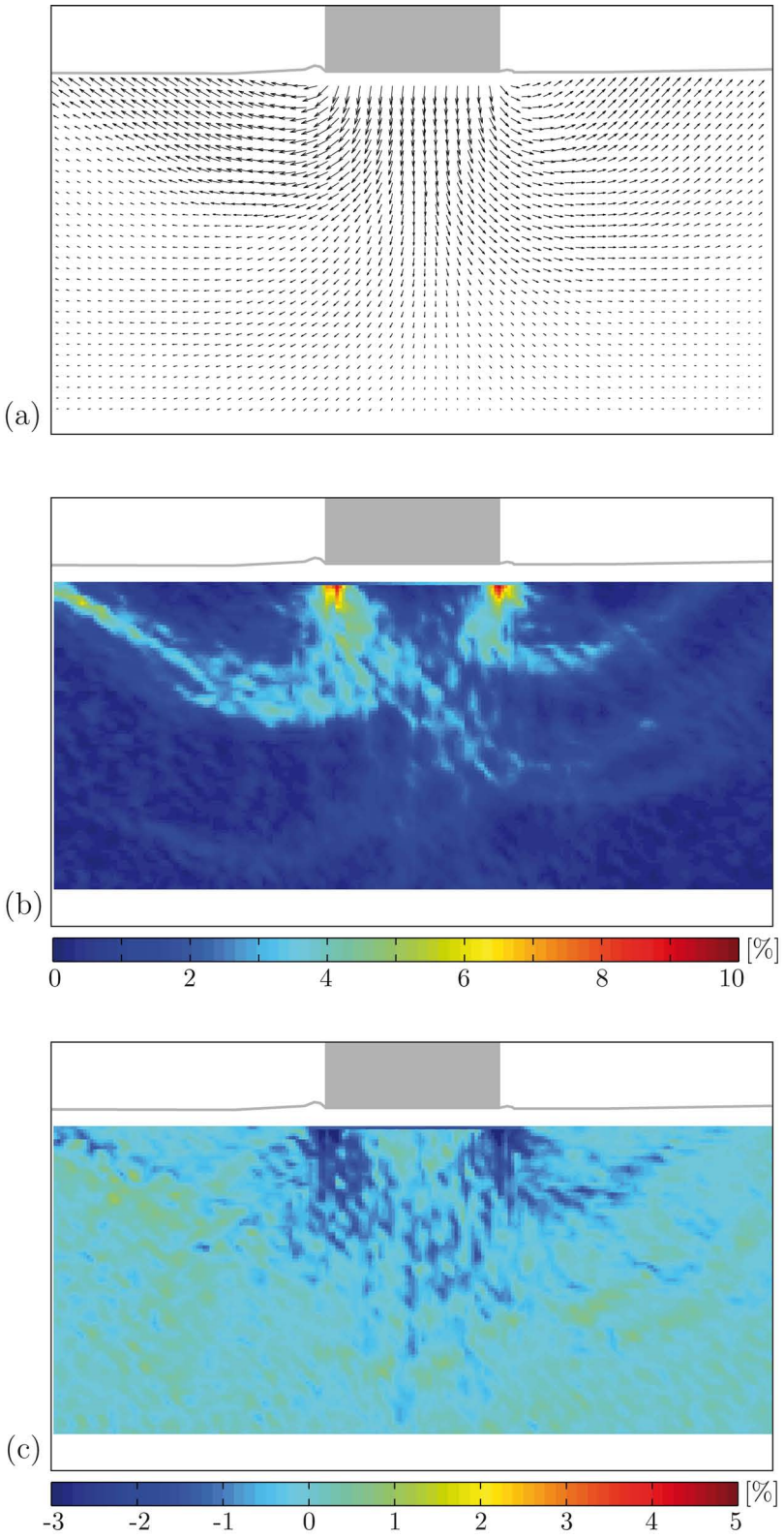

Figure D.3: PIV results for shallow penetration test SP-3 in dense sand ($D_{r0} = 78\,\%$) at $z/B = 0.01$. (a) Incremental displacement scaled up by a factor of 10, (b) incremental maximum shear strain, (c) incremental volumetric strain (positive if compressive).

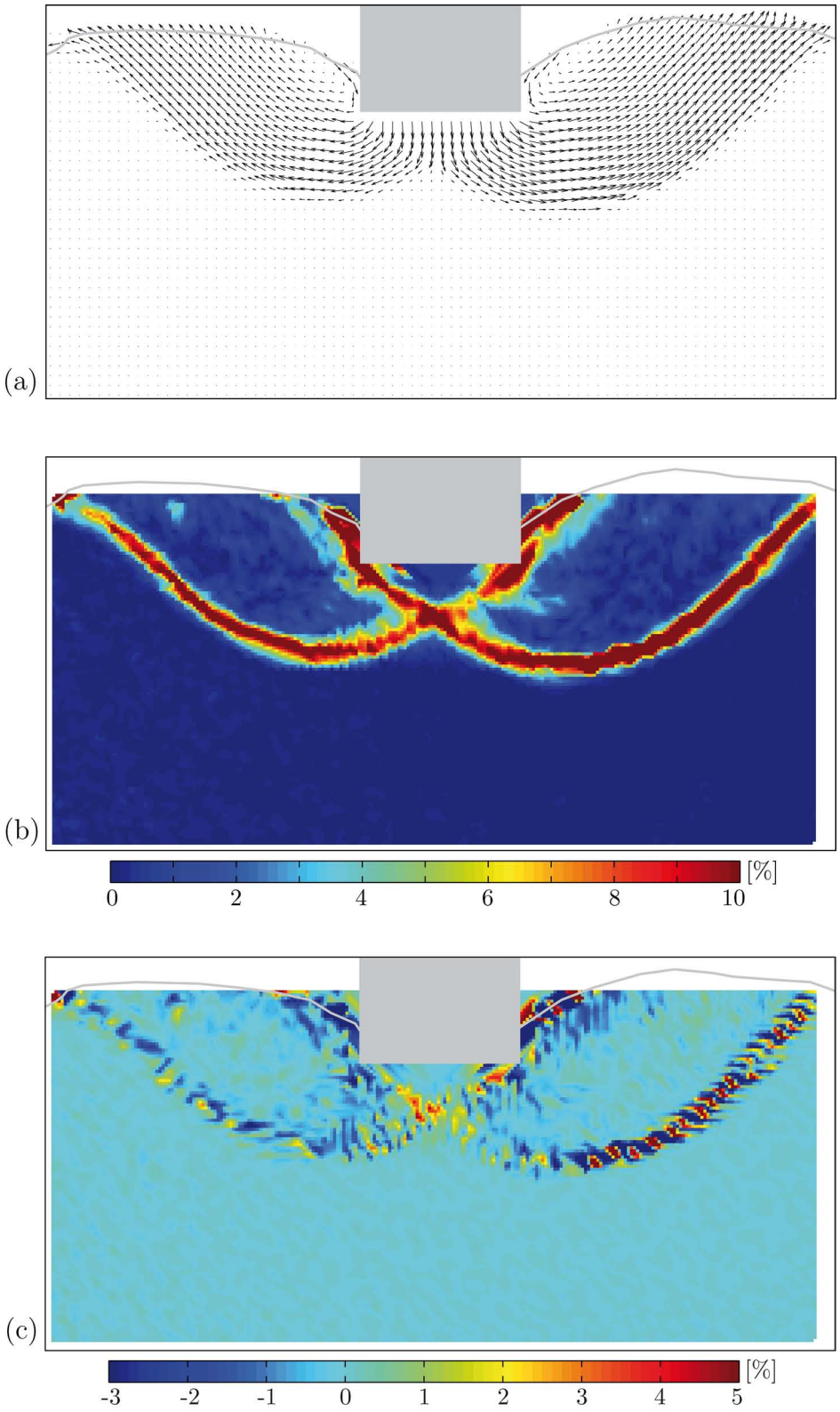

Figure D.4: PIV results for shallow penetration test SP-3 in dense sand ($D_{r0} = 78\,\%$) at $z/B = 0.31$. (a) Incremental displacement scaled up by a factor of 5, (b) incremental maximum shear strain, (c) incremental volumetric strain (positive if compressive).

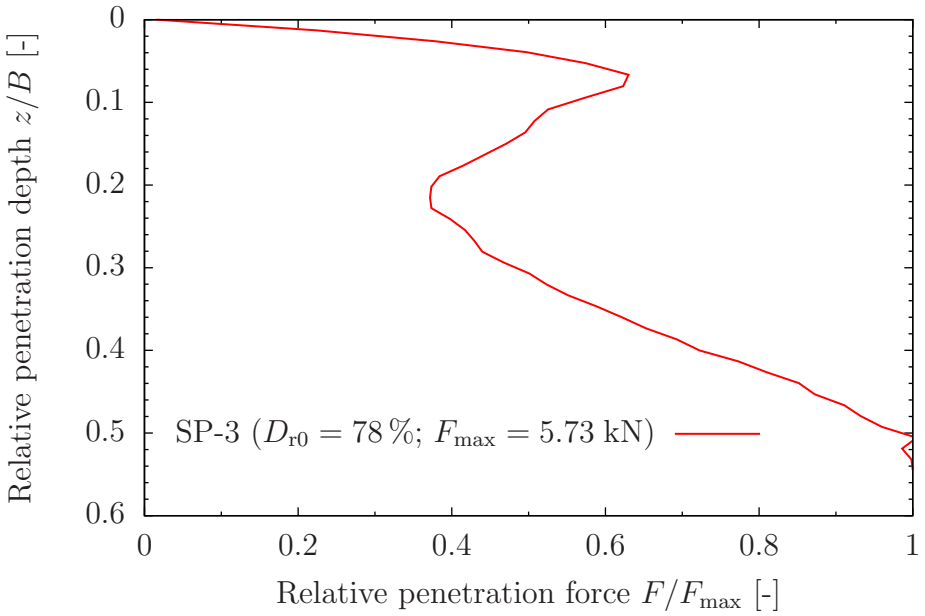

Figure D.5: Measured load-displacement curve of shallow penetration test SP-3.

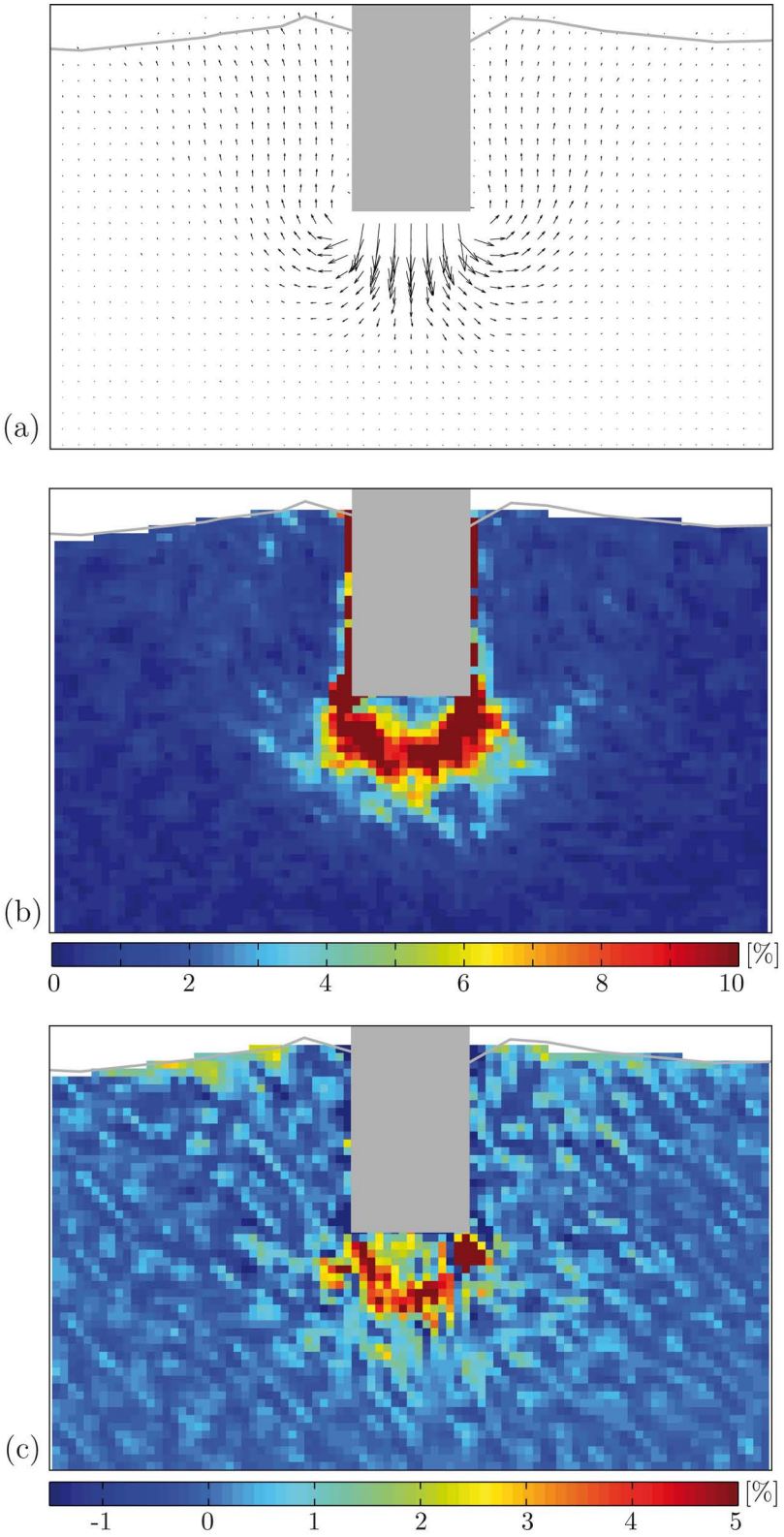

Figure D.6: PIV results for pile penetration test PP-5-F in very dense sand (D_{r0} = 93 %) at z/D = 1.4. (a) Incremental displacement scaled up by a factor of 10, (b) incremental maximum shear strain, (c) incremental volumetric strain (positive if compressive).

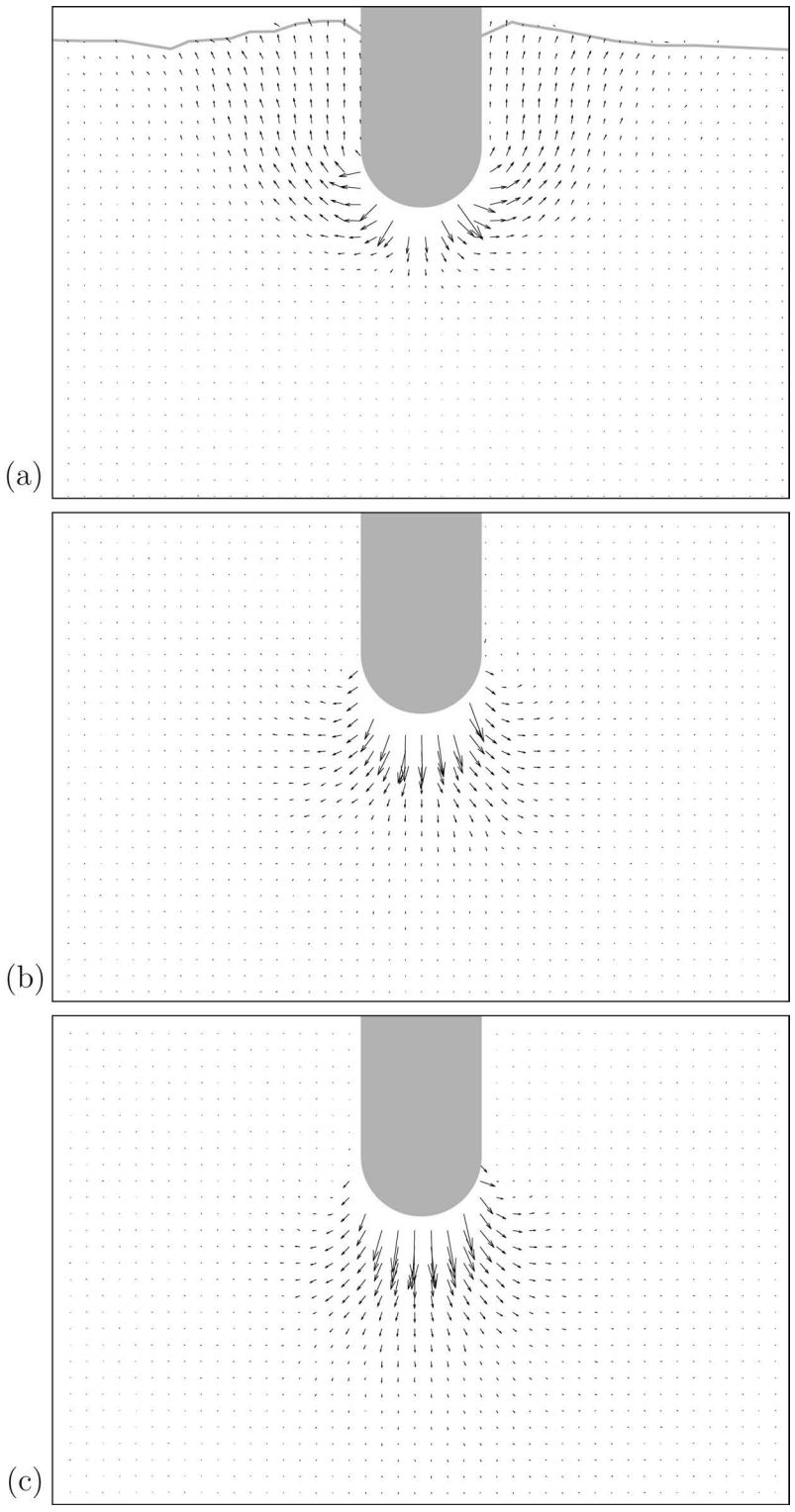

Figure D.7: PIV results for pile penetration test PP-7-H in very dense sand (D_{r0} = 92 %). Incremental displacement scaled up by a factor of 10 (a) at $z/D = 1.5$, (b) at $z/D = 5.1$, (c) at $z/D = 8.8$.

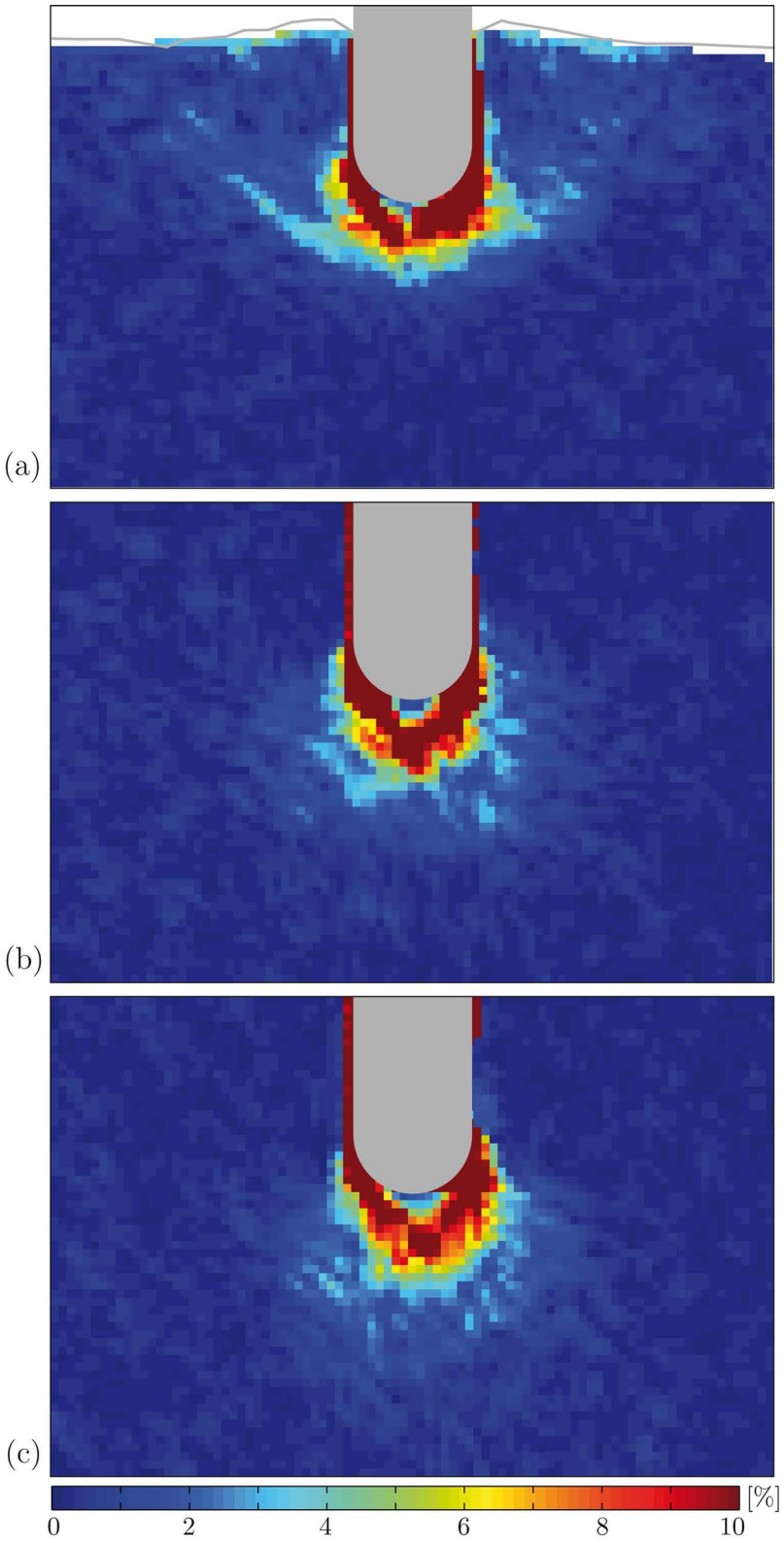

Figure D.8: PIV results for pile penetration test PP-7-H in very dense sand (D_{r0} = 92 %). Incremental maximum shear strain (a) at $z/D = 1.5$, (b) at $z/D = 5.1$, (c) at $z/D = 8.8$.

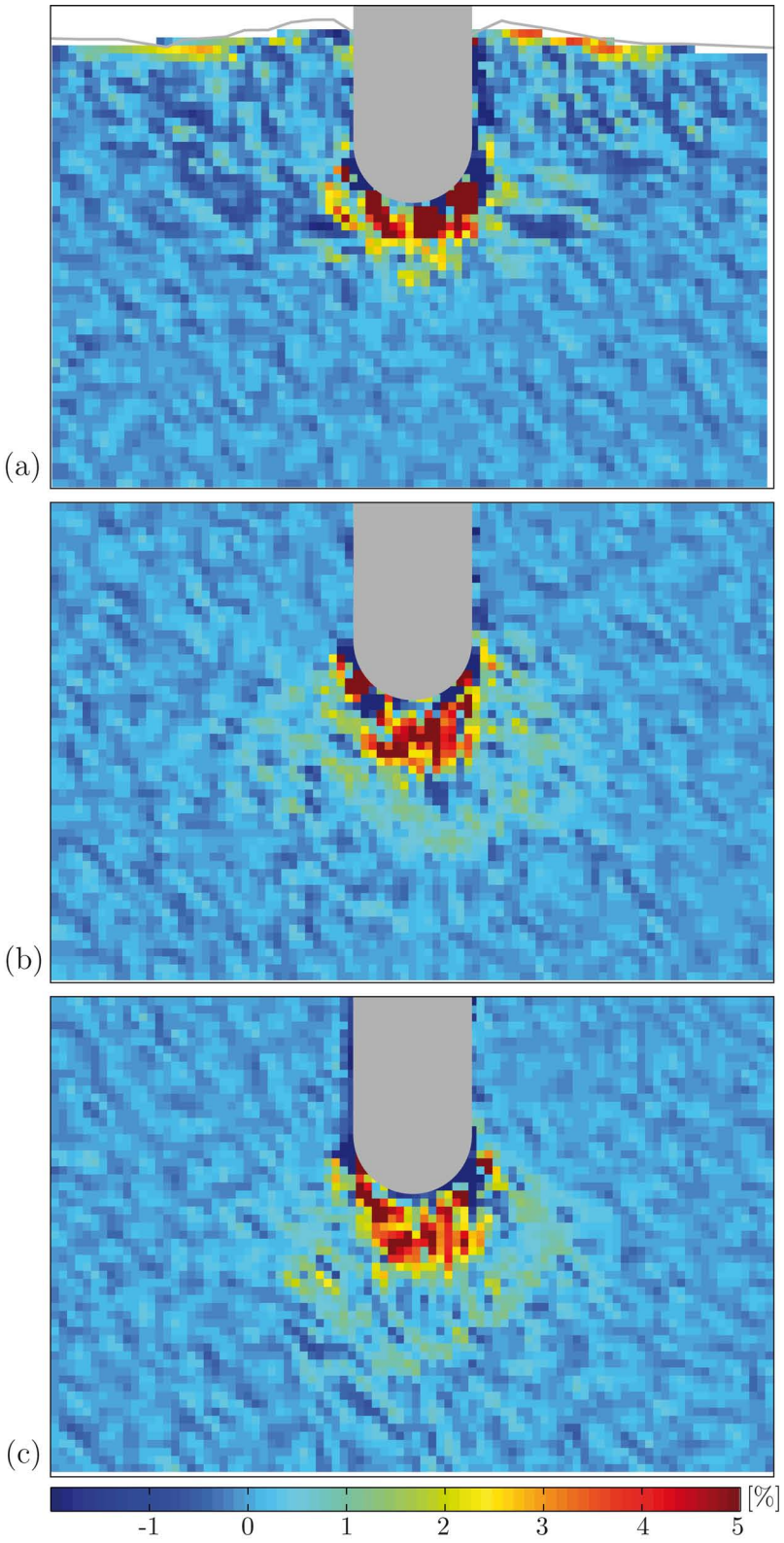

Figure D.9: PIV results for pile penetration test PP-7-H in very dense sand (D_{r0} = 92 %). Incremental volumetric strain (a) at $z/D = 1.5$, (b) at $z/D = 5.1$, (c) at $z/D = 8.8$ (positive if compressive).

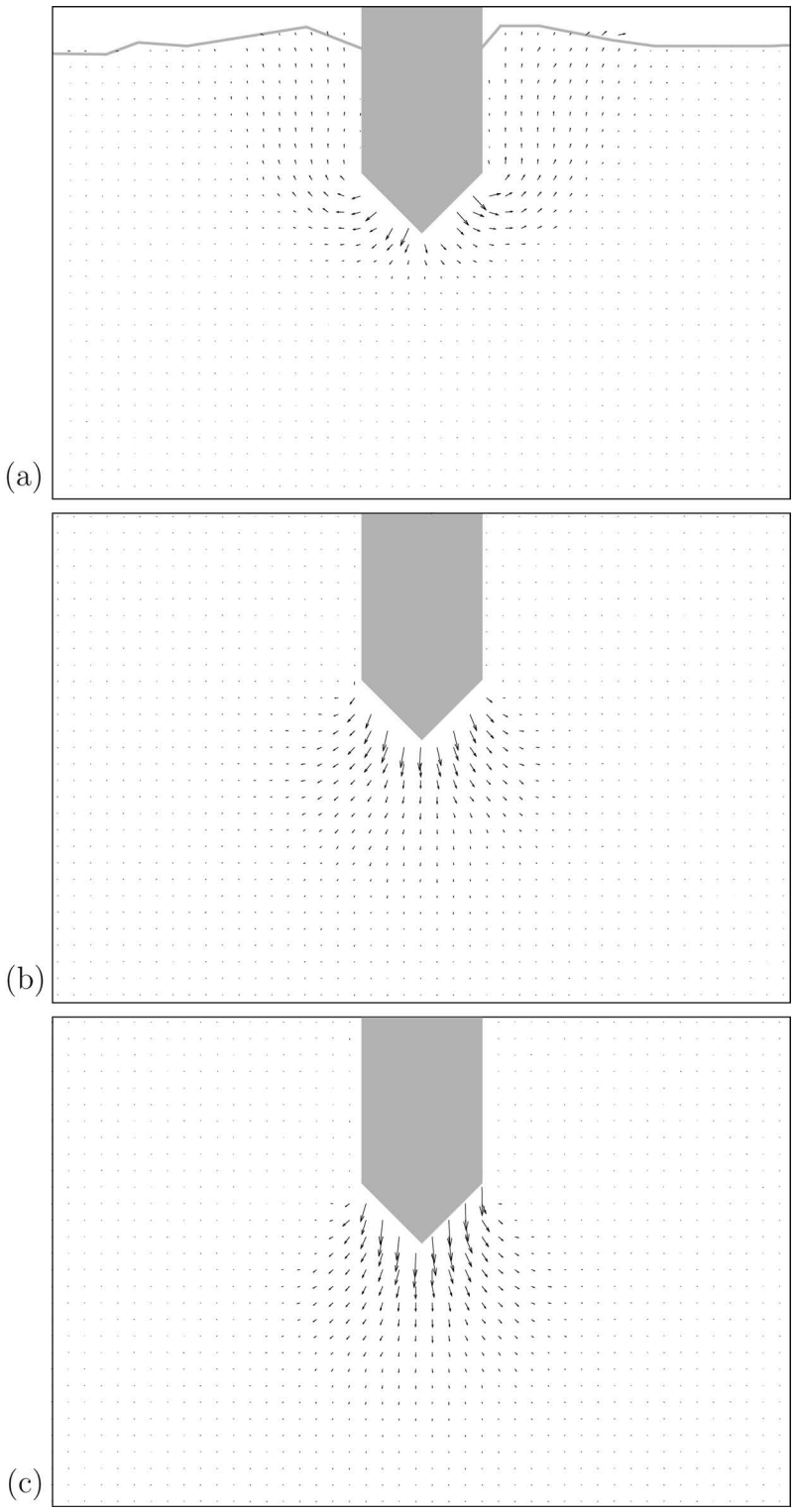

Figure D.10: PIV results for pile penetration test PP-10-C in very dense sand (D_{r0} = 95 %). Incremental displacement scaled up by a factor of 5 (a) at $z/D = 1.5$, (b) at $z/D = 4.8$, (c) at $z/D = 8.3$.

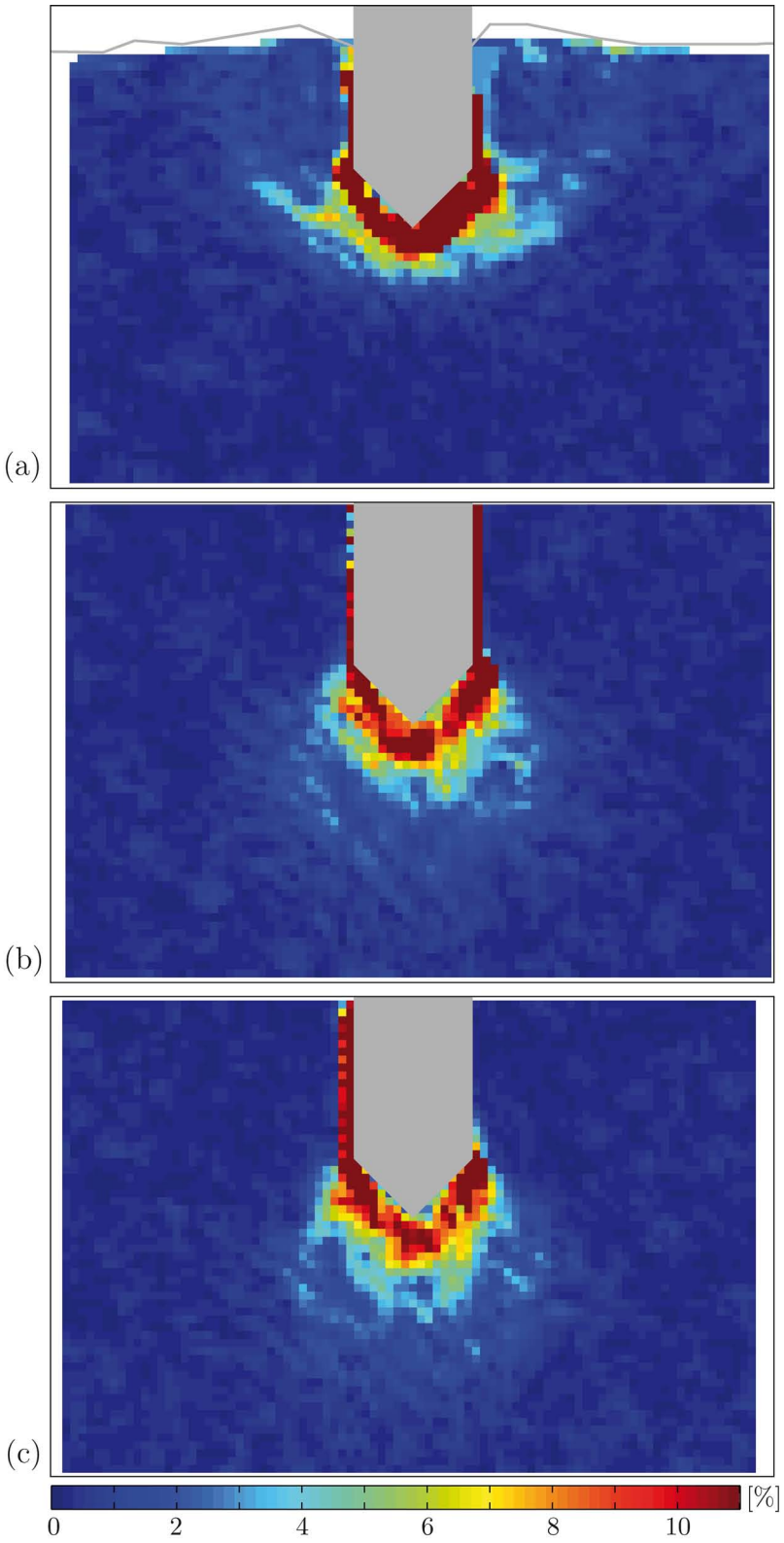

Figure D.11: PIV results for pile penetration test PP-10-C in very dense sand (D_{r0} = 95 %). Incremental maximum shear strain (a) at $z/D = 1.5$, (b) at $z/D = 4.8$, (c) at $z/D = 8.3$.

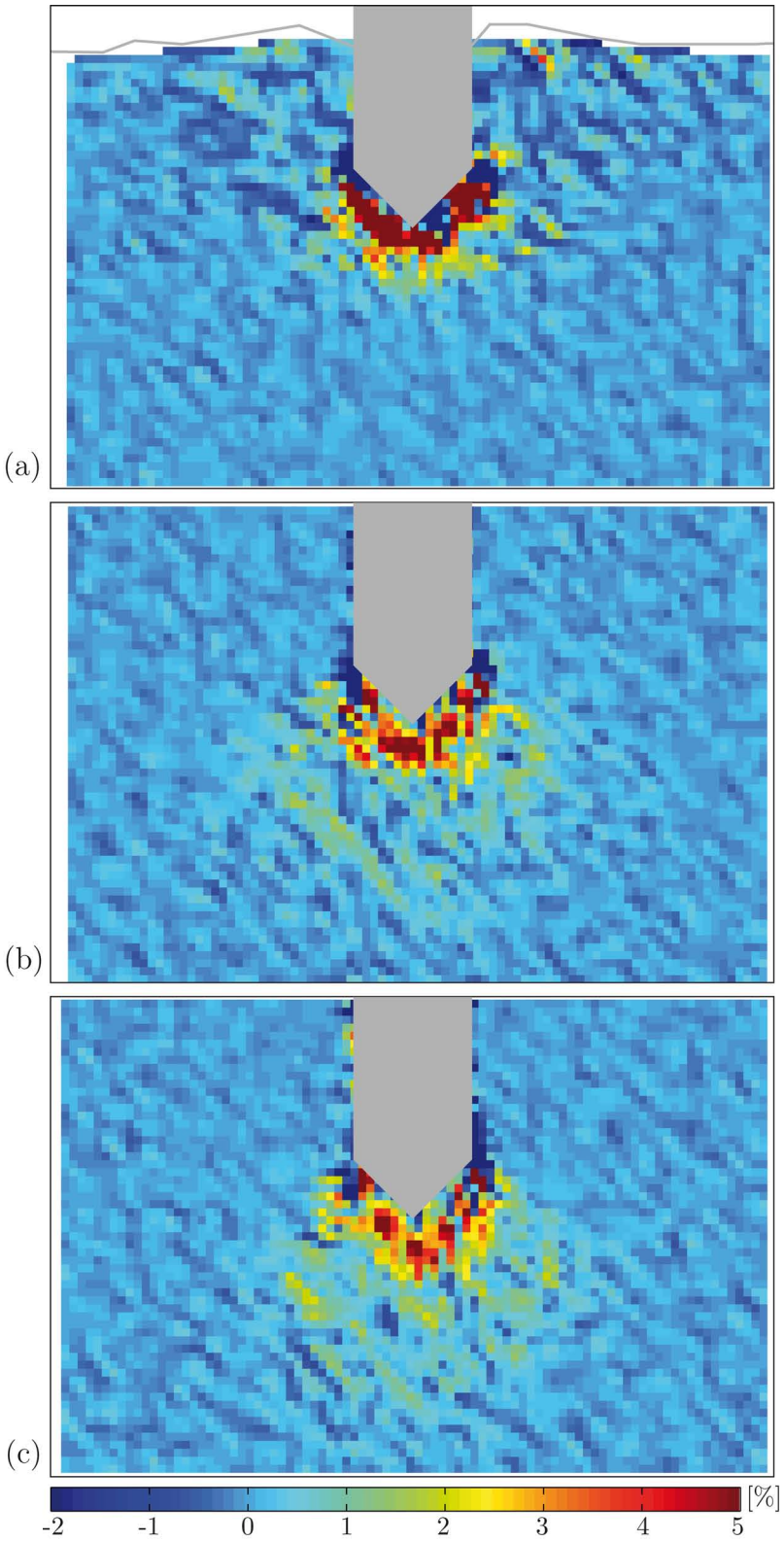

Figure D.12: PIV results for pile penetration test PP-10-C in very dense sand (D_{r0} = 95 %). Incremental volumetric strain (a) at z/D = 1.5, (b) at z/D = 4.8, (c) at z/D = 8.3 (positive if compressive).

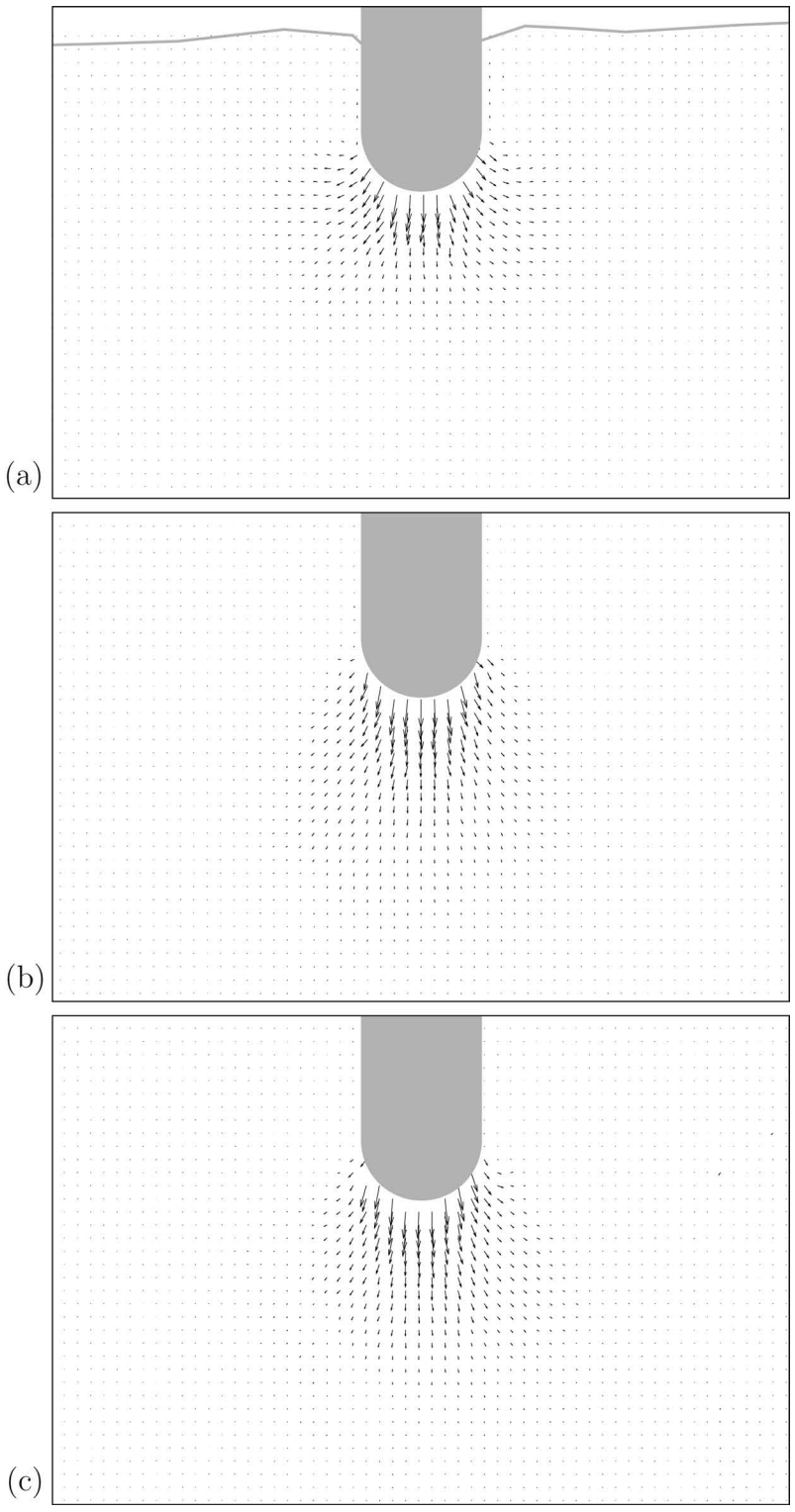

Figure D.13: PIV results for pile penetration test PP-26-H in loose sand ($D_{r0} = 34\,\%$). Incremental displacement scaled up by a factor of 5 (a) at $z/D = 1.4$, (b) at $z/D = 5.0$, (c) at $z/D = 8.5$.

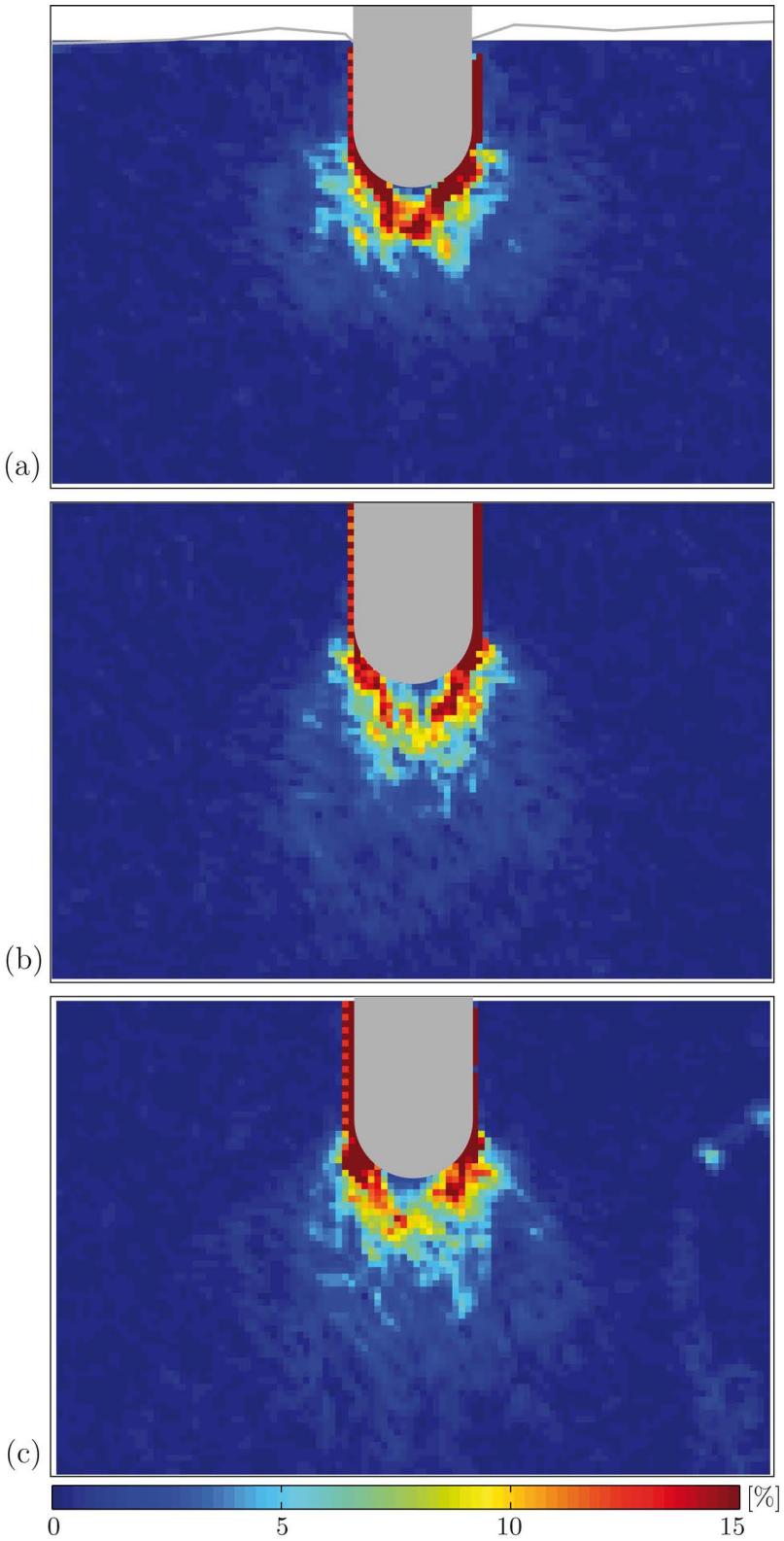

Figure D.14: PIV results for pile penetration test PP-26-H in loose sand ($D_{r0} = 34\,\%$). Incremental maximum shear strain (a) at $z/D = 1.4$, (b) at $z/D = 5.0$, (c) at $z/D = 8.5$.

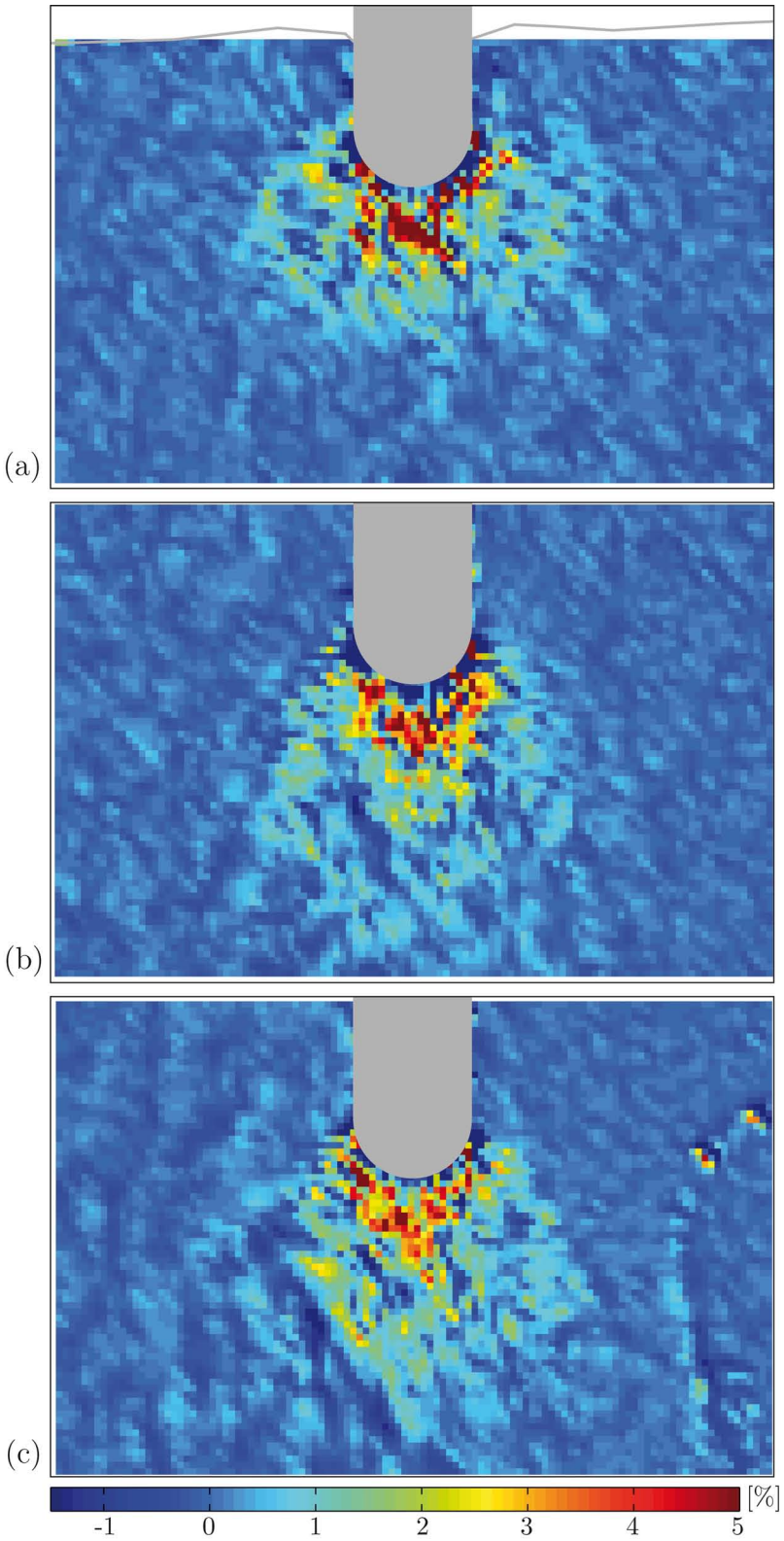

Figure D.15: PIV results for pile penetration test PP-26-H in loose sand ($D_{r0} = 34\,\%$). Incremental volumetric strain (a) at $z/D = 1.4$, (b) at $z/D = 5.0$, (c) at $z/D = 8.5$ (positive if compressive).

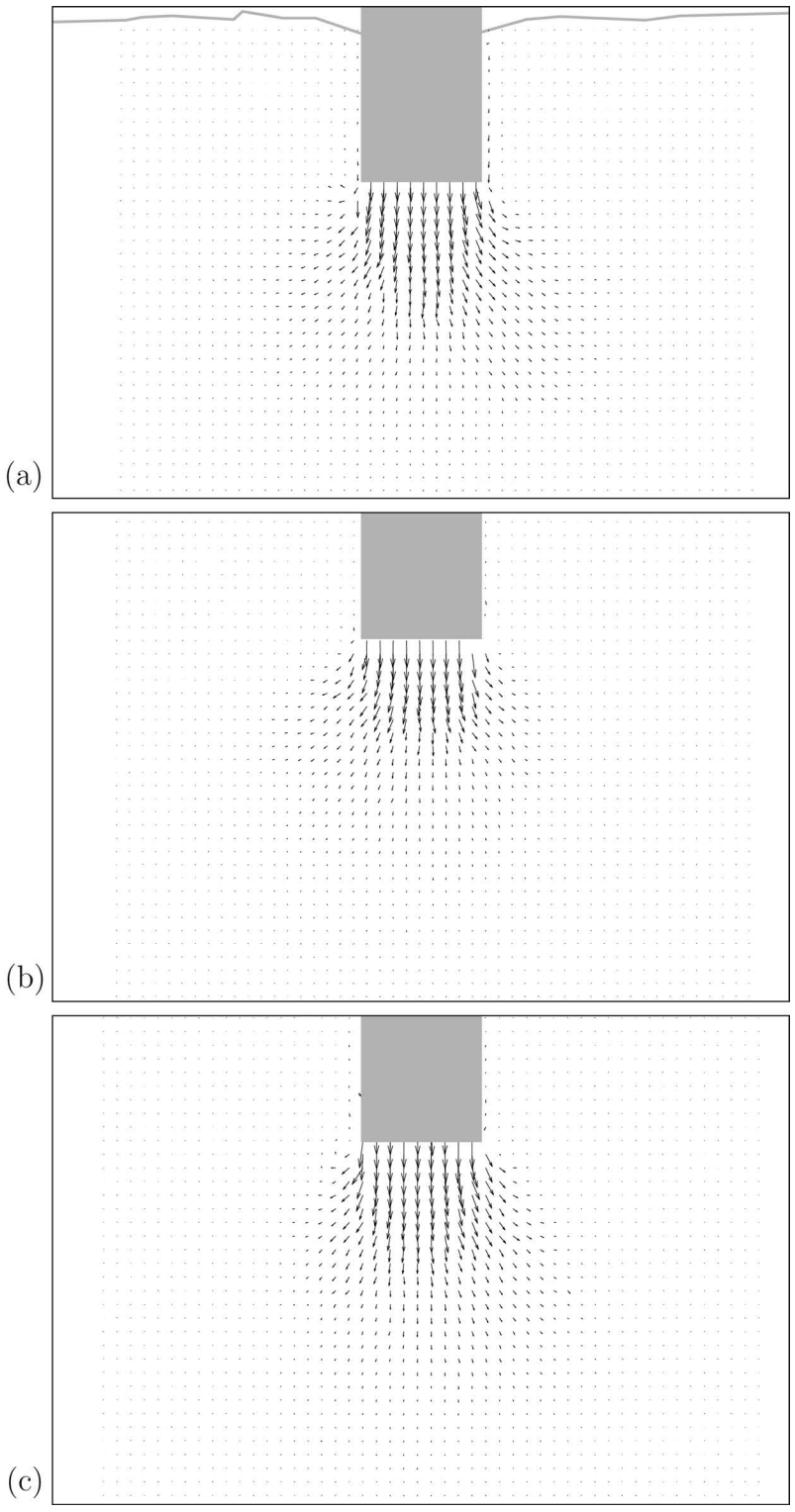

Figure D.16: PIV results for pile penetration test PP-27-F in loose sand ($D_{r0} = 21\,\%$). Incremental displacement scaled up by a factor of 5 (a) at $z/D = 1.3$, (b) at $z/D = 5.0$, (c) at $z/D = 8.5$.

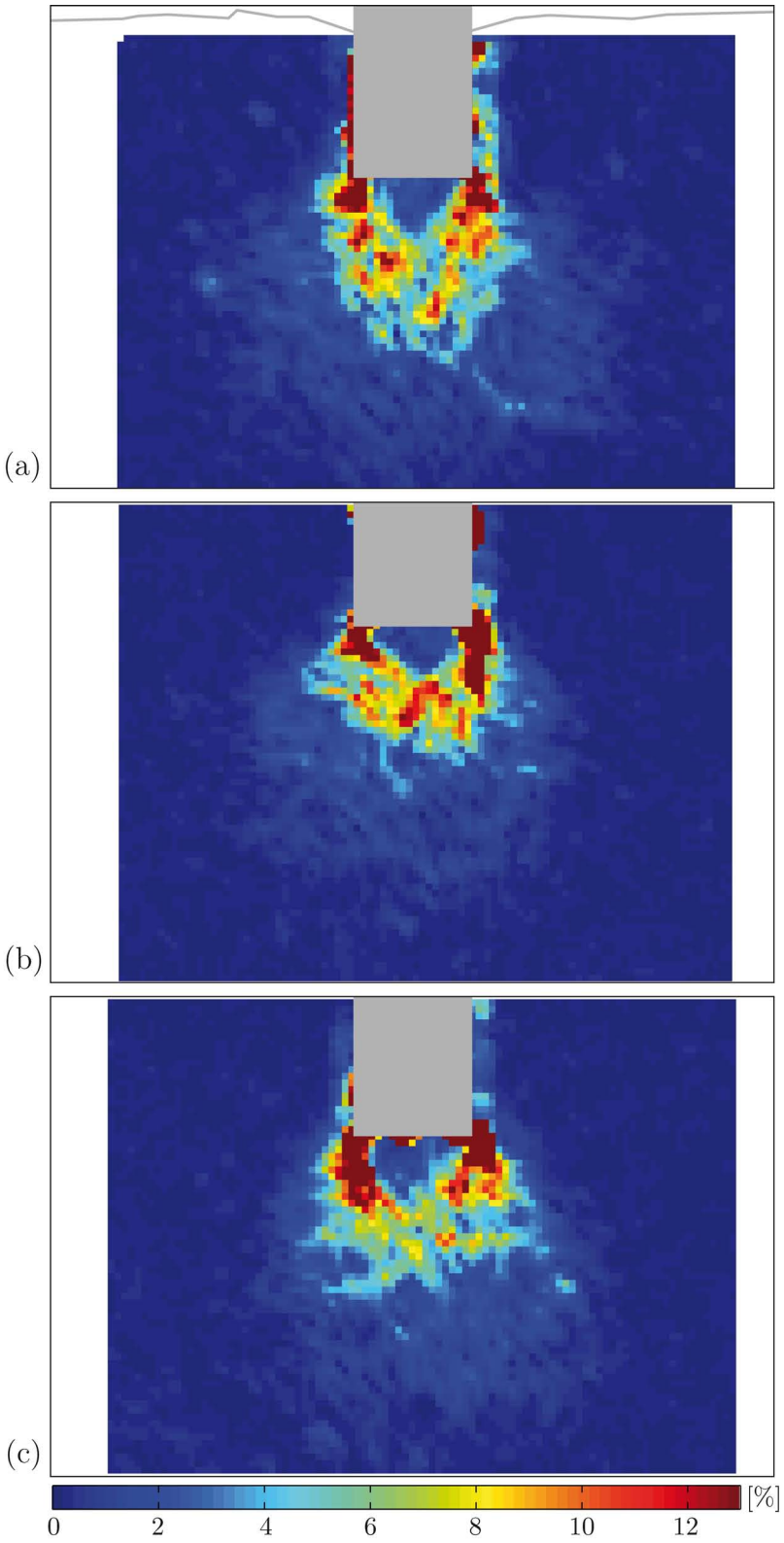

Figure D.17: PIV results for pile penetration test PP-27-F in loose sand ($D_{r0} = 21\,\%$). Incremental maximum shear strain (a) at $z/D = 1.3$, (b) at $z/D = 5.0$, (c) at $z/D = 8.5$.

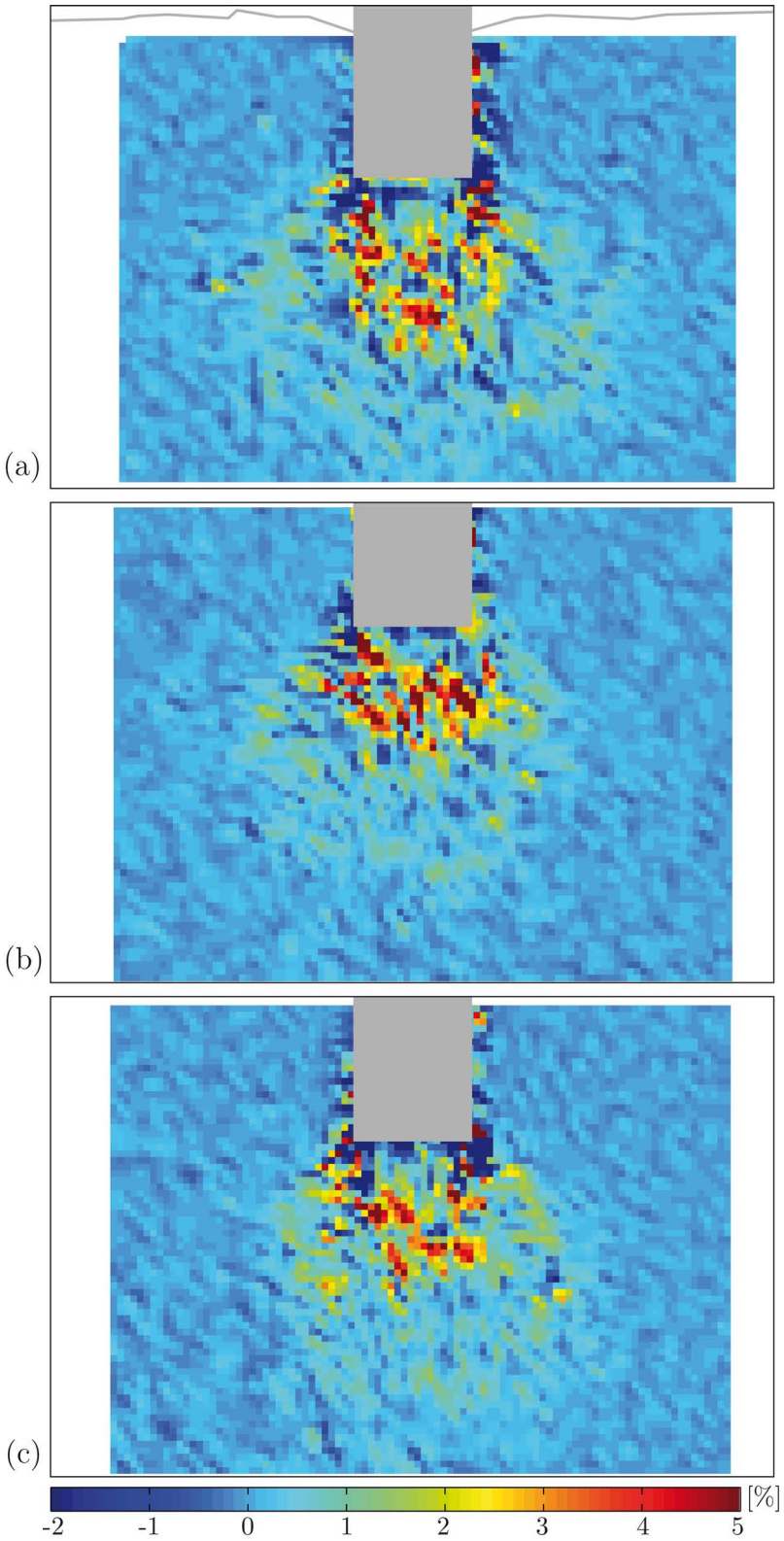

Figure D.18: PIV results for pile penetration test PP-27-F in loose sand ($D_{r0} = 21\,\%$). Incremental volumetric strain (a) at $z/D = 1.3$, (b) at $z/D = 5.0$, (c) at $z/D = 8.5$ (positive if compressive).

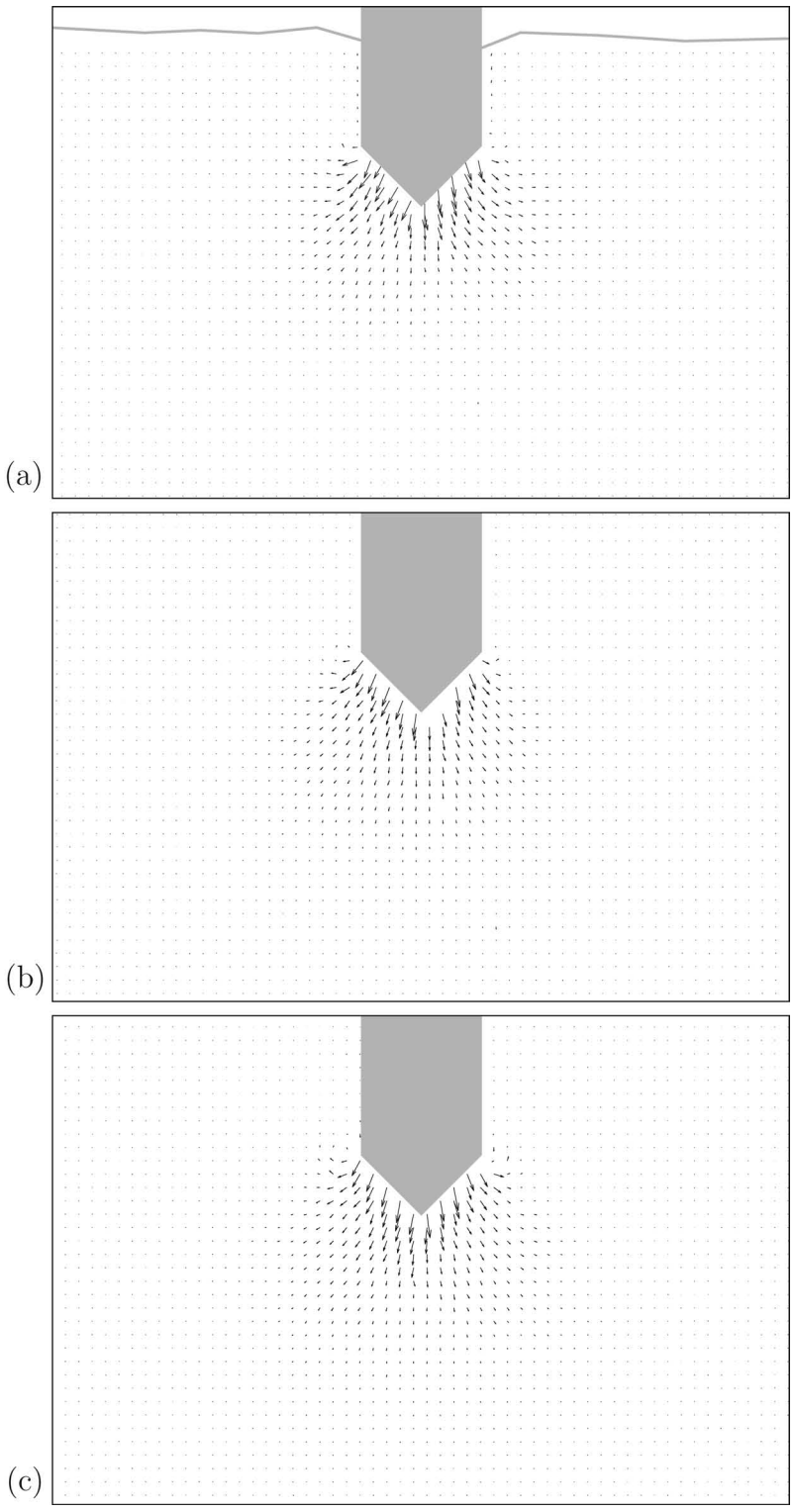

Figure D.19: PIV results for pile penetration test PP-28-C in loose sand ($D_{r0} = 21\,\%$). Incremental displacement scaled up by a factor of 5 (a) at $z/D = 1.4$, (b) at $z/D = 4.8$, (c) at $z/D = 8.5$.

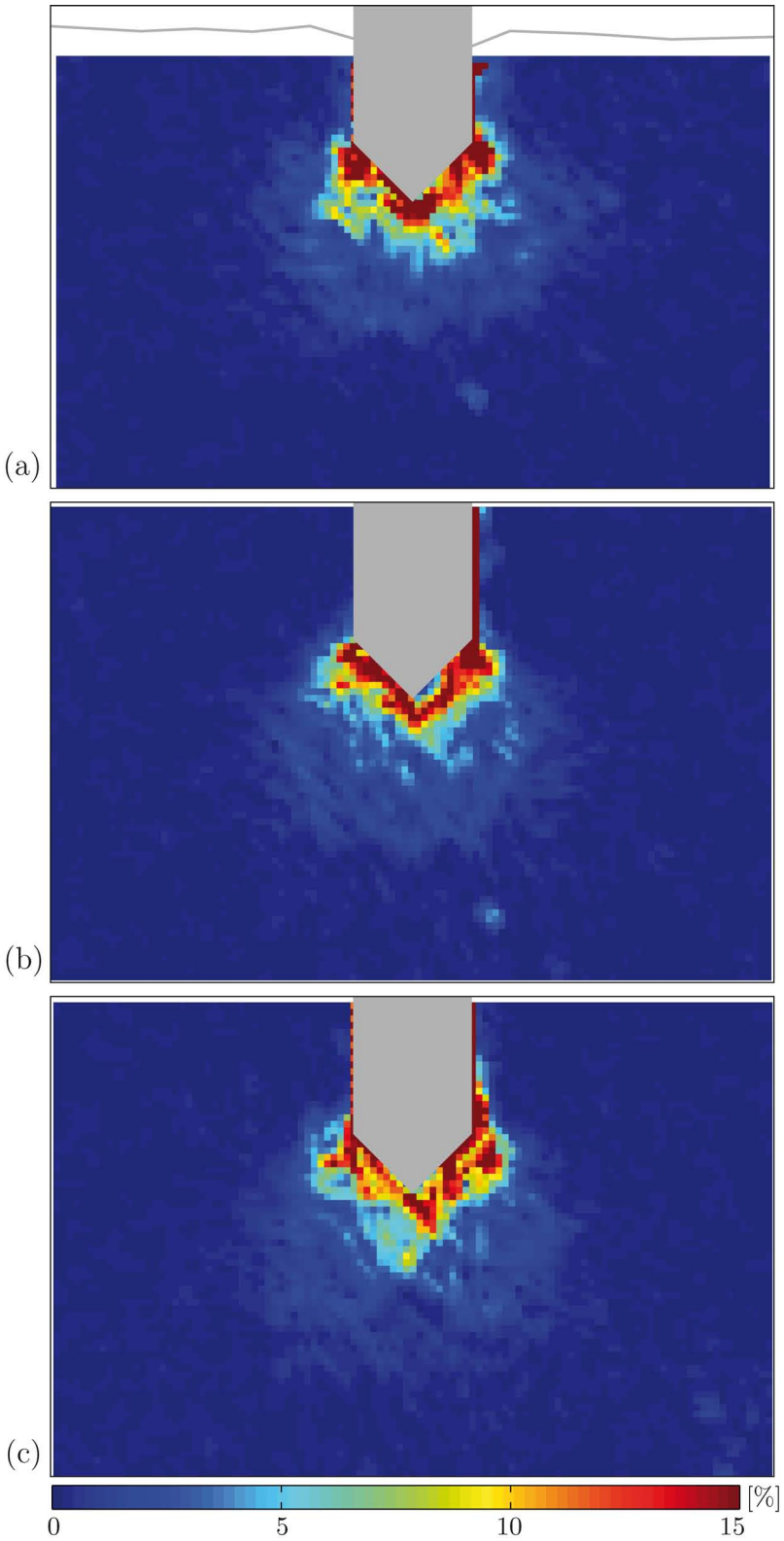

Figure D.20: PIV results for pile penetration test PP-28-C in loose sand ($D_{r0} = 21\,\%$). Incremental maximum shear strain (a) at $z/D = 1.4$, (b) at $z/D = 4.8$, (c) at $z/D = 8.5$.

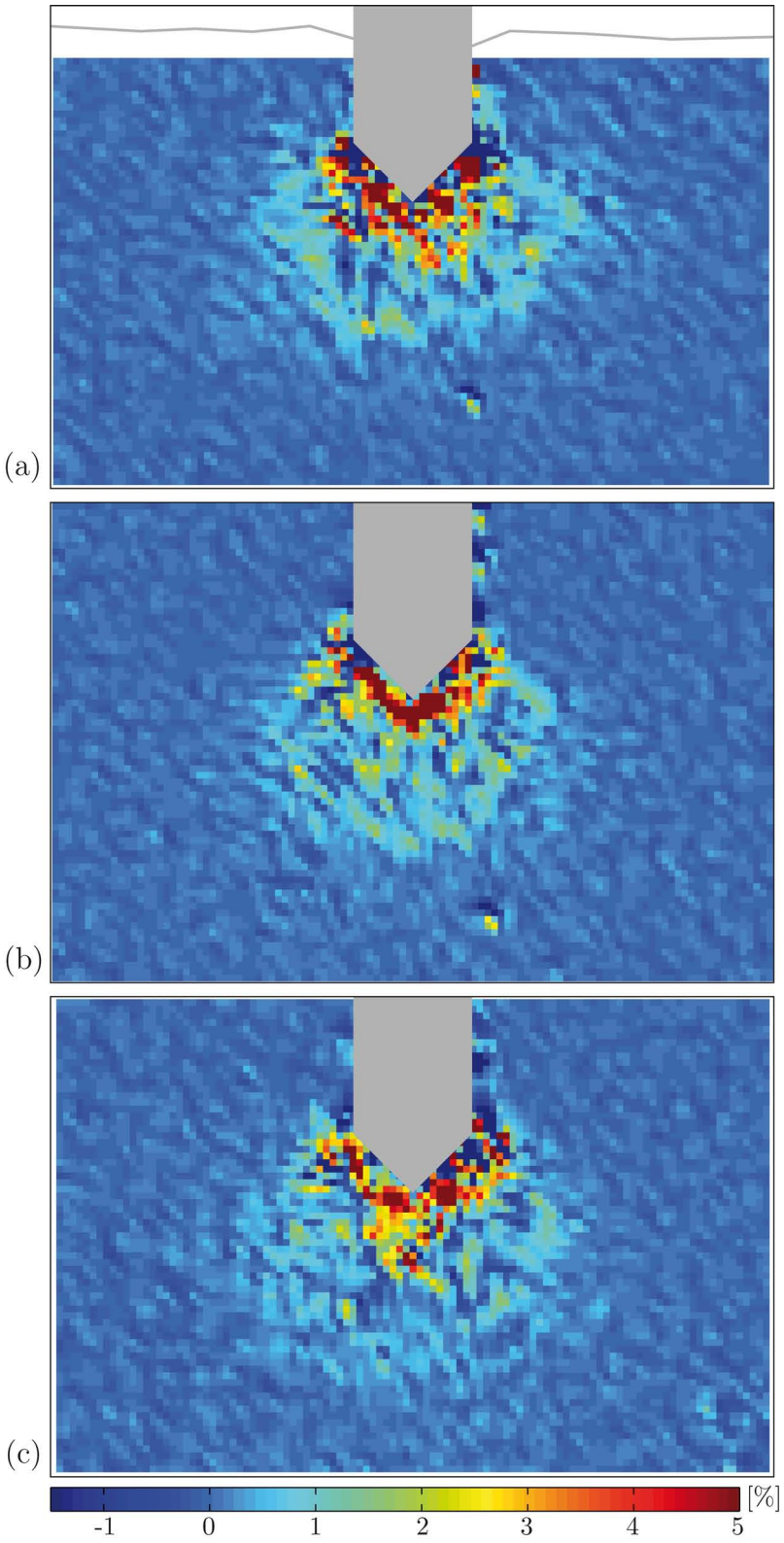

Figure D.21: PIV results for pile penetration test PP-28-C in loose sand ($D_{r0} = 21\,\%$). Incremental volumetric strain (a) at $z/D = 1.4$, (b) at $z/D = 4.8$, (c) at $z/D = 8.5$ (positive if compressive).

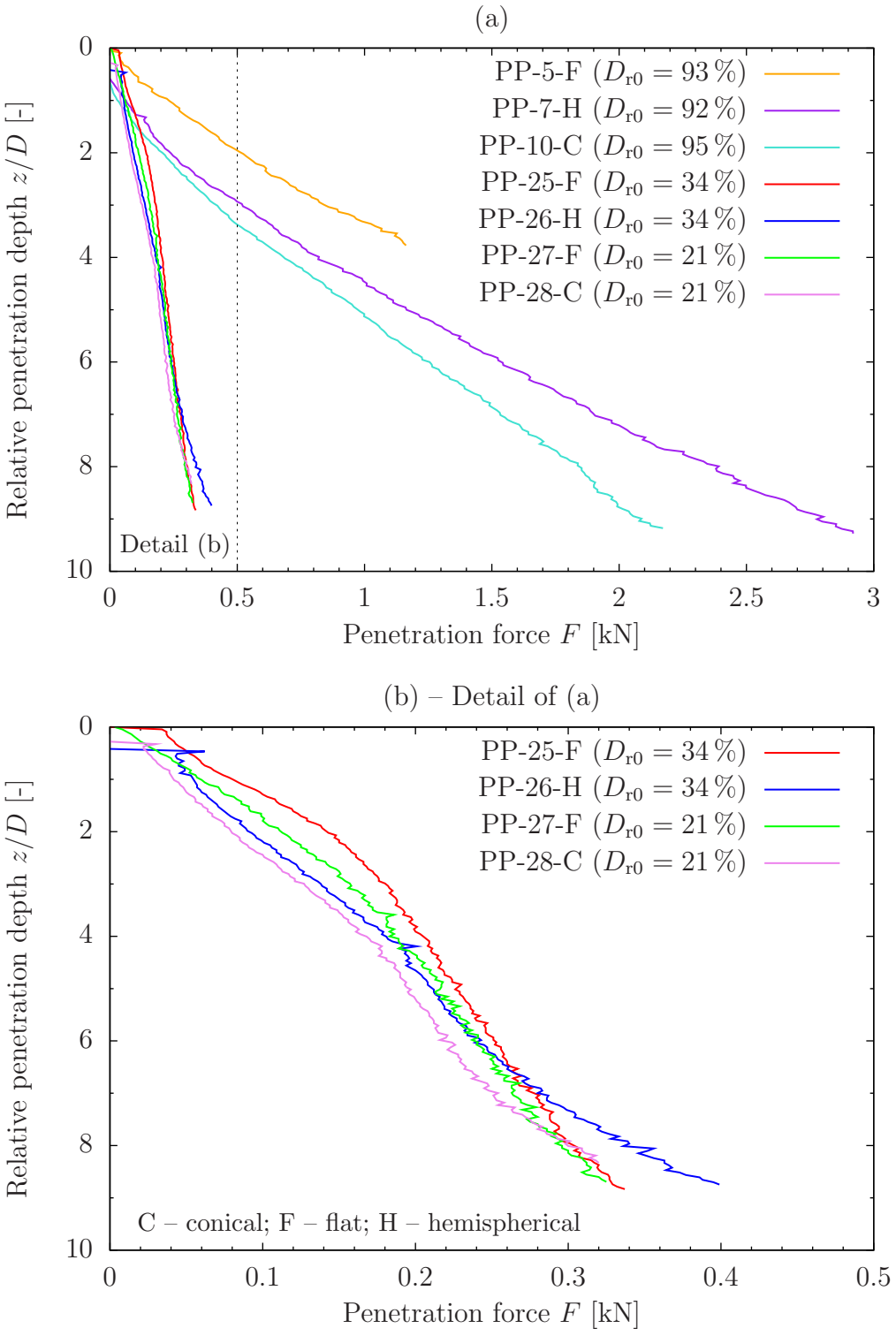

Figure D.22: Measured load-displacement curves of selected pile penetration tests.

Bibliography

R. Abraham, J. E. Marsden, and T. Ratiu. *Manifolds, Tensor Analysis, and Applications*. Addison-Wesley, Reading, Massachusetts, 1983.

F. L. Addessio, J. R. Baumgardner, J. K. Dukowicz, N. L. Johnson, B. A. Kashiwa, R. M. Rauenzahn, and C. Zemach. CAVEAT: A Computer Code for Fluid Dynamics Problems with Large Distortion and Internal Slip. Report LA-10613-MS-REV. 1, Los Alamos National Laboratory, Los Alamos, USA, 1990. (revised edition).

R. J. Adrian. Scattering particle characteristics and their effect on pulsed laser measurements of fluid flow: speckle velocimetry vs. particle image velocimetry. *Applied Optics*, 23(11):1690–1691, 1984.

R. J. Adrian. Particle-imaging techniques for experimental fluid mechanics. *Annual Review of Fluid Mechanics*, 23:261–304, 1991.

R. J. Adrian. Twenty years of particle image velocimetry. *Experiments in Fluids*, 39: 159–169, 2005.

T. Akenine-Möller, E. Haines, and N. Hoffman. *Real-Time Rendering*. A K Peters, Ltd., Wellesley, Massachusetts, 3rd edition, 2008.

N. Amenta, M. Bern, and D. Eppstein. Optimal point placement for mesh smoothing. *Journal of Algorithms*, 30:302–322, 1999.

A. A. Amsden and C. W. Hirt. YAQUI: An Arbitrary Lagrangian-Eulerian Computer Program for Fluid Flow at All Speeds. Report LA-5100, Los Alamos National Laboratory, Los Alamos, USA, 1973.

A. A. Amsden, H. M. Ruppel, and C. W. Hirt. SALE: A Simplified ALE Computer Program for Fluid Flow at All Speeds. Report LA-8095, Los Alamos National Laboratory, Los Alamos, USA, 1980.

Ch. E. Anderson, Jr. An overview of the theory of hydrocodes. *International Journal of Impact Engineering*, 5:33–59, 1987.

ANSYS. *ANSYS User Material Subroutine USERMAT*. ANSYS, Inc., Canonsburg, Pennsylvania, USA, 1999.

ANSYS. *Theory Reference for ANSYS and ANSYS Workbench, ANSYS Release 11.0*. ANSYS, Inc., Canonsburg, Pennsylvania, USA, 2007a.

ANSYS. *Programmer's Manual for ANSYS, ANSYS Release 11.0*. ANSYS, Inc., Canonsburg, Pennsylvania, USA, 2007b.

ANSYS. *ANSYS Parametric Design Language Guide, ANSYS Release 11.0*. ANSYS, Inc., Canonsburg, Pennsylvania, USA, 2007c.

ANSYS. *Basic Analysis Guide, ANSYS Release 11.0*. ANSYS, Inc., Canonsburg, Pennsylvania, USA, 2007d.

L. Armijo. Minimization of functions having Lipschitz continuous first partial derivatives. *Computational Mechanics*, 16:1–3, 1966.

H. Askes, L. Bodé, and L. J. Sluys. ALE analysis of localization in wave propagation problems. *Mechanics of Cohesive-Frictional Materials*, 3:105–125, 1998.

D. Aubram. *Differential Geometry Applied to Continuum Mechanics*. Number 44 in Veröffentlichungen des Grundbauinstitutes der Technischen Universität Berlin. Shaker Verlag, Aachen, 2009. URL `http://opus.kobv.de/tuberlin/volltexte/2009/2270/`.

B. Avci and P. Wriggers. A DEM-FEM coupling approach for the direct numerical simulation of 3d particulate flows. *Journal of Applied Mechanics*, 79(1):010901, 2012.

J. L. F. Aymone. Mesh motion techniques for the ALE formulation in 3d large deformation problems. *International Journal for Numerical Methods in Engineering*, 59: 1879–1908, 2004.

J. L. F. Aymone, E. Bittencourt, and G. J. Creus. Simulation of 3d metal-forming using an arbitrary Lagrangian-Eulerian finite element method. *Journal of Materials Processing Technology*, 110:218–232, 2001.

M. M. Baligh. Strain path method. *Journal of Geotechnical Engineering*, 111(9): 1108–1136, 1985.

J.-P. Bardet. *Experimental Soil Mechanics*. Prentice Hall, Inc., New Jersey, 1997.

W. D. Barfield. An optimal mesh generator for Lagrangian hydrodynamic calculations in two space dimensions. *Journal of Computational Physics*, 6:417–429, 1970.

T. Barth and M. Ohlberger. *Finite Volume Methods: Foundation and Analysis*, volume 1 of *Encyclopedia of Computational Mechanics*, chapter 15. John Wiley & Sons, Ltd., 2004.

T. J. Barth and D. C. Jespersen. The design and application of upwind schemes on unstructured meshes. In *Proceedings 27th Aerospace Sciences Meeting, Reno, Nevada, USA*. American Institute of Aeronautics and Astronautics (AIAA), 1989. (published as AIAA Paper 89-0366).

R. Barzel. *Graphics Tools: The JGT Editors' Choice*. A K Peters, Ltd., 2005.

G. Bashein and P. R. Detmer. *Centroid of a Polygon*, volume IV of *Graphics Gems*, pages 3–6. Academic Press, Inc., 1994.

K.-J. Bathe. *Finite Element Procedures*. Prentice Hall, Inc., New Jersey, 1996.

K.-J. Bathe, E. Ramm, and E. L. Wilson. Finite element formulation for large deformation dynamic analysis. *International Journal for Numerical Methods in Engineering*, 9:353–386, 1975.

E. Bauer. Calibration of a comprehensive constitutive equation for granular materials. *Soils and Foundations*, 36(1):13–26, 1996.

H. N. Bayoumi and M. S. Gadala. A complete finite element treatment for the fully coupled implicit ALE formulation. *Computational Mechanics*, 33:435–452, 2004.

K. Been and M. G. Jefferies. A state parameter for sands. *Géotechnique*, 35(2):99–112, 1985.

T. Belytschko, Y. Y. Lu, and L. Gu. Element-free galerkin methods. *International Journal for Numerical Methods in Engineering*, 37:229–256, 1994.

T. Belytschko, Y. Krongauz, D. Organ, M. Fleming, and P. Krysl. Meshless methods: An overview and recent developments. *Computer Methods in Applied Mechanics and Engineering*, 139:3–47, 1996.

T. Belytschko, W. K. Liu, and D. Moran. *Nonlinear Finite Elements for Continua and Structures*. John Wiley & Sons, Ltd., 2000.

T. B. Belytschko and J. M. Kennedy. Computer models for subassembly simulation. *Nuclear Engineering and Design*, 49:17–38, 1978.

D. J. Benson. An efficient, accurate, simple ALE method for nonlinear finite element programs. *Computer Methods in Applied Mechanics and Engineering*, 72(3):305–350, 1989.

D. J. Benson. Computational methods in Lagrangian and Eulerian hydrocodes. *Computer Methods in Applied Mechanics and Engineering*, 99(2-3):235–394, 1992.

D. J. Benson. A multi-material Eulerian formulation for the efficient solution of impact and penetration problems. *Computational Mechanics*, 15:558–571, 1995.

D. J. Benson. A mixture theory for contact in multi-material Eulerian formulations. *Computer Methods in Applied Mechanics and Engineering*, 140:59–86, 1997.

D. J. Benson. An implicit multi-material Eulerian formulation. *International Journal for Numerical Methods in Engineering*, 48:475–499, 2000.

D. J. Benson. Momentum advection on unstructured staggered quadrilateral meshes. *International Journal for Numerical Methods in Engineering*, 75:1549–1580, 2008.

D. J. Benson and S. Okazawa. Contact in a multi-material Eulerian finite element formulation. *Computer Methods in Applied Mechanics and Engineering*, 193:4277–4298, 2004.

V. G. Berezantsev, V. S. Khristoforov, and V. N. Golubkov. Load bearing capacity and deformation of piled foundations. In *Proceedings 5th International Conference of Soil Mechanics and Foundation Engineering*, volume 2, pages 11–15, 1961.

L. Beuth. *Formulation and Application of a Quasi-Static Material Point Method*. Dissertation, Fakultät für Bau- und Umweltingenieurwissenschaften, Universität Stuttgart, Germany, 2012.

R. B. Bird. The equations of change and the macroscopic mass, momentum, and energy balances. *Chemical Engineering Science*, 6:123–131, 1957.

R. B. Bird, W. E. Stewart, and E. N. Lightfoot. *Transport Phenomena*. John Wiley & Sons, Inc., 1960.

R. L. Bishop and S. I. Goldberg. *Tensor Analysis on Manifolds*. The Macmillan Company, New York, 1968.

M. D. Bolton, M. W. Gui, and R. Phillips. Review of miniature soil probes for model tests. In S. L. Lee, Kwet Yew Yong, and Y. K. Chow, editors, *Proceedings of the Eleventh Southeast Asian Geotechnical Conference, Singapore*, pages 85–90. Southeast Asian Geotechnical Society, 1993.

M. D. Bolton, M. W. Gui, J. Garnier, J. F. Corte, G. Bagge, J. Laue, and R. Renzi. Centrifuge cone penetration tests in sand. *Géotechnique*, 49(4):543–552, 1999.

J. U. Brackbill and J. S. Saltzman. Adaptive zoning for singular problems in two dimensions. *Journal of Computational Physics*, 46:342–368, 1982.

H. Braess. *Untersuchungen von Strömungen in zeitlich veränderlichen Gebieten mit der Methode der Finiten Elemente*. Dissertation, Fachbereich Bauingenieur- und Vermessungswesen, Universität Hannover, Germany, 2000. (published in Institute Series; in German).

H. Braess and P. Wriggers. Arbitrary Lagrangian Eulerian Finite Element Analysis of Free Surface Flow. *Computer Methods in Applied Mechanics and Engineering*, 190: 95–109, 2000.

I. N. Bronstein, K. A. Semendjajew, G. Musiol, and H. Mühlig. *Taschenbuch der Mathematik*. Verlag Harri Deutsch, Thun und Frankfurt am Main, 5th edition, 2001. (in German).

I. N. Bronstein, K. A. Semendjajew, G. Musiol, and H. Mühlig. *Handbook of Mathematics*. Springer-Verlag Berlin Heidelberg, 5th edition, 2007.

A. N. Brooks and T. J. R. Hughes. Streamline upwind/Petrov-Galerkin formulations for convection dominated flows with particular emphasis on the incompressible Navier-Stokes equations. *Computer Methods in Applied Mechanics and Engineering*, 32: 199–259, 1982.

K. H. Brown, S. P. Burns, and M. A. Christon. Coupled Eulerian-Lagrangian methods for earth penetrating weapon applications. Report SAND2002-1014, Sandia National Laboratories, USA, 2002.

O. T. Bruhns, A. Meyers, and H. Xiao. On non-corotational rates of Oldroyd's type and relevant issues in rate constitutive formulations. *Proceedings of the Royal Society of London. Series A*, 460:909–928, 2004.

D. Bruno. *Dynamic and Static Load Testing of Driven Piles in Sand*. PhD thesis, University of Western Australia, 1999.

W. R. Buell and B. A. Bush. Mesh generation – a survey. *Journal of Engineering for Industry (ASME)*, 95(1):332–338, 1973.

H. H. Bui, R. Fukagawa, K. Sako, and S. Ohno. Lagrangian meshfree particles method (SPH) for large deformation and failure flows of geomaterial using elastic-plastic soil onstitutive model. *International Journal for Numerical and Analytical Methods in Geomechanics*, 32:1537–1570, 2008.

H. H. Bui, R. Fukagawa, K. Sako, and J. C. Wells. Slope stability analysis and discontinuous slope failure simulation by elasto-plastic smoothed particle hydrodynamics (SPH). *Géotechnique*, 61(7):565–574, 2011.

Ch. Carow. Anwendung der PIV-Methode zur Quantifizierung der Bodenbewegungen bei Pfahleindringung auf der Grundlage kleinmaßstäblicher Modellversuche in Sand. Bachelor's thesis, Chair of Soil Mechanics and Geotechnical Engineering, Technische Universität Berlin (TU Berlin), Germany, 2009. (unpublished; in German).

B. Carter and H. Quintana. Foundations of general relativistic high-pressure elasticity theory. *Proceedings of the Royal Society of London. Series A*, 331:57–83, 1972.

J. P. Carter, M. F. Randolph, and C. P. Wroth. Stress and pore pressure changes in clay during and after the expansion of a cylindrical cavity. *International Journal for Numerical and Analytical Methods in Geomechanics*, 3:305–322, 1979.

G. Castro. Liquefaction and cyclic mobility of saturated sands. *Journal of the Geotechnical Engineering Division, ASCE*, 101(6):551–569, 1975.

R. K.-C. Chan. A generalized arbitrary Lagrangian-Eulerian method for incompressible flows with sharp interfaces. *Journal of Computational Physics*, 17:311–331, 1975.

W. F. Chen and D. J. Han. *Plasticity for Structural Engineers*. Springer-Verlag New York, Inc., 1988.

Y. M. Cheng and Y. Tsui. Limitations to the large strain theory. *International Journal for Numerical Methods in Engineering*, 33:101–114, 1992.

A. J. Chorin, T. J. R. Hughes, M. F. McCracken, and J. E. Marsden. Product formulas and numerical algorithms. *Communications on Pure and Applied Mathematics*, 31: 205–256, 1978.

F. C. Chow. *Investigations into the behaviour of displacement piles for offshore foundations*. PhD thesis, Imperial College, London, UK, 1997.

F. C. Chow, R. J. Jardine, J. F. Nauroy, and F. Brucy. Time-related increases in the shaft capacities of driven piles in sand. *Géotechnique*, 47(2):353–361, 1997.

P. G. Ciarlet. *Mathematical Elasticity, Volume I: Three-Dimensional Elasticity*. Elsevier Science Publishers B.V., Amsterdam, The Netherlands, 1988.

A. Cividini and G. Gioda. A simplified analysis of pile penetration. In G. Swoboda, editor, *Proceedings Sixth International Conference on Numerical Methods in Geomechanics, Innsbruck, Austria*, pages 1043–1049. A. A. Balkema, 1988.

P. Colella. Multidimensional upwind methods for hyperbolic conservation laws. *Journal of Computational Physics*, 87:171–200, 1990.

B. D. Coleman and M. E. Gurtin. Thermodynamics with internal state variables. *The Journal of Chemical Physics*, 47(2):597–613, 1967.

B. D. Coleman and V. J. Mizel. Existence of caloric equations of state in thermodynamics. *The Journal of Chemical Physics*, 40(4):1116–1125, 1964.

B. D. Coleman and W. Noll. The thermodynamics of elastic materials with heat conduction and viscosity. *Archive for Rational Mechanics and Analysis*, 13:167–178, 1963.

R. Courant, K. Friedrichs, and H. Lewy. Über die partiellen Differenzengleichungen der mathematischen Physik. *Mathematische Annalen*, 100:32–74, 1928. (in German; republished in English as: "On the Partial Difference Equations of Mathematical Physics", IBM Journal 11(2):215–234, 1967).

R. Courant, E. Isaacson, and M. Rees. On the solution of nonlinear hyperbolic differential equations by finite differences. *Communications on Pure and Applied Mathematics*, 5(3):243–255, 1952.

R. F. Craig. *Craig's Soil Mechanics*. E & FN Spon, London, New York, 7th edition, 2007.

R. O. Cudmani. *Statische, alternierende und dynamische Penetration in nichtbindige Böden*. Dissertation, Fakultät für Bauingenieur- und Vermessungswesen der Universität Karlsruhe (TH), Germany, 2001. (published in Institute Series; in German).

P. A. Cundall and O. D. L. Strack. A discrete numerical model for granular assemblies. *Géotechnique*, 29(1):47–65, 1979.

Y. F. Dafalias. Bounding surface plasticity. i: Mathematical foundation and hypoplasticity. *Journal of Engineering Mechanics*, 112(9):966–987, 1986.

E. A. Dari and G. C. Buscaglia. Mesh optimization: How to obtain good unstructured 3d finite element meshes with not-so-good mesh generators. *Structural and Multidisciplinary Optimization*, 8:181–188, 1993.

B. M. Das. *Advanced Soil Mechanics*. Taylor & Francis, USA, 3rd edition, 2008.

R. de Boer. *Theory of Porous Media*. Springer-Verlag, Berlin, 2000.

R. de Borst and P. A. Vermeer. Possibillities and limitations of finite elements for limit analysis. *Géotechnique*, 34(2):199–210, 1984.

A. de Nicola. *The performance of pipe piles in sand*. PhD thesis, University of Western Australia, 1996.

A. de Nicola and M. F. Randolph. The plugging behaviour of driven and jacked piles in sand. *Géotechnique*, 47(4):841–856, 1997.

D. Demirdžić and M. Perić. Space conservation law in finite volume calculations of fluid flow. *International Journal for Numerical Methods in Fluids*, 8(9):1037–1050, 1988.

D. Demirdžić and M. Perić. Finite volume method for prediction of fluid flow in arbitrarily shaped domains with moving boundaries. *International Journal for Numerical Methods in Fluids*, 10(7):771–790, 1990.

Y. Di, J. Yang, and T. Sato. An operator-split ALE model for large deformation analysis of geomaterials. *International Journal for Numerical and Analytical Methods in Geomechanics*, 31:1375–1399, 2007.

J. K. Dienes. On the analysis of rotation and stress rate in deforming bodies. *Acta Mechanica*, 32:217–232, 1979.

J. K. Dienes. A discussion of material rotation and stress rate. *Acta Mechanica*, 65: 1–11, 1986.

F. L. DiMaggio and I. S. Sandler. Material model for granular soils. *Journal of the Engineering Mechanics Division*, 97(3):935–950, 1971.

DIN 1054. Baugrund – Sicherheitsnachweise im Erd- und Grundbau. Beuth Verlag, Berlin, January 2005. (German Code).

DIN 18123. Baugrund, Untersuchung von Bodenproben – Bestimmung der Korngrößenverteilung. Beuth Verlag, Berlin, April 2011. (German Code).

DIN 18126. Baugrund, Untersuchung von Bodenproben – Bestimmung der Dichte nichtbindiger Böden bei lockerster und dichtester Lagerung. Beuth Verlag, Berlin, November 1996. (German Code).

DIN 4094-1. Baugrund – Felduntersuchungen, Teil 1: Drucksondierungen. Beuth Verlag, Berlin, June 2002. (German Code).

DIN EN ISO 14688-1. Geotechnische Erkundung und Untersuchung — Benennung, Beschreibung und Klassifizierung von Boden — Teil 1: Benennung und Beschreibung. Beuth Verlag, Berlin, January 2003. (German Code).

DIN EN ISO 14688-2. Geotechnische Erkundung und Untersuchung — Benennung, Beschreibung und Klassifizierung von Boden — Teil 2: Grundlagen für Bodenklassifizierungen. Beuth Verlag, Berlin, November 2004. (German Code).

DoDI 5000.61. DoD Modeling and Simulation (M&S) Verification, Validation, and Accreditation (VV&A), December 2009. (U.S. Department of Defense Instruction).

J. Donea and A. Huerta. *Finite Element Methods for Flow Problems*. John Wiley & Sons, Ltd., Chichester, England, 2003.

J. Donea, S. Giuliani, J. P. Halleux, P. Granet, P. Hamon, and P. Permezel. Response of fast-reactor core subassemblies to pressure transients. *Nuclear Engineering and Design*, 68:153–174, 1981.

J. Donea, S. Giuliani, and J. P. Halleux. An arbitrary Lagrangian-Eulerian finite element method for transient dynamic fluid-structure interactions. *Computer Methods in Applied Mechanics and Engineering*, 33:689–723, 1982.

J. Donea, A. Huerta, J.-Ph. Ponthot, and A. Rodríguez-Ferran. *Arbitrary Lagrangian-Eulerian Methods*, volume 1 of *Encyclopedia of Computational Mechanics*, chapter 14. John Wiley & Sons, Ltd., 2004.

L. Dormieux, D. Kondo, and F.-J. Ulm. *Microporomechanics*. John Wiley & Sons, Inc., 2006.

D. A. Drew. Mathematical modeling of two-phase flow. *Annual Review of Fluid Mechanics*, 15:261–291, 1983.

V. Dyadechko, R. Garimella, and M. Shashkov. Reference Jacobian rezoning strategy for arbitrary Lagrangian-Eulerian methods on polyhedral grids. Report LA-UR-05-8159, Los Alamos National Laboratory, Los Alamos, USA, 2005.

D. G. Ebin and J. E. Marsden. Groups of diffeomorphisms and the motion of an incompressible fluid. *Annals of Mathematics*, 92:102–163, 1970.

Ch. Eichstädt. Untersuchung der Eindringung von Modellpfählen mit der PIV-Methode. Diploma thesis, Chair of Soil Mechanics and Geotechnical Engineering, Technische Universität Berlin (TU Berlin), Germany, 2006. (unpublished; in German).

A. Einstein. Die Grundlage der allgemeinen Relativitätstheorie. *Annalen der Physik*, 354(7):769–822, 1916. (in German).

B. E. Engelmann and J. O. Hallquist. NIKE2D: A Nonlinear, Implicit, Two-Dimensional Finite Element Code for Solid Mechanics - User Manual. Report UCRL-MA-105413, Lawrence Livermore National Laboratory, California, USA, 1991. URL `https://www-eng.llnl.gov/mdg/mdg_codes_nike2d.html`.

M. Epstein and R. Segev. Differentiable manifolds and the principle of virtual work in continuum mechanics. *Journal of Mathematical Physics*, 21(5):1243–1245, 1980.

T. Erhart. *Strategien zur numerischen Modellierung transienter Impaktvorgänge bei nichtlinearem Materialverhalten*. Dissertation, Fakultät Bau- und Umweltingenieurwissenschaften, Universität Stuttgart, Germany, 2004. (published in Institute Series; in German).

A. C. Eringen. *Mechanics of Continua*. Robert E. Krieger Publishing Company, New York, 2nd edition, 1980.

M. W. Evans and F. H. Harlow. The particle-in-cell method for hydrodynamic calculations. Report LA-2139, Los Alamos Scientific Laboratory, Los Alamos, New Mexico, USA, 1957.

C. Farhat, Ph. Geuzaine, and C. Grandmont. The discrete geometric conservation law and the nonlinear stability of ale schemes for the solution of flow problems on moving grids. *Journal of Computational Physics*, 174:669–694, 2001.

J. H. Ferziger and M. Perić. *Computational Methods for Fluid Dynamics*. Springer-Verlag Berlin Heidelberg New York, 2002.

D. A. Field. Laplacian smoothing and Delaunay triangulations. *Communications in Applied Numerical Methods*, 4:709–712, 1988.

D. A. Field. Qualitative measures for initial meshes. *International Journal for Numerical Methods in Engineering*, 47:887–906, 2000.

W. D. L. Finn, P. L. Bransby, and D. J. Pickering. Effect of strain history on liquefaction of sand. *Journal of the Soil Mechanics and Foundations Division*, 96(6): 1917–1934, 1970.

W. D. L. Finn, D. J. Pickering, and P. L. Bransby. Sand liquefaction in triaxial and simple shear tests. *Journal of the Soil Mechanics and Foundations Division*, 97(4): 639–659, 1971.

D. P. Flanagan and L. M. Taylor. An accurate numerical algorithm for stress integration with finite rotations. *Computer Methods in Applied Mechanics and Engineering*, 62: 305–320, 1987.

J. D. Foley, A. van Dam, S. K. Feiner, and J. F. Hughes. *Computer Graphics: Principles and Practice*. Addison-Wesley Professional, 2nd edition, 1995.

R. M. Frank and R. B. Lazarus. *Mixed Lagrangian-Eulerian Method*, pages 47–67. Methods in Computational Physics. Advances in Research and Applications. Volume 3: Fundamental Methods in Hydrodynamics. Academic Press, New York and London, 1964.

L. Freitag. On combining Laplacian and optimization-based mesh smoothing techniques. In S. A. Canann and S. Saigal, editors, *Trends in Unstructured Mesh Generation*, volume 220 of *AMD Series*. ASME, New York, 1997.

D. Freßmann. *On Single- and Multi-Material Arbitrary Lagrangian-Eulerian Approaches with Application to Micromechanical Problems at Finte Deformations*. Dissertation, Fachbereich Bauingenieur- und Vermessungswesen, Universität Hannover, Germany, 2004. (published in Institute Series; in German).

D. Freßmann and P. Wriggers. Advection approaches for single- and multi-material arbitrary Lagrangian-Eulerian finite element procedures. *Computational Mechanics*, 39:153–190, 2007.

P. J. Frey and P.-L. George. *Mesh Generation: Application to Finite Elements*. HERMES Science Europe Ltd., Oxford, United Kingdom, 2000.

V. G. Ganzha and E. V. Vorozhtsov. *Numerical Solutions for Partial Differential Equations: Problem Solving Using Mathematica*. Symbolic and Numeric Computation Series. CRC Press, Boca Raton, Florida, USA, 1996.

P. L. George, H. Borouchaki, P. J. Frey, P. Laug, and E. Saltel. *Mesh Generation and Mesh Adaptivity: Theory and Techniques*, volume 1 of *Encyclopedia of Computational Mechanics*, chapter 17. John Wiley & Sons, Ltd., 2004.

S. Ghosh. Arbitrary Lagrangian-Eulerian finite element analysis of large deformation in contacting bodies. *International Journal for Numerical Methods in Engineering*, 33:1891–1925, 1992.

S. Ghosh and N. Kikuchi. An arbitrary Lagrangian-Eulerian finite element method for large deformation analysis of elastic-viscoplastic solids. *Computer Methods in Applied Mechanics and Engineering*, 86:127–188, 1991.

R. A. Gingold and J. J. Monaghan. Smoothed particle hydrodynamics: Theory and application to non-spherical stars. *Monthly Notices of the Royal Astronomical Society*, 181:375–389, 1977.

S. Giuliani. An algorithm for continuous rezoning of the hydrodynamic grid in arbitrary Lagrangian-Eulerian computer codes. *Nuclear Engineering and Design*, 72:205–212, 1982.

S. K. Godunov. A difference method for numerical calculation of discontinuous solutions of the equations of hydrodynamics. *Matematicheskii Sbornik*, 47(3):271–306, 1959. (in Russian; translated by US Joint Publication Research Service, JPRS 7226, 1969).

M. Goldscheider. Dilatanzverhalten von Sand bei geknickten Verformungswegen. *Mechanics Research Communications*, 2:143–148, 1975. (in German).

M. Goldscheider. Grenzbedingung und Fließregel von Sand. *Mechanics Research Communications*, 3:463–468, 1976. (in German).

M. Goldscheider and G. Gudehus. Rectilinear extension of dry sand: Testing apparatus and experimental results. In *Proceedings 8th International Conference on Soil Mechanics and Foundation Engineering, Moscow*, volume 1, pages 143–149, 1973.

A. A. Goldstein and J. F. Price. An effective algorithm for minimization. *Numerische Mathematik*, 10:184–189, 1967.

J. Grabe and F. König. Zeitabhängige Traglaststeigerung von Verdrängungspfählen. In *Vorträge der 29. Baugrundtagung 2006, September 27-29, 2006, Bremen, Germany*, pages 291–298, 2006. (in German).

J. Grabe, S. Henke, and B. Schümann. Numerical simulation of pile driving in the passive earth pressure zone of excavation support walls. *Bautechnik, Special issue 2009 - Geotechnical Engineering*, 86(S1):40–45, 2009.

A. E. Green and P. M. Naghdi. A general theory of an elastic-plastic continuum. *Archive for Rational Mechanics and Analysis*, 18:251–281, 1965.

D. V. Griffiths. Elasto-plastic analysis of deep foundations in cohesive soil. *International Journal for Numerical and Analytical Methods in Geomechanics*, 6:211–218, 1982.

G. Gudehus. A comprehensive constitutive equation for granular materials. *Soils and Foundations*, 36(1):1–12, 1996.

G. Gudehus and D. Kolymbas. A constitutive law of the rate type for soils. In W. Wittke, editor, *Proceedings Third International Conference on Numerical Methods in Geomechanics, Aachen, Germany*, pages 319–329. A. A. Balkema, 1979.

M. W. Gui and M. D. Bolton. Geometry and scale effects in CPT and pile design. In P. W. Mayne and P. K. Robertson, editors, *Proceedings First International Conference on Site Characterization, Atlanta, Georgia, USA*, pages 1063–1068. Balkema, 1998.

P. R. Gummert. *General Constitutive Equations for Simple and Non-Simple Materials*, volume 399 of *CISM Courses and Lectures*. Springer-Verlag Wien New York, 1999.

Z.-H. Guo. Time derivatives of tensor fields in non-linear continuum mechanics. *Archiwum Mechaniki Stosowanej*, 15(1):131–161, 1963.

M. E. Gurtin. *An Introduction to Continuum Mechanics*. Academic Press, Inc., 1981.

R. B. Haber. A mixed eulerian-lagrangian displacement model for large-deformation analysis in solid mechanics. *Computer Methods in Applied Mechanics and Engineering*, 43(3):277–292, 1984.

E. C. Hambly. Sand response to cyclic rotation of principal stress directions as induced by wave loads. *Géotechnique*, 18(2):307–309, 1969.

F. H. Harlow. Hydrodynamic problems involving large fluid distortions. *Journal of the Association for Computing Machinery*, 4(2):137–142, 1957.

J. W. Harris and H. Stöcker. *Handbook of Mathematics and Computational Science*. Springer Science+Business Media, LLC, 2006.

C. Hauser and B. Walz. Bildbasierte Verformungsmessung mit der PIV-Methode. *Geotechnik*, 27(4):339–343, 2004.

E. P. Heerema. Predicting pile driveability: Heather as an illustration of the friction fatigue theory. *Ground Engineering*, 13(April):15–37, 1980.

E. Heesen. *Zur Modellierung der Pfahlinstallation mit der Discrete Element Method*. Dissertation, Technische Universität Hamburg-Harburg, Germany, 2010. (published by Shaker Verlag, Aachen; in German).

W. F. Heinz. *Zur Tragfähigkeit von Flachgründungen auf rolligem Boden*. PhD thesis, Fakultät für Bauingenieurwesen, Technische Universität Berlin, Germany, 1970. (in German).

S. Henke. *Herstellungseinflüsse aus Pfahlrammung im Kaimauerbau*. Dissertation, Technische Universität Hamburg-Harburg, Germany, 2008. (published in Institute Series; in German).

S. Henke. Influence of pile installation on adjacent structures. *International Journal for Numerical and Analytical Methods in Geomechanics*, 34(11):1191–1210, 2010.

S. Henke, G. Qiu, and J. Grabe. A coupled Eulerian-Lagrangian approach to solve geotechnical problems involving large deformations. In T. Benz and S. Nordal, editors, *Proceedings 7th European Conference on Numerical Methods in Geotechnical Engineering (NUMGE 2010)*, pages 233–238. Taylor & Francis Group, London, UK, 2010.

I. Herle. *Hypoplastizität und Granulometrie einfacher Korngerüste.* Dissertation, Fakultät für Bauingenieur- und Vermessungswesen der Universität Karlsruhe (TH), Germany, 1997. (published in Institute Series; in German).

I. Herle and G. Gudehus. Determination of parameters of a hypoplastic constitutive model from properties of grain assemblies. *Mechanics of Cohesive-Frictional Materials*, 4:461–486, 1999.

I. Herle and P.-M. Mayer. Verformungsberechnung einer Unterwasserbetonbaugrube auf der Grundlage hypoplastisch ermittelter Parameter des Berliner Sandes. *Bautechnik*, 76(1):34–48, 1999. (in German).

E. S. Hertel. A survey of numerical methods for shock physics applications. Report SAND97-1015C, Sandia National Laboratories, USA, 1997.

R. Hill. Some basic principles in the mechanics of solids without a natural time. *Journal of the Mechanics and Physics of Solids*, 7(3):209–225, 1959.

R. Hill. *The Mathematical Theory of Plasticity.* Oxford University Press, 1998. (Reprint; first published 1950).

Ch. Hirsch. *Numerical Computation of Internal and External Flows*, volume 1. Butterworth-Heinemann, Burlington, MA, USA, 2nd edition, 2007.

C. W. Hirt, A. A. Amsden, and J. L. Cook. An arbitrary Lagrangian-Eulerian computing method for all flow speeds. *Journal of Computational Physics*, 14:227–253, 1974.

K. Ho-Le. Finite element mesh generation methods: A review and classification. *Computer Aided Design*, 20:27–38, 1988.

G. A. Holzapfel. *Nonlinear Solid Mechanics - A Continuum Approach for Engineering.* John Wiley & Sons, Ltd., 2000.

Y. Hu and M. F. Randolph. A practical numerical approach for large deformation problems in soil. *International Journal for Numerical and Analytical Methods in Geomechanics*, 22:327–350, 1998.

A. Huerta and F. Casadei. New ALE applications in non-linear fast-transient solid dynamics. *Engineering Computations*, 11:317–345, 1994.

T. J. R. Hughes. Numerical implementation of constitutive models: Rate-independent deviatoric plasticity. In S. Nemat-Nasser, R. J. Asaro, and G. A. Hegemier, editors, *Theoretical Foundation for Large-Scale Computations for Nonlinear Material Behavior*, pages 29–63. Martinus Nijhoff Publishers, Dordrecht, Niederlande, 1984.

T. J. R. Hughes and K. S. Pister. Consistent linearization in mechanics of solids and structures. *Computers and Structures*, 8:391–397, 1978.

T. J. R. Hughes and J. Winget. Finite rotation effects in numerical integration of rate constitutive equations arising in large-deformation analysis. *International Journal for Numerical Methods in Engineering*, 15(12):1862–1867, 1980.

T. J. R. Hughes, W. K. Liu, and T. K. Zimmermann. Lagrangian-Eulerian finite element formulation for incompressible viscous flows. *Computer Methods in Applied Mechanics and Engineering*, 29:329–349, 1981.

J. Huétink. Analysis of metal forming processes based on a combined Eulerian-Lagrangian finite element formulation. In J. F. T. Pittman, editor, *Proceedings International Conference of Numerical Methods in Industrial Forming Processes*, pages 501–509. Pineridge Press, Swansea, Großbritannien, 1982.

J. Huétink, P. T. Vreede, and J. van der Lugt. Progress in mixed Eulerian-Lagrangian finite element simulation of forming processes. *International Journal for Numerical Methods in Engineering*, 30:1441–1457, 1990.

K. Ishihara and I. Towhata. Sand response to cyclic rotation of principal stress directions as induced by wave loads. *Soils and Foundations*, 23(4):11–26, 1983.

K. Ishihara and F. Yamazaki. Cyclic simple shear tests on saturated sand in multi-directional loading. *Soils and Foundations*, 20(1):45–59, 1980.

K. Ishihara, F. Tatsuoka, and S. Yasuda. Undrained deformation and liquefaction of sand under cyclic stresses. *Soils and Foundations*, 15(1):29–44, 1975.

G. Jaumann. Geschlossenes System physikalischer und chemischer Differentialgesetze. *Sitzungsberichte der Mathematisch-Naturwissenschaftlichen Classe der Kaiserlichen Akademie der Wissenschaften 2a*, 120:385–530, 1911.

M. J. Jiang, H.-S. Yu, and D. Harris. Discrete element modelling of deep penetration in granular soils. *International Journal for Numerical and Analytical Methods in Geomechanics*, 30:335–361, 2006.

W. E. Johnson and Ch. E. Anderson, Jr. History and application of hydrocodes in hypervelocity impact. *International Journal of Impact Engineering*, 5:423–439, 1987.

M. S. Joun and M. C. Lee. Quadrilateral finite-element generation and mesh quality control for metal forming simulation. *International Journal for Numerical Methods in Engineering*, 40:4059–4075, 1997.

S. R. Kennon and G. S. Dulikravich. Generation of computational grids using optimization. *AIAA Journal*, 24(7):1069–1073, 1986.

N. Kikuchi and J. T. Oden. *Contact Problems in Elasticity: A Study of Variational Inequalities and Finite Element Methods*. Society for Industrial and Applied Mathematics (SIAM), Philadelphia, 1988.

P. D. Kiousis, G. Z. Voyiadjis, and M. T. Tumay. A large strain theory for the two dimensional problems in geomechanics. *International Journal for Numerical and Analytical Methods in Geomechanics*, 10:17–39, 1986.

P. D. Kiousis, G. Z. Voyiadjis, and M. T. Tumay. A large strain theory and its application in the analysis of the cone penetration mechanism. *International Journal for Numerical and Analytical Methods in Geomechanics*, 12:45–60, 1988.

E. U. Klotz and M. R. Coop. An investigation of the effect of soil state on the capacity of driven piles in sands. *Géotechnique*, 51(9):733–751, 2001.

F. König. *Zur zeitlichen Traglastentwicklung von Pfählen und der nachträglichen Erweiterung bestehender Pfahlgründungen.* Dissertation, Technische Universität Hamburg-Harburg, Germany, 2008. (published in Institute Series; in German).

P. M. Knupp. Winslow smoothing on two-dimensional unstructured meshes. *Engineering with Computers*, 15:263–268, 1999.

P. M. Knupp. Algebraic mesh quality metrics. *SIAM Journal on Scientific Computing*, 23(1):193–218, 2001.

P. M. Knupp. Algebraic mesh quality metrics for unstructured initial meshes. *Finite Elements in Analysis and Design*, 39:217–241, 2003.

P. M. Knupp, L. G. Margolin, and M. Shashkov. Reference Jacobian optimization-based rezone strategies for arbitrary Lagrangian Eulerian methods. *Journal of Computational Physics*, 176:93–128, 2002.

D. Kolymbas. *Ein nichtlineares viskoplastisches Stoffgesetz für Böden*, volume 77 of *Veröffentlichungen des Institutes für Bodenmechanik und Felsmechanik der Universität Fridericiana in Karlsruhe.* 1978. (Institute Series; in German).

D. Kolymbas. *Eine konstitutive Theorie für Böden und andere körnige Stoffe*, volume 109 of *Veröffentlichungen des Institutes für Bodenmechanik und Felsmechanik der Universität Fridericiana in Karlsruhe.* 1988. (Institute Series; in German).

D. Kolymbas. An outline of hypoplasticity. *Archive of Applied Mechanics*, 61(3):143–151, 1991a.

D. Kolymbas. Computer-aided design of constitutive laws. *International Journal for Numerical and Analytical Methods in Geomechanics*, 15:593–604, 1991b.

K. Kondo, editor. *RAAG Memoirs of the Unifying Study of Basic Problems in Engineering and Physical Sciences by Means of Geometry.* Gakujutsu Bunken Fukyu-Kai, Tokyo, 1955–1968. (4 vols.).

A. Krawietz. *Materialtheorie: Mathematische Beschreibung des phänomenologischen thermomechanischen Verhaltens.* Springer-Verlag Berlin Heidelberg, 1986. (in German).

J. Kérisel. Fondations profondes en millieux sableux. In *Proceedings 5th International Conference of Soil Mechanics and Foundation Engineering, Paris, France*, volume 2, pages 73–83, 1961.

J. Kérisel. Deep foundations basic experimental facts. In *Proceedings Deep Foundations Conference, Mexiko*, volume 1, pages 5–44, 1964.

J. Kérisel. Fondations profondes en millieux sableux. In *Proceedings 11th International Conference of Soil Mechanics and Foundation Engineering, San Francisco, USA*, volume Golden Jubilee Volume, pages 3–93, 1985.

P. Lancaster and K. Salkauskas. Surfaces generated by moving least squares methods. *Mathematics of Computations*, 37:141–158, 1981.

P. Lax and B. Wendroff. Systems of conservation laws. *Communications On Pure and Applied Mathematics*, 13:217–237, 1960.

E. Lesoinne and C. Farhat. Geometric conservation laws for flow problems with moving boundaries and deformable meshes, and their impact on aeroelastic computations. *Computer Methods in Applied Mechanics and Engineering*, 134:71–90, 1996.

C. F. Leung, F. H. Lee, and N. S. Yet. The role of particle breakage in pile creep in sand. *Canadian Geotechnical Journal*, 33(6):888–898, 1996.

C. F. Leung, F. H. Lee, and N. S. Yet. Centrifuge model study on pile subject to lapses during installation in sand. *International Journal of Physical Modelling in Geotechnics*, 1(1):47–57, 2001.

R. J. LeVeque. *Numerical Methods for Conservation Laws*. Birkhäuser Verlag, Basel, Switzerland, 2nd edition, 1992.

R. J. LeVeque. *Finite Volume Methods for Hyperbolic Problems*. Cambridge University Press, Cambridge, UK, 3rd edition, 2002.

R. W. Lewis and B. A. Schrefler. *The Finite Element Method in the Static and Dynamic Deformation and Consolidation of Porous Media*. John Wiley & Sons, Ltd., Chichester, 2nd edition, 1998.

R. Löhner, K. Morgan, and O. C. Zienkiewicz. Adaptive grid refinement for the compressible euler equations. In I. Babuška, O. C. Zienkiewicz, J. Gago, and E. R. A. Oliviera, editors, *Accuracy Estimates and Adaptive Refinements in Finite Element Computations*, pages 281–297. John Wiley & Sons, Ltd., 1986.

X. S. Li. Analysis of seismic response of granular soil deposits. In F. Rackwitz, editor, *Entwicklungen in der Bodenmechanik, Bodendynamik und Geotechnik*, pages 139–151. Springer-Verlag Berlin Heidelberg, 2006.

X. S. Li and Y. F. Dafalias. Dilatancy for cohesionless soils. *Géotechnique*, 50(4): 449–460, 2000.

X. S. Li and Y. F. Dafalias. A constitutive framework for anisotropic sand including non-proportional loading. *Géotechnique*, 54(1):41–55, 2004.

X. S. Li and Y. Wang. Linear representation of steady-state line for sand. *Journal of Geotechnical and Geoenvironmental Engineering*, 124(12):1215–1217, 1998.

X. S. Li, Y. F. Dafalias, and Z.-L. Wang. State-dependent dilatancy in critical-state constitutive modelling of sand. *Canadian Geotechnical Journal*, 36:599–611, 1999.

W.-R. Linder. *Zum Eindring- und Tragverhalten von Pfählen in Sand.* PhD thesis, Fachbereich für Bauingenieur- und Vermessungswesen, Technische Universität Berlin, Germany, 1977. (in German).

A. Liu and B. Joe. Relationship between tetrahedron shape measures. *BIT*, 34:268–287, 1994.

W. K. Liu, T. Belytschko, and H. Chang. An arbitrary Lagrangian-Eulerian finite element method for path-dependent materials. *Computer Methods in Applied Mechanics and Engineering*, 58:227–245, 1986.

W. K. Liu, H. Chang, J.-S. Chen, and T. Belytschko. Arbitrary Lagrangian-Eulerian petrov-galerkin finite elements for nonlinear continua. *Computer Methods in Applied Mechanics and Engineering*, 68:259–310, 1988.

D. S. Liyanapathirana. Arbitrary Lagrangian Eulerian based finite element analysis of cone penetration in soft clay. *Computers and Geotechnics*, 36:851–860, 2009.

D. S. Liyanapathirana, A. J. Deeks, and M. F. Randolph. Numerical modelling of large deformations associated with driving of open-ended piles. *International Journal for Numerical and Analytical Methods in Geomechanics*, 24:1079–1101, 2000.

A. S. Lodge. On the use of convected coordinate systems in the mechanics of continuous media. *Proceedings of the Cambridge Philosophical Society*, 47:575–584, 1951.

Q. Lu, M. F. Randolph, Y. Hu, and I. C. Bugarski. A numerical study of cone penetration in clay. *Géotechnique*, 54(4):257–267, 2004.

L. B. Lucy. A numerical approach to the testing of the fission hypothesis. *The Astronomical Journal*, 82:1013–1024, 1977.

D. G. Luenberger and Y. Ye. *Linear and Nonlinear Programming.* Springer Science+Business Media, LLC, 3rd edition, 2008.

M. E. Mabsout and J. L. Tassoulas. A finite element model for the simulation of pile driving. *International Journal for Numerical Methods in Engineering*, 37:257–278, 1994.

R. W. MacCormack and A. J. Paullay. Computational efficiency achieved by time splitting of finite difference operators. In *Proceedings AIAA 10th Aerospace Science Meeting, January 17-19, 1972, San Diego, California, USA*. American Institute of Aeronautics and Astronautics (AIAA), 1972. (published as AIAA Paper 72-154).

K.-P. Mahutka. *Zur Verdichtung von rolligen Böden infolge dynamischer Pfahleinbringung und durch Oberflächenrüttler.* Dissertation, Technische Universität Hamburg-Harburg, Germany, 2007. (published in Institute Series; in German).

K.-P. Mahutka and J. Grabe. Erschütterungs- und Sackungsprognose im Nahfeld von Rammarbeiten. In *Tagungsband Pfahl-Symposium 2005*, pages 97–112. Institute of

Geotechnics and Soil Mechanics, Technical University of Brunswick, Germany, 2005. (in German).

K.-P. Mahutka and S. Henke. Numerische Untersuchungen zur herstellungsbedingten Tragfähigkeit von Pfählen. In *Tagungsband Pfahl-Symposium 2009*, pages 471–491. Institute of Geotechnics and Soil Mechanics, Technical University of Brunswick, Germany, 2009. (in German).

H. U. Mair. Review: Hydrocodes for structural response to underwater explosions. *Shock and Vibration*, 6:81–96, 1999.

P.-H. Maire. A high-order cell-centered Lagrangian scheme for compressible fluid flows in two-dimensional cylindrical geometry. *Journal of Computational Physics*, 228(18): 6882–6915, 2009.

K. Maisch. *Bodenstabilisierung durch Einpressen von Trockengranulaten*, volume 149 of *Veröffentlichungen des Institutes für Bodenmechanik und Felsmechanik der Universität Fridericiana in Karlsruhe*. 2000. (Institute Series; in German).

L. E. Malvern. *Introduction to the Mechanics of a Continuous Medium*. Prentice Hall, Inc., New Jersey, 1969.

L. G. Margolin and M. Shashkov. MPDATA: Gauge transformations, limiters and monotonicity. *International Journal for Numerical Methods in Fluids*, 50(10):1193–1206, 2006.

J. E. Marsden and T. J. R. Hughes. *Mathematical Foundations of Elasticity*. Dover Publications, New York, 1994. (originally published: Prentice-Hall, 1983).

G. R. Martin, W. D. L. Finn, and H. B. Seed. Fundamentals of liquefaction under cyclic loading. *Journal of the Geotechnical Engineering Division, ASCE*, 101(5):423–438, 1975.

H. Matsuoka and T. Nakai. Stress-strain relationship of soil based on the 'SMP'. In *Constitutive Equations of Soils, Proceedings of Specialty Session 9, Ninth International Conference on Soil Mechanics and Foundation Engineering, Tokio, Japan*, 1977.

P.-M. Mayer. *Verformungen und Spannungsänderungen im Boden durch Schlitzwandherstellung und Baugrubenaushub*, volume 151 of *Veröffentlichungen des Institutes für Bodenmechanik und Felsmechanik der Universität Fridericiana in Karlsruhe*. 2000. (Institute Series; in German).

J. M. McGlaun, S. L. Thompson, and M. G. Elrick. CTH: A three-dimensional shock wave physics code. *International Journal of Impact Engineering*, 10:351–360, 1990.

R. M. McMeeking and J. R. Rice. Finite-element formulations for problems of large elastic-plastic deformation. *International Journal of Solids and Structures*, 11:601–616, 1975.

G. G. Meyerhof. The ultimate bearing capacity of foundations. *Géotechnique*, 2(4): 301–332, 1951.

G. G. Meyerhof. Penetration tests and bearing capacity of cohesionless soils. *Journal of the Soil Mechanics and Foundations Division, ASCE*, 82(SM1):1–19, 1956. (paper 886).

G. G. Meyerhof. Bearing capacity and settlement of pile foundations. *Journal of the Geotechnical Engineering Division, ASCE*, 102(GT3):197–228, 1976.

M. Mikasa and N. Takada. Significance of centrifugal model tests in soil mechanics. In *Proceedings 8th International Conference of Soil Mechanics and Foundation Engineering, Moskau*, pages 273–278, 1973.

C. W. Misner, K. S. Thorne, and J. A. Wheeler. *Gravitation*. W. H. Freeman and Company, San Francisco, 1973.

C. R. Molenkamp. Accuracy of finite-difference methods applied to the advection equation. *Journal of Applied Meteorology*, 7:160–167, 1968.

J. J. Monaghan. Particle methods for hydrodynamics. *Computater Physics Report*, 3: 71–124, 1985.

P. M. Naghdi and W. L. Wainwright. On the time derivatives of tensors in mechanics of continua. *Quarterly of Applied Mathematics*, 19(2):95–109, 1961.

J. C. Nagtegaal. On the implementation of inelastic constitutive equations with special reference to large deformation problems. *Computer Methods in Applied Mechanics and Engineering*, 33:469–484, 1982.

J. C. Nagtegaal and F. E. Veldpaus. On the implementation of finite strain plasticity equations in a numerical model. In J. F. T. Pittman, O. C. Zienkiewicz, R. D. Wood, and J. M. Alexander, editors, *Numerical Analysis of Forming Processes*. John Wiley & Sons, Ltd., 1984. chapter 12.

J. C. Nagtegaal, D. M. Parks, and J. R. Rice. On numerical accurate finite element solutions in the fully plastic range. *Computer Methods in Applied Mechanics and Engineering*, 4:153–177, 1974.

E. J. Nanson. Note on hydrodynamics. *The Messenger of Mathematics*, 7:182–185, 1878.

M. Nazem. *Numerical Algorithms for Large Deformation Problems in Geomechanics*. PhD thesis, University of Newcastle, Australia, 2006.

M. Nazem, D. Sheng, and J. P. Carter. Stress integration and mesh refinement for large deformation in geomechanics. *International Journal for Numerical Methods in Engineering*, 65:1002–1027, 2006.

M. Nazem, D. Sheng, J. P. Carter, and S. W. Sloan. Arbitrary Lagrangian-Eulerian method for large-strain consolidation problems. *International Journal for Numerical and Analytical Methods in Geomechanics*, 32(9):1023–1050, 2008.

K. Nübel and A. Niemunis. umat.f - Hypoplasticity Subroutine for Abaqus. Personal communication F. Rackwitz (2007), F. Rackwitz and P.-A. von Wolffersdorff (2006), 1999.

K. Nübel and V. Weitbrecht. Visualization of localization in grain skeletons with particle image velocimetry. *Journal of Testing and Evaluation*, 30(4):322–329, 2002.

A. Niemunis. *Extended Hypoplastic Models for Soils*, volume 34 of *Schriftenreihe des Instituts für Grundbau und Bodenmechanik der Ruhr-Universität Bochum*. 2003. (Institute Series).

A. Niemunis and I. Herle. Hypoplastic model for cohesionless soils with elastic strain range. *Mechanics of Cohesive-Frictional Materials*, 2:279–299, 1997.

J. Nocedal and S. J. Wright. *Numerical Optimization*. Springer Science+Business Media, LLC, 2nd edition, 2006.

W. F. Noh. *CEL: A Time-Dependent, Two-Space-Dimensional, Coupled Eulerian-Lagrange Code*, pages 117–179. Methods in Computational Physics. Advances in Research and Applications. Volume 3: Fundamental Methods in Hydrodynamics. Academic Press, New York and London, 1964.

W. Noll. A mathematical theory of the mechanical behavior of continuous media. *Archive for Rational Mechanics and Analysis*, 2:197–226, 1958.

W. Noll. Materially uniform simple bodies with inhomogeneities. *Archive for Rational Mechanics and Analysis*, 27(1):1–32, 1967.

W. Noll. A new mathematical theory of simple materials. *Archive for Rational Mechanics and Analysis*, 48(1):1–50, 1972.

W. Noll. Lectures on the foundations of continuum mechanics and thermodynamics. *Archive for Rational Mechanics and Analysis*, 52(1):62–92, 1973.

J. T. Oden. *Finite Elements of Nonlinear Continua*. McGraw-Hill, Inc., New York, 1972.

R. W. Ogden. *Non-Linear Elastic Deformations*. Dover Publications, New York, 1997. (first published by John Wiley & Sons, 1984).

J. O'Rourke. *Computational Geometry in C*. Cambridge University Press, New York, 2nd edition, 1998.

M. Ortiz and J. J. Quigley. Adaptive mesh refinement in strain localization problems. *Computer Methods in Applied Mechanics and Engineering*, 90:781–804, 1991.

M. Ortiz and J. C. Simo. An analysis of a new class of integration algorithms for elastoplastic constitutive relations. *International Journal for Numerical Methods in Engineering*, 23:353–366, 1986.

G. N. Pande and O. C. Zienkiewicz, editors. *Soil Mechanics - Transient and Cyclic Loads*. John Wiley & Sons, Ltd., 1982.

W. H. Peacock and H. B. Seed. Sand liquefaction under cyclic loading simple shear conditions. *Journal of the Soil Mechanics and Foundations Division*, 94(3):689–708, 1968.

J. S. Peery and D. E. Carroll. Multi-material ALE methods in unstructured grids. *Computer Methods in Applied Mechanics and Engineering*, 187:591–619, 2000.

C. J. D. Pickering and N. A. Halliwell. Speckle photography in fluid flows: signal recovery with two-step processing. *Applied Optics*, 23(8):1128–1129, 1984.

G. F. Pinder and W. G. Gray. *Essentials of Multiphase Flow and Transport in Porous Media*. John Wiley & Sons, Inc., 2008.

P. M. Pinsky, M. Ortiz, and K. S. Pister. Numerical integration of rate constitutive equations in finite deformation analysis. *Computer Methods in Applied Mechanics and Engineering*, 40:137–158, 1983.

A. Pogany. Phénomène d'écoulement dans le cas de fondations sur pieux. *Annales de l'Institut Technique du Bâtiment et des Travaux Publics*, 6(63-64):387–389, 1953.

W. E. Pracht. Calculating three-dimensional fluid flows at all speeds with an Eulerian-Lagrangian computing mesh. *Journal of Computational Physics*, 17(2):132–159, 1975.

W. Prager. An elementary discussion of definitions of stress rate. *Quarterly of Applied Mathematics*, 18(4):403–407, 1961.

L. Prandtl. Über die Härte plastischer Körper. *Nachrichten von der Königlichen Gesellschaft der Wissenschaften zu Göttingen, Mathematisch-Physikalische Klasse*, pages 74–85, 1920. (in German).

W. H. Press, S. A. Teukolsky, W. T. Vetterling, and B. P. Flannery. *Numerical Recipes: The Art of Scientific Computing*. Cambridge University Press, New York, 3rd edition, 2007.

F. Rackwitz. *Numerische Untersuchungen zum Tragverhalten von Zugpfählen und Zugpfahlgruppen in Sand auf der Grundlage von Probebelastungen*. Dissertation, Fakultät VI - Bauingenieurwesen und Angewandte Geowissenschaften, Technische Universität Berlin, Germany, 2003. (published in Institute Series; in German).

B. Ramaswamy. Numerical simulation of unsteady viscous free surface flow. *Journal of Computational Physics*, 90:396–430, 1990.

B. Ramaswamy and M. Kawahara. Arbitrary Lagrangian-Eulerian finite element method for unsteady, convective, incompressible viscous free surface fluid flow. *International Journal for Numerical Methods in Fluids*, 7:1053–1075, 1987.

M. F. Randolph and C. P. Wroth. Driven piles in clay - the effects of installation and subsequent consolidation. *International Journal for Numerical and Analytical Methods in Geomechanics*, 3:217–229, 1979.

M. F. Randolph, J. P. Carter, and C. P. Wroth. Driven piles in clay - the effects of installation and subsequent consolidation. *Géotechnique*, 29(4):361–396, 1979.

M. F. Randolph, J. Dolwin, and R. Beck. Design of driven piles in sand. *Géotechnique*, 44(3):427–448, 1994.

P. K. Raschewski. *Riemannsche Geometrie und Tensoranalysis*. Verlag Harri Deutsch, GmbH, 2nd edition, 1995. (in German).

M. M. Rashid. Incremental kinematics for finite element applications. *International Journal for Numerical Methods in Engineering*, 36:3937–3956, 1993.

O. Reuter. *Der Spreebogen 1994–2001*. Luftbildverlag, Berlin, 2001.

O. Reynolds. On the dilatancy of media composed of rigid particles in contact. With experimental illustrations. *Philosophical Magazine Series 5*, 20(127):469–481, 1885.

W. J. Rider. A very brief history of hydrodynamic codes (i.e. hydrocodes). Lecture 1/27: Introduction to Methods for Eulerian Hydrodynamics, Report LA-UR-05-7300, Sandia National Laboratories, USA, 2005. URL `https://cfwebprod.sandia.gov/cfdocs/CCIM/docs/Rider_CSRI_June27_2007.pdf`. (online; accessed 22-February-2013).

B. Riemann. Über die Hypothesen, welche der Geometrie zu Grunde liegen. *Abhandlungen der Königlichen Gesellschaft der Wissenschaften zu Göttingen*, 13, 1868. (Print of inaugural lecture held in 1854, in German).

B. Riemann. On the hypotheses which lie at the bases of geometry. *Nature*, 8(183-184): 14–17, 36, 37, 1873. (Reprint, translated by W.K. Clifford).

A. W. Rizzi and M. Inouye. Time-split finite-volume method for three-dimensional blunt-body flow. *AIAA Journal*, 11(11):1478–1485, 1973.

E. I. Robinsky and C. F. Morrison. Sand displacement and compaction around model friction piles. *Canadian Geotechnical Journal*, 1(2):81–93, 1964.

A. Rodríguez-Ferran, F. Casadei, and A. Huerta. ALE stress update for transient and quasistatic processes. *International Journal for Numerical Methods in Engineering*, 43:241–262, 1998.

A. Rodríguez-Ferran, A. Pérez-Foguet, and A. Huerta. Arbitrary Lagrangian-Eulerian (ALE) formulation for hyperelastoplasticity. *International Journal for Numerical Methods in Engineering*, 53:1831–1851, 2002.

G. Romano and R. Baretta. Continuum mechanics on manifolds. Lecture notes, Department of Structural Engineering, University of Naples Federico II, Italy, 2009. URL `http://wpage.unina.it/romano/`.

K. H. Roscoe and J. B. Burland. *On the generalised stress-strain behaviour of 'wet' clay*, pages 535–609. Engineering Plasticity. Cambridge University Press, 1968.

K. H. Roscoe and A. N. Schofield. Mechanical behaviour of an idealized 'wet-clay'. In *Proceedings European Conference of Soil Mechanics and Foundation Engineering, Wiesbaden, Germany*, volume 1, pages 47–54, 1963.

K. H. Roscoe, A. N. Schofield, and C. P. Wroth. On the yielding of soils. *Géotechnique*, 8(1):22–53, 1958.

P. W. Rowe. The stress-dilatancy relation for static equilibrium of an assembly of particles in contact. *Proceedings of the Royal Society of London. Series A*, 269: 500–527, 1962.

R. Rubinstein and S. N. Atluri. Objectivity of incremental constitutive relations over finite time steps in computational finite deformation analysis. *Computer Methods in Applied Mechanics and Engineering*, 36:277–290, 1983.

J. Sarrate, A. Huerta, and J. Donea. Arbitrary Lagrangian-Eulerian formulation for fluid-rigid body interaction. *Computer Methods in Applied Mechanics and Engineering*, 190:3171–3188, 2001.

S. A. Savidis and J. Mittag. Vibration measurements in deep excavation pits in Berlin. In *Proceedings Civil and Environmental Engineering Conference - New Frontiers and Challenges, Bangkok, Thailand*, pages II–49–II–54, 1999.

S. A. Savidis and R. Schuppe. Dynamisches Triaxialgerät zur Untersuchung des Verflüssigungsverhaltens von isotrop und anisotrop konsolidierten Sanden. *Bautechnik*, 59(1):21–24, 1982. (in German).

P. J. Schneider and D. H. Eberly. *Geometric Tools for Computer Graphics*. Morgan Kaufmann, 2003.

U. Schran. *Untersuchungen zu Verschiebungen von Schlitzwänden beim Unterwasseraushub in Berliner Sanden*. Dissertation, Fakultät VI - Bauingenieurwesen und Angewandte Geowissenschaften, Technische Universität Berlin, Germany, 2003. (published in Institute Series; in German).

G. Scovazzi. Galilean invariance and stabilized methods for compressible flows. *International Journal for Numerical Methods in Fluids*, 54:757–778, 2007.

G. Scovazzi and T. J. R. Hughes. Lecture notes on continuum mechanics on arbitrary moving domains. Report 2007-6312P, Sandia National Laboratories, USA, 2007. (Lecture Notes).

H. B. Seed. Soil liquefaction and cyclic mobility evaluation for level ground during earthquakes. *Journal of the Geotechnical Engineering Division, ASCE*, 105(2):201–255, 1979.

H. B. Seed and K. L. Lee. Liquefaction of saturated sands during cyclic loading. *Journal of the Soil Mechanics and Foundations Division*, 92(6):105–134, 1966.

H. B. Seed and W. H. Peacock. Test procedures for measuring soil liquefaction characteristics. *Journal of the Soil Mechanics and Foundations Division*, 97(8):1099–1119, 1971.

R. Segev. Forces and the existence of stresses in invariant continuum mechanics. *Journal of Mathematical Physics*, 27(1):163–170, 1986.

R. Segev. The geometry of Cauchy's fluxes. *Archive for Rational Mechanics and Analysis*, 154(3):183–198, 2000.

R. Segev. Notes on metric independent analysis of classical fields. *Mathematical Methods in the Applied Sciences*, 36(5):497–566, 2013.

D. Sheng, K. D. Eigenbrod, and P. Wriggers. Finite element analysis of pile installation using large-slip frictional contact. *Computers and Geotechnics*, 32:17–26, 2005.

D. Sheng, P. Wriggers, and S. W. Sloan. Improved numerical algorithms for frictional contact in pile penetration analysis. *Computers and Geotechnics*, 33:341–354, 2006.

D. Sheng, M. Nazem, and J. P. Carter. Some computational aspects for solving deep penetration problems in geomechanics. *Computational Mechanics*, 44:549–561, 2009.

J. C. Simo. The (symmetric) Hessian for geometrically nonlinear models in solid mechanics: Intrinsic definition and geometric interpretation. *Computer Methods in Applied Mechanics and Engineering*, 96:189–200, 1992.

J. C. Simo and T. J. R. Hughes. *Computational Inelasticity*. Springer-Verlag Berlin, 1998.

J. C. Simo and J. E. Marsden. On the rotated stress tensor and the material version of the Doyle-Ericksen formula. *Archive for Rational Mechanics and Analysis*, 86(3): 213–231, 1984.

J. C. Simo and G. Meschke. A new class of algorithms for classical plasticity extended to finite strains. Application to geomaterials. *Computational Mechanics*, 11:253–278, 1993.

J. C. Simo and K. S. Pister. Remarks on rate constitutive equations for finite deformation problems: Computational implications. *Computer Methods in Applied Mechanics and Engineering*, 46:201–215, 1984.

J. C. Simo and R. L. Taylor. Consistent tangent operators for rate-independent elastoplasticity. *Computer Methods in Applied Mechanics and Engineering*, 48:101–118, 1985.

J. C. Simo, J. E. Marsden, and P. S. Krishnaprasad. The Hamiltonian structure of nonlinear elasticity: The convective representation of solids, rods, and plates. *Archive for Rational Mechanics and Analysis*, 104(2):125–183, 1988.

J. C. Slattery. *Momentum, Energy, and Mass Transfer in Continua*. McGraw-Hill, Inc., New York, 1972.

S. W. Sloan. Substepping schemes for the numerical integration of elastoplastic stress-strain relations. *International Journal for Numerical Methods in Engineering*, 24: 839–911, 1987.

S. W. Sloan, A. J. Abbo, and D. Sheng. Refined explicit integration of elastoplastic models with automatic error control. *Engineering Computations*, 18(1/2):121–154, 2001.

M. Spivak. *Calculus on Manifolds*. Benjamin, New York, 1965.

M. Spivak. *A Comprehensive Introduction to Differential Geometry*, volume 1. Publish or Perish, Inc., Houston, Texas, 3rd edition, 1999.

G. Strang. Accurate partial difference methods i: Linear Cauchy problems. *Archive for Rational Mechanics and Analysis*, 12(1):392–402, 1963.

G. Strang. Accurate partial difference methods ii. non-linear problems. *Numerische Mathematik*, 6:37–46, 1964.

G. Strang. On the construction and comparison of difference schemes. *SIAM Journal on Numerical Analysis*, 5(3):506–517, 1968.

H. Stumpf and U. Hoppe. The application of tensor algebra on manifolds to nonlinear continuum mechanics - invited survey article. *Zeitschrift für Angewandte Mathematik und Mechanik (ZAMM)*, 77(5):327–339, 1997.

D. Sulsky and H. L. Schreyer. Axisymmetric form of the material point method with applications to upsetting and Taylor impact problems. *Computer Methods in Applied Mechanics and Engineering*, 139:409–429, 1996.

W. Sun and Y.-X. Yuan. *Optimization Theory and Methods - Nonlinear Programming*. Springer Science+Business Media, LLC, 2006.

E. Susila and R. D. Hryciw. Large displacement FEM modelling of the cone penetration test (CPT) in normally consolidated sand. *International Journal for Numerical and Analytical Methods in Geomechanics*, 27:585–602, 2003.

J. L. Synge and A. Schild. *Tensor Calculus*. Dover Publications, New York, 1978. (originally published: University of Toronto Press, 1949).

C. I. Teh and G. T. Houlsby. An analytical study of the cone penetration test in clay. *Géotechnique*, 41(1):17–34, 1991.

K. Terzaghi. *Theoretical Soil Mechanics*. John Wiley & Sons, Inc., New York, 1943.

G. B. Thomas and R. L. Finney. *Calculus and Analytic Geometry*. Addison-Wesley, Reading, Massachusetts, 9th edition, 1996.

P. D. Thomas and C. K. Lombard. Geometric conservation law and its application to flow computations on moving grids. *AIAA Journal*, 17(10):1030–1037, 1979.

J. F. Thompson, B. K. Soni, and N. P. Weatherill, editors. *Handbook of Grid Generation*. CRC Press, Boca Raton, Florida, USA, 1999.

P. A. Thompson. *Compressible-Fluid Dynamics*. McGraw-Hill, Inc., New York, 1972.

E. F. Toro. *Riemann Solvers and Numerical Methods for Fluid Dynamics – A Practical Introduction*. Springer-Verlag Berlin Heidelberg, 2nd edition, 1999.

I. Towhata and K. Ishihara. Undrained strength of sand undergoing cyclic rotation of principal stress axes. *Soils and Foundations*, 25(2):135–147, 1985.

T. Triantafyllidis. Neue Erkenntnisse aus Messungen an tiefen Baugruben am Potsdamer Platz in Berlin. *Bautechnik*, 75(3):133–154, 1998. (in German).

T. Triantafyllidis, editor. *Cyclic Behaviour of Soils and Liquefaction Phenomena*, 2004. A.A. Balkema Publishers, The Netherlands.

C. Truesdell. The simplest rate theory of pure eleasticity. *Communications on Pure and Applied Mathematics*, 8:123–132, 1955a.

C. Truesdell. Hypo-elasticity. *Journal of Rational Mechanics and Analysis*, 4(1):83–133, 1955b.

C. Truesdell and W. Noll. *The Non-Linear Field Theories of Mechanics*. Springer-Verlag Berlin Heidelberg New York, 3rd edition, 2004.

C. Truesdell and R. A. Toupin. *The Classical Field Theories*, volume III/1 of *Encyclopedia of Physics*, pages 226–793. Springer-Verlag Berlin Göttingen Heidelberg, 1960.

J. G. Trulio. Theory and structure of the AFTON codes. Report AFWL-TR-66-19, Air Force Weapons Laboratory, Kirtland Air Force Base, New Mexico, USA, 1966.

J. G. Trulio and K. R. Trigger. Numerical solution of the one-dimensional hydrodynamic equations in an arbitrary time-dependent coordinate system. Report UCRL-6522, Lawrence Radiation Laboratory, University of California, Livermore, USA, 1961.

M. J. Turner, R. W. Clough, H. C. Martin, and L. P. Topp. Stiffness and deflection analysis of complex structures. *Journal of the Aeronautical Sciences*, 23(9):805–823, 1956.

V. M. Ulitskii. History of pile foundation engineering. *Soil Mechanics and Foundation Engineering*, 32(3):110–114, 1995.

Y. P. Vaid and J. Thomas. Liquefaction and postliquefaction behavior of sand. *Journal of Geotechnical Engineering*, 121(2):163–173, 1995.

P. van den Berg. *Analysis of Soil Penetration*. PhD thesis, Faculty of Civil Engineering, Delft University of Technology, The Netherlands, 1994.

P. van den Berg and P. A. Vermeer. Undrained strength from CPT and finite element calculations. In G. Swoboda, editor, *Proceedings Sixth International Conference on Numerical Methods in Geomechanics, Innsbruck, Austria*, pages 1095–1100. A. A. Balkema, 1988.

P. van den Berg, R. de Borst, and H. Huétink. An Eulerian finite element model for penetration in layered soil. *International Journal for Numerical and Analytical Methods in Geomechanics*, 20:865–886, 1996.

M. J. van Haaren, H. C. Stoker, A. H. van den Boogaard, and J. Huétink. The ALE-method with triangular elements: Direct convection of integration point values. *International Journal for Numerical Methods in Engineering*, 49:697–720, 2000.

B. van Leer. Towards the ultimate conservative difference scheme. iv. A new approach to numerical convection. *Journal of Computational Physics*, 23:276–299, 1977.

R. Verdugo and K. Ishihara. The steady state of sandy soils. *Soils and Foundations*, 36(2):81–91, 1996.

P. A. Vermeer, L. Beuth, and T. Benz. A quasi-static method for large deformation problems in geomechanics. In *Proceedings 12th International Conference of the International Association for Computer Methods and Advances in Geomechanics (12IACMAG), October 1-6, 2008, Goa, India*, pages 55–63, 2008.

A. S. Vesic. Bearing capacity of deep foundations in sand. *Highway Research Record*, 39:112–153, 1963.

A. S. Vesic. Expansion of cavities in an infinite soil mass. *Journal of the Soil Mechanics and Foundations Division, ASCE*, 98(SM3):265–290, 1972.

A. S. Vesic. Analysis of ultimate loads of shallow foundations. *Journal of the Soil Mechanics and Foundations Division, ASCE*, 99(SM1):45–73, 1973.

M. Vierhaus. Modellversuche zur Pfahleindringung in Sand unter Anwendung der PIV-Methode. Diploma thesis, Chair of Soil Mechanics and Geotechnical Engineering, Technische Universität Berlin (TU Berlin), Germany, 2007. (unpublished; in German).

M. Vinokur. An analysis of finite-difference and finite-volume formulations of conservation laws. *Journal of Computational Physics*, 81:1–52, 1989.

E. Vitali and D. J. Benson. Contact with friction in multi-material arbitrary Lagrangian-Eulerian formulations using x-fem. *International Journal for Numerical Methods in Engineering*, 76:893–921, 2008.

E. Vitali and D. J. Benson. Kinetic friction for multi-material arbitrary Lagrangian Eulerian extended finite element formulations. *Computational Mechanics*, 43:847–857, 2009.

P.-A. von Wolffersdorff. A hypoplastic relation for granular materials with a predefined limit state surface. *Mechanics of Cohesive-Frictional Materials*, 1:251–271, 1996.

P.-A. von Wolffersdorff and R. Schwab. The Uelzen I lock - hypoplastic finite-element analysis of cyclic loading. *Bautechnik, Special issue 2009 - Geotechnical Engineering*, 86(S1):64–73, 2009.

C. C. Wang and C. Truesdell. *Introduction to Rational Elasticity*. Noordhoff International Publishing, Leyden, 1973.

Z.-L. Wang, Y. F. Dafalias, and C.-K. Shen. Bounding surface hypoplasticity model for sand. *Journal of Engineering Mechanics*, 116(5):983–1001, 1990.

D. J. White. *An Investigation Into the Behaviour of Pressed-In Piles*. PhD thesis, University of Cambridge, UK, 2002.

D. J. White. GeoPIV - Particle Image Velocimetry (PIV) software for use in geotechnical testing. Personal communication D. Aubram (February 2009), 2009.

D. J. White and W. A. Take. GeoPIV: Particle image velocimetry (PIV) software for use in geotechnical testing. Report CUED/D-SOILS/TR322, Geotechnical and Environmental Research Group, University of Cambridge, UK, 2002.

D. J. White, H. K. Sidhu, T. C. R. Finlay, M. D. Bolton, and T. Nagayama. Press-in piling: the influence of plugging on driveability. In *Proceedings 8th International Conference of the Deep Foundations Institute, New York*, pages 299–310, 2000.

D. J. White, W. A. Take, and M. D. Bolton. Soil deformation measurement using particle image velocimetry (PIV) and photogrammetry. *Géotechnique*, 53(7):619–631, 2003.

Z. Więckowski, S.-K. Youn, and J.-H. Yeon. A particle-in-cell solution to the silo discharging problem. *International Journal for Numerical Methods in Engineering*, 45:1203–1225, 1999.

M. L. Wilkins. *Computer Simulation of Dynamic Phenomena*. Scientific Computation. Springer-Verlag Berlin Heidelberg New York, 1999.

D. M. Wood. *Soil Behaviour and Critical State Soil Mechanics*. Cambridge University Press, USA, 1990.

P. Wriggers. *Computational Contact Mechanics*. Springer-Verlag Berlin Heidelberg, 2nd edition, 2006.

P. Wriggers. *Nonlinear Finite Element Methods*. Springer-Verlag Berlin Heidelberg, 2008.

W. Wu and E. Bauer. A simple hypoplastic constitutive model for sand. *International Journal for Numerical and Analytical Methods in Geomechanics*, 18:833–862, 1994.

XANSYS Mailing List. XANSYS Message 67168, February 2004. URL `http://x.ansys.net/posting/67168`. Message posted by Guoyu Lin on Feb 24, 2004 12:35 pm.

H. Xiao, O. T. Bruhns, and A. Meyers. The choice of objective rates in finite elastoplasticity: General results on the uniqueness of the logarithmic rate. *Proceedings of the Royal Society of London. Series A*, 456:1865–1882, 2000.

S. Yaghmai. Incremental analysis of large deformations in mechanics of solids with applications to axisymmetric shells of revolutions. Report CR-1350, National Aeronautics and Space Administration (NASA), Washington, D.C., 1969. (PhD thesis at University of California, Berkeley).

Y. Yamada and K. Ishihara. Anisotropic deformation characteristics of sand under three-dimensional stress conditions. *Soils and Foundations*, 19(2):79–94, 1979.

Y. Yamada and K. Ishihara. Undrained deformation characteristics of loose sand under three-dimensional stress conditions. *Soils and Foundations*, 21(1):61–79, 1981.

Y. Yamada and K. Ishihara. Undrained deformation characteristics of sand in multidirectional shear. *Soils and Foundations*, 23(1):61–79, 1983.

N. Yasufuku, H. Ochiai, and S. Ohno. Pile end-bearing capacity of sand related to soil compressibility. *Soils & Foundations*, 41(4):59–71, 2001.

A. Yavari and A. Ozakin. Covariance in linearized elasticity. *Zeitschrift für Angewandte Mathematik und Physik (ZAMP)*, 59(6):1081–1110, 2008.

M. Yoshimine, K. Ishihara, and W. Vargas. Effects of principal stress direction and intermediate principal stress on undrained shear behaviour of sand. *Soils and Foundations*, 38(3):179–188, 1998.

H. S. Yu and G. T. Houlsby. Finite cavity expansion in dilatant soils: loading analysis. *Géotechnique*, 41(2):173–183, 1996.

S. T. Zalesak. Fully multidimensional flux-corrected transport algorithms for fluids. *Journal of Computational Physics*, 31(3):335–362, 1979.

S. Zaremba. Sur une forme perfectionée de la théorie de la relaxation. *Bulletin international de l'Académie des Sciences de Cracovie, Classe des Sciences Mathematiques et Naturelles*, 124:594–614, 1903.

P. D. Zavattieri, E. A. Dari, and G. C. Buscaglia. Optimization strategies in unstructured mesh generation. *International Journal for Numerical Methods in Engineering*, 39:2055–2071, 1996.

H. Zhang, M. Reggio, J. Y. Trépanier, and R. Camarero. Discrete form of the GCL for moving meshes and its implementation in cfd schemes. *Computers & Fluids*, 22 (1):9–23, 1993.

H. Zhou and M. F. Randolph. Computational techniques and shear band development for cylindrical and spherical penetrometers in strain-softening clay. *International Journal of Geomechanics, ASCE*, 7(4):287–295, 2007.

O. C. Zienkiewicz and Y. K. Cheung. Buttress dams on complex rock foundations. *Water Power*, 16:193–198, 1964.

O. C. Zienkiewicz and Y. K. Cheung. Stresses in buttress dams. *Water Power*, 17: 69–75, 1965.

O. C. Zienkiewicz and R. L. Taylor. *The Finite Element Method*, volume 1: The Basis. Butterworth-Heinemann, 5th edition, 2000a.

O. C. Zienkiewicz and R. L. Taylor. *The Finite Element Method*, volume 2: Solid Mechanics. Butterworth-Heinemann, 5th edition, 2000b.

O. C. Zienkiewicz and R. L. Taylor. *The Finite Element Method*, volume 3: Fluid Dynamics. Butterworth-Heinemann, 5th edition, 2000c.

Veröffentlichungen des Grundbauinstitutes der Technischen Universität Berlin

Erschienene Hefte:

Herausgegeben von H. Müller-Kirchenbauer

[1] Aufbau und Arbeitsgebiete des Instituts 1977, 166 S. (vergriffen)
Universitätsverlag der TU Berlin
ISBN 3 7983 578 1

[2] Allgemeine experimentelle Ergebnisse und Betrachtungen des Spannungs-Deformationsverhaltens von Sand 3,00 €
Savidis, S. A.
Über die theoretische Erfassung nichtlinearen Spannungs-Verformungsverhaltens von Boden
Richter, T., 1978, 100 S.
Universitätsverlag der TU Berlin
ISBN 3 7983 0622 2

[3] Experimentelle und Theoretische Untersuchungen zum Tragverhalten der Spundwand mit Sporn 4,50 €
Prager, J., 1978, 165 S.
Universitätsverlag der TU Berlin
ISBN 3 7983 0621 4

[4] Der Nachweis der äußeren Standsicherheit suspensionsgestützter Erdwände nach der Elementscheibentheorie 3,50 €
Walz, B.; Prager, J., 1978, 124 S.
Universitätsverlag der TU Berlin
ISBN 3 7983 0627 3

[5] Berechnungsverfahren zum aktiven räumlichen Erddruck 4,50 €
1979, 124 S.
Universitätsverlag der TU Berlin
ISBN 3 7983 0665 6
enthält:
Vergleichende Untersuchungen der Berechnungsverfahren zum Nachweis der Sicherheit gegen Gleitflächenbildung bei suspensionsgestützten Erdwänden
Müller-Kirchenbauer, H.; Walz, B.; Kilchert, M.

Berechnungen zum dreidimensionalen aktiven Erddruckproblem
bei rolligen Böden
Karstedt, J.
Grundlagen und Anwendung der Erdscheibentheorie
Walz, B.

[6] Pressenkräfte und Bodenverformungen beim Rohrvortrieb 4,00 €
Salomo, K.-P., 1980, 162 S.
Universitätsverlag der TU Berlin
ISBN 3 7983 0666 4

[7] Experimentelle und theoretische Untersuchungen zum 4,00 €
Erddruckproblem auf radialsymetrische Senkkästen und Schächte
Müller-Kirchenbauer, H.; Walz, B.; Klapperich, H. 1980, ca. 200 S.
Universitätsverlag der TU Berlin
ISBN 3 7983 0705 9

[8] Klassische Verfahren zur Berechnung des seismischen Erddruckes 2,50 €
Savidis, S.A.; Klapperich, H.; Abdel-Karim, M.
Berechnung der zeitabhängigen Verformung einer mehrfach
verankerten chemisch verfestigten Baugrubenwand
Borchert, K.-M.; Müller-Kirchenbauer, H.;
Hebener, H.; Richter, T., 1980, 73 S.
Universitätsverlag der TU Berlin
ISBN 3 7983 0706 7

[9] Untersuchung zur Eignung von Silikatgelen für Abdichtungsinjektionen 4,00 €
Tausch, N., 1980, 191 S.
Universitätsverlag der TU Berlin
ISBN 3 7983 0733 4

[10] Untersuchungen zum aktiven räumlichen Erddruck im rolligen Boden 8,00 €
bei hydrostatischer Stützung der Erdwand
Karstedt, J., 1982, 160 S.
Universitätsverlag der TU Berlin
ISBN 3 7983 0807 1

Herausgegeben von H. Müller-Kirchenbauer und S.A. Savidis

[11] Grundwasserbeeinflussung durch Silikatgelinjektionen 12,00 €
zweite unveränderte Auflage 1984
Müller-Kirchenbauer, H. u.a., 1984, 378 S.
Universitätsverlag der TU Berlin
ISBN 3 7983 0817 9

[12] Untersuchungen zum Tragverhalten von Verpreßankern in Sand — 8,00 €
Mayer, G., 1983, 171 S.
Universitätsverlag der TU Berlin
ISBN 3 7983 0841 1

Herausgegeben von S.A. Savidis

[13] Beiträge aus Forschungsschwerpunkten des Grundbauinstituts — 10,50 €
Savidis, S.A. u.a., 1983, 200 S.
Universitätsverlag der TU Berlin
ISBN 3 7983 0930 2

[14] Untersuchungen zum dynamischen Erddruck — 10,00 €
Klapperich, H., 1983, 192 S.
Universitätsverlag der TU Berlin
ISBN 3 7983 3940 X

[15] Vergleich zwischen berechneten und gemessenen Kriechverformungen an mit Silikatgel verfestigtem Sand — 11,50 €
Borchert, K.-M., 1985, 200 S.
Universitätsverlag der TU Berlin
ISBN 3 7983 1042 4

[16] Zur Mechanik der Entwicklung von Erosionskanälen in geschichtetem Untergrund unter Stauanlagen — 10,50 €
Hanses, U., 1985, 200 S.
Universitätsverlag der TU Berlin
ISBN 3 7983 1042 4

[17] Ein allgemeines Berechnungsverfahren für Grenzlastzustände im Grundbau, dargestellt am Beispiel des Grund- und Böschungsbruchs — 10,50 €
Sturm, U., 1987, 189 S.
Universitätsverlag der TU Berlin
ISBN 3 7983 1174 9

[18] Beiträge zur Modellversuchstechnik in der Geotechnik — 10,50 €
1988, 188 S.
Universitätsverlag der TU Berlin
ISBN 3 7983 1269 9

[19] Beiträge zur Umwelttechnik — 10,50 €
1989, 104 S.
Universitätsverlag der TU Berlin
ISBN 3 7983 1320 2

[20] Beiträge zur Probabilistik in der Geotechnik — 10,50 €
1989, 104 S.
Universitätsverlag der TU Berlin
ISBN 3 7983 1409 8

[21] Zur analytischen Lösung der dreidimensionalen Wellenausbreitung in elastischen Halbraum mit Anwendung auf Interaktionsprobleme Baugrund - Bauwerk — 10,50 €
Mitakidis, A., 1991, 257 S.
Universitätsverlag der TU Berlin
ISBN 3 7983 1417 9

[22] Numerische Verfahren zur dynamischen Boden - Bauwerk Interaktion — 2,60 €
Sarfeld, W., 1994, 147 S.
Universitätsverlag der TU Berlin
ISBN 3 7983 1624 4

[23] Vorhersage gebirgsrelevanter Parameter im Tunnelbau mittels stochastischer Prozesse — 2,60 €
Kleen, H., 1994, 243 S.
Universitätsverlag der TU Berlin
ISBN 3 7983 1626 0

[24] Selbstheilungsvermögen toniger Erdstoffe in Dichtungssystemen von Deponien bei Schädigung durch mechanische Risse und Austrocknung — 2,60 €
Mallwitz, K., 1996, 266 S.
Universitätsverlag der TU Berlin
ISBN 3 7983 1693 7

[25] Einflußfunktionen für inhomogene Böden und ihre Anwendung bei der Boden-Bauwerk Interaktion — 9,20 €
Vrettos, C., 1997, 138 S.
Universitätsverlag der TU Berlin
ISBN 3 7983 1750 X

[26] Experimentelle Untersuchung des dynamischen Verhaltens starrer Fundamente mit Impulserregungen in situ und an kleinmaßstäblichen Modellen — 15,30 €
Fritsche, M., 2000, 234 S.
Universitätsverlag der TU Berlin
ISBN 3 7983 1854 9

[27] Untersuchungen zum Filtrationsverhalten von Feinstbindemittel-suspensionen bei der Injektion in Sande — 17,90 €
Mittag, J., 2000, 208 S.
Universitätsverlag der TU Berlin
ISBN 3 7983 1855 7

[28] Numerische Verfahren zur Berechnung von Baugrund-Bauwerk-Interaktionen im Zeitbereich mittels GREENscher Funktionen für den Halbraum — 16,00 €
Bode, C., 2000, 168 S.
Universitätsverlag der TU Berlin
ISBN 3 7983 1856 5

[29] Oberflächenabdichtungen für Deponien - Technische Entwicklungen, Wirtschaftlichkeit, Genehmigungsfähigkeit — 30,70 €
Gemeinschaftstagung TUB, BAM, LUAB
2001, 116 S.
Universitätsverlag der TU Berlin
ISBN 3 7983 1857 3

[30] Verformbarkeit von Dichtungsasphalt — 15,30 €
Franke, J., 2001, 147 S.
Universitätsverlag der TU Berlin
ISBN 3 7983 1862 X

[31] Kopplung von Finiten Elementen mit Rand-Elementen zur Berechnung der dynamischen Baugrund-Bauwerk-Interaktion — 18,00 €
Hirschauer, R., 2001, 150 S.
Universitätsverlag der TU Berlin
ISBN 3-7983-1883-2

[32] Numerische Untersuchungen zum Tragverhalten von Zugpfählen und Zugpfahlgruppen in Sand auf der Grundlage von Probebelastungen — 18,00 €
Rackwitz, F., 2003, 206 S.
Universitätsverlag der TU Berlin
ISBN 3-7983-1907-3

[33] Untersuchungen zu Verschiebungen von Schlitzwänden beim Unterwasseraushub in Berliner Sanden — 19,00 €
Schran, U., 2003, 248 S.
Universitätsverlag der TU Berlin
ISBN 3-7983-1919-7

[34] Untersuchungen zum Trag- und Schädigungsverhalten fester Schienenfahrbahnen in Betonbauweise — 19,00 €
Bergmann, S., 2005, 230 S.
Universitätsverlag der TU Berlin
ISBN 3-7983-1923-5

[35] Untersuchungen zum Einfluß der Geologie im Großraum Köln auf die Form elastischer Beschleunigungsantwortspektren — 25,00 €
Röhner, J., 2005, 60 S. + Anlagen
Universitätsverlag der TU Berlin
ISBN 3-7983-1925-1

[36] Qualitätsverbesserung von Schlitzwand- und Düsenstrahlarbeiten unter besonderer Berücksichtigung der Baugrundverhältnisse im Zentralen Bereich Berlins — 16,50 €
Windelschmidt, B., 2003, 290 S.
Universitätsverlag der TU Berlin
ISBN 3-7983-1928-6

[37] Untersuchung des Setzungsverhaltens von Bahnschotter und der Hohllagenentwicklung auf Schotterfahrbahnen — 18,00 €
Holtzendorff, K., 2004, 142 S.
Universitätsverlag der TU Berlin
ISBN 3-7983-1936-7

[38] Vorträge zum 1. Hans Lorenz Symposium, Berlin 2005 — 45,00 €
Universitätsverlag der TU Berlin
ISBN 3-7983-1993-6

[39] Vorträge zum Spundwandseminar 2006, Berlin 2006 — 45,00 €
Universitätsverlag der TU Berlin
ISBN 3-7983-2012-8

[40] Vorträge zum 2. Hans Lorenz Symposium, Berlin 2006 — 45,00 €
Universitätsverlag der TU Berlin
ISBN 3-7983-2024-1

[41] Vorträge zum 3. Hans Lorenz Symposium, Berlin 2007 — 45,00 €
Universitätsverlag der TU Berlin
ISBN 3-7983-2063-5

[42] Vorträge zum 4. Hans Lorenz Symposium, Berlin 2008 — 49,80 €
SHAKER Verlag
ISBN 978-3-8322-7597-6

[43] Vorträge zum Spundwandseminar 2009, Berlin 2009 — 48,80 €
SHAKER Verlag
ISBN 978-3-8322-8035-2

[44] Differential Geometry Applied to Continuum Mechanics — 45,80 €
Aubram, D., 2009, 124 S.
SHAKER Verlag
ISBN 978-3-8322-8154-0

[45] Lageveränderungen des Schottergleises durch zyklische und dynamische Beanspruchungen
Baessler, M.
SHAKER Verlag
in Vorbereitung

[46] Einflussgrößen für das Schwingungsverfahren von Gebäuden zur Prognose von Erschütterungsimmissionen — 48,80 €
Meinhardt, C., 2011, 161 S.
SHAKER Verlag
ISBN 978-3-8440-0334-5

[47] Vorträge zum 5. Hans Lorenz Symposium, Berlin 2009 — 49,80 €
SHAKER Verlag
ISBN 978-3-8322-8336-0

[48] Modeling and Numerical Analysis of Wave Propagation in Saturated and Partially Saturated Porous Media — 49,80 €
Albers, B., 2010, 342 S.
SHAKER Verlag
ISBN 978-3-8322-9008-5

[49] Der Einfluss der Gestängelänge auf die Ergebnisse von Rammsondierungen — 48,80 €
Röhner, R., 2010, 166 S.
SHAKER Verlag
ISBN 978-3-8322-9373-4

[50] Vorträge zum 6. Hans Lorenz Symposium, Berlin 2010 — 49,80 €
SHAKER Verlag
ISBN 978-3-8322-9457-1

[51] State-of-the-Art. Fault Rupture Propagation to the Ground Surface and Soil-Structure Interaction — 45,80 €
El Soud, S. A., 2011, 107 S.
SHAKER Verlag
ISBN 978-3-8440-0312-3

[52] Zur Dimensionierung der Monopile-Gründungen von Offshore Windenergieanlagen
Tasan, E.
in Vorbereitung

[53] Preloading Effects on Dynamic Sand Behavior by Resonant Column Tests 49,80 €
Bai, L., 2011, 224 S
SHAKER Verlag
ISBN 978-3-8440-0120-4

[54] Piled foundations for offshore wind turbines: Numerical and experimental investigations for a design model
Cuellar, P.
in Vorbereitung

[55] Einfluss der Steifigkeit von Baugrund und Gründung auf die Abschirmung von Schienenverkehrserschütterungen mit Elastomermatten
Appel, S.
in Vorbereitung

[56] Vorträge zum Workshop OWEA Gründungen, Berlin 2011 49,80 €
SHAKER Verlag
ISBN 978-3-8440-1090-9

[57] Durch Tunnelblick zu erweiterter Perspektive 39,80 €
Balthaus, H., 2011, 64 S.
SHAKER Verlag
ISBN 978-3-8440-0239-3

[58] Vorträge zum 7. Hans Lorenz Symposium, Berlin 2011 49,80 €
SHAKER Verlag
ISBN 978-3-8440-0407-6

[59] Untersuchungen zum Trag-und Verformungsverhalten von Untergrund-verbesserungen mit Sandsäulen in Böden mit organischen Anteilen 49,80 €
Schüssler, M., 2012, 374 S.
SHAKER Verlag
ISBN 978-3-8440-0943-9

[60] Vorträge zum 8. Hans Lorenz Symposium, Berlin 2012 49,80€
Gründungen von Offshore-Bauwerken
SHAKER Verlag
ISBN 978-3-8440-1377-1

[61] Numerical Investigation of Dynamic Railway Vehicle-Track-Subgrade Interaction — 45,80€
Shan, Y., 2013, 130 S.
SHAKER Verlag
ISBN 978-3-8440-2294-0

[62] An Arbitrary Lagrangian-Eulerian Method for Penetration into Sand at Finite Deformation
Aubram, D.
SHAKER Verlag
in Vorbereitung

[63] Vorträge zum 9. Hans Lorenz Symposium, Berlin 2013 — 49,80€
SHAKER Verlag
ISBN 978-3-8440-2201-8

Weitere Veröffentlichungen des Grundbauinstituts

Empfehlungen des Arbeitskreises "Baugrunddynamik" — (vergriffen)
Herausgegeben von der DGGT, 2003, 67 S.
ISBN 3-7983-1909-X

Grundbauseminar — 25,00 €
Vorstellung der neuen EAB mit dem Teilsicherheitskonzept, 2007, 236 S

DIN 1054 Seminar — 25,00 €
Neues Sicherheitskonzept in der Geotechnik, 2009, 156 S.